Erasmus Mundus Joint Doctorate

International Relativistic Astrophysics Program Ph.D.

Multi-Frequency Studies of Very High Energy Peaked Blazars

PhD student:

Yu-Ling Chang

Supervisor:

Paolo Giommi

Academic Years: 2014-2018

Abstract

Observations have shown that blazars (a special sub-class of active galactic nuclei) of the high synchrotron peak type (HSPs) play a crucial role in TeV/Very High Energy (VHE) astronomy. To provide a large list of potential VHE emitters, and therefore candidate targets for current and future TeV instruments, we have assembled a catalog including over 2000 confirmed and candidate HSP blazars selected on the basis of multi-frequency data. The catalog, named 3HSP, is currently the largest and most complete sample of HSP blazars, and can be used for detailed statistical properties of the whole HSP population and may shed light on some of the the long-standing issues in the cosmological evolution of blazars.

The most recent successful case is a new TeV source, PGC 2402248, was detected by the MAGIC (Major Atmospheric Gamma Imaging Cherenkov Telescopes), applying a 3HSP source as observation seed. Moreover, with a dedicated gamma-ray analysis on the position of bright 3HSP sources using Fermi PASS8 data, we have found 150 new gamma-ray detections recently published in the 1BIGB catalog.

To optimise the search for new blazars making full use of all available multi-frequency data we have developed a new software tool, called VOU-Blazars. The tool, based on Virtual Observatory (VO) protocols and developed within the Open Universe initiative, can identify blazars in relatively large regions of the sky, such as γ-ray and neutrino uncertainty regions.

Using radio and γ-ray flux limited and largest ever subsamples of the 3HSP catalog we explored the statistical and evolution properties of HSP blazars, deriving the radio and γ-ray LogN-LogS, luminosity function, as well as testing for the presence of cosmological evolution using the V/Vmax test. Our results confirm with unprecedented statistical robustness the presence of negative evolution. The luminosity function and LogN-LogS of HSP blazars imply that there is no preference for high $\nu_{\rm peak}$ sources in faint luminous/flux bins, contrary to the predictions of the "blazar sequence".

Multi-Frequency Studies of Very High Energy Peaked Blazars

A thesis presented

by

Yu-Ling Chang

to

The department of physics

In fulfillment of the requirements

for the PhD degree in

international relativistic astrophysics

IRAP PhD

La Sapienza University

Rome, Italy

July 2018

Advisor: Paolo Giommi

Board of examiners

Antonio Capone

Paolo Padovani

Marco Tavani

External evaluator

Chorng-Yuan Hwang

Bruno Arsioli

The thesis is dedicated to my parents. I love you and thanks for everything.

Acknowledgement

During the PhD, I received a lot of help to finish my thesis and obtain the degree. First of all, I would like to thank Paolo Giommi for the uncountable lessons during my PhD period. Thanks for giving me many very useful advice and instructions and helping me overcome the bottleneck of my research. Without you, I could not finish this thesis and the PhD research, and I am really lucky to have you as my supervisor.

I also would like to express my sincere appreciation to Bruno, who has been advising me since the very beginning of my PhD. Bruno, Thanks for every discussions and comments, I really appreciate that. Besides, I thank Paolo Padovani for kindly suggestions and advice, it is very pleasure and fortunate to work with a world-class scientist.

Moreover, I would like to thank the Government of Republic of China (Taiwan) for providing me full scholarship to complete my PhD. I also thank Prof. Remo Ruffini for kindly financial support every months. Special thanks to Federica and Cinzia, thank you very much for countless help when I was in Pescara. Things like permit of stay and visa will not go smoothly without your help, and I really appreciate your hospitable welcome and support during my PhD period.

I would like to thank Prof. Hwang, Prof. Capone, and Dr. Tavani for being the committee member of my thesis defense. Thanks for arranging time to joint my oral defense and for reading my thesis and giving me useful comments. I thank Carlo Bianco and Jorge as well for helping me arrange the defense.

Thank you to Carlos for helping me to deal with some technical issues, without your help, the VOU-Blazars will not successfully work. Apart from that, during the PhD, I meet many kind and great people, Andreas, Camilo, Daria, and Yerlan. It is a great pleasure to do the PhD and learn Italian together with all of you. Furthermore, I would like to give my honest thank you to Wang Yu, Judy, and Yen-Chen. It is very happy to meet you guys, and every time after chatting with you, I feel refresh and have the energy to keep fighting with crazy puzzles.

Some of my friends, Wendy, Terry, Cheyenne, and Mandy, have been here to visit me and bring me a lot of stuff from Taiwan. Thank you very much for flying such a long distance to here and giving me warmest support. A special thank goes to Tina Chiu, thank you for always being there when I feel frustrated. Yours encourage make me come through the most difficult time.

Last but not least, I would like to thank my family. Thank you for unconditionally support me to complete my dream and study aboard without worries. They are always the most important people to me and no word in the dictionary could express my gratitude to them.

Acronyms

1SWXRT The seven year Swift-XRT point source catalog

2/3FHL Second/Third Catalog of Hard *Fermi*-LAT Sources

3FGL *Fermi* LAT 4-Year Point Source Catalog

3XMM XMM-Newton Serendipitous Source Catalog

5BZCat 5th *Roma-BZCAT*

AGN Active Galactic Nucleus

BMW-HRI Brera Multi-scale Wavelet (BMW) ROSAT HRI Source Catalog

CTA Cherenkov Telescope Array

Einstein IPC Einstein Observatory Image Proportional Counter

FIRST Faint Images of the Radio Sky at Twenty-Centimeters

FL8Y *Fermi*-LAT 8 years catalog

GALEX Galaxy Evolution Explorer

GB6 Green Bank 6-cm Radio Source Catalog

HSP high synchrotron peaked blazar

MCXC Meta-Catalog of X-Ray Detected Clusters of Galaxies

NVSS National Radio Astronomy Observatory (NRAO) Very Large Array (VLA) Sky Survey

Pan-STARRS Panoramic Survey Telescope and Rapid Response System

PGC Principal Galaxy Catalog 2003

Planck SZ2	Planck 2nd Sunyaev-Zeldovich Source Catalog
PMN	Parkes-MIT-NRAO Surveys
RASS BSC	ROSAT All-Sky Survey Bright Source Catalog
RASS FSC	ROSAT All-Sky Survey Faint Source Catalog
SDSS	Sloan Digital Sky Survey
SDSS WHL	Sloan Digital Sky Survey Galaxy Clusters Catalog
SED	spectral energy distribution
SSDC	ASI Space Science Data Center
SUMSS	Sydney University Molonglo Sky Survey
SwiftFT	The Swift serendipitous survey in deep XRT GRB fields
VHE	very high energy
WISE	Wide-field Infrared Survey Explorer mission
XMMOMSUMSS	XMM-Newton Optical Monitor Serendipitous UV Source Survey
XMMSL	XMM-Newton Slew Survey Source Catalog
ZW	Zwicky Clusters

Contents

List of Figures

List of Tables

Chapter 1

Introduction

The statistical properties of blazars is a long-lasting mystery for around 20 years. The main purpose of this thesis is to build a latest and largest high synchrotron peaked blazars (HSPs) catalog and discussing the intrinsic and statistical properties of HSPs. Another aim to build a new generation HSP catalog is for future very high energy (VHE) observations, to unveil more γ-ray or TeV sources effectively with multi-frequency analysis knowledge. Apart from that, the thesis also introduces a tool to find more blazars candidates to make the HSP catalog more complete.

1.1 AGNs and Unification Model

Compared with normal galaxies, some galaxies have special spectra or variability such as extremely broad emission lines or obviously brightness changes in a short time. These abnormal phenomena usually come from the center part of the galaxies, and the special phenomena are called "active galactic nuclei (AGNs)." HSPs are a special type of AGNs which are expected to emit the highest frequency non-thermal emission among AGNs. According to the observations, there are several different types of AGNs (Carroll and Ostlie, 2006; Peterson, 1997; Padovani, 2017)[27, 110, 95]:

1. Quasars

   (a) Radio-loud quasars: They are strong radio sources with variations in all observed wavelengths. They have broad emission lines in their spectra and usually have high redshifts.

   (b) Radio-quiet quasars: They also have broad emission lines in spectra, high redshifts, and variability in all studied wavelengths, but they are weak in radio.

They usually are brighter than -23 magnitude in B band.

2. Seyfert Galaxies

   (a) Type 1 Seyfert galaxies: They are similar as radio quiet quasars, while dimmer than -23 magnitude in B band by definition. The width of Hβ is larger than 2000 km/s, and the line ratio of [OIII] to Hβ is smaller than 3. They have X-ray emission. Most of them are located in spiral galaxies.

   (b) Type 2 Seyfert galaxies: They are not variable and merely have weak X-ray and radio emission. They have only narrow lines in their spectra. The width of Hβ is lower than 2000 km/s, and the line ratio of [OIII] to Hβ is greater than 3. They also host in spiral galaxies mostly.

   (c) Narrow-line Seyfert 1 galaxies: They are similar as Seyfert 1 galaxies, but they are narrow line targets. The width of Hβ is less than 2000 km/s, and the line ratio of [OIII] to Hβ is smaller than 3.

3. Radio galaxies

   (a) FR Is: They are radio sources from core-halo with no variation. They usually have narrow lines in their spectra only. The majority of them are located in elliptical galaxies.

   (b) FR IIs: They are strong radio sources from double-lobe. Some of them are variable in all studied wavelengths, and some of them have broad emission lines in their spectra. Most of their host galaxies are elliptical.

4. Blazars

   (a) BL Lacs objects: They have strong radio emission and rapid variability at visible wavelengths. The spectra are almost devoid of emission lines. They host in elliptical galaxies mostly.

   (b) Flat spectrum radio quasars (FSRQs): They are also strong radio sources and are rapid variable in all observed wavelengths. However, they have broad emission lines in their spectra.

5. Low ionization nuclear emission-line regions (LINERs): Their spectra are similar to low-luminosity Seyfert 2 with low-ionization emission lines in their spectra. They

might be related to star-burst phenomena. Most of the host galaxies of LINERs are elliptical.

6. Broad absorption line quasars (BAL quasars): They have broad absorption lines instead of emission lines in their spectra.

7. Ultra-luminous infrared galaxies (ULIRGs): They might be dust-enshrouded quasars, and alternatively might be star burst phenomena.

Unfortunately, scientists have no certain conclusions about the properties and classification of AGNs; there are many uncertainties lie in the classification of AGNs. Till now, the "unification model" (Blandford and Rees, 1978; Antonucci, 1993; Urry and Padovani, 1995)[19, 11, 140] is the most accepted model of AGNs. Type 1 and type 2 AGNs has been remarkably successful connected by the unification model. The schematic picture of the unification model is shown in Figure 1.1.

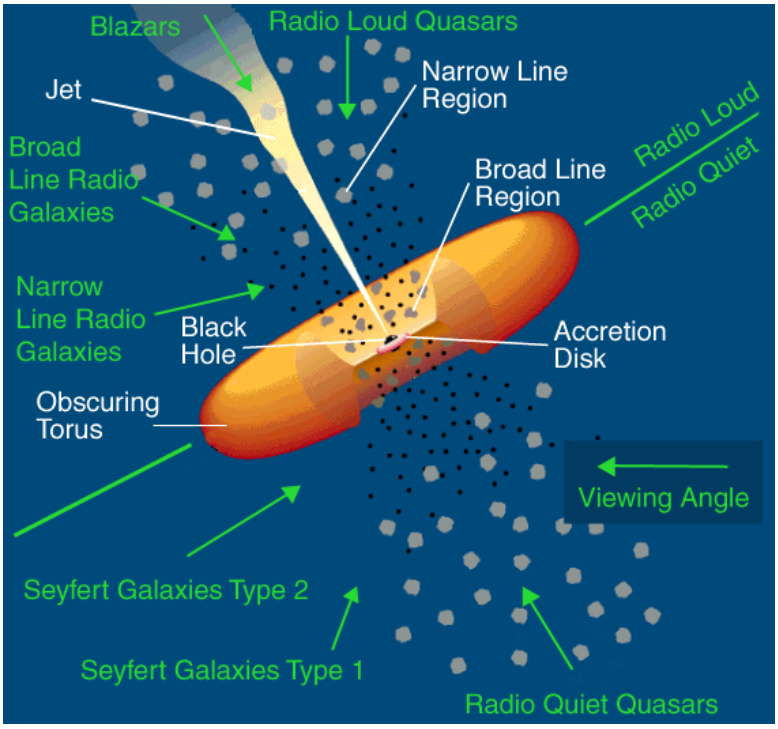

Figure 1.1: The unification model of AGNs. Picture credit: Urry and Padovani, 1995[140]

The unification model assumes a super massive black hole (SMBH) at the center of AGNs. There are several components surrounding the SMBH. The materials near the SMBH will be attracted, circling around the SMBH, falling into the black hole, and forming an accretion disk. The materials in the inner part of the accretion disk may emit X-ray when falling into the SMBH, while the materials located at the outer part of the accretion disk will generate ultraviolet and optical with a lower velocity. There is a torus outside the accretion disk, absorbing optical and ultraviolet and re-radiating at infrared. There are also some gas clouds in AGNs. The gas clouds near the black hole will be excited by stronger radiation, generating broader emission lines called broad line region (BLR). The gas clouds farther away from the SMBH will be excited by weaker radiation, emitting narrow lines called narrow line region (NLR). Jets might appear perpendicularly to the accretion disk when the materials fall into the SMBH.

According to the unification model, observations of different phenomena of AGNs are caused by different angles. Torus is the region that optical cannot penetrate. When observing the AGNs from different angles, one will see particular phenomena due to the shielding of the torus. There were separated the AGN by radio-quiet and radio-loud. For radio-quiet AGNs (mostly non-jetted AGN [95]), if observing from the face-on direction, one might see the BLR mainly. This is the phenomenon of radio-quiet quasars. If observing from an angle away from the face-on direction, one can see both BLR and NLR-the classification of Seyfert 1 galaxies. Finally, if observing from the edge-on direction, the BLR is covered by the torus, and one can see only the NLR. This is the observation of Seyfert 2 galaxies. For radio-loud AGNs (mostly jetted AGN [95]), there are jets at the face-on direction. If observing from that direction, one would see jets coming toward us, the observation of blazars. If observing from an angle away from the face-on direction, one could see the phenomena of broad-line radio galaxies and radio-loud quasars. At last, if one observes at the edge-on direction, there will be seen NLR only, the classification of narrow-line radio galaxies.

Recently, there are some evidences from [95] and [92] suggest that a unified picture based primarily on orientation and obscuring material is incomplete. Padovani 2017 [95] suggests that there are other key elements necessary to describe the model of AGNs, such as accretion rate, torus covering factor, jet strength, and host galaxy properties. A schematically new unified model with accretion rate and jet strength is proposed in [95] and shown in Figure 1.2.

From the new model in [95], AGNs are divided into two main classes, jetted or non-jetted AGNs. The jetted AGNs mostly are known as radio-loud sources, while the non-jetted AGN mainly are radio-quiet. They further introduced radiatively efficiency factor into the model to separate jetted and non-jetted AGNs. For example, according to this new model, blazars are jetted AGNs comprises high-accretion (radiatively efficient) radio flat quasars and low-accretion (radiatively inefficient) BL Lacs. Note that radiatively

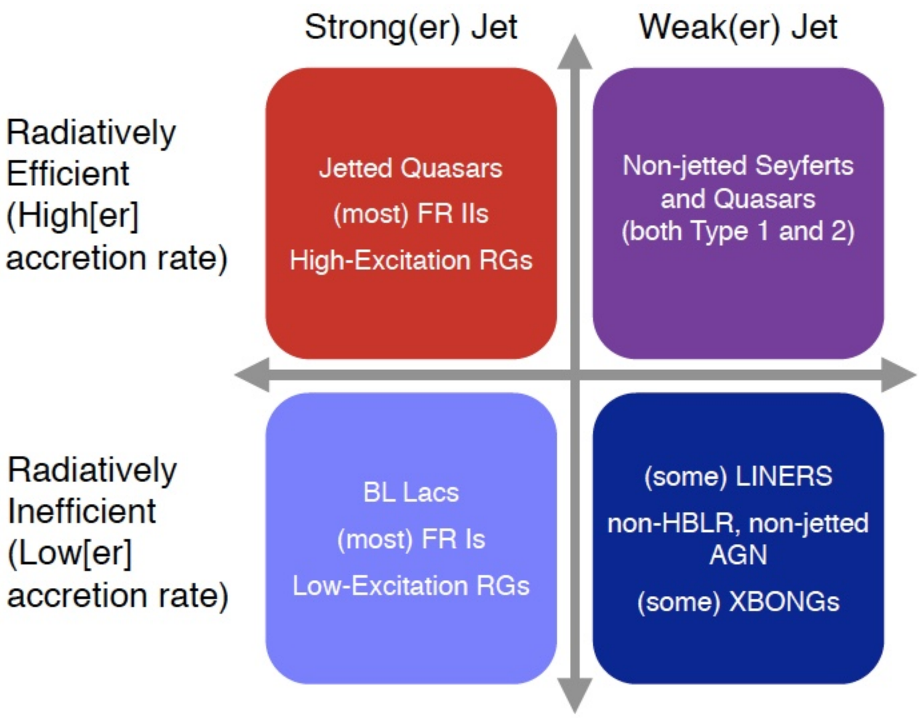

Figure 1.2: Scheme of new unified model of AGNs with two parameters, jet and accretion. Picture credit: Padovani et al. 2017 [95]

efficient blazars usually has radio flat spectrum given that they are not radio extended. It is believed that the high-extinction radio galaxy (HERG) and low-extinction radio galaxy (LERG) are the parent population of FSRQ and BL Lac, respectively.

1.2 Brief introduction of blazars

It is known that BL Lac objects and flat spectrum radio quasars (FSRQs), also known as optical violent variable quasars (OVVs) are collectively called "blazars, " and blazars are a class of active galactic nuclei (AGN) hosting a jet oriented at a small angle with respect to the line of sight [140]. However, the optical spectra of BL Lacs objects and FSRQs are very distinct. The FSRQs generally have broad emission lines which dominate in their spectra, while the emission and absorption lines of BL Lac objects are very weak relative to the continuum. The example spectra of FSRQs and BL Lac objects are shown in Figure 1.3. Compared with those of the BL Lac objects, the redshifts of FSRQs tend to be large.

Both of the BL Lac objects and FSRQs are characterized by rapid and large amplitude spectral variability due to the presence of a relativistic jet from the observed direction (See the example light curves in Edelson et al, 1995)[45]. In a few months, the optical fluxes of blazars can vary over several magnitudes. The apparent luminosities and the degree of continuum polarization could determine the strength of the continuum variations, indicating strongly for a non-thermal origin of the continuum of BL Lac objects (Edelson, 1992)[44]. All observed blazars are radio-loud sources dominated by center AGNs; no radio-quiet blazars have been found, although they have been searched for (Stocke et al., 1990)[130].

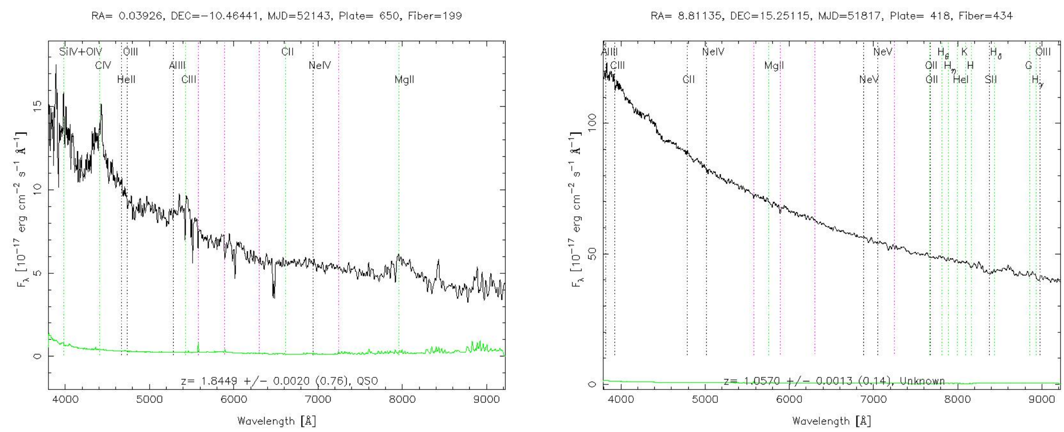

Figure 1.3: Example spectra of FSRQs and BL Lacs. Spectra Credit: Sloan Digital Sky Survey. The left one is a sample spectrum of FSRQs, and the right one is a sample spectrum of BL Lac objects.

Blazars are believed to emit non-thermal over most or the entire electromagnetic spectrum, from radio frequencies to hard γ-rays. The observed spectral energy distribution (SED) of them presents a general shape composed of two bumps. One typically is located in the infrared (IR), and sometimes extending to the X-ray band, and the other is in the hard X-ray to γ-rays. The low-energy bumps are from synchrotron emission, while the high-energy bumps are from inverse Compton emission. According to the locations of the peaks on the SEDs, blazars can be divided into three groups: low synchrotron peaked blazars (LSP), intermediate synchrotron peaked blazars (ISP), and high synchrotron peaked blazars (HSP) (Abdo et al., 2010; Padovani and Giommi, 1995) [1, 97]. If the peaked frequency of the synchrotron bump ($\nu_{\rm peak}$) in ν - νF_ν space is larger than 10^{15} Hz (corresponding to $\sim$ 4 eV), a source is usually called high synchrotron peaked (HSP) blazars. On the other hand, if the synchrotron emission peaked in IR or optical ($\nu_{\rm peak}$less than 10^{14} Hz), it will be classified as LSP. Figure 1.4 shows the example SEDs of several blazars.

There were selected SEDs of four well-known bright blazars to illustrate in Figure 1.4.

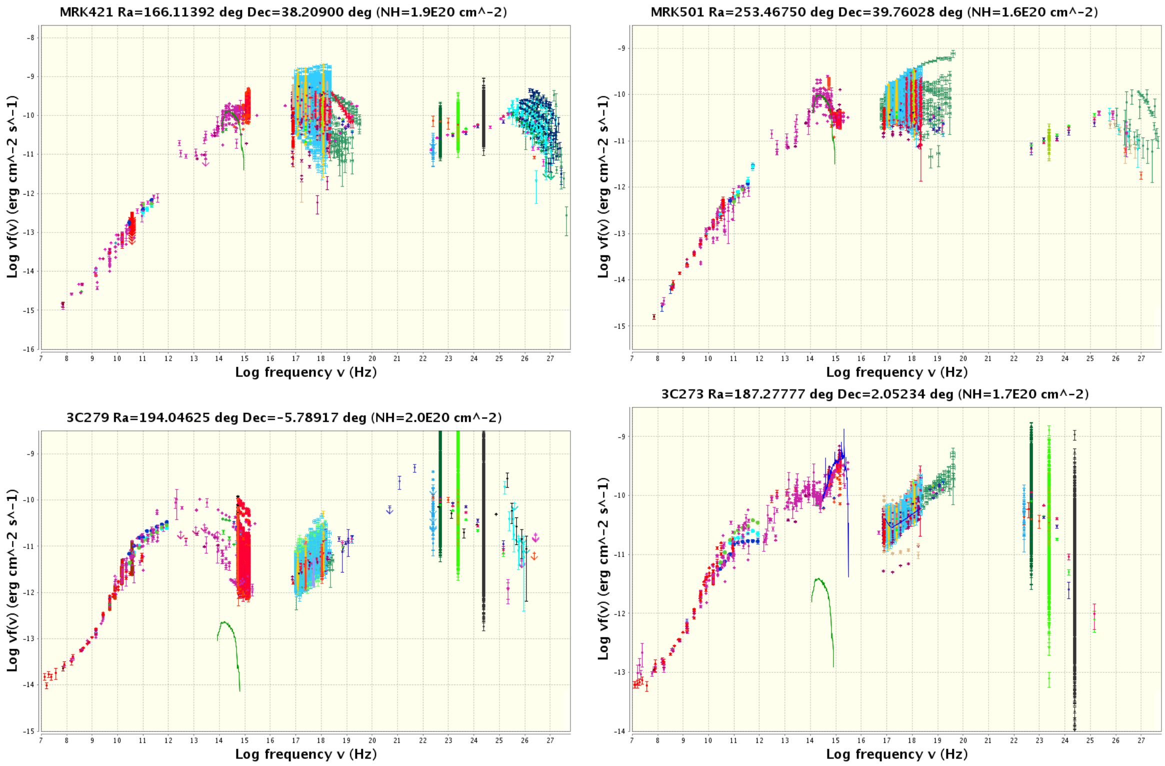

Figure 1.4: Sample SEDs of blazars. SED credit: SSDC SED builder. Up: example SEDs of high synchrotron peaked blazars. Bottom: example SED of low synchrotron peaked blazars. Green lines represent the emission from host galaxy, and the blue lines mean the emission from accretion and BLR.

From upper left to lower right, there is Mrk 421, Mrk 501, 3C 279, and 3C 273. Mrk 421 and Mrk 501 are high synchrotron peaked BL Lacs with no accretion and BLR clues from SED. The host galaxy emission (green line) from Mrk 421 is more or less the similar level as AGN emission, while for Mrk 501, the host galaxy dominated the other non-thermal emission in IR and optical. 3C 279 and 3C 273 both are LSP blazars; however, 3C 279 is a BL Lac with radiatively inefficient accretion at the center SMBH, while 3C 273 is an FSRQ with radiatively efficient accretion. There is no accretion feature from the SED of 3C 279, implying a featureless optical spectrum for the source. For 3C 273, the UV and part of X-ray are dominated by the accretion and BLR emission (blue lines, with radio-optical spectral slope, assumed 0.6) from center AGN. The emission from host galaxies (green lines) of both 3C 279 and 3C 273 are swamped by the non-thermal from jet; the green line in the 3C 279 case are plotted with redshift 0.536 ([80]) and that in the 3C 273 case are plotted with z=0.158 ([133]).

From the SEDs of the BL Lacs, it is known that sometimes (like the cases of 3C 279) there are no identifiable features (such as the big blue bump and the sub-millimeter break) at particular frequencies, as there are in non-blazar AGN SEDs (Peterson,1997)[110]. The missing of characteristic features of AGN SEDs in the SEDs of BL Lacs suggests a non-thermal origin of the spectra of BL Lacs, and the estimation of redshift is relatively hard for these featureless sources.

Apart from classifying blazars with optical spectrum, Giommi and Padovani (2012) [60] proposed "a simplified view" of blazars and suggested a more clear classification for blazars. According to the simplified view of blazars, there were two groups of blazars, separated by the accretion efficiency, either LERG or HERG observed at the direction of the jet. They suggested that some of the cataloged BL Lac are actually FSRQ with high accretion rate but the SED features from accretion and BLR are overwhelmed by the non-thermal jet. These sources are called "masquerading" BL Lac as there is no emission line from their optical spectra. Moreover, some of the BL Lacs are misclassified as radio galaxies when the IR and optical part of their SED are dominated by the host galaxy, while in fact, they are good blazars with non-thermal emission from jet also very strong. Padovani, Giommi, and Polenta (2015) [98] concludes their results in a table, which are shown in Table 1.1 here.

	LERG	HERG	viewing angle
strong jet dilution (EW< 5Å; Ca H&K< 0.4)	BL Lac	*BL Lac* [1]	$\theta < \theta_{\rm blazar}$
weak jet dilution	*Radio Galaxy* [2]	FSRQ	$\theta < \theta_{\rm blazar}$
misdirected jet	Radio Galaxy	Radio Galaxy	$\theta > \theta_{\rm blazar}$

Italic denote "masquerading" sources, [1] misclassified FSRQ, [2] misclassified BL Lac

where $\theta_{\rm blazar} \sim 15 - 20^\circ$ [140]

Table 1.1: The simplified blazar view scenario. Table from Padovani and Giommi, 2015 [98].

The observed radiation of HSP blazars shows extreme properties, mostly owing to relativistic amplification effects. They are also considered as extreme sources since the Lorentz factor of the electrons radiating at the peak of the synchrotron bump γ_{peak} are the highest within the blazar population, and likely of any other type of steady cosmic sources. Considering a simple SSC model, where $\nu_{\rm peak} = 3.2 \times 10^6 \gamma_{\rm peak}^2 B\delta$ [60], assuming $B = 0.1$ Gauss and Doppler factor $\delta = 10$, HSPs characterized by $\nu_{\rm peak}$ ranging between 10^{15} and $\gtrsim 10^{18}$ Hz demand $\gamma_{\rm peak} \approx 10^4 - 10^6$.

The typical two-bump SED of blazars and the high energies that characterize HSPs imply that these objects occupy a distinct position in the optical to X-ray spectral index ($\alpha_{\rm ox}$) versus the radio to optical spectral index ($\alpha_{\rm ro}$) color-color diagram [131]. Considering the distinct spectral properties of blazars over the whole electromagnetic spectrum, selection methods based on $\alpha_{\rm ox}$ and $\alpha_{\rm ro}$ have long been used to search for new blazars. For example, [124] discovered 10 new BL Lacs via a multi-frequency approach with radio, optical, and X-ray data, and their BL Lac nature with optical spectra.

In a series of papers, [84, 37, 83] show that most blazars occupy a specific region of the IR colour-colour diagram, which they termed the blazar strip. In 1WHSP, they extended the blazar strip in the WISE colour-colour diagram to include all the Sedentary Survey blazars and called it the *Sedentary WISE colour domain* (SWCD). The SWCD is wider than the WISE blazar strip since it contains some blazars whose host galaxy is very bright, such as Mrk 421 and MKN 501 (see Figure 1.4). It is understood from previous works that many low-luminosity HSP blazars have the IR colours dominated by the thermal component of the host giant elliptical galaxy. Therefore, a selection scheme adopting IR colour restrictions may work effectively for selecting cases where the non-thermal jet component dominates the IR band but is less efficient for selecting galaxy-dominated sources (since they are spread over a larger area in the IR colour-colour plot).

HSP blazars play a crucial role in very high energy (VHE) astronomy. Observations have shown that HSPs are bright and variable sources of high energy γ-ray photons (TeVCat)[1] and that they are likely the dominant component of the extragalactic VHE background [96, 56, 41, 59, 9]. In fact, most of the extragalactic objects detected so far above a few GeV are HSPs [57, 98, 14, 135], see also TeVCat. However, only a few hundred HSP blazars are above the sensitivity limits of currently available γ-ray surveys.

For example, the 1WHSP catalog (Arsioli et al. 2015, hereafter 1WHSP) [14], which was the largest sample of HSP blazars when it was published, shows that out of the 992 objects in it, 299 have an associated γ-ray counterpart in the *Fermi* 1/2/3FGL catalogs. Nevertheless there is a considerable number of relatively bright HSPs which still lack a γ-ray counterpart. These are likely faint, point-like sources at or below the *Fermi*-LAT, detectability threshold and were not found by the automated searches carried out so far. Indeed, [13] have detected $\approx$ 150 new γ-ray blazars based on a specific search around bright WHSP sources, using over seven years of *Fermi*-LAT Pass 8 data.

In the most energetic part of the γ-ray band photons from high redshift sources are absorbed by the extragalactic background light (EBL) emitted by galaxies and quasars

[1]http://tevcat.uchicago.edu

[40, 112, 23]. Therefore, the TeV flux can drop by a very large factor compared to GeV fluxes, making distant TeV sources much more difficult to detect. 1WHSP paper has shown that, with the help of multi-wavelength analysis, HSP catalogs can provide many good candidates for VHE detection.

1.3 Current HSP catalogs

The currently known HSP blazars are listed in catalogs such as the 5th *Roma-BZCAT* [82] (hereafter 5BZCat), the Sedentary Survey [58, 61, 115], Deep X-ray Radio Blazar Survey (DXRBS) [109, 74, 99], Kapanadze 2013 catalog[73], and 1WHSP..etc.

[14] (1WHSP) built an HSP catalog, 1WHSP, based on the color-color diagram, using data from the Wide-field Infrared Survey Explorer mission (WISE) color-color diagram and selecting sources only inside the SWCD region. They cross-matched the AllWISE sources [36] in the SWCD with different radio and X-ray catalogs using TOPCAT[2], applied three spectral slope criteria, and selected sources with $\nu_{\rm peak} > 10^{15}$ Hz. There were NVSS, FIRST, and SUMSS radio catalogs applied in 1WHSP; for X-ray catalogs, the 1WHSP make use of RASS, IPC, XMM, SWIFT. The slope criteria[3] applied in Paper I are the radio to IR spectral slope, IR to X-ray spectral slope, and the AllWISE channels W1 to W3 spectral slope; the criteria are obtained from normalized and rescaled SEDs of three well-known HSP blazars. It includes 992 known, newly-identified, and candidate high galactic latitude ($b > |20°|$) HSPs.

The 5BZCat is the largest compilation of confirmed blazars, containing 3 561 sources, around 500 of which are of the HSP type. It collected blazars discovered in surveys carried out in all parts of the electromagnetic spectrum and is also based on an extensive review of the literature and optical spectra. [73] built a catalog of 312 HSPs with flux ratio ($f_{\rm x}/f_{\rm r} \geq 10^{-11}$ erg cm^{-2} s^{-1} Jy^{-1}) selected from various X-ray catalogs, the NVSS catalog of radio sources, and the first edition of the $Roma-BZCAT$ catalog [81].

The Sedentary catalog, built with X-ray to radio flux ratio $\rm f_x/f_r \geq 3{\times}10^{-10}$ erg cm^{-2} s^{-1} Jy^{-1}, implying that the synchrotron peaked of Sedentary sources (log$\nu_{\rm peak}\gtrsim$ 16.5 Hz) will be at higher energy then that of typical HSP sources (log$\nu_{\rm peak}\geq$ 15 Hz). They began with cross-matching The NRAO VLA Sky Survey (NVSS) with the ROSAT All-Sky Survey Bright Source catalog (RASS-BSC) with cross-matched radius 0.8 arcmin and then taking the

[2] `http://www.star.bris.ac.uk/~mbt/topcat/`

[3] $0.05 < \alpha_{1.4{\rm GHz}-3.4\mu{\rm m}} < 0.45, 0.4 < \alpha_{4.6\mu{\rm m}-1{\rm keV}} < 1.1,$
and $-1.0 < \alpha_{3.4\mu{\rm m}-12.0\mu{\rm m}} < 0.7$

radio-X-ray matched sources with the optical counterpart in the APM [71] or COSMOS [150] catalog. The Sedentary sample selected only sources with $\delta > -40°$ and out of the Galactic plane ($|b| > 20°$). Apart from that, a radio cut at $f_r > 3.5$ mJy, X-ray cut at cts/s > 0.1, and optical cut at $V \leq 21$ are applied to the Sedentary.

The Sedentary paper further employed the α_{ox}-α_{ro} diagram to narrow down the number of candidates, taking the sources only in HBL zone in the diagram[4]. After removing the sources with broad emission lines or with ROSAT hardness ratio HRI < -0.5, in the end, the Sedentary catalog contains 150 extreme HBL.

DXRBS applied all serendipitous X-ray sources in WGACAT with quality flag > 5 and cross-matching the WGACAT with the Green Bank 6-cm survey (GB6) catalog [63] in the north celestial sphere and with Parkes-MIT-NRAO survey (PMN) catalog [64] in the south. They further cross-matched the northern sources with NORTH20CM [146], the sources having $-40° < \delta < 0°$ with NVSS, and the sources having $\delta \leq 40°$ with Australia Telescope Compact Array[5] (ATCA) at 3.6 cm and 6 cm. To select sources efficiently, they adopt a spectral index cut $\alpha_r \leq 0.7$, selecting all FSRQ and basically all BL Lacs and excluding most of the radio galaxies; that is $\alpha_{6-20} \leq 0.7$ for $\delta > -40°$ and $\alpha_{3.6-6} \leq 0.7$ for $\delta \leq -40°$. Note that the DXRBS covers almost all the fields of WGACAT but excluding the areas such as $\delta > 75°$ (outside of the NORTH20CM coverage), $|b| < 10°$ (avoid the Galactic plane region), several regions not observed by the PMN and the GB6 surveys, and circular regions around M31, LMC, SMC, and the Orion Nebula.

Moreover, the flux cuts $f_{20cm} \geq 150$ mJy for NORTH20CM, $f_{6cm} \geq 51$ mJy for PMN at $-87.5° \leq \delta < -37°$ and $-29° < \delta < -0°$, and $f_{6cm} \geq 72$ mJy for PMN at $-37° \leq \delta \leq -29°$ were applied to the sample. Ultimately, there are 129 FSRQs, 24 BL Lacs, and 16 unidentified sources in DXRBS catalog. DXRBS contains both FSRQs and BL Lacs selected in the same sample, providing the possibility to compare the properties of the two classes. In particular, the DXRBS is the first catalog to include both LBL and HBL within one sample in sizeable numbers, and this makes it possible to compare their properties independently of different selection bands and methods which result in salient selection effect [60].

The thesis is structured as follows. Chapter 2 describes how an HSP catalog is built. The statistical properties, evolution, and selection effects are discussed in Chapter 3. In Chapter 4, there was introduced a new tool, VOU-blazars, to find more blazar candidates

[4] $\alpha_{ro} > 0.2$ and $\alpha_{rx} > 0.65$, the later equivalent to $f_x/f_r \geq 3 \times 10^{-10}$ erg cm^{-2} s^{-1} Jy^{-1}

[5] `http://www.narrabri.atnf.csiro.au/observing/`

and identify possible counterpart for VHE detections. Chapter 5 explains the possible connection between VHE astronomy and HSP blazars. Discussion and Conclusion are in the last Chapter. Throughout the thesis, there were adopt a Flat-ΛCDM cosmology with the following parameters [28]: $\Omega_{\rm m} = 0.3$ and $H_0 = 70$ km s^{-1} Mpc^{-1}. Besides, the $1 - \sigma$ Poisson errors [54] was applied when the number counts is ≤ 50 in logN-logS and luminosity functions.

Chapter 2

The 3HSP Catalog

HSPs are extremely essential objects for γ-ray or TeV researches. The number of known HSPs is still relatively small compared to other types of AGNs, with less than $\approx 1,000$ cataloged HSPs in 1WHSP catalog (Arsioli et al., 2015; hereafter 1WHSP)[14]. Significantly, enlarging the number of high energy blazars is important to better understand their role within the AGN phenomenon, and should shed light on the cosmological evolution of blazars, which is still a matter of debate. By extending the 1WHSP catalog to lower Galactic latitudes ($b > |10°|$), a larger catalog including $\approx$ 2000 HSP blazars expected to emit at VHE energies by means of multi-frequency data was established. The main purpose of building a new and more complete HSP catalog is to provide seed sources for TeV surveys and to better understand the TeV background. The processes of building the catalog are shown in this Chapter.

2.1 Initial data selection, cross-matching, and slope criteria

Blazars are known to emit electromagnetic radiation over a very wide spectral range, from radio to VHE photons. As discussed in the 1WHSP paper, an effective way of building large blazar samples is to work with multi-frequency data, especially from all-sky surveys, and to apply selection criteria based on spectral features that are known to be specific to blazar SEDs. At least three points are needed to describe the Synchrotron emission with a parabolic curve and to examine if the spectral shape is similar as typical HSPs. In general, there are much more sources detected in Infrared and optical than in X-ray and radio. Thus, the idea to find the blazar candidates is to identify the sources with both radio and X-ray counterparts and check if the radio-X-ray matched sources have IR/optical data or not. In this way, the pre-selected candidates will reduce to the minimum, and will not miss the majority of blazar candidates.

Following the 1WHSP catalog, the very first step of building an HSP catalog started by cross-matching the AllWISE whole sky infrared catalog (Cutri et al., 2013 [36]) with three radio survey, NVSS, FIRST, and SUMSS (Condo et al., 1998; White et al 1997; and Manch et al., 2003). [34, 147, 69, 77]. Taking into account the positional uncertainties associated with each target, the matching radii of 0.3 arcmin was applied for the NVSS and the SUMSS surveys and 0.1 arcmin for the FIRST catalog. Then an internal match for all IR-radio sources to eliminate duplicate entries coming from the different radio catalogs was performed. Keeping only the best matches between radio and IR, there were 2 137 505l selected objects. The reason to start by cross-matching radio and IR catalogs since the position accuracy in these two wavelengths bands is generally better than in the X-ray band.

After this, there were demanded all radio-IR matching sources to have a counterpart in one of the X-ray catalogs available to us (RASS BSC and FSC, 1SWXRT, Swift deep XRT GRB (SwiftFT), 3XMM, XMM slew, Einstein IPC, IPC slew, WGACAT, Chandra, and BMW: [141, 142, 39, 118, 143, 123, 67, 90, 145, 46, 106]). Therefore cross-matching the IR-radio subsample with each X-ray catalog individually was done, taking into account their positional errors. For instance, a radius of 0.1 arcmin was adopted for the cross-correlations (as in 1WHSP), unless the positional uncertainty of a source was reported to be larger than 0.1 arcmin, as in the case of many X-ray detections in the RASS survey. In these cases, there were applied the 95% uncertainty radius (or ellipse major axis) of each source as maximum distance for the cross-match. Some X-ray catalogs have a very wide range of positional uncertainties, thus separating the data by positional errors and used different cross-matching radii for these X-ray catalogs is necessary. The radii used for cross-matching the IR-radio subsample with each X-ray catalog are reported in Table 2.1. The sample also is restricted by Galactic latitude $|b| > 10^{\circ}$ to avoid complications in the Galactic plane. There were combined all the IR-radio-X-ray matching sources and applied an internal cross-check, keeping only single IR sources within 0.1 arcmin radius; this procedure reduced the sample to 28 376 objects.

Next, taking advantage of the fact that HSP blazars show radio to X-ray SEDs which distinguish them from any other type of extragalactic sources, two constraints on the spectral slopes were imposed, namely

Catalog	Error position	Cross-matched radius
RASS	0-36 arcsec	0.6 arcmin
	>37 arcsec	0.8 arcmin
Swift 1SWXRT	0-5 arcsec	0.1arcmin
	>5 arcsec	0.2 arcmin
Swift deep XRT GRB	all data	0.2 arcmin
3XMM DR4	0-5 arcsec	0.1 arcmin
	>5 arcsec	0.2 arcmin
XMM Slew DR6	all data	10 arcsec
Einstein IPC	all data	40 arcsec
IPC Slew	all data	1.2 arcmin
WGACAT2	all data	50 arcsec
Chandra	all data	0.1 arcmin
BMW-HRI	all data	0.15 arcmin

Table 2.1: The cross-matching radii of the X-ray catalogs.

$$\begin{aligned} 0.05 < \alpha_{1.4\mathrm{GHz}-3.4\mu\mathrm{m}} &< 0.45 \\ 0.4 < \alpha_{4.6\mu\mathrm{m}-1\mathrm{keV}} &< 1.1, \end{aligned} \tag{2.1}$$

where $\alpha_{\nu1-\nu2} = -\frac{\log(f_{\nu1}/f_{\nu2})}{\log(\nu_1/\nu_2)}$, which are the same conditions applied to the 1WHSP catalog, with the exception that here we do not apply the criterion $-1.0 < \alpha_{3.4\mu\mathrm{m}-12.0\mu\mathrm{m}} < 0.7$. This choice was necessary to prevent the loss of IR galaxy-dominated HSPs, which could still be promising VHE candidates (See Massaro et al (2011) and Arsioli et al. (2015) for detail) [84, 14].

The parameter ranges given in equation 2.1 are derived from the shape of the SED of HSP blazars, which is assumed to be similar to those of three well-known bright HSPs, i.e. Mrk 421, Mrk 501, and PKS 2155−304 shown in Fig. 3 of Paper I, which also fit within the limiting slopes ($\alpha_{1.4\mathrm{GHz}-3.4\mu\mathrm{m}}$ and $\alpha_{4.6\mu\mathrm{m}-1\mathrm{keV}}$) used for the selection. By avoiding the application of the IR slope constraints used for the 1WHSP, more HSP candidates were selected, reducing the incompleteness at low radio luminosities where the IR flux is often dominated by the host galaxy.

The final pre-selection led to a sample of 5,518 HSP-candidates, 922 of which are also 1WHSP sources. Note that this initial sample includes most of the HSP blazars that had to be added to the 1WHSP sample as additional previously known sources that were missed during the original selection procedure.

2.2 Deriving $\nu_{\rm peak}$ and classifying the sources

The 5,518 pre-selected candidates derived from section 2.1 contain not only HSPs but all kind of sources with radio, X-ray, and Infrared emissions and with SED slope similar to HSP blazars. To refine and further improve the quality of the sample, there were used the SSDC SED builder tool[1] to examine in detail all the candidates, accepting only those with SEDs that are consistent with that of genuine HSPs. The synchrotron component of each object that passed our screening was fitted using a third-degree polynomial function to estimate parameters such as $\nu_{\rm peak}$, and $\nu_{\rm peak}{\rm f}_{\nu_{\rm peak}}$, the energy flux at the synchrotron peak.

The host galaxies of HSP blazars are typically giant ellipticals, and their optical and near IR thermal flux sometimes dominate the SED in these bands. To only fit the synchrotron component of HSP blazars, it is crucial to distinguish the non-thermal nuclear radiation from the flux coming from the host galaxy. A standard giant elliptical galaxy template (CWW elliptical template, [31]) of the SSDC SED builder tool was applied to judge if the optical and IR data points were due to the host galaxy or from non-thermal synchrotron radiation. If the source under examination had ultraviolet data (such as Swift-UVOT or GALEX [89] measurements) it was straightforward to tell that there was non-thermal emission from the object. Sometimes the SDSS [20, 3] flux near UV bands are apparently higher than the other optical bands (g and r band), and such excess implies that the near UV band data are from non-thermal emission. On the other hand, if the WISE W2 flux drop quickly regarding the W1 flux, then both W1 and W2 emission are from the host galaxy. Note that sources with less than 3 data from non-thermal at different frequencies are eliminated directly to avoid extremely uncertain sources.

Additionally, to avoid selecting objects with misaligned jets, which are expected to be radio-extended, the accepted spatial extension of the radio counterparts (as reported in the original catalogs) was limited to 1 arcmin. This procedure was carried out whenever possible, based on the 1.4 GHz radio image from NVSS, which includes the entire sky north of $\delta = -40°$, similarly to what had been done for the 1WHSP catalog. It is possible to identify radio extended sources from their SED since radio extended objects typically display a steep radio spectrum. All cases where there are shreds of evidence of radio (or X-ray, typically from clusters: see section 2.2.1) extension found were eliminated from the sample.

[1]http://tools.asdc.asi.it/SED

For some cases, the optical data were consistent with thermal emission from the host galaxy, and the remaining few radio, IR, or X-ray measurements that could be related to non-thermal emission were very sparse. More multi-frequency data are needed for these sources to beter determine the $\nu_{\rm peak}$ value. Many of the candidates have been observed by Swift with multiple short exposures. To allow for a more accurate estimation of $\nu_{\rm peak}$ and $\nu_{\rm peak}{\rm f}_{\nu_{\rm peak}}$, there were summed all the Swift XRT observations that were taken within a three-week interval. For those without SWIFT observations or data yet but with relatively bright $\nu_{\rm peak}{\rm f}_{\nu_{\rm peak}}$, there were collected as a observation proposal to Swift. A total of 210 proposed souces has been submited to Swift, and 151 of them have been observed and applied to calibrate the $\nu_{\rm peak}$ estimation already. Another 59 sources are still observing and the upcoming data will be used to increase the accuracy of the Synchrotron peak estimation. All the sources submitted to XRT are list in table G.3, and the dedicated analysis for these sources are further discusses in section 2.4.2.

There was still a number of unclear cases owing to the lack of good multi-frequency data, and these unclear sources were flagged asteroid accordingly. There were no reasons to exclude these unclear sources. In addition, since the positional accuracy in X-ray surveys is usually not as precise as that of optical or radio surveys, the position of the X-ray counterparts sometimes may be 20 to 40 arcsec away from the radio and optical counterparts, introducing more uncertainty.

At the end of the selecting process, only objects with $\nu_{\rm peak} > 10^{15}$ Hz (Padovani and Giommi, 1995)[97] are accepted, leading to the selection of 734 new HSPs in addition to those already included in the 1WHSP catalog. For each source, we adopted as best coordinates those taken from the WISE catalog. The new sample including previously known, newly discovered, and candidate blazars. Clearly, most bright sources in the current list are also included in the 1WHSP catalog. Many of the new catalog entries are fainter sources or objects located at low Galactic latitudes ($10^\circ < |b| < 20^\circ$).

2.2.1 Avoiding X-ray contamination from cluster of galaxies

Blazars are certainly not the only objects that emit X-rays. For instance, galaxy clusters also show X-ray emission that is, however, normally spatially extended with a spectrum that peaks at $\approx 1 - 3$ KeV resulting from the emission of giant clumps of hot and low density diffused gas ($\approx 10^8$ K and $\approx 10^{-3}$ atoms/cm^3: [122, 21, 108].) Since blazars and radio galaxies are often located in clusters of galaxies, the X-rays of clusters from the hot gas, if not correctly identified, might cause the SED of the candidate source to look like that of an HSP object, introducing source contamination for our sample. That is, even though the sources are detected in both X-ray and radio, and optical emission like elliptical galaxies. Obviously, it is necessary to avoid selecting sources where the X-rays are due to extended cluster emission instead of the non-thermal Synchrotron.

HSPs usually have a steep X-ray spectrum, but if there is not enough spectral information in the X-ray band, it is difficult to tell whether the X-ray spectrum is steep or hard. Apart from that, the optical spectra and SEDs from clusters could mimic a giant elliptical galaxy. To avoid this problem an extensive check of bibliographic references[2] and catalogs of clusters of galaxies (e.g. ABELL, PGC, MCXC, ZW, SDSS WHL...etc: [2, 107, 114, 152, 144]) have carried out, excluding cases where cluster emission could be responsible for the observed X-rays. There were cross-matched the sample with the positions of RASS extended sources and with those of the Planck SZ sources [116] to further rule out the ones already classified as a cluster member.

In addition, Swift XRT imaging data (which are available for $\approx 60\%$ of the sample) were applied to distinguish between X-ray emission from blazar jets, which is point-like in the XRT count maps, and that from the clusters, which is often extended. The same procedure was followed using XMM images, whenever these could be found in the public archive. Visually inspecting optical images and the error circle maps built with the SSDC explorer tool[3] also works to look for targets that could be related to clusters of galaxies. When the error circle map shows that the region around the source is very crowded and there are several X-ray detections around the source, the source might be a cluster member and X-ray is extended.

To illustrate the processes above, which removing objects that satisfy our multi-frequency selection criteria but where the X-ray flux is likely due to extended emission from a cluster of galaxies, 3 cases are shown here. First, WHL J151056.1+054441, a giant cluster of galaxies also cataloged as Abell2029. The X-ray peak in the SED is located at around 1 KeV, meaning that the X-ray might be from the hot gas in the clusters not from the jet of the blazars. The radio emissions also are extended since there are several detections at 10^9 Hz and the radio spectrum is clearly steep from the SED. Since the strong X-ray emission is clearly extended both in the Swift-XRT and XMM images (see Fig. 2.1), this source was not selected to the HSP catalog.

[2]For the cross-check with ADS references on each source there were used the Bibliographic Tool available on the SSDC website.

[3]http://tools.asdc.asi.it

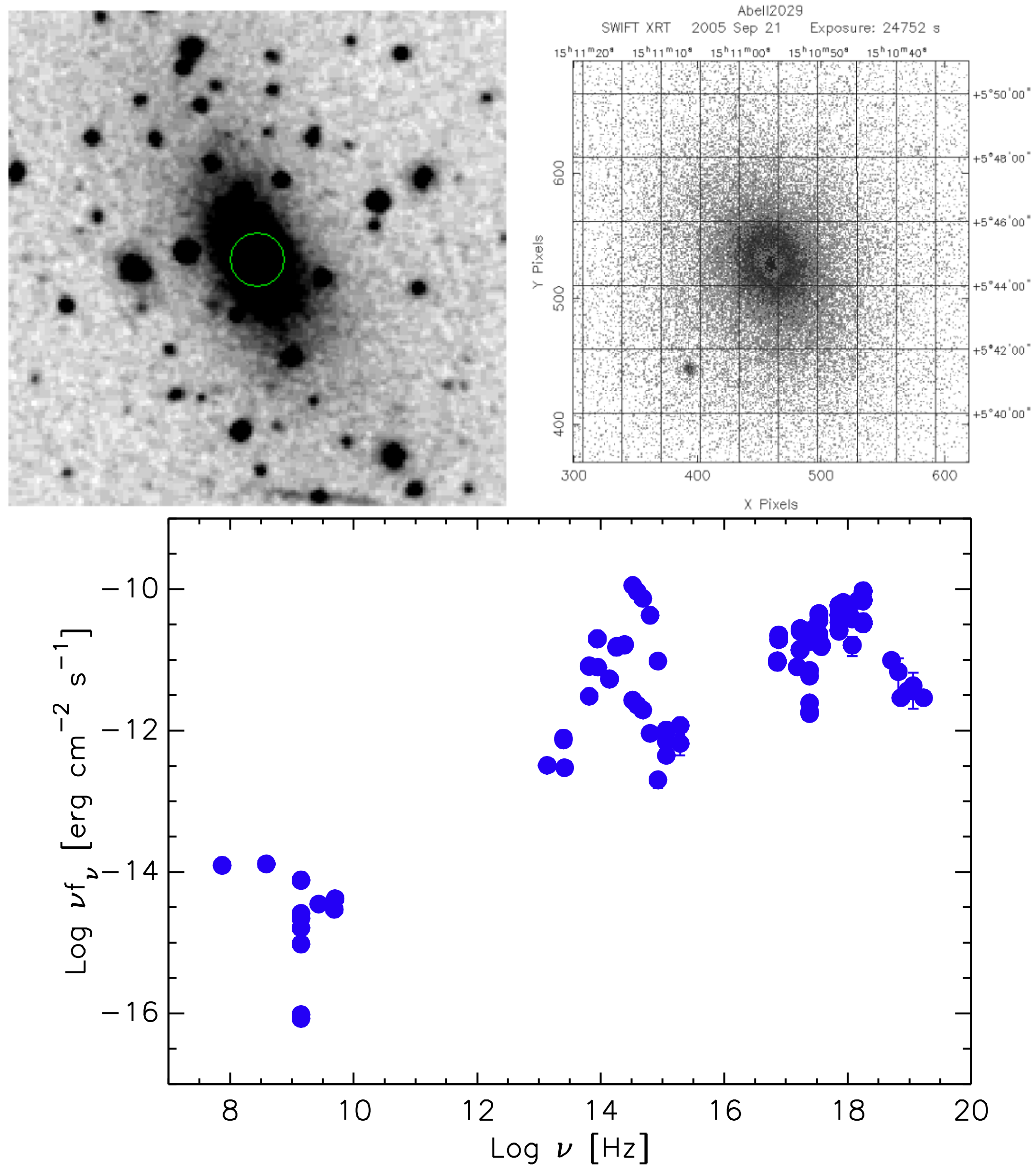

Figure 2.1: Up: optical (left) and X-ray (right: XRT count map) images of WHL J151056.1+054441. Bottom: the SED of WHL J151056.1+054441. See text for details.

Another example is shown in Fig. 2.2, where the candidate blazar is at the center of a cluster of galaxies LCRS B113851.7−115959. Although the X-ray emission is overall extended, the region around the sources shows clumps, and there are several X-ray detections; the non-thermal emission is very clear in the SED. Apparently, there is an AGN at the center that also emits in the UV. However, based on the available data, we cannot know if the X-ray is mainly from the non-thermal jet or from the cluster. Only the sources which show conspicuous non-thermal X-ray emission would be selected, therefore, this source is not included in the catalog.

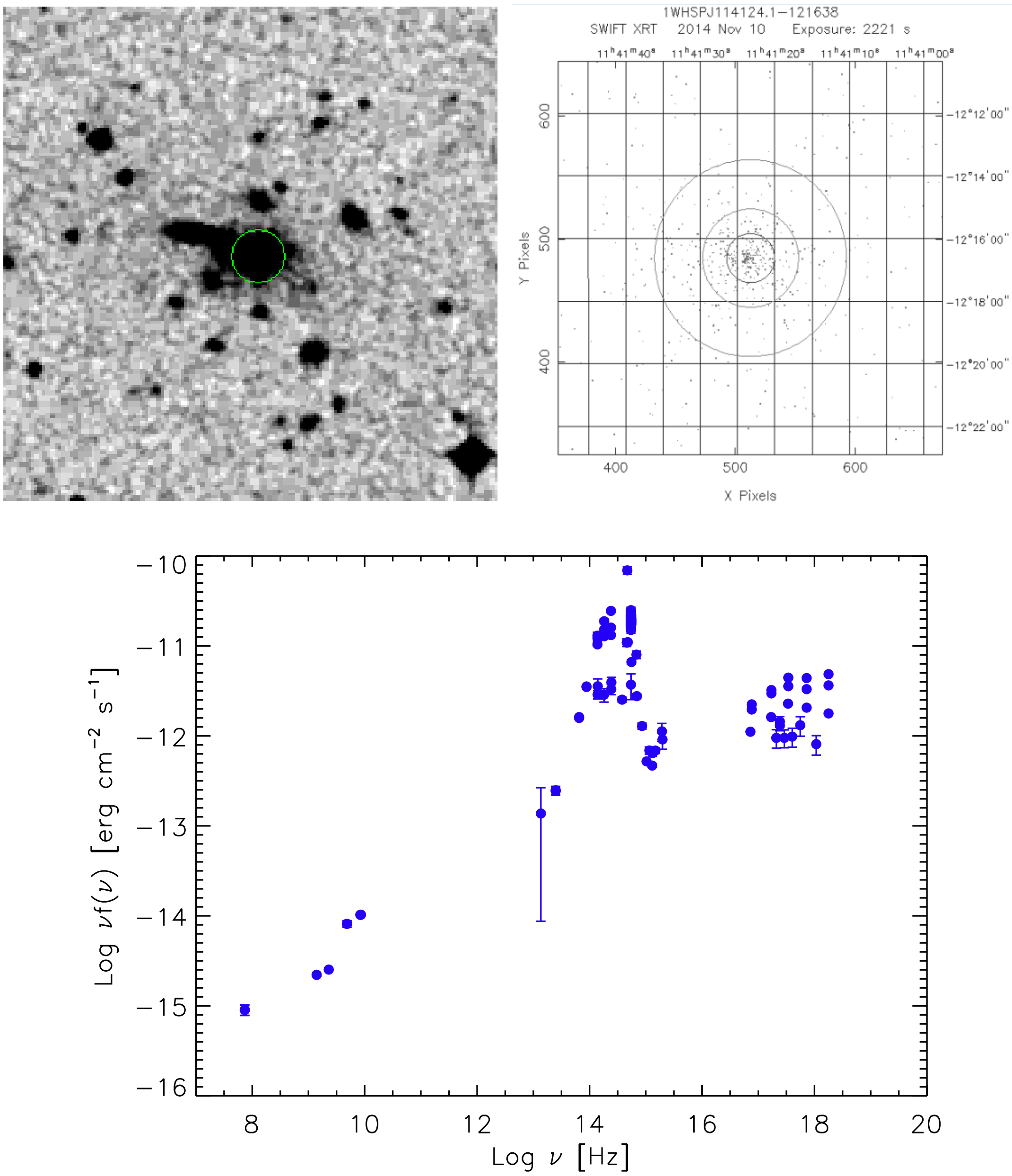

Figure 2.2: Up: optical (left) and X-ray (right: XRT count map) images of LCRS B113851.7−115959. Bottom: the SED of LCRS B113851.7−115959. See text for details.

Last, 5BZBJ0837+1458, Fig.2.3, is a known HSP with both host galaxy and central point source are very bright. The X-ray count map looks accumulate at the center, and the SED indicates that X-ray emissions mainly are from the non-thermal jet. Besides, the optical spectrum shows clear non-thermal emission and looks like a typical BL Lac. Without a doubt, this source is selected to the catalog.

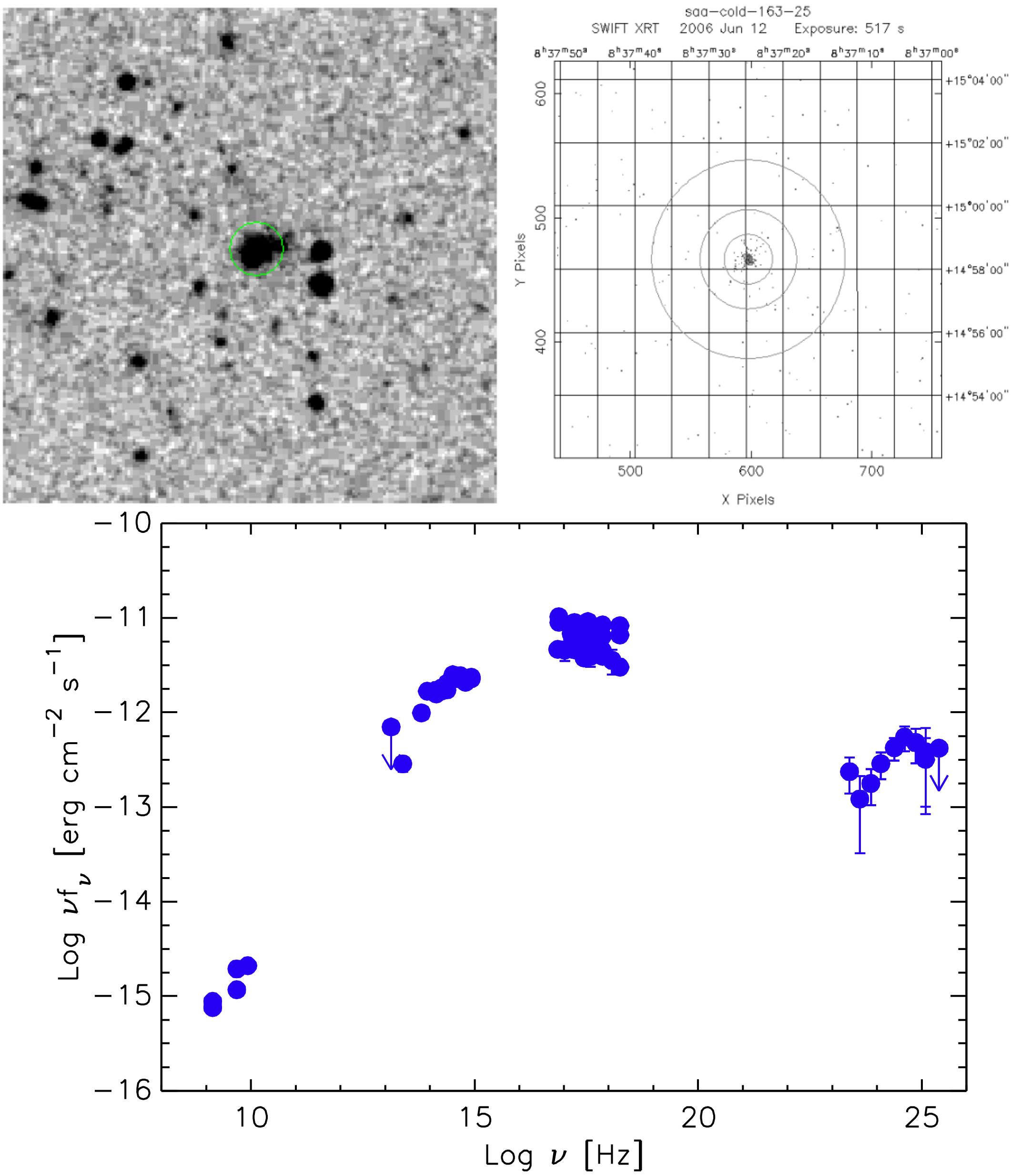

Figure 2.3: Up: optical (left) and X-ray (right: XRT count map) images of 5BZBJ0837+1458. Bottom: the SED of 5BZBJ0837+1458. See text for details.

2.2.2 Improving the sample completeness

The procedure described above totally select 734 sources, containing previously known, newly discovered, and candidate HSP blazars. To evaluate the efficiency of the method that selecting VHE emission blazars, there were cross-matched the sample of 1,645 objects (combining 1WHSP sources) with the *Fermi* 2FHL [8] and with TeVCat. Unfortunately, there are still several missing cases.

The 2FHL sources are detected by the *Fermi*-Large Area Telescope (LAT) in 50 GeV-2 TeV energy band with the newly delivered PASS-8 event-level analysis. Only 146 out of the 360 sources in the 2FHL catalog (257 at $|b| > 10°$) are also in this preliminary sample. To verify if there are genuine HSPs in the 2FHL catalog that were missed during the selection, there were closely examined the remaining 214 2FHL sources to see if they are good blazars or blazar candidates. 31 high Galactic latitude blazars with $\nu_{\rm peak} > 10^{15}$ Hz were found to be added to the catalog. These sources were initially missed since they just did not match the slope criteria (equation 2.1) during the preliminary selection process. To sum up, out of the 177 HSPs located at $|b| > 10°$ in the 2FHL catalog, the selection method detected 146 objects, for an efficiency of 82.5%.

In addition, there are 14 HSP blazars in the 2FHL catalog that are located at Galactic latitudes $|b| < 10°$; the area of sky was not considered in previous processes as reducing complications connected to the Galactic plane. Since the aim of the work is to provide the most complete list of HSPs for VHE energy and these sources are detected in hard γ-ray, these 14 low latitude objects were added to the sample. Totally, there were 45 additional HSPs found in the 2FHL catalog. Only one good HSP blazar found among the 2FHL low Galactic latitude sources had no WISE data (J135340.2−663958.0). The radio position instead of the IR position was applied in this case.

Next is to check catalogs of sources detected at TeV energies. Currently, the most complete list of objects detected in this band is TeVCat, which consists of 175 sources detected by Imaging Atmospheric/Air Cherenkov Telescope/Technique (IACT). At present, there are three main IACT systems operating in the $\sim$ 50 GeV to 50 TeV range: the High Energy Stereoscopic System (H.E.S.S.), MAGIC (Major Atmospheric Gamma Imaging Cherenkov Telescopes), and VERITAS (Very Energetic Radiation Imaging Telescope Array System). There are 38 TeVCat sources that are also in the preliminary catalog, and the other high Galactic latitude sources are checked to see if they were classified as HSP blazars, concluding that only one HSP source was missed. Note that, previously, three TeV sources were added to the 1WHSP catalog, since these were missed during its selection. In total there are 39 HSPs at $|b| > 10°$ in TeVCat, 35 of which satisfy the selection criteria. The selection efficiency, in this case, is 89.7%.

Similar as in the case of the 2FHL catalog, all missing TeV sources have been lost because they just did not meet the slope criteria used in section 2.1. In all cases, the spectral parameters turned out to be very close to the limits of the selection criteria, with $\nu_{\rm peak} \approx 10^{15}$ Hz or with host galaxy dominated the non-thermal emission. This selection inefficiency could be due to flux variability, lack of sufficiently high-quality multi-frequency data, or simply to a non-optimal choice of parameter values in Equation 2.1. Two sources are missed due to no AllWISE data but in the first generation of the WISE survey. Note that there are ≈ 10 sources in the catalog that have only first generation WISE survey data rather than have AllWISE data.

At the end of the all selecting processes, 1,691 sources remained. Since most of the "missing" sources result from the slope criteria, some source with $\nu_{\rm peak}$at around 10^{15}Hz or with host galaxy dominated in IR will not be selected. This kind of sources might be ruled out by slope criteria as the X-ray fluxes are just below the standard or as the IR fluxes are slightly brighter than the criteria or, but they are HSP with the $\nu_{\rm peak}\geq 10^{15}$Hz. To avoid this problem, extending the range of slope criteria might be a choice; however, it will remain a bulk number of subsample to be clean. Detail discussion about the slope criteria is written in section 2.3.2.

2.2.3 The 2WHSP catalog

The final sample after the whole selections includes a total of 1,691 sources, 288 of which are newly identified HSPs, 540 are previously known HSPs, 814 are HSP candidates, 45 are HSP blazars taken from the 2FHL catalog, and four from TeVcat. The sample is called 2WHSP, and the name "WHSP" stands for WISE high synchrotron peaked blazars given that almost all 2WHSP sources have WISE counterparts, except for 2WHSP J135340.2-663958. The catalog has been published in A&A (Chang et al., 2017 [30]: hereafter 2WHSP). The complete list of 2WHSP sources is available in electronic form at the CDS via anonymous ftp to cdsarc.u-strasbg.fr (130.79.128.5) or via `http://www.ssdc.asi.it/2whsp/`.

The 2WHSP has been used as a seed to HE and VHE observations to find new VHE detections or counterparts of VHE catalogs. Works like [13] and [103] have shown that the HSPs are good proposed sources for future γ-ray or VHE surveys and shown that, among the blazar family, HSPs may be the most possible counterparts for high energy neutrinos. There will be more details about the VHE and HSP blazars in Chapter 5.

2.3 Testing the completness of the 2WHSP

Apparently, there are still some good HSPs not selected in the catalog. When a source did not have Infrared data yet, obviously, it will not be selected to 2WHSP. For example, 5BZB J0403-2429 (Fig.2.4, left), which does not have infrared counterpart, but is a good extreme HSP in 5BZCat with *Fermi* counterpart (3FHL J0403.2−2428). The source is missed in the current version of the 2WHSP, simply because there is no infrared detection

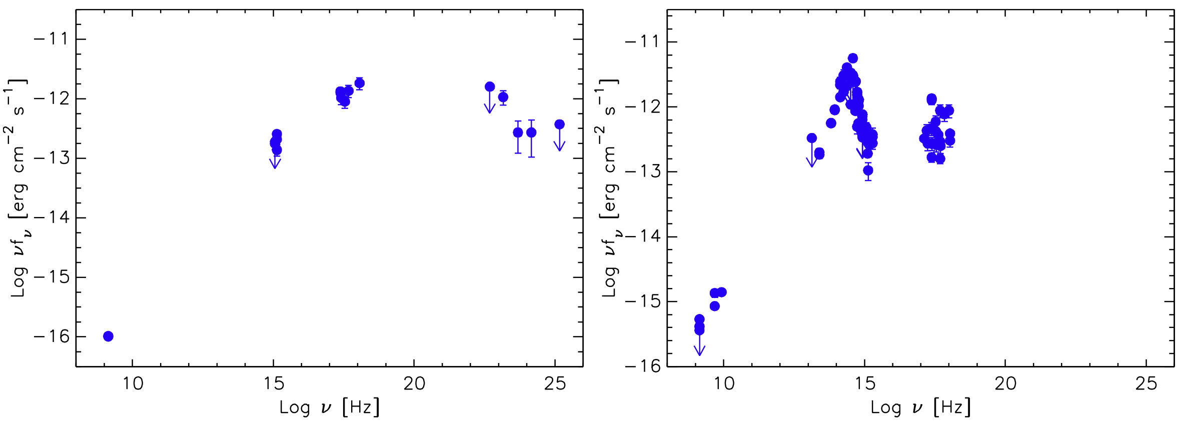

Figure 2.4: The SEDs of 5BZB J0403-2429 (Left) and 5BZG J0903+4055 (Right). The two sources were not selected to 2WHSP due to the slope criteria and no IR data.

for this source.

Moreover, for sources with bright host galaxy dominated in Infrared and optical will affect the $\alpha_{1.4\mathrm{GHz}-3.6\nu\mathrm{m}}$ to a smaller value and out of the radio-Infrared slope criterion. Like 5BZG J0903+4055 (Fig.2.4, right), which is not in our catalog since it violates the slope criteria owing to host galaxy contamination in IR; though it is another good 5BZCat HSP with X-ray counterpart originating from non-thermal emission. This would be an HSP worth concern as the X-ray emission from this source might vary with time, causing the ν_{peak} value change during the different period. v

Last but not least, some sources without radio data could be good HSPs with extreme ν_{peak}value. For instance, 6dF J0213586-695137 (Fig. 2.5), is clearly an HSP without radio counterpart except for upper limit from SUMSS (orange arrow), but it is an HSP with 3FHL counterpart. Apparently, this kind of very faint radio sources will not be selected when using current 2WHSP selection setup. The *Fermi* Pass 8 analysis was done for this sources, showing that the γ-ray fluxes are consistent with data from the lower energy bands. In the sense that this source is classified as an HSP, the γ-ray data suggests that its Inverse Compton emission will peak at TeV.

Besides the cases above, the sources with ν_{peak}close to 10^{15} Hz sometimes will out of the X-ray-Infrared slope criterion. Lots of sources with ν_{peak} on the border between ISP and HSP might be lost during the selection. Further discussions of the incompleteness owing to the inefficiency or criteria in finding sources in 2WHSP are written in later sections.

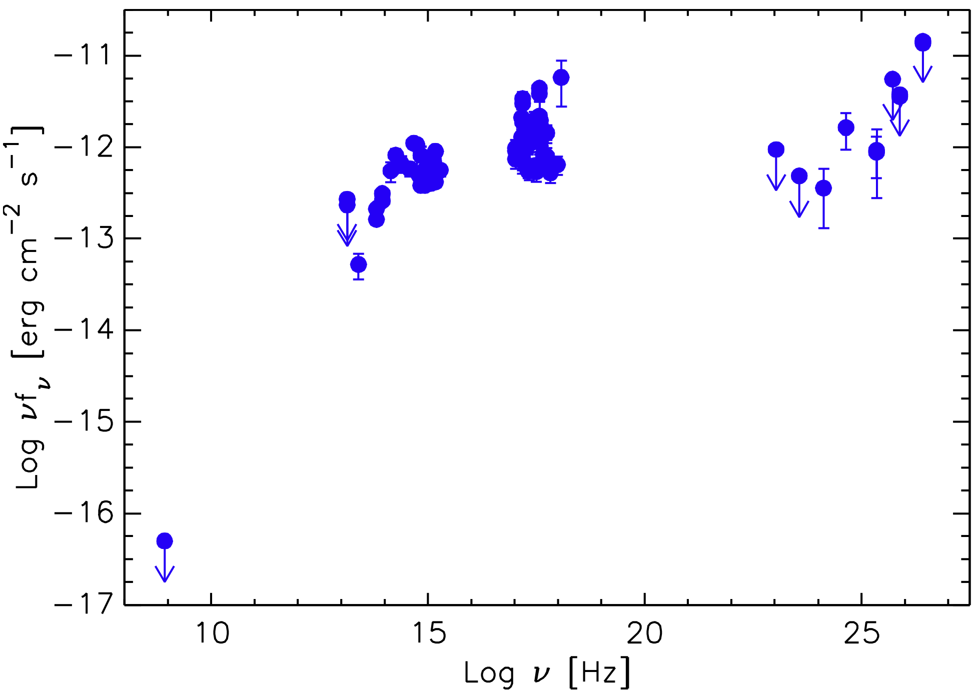

Figure 2.5: The SED of 6dF J0213586-695137. This source was missed in 2WHSP since there is no radio data available for the source.

2.3.1 Radio-X-ray flux plane

As that the 2WHSP are selected from various radio and X-ray catalogs and that the IR catalog usually has better sensitivity than the radio and X-ray ones, the inefficiency tests beginning with the constraints due to the radio and X-ray catalogs. Among the radio and X-ray catalogs been applied to the 2WHSP selection, NVSS and RASS have the largest coverage, thus in this section, all the test are focused on the subsample of 2WHSP sources with both NVSS and RASS counterparts. Figure 2.6 illustrates the radio - X-ray flux plane of 2WHSP, comparing with Sedentary and DXRBS. The corresponding proximate synchrotron peak frequency using extrapolation and the relationship between $\nu_{\rm peak}$ and X-ray to radio flux ratio (f_x/f_r) were estimated with the equation, $\nu_{\rm peak} = (f_x/f_r + 14.62) / 0.298$.

The black dotted line stands for X-ray to radio flux ratio that distinguishes between the low-energy peaked BL Lacs (LBL) and high-energy peaked BL Lacs (HBL), which is $f_x/f_r = 3.2 \times 10^{-12}$ erg cm^{-2} s^{-1} Jy^{-1} in [101, 99]. Three black dashed lines represent the flux ratios, from left to right, $f_x/f_r = 8 \times 10^{-14}, 3 \times 10^{-10}$, and 2×10^{-9} erg cm^{-2} s^{-1} Jy^{-1}, respectively. The ratio, 8×10^{-14} erg cm^{-2} s^{-1} Jy^{-1} ($\nu_{\rm peak} \approx 10^{5.1}$ Hz), is the minimum radio to X-ray flux ratio for both BL Lac objects and FSRQs ([99], based on the data

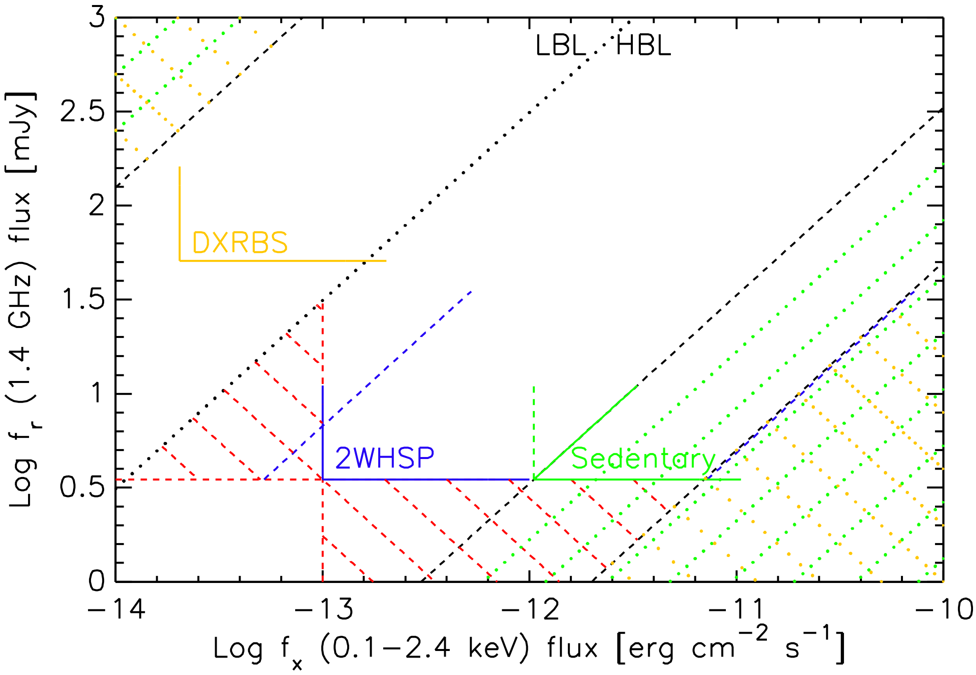

Figure 2.6: The sampling of the radio flux density - X-ray flux plane with the 2WHSP, Sedentary, and DXRBS. The black dashed lines are the slope limits for BL Lacs and FSRQs. The black dotted line is the flux ratio that separates the LBL and HBL. The green and yellow dotted lines mean the forbidden region for BL Lacs and FSRQ. The red dashed lines are the incomplete regions of 2WHSP.

from: [93, 128]). The maximum flux ratio for FSRQs is 3×10^{-10} erg cm^{-2} s^{-1} Jy^{-1} ($\nu_{\rm peak} \approx 10^{17}$ Hz), while that for BL Lacs is 2×10^{-9} erg cm^{-2} s^{-1} Jy^{-1} ($\nu_{\rm peak} \approx 10^{20}$ Hz) [101, 99].

Given that the minimum radio flux cut applied is 3.5 mJy for NVSS-RASS-2WHSP subsample, the radio limit of 2WHSP on this figure is set to 3.5 mJy. Besides, the 2WHSP X-ray limit is set to the minimum RASS flux value, $\approx 10^{-13}$ erg cm^{-2} s^{-1}, of the subsample. However, note that the true radio and X-ray flux limits of the whole 2WHSP catalogue is not 3.5 mJy and 10^{-13} erg cm^{-2} s^{-1} as there were cross-matched/internal cross-matched with several radio and X-ray catalogs, not only with the NVSS and RASS samples, to build the 2WHSP. Practically, the exact radio and flux limits of 2WHSP might be slightly smaller than the limits set here; there exits 2WHSP sources with radio flux $<$ 3.5 mJy and X-ray flux $< 10^{-13}$ erg cm^{-2} s^{-1}.

According to the Figure 2.6, the 2WHSP is not complete neither in radio nor in X-ray; the Sedentary is more complete than 2WHSP when selecting relatively extreme HBLs. For some sources with radio flux brighter than 3.5 mJy but X-ray flux fainter than

10^{-13} erg cm^{-2} s^{-1} (the red triangle region in Fig. 2.6), they are not selected to the current catalog as they are dim X-ray sources and are not detected by current X-ray surveys. On the other hand, some bright X-ray but faint radio sources (the red trapezoid region in Fig. 2.6) were missed; these sources are not included in today's large-area radio catalogs since their radio flux densities could even be less than 1 mJy. If there were enlarged the radio flux limit to $\approx$ 22 mJy, there will select all sources with radio flux larger than that; similarly, when setting the X-ray flux limit to a higher value $\approx 7\times\ 10^{-12}$ erg cm^{-2} s^{-1}, the sample becomes complete in X-ray. It is compatible with the radio and X-ray logN-logS results in the 2WHSP paper.

It is believed that the lost sources in red triangle region are principally lower $\nu_{\rm peak}$ blazars, while those in red trapezoid region are mainly higher $\nu_{\rm peak}$ blazars. The consequences of the slope criteria are the blue dashed lines displayed in Fig. 2.6, and the estimated lower and upper limits of f_x/f_r for 2WHSP are 1.490×10^{-11} erg cm^{-2} s^{-1} Jy ($\nu_{\rm peak} \approx 10^{14.2}$ Hz) and 2.063×10^{-9} erg cm^{-2} s^{-1} Jy ($\nu_{\rm peak} \approx\ 10^{19}$ Hz), respectively. The two 2WHSP slope criteria limits are estimated with the assumption that the average X-ray spectral slope is 0.9 and IR slope is 0.3. Further description about the conversion between the slope criteria in equation refeq:slope and f_x/f_r are in Appendix C.

Thus, to build an X-ray complete sample, one need deeper radio surveys and vice versa. Although the 2WHSP is not exactly a complete sample in radio, it is practically complete "thanks to" the slope criteria. The sources in red triangle region mostly are low synchrotron peaked blazars and are out of our slope criteria. Apart from that, there might miss more very faint radio sources with X-ray flux $\geq 10^{-13}$ erg cm^{-2} s^{-1} than expected; the red trapezoid might be extended down to become a triangle region.

The 2WHSP is far from completeness in X-ray, and there were lost lots of sources (in red trapezoid area) due to the flux limit from the radio surveys, like the Figure 2.5 shown. However, by examining all the possible blazar counterparts in γ-ray catalogs, there are able to find these sources with γ-ray emission and will not miss important HSPs that might be the seed for future VHE surveys. Another way to select more HSPs is to avoid using radio databases and cross-matching the X-ray catalogs with HE/VHE catalog; in doing so, we may find fainter radio sources and enhance the sample completeness in X-ray.

2.3.2 The slope criteria

To further understand the influences of slope criteria, they are discussed with a well-known host galaxy dominated HSP, Mrk 421 (2WHSP J110427.3+381230) in this section,

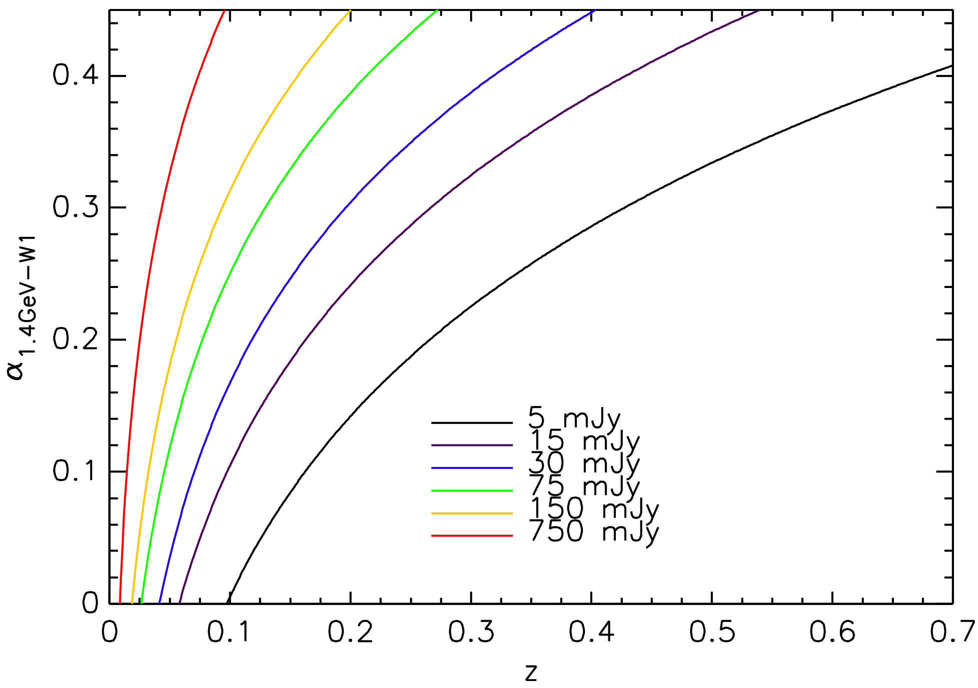

Figure 2.7: The radio-IR slope and redshift relationship under different fix radio fluxes for Mrk421.

under the hypothesis that the IR luminosity here is fixed to that of Mrk 421 as the luminosity of the host galaxy will not change much. Figure 2.7 shows the radio-infrared spectral slope with respect to redshift and different radio flux densities. Figure 2.8 illustrates the relationship between radio flux density and redshift under different $\alpha_{1.4\mathrm{GHz}-3.4\nu\mathrm{m}}$.

Both figures indicate that when the redshifts are low, only high radio flux density sources match the $\alpha_{1.4\mathrm{GHz}-3.4\nu\mathrm{m}}$ criterion, and vice versa. The radio flux density would be decreasing if the redshift is increasing. Once there were lower the $\alpha_{1.4\mathrm{GHz}-3.4\nu\mathrm{m}}$ to < 0.05, there may be able to select low redshift faint radio sources (the bottom left corner in Fig. 2.8). It is suggested that there were lost some nearby faint radio sources in 2WHSP due to $\alpha_{1.4\mathrm{GHz}-3.4\nu\mathrm{m}}$ criterion and host galaxy.

Fig. 2.7 also suggests that there exist such correlations between $\alpha_{1.4\mathrm{GHz}-3.4\nu\mathrm{m}}$ and redshift and between $\alpha_{1.4\mathrm{GHz}-3.4\nu\mathrm{m}}$ and radio flux density. It is known that all low $\alpha_{1.4\mathrm{GHz}-3.4\nu\mathrm{m}}$ sources are also nearby faint radio sources. There were intimated that the correlations might be bona fide; however, when the $\alpha_{1.4\mathrm{GHz}-3.4\nu\mathrm{m}}$ is higher, the correlated trends become not transparent. Besides, the average radio fluxes for 2WHSP is ≈ 25 mJy, average redshift is ≈ 0.3, and average $\alpha_{1.4\mathrm{GHz}-3.4\nu\mathrm{m}}$ is ≈ 0.3. From these values and according to Fig. 2.8, there were spatulated that the HSPs non-thermal emission averagely is ≈ 6 times brighter than the host galaxy emission.

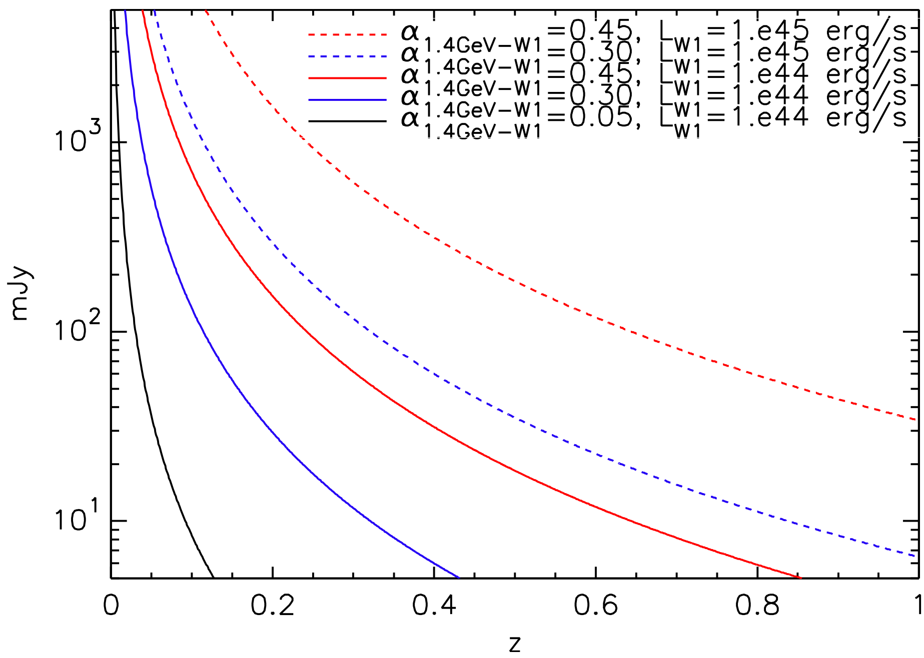

Figure 2.8: The radio flux with respect to z for a given radio-IR slope and IR luminosity of Mrk421. The IR luminosity is set to 10^{44} erg s^{-1} (solid lines), the typical luminosity of the host galaxy, or 10^{45} erg s^{-1} (dashed lines), 10 times the galaxy luminosity. In the dashed line cases, there were assumed that the galaxy is swamped by the non-thermal emission and the IR luminosity are brighter than typical elliptical galaxy luminosity by an order.

The relation among IR-X-ray slope, X-ray 1 keV flux, and redshift are shown in Figure 2.9, inferring that the bright X-ray sources located in the nearby universe, while the faint sources are more distant. Clearly, there were missed faint X-ray low redshift sources, and these lost sources are generally low synchrotron peaked sources, as low $\nu_{\rm peak}$ sources have fainter X-ray. Majority of these sources are also non-featureless sources, as the host galaxy contamination would induce large slope value. Apart from that, the mean radio flux density of low redshift sources is believed to be higher than that of the high redshift sources. To sum up, the faint X-ray and low redshift sources would easily be missed in 2WHSP, and these sources mostly are also bright radio low $\nu_{\rm peak}$ HSPs.

The low $\alpha_{1.4{\rm GHz}-3.4\nu{\rm m}}$ sources missed in 2WHSP are mainly host galaxy dominated but faint in radio. It is suggested that although those sources (might be low $\nu_{\rm peak}$ or high $\nu_{\rm peak}$) are with good redshift measurement, they are low radio flux sources due to the extremely low $\alpha_{1.4{\rm GHz}-3.4\nu{\rm m}}$. On the other hand, the low $\nu_{\rm peak}$ sources with low z, faint X-ray flux, and bright radio flux lost due to $\alpha_{3.4\nu{\rm m}-1{\rm keV}}$ might actually be high $\alpha_{1.4{\rm GHz}-3.4\nu{\rm m}}$ sources.

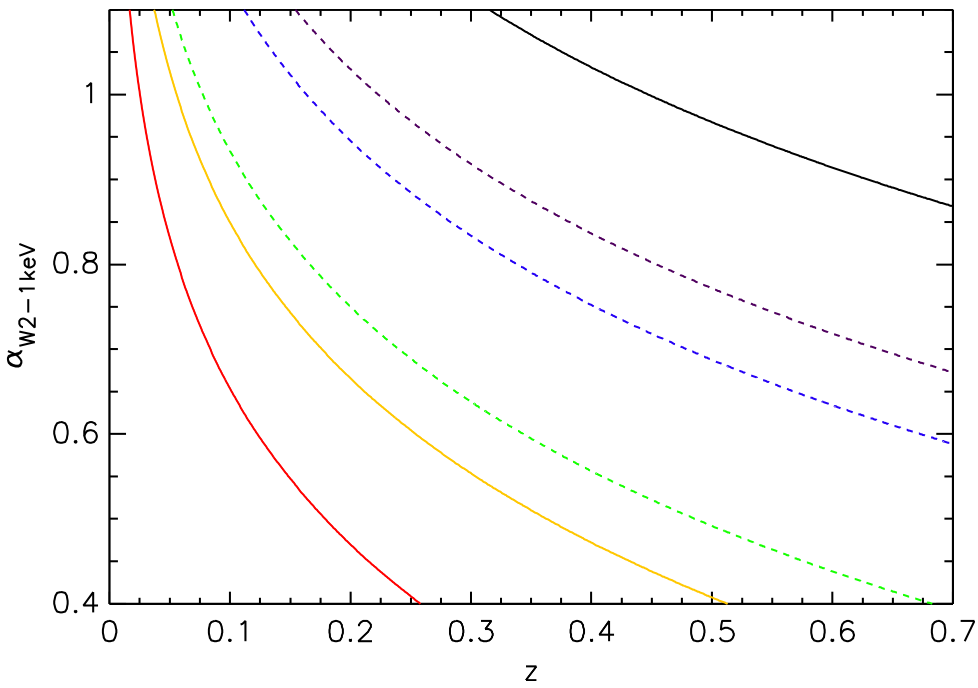

Figure 2.9: The IR-X-ray slope versus redshift with certain X-ray flux 1.01×10^{-12} (black), 3.03×10^{-12} (purple), 6.06×10^{-12} (blue), 1.52×10^{-11} (green), 3.03×10^{-11} (yellow), and 1.52×10^{-10} (red) erg s^{-1} Hz^{-1} cm^{-2}, for Mrk421.

Radio flux density (mJy)	Lower limit of z	Upper limit of z
3.5	0.151	0.987
5.0	0.128	0.854
7.0	0.109	0.745
10.0	0.093	0.644
15.0	0.077	0.544
20.0	0.067	0.483
30.0	0.055	0.407
50.0	0.043	0.327
70.0	0.037	0.283
100.0	0.031	0.242
300.0	0.018	0.147
1000.0	0.010	0.084

Table 2.2: The corresponding redshift range that agrees with the slope criteria with a certain radio flux density.

Note that for the same color lines in Fig. 2.7 and 2.9, the radio flux and X-ray flux they represent have the identical ratio with the radio and X-ray fluxes of Mrk 421. Table 2.2 illustrates the corresponding redshift range that will match the slope criteria for a given radio flux density. Unfortunately, the $\alpha_{4.6\nu m-1keV}$, are highly related to the synchrotron peak frequency. Here there were just displayed an approximately brief test using Mrk 421, with no consideration of various ν_{peak} values. The radio and X-ray fluxes here in the Figures also refer to Mrk 421; a 75 mJy source other than Mrk 421 might be with X-ray flux density $\leq 1.01 \times 10^{-12}$ erg s^{-1} Hz^{-1} cm^{-2}.

2.3.3 Concluding the lost sources in 2WHSP

In this subsection, there were concluded on the overall incompleteness to which the 2WHSP is subjected to and also on the nature of sources probably missed during the selection processes. Collective all of the evidence discussed in previous sections suggest that the 2WHSP is neither complete in radio nor X-ray; although it is close to a radio complete catalog. Because of the instrumental constrain, it is not able to select some faint X-ray or faint radio sources to the catalog; generally, they are not included in current large-area radio and X-ray catalogs. The missing faint X-ray sources mostly are higher synchrotron peaked blazars, while the lost faint radio sources mainly are lower ν_{peak} blazars.

Given that the sensitivity of X-ray surveys might not be the same on the whole sky, there were some faint X-ray sources lost, as the observed area of them are smaller than the bright X-ray sources. The faint X-ray sources typically are low ν_{peak}sources; therefore the sources missed are faint X-ray sources with low synchrotron peak frequency. Note that faint X-ray flux does not necessarily imply faint radio flux.

Furthermore, as section 2.3.2 depicts, there were not able to select some of the low redshift and faint X-ray sources with Synchrotron slope close to 10^{15} Hz. The faint X-ray low ν_{peak} HSPs with host galaxy spectral feature will tend to be rejected by the IR-X-ray slope criterion. Given that the radio flux densities of firm z sources will be higher than the others on average and that the sources with host galaxy contaminant are mainly nearby, there were some high radio fluxes, low ν_{peak}, and low z sources missed in 2WHSP.

From section 2.3.2, there were summarized that the losing of faint radio flux low redshift sources in 2WHSP ascribed to the radio-IR slope criterion and host galaxy. Both low ν_{peak} sources and high ν_{peak} sources will suffer this deficiency. The overall deficiency of the 2WHSP can be summarized in Table. 2.3.

Next, the selection bias of 2WHSP will also be concluded in this section. Fig. 2.7 and 2.8 indicate that high redshift and bright radio flux are the only two sufficient conditions for high $\alpha_{1.4\mathrm{GHz}-3.4\nu\mathrm{m}}$ sources. The Figures also suggest that low radio flux or low redshift are the necessary conditions for low $\alpha_{1.4\mathrm{GHz}-3.4\nu\mathrm{m}}$ sources. The three common trends of

	Low $\nu_{\rm peak}$ Sources
Instrumental constrain	faint radio sources
$\alpha_{\rm 1.4GHz-3.4\nu m}$ criterion	faint radio low z sources
$\alpha_{\rm 4.6\nu m-1keV}$ criterion	bright radio low z faint X-ray sources
RASS sensitivity map	faint X-ray sources
	High $\nu_{\rm peak}$ Sources
Instrumental constrain	faint X-ray sources
$\alpha_{1.4GHz-3.4\nu m}$ criterion	faint radio low z sources

Table 2.3: The general lost sources of the 2WHSP catalog.

2WHSP could be inferred as:

- Low $\alpha_{\rm 1.4GHz-3.4\nu m}$, low z, and low radio flux sources.
- High $\alpha_{\rm 1.4GHz-3.4\nu m}$, low z, and high radio flux sources.
- High $\alpha_{\rm 1.4GHz-3.4\nu m}$, high z, and low radio flux sources.

The first trend mainly contains host galaxy dominated sources. As the slope criteria do not allow us to select faint radio nearby source, some sources obey the first trend are probably missed during the 2WHSP selection procedure. Additionally, the host galaxy dominated sources are practically extended and easily be classified as radio galaxies. The majority of the second trend sources are high synchrotron peak, since the low $\nu_{\rm peak}$, firm z (relatively lower z), and bright radio sources would frequently be out of the IR-X-ray slope criterion. That is, there were missed some sources following the second trend in our catalog. Hence, it is suggested that the 2WHSP tend to select third trend sources, high $\alpha_{\rm 1.4GHz-3.4\nu m}$, high z, and low radio flux sources.

2.4 Adding "missing" sources

The 2WHSP catalog is close to complete; however as section 2.3 described, there are still some good HSPs are missing in the catalog. Apparently, it is necessary to add more source to the 2WHSP to establish a more complete catalog. Among the factors that cause the deficiency of 2WHSP, the slope criteria are the most relevant reason; also, as Fig.2.4 shown, a good HSP does not necessary detected by WISE. To "find out" those missing sources, there were freed the slope criteria, not demand all candidates to have an IR counterpart, and applied only X-ray to radio flux ratio. The first step to increase the completeness of the 2WHSP is cross-matching the RASS and NVSS catalogs with radius

0.8 arcmin and choosing sources with X-ray to radio flux ratio larger than 9×10^{-11}. Sources that already in the 2WHSP catalog are ruled out using cross-matching radius 0.3 arcmins. There are $\approx$ 3000 candidate sources additional to the original sample to be examined.

To narrow down the number of candidates and make the selection become more effective, the further cross-matching of these 3000 sources with 5BZCat [82], XMMOM [105], and *Fermi* 3FHL [135], individually, are done. The cross-matched radii for 5BZCat, XMMOM, and 3FHL are 0.3, 0.3, and 20 arcmin, respectively. After the cross-matching, the number of pre-selected candidates reduces to $\approx$ 300, and around 60 of them are good HSPs or HSP candidates.

Note that a good HSPs, especially the one with γ-ray detection, is not necessary with both radio or X-ray data, as Figure 2.5 illustrated. Missing HSPs with γ-ray emission is not what has been expected for the catalog; however, there are still some sources out of the radio-X-ray flux ratio criteria or out of RASS/NVSS catalog but are detected in γ-ray. To find these missing sources, a careful examination of the 3FHL detected sources and their counterparts were performed. In total, $\approx$ 160 missing sources with 3FHL counterparts were further added to the catalog. These sources are either without radio or X-ray data or have special X-ray to radio flux ratio.

Apart from the *Fermi* 3FHL catalog, the FL8Y catalog [4] also detected some good HSP candidates but not in the 2WHSP yet. Thus, there were checked each FL8Y sources with hard γ-ray photon index ($\Gamma < 2.0$) that are not in the 2WHSP as well; 120 HSP blazars/candidates out of $\approx$ 400 sources were added to the catalog. As expected, the FL8Y sources selected here mostly do not have radio or X-ray detection yet.

While adding and cleaning the sources for 2WHSP catalog, there is a tool, VOU-Blazars, being developed (See Chapter 4). There were 10-20 good HSP candidates selected to the catalog with VOU-Blazars; given that the tool is still under development, there will be more new HSP candidates found in future. Most of these sources have X-ray detections only from Swift or 3XMM, which the latest data are not always available from the SED tool, thus lost X-ray data to be selected by all of the above procedures. However, with VOU-Blazars, there were more data could be retrieved and more HSP candidates could be found.

Eventually, there are 379 new sources apart from the 2WHSP catalog selected after all the processes above. The comparison between the new sources and the 2WHSP sources

[4] https://fermi.gsfc.nasa.gov/ssc/data/access/lat/fl8y/

are shown bellow.

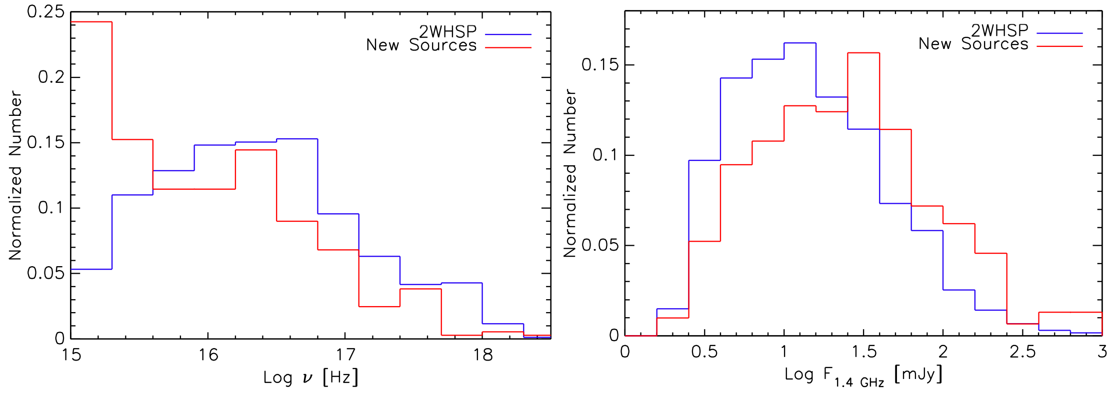

Figure 2.10: The $\nu_{\rm peak}$ (left) and radio flux density (right) distribution of the new sources and the 2WHSP.

Figure 2.10 clearly depicts that most of the new sources added in this section are low $\nu_{\rm peak}$ sources and shows that the new sources averagely have higher radio flux, compared to the old 2WHSP sample. Note that the majority of the new sources are with γ-ray counterpart, which might affect the radio flux density distribution as well, leading to a sample with more bright sources.

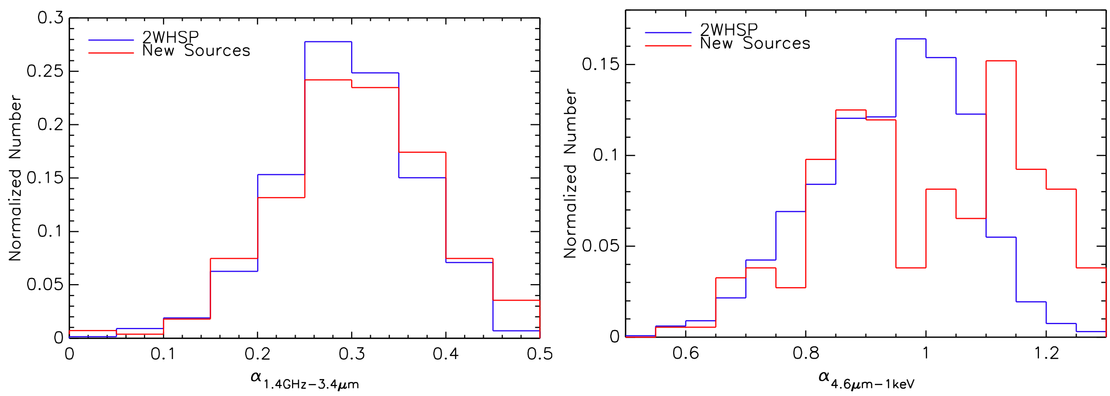

Figure 2.11: The radio-IR slope (Left) and the X-ray-IR slope (Right) distribution of the new sources and the 2WHSP.

It is illustrated in Figure 2.11 that there are several low $\alpha_{\rm r-IR}$ sources, most are host galaxy dominated, found in the new sample. The new sample comprises some sources with relatively high $\alpha_{\rm r-IR}$ as well. Moreover, the Figure also indicates that there are more high $\alpha_{\rm IR-X-ray}$ sources selected in the new sample, suggesting that relaxing the slope criteria works for selected more new HSPs to the catalog.

Figure 2.12 suggests that there is no big difference in X-ray flux between the new sample and 2WHSP; however, it shows that the new samples generally have lower z than

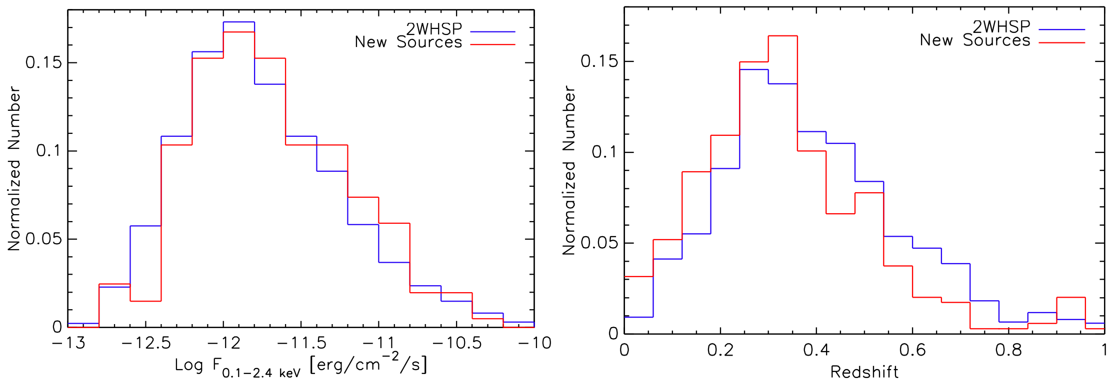

Figure 2.12: The X-ray flux density (Left) and redshift (Right) distribution of the new sources and the 2WHSP.

the old one. Majority of the high z sources are already in 2WHSP, implying that most of the new sources added here are not non-thermal dominated.

In conclusion, compared with the sources in 2WHSP, there were more low $\nu_{\rm peak}$ sources, more bright radio sources, and more low redshift sources added, meaning that after removing the slope criteria, there were more sources with $\nu_{\rm peak}$ on the border of the ISP and HSP selected. Given that there are no slope criteria applied anymore and that most of the new sources here are with $\nu_{\rm peak}$ around 10^{15} Hz, from the Table 2.3, sources with low redshift, low X-ray flux, and bright radio flux density lost due to X-ray-IR criterion may be selected to the catalog now. The new sample does fill some of the missing sources (most are high $\alpha_{\rm IR-X-ray}$ low $\nu_{\rm peak}$) from slope criteria. Moreover, there are less host galaxy dominated sources in the new sample than expected.

2.4.1 Redshift estimations

It is known that some BL Lacs are not easy to measure the redshift as there are little features on their optical spectrum. Some HSP sources lack redshift due to their completely featureless optical spectrum; however, from their SED, most of the time, the thermal emissions from the host galaxy still could be recognized. Even though the host galaxy features could not be seen in optical, sometimes, they could be told in IR. Therefore, there were estimated the photo-z for sources without optical spectrum yet or with featureless spectrum, when the host galaxy contributions of these sources could be distinguished from the non-thermal emission on SED. In this cases, the reason which causes the featureless spectrum is inconspicuous 4000Å calcium break, synchrotron emission has similar flux density with thermal component, with blue part of the optical data are from non-thermal while red part of that is from the host galaxy. By fitting the host galaxy contributions using CWW elliptical template (Coleman, Wu, and Weedman 1980)[31] and assuming that the luminosity of the elliptical galaxy is the same, the approximately photometric redshift could be estimated for those sources.

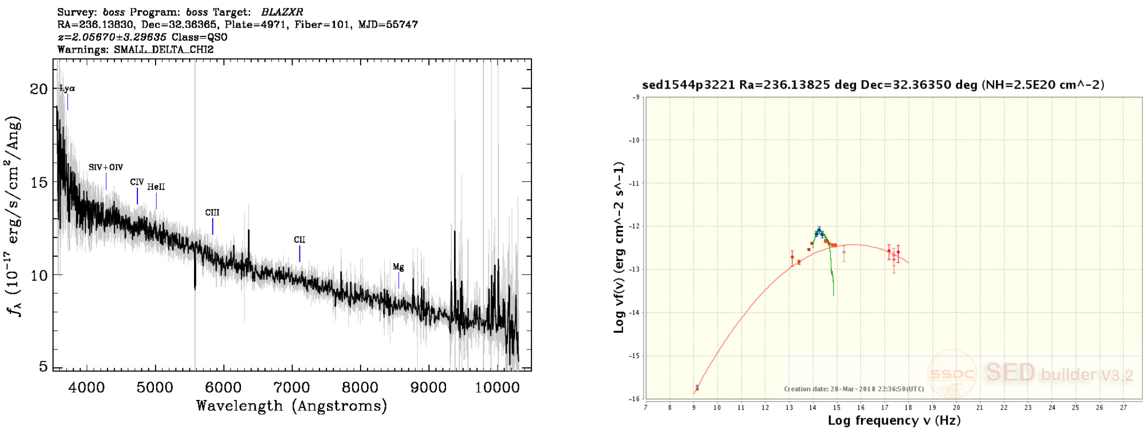

Figure 2.13: Illustrated of the photo-z. Spectrum (Left) and SED (Right) of J154433.1+322148.

The evaluation of photo-z is depicted in Figure 2.13 with an example source J154433.1+322148. Clearly, from the SED, host galaxy emission of this source still could be distinguished even it with featureless optical spectrum like the one observed by SDSS Dr14 [20, 3]. According to the SED (right of the Figure 2.13), the 2MASS data (blue points) and the WISE W1 and W2 data (dark purple points) of the source are from its host galaxy instead of non-thermal processes. By fitting the 2MASS, W1, W2, and part of SDSS data using the elliptical model from SSDC SED builder (the green line on the SED), the photo-z is estimated with 0.32.

For the other sources with non-thermal dominated in all wavelength on SED and with featureless spectrum, as in 1WHSP, there were estimated lower limit redshifts for these sources. Assuming that in the optical band the host galaxy is swamped by the non-thermal emissions and leaves no imprint on the optical spectrum when the observed non-thermal flux is at least ten times larger than the host galaxy flux, there were used the distance modulus (for details, see Eq. 5 in 1WHSP paper) to calculate the lower limits redshifts. Note that, some of the redshifts obtained from the several references and are listed accordingly in the final sample.

Apart from that, some of the sources in the catalog still do not have redshift measurements/estimations yet, either photo-z or spectral-z. For those non-thermal dominated sources but without available optical spectrum yet, the redshift is left to 0. It is supposed that most of those without spectral observations are featureless or too faint in optical; the redshift of these sources is much higher than the observed value. According to [60], the average predicted redshift of BL Lacs with featureless spectrum is around 1.2. Moreover, according to Figure 9 of 2WHSP paper, the sources with featureless spectra might be much more distant than we thought. Therefore, there were assumed the mean redshift of those sources is 1.2 and randomly assigned them redshift values assuming a Gaussian distribution with mean value 1.2 and sigma 0.3 in next Chapter.

2.4.2 XRT data analysis with Swift Deepsky pipline

During the selection of 3HSP, there were 210 sources proposed to Swift (50 from 1WHSP, 80 from 2WHSP, and 80 from 3HSP), 190 out of 210 are in 3HSP. Before March 2018, 151 of them have been observed by XRT team. For these 151 sources, there were running the Swift DeepSky pipline[5], which provides deep observations of the X-ray sky seen by the Swift XRT via contaminating all the observations up to date.

After analyzing the data with Swift DeepSky, there were 147 new detections at the 3HSP position out of 151 observations. Around 97% of the proposed 3HSPs with detections, proving that with multi-frequencies analysis HSP sample, it is more effective to find potential X-ray sources. There were re-estimation the $\nu_{\rm peak}$ of the 3HSPs with these 147 detections, as the pipeline provides more dedicated analysis in X-ray. The four sources without detections might be due to a non-enough exposure time. The 147 sources are listed in table G.3, and the rest no-observation or no-detection sources are also shown in Appendix G.3.

2.5 The 3HSP catalog - the most complete HSP catalog nowadays

Compared with 2WHSP, there are totally 379 new HSP blazars/candidates selected in section 2.4. Furthermore, with new optical spectrum or XRT data, 58 sources in 2WHSP were eliminated since these sources are either ISP/FSRQ or part of X-ray extended cluster. In total, the new version of the catalog contains 2012 sources with 88 source close to Galactic plane $b < |10|^{\circ}$. This new 2WHSP catalog is named 3HSP, which means the third catalog for HSP blazars. Among these 2012 sources, 1633 sources are also in 2WHSP, 999 have *Fermi* counterpart.

[5]https://github.com/chbrandt/swift_deepsky

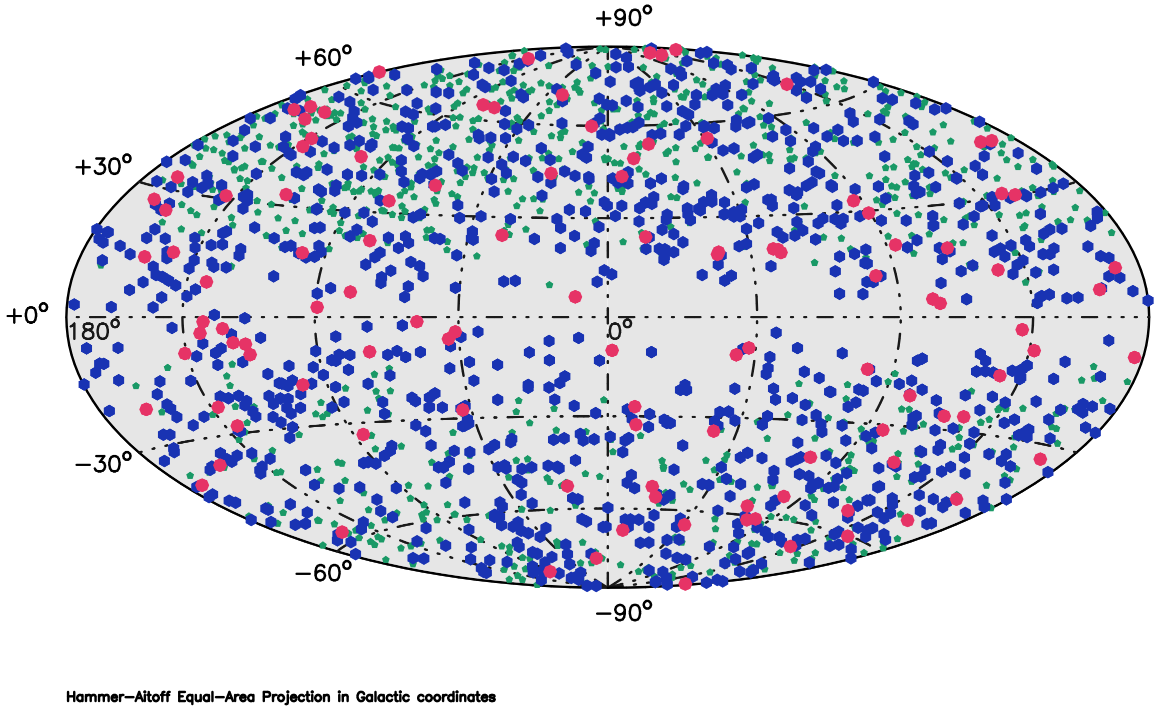

Figure 2.14: Aitoff projection of 3HSP sources. Figure credit: Paolo Giommi. The Galactic coordinate system are applied here. Red, blue and green points represents FOM > 1.0, $0.2 <$ FOM < 1, and FOM < 0.2, individually.

The procedures of building the 3HSP catalog are concluded as

1. Cross-matching radio-IR-matched sample with various X-ray catalogs
2. Applying slope criteria and selecting sources with log $\nu_{\text{peak}} \geq 15$ Hz
3. Checking miss source with *Fermi* 2FHL and TeVCat $\Rightarrow$ **2WHSP**
4. Cutting NVSS-RASS matched sources with flux ratio $\geq 9 \times 10^{-11}$
5. Cross-matching with 5BZCat, *Fermi* 3FHL, and XMMOM
6. Adding more hard-photon-index good HSPs from 3FHL and *Fermi* 8 years catalogs
7. Applying Swift DeepSky and VOU-Blazars to refine the ν_{peak} and find more sources
8. Cleaning 2WHSP sources, especially the one with no *Fermi* detections

The 3HSP catalog are listed in Appendix G.5 and the electronic form of the 3HSP blazars table is available via `http://wwwdev.asdc.asi.it/3hsp/`. In the table, there were ν_{peak} value, redshift, γ-ray counterpart, 2WHSP counterpart, BZCat counterpart, and Figure of Merit (FOM) presented. The FOM value, defined in [14] as the ratio between the synchrotron peak flux $\nu_{\rm peak} f_{\nu_{\rm peak}}$ of a given source and that of the faintest blazar in the 1WHSP sample that has already been detected in the TeV band was introduced to provide a simple quantitative measure of potential detectability of HSPs by TeV instruments (See 1WHSP paper and Chapter 5 for more detail).

There were flags for $\nu_{\rm peak}$ and redshift value which also are listed in the table. For flag 1, 2, and 3 means firm estimation, uncertain value, and lower limit, individually. Two extra flags, 4 and 5, are applied for redshift, and which represents that the redshift is photo redshift as that could not be measured from optical spectrum. The difference between these two flags is that sources with flag 4 have optical spectrum while with flag 5 has no available spectrum yet. Like the Figure 2.13 illustrated, flag 4 sources are with featureless spectrum but the non-thermal emissions are not totally overwhelmed by the host galaxy, thus the photo-z still could be estimated from IR data or part of the optical data on SED. Redshift flag 3 (upper limits) sources also with featureless spectrum; however, from their SED, the Synchrotron radiation swamp over the host galaxy emission and left no host galaxy "clue" on SED.

There are still some non-thermal sources without optical spectrum observation yet, and the redshift for them remain 0 with flag 0. Only 12.72% of sources in 3HSP does not have estimated redshift value. To sum up, for no optical spectrum sources, there were flag 0 or 5; for non-thermal dominated sources, there were flag 0 or 3; for featureless optical spectrum, there were flag 3 or 4; and for photo-z, there were flag 4 or 5.

The 3HSP catalog is currently the largest and probably most complete HSP catalog, and the statistical properties, such as $\nu_{\rm peak}$ distribution, completeness, evolution, bias, et cetera, of the 3HSP is worth testing. With multi-messenger analyzed HSP catalogs like 3HSP, it is possible to find more VHE sources, as HSPs are suggested to be one of the few kinds of objects that emit the most energetic radiation. Chapter 3 will describe various properties, evolution, deficiencies, and biases for 3HSP and Chapter 5 will show the importance, applications, and connections of 3HSP with very high energy astronomy.

Chapter 3

Statistical Properties of the HSP Blazars

The demographic and evolution of blazars have been a debating issue for a long time. The existence of the blazar sequence also is one of the controversial topics among blazars. In this chapter, with largest ever HSP blazar catalog, the overall properties of the 3HSP will be discussed thoroughly. There were two different 3HSP subsamples, 3HSP-NVSS-RASS, 3HSP-NVSS-Fermi considered in this chapter as well, cutting the 3HSP with radio (NVSS) and with X-ray (RASS) or γ-ray (FL8Y). The 3HSP-NVSS-RASS subsample includes 1247 sources, while the 3HSP-NVSS-Fermi subsample has 727 HSP candidates; the whole 3HSP catalog contains 2012 sources in total. These cut catalogs are built to construct more complete subsamples, avoiding the missing sources due to instrumental constrain. Note that all these two subsamples are independent; the source detected by RASS does not imply the detection in *Fermi*.

3.1 General properties of the 3HSP catalog

3.1.1 Synchrotron peak

The $\nu_{\rm peak}$ distributions of the 3HSP sources with three different samples are shown in Fig. 3.1. For the whole sample, the peak of the distribution locates at $\approx 10^{16.3}$ Hz and not at the threshold of $\nu_{\rm peak} = 10^{15}$ Hz used for the sample selection. This is very likely due to the incompleteness of the sample near the $\nu_{\rm peak}$ border for HSPs, as the selection criteria in Chapter 2 were tuned to avoid too large an LSP contamination. The distribution is similar to that of the 1WHSP sample and of the subsample of HSP sources in the 5BZCat.

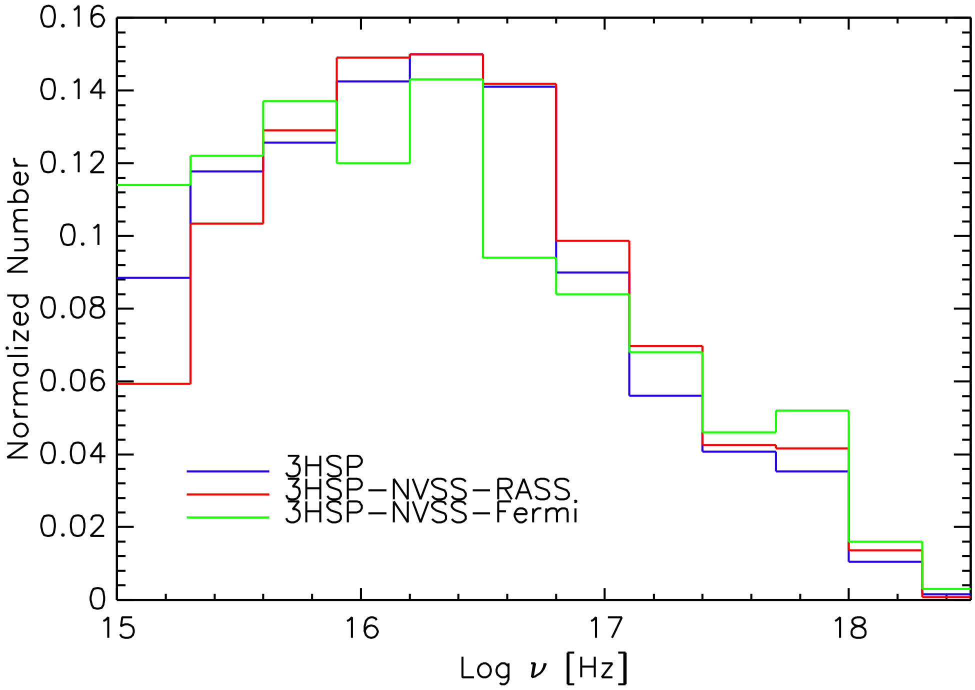

Figure 3.1: $\nu_{\rm peak}$ distribution between 3HSP and 3HSP subsamples. The different color lines mean different subsample. The samples are independence.

When compared with other catalogs of extreme blazars, the peak value of the $\nu_{\rm peak}$ distribution of our sample is a bit lower. For example the Sedentary and the [73](hereafter K13) catalogs have peak values $\approx 10^{16.8}$ and $\approx 10^{16.7}$ Hz, respectively. This difference results from the criteria and different selected methods applied. The Sedentary and [73] catalogs, for example, were tuned to select sources with relatively large $\nu_{\rm peak}$ values. Note that the $\nu_{\rm peak}$ of some 3HSP sources is particularly high, with values $\gtrsim 10^{18}$ Hz, which is especially crucial for VHE astronomy, and are described in section 5.1.1.

Sometimes, the severe variability of HSPs may result in displacements for $\nu_{\rm peak}$in different phases, such as MRK501 (See Fig. 5.3); not to mention that the intense variability will make the $\nu_{\rm peak}f_{\nu_{\rm peak}}$vary by an order of 1-2 or even worse. In these cases, there were fit the $\nu_{\rm peak}$and $\nu_{\rm peak}f_{\nu_{\rm peak}}$with the mean values to estimate the proper values for the synchrotron component averagely, avoiding having extreme values for the synchrotron peak and reduce the effects of variability.

The green lines in Figure 3.1 suggests that the subsample cut with *Fermi* catalogs are more complete in $\nu_{\rm peak}$ than the whole sample, while the blue lines indicate that a RASS cut subsample is less complete than the entire 3HSP catalog. Obviously, the 3HSP is not complete for lower $\nu_{\rm peak}$ sources, owing to those sources may have relatively faint X-ray flux, radio flux, or γ-ray flux to be detected by current instruments (See section 2.3.1 for more details). Subsamples with flux cut are expected to solve this problem; however, it seems worse for X-ray cut sample. The problem may come from the RASS catalog.

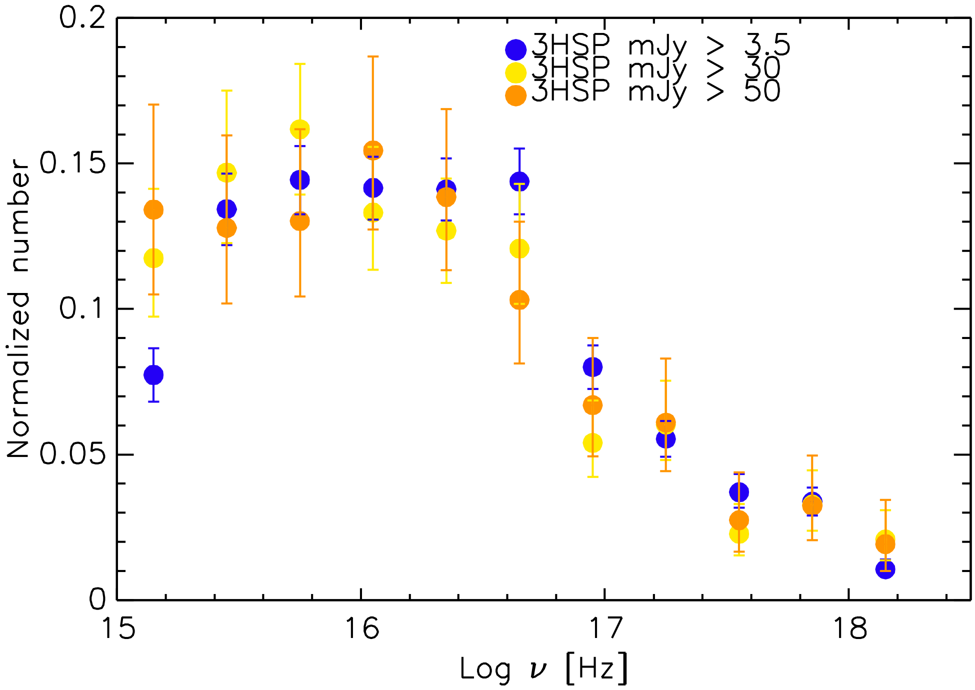

Figure 3.2: Calibrated ν_{peak} distribution for X-ray cut subsample with different mjy cuts.

The sensitivities of a telescope or a survey may not be the same everywhere in the sky, like ROSAT survey; especially, only a small fraction of sky is actually observed with the highest sensitivities. Given that fainter sources need better sensitivities or more exposure time to be detected by the telescope and that for RASS catalog, there are only a few degrees in the sky to have deep enough sensitivity to detected faint X-ray sources, causing that some of the faint X-ray sources might be lost. Clearly, area calibrations need to be done before comparison general properties for RASS selected sample in order to get reasonable results, considering the observed area of each source according to the RASS whole sky sensitivity map [141, 142]. The RASS detected sources should be counted regarding the survey coverage area, counting the source in same degrees of the area; otherwise, there may underestimate the number for the faint sources.

It is expected that after the calibrations with the observed area for X-ray selected sample, the radio-X-ray cut subsample will be more complete in ν_{peak} than the whole 3HSP catalog. As Figure 3.2 illustrates, there are more low ν_{peak} sources, as most of them are with faint X-ray flux than in Figure 3.1. It seems that there are still some sources with ν_{peak} close to the threshold miss for the bright sources in the double cut subsample, suggesting that the incompleteness probably results from the slope criteria or flux ratio criteria applied to distinguish between ISP and HSP. The figure also suggested that 3HSP subsample with both radio and X-ray cuts should be complete when $\nu_{\rm peak}$ larger than 10^{16} Hz.

3.1.2 Flux

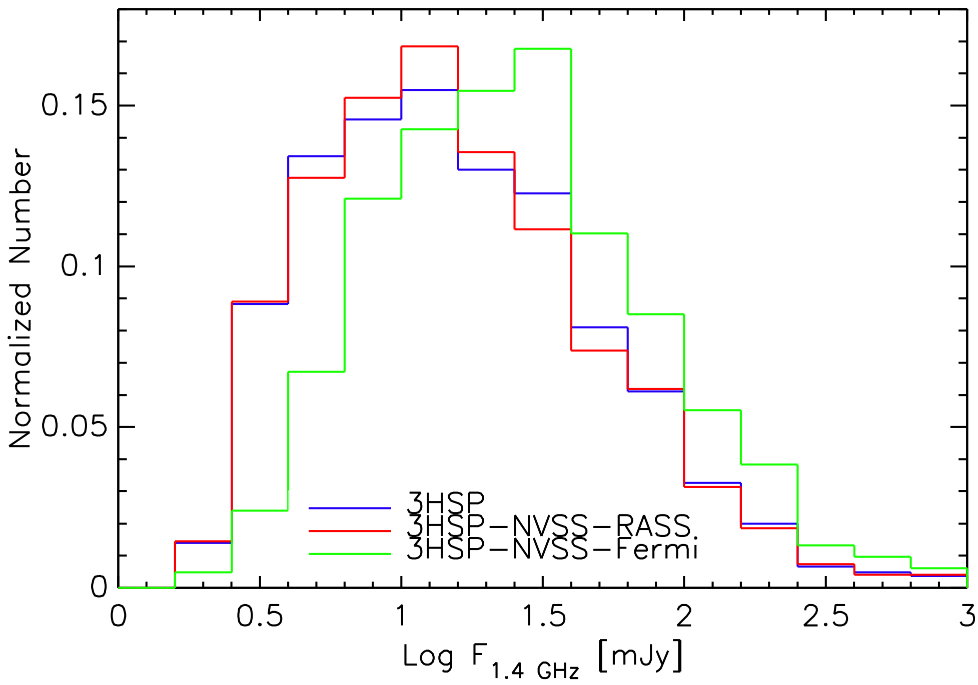

Figure 3.3: Radio flux density distribution between 3HSP and 3HSP subsamples.

Next, distribution of the radio flux density for 3HSP sources is depicted in Figure 3.3. Like the last subsection, there are 3 different samples shown in the Figure. The Figure indicates that all the threes subsample are not complete in radio. The peak of the distribution for all 3HSP sources is at around 25 mJy, similar to the X-ray-radio cut subsample, while that for γ-ray-radio selected subsample is higher. It seems that the *Fermi* selected subsample in averagely are brighter in radio than the whole 3HSP sources, may resulting from the constraint of *Fermi* sensitivity.

The X-ray cut sample is expected to be more complete in radio after the calibration for RASS observed area, and Figure 3.4 is the distribution of radio flux density for radio-X-ray selected subsample with area calibration. Obviously, there are many more faint sources "appear" after considering number count with the same area. From the Figure, the double cut subsample are very close to complete when the radio flux density $F_{1.4\ \rm GHz} \gtrsim 6$ mJy; however, comparing with the distribution from Sedentary, the slope is flatter. There still

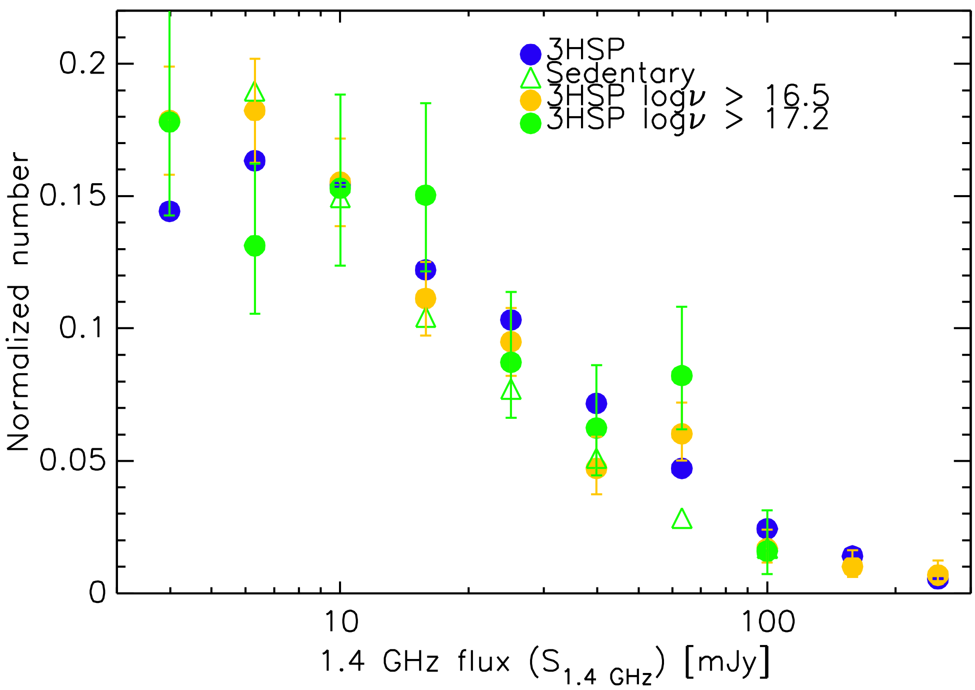

Figure 3.4: Radio flux density distribution with different $\nu_{\rm peak}$ cuts.

some sources with $F_{1.4\ \rm GHz}$ between 6 to $\approx$ 25 mJy lost for the X-ray selected sample, implying that the 3HSP is not complete unless the radio flux is brighter than 25 mJy. The figure also shows that the subsample is not complete even for higher $\nu_{\rm peak}$ cut, some faint radio sources with higher $\nu_{\rm peak}$ values are not selected to 3HSP. Those relatively high $\nu_{\rm peak}$ sources might be lost due to evolution since there was already radio cut applied for the subsample and it is not expected to loss high $\nu_{\rm peak}$ sources.

Figure 3.5 is the RASS flux distribution for X-ray and radio cut subsample after the RASS coverage calibration. All the subsample are far from complete in X-ray as these faint sources in X-ray mostly with relatively lower $\nu_{\rm peak}$ value; low $\nu_{\rm peak}$ sources, especially the ones close to the $\nu_{\rm peak}$ threshold, might not be selected due to slope/flux ratio criteria. It is suggested from the Figure that the higher the $\nu_{\rm peak}$ cut, the less the faint RASS flux sources, resulting from the selection effect that it is more likely to find high $\nu_{\rm peak}$ sources for an X-ray selected sample.

3.1.3 Redshift

Fig. 3.6 shows the redshift distribution for the whole 3HSP sample, which peaks just above 0.25. For all 3HSP sources, $\langle z_{all} \rangle = 0.363 \pm 0.004$; for firm redshift 3HSP sources, $\langle z \rangle = 0.311 \pm 0.007$. Clearly, sources without firm redshift are, on average, farther away than sources with firm redshift. That is, the redshifts of distant sources are not easy

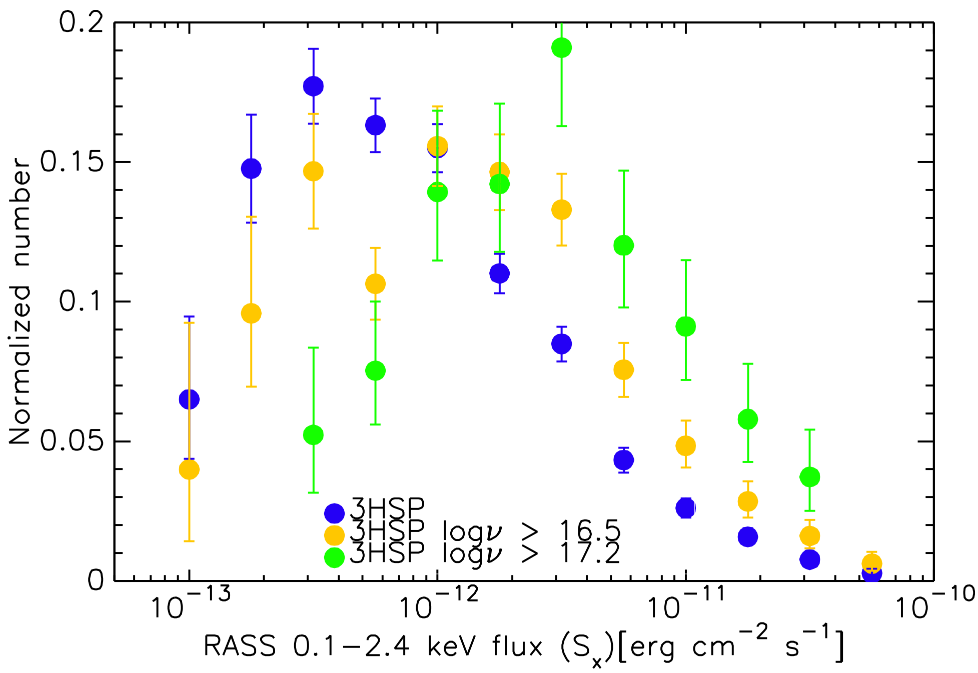

Figure 3.5: RASS flux distribution with different $\nu_{\rm peak}$ cuts.

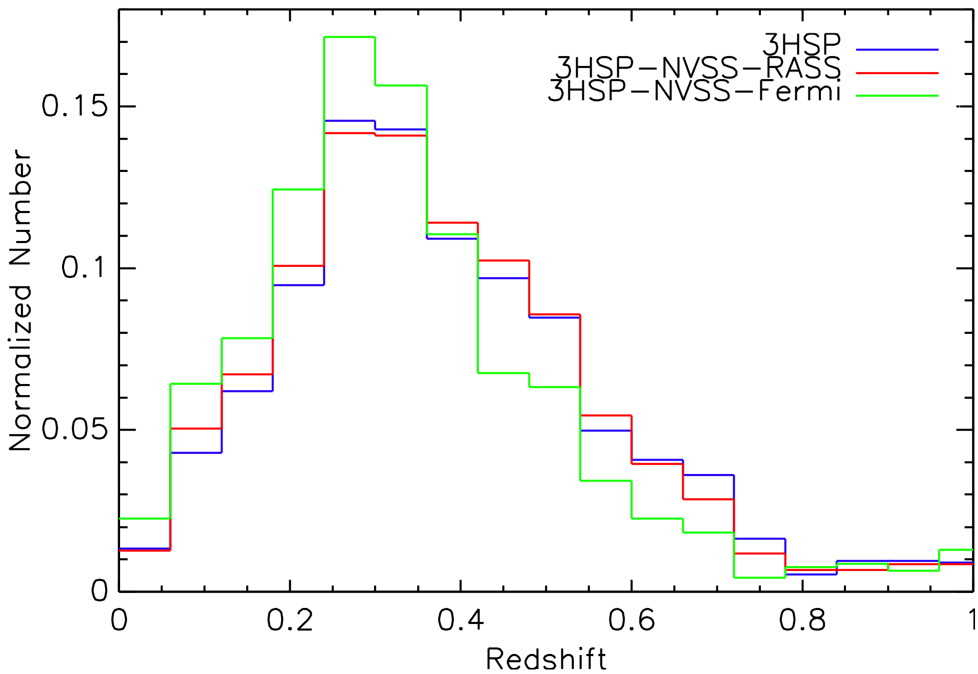

Figure 3.6: The redshift distribution between 3HSP and 3HSP subsamples.

to estimate since the optical spectra of far and bright blazars usually are dominated by the non-thermal emission. High redshift sources in flux-limited samples tend to have featureless optical spectra as those sources usually have brighter luminosity in average and the host galaxy contribution is overwhelmed by the synchrotron emission. [60] have predicted that the redshift distribution of BL Lacs without redshift in radio flux-limited surveys will peak around $z_{predict} \approx 1.2$. The results again suggest that source with only lower limit redshift, or without redshift, could be much further away than objects with measured redshift.

Considering only sources with firm z values, the redshift distribution of 3HSP sources is similar but not identical to other HSP catalogs/subsamples. The average redshift of the 1WHSP catalog is $\langle z_{1whsp} \rangle = 0.306$, that of the subsample of HSPs ($\nu_{\rm peak} > 10^{15}$ Hz) in 5BZCat is $\langle z_{bzcat} \rangle = 0.294$, that of the Sedentary sources is $\langle z_s \rangle = 0.320$, and that of the K13 catalog is $\langle z_k \rangle = 0.289$. The differences between may come from, for instance in K13, the redshifts range is $0.031 < z_k < 0.702$ while, in 3HSP, there were selected several sources with relatively high redshift ($z > 0.7$) that are not in previous catalogs.

Comparison of redshift distribution between 3HSP and the subsamples are shown in Fgiure 3.6. It seems that there are no big differences in redshift between whole 3HSP and X-ray subsample, while for *Fermi* cut sample, the average redshift is lower, suggesting that most of the sources with high z may not be detected by *Fermi* yet. Given that high redshift sources typically with lower flux, those sources might be fainter than the *Fermi* limit.

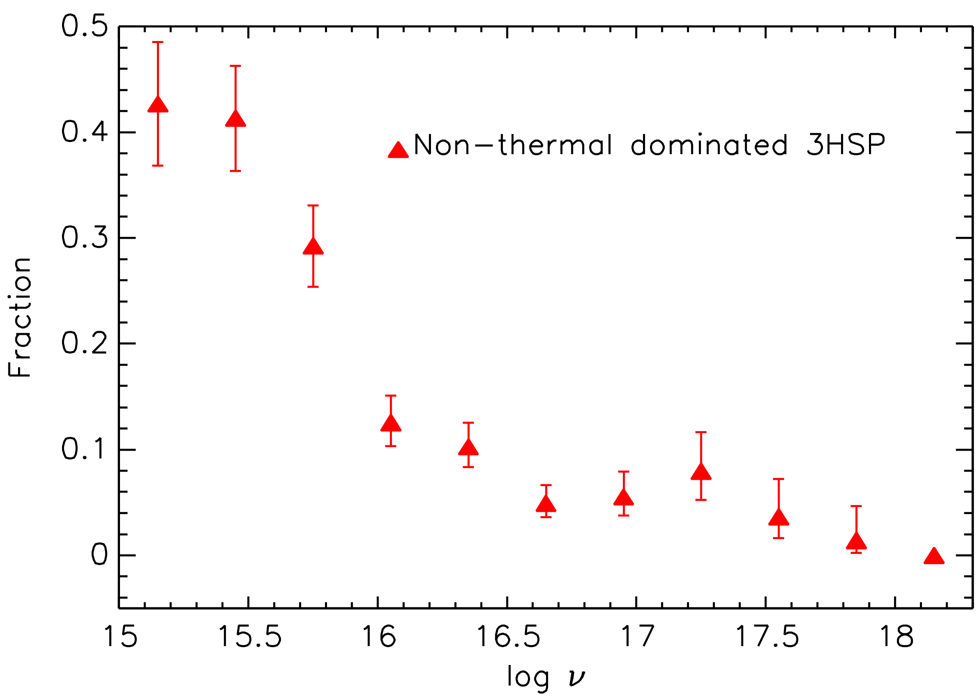

Figure 3.7: Fraction of non-thermal dominated sources w.r.t. $\nu_{\rm peak}$.

Figure 3.7 suggests that most of the non-thermal dominated sources are with relatively lower $\nu_{\rm peak}$. However, it is believed that the opportunities to find a non-thermal dominated sources among low $\nu_{\rm peak}$ HSPs and high $\nu_{\rm peak}$ HSPs are same. The tread may result from several facts. First of all, there are less/no high luminous high $\nu_{\rm peak}$sources in 3HSP, implying that the high $\nu_{\rm peak}$ sources may have totally different evolution properties than low $\nu_{\rm peak}$ sources. It is not expected to lose high $\nu_{\rm peak}$ sources with such bright luminosity, so the only explanation for this scene is that there are no such bright high $\nu_{\rm peak}$ sources, at least it is not easy to find them than expected. Another fact from Figure 3.7 is that there are some low luminous low $\nu_{\rm peak}$ sources missed in 3HSP. As there were discussed before, the 3HSP catalog loses some low $\nu_{\rm peak}$ faint sources due to flux ratio criteria. Note that since there are more low $\nu_{\rm peak}$ sources with no available optical spectra than high $\nu_{\rm peak}$ sources and since the mean redshift value assumed for sources without spectra is higher than the observed one, there exists an artificial anti-correlation between synchrotron peak and z.

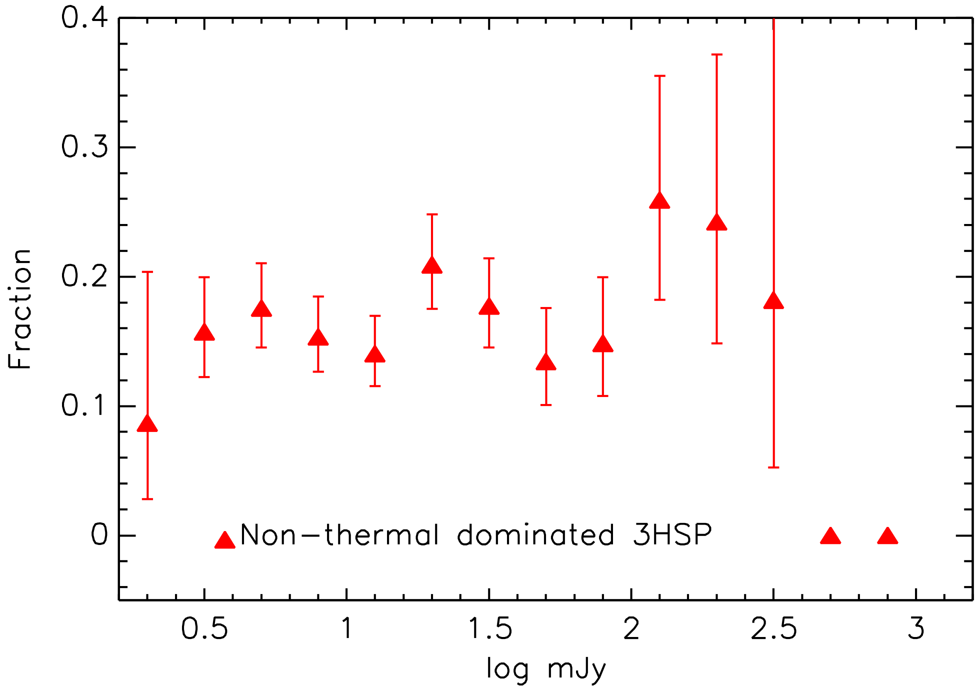

Figure 3.8: Fraction of non-thermal dominated sources w.r.t. mJy.

According to Figure 3.8, the ratio of non-thermal dominated sources are not depend on radio fluxes. However, there were expected to have more high luminosity sources when fluxes go higher. Again it is no possible to miss bright fluxes sources, there might be no such sources in reality. Thus it may be the evolution that causes no high fluxes bright luminous sources in 3HSP. Note that for very faint radio flux sources, most of them are with host galaxy dominated.

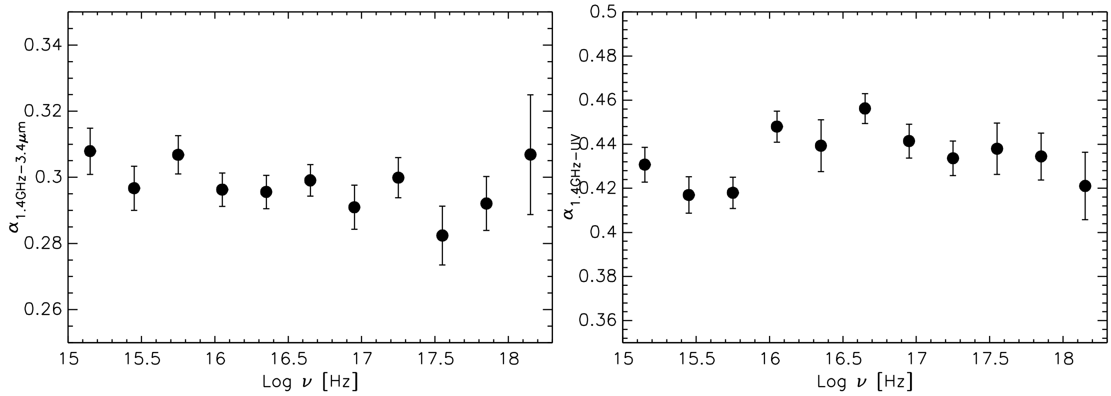

Figure 3.9: The radio-IR slope and radio-UV slope w.r.t. ν_{peak}

3.1.4 Slope and synchrotron peak

The relation between spectral slope and synchrotron peak frequency are explored in this subsection. Figure 3.9 illustrates that the average radio-IR slope ($\alpha_{1.4\text{GHz}-3.4\mu\text{m}}$) and radio-UV slope ($\alpha_{1.4\text{GHz}-\text{NUV}}$) does not depend on ν_{peak}. The mean value for radio-IR slope is ≈ 0.3, while that of radio-UV slope is ≈ 0.43. Regardless of the ν_{peak}, the radio-IR slope remains the same, indicating that the host galaxy plays little role on averagely and the slope of non-thermal emission for each source does not vary much. Note that the radio-UV slope is slightly flatter than that of the radio-IR slope is simply because that the UV is more close to the synchrotron peak for HSPs. The mean $\alpha_{1.4\text{GHz}-3.4\mu m}$ value between non-thermal dominated sources and sources with features from host galaxy on SED does not have a big difference. The host galaxy affections on radio-IR slope generally will not bias the statistics.

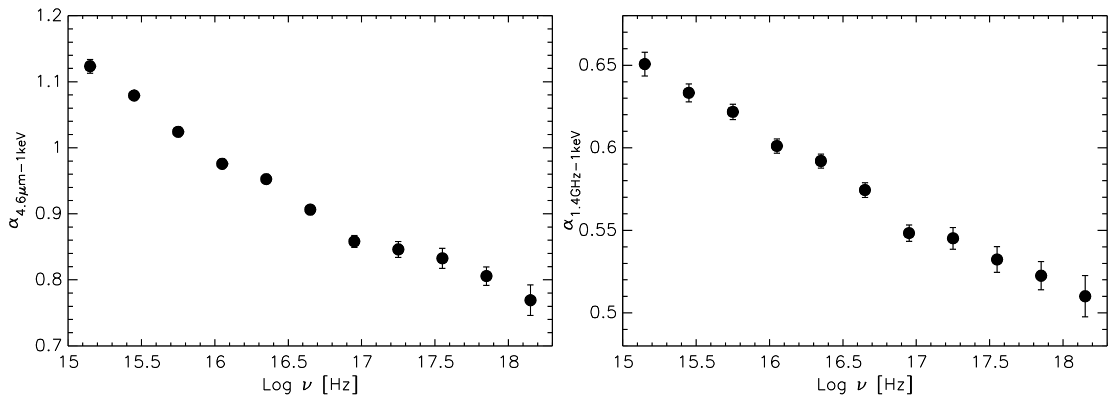

Figure 3.10: The IR-X-ray slope and radio-X-ray slope w.r.t. ν_{peak}

From Figure 3.10, the average IR-X-ray slope ($\alpha_{4.6\mu\text{m}-1\text{kev}}$) and radio-X-ray slope

($\alpha_{1.4\mathrm{GHz}-1\mathrm{kev}}$) are decending while ν_{peak} are increasing. The flatness between 10^{17} to 10^{18} Hz is absolutely where the location of the synchrotron peak for X-ray peaked blazars. The anti-correlation between radio-X-ray flux and synchrotron peak frequency could be applied to estimate the approximate ν_{peak} value for a radio-X-ray matched blazars. $\alpha_{4.6\mu\mathrm{m}-1\mathrm{kev}} = 1$, the turning point, locates at $\log\nu \approx 15.8$, which is exactly the middle frequency between 4.6μm and 1 keV.

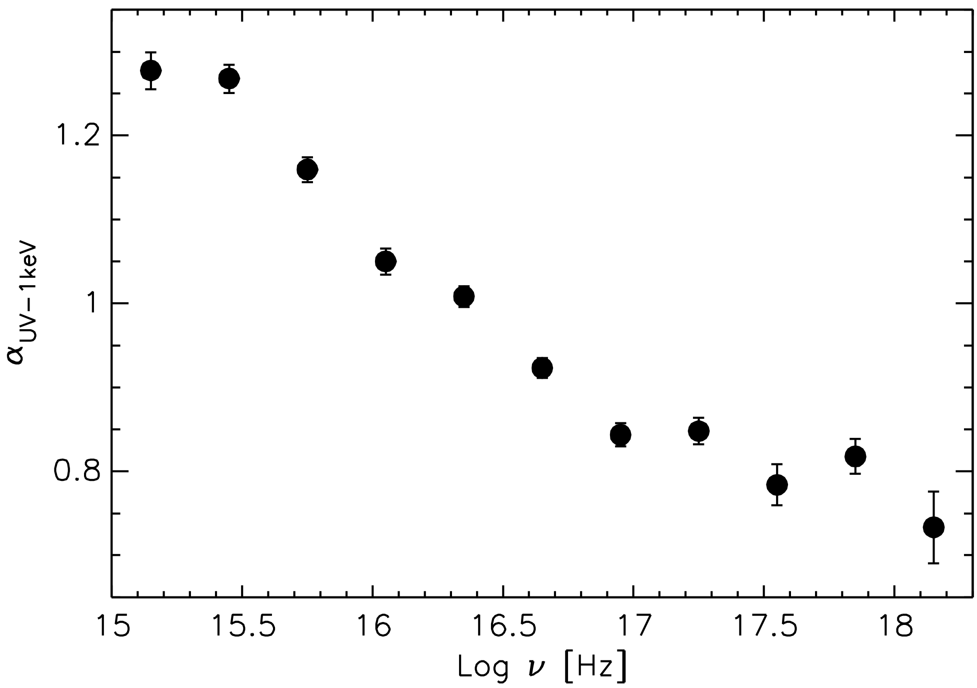

Figure 3.11: The UV-X-ray slope w.r.t. ν_{peak}

The Figure 3.11 suggests that there is an anti-correlation between the UV-X-ray slope ($\alpha_{\mathrm{UV}-1\mathrm{kev}}$); however, the anti-correlation is not strictly decreasing as there are two flatnesses in the plot. It is not surprising that the first flatness occurs at the UV band and the second flatness is at the X-ray band. When the ν_{peak} goes to a higher frequency, the UV-X.ray slope will be slightly smaller than 0.8 and then remain constant if the ν_{peak} extended to more extreme value.

3.1.5 Synchrotron component and Flux

In this section, there were discussion the flux and ν_{peak}relation. The average radio flux density with respect to the Synchrotron ν_{peak} are shown in Figure 3.12, suggesting that the radio flux density does not depend on the synchrotron peak. The probability to find high ν_{peak} sources is the same as to find low ν_{peak} sources in every radio flux bins. Without radio cut, the average radio flux density is slightly higher on both ends, probably resulting from the incompleteness of the faint radio sources. If there were applied the radio cut with 30 mJy, likes the blue points in the Figure, the relation is more clear that the radio flux density does not depend on the $\nu_{\rm peak}$.

Generally, for certain slope and synchrotron peak flux, the synchrotron peak frequency decreases with increasing radio flux density averagely. Our result is not similar to this statement but is similar to those of [97] and the Sedentary and DXRBS Papers. It might be genuine that the radio flux has no relationship with $\nu_{\rm peak}$, indicating that the fraction of HSP among blazars is independent of radio fluxes. Moreover,3HSP also applied radio cut, avoiding selecting the very faint infrared sources and thus faint radio sources when $\nu_{\rm peak}$ is higher. Apart from that, the previous results indicate that there were less faint radio high synchrotron peaked sources and missed both faint and bright low $\nu_{\rm peak}$ sources, resulting in the overestimation of radio flux for high $\nu_{\rm peak}$ sources. Definitely, the bias will increase the controversy of radio flux - $\nu_{\rm peak}$ relationship. Conclusively, the intrinsic relationship between radio flux and Synchrotron peak frequency is still a debating issue, but our work suggests that there may be neither no correlation nor anti-correlation between radio flux and Synchrotron peak frequency.

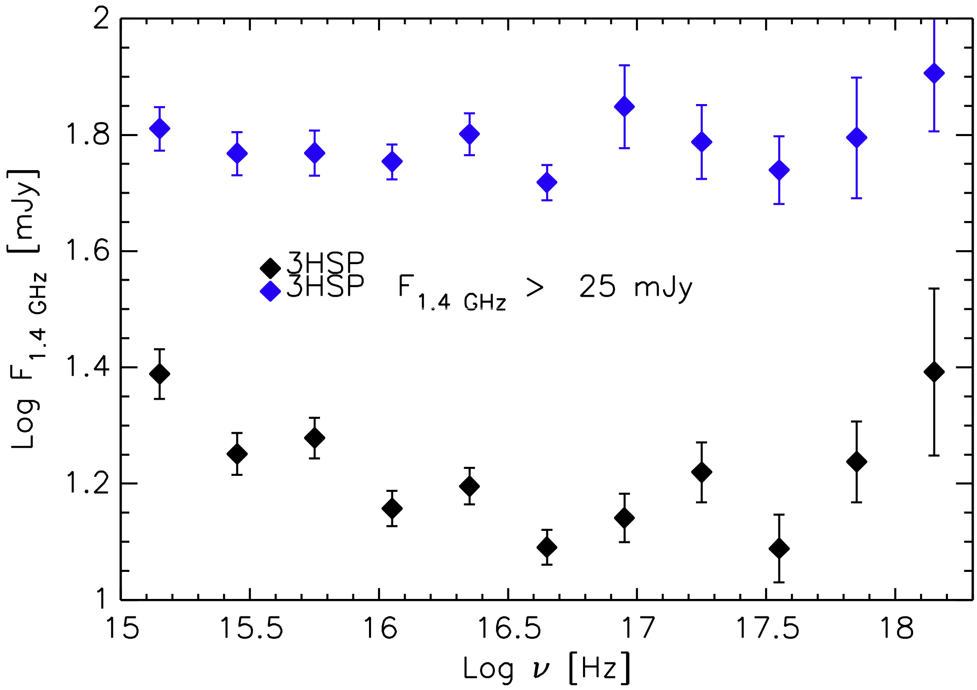

Figure 3.12: The radio flux density versus $\nu_{\rm peak}$.

The last properties of the 3HSP sources to be discussed in this thesis is the *Fermi* photon fluxes and photon indexes. Figure 3.13 shows that the *Fermi* fluxes averagely do not depend on ν_{peak} and it is similar to Figure 3.12. The ν_{peak} does not have any relationship with both radio flux and γ-ray photon flux.

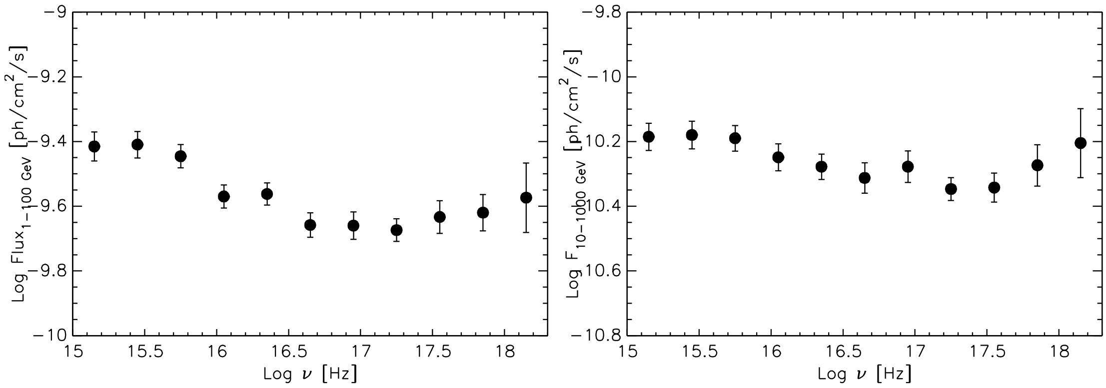

Figure 3.13: The γ-ray flux versus ν_{peak}.

The relationship between the γ-ray photon indexes and ν_{peak} are presented in Figure 3.14; as expected, the higher the ν_{peak}, the harder the γ-ray spectrum. With this anti-correlation between the ν_{peak} andΓ, there could estimate approximate synchrotron peak value from the observed γ-ray photon index. The γ-ray photon index $\Gamma = 2$ between energy from $1 - 100$ GeV is at $\approx 10^{15}$ Hz while that between $10 - 1000$ GeV is at $\approx 10^{16}$ Hz, indicating that the Inverse Compton peak might be located at ≈ 50 GeV and ≈ 500 GeV for them, respectively.

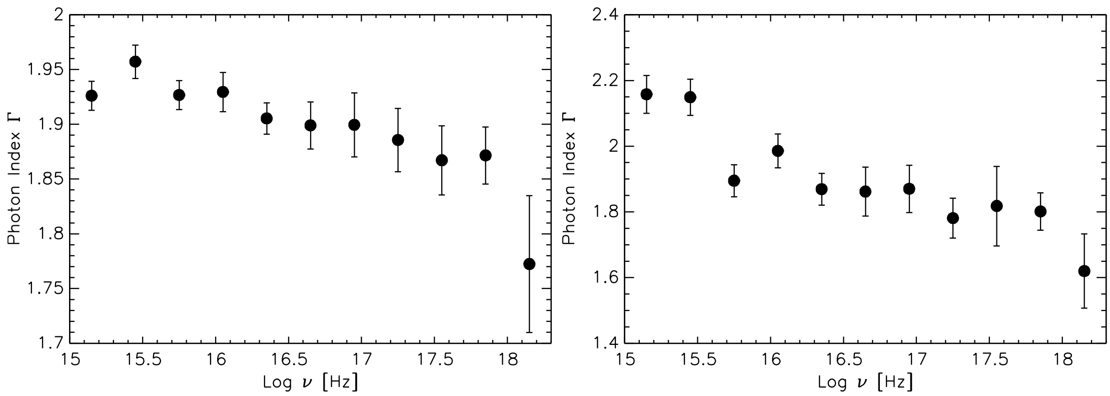

Figure 3.14: The γ-ray phpton index versus ν_{peak}.

3.2 Number count and completeness

A good way to check the completeness of the catalog is to evaluate the logN-logS figures. The integral radio logN-logS for the 3HSP sample with different ν_{peak} cuts is

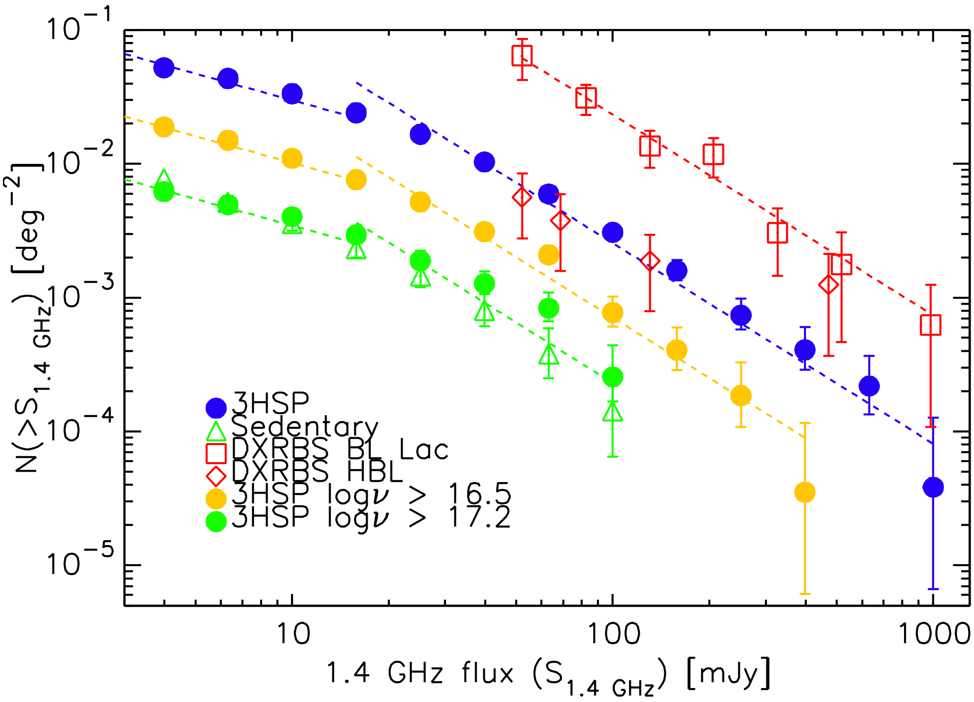

Figure 3.15: The radio logN-logS.

shown in Fig. 3.15. Number counts for Sedentary HBL [58, 61, 115], the Deep X-ray Radio Blazar Survey (DXRBS) BL Lacs , and DXRBS HBL only ([99]) are shown as well for comparison. The logN-logS for DXRBS are in 5 GHz; however, given that BL Lacs typically have flat radio spectra, there is no conversion between the 5 GHz counts and 1.4 GHz. The dashed lines in bright bins correspond to a fixed slope of -1.5, the expected value for a complete sample of a non-evolving population in a Euclidean Universe. Since the radio surveys that we use have different sensitivities in the northern and southern sky, we only considered sources with $\delta > -40^\circ$ and radio flux density ≥ 3.5 mJy.

It is clear from Fig. 3.15 that the surface density of the 3HSP sample is approximately a factor of ten larger than that of the Sedentary Survey, which is expected since the latter includes more extreme sources (its $\nu_{\rm peak}$ distribution peaks at $\log \nu_{\rm peak} \sim 16.8$, as compared to $\log \nu_{\rm peak} \sim 15.5$ for the 3HSP sample). Similarly, the DXRBS all BL Lacs outnumbers the 3HSPs in every flux bins. For 3HSP subsamples, the higher the $\nu_{\rm peak}$ cut, the lower the density, and the Sedentary number density are consistent with 3HSP subsample with a $\nu_{\rm peak}$ cut at $10^{17.2}$ Hz. The DXRBS HBLs are also in very good agreement with the 3HSP number counts in the region of overlap, which shows that our selection criteria are robust.

Apart from the different normalizations, the logN-logS of every samples/subsamples show similar trends deviating from the Euclidean slope at radio flux densities lower than

≈ 25 mJy. The number densities for different BL Lac group and different $\nu_{\rm peak}$HBL are almost parallel to each other, implying that the ratio between high $\nu_{\rm peak}$ BL Lacs and low $\nu_{\rm peak}$ BL Lacs remains the same regardless of the radio flux. It is consistent with Figure 3.12 that the average radio flux does not depend on synchrotron peak frequency and it seems that there is no preference for high $\nu_{\rm peak}$ sources with faint flux and vice versa. A clear trend can be seen going from the Sedentary Survey extreme HSP to the 3HSP sample and to the whole DXRBS BL Lac population, with an increase in number by a factor ≈ 10 at every step.

The logN-logS indicates that both samples are complete in the bright end but do not obey the non-evolution slope, -1.5 (dashed line), in the faint end. The Sedentary is believed to be complete in radio, and the flattening for faint sources may due to its cosmological evolution, meaning there are less faint radio sources in the young universe. The 3HSP flattening; however, appears to be stronger than that of the Sedentary Survey, which suggests the onset of some degree of incompleteness at lower radio flux densities, on top of the evolutionary effects discussed by the Sendentary paper.

The faintest bins for 3HSP has number density $\approx 0.06\text{deg}^{-2}$, indicating the 3HSP maximum surface density corresponds to a total of $\sim 2,400$ HSP blazars over the whole sky with radio flux above 3.5 mJy. Given that this number refers only to sources with 1.4 GHz flux density ≥ 3.5 mJy, and because of the incompleteness discussed above, this has to be considered a robust lower limit.

Fig. 3.16 illustrates the X-ray logN-logS for 3HSP and Sedentary catalogues. Both catalogs manifest significant incompleteness for dim sources. The deviation from the euclidean slope happens at RASS flux $\approx 4 \times 10^{-12}$ erg cm^{-2} s^{-1} for 3HSP. Although the Sedentary is complete in radio [58], it is not complete in X-ray due to instrumental and observational restrictions. Not like in radio, the 3HSP and Sedentary have similar number counts in the X-ray band. When X-ray flux is brighter, it will be easier to find more extreme (high $\nu_{\rm peak}$) blazars, while there are more low $\nu_{\rm peak}$ blazars for faint X-ray flux sources. It is a consequence of the selection effect among blazars as more extreme blazars typically peak in the X-ray band. The logN-logS for the Sedentary is flatter and less than that for the 3HSP at X-ray flux $\lesssim 9 \times 10^{12}$ erg cm^{-2} s^{-1}.

The maximum number densities for 3HSP in X-ray is $\approx 0.07\text{deg}^{-2}$, corresponding to roughly 2800 HSPs detected in X-ray in the whole sky. It is suggested that there might be more HSPs in the whole sky since the 3HSP catalog is not complete in X-ray, and the "intrinsic" number of HSPs detected by X-ray may be much more than 2800 due to the

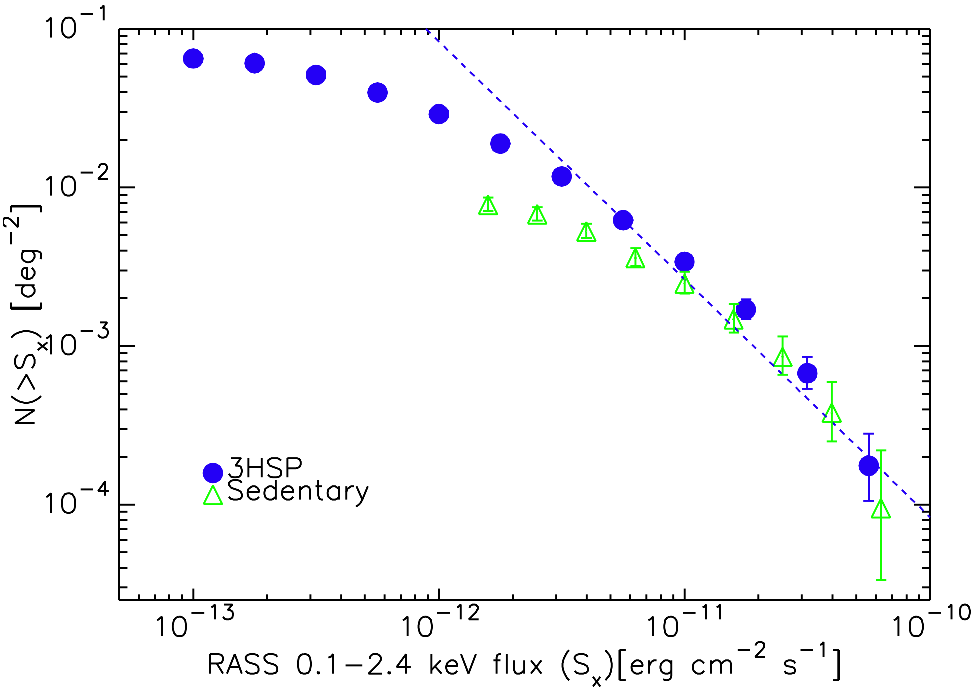

Figure 3.16: The X-ray logN-logS.

severe incompleteness in X-ray. Note that the number is more than that selected in radio as the fact that it is more easier to find high synchrotron peaked blazars in X-ray and the fact that there was no radio cut applied in Figure 3.16. Figure 2.6 in the previous Chapter also shown that the “red trapezoid” area, in which the sources might not be detected by current radio survey but with detectable X-ray flux, is much larger than “red triangle” in size.

If we select blazars in radio, we will find more sources with relatively low energy synchrotron peak; extreme peaked HSPs only constitute a small fraction of all blazars in radio-selected samples. Conversely, we will find more extreme blazar if we select from X-ray since extreme blazars usually have their synchrotron peak in the X-ray band.

There were illustrated the cumulative distribution of $\nu_{\rm peak}$ with different radio cuts in Figure 3.17. The Figure suggests that there were less both high $\nu_{\rm peak}$ sources and low $\nu_{\rm peak}$ sources in faint radio cuts, while there are only miss low $\nu_{\rm peak}$ sources for higher radio cuts. For low $\nu_{\rm peak}$ sources, the missing might due to those sources are very close to the critical point of flux ratio/slope criteria. While for high $\nu_{\rm peak}$ sources, the lost of faint sources is evidence for negative evolution for HSPs.

The dashed lines in the Figure is fitting with a fixed slope, which is estimated from the intercepts between the different $\nu_{\rm peak}$ cut sample in radio logN-logS with the bright source. After the fitting, there were applied the intercept difference between 3.5 mJy

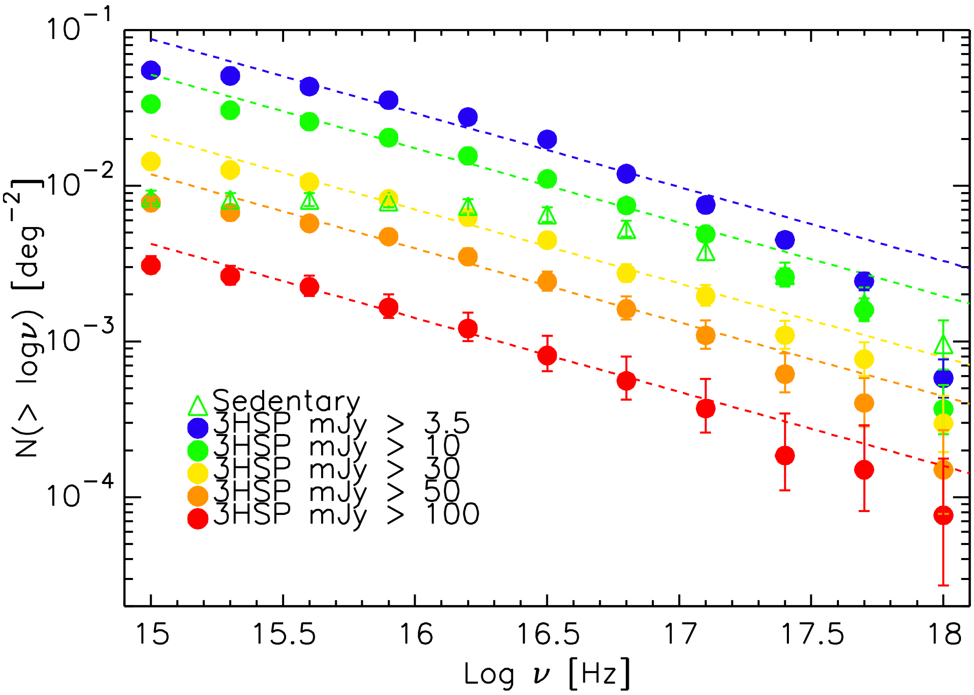

Figure 3.17: Cumulative distribution of $\nu_{\rm peak}$w.r.t. different mJy cuts.

and 30 mJy in this figure to obtain the slope for faint bins in radio logN-logS, which is around 0.5 and re-fit the faint part of the radio number density. There were double check the slope of number density for bright radio sources by using the intercepts difference in Figure 3.17, and the estimated slope is 1.3, not very different than what expected.

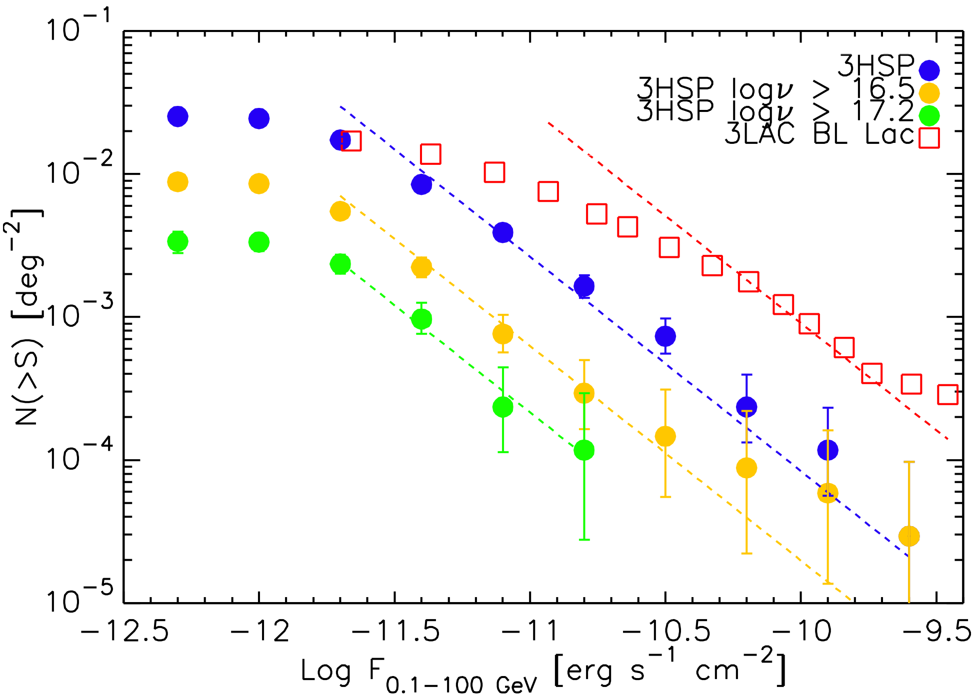

Figure 3.18: The γ-ray logN-logS.

LogN-logS in γ-ray between 0.1-100 GeV for 3HSP subsamples as well as 3 LAC all BL Lac [7] is shown in Figure 3.18. Conversion between photon flux and energy flux are written in Appendix D. Note that the 3 LAC BL Lac suffers from severe incompleteness as they did not include the blazars with uncertain types in their logN-logS for BL Lac. From the Figure, it is clear that the number surface density with respect to γ-ray flux for several different $\nu_{\rm peak}$ blazar subsamples has no relationship with synchrotron peaks. This is consistent with the radio logN-logS, suggesting the HSPs only consist around 10% of all BL Lacs. There are no more high $\nu_{\rm peak}$ sources among all BL Lacs for faint γ-ray fluxes and no more low $\nu_{\rm peak}$ sources for bright γ-ray fluxes.

3.3 V/Vmax value and evolution

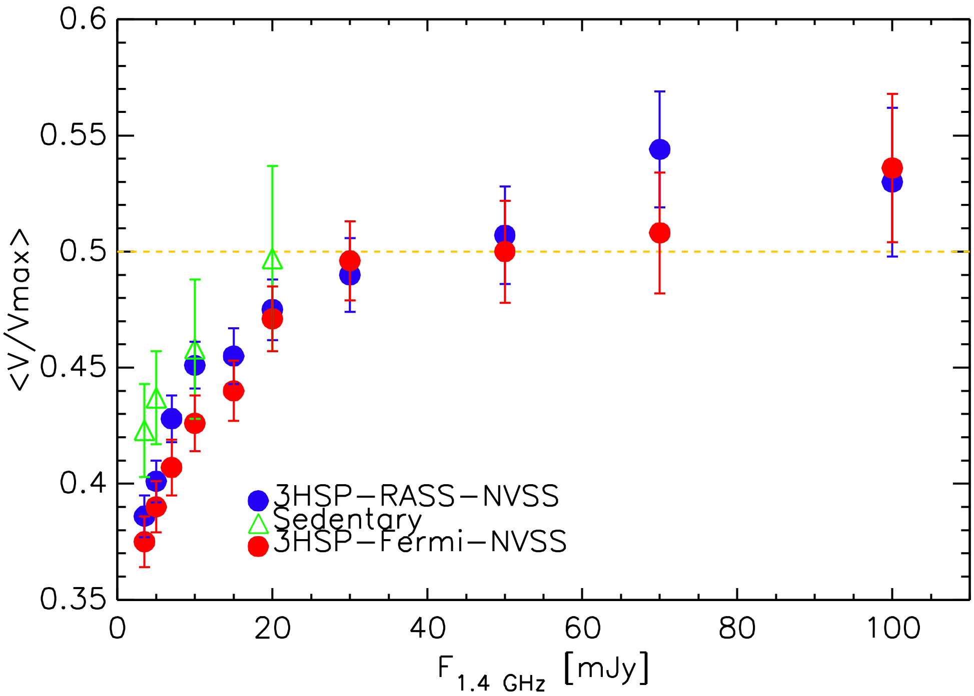

Figure 3.19: The average V/Vmax for three different samples with various mJy cuts.

To test the cosmological evolution and deficiency for 3HSP sources, there were calculated the $V/V_{\rm max}$ value, the ratio between enclosed volume and maximum available volume for a source [125, 15], with respect to different radio cuts in Fig. 3.19. The statistical error of $\langle V/V_{\rm max}\rangle$ for a catalogue is given by $1/\sqrt{12\rm N}$, where N is the number of sources in the catalogue [15].

To explore the $V_{\rm max}$ properties, there were 2 subsamples, 3HSP-RASS-NVSS and 3HSP-Fermi-NVSS considered. The radio flux limit is set to various values in this section;

the subsample undergoes various radio flux cuts here. The X-ray flux limit is the RASS sensitivity map, while the *Fermi* flux limits are obtained with the 8 years catalogs (See Figure F.1 and Appendix F for more details). For those 3HSP sources without redshift measurements, their redshifts were assumed to abide by a normal distribution with average 1.2 [60].The V/V_{max} values with the Sedentary ones (the green triangles) are also shown in the Figures for comparison.

A sample with $\langle V/V_{max} \rangle = 0.5$ is believed to be complete and non-evolving. HSP blazars are believed to have little negative cosmological evolution, with $\langle V/V_{max} \rangle \approx 0.5$, from previous results (Padovani and Giommi 1995[97],Sedentary Paper, DXRBS Paper, and so on). Figure 3.19 shows that for lower radio cuts (which select more sources), the $\langle V/V_{max} \rangle$ for both 3HSP subsamples are lower than 0.5, while the $\langle V/V_{max} >$ are slightly higher than 0.5 for higher radio cuts. There are more low V/V_{max} sources for low radio cuts; conversely, the high V/V_{max} sources dominate in the high radio cut cases.

By definition, for a certain radio cut and certain source, the higher the radio flux density, the lower the V/V_{max} value. When radio cuts are smaller than ≈ 20 mJy, the low $\langle V/V_{max} \rangle$ indicates that we might lose some faint radio and high V/V_{max} sources. Comparing with the Sedentary $\langle V/V_{max} \rangle$ values, the catalog is complete in radio, and the lower value of the $\langle V/V_{max} \rangle$ indicates that there are less faint radio HSPs in the universe.

However, for the 3HSP sources, in cases of low flux radio cuts, the lower $\langle V/V_{max} \rangle$ values mean not only that evolution might exist among HBLs but also mean that the 3HSP do lose some faint radio sources. The 3HSP double cut subsamples are more or less complete for radio flux densities larger than around 30 mJy, as the $\langle V/V_{max} \rangle$ value is around 0.5. For our V/V_{max} results, the incompleteness in faint radio flux bins ($\lesssim 20$ mJy) are caused by the absence of low radio and relatively low synchrotron peaked sources.

The $\langle V/V_{max} \rangle$ values for *Fermi* selected subsample is lower than that for X-ray selected subsample, may resulting from missing of the faint radio sources in *Fermi* catalog. With dedicated γ-ray analysis, like the 1BIGB catalog [13] (section 5.2.1) or future 2BGIB, the *Fermi* subsample will be more complete in radio.

Figure 3.20 depicts the $\langle V/V_{max} \rangle$ value with respect to differenet ν_{peak} cuts. It is clear that the overall $\langle V/V_{max} \rangle$ values for lower ν_{peak}subsample is larger than that for higher ν_{peak} subsamples. This trend is due to the negative evolution of high ν_{peak} BL Lacs, causing less faint radio sources in the high ν_{peak} subsample. As it is believed that 3HSP is complete in radio for the high ν_{peak} subsample, the lower $\langle V/V_{max} \rangle$ values of them may represent the true evolution feature for HBL on V/Vmax. Note that the Sedentary

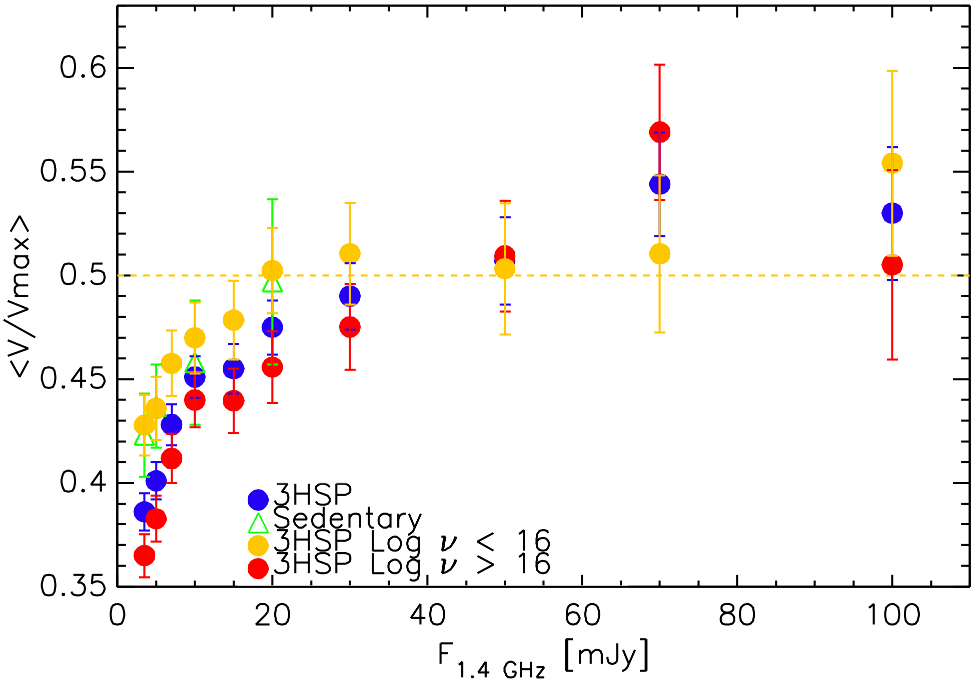

Figure 3.20: The average V/Vmax for different $\nu_{\rm peak}$ subsamples.

catalog, which is also complete in radio, have higher $\langle V/V_{\rm max}\rangle$ values than high $\nu_{\rm peak}$ subsample. It may due to the fact that not all the sources in Sedentary have relatively high $\nu_{\rm peak}$, even though most of the sources in that are high $\nu_{\rm peak}$.

When the radio cuts are higher, the $\langle V/V_{\rm max}\rangle$ are slightly larger than 0.5. The divergence seems fine as it is within the error. However, it may also result from the contamination of 3HSP with low $\nu_{\rm peak}$ blazars in high radio cut cases. These lower synchrotron peaked blazars are supposed to be evolving sources, with higher $\langle V/V_{\rm max}\rangle$.

The average V/Vmax with respect to various γ-ray cuts for different $\nu_{\rm peak}$ subsamples of 3HSP is shown in Figure 3.21. The *Fermi* cut subsample is not complete in γ-ray given that there are some faint γ-ray sources miss in *Fermi* catalogs, and dedicated *Fermi* analysis with multi-frequency knowledge is need to get a more complete sample in γ-ray (see Arsioli and Chang (2017) [13] for more details). The Figure also suggests that the incompleteness in γ-ray mostly are from low $\nu_{\rm peak}$ sources.

Besides various radio cuts there were tested other possible $V/V_{\rm max}$ dependencies with radio-X-ray selected subsample. Figure 3.22 is the $\langle V/V_{\rm max}\rangle$ with respect to synchrotron peak frequency. The $\langle V/V_{\rm max}\rangle$ for high $\nu_{\rm peak}$ sources are lower than 0.5 when setting the radio cut to ≤ 10 mJy, implying that there are less faint radio sources for high $\nu_{\rm peak}$sources. While for higher radio cuts, the trend is not clear, and the $\langle V/V_{\rm max}\rangle$ are around 0.5 for

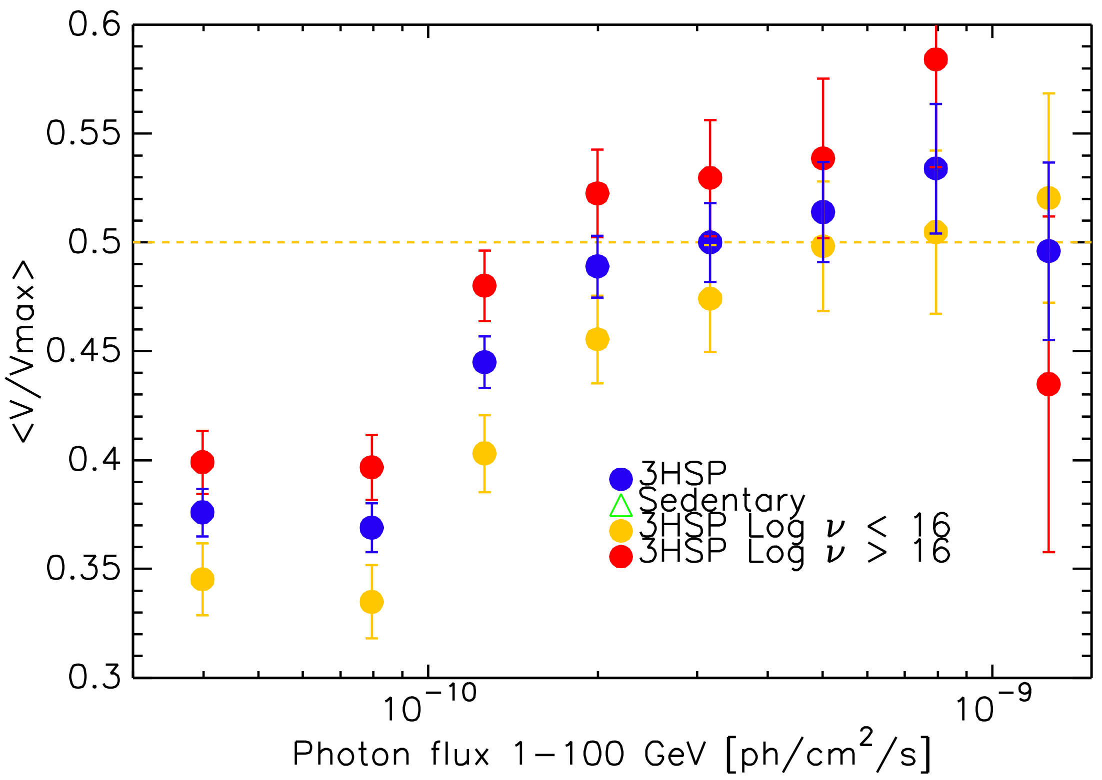

Figure 3.21: The average V/Vmax w.r.t various γ-ray cuts for different $\nu_{\rm peak}$ subsamples.

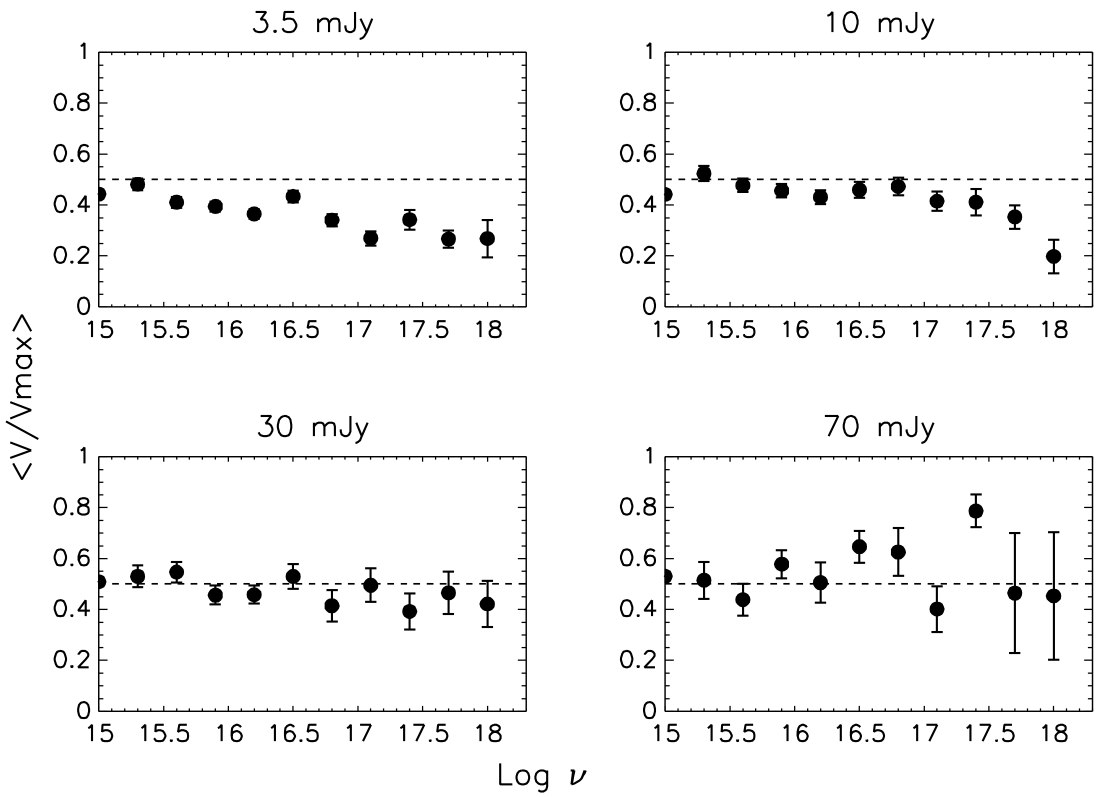

Figure 3.22: The average V/Vmax w.r.t to different $\nu_{\rm peak}$.

every $\nu_{\rm peak}$ bins.

There seems to be an anti-correlation between the $\langle V/V_{\rm max}\rangle$ and synchrotron peak for the 3HSP-RASS-NVSS subsample (radio cut = 3.5 mJy), and in Sedentary, the $\langle V/V_{\rm max}\rangle$ is also decreasing when the $\nu_{\rm peak}$ values are rising. The anti-correlation exits only for faint radio cut cases. This tendency might be a genuine result from the negative evolution nature for high $\nu_{\rm peak}$ blazars; the higher the synchrotron peak frequency, the less faint radio or evolving sources were found.

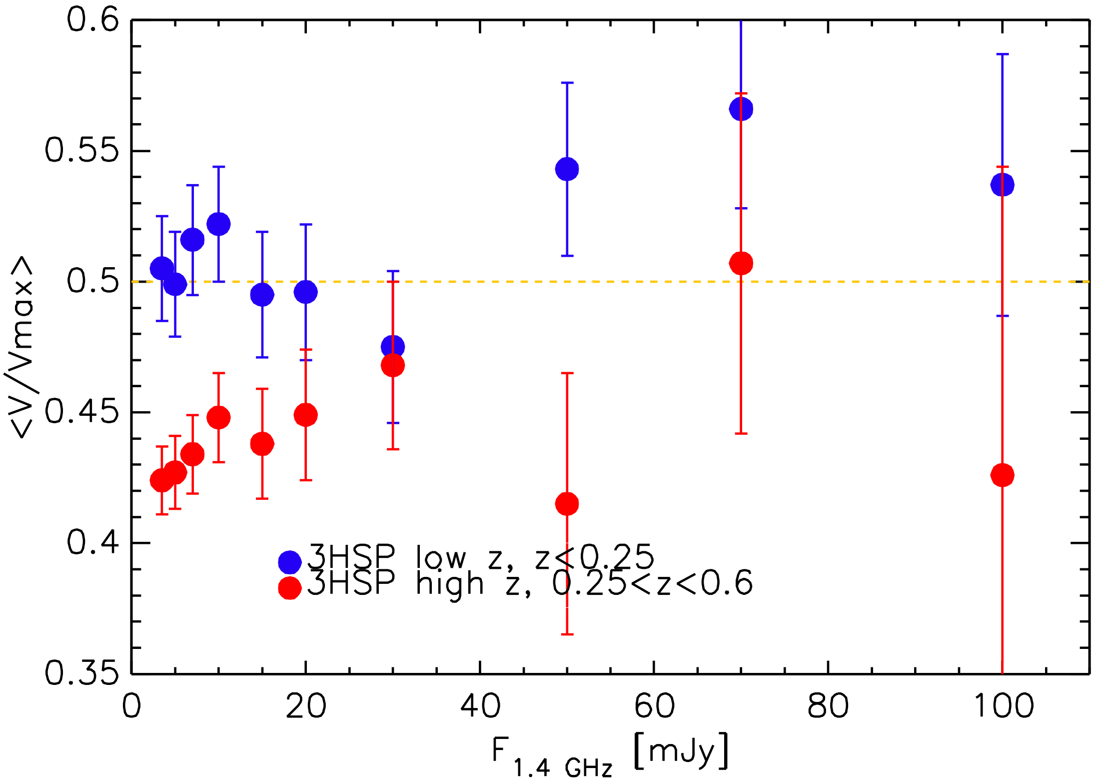

Figure 3.23: The V/Vmax for different redshift cut subsamples.

Given that the 3HSP radio-X-ray selected subsample is complete when $\nu_{\rm peak}$ is larger than 10^{16} Hz, the further V/Vmax tests will apply $\nu_{\rm peak}$ cut at 10^{16} Hz. The $\langle V/V_{\rm max}\rangle$ for subsample with two different redshift cuts is illustrated in Fig. 3.23, suggesting that the higher redshift cut subsample have lower $\langle V/V_{\rm max}\rangle$ value. The two subsamples are adopted with redshift cut $0 < z \leq 0.25$ and $0.25 < z \leq 0.6$, respectively. There were assumpted that the universe is limited by the cuts; that is, the maximum distant could be observed is the applied z cuts. The difference between $\langle V/V_{\rm max}\rangle$ for the subsamples means that the there is a de-evolution effect among HSPs. HSPs are not distributed uniformly between these two bins, especially for high z bin. As redshift go higher, the sources are less in density or in luminosity, causing less faint flux sources and low $\langle V/V_{\rm max}\rangle$ value. It is obvious evidence that the HSP blazars are encounter negative evolution.

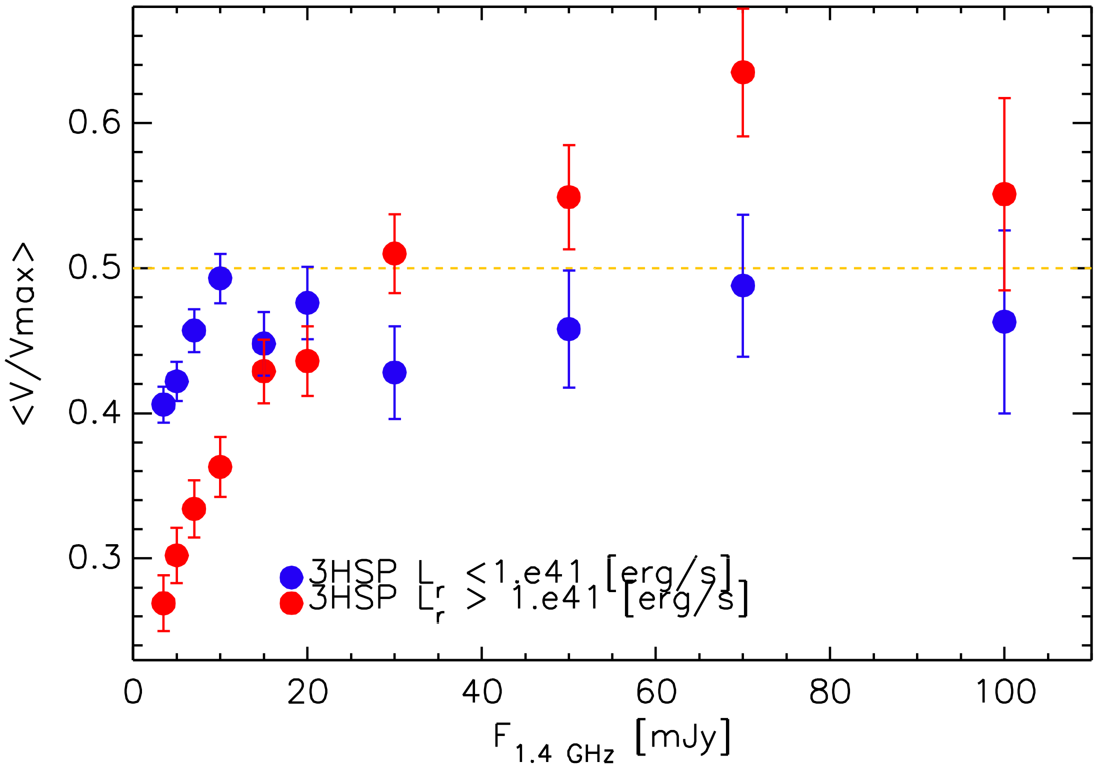

Figure 3.24: The V/Vmax for different luminosity subsample.

Figure 3.24 is $\langle V/V_{max} \rangle$ for different luminosity bins, showing that the low luminous sources and high luminous sources have totally different evolution. The Figure suggests that there are less high luminosity sources in the universe, which is another evidence for negative evolution, and the negative evolution is stronger in faint radio sources.

3.4 Luminosity function

In this section, there were calculated and discussed the luminosity function, number of sources per luminosity within the maximum available volume [126, 33], in radio and γ-ray to explore the evolution of the 3HSP catalog. To obtain the luminosity function, there were applied double cut subsample (in radio and X-ray for radio luminosity function and in radio and γ-ray for γ-ray luminosity function) to estimate the maximum available volume for a source since the 3HSP catalogue is constrained mainly by both radio and X-ray fluxes or selected according to γ-ray catalogs. The radio flux limit is set to 3.5 mJy at 1.4 GHz, the X-ray flux limit is same as the RASS sensitivity, and the γ-ray flux limit is defined source by source with γ-ray photon index.

Figures 3.25 and 3.26 present the luminosity function for 3HSP (all HSPs) in radio and

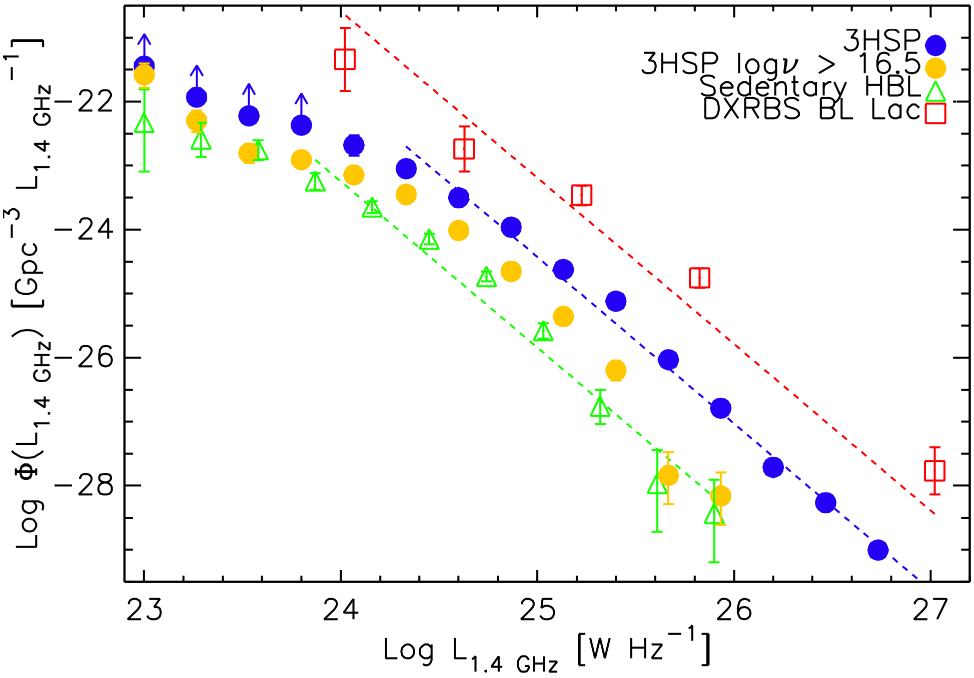

Figure 3.25: The radio luminosity function.

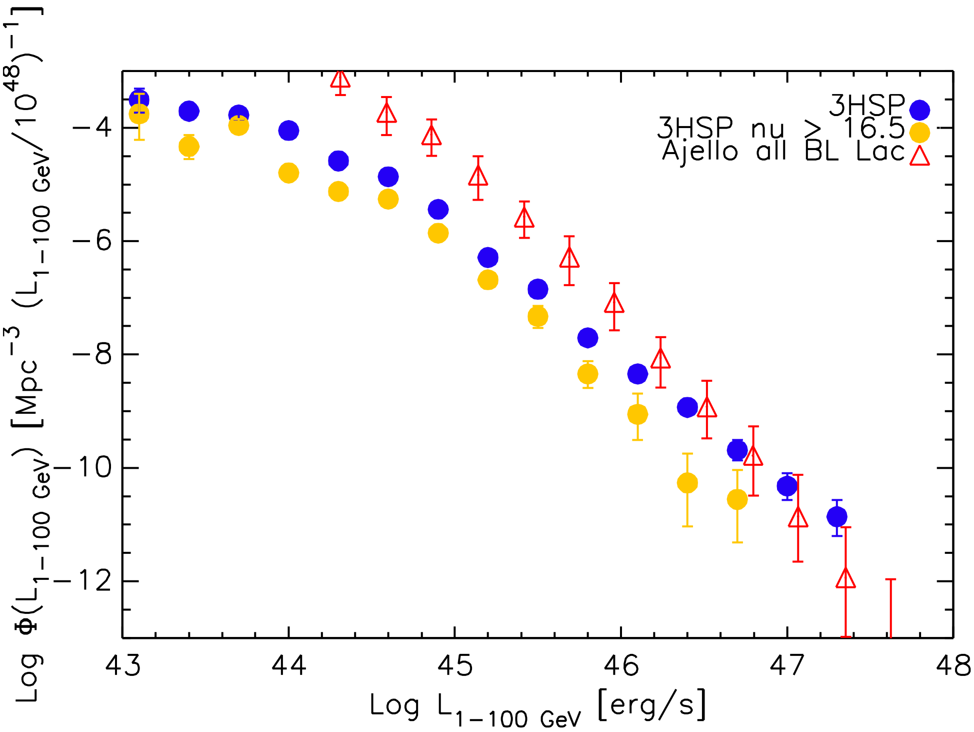

Figure 3.26: The γ-ray luminosity function.

γ-ray respectively. Besides, there were also compared the radio luminosity functions with that of the DXRBS all $\nu_{\rm peak}$ blazars and more extreme $\nu_{\rm peak}$ Sedentary HSPs (Section 1.3), and there were compare the γ-ray luminosity function with all BL Lac from Ajello et al.

2014 [10]. The luminosity function for all BL Lacs in Ajello et al. 2014 [10] is de-evoluted to z=0, so the slope is different and steeper than that of 3HSP subsamples.

Both 3HSP luminosity functions in radio and γ-ray are consistent with the logN-logS in section 3.2. That is, the ratio between high $\nu_{\rm peak}$ sources and low $\nu_{\rm peak}$ sources does not go higher or lower when luminosity goes brighter. The luminosity functions for different mean $\nu_{\rm peak}$ subsamples of blazars have the similar slope. The high $\nu_{\rm peak}$ sources do not have higher number density in low luminosity bins or lower number density in high luminosity bins. Note that for the last two points of the 3HSP subsample with $\nu_{\rm peak}> 10^{16.5}$, there are obviously lower than the others, and the density for the most luminous bins of that subsample seems lower. It may due to the negative evolution facts that the high luminous sources tend to close to us.

The 3HSP catalogue suffer from incompleteness when radio luminosity density is lower than $\approx 10^{24.4}$ W Hz^{-1} and when γ-ray luminosity is fainter than $\approx 10^{44.5}$ erg s^{-1}. The slope for radio and γ-ray luminosity functions are -2.598 and -2.263, individually, which are very similar to the DXRBS one, -2.12 ± 0.16. Given that 3HSP undergoes deficiency when radio luminosity density is $\lesssim 10^{24}$ W Hz^{-1}, there were applied lower limits instead of the real value here. Those faint luminosity sources mostly are low $\nu_{\rm peak}$ on the threshold of 3HSP selection criteria.

In conclusion, our radio luminosity function and logN-logS results are consistent with the results from the Sedentary and DXRBS Papers, indicating that the HSPs constitute $\sim 10\%$ of all BL Lacs, and only $\sim 10\%$ of the HSPs are extreme objects with synchrotron peak$\gtrsim 10^{17}$ Hz, independent of the radio flux/luminosity density. In the X-ray band, the position of $\nu_{\rm peak}$ tells a different story: the number ratio between higher $\nu_{\rm peak}$ HSPs and lower $\nu_{\rm peak}$ HSPs increases at lower X-ray flux/luminosity. When the energy goes to γ-ray it is similar to what radio results show. The number density ratio between different $\nu_{\rm peak}$ subsamples remains almost the same for every γ-ray bins. Our results deviate from the predictions of the blazar sequence [50, 51, 94], in which the number ratio between high $\nu_{\rm peak}$ and low $\nu_{\rm peak}$ blazars will be smaller when at higher radio luminosity/flux density and more or less constant with X-ray luminosity bin (see Table 3. in [50]).

The relative number of low $\nu_{\rm peak}$ BL Lacs and high $\nu_{\rm peak}$ BL Lacs are different in the radio and in the X-ray bands, and the number ratio between low peaked BL Lacs and high peaked BL Lacs is a debatable topic. However, given the unbiased nature of radio selection with respect to $\nu_{\rm peak}$, this is a direct consequence of BL Lac demographics, with HBL making up only $\sim$ 10% of the total BL Lacs see also, for example, [99]. There does exist some current evidence support a scenario that the high synchrotron peaked BL Lacs only occupy a small minority ($\approx 10\%$) of the BL Lac family. [97, 60]...etc. Aside from that, the luminosity function and logN-logS results tend to support low synchrotron peaked blazar leading scheme as well, with high $\nu_{\rm peak}$ blazars being the minority in the whole blazar family.

The luminosity function presented in Figure 3.25 could not illustrate the number density with respect to different redshifts, thus could not show the evolution in redshift. Luminosity function results from [88] have show that X-ray selected BL Lacs (mostly high $\nu_{\rm peak}$BL Lacs) undergoes negative evolution. To illustrate the negative evolution of HSPs, as we know from Figure 3.23 that there is a negative evolution exists, it is necessary to plot the luminosity function in different z. Figure 3.27 is the radio luminosity function from two different redshift subsamples, $z < 0.15$ and $0.45 < z < 0.7$.

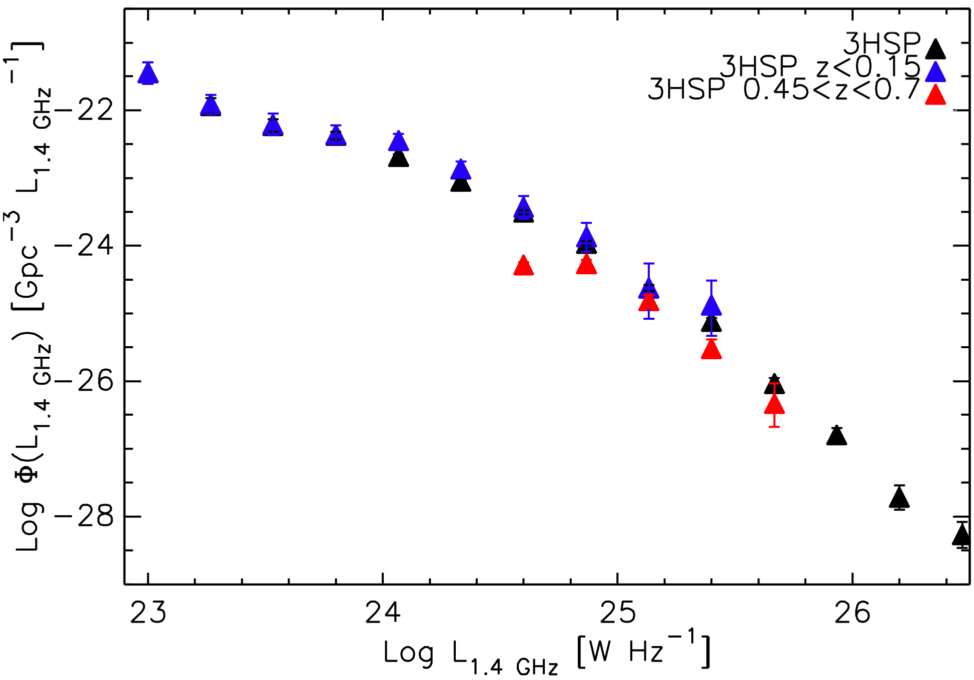

Figure 3.27: The radio luminosity function for two different z subsamples.

It could infer from the Figure that sources in high z bin generally are less dense or less luminous than that of in low z bin. That is, the red points are either shift down (density evolution) or shift left (luminosity evolution), compared with the blue points. There is evidence of de-evolution trend in HSPs. Note that there were avoid the sources in higher redshifts as most of them are with featureless spectrum and no observed redshift available. Simulation is necessary for further analysis in future, but definitely, the conclusion that negative evolution exists among high $\nu_{\rm peak}$ blazars is still true.

3.5 Exploring the statistical properties and the selection effects of the sample of HSP blazars

A full understanding of the selection effects and of the incompleteness level among 3HSP sources is essential to explore the intrinsic statistical properties of HSP blazars. If there were no double cuts (in radio and X-ray flux) applied to 3HSP catalog, there would be significant incompleteness at low radio or X-ray fluxes as many sources near the flux limit would be lost in the selection process. Therefore, all the discussion here concerns results obtained using radio and X-ray cut subsamples.

The main cause for the incompleteness of the 3HSP catalog is the flux ratio criteria, which, because of the non-uniform coverage of the existing X-ray catalogs, results in the loss of some weak sources with $\nu_{\rm peak}$ close to the selection threshold of 10^{15} Hz. From Figure 3.17, Figure 3.3, and Figure 3.12, we note that there are some high $\nu_{\rm peak}$ sources with faint flux that seem to be missing; however, because of the radio flux cut applied, no significant loss of high $\nu_{\rm peak}$ sources is expected, and therefore this is likely due to negative evolution of high $\nu_{\rm peak}$ objects. The V/Vmax results (Figure 3.23 and 3.24) and Luminosity function for different redshift bins subsamples (Figure 3.27) indicate a negative evolution for HSP blazars. A de-evoluted sample means that the sources are either less common or less luminous in high redshift. That is the sources in a negative evolution sample are concentrated in the recent, and especially, bright sources are accumulated in low redshift. Either way will result in less faint flux sources.

As the high luminosity sources are rare to find and required larger space in the universe to find one; for non-evolution sample, the average z of bright L sources is higher than that of faint L sources. However, the de-evoluted sample will cause the bright sources mean redshift lower. Thus, there was not enough space to find one bright source as they gather in a relatively small region, resulting in missing of bright sources, unless one is lucky enough to focus on a region just next to the luminous sources. The missing of high luminosity sources will lead to loss of non-thermal dominated sources as non-thermal dominated sources are also bright luminosity sources. Since the negative evolution is stronger for high $\nu_{\rm peak}$sources, most of the high $\nu_{\rm peak}$sources are not non-thermal dominated, as shown in Figure 3.7.

Conclusively, the 3HSP should be complete when $\nu_{\rm peak}$ is larger than 10^{16} Hz and applying both radio and X-ray cuts. Apart from that, for high $\nu_{\rm peak}$ sources, given that they are undergone negative evolution, there are less faint radio flux sources and less high luminosity sources. Table 3.1 lists all the possible selection effects and evolution consequences for 3HSP catalog.

Selection Effect	Consequence
Instrumental constrain	miss faint radio low $\nu_{\rm peak}$ sources
Instrumental constrain	miss faint X-ray high $\nu_{\rm peak}$ sources
RASS sensitivity map	miss faint X-ray sources
flux ratio / slope criteria	miss low $\nu_{\rm peak}$ sources
Negative Evolution Fact	Consequence
average flux higher	less faint radio high $\nu_{\rm peak}$ sources
not enough volume	could not find high L high $\nu_{\rm peak}$ sources

Table 3.1: The general statistical of 3HSP catalog.

Note that according to the logN-logS and luminosity function in radio, the probability that a found blazar is a high $\nu_{\rm peak}$ source or a low $\nu_{\rm peak}$ source remains almost the same at arbitrary luminosities/fluxes for whole redshift sample. Thus, in the entire universe, the high $\nu_{\rm peak}$ sources are not average brighter or fainter than low $\nu_{\rm peak}$ sources. The high luminosity sources with high $\nu_{\rm peak}$, although is extremely rare, are there, and it is the negative evolution of high $\nu_{\rm peak}$blazars that cause them very difficult to find. The negative evolution does not mean that there are no high $\nu_{\rm peak}$ sources with high luminosity nor means most of the high $\nu_{\rm peak}$ sources are less luminous. This is totally different than what is expected with the "blazar sequence".

The missing of high luminosity high $\nu_{\rm peak}$sources on luminosity function should not affect the fact that there is no privilege for finding high $\nu_{\rm peak}$ sources in low luminosity/flux conditions. If the blazars sequence exists, the luminosity function for higher $\nu_{\rm peak}$ blazars should be steeper than that of lower $\nu_{\rm peak}$blazars. Blazar sequence may be one of the selection effects because of the nonuniform distribution of the high $\nu_{\rm peak}$ source on the sky. Moreover, if there does exist such sequence, there will be more high $\nu_{\rm peak}$ blazars found as there are low luminous than low $\nu_{\rm peak}$ blazars; however, observations have shown that the high $\nu_{\rm peak}$ sources only consist at most 10 % of the blazars.

Chapter 4

The VOU-Blazars Tool

In this Chapter, a brand new tool, VOU-Blazars, that find the potential interesting blazar candidates automatically are presented.

4.1 Brief introduction

VOU-Blazars tool is being developed in the framework of the United Nations Open Universe initiative[1] using Virtual Observatory protocols[2] (VO). The main purpose to build this tool is to search blazar candidates effectively at a certain position within a specified area. The name, VOU, is taken from the combination of VO and OU (open universe). It was written in BASH shell to run several programs compiled with Fortran and Python under macOS or Linux system. The PGPLOT[3] were applied to plot the figures.

The tool is made up with two phases; the first phase "points out" all the candidates in a relatively large area, while the second phase deal with one interested candidate at a time, plotting the SED and error circle map for that candidate. Given that the majority of blazars are detected in both radio and X-ray, the VOU-Blazars find sources in all available lists of radio and X-ray emitters in the first phase. It searches the data from plenty of catalogs through VO services and estimates the possible blazar candidates. After the first phase is done, a list with all the implicit candidates as well as the coordinate and radio and X-ray flux of them will be readily passed to the second phase.

The user then specifies an interested source from the candidate list to send to the second phase. VOU-Blazars will further retrieve the data from catalogs other than radio and X-ray which already applied in the first phase, such as high-frequency radio, far IR,

[1]http://www.openuniverse.asi.it/

[2]http://www.ivoa.net/

[3]http://www.astro.caltech.edu/ tjp/pgplot/

IR, optical, UV, and γ-ray, for that source via VO conesearch. The second phase will do the data analysis as well as the source classification to plot the SED for the source or to rule out the source if no further non-thermal data could be found. The SED data could further be upload to the SSDC SED builder tool [4].

A particular process might be "triggered" automatically to find more possible candidates as intermediate phase before running the second phase. The intermediate phase checks the sources inside the error region but without radio-X-ray matched. The checked sources with GALEX [89, 18] counterpart or GB6 [63]/PMN [65, 66, 148, 64, 149] counterpart will be delivered to second phase as well. If no sources without radio-X-ray matched inside the error area, the intermediate phase will not be called.

The VOU-Blazars is already applied to point out potential neutrinos counterpart, it could effectively show all the possible blazar candidates around VHE detected region. Apart from that, the tool also finds several good HSPs HSP candidates and contributes several sources to 3HSP catalog. The tool is still under developing and could be download from `https://github.com/ecylchang/VOU_Blazars`.

4.1.1 Aims and motivations

There are more and more VHE sources detected; however, some of the γ-ray or VHE cataloged sources (in *Fermi* catalogs[5], TeVCat[6], or neutrino event[136]) are not associted to lower frequency sources yet. Association of the VHE sources always is a highly concerned issue, especially the connection between neutrino / cosmic ray and astronomical objects. Motivating by the fact that most of the extra-Galactic γ-ray sources are believed to be blazars (See TeVCat or 3FHL[135]), to find more possible counterparts for the VHE sources, a tool to quickly identify all the possible blazars or blazar candidates was built.

Apart from that, as Chapter 2 mentioned, a complete HSP catalog is essential for VHE astronomy, while it is known that there are still some blazars which are not in current blazar catalogs yet. Making the current blazar catalogs more complete and finding still missing blazars is an critical work. Unfortunately, it is time-taking to go through all the possible candidates; For example, in 3HSP, there were checked around 6000 sources one by one to selected 2000 HSPs. Thus, VOU-Blazars also was built to find more blazars candidates effectively based on searching with various multi-frequency VO catalogs. It

[4]https://tools.asdc.asi.it/SED/

[5]https://fermi.gsfc.nasa.gov/

[6]http://tevcat.uchicago.edu/

could examine every possible radio or X-ray sources, rule out most of the uncertain or non-blazars sources automatically from an enormous sample, and then pass back only good blazar candidates. That is, the VOU-Blazars will help the users to save time and focus on only the interesting plausible blazars; by doing this, the numbers of pre-selected candidates are substantially reduced.

The SSDC SED builder is an excellent tool to explore the full band SED of a source, while there are some of the catalogs not applied by the SED builder yet, such as Gaia [53, 52], Pan-STARRs[29], and XMMOMSUMSS[105]...etc. The data from these catalogs could be attained from VO conesearch; besides, the latest version of XMMSL [123], Chandra[46], and GALEX...etc also could be obtained from the conesearch. With a tool retrieving data using VO, an SED with more data than the SED builder could be displayed.

Conclusively, the main purpose of the VOU-Blazars is to figure out potential blazar counterpart for VHE detections. Moreover, cutting down the pre-selecting sample and to check only reasonable good sources when finding new blazars is another goal of the tool. Last, plotting the SED for interesting sources also is an important purpose for the tool.

4.1.2 Setting up for the tool

The dependencies of the VOU-Blazars are:

- Fortran: GFortran compiler
- Python: astropy, pyvo, and pyyaml packages
- Anaconda: to install eada environment and conesearch pipeline
- PGPLOT
- BASH: awk, ps2eps, open...etc

To run the VOBlazars, one need Fortran and Python compilers and PGPLOT first. Given that the GFortran compiler is fully compliant with the Fortran 95 Standard and includes legacy F77 support, it is applied to compile all Fortran programs in the tool. The GFortran compiler and Python could be download from `https://gcc.gnu.org/wiki/GFortran` and `https://www.python.org/downloads/`, correspondingly. For MacOS user, the PGPLOT could be installed with homebrew[7] via command brew install

[7]https://brew.sh/

pgplot; otherwise, PGPLOT could installed following the instruction from `http://www.astro.caltech.edu/~tjp/pgplot/install.html`.

Besides, Anaconda and "conesearch" pipeline are also required. The Anaconda is available through `https://www.anaconda.com/download/#macos`, while the conesearch pipeline to obtain the various catalogs data from VO link could be cloned from `https://github.com/chbrandt/eada`. After cloning everything and putting the whole conesearch setup files/folders under Anaconda folder, there were set up a Python environment called "eada" via the comment conda create -n eada ipython python=2 astropy[8]. Note that eada environment should be built under the conesearch installation main folder and that the environment will contain all packages required by VO conesearch pipeline.

The commands source activate eada and source deavtivate are use to activate and deactivate the eada environment. To install the pipeline and related mandatory packages under eada environment, there were activated the environment before the next step of the installation. There are three Python packages, astropy, pyvo, and pyyaml, nessaccary when running the conesearch, and commands pip install XXX or conda install XXX are applied to install them to eada environment. The python setup.py develop command is the final step of the whole installation of the conesearch pipeline.

Once the pipeline is installed, try to run conesearch to see if it works. It is worth mentioning that the conesearch pipeline needs to be run under eada environment. A file, "setupeada", written all the commands to install the conesearch pipeline and set up the eada environment, might be an easier choice to set up the conesearch. With setupeada, one could simply use source setupeada to run all the processes at a time.

The last thing to set up the VOU-Blazars is to compile all the Fortran programs as well as subroutines, "mylib.f", into object files. Note that the -c option tells gfortran to create an object file; using gfortran -c XXX.f -ffixed-line-length-132 to compile a program into object file. To compile other Fortran main programs, command gfortran -o XXX XXX.f -ffixed-line-length-132 mylib.o -lpgplot is used. A script with all the compiling commands, compile.sh, could be applied to compile the Fortran programs in a more convenient way. With compile.sh, the user could simply compile all the program and subroutine at once by running the script.

Conclusivelly, there are 7 Fortran executable files (Find_candidates1, Find_candidates2, Find_Candidates_int, plot_sed, gnomo_plot_types, readcat, and convert_sed), 1 Fortran object file (mylib.o), 2 shell scripts (vou-blazars and quesh.sh), 2 conesearch catalog lists

[8]To remove the environment, using: conda remove -n eada –all.

(cats1.ini and cats2.ini), one staus code, and one folder contains filter responses for X-ray surveys (count_rate) required to run VOU-Blazars.

The overall steps to set up the tool are sumarized here:

1. Installing the Fortran compile, PGPLOT, and Python.
2. Cloning the conesearch pipline and downloading the Anaconda.
3. Command: conda create -n eada ipython python=2 astropy
4. Command: source avtivate eada
5. Command: pip install astropy
6. Command: pip install pyvo
7. Command: pip install pyyaml
8. Command: python setup.py develop
9. Compiling mylib.f into object files.
10. Compiling other Fortran programs into executable files.

4.1.3 Included programs and files

There are totally 15 files/folder which makes up the VOU-Blazars; in addition, two files to set up the conesearch pipline and compile all the fortran programs as well as 1 readme document is availalbe.

- **vou-blazars**
  Main shell script to run the VOU-Blazars.
- **cats1.ini**
  A list for the conesearch pipline to search the first phase data.
- **cats2.ini**
  A list for the conesearch pipline to search the second phase data.
- **queue.sh**
  A script to run conesearch in parallel.

- **Folder: count_rate**

  A Folder with X-ray telescopes filter responses that use to calibrate the X-ray data. There are XRT, IPC, ROSAT PSPC, and ROSAT HDI responses as well as a configuration file inside the count_rate.

- **mylib.f**

  Fortran subroutine that contains several common used subroutines and functions that are necessary for the Fortran main programs which are run in VOU-Blazars. Including subroutine to calibrate the X-ray countrate into integral flux with calibrated the absorption from neutral Hydrogen and subroutine to convert the equatorial coordinate system from hours:minutes:seconds/degrees:minutes:seconds to decimal degrees.

- **status.code**

  The status code that required by mylib.f

- **readcat.f**

  Fortran program to read the various output from VO searching into a single file in unified format.

- **find_candidates1.f**

  Fortran program running the first phase.

- **gnomo_plot_types.f**

  Fortran program plotting the source map.

- **find_candidates_int.f**

  Fortran program running the Intermediate phase.

- **find_candidates2.f**

  Fortran program running the second phase.

- **plot_sed.f**

  Fortran program to plot the SED.

- **convert_sed.f**

  Fortran program to convert the SED into format used by SSDC SED tool.

- compile.sh

  A script to compile all the fortran programs/subroutines at a time.

- setupeada

  All the commands to set up the eada environment and to install the conesearch pipline.

4.2 How does it work?

In this section, the detailed operated process of the VOU-Blazars are introduced. A brief sheme for the VOU-Blazars is shown in Fig. 4.1.

4.2.1 To run the tool

In order to run the VOU-Blazars, make sure all the necessary files/folders are put in the working directory, all the set up in section 4.1.2 are done, and all the required programs are compiled. Besides, the eada environment needs to be activated and BASH shell is obligatory to operate it.

The tool requires the user to specify an interested position in Equatorial system and interested size of the area to run. Three parameters, RA, Dec, and searching radius, are mandatory to input to the tool. The RA and Dec are in the unit of degree, and the searching radius is in the unit of arcmin. For example, the tool could be run with the command source vou-blazars 77.43 5.72 80.

The other parameters, such as nH column density and error circles and/or ellipticals, also could be inserted into the tool. One circle, one elliptical, one circle and one elliptical, two circles, or two ellipticals could be input as error regions. Unit of the nH applied in the tool is cm^{-2}, that of the radius and axes for error circle and elliptical are arcmin, and that of the position angle for error elliptical is degree, north to east on the sky. The input parameters are sorted by R.A., Dec., Searching Radius, nH (if specified), and error circles or/and ellipticals (if specified). One cardinal thing to mention is that if two error circles or ellipticals are specified, the one with a larger size should input first.

Several examples of input are listed below:

∗ **source vou-blazars 77.43 5.72 80**

  The simplest input.

∗ **source vou-blazars 77.43 5.72 80 3.e21**

  Specify the nH with 3×10^{21} cm^{-2}.

∗ **source vou-blazars 77.43 5.72 80 3.e21 50**

  Specify nH value and an error circle radius 50 arcmin.

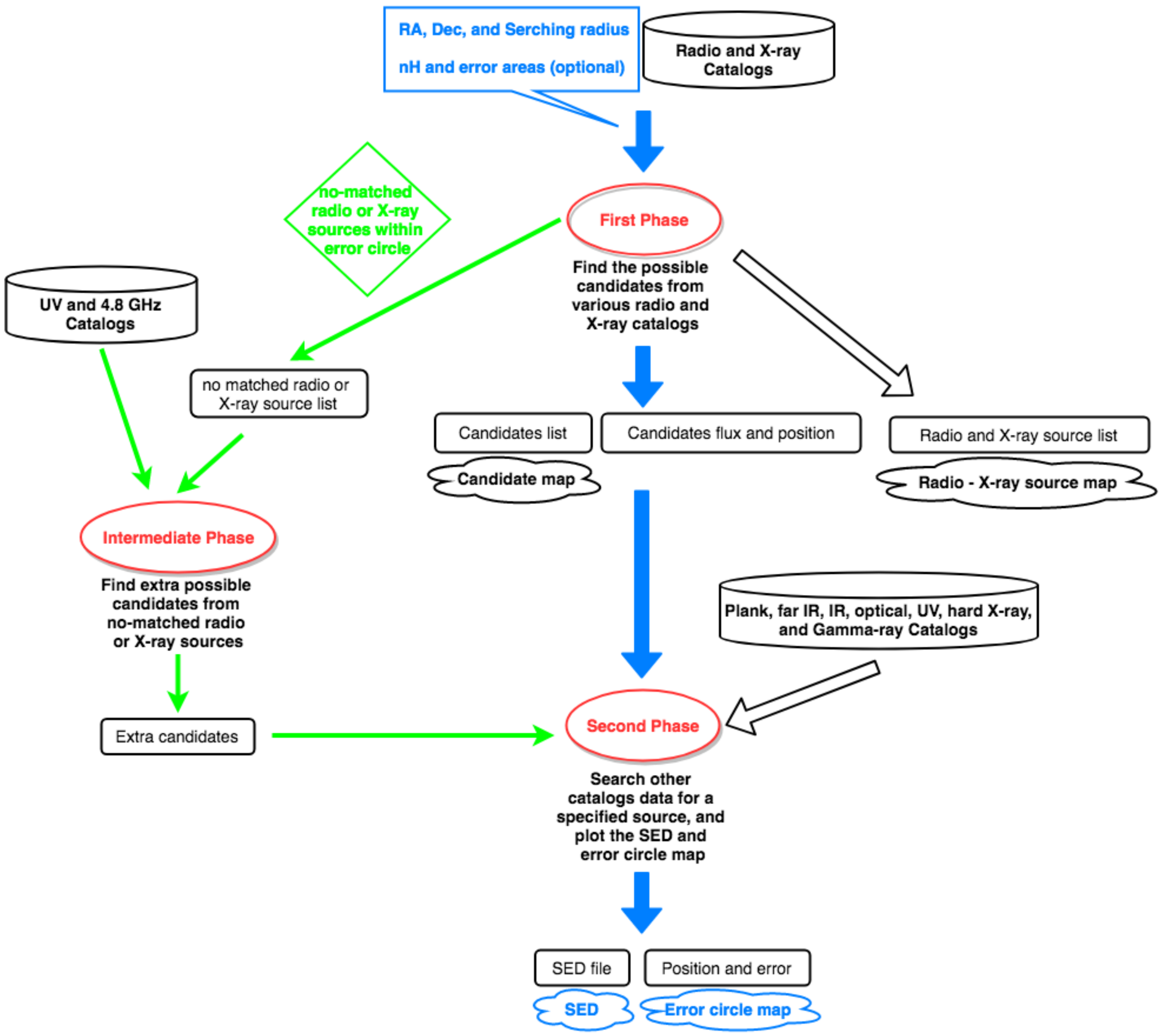

Figure 4.1: A simple scheme of the VOU-Blazars. The blue part means the mandatory processes as well as the initial input parameters and final outputs. The green part is the conditional processes which are executed only if there are further sources need to be checked. Under the conditions inside "diamond", the tool will further go through the green processes. The red ellipticals are three main phases of the VOU-Blazars. Round rectangles represent the file that input to or output from the tool, and clouds indicate the resulting figures. Cylinders illustrate the data from VO conesearch.

* **source vou-blazars 77.43 5.72 80 50**

  Specfiy error circle radius 50 armin, but did not specify nH value.

* **source vou-blazars 77.43 5.72 80 50 30**

  Specify two error circles with radii 50 and 30 arcmin, respectively.

* **source vou-blazars 77.43 5.72 80 3.e21 60 25 45**

Specify nH value and a error elliptical with major axis 60 arcmin, minor axis 25 arcmin, and position angle 45 degree.

* **source vou-blazars 77.43 5.72 80 50 60 25 45**
  Specify one error circle and one error elliptical. Note that if one circle and one elliptical are inserted as error areas, circle go first. If the elliptical major axis is larger than the error radius of the circle, the tool will plot the error elliptical first; otherwise, the circle will be plot first.

* **source vou-blazars 77.43 5.72 80 3.e21 50 60 25 45**
  Specify nH value, one circle, and one elliptical.

* **source vou-blazars 77.43 5.72 80 60 25 45 30 15 200**
  Specify two error ellipticals. The second one has major axis 30 arcmin, minor axis 15 arcmin, and position angle 200 degree.

* **source vou-blazars 77.43 5.72 80 3.e21 60 25 45 30 15 200**
  The maximum parameters that could be input to the VOU-Blazars. Specify nH value and two error ellipticals.

If the nH are not assigned to the VOU-Blazars, the default value is 5×10^{20} cm^{-2}; if no error circles and ellipticals are specified, the error radii are set to 0. Note that if there was HEASoft[9] installed and if the user did not input the nH value to the tool, the nH value will be calculated by the HEASoft instead of the value 5×10^{20} cm^{-2}.

The tool will then read all the input parameters and return a candidate map with all the blazars and blazar candidates it found during the first phase. A map with all radio and X-ray sources found from conesearch also are presented. Figure 4.2 (Left) is an example of the candidate maps and Figure 4.2. (Right) is the map of every radio and X-ray sources in the first phase. The indications of the color and symbol for these maps are presented in Table 4.4 Further information about the candidates are shown as well and will be discussed in section 4.3.

All sources returned are with number on the candidate map, and the user could select an interested source from the map and pass the source to the VOU-Blazars. By entering the source number to the tool, it will process to get further data for that source. Only one source could be sent to the tool during this period at a time. The zoom in area for

[9] https://heasarc.nasa.gov/lheasoft/

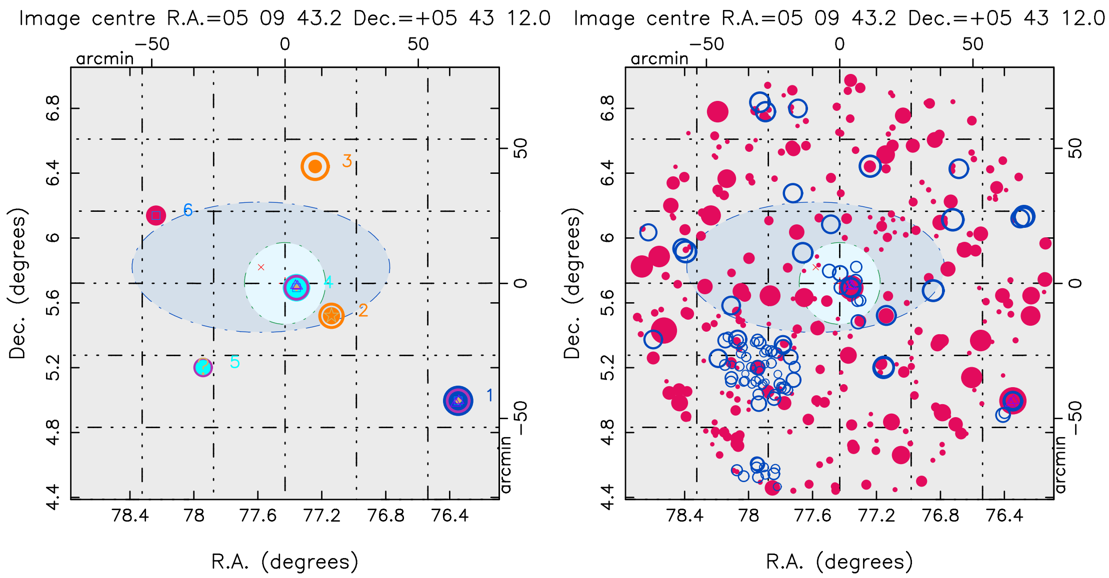

Figure 4.2: Example output of the candidates map (left) and RX sources map (right).

the error circle map, size of the error circle map, of that candidate also could be specified, in arcsec. Besides, if the user wants to check the SED points flux value or the points are from which catalogs, there is an option to show all the SED data for that source as well, with typing "osed" to the tool before it runs the second phase.

To sum up, all the available parameters input to the tool at this stage are following the order like, the candidate number, the zoom in radius (optional), and open sed option. If there is no zoom in radius inserted, the default size of the error circle map will be zoomed into 1 arcmin. The VOU-Blazar will output the SED and the error circle map of that interested source at the end of running the whole process. Examples of the SED and error circle map are shown in Figure 4.3.

The procedures described above are in a loop, which means that the user could keep inserting the source number for every candidates many times. To stop the loop and leave the VOU-Blazars, type "q" to quit the whole blazar finding process. All the figures and the coneserch outputs with being sorted in the folder "Results." The detailed explanation of the output results from the tool will be described in section 4.3.

In the "Results", there are folders represent every run, with different coordinates and different searching radius, from the VOU-Blazars. The name of the folder is the combination of RA value, dec value, and the searching radius. Furthermore, all the SED data produced by VOU-Blazars could be uploaded to SSDC SED builder. The data for SED builder, one file means one source/candidate, are saved inside the "SEDtool" folder

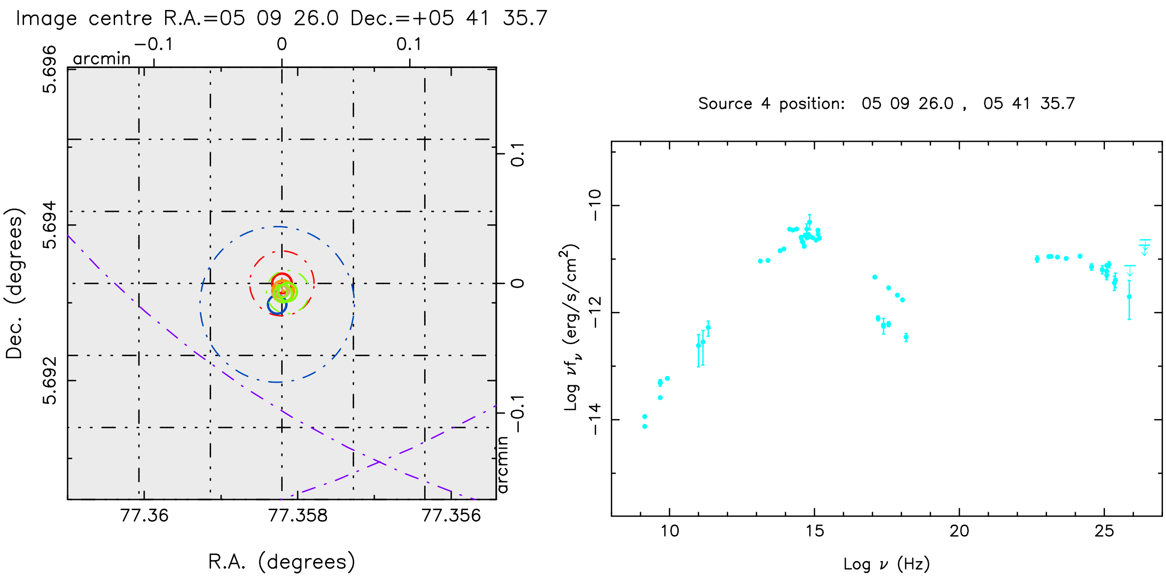

Figure 4.3: Example output of the error circle map and the SED.

under "Results".

One thing needs to be mention is that the VOU-Blazars might stop before the intermediate phase and before asking the user to insert an interested source number. When the radius or major axis of first specified error circle or error elliptical is larger than 20 arcmin, the tool will stop and ask if the user want to keep processing the Intermediate phase. If the user wants to skip the intermediate phase and directly go to the second phase, type "n"; otherwise, press "ENTER" key to keep searching candidates in the intermediate phase.

There is an option in VOU-Blazars to skip finding blazars candidates and only plot the SED and error circle map of a source at the given position called "SED mode." SED mode is run by replacing the output comment "vou-blazars" with " vou-sed", and followed by specified RA DEC. In principle, there are no big differences between the SED mode and Find Candidate mode, except that there is no candidate list and candidate map returned, and the SED mode is built to illustrate the SED with all the possible counterparts around the inserted coordinate.

4.2.2 First phase

Now the details process of the first phase in VOU-Blazars will be introduced. As described in section 2.1, the most effective way to find blazar candidates is beginning with multi-frequency data, especially the radio and X-ray catalogs. The main purpose of the first phase is to identify a number of possible blazar candidates within a large area (few tenths arcmin to several degrees) from various radio and X-ray catalogs.

Once the user specifies the input parameters to the tool, the tool will begin to recognize the parameters. Examples of the input parameters are shown in section 4.2.1. The minimum number of the input is 3, and the maximum number of that is 10; the tool will begin the next step until the number of input parameter is between 3 and 10. VOU-Blazars basically determined the parameters, like does the nH be specified or does the error circles/ellipticals be specified, from the number of inputs. If the nH is not inserted into the tool, a mean value of 5×10^{20} cm^{-2} all over the sky will be applied to that. The error radii will be set to 0 if no error circles or error ellipticals are input.

The tool then checked if HEASoft and Docker[10] is installed or not. Under the condition when the nH is not specified, if the HEASoft was installed, the nH value will be calculated by the HEASoft; otherwise, nH will be the set value 5×10^{20} cm^{-2}. The further SWIFT-XRT data could be retrieved from a pipeline, Swift DeepSky[11], if Docker was installed. The Swift DeepSky pipeline combines multiple latest observations made by Swift XRT at a given position in the sky, and the data will later be applied in the first phase. This option is turned down by default, but if the user wants to get the deep data from XRT survey with the pipeline, they could remove the comment symbol in regarding lines in the vou-blazars script. Note that the Swift Deepsky pipeline could do the data reduction only with largest area 16 arcmin, and that the field of view for XRT is 12 arcmin.

With all the input parameters are ready, the coordinate and the searching radius will be passed to the conesearch pipeline to retrieve the data from various radio and X-ray catalogs. The conesearch will obtain the data from VO in parallel. Not only the radio and X-ray catalogs, in the first phase, there were made used of other blazars, pulsar, and cluster catalogs. In the first phase, there were totally 28-catalog data searching through VO conesearch. The catalogs applied in the first phase are listed in Table 4.1, and Table 4.2 presents the retrieved frequencies of the X-ray data from each catalog.

After getting all the first phase data, the VOU-blazars is ready to reduce the data. For the intensity of the X-ray data, there were count rates or absorbed flux obtained from the VO. The subroutine "nhdeabsorb" will calculate the de-absorbed flux assuming X-ray spectral slope $\alpha_{\rm x} = 0.9$, following power law relation $F_\nu \propto \nu^{-\alpha}$. For those catalogs that count rate is obtained, the filter responses are considered when estimated the de-absorbed flux. For the RASS and WGA catalog, the ROSAT PSPC filter responses are applied;

[10]https://store.docker.com/

[11]https://github.com/chbrandt/swift_deepsky

Radio/Fermi Catalog	X-ray Catalog	Blazar/Pulsar/Cluster Catalog
NVSS [34]	XMMSL Dr2 Clean [123]	5BZCat [82]
FIRST [147, 69]	3XMM Dr7 [143]	3HSP
SUMSS V2.1 [77]	RASS 2RXS [22]	ATNF PULSAR [78]
CRATES [68]	WGACAT2 [145]	*Fermi* 2PSR [134]
Fermi 8YRS	Swift 1SXPS [47]	ZW CLUSTERS [152]
Fermi 3FHL [135]	SDS82[a]	PLANCK SZ2 [116]
Fermi 3FGL [6]	Einstein IPC [67]	ABELL [2]
1BIGB SED [12]	Einstein IPC slew [90]	MCXC [114]
	BMW-HRI [106]	SDSS WHL [144]
	Chandra[46]	SW XCS [76]

[a] Swift DeepSky data over Stripe82, http://vo.bsdc.icranet.org/sds82/q/cone/info

Table 4.1: Catalogs applied in the first phase

and for 1SXPC catalog, the XRT filter response are applied. For IPC / IPC slew and BMW-HDI catalogs, there were IPC and ROSAT HDI filter responses regarded. For other catalogs like 3XMM, XMMSL, and Chandra, there were absorbed flux retrieved from the VO; thus, no filter response necessary.

The de-absorbed flux then are converted to flux density at 1 keV (for total-band flux) or other certain frequency (for other band flux, if available) with α_x set to 0.9; detail description is written in Appendix D. For a detection from a catalog with at least three different bandwidths, like XMMSL, when the soft band has detected value while the hard band has not, there were assumed that the majority detected photons are coming from the soft band. Hard-band flux is more difficult to be detected than soft-band. So, the total-band fluxes are always converted to 1 keV, to avoid bias in cases of no hard band flux.

According to different catalogs, the corresponding photometric flag/criteria are applied. For example, there were only detections with sidelobe probabilities p(s) $<$ 0.15 in FIRST catalog are accepted. Besides, the XMM catalogs have several different fluxes from different cameras, PN, M1, M2, and EPIC, and there were applied the value from EPIC, which is the mean of the band-specific detections in all cameras.

Sometimes, there is no flux value or only upper limit for the sources in X-ray total band, like the b8 in 3XMM / XMM slew, C0 in 1SXPS, and total band in Chandra, the 1 keV flux then converted from the other nearby frequency band. There were only flux data with the error smaller than the value accepted. For the 1SXPS and Chandra catalogs,

X-ray Catalog	Retrived Frequencies	Converted Frequency
XMMSL Dr2 Clean	b8 (0.2 - 12 keV)	1 keV
	b6 (0.2 - 2 keV)	1.1 keV
	b7 (2 - 12 keV)	7 keV
3XMM Dr7	EP8 (0.2 - 12 keV)	1 keV
	EP1 (0.2 - 0.5 keV)	0.35 keV
	EP2 (0.5 - 1 keV)	0.75 keV
	EP3 (1 - 2 keV)	1.5 keV
	EP4 (2 - 4.5 keV)	3.25 keV
	EP5 (4.5 - 12 keV)	8.25 keV
RASS 2RXS	0.1 - 2.4 keV	1 keV
WGACAT2	0.24 - 2 keV	1 keV
Swift 1SXPS	Total 0.3 - 10 keV	1 keV
	Soft 0.3 - 1 keV	0.65 keV
	Medium 1 - 2 keV	1.5 keV
	Hard 2 - 10 keV	6 keV
XRT DeepSky / SDS82	Total 0.3 - 10 keV	3 keV
	Soft 0.3 - 1 keV	0.5 keV
	Medium 1 - 2 keV	1.5 keV
	Hard 2 - 10 keV	4.5 keV
Einstein IPC / IPC slew	0.2 - 3.5 keV	1 keV
BMW-HRI	0.1 - 2.4 keV	1 keV
Chandra	Full band 0.5 - 7 keV	1 keV
	Ultra Soft 0.2 - 0.5 keV	0.35 keV
	Soft 0.5 - 1.2 keV	0.85 keV
	Medium 1.2 - 2 keV	1.6 keV
	Hard 2 - 7 keV	4.5 keV

Table 4.2: Retrived frequencies of X-ray catalog

some data with only upper errors but no flux values, thus there were applied $3-\sigma$ upper limits for the data.

For radio catalogs, the position error will be applied as the geometric average of the fitted Gaussian model for the deconvoluted flux instead of the error value from the catalogs, which is the accuracy of the position value and not always works for extended radio sources. The position may be good, but for radio extended sources, the other counterpart of the extended sources may not exactly close to the position from radio catalogs. Thus there were applied the deconvoluted flux size as the position error not the error value from radio catalogs. However, sometimes the fitted major axis and minor axis from the NVSS catalog have only upper limit value instead of real value. When there is no real fitted value from NVSS, the position error will be the error value from the catalogs.

Still, there are some catalogs applied in the first phase without position error could be retrieved from VO, like the second version of RASS catalog (2RXS) and SWIFT catalogs. If the 2RXS count rate is larger than 0.1, the position error is set to 20 arcsecs; otherwise, the position error is assumed 40 arcsecs. For SWIFT catalogs, the position errors are limited to 10 arcsecs.

The VOU-Blazars begins the cross-matching when the data are properly reducted. There were considered the radio sources one by one to find nearby X-ray detections. Each radio sources is cross-matched with every X-ray catalogs, checking if that radio source has matched X-ray data nearby. The cross-matched radius between radio sources and the X-ray catalogs depends on sources by sources, and that will be the propagation of the position errors from both radio and X-ray sources to be matched. That is the radius is $\sqrt{(\text{radio position error})^2 + (\text{Xray position error})^2}$. If the cross-matched radius from both catalogs is smaller than 2 arcsec, it will be set to 2 arcsec.

Once the radio source has any X-ray counterpart nearby (radio-X-ray matched source), the VOU-Blazars will calculate the spectral slope $\alpha_{1.4\mathrm{GHz}-1\mathrm{keV}}(\alpha_{\mathrm{rx}})$ and define the type of the source in the first phase preliminary. If spectral slope $0.42 < \alpha_{\mathrm{rx}} \leq 0.78$, the source probably is HBL or IBL, then the tool will estimated the approximately ν_{peak} with $\log \nu_{\mathrm{peak}} = (1.44 - \alpha_{\mathrm{rx}})/0.05$. The source will be classified as HBL if $\log \nu_{\mathrm{peak}} > 15.5$; Otherwise, it will be classified as IBL. Apart from that, the source will be catalogrized as LBL, if spectral slope $0.78 < \alpha_{\mathrm{rx}} \leq 0.95$. For those radio-X-ray matched sources with spectral slope $\alpha_{\mathrm{rx}} \leq 0.42$, the tool will classify them as non-jet AGN. Other sources will be called unknown type, as they have unusual slope $\alpha_{\mathrm{rx}} > 0.95$; those sources probably with very faint X-ray flux. Some sources without X-ray flux values, maybe only with upper limits in 3XMM in all wavebands, will be defined as unknown type too.

As the radio sources might have more than one X-ray detections from various of catalogs, and the α_{rx} also are different for different X-ray catalogs. The types classified from those X-ray catalogs might be different; a source might be classified as IBL with 3XMM data, but might be classified as HBL with RASS data. The final type of each matched sources in the first phase will be defined as the majority type. All the radio-X-ray matched sources, as well as the radio and X-ray data of them, will be sent to the second phase. Considering the radio position is more accurate than that of X-ray, there was radio position applied to be passed to the second phase.

After the final type of the radio-X-ray matched sources are determined, the VOU-Blazars then checks if there the sources are already cataloged in 5BZCat, 3HSP, Cluster catalogs, or Pulsar catalogs. The matching radius is the maximum value between the position error of the matched radio sources and 10 arcsecs. There were considered the matched source is part of those catalogs if the distance between the matched source and cataloged position is within the 10 arcsecs, even though the radio position error is smaller than 10 arcsec. If the radio-X-ray matched sources are in those catalogs, they will be shown on the candidate source map as well.

As each candidate is found by matching every radio sources with each X-ray catalogs, there may be two radio sources, one from FIRST and one from NVSS, from the same object be treated as different candidates. If the two radio detections are very close to each other, says the distances between them are smaller than 0.1 arcsecs, the tool will consider the two detections are from the same source. Therefore, in this multiple radio detection case, only one candidate instead of two candidates being sent to the next step, following the order of priority, FIRST, NVSS, SUMSS. If the multiple radio detections are from the same catalog, the coordinate of the brighter one will be applied in the second phase. Although there was only one candidate position passed to the second phase for multiple radio situation, all the fluxes and position error values from every multiple detections (required by the second phase) will be passed.

Till now, all the radio-x-ray matched sources have been sent to the second phase; however, some good cataloged blazars does not have both radio and X-ray counterparts, but should not be missed. Thus, the tool checks every cataloged sources (3HSP, 5BZCat, and PSR) without radio and X-ray matched along with their radio or X-ray data and passes them to the second phase as well. The cross-matched radius is defined as the position error of the radio or X-ray sources to be matched, with accepted minimum value 10 arcsecs.

Last, there are some sources without radio-X-ray matched, hereafter single radio or single X-ray sources could be interesting as well. A particular phase is designed to deal with them; the phase is triggered between first and second phase thus called intermediate phase. If those single radio or single X-ray sources are inside the error region specified to the tool and if the sources are not in other blazars/clusters/pulsars catalogs, they will also be passed to the intermediate phase. The intermediate phase will further examine those sources.

Now all the possible blazar candidates, that is radio-X-ray matched source, no radio-X-ray matched cataloged sources, and single radio or single X-ray source been sent to intermediated phase, are selected, the VOU-Blazars then plots the source map of all the candidates. Another source map which illustrates all the radio and X-ray sources also are shown. The example of the candidate map and radio-X-ray sources map are shown in Fig.4.2 and will be described in section 4.3. After saving all the output figures and VO results, the VOU-Blazars has done the first phase and processes the next step.

4.2.3 Intermediate phase

Intermediate phase is built to find extra good blazar candidates without both radio and X-ray data. An LSP blazar might not be detected in X-ray as the X-ray are too faint, while an HSP with relatively high ν_{peak} value might not be detected in radio. That is, for HSPs with very faint flux, might not be detected by current radio survey, as Fig.2.5 depicted, especially for those extreme ν_{peak} blazars. It is worth checking those single radio or single X-ray sources in order not to lose good blazar candidates.

As there are too many single radio or single X-ray sources, the VOU-Blazars checks only the sources inside the error area. The intermediate phase will be activated only if there are any single radio or single X-ray sources within the error circle/elliptical; otherwise, the tool will directly go to the second phase. If the error circle radius or error elliptical major axis $\geq$ 20 acrmin, the tool will ask the user want to continue the intermediated phase or not. To skip the intermediate phase, input "n", and then the tool will jump to the second phase. Once the user wants to keep processing the intermediate phase for the occasion of large error circle, the intermediate phase will be operated.

In the intermediate phase, there were only GALEX, PMN, and GB6 catalogs applied. The preliminary step to find extra interesting candidates from single radio or X-ray sources is to search the UV counterparts around them. Except for radio and X-ray emission, a good blazars candidates usually have UV emission as well. If a source only has the radio from non-thermal but without X-ray and UV or a source only have X-ray but not radio and UV data, it is too uncertain to be selected as a blazar candidate. Moreover, for single radio sources, there were searched the 4.8 GHz radio catalogs as well to find steep radio sources. The searching radius for VO conesearch in this step is set to same as the input radius, same as in the first phase. The GALEX data then be reduced and de-reddened using Fitzpatrick extinction rule [49].

There might be more than one X-ray detections (either from the same catalog like 3XMM or from different X-ray catalogs) very close to each other. If the distance between two X-ray detections is less than 12 arcsec, the tool considers them are from the same sources. Likewise, there might be both NVSS and FIRST detections for a radio source, and these detections are regarded as the same source when they are closer than 6 arcsec, as that are been done in the first phase.

Here there were 12 arcsec applied for X-ray as the position uncertainties of X-ray catalogs generally are larger than that of radio catalogs. Note that the order of priority for multiple X-ray detections sent to next step during the intermediate phase is SWIFT, Chandra, XMM, BMW, ROSAT, and IPC. If the detections for a source are from the same catalog, such as the multiple detections from 3XMM, the position with the smallest error among them will be passed to the second phase.

The tool then cross-matching each X-ray detections and radio detections sources by sources with every GALEX data. For radio sources, there were further cross-matching with 4.8 GHz PMN and GB6 catalogs. Like the cross-matching in the first phase, the matched radius is the combination of the position error of two sources being matched and the minimum value of that is set to 2 arcsec. Slope between UV and X-ray sources are calculated for matched sources, and there are only matched sources with $\alpha_{\mathrm{UV-X-ray}} \leq 1.4$, $\alpha_{\mathrm{r-UV}} \leq 0.75$, or $\alpha_{\mathrm{1.4GHz-4.8GHz}} \leq 0.7$ accepted. If there are UV sources matched one of the X-ray detections from an X-ray source and there are either UV sources or 4.8 GHz sources matched one of the radio detection from a radio source, the sources will be passed to the second phase.

Once the intermediate phase was triggered and found further single radio and X-ray candidates, the VOU-Blazars will plot the candidate map again with those further candidates. The differences between the sources maps with/without the intermediate phase are presented in Figure 4.4 with a *Fermi* 8 years detection, FL8Y J0439.4-3202.

Figure 4.4 shows that there were two extra candidates without radio and X-ray matched found from the intermediate phase. One single X-ray and one single radio sources within larger error are found during the Intermediate phase.

4.2.4 Second phase

Plotting the SED, refining the type of the candidates, and showing only good blazar candidates is the purpose of the second phase. Before processing the second phase, the VOU-Blazars required users to input source number of an interested candidate, one candidate at a time. Other optional inputs to the second phase are discussed in section 4.2.1. The tool then reads the radio position of that candidate assigned and begin to retrieve further data, like 4.8 GHz, far IR, IR, optical, UV, Gamma-ray, for that sources with VO. In the second phase, the searching radius of conesearch is not the parameter inserted

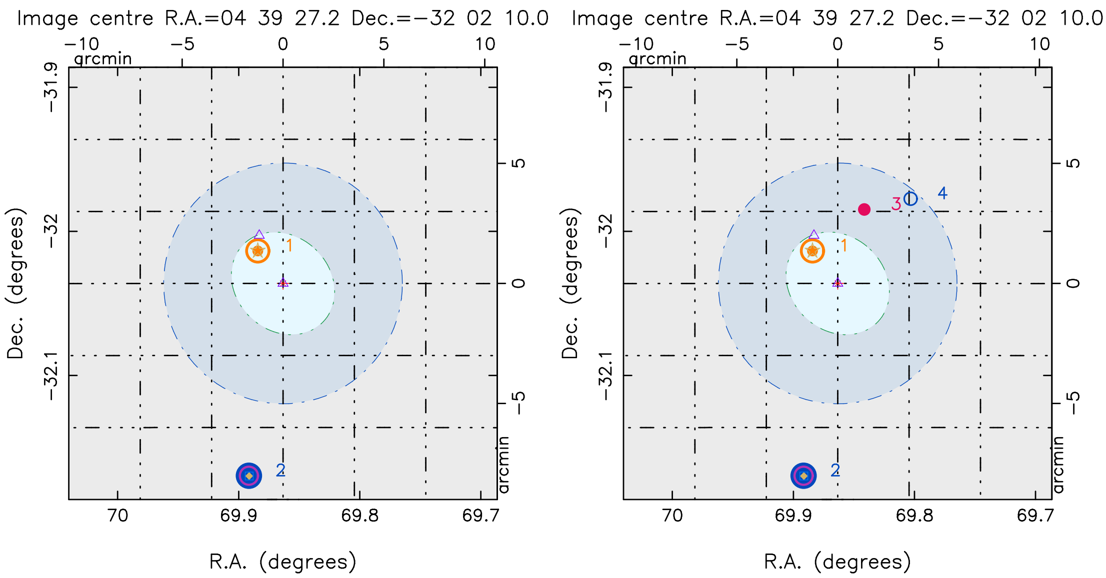

Figure 4.4: Example output with (right) and w/o (left) intermediate phase.

into the tool but set to some values according to the waveband of the searching catalog. As the aim is to find more data for the interested candidate and the reason that those catalogs usually have much more data than radio and X-ray, the tool only searching the data for the candidate within a small radius. The catalogs applied in the second phase are shown in Table 4.1.

There were only flux data with an error smaller than the value accepted except for the Fermi data, that described in the catalog, those points are upper limits. Several catalogs, like GB6, PMN, AT, WISE...etc, are with the photometric quality available, if the data already marked as problematic/unreliable points, they will be illustrated with a different symbol on SED in the later phase. The SDSS points will be considered doubtful with VOU-Blazars, if the flux is smaller than 10 times zero-magnitude flux, meaning that the observed magnitude maybe is differed by larger than 1 %, as largest as 0.25 magnitude deviation (Stoughton et al. 2002)[132]. Apart from that, no flux error available from NORTH20CM, CRATES, USNO, and GAIA catalogs. When the flux/magnitude error retrieved from the conesearch is 0, there were upper limits applied to the SED.

Note that the reduction of IR, optical, and UV catalogs required the calibration of extinction. Fitzpatrick (1999) [49] template are applied to de-redden the magnitude of these catalogs, and Appendix B explains all the details to do the reduction. Effective wavelengths and zero-magnitude fluxes applied for every bands of those catalogs are listed in Table 4.6.

4.8/8.6 GHz Catalog	Searching Radius	WISH and Plank Catalog	Searching Radius
GB6 [63]	30 arcsec	WISH 352 MHz [38]	15 arcsec
GB87 [62]	30 arcsec	PCCS2 44 GHz [138]	3 arcmin
PMN [65, 66, 148, 64, 149]	30 arcsec	PCCS2 70 GHz [138]	3 arcmin
ATPMN [85]	15 arcsec	PCCS2 100 GHz [138]	3 arcmin
AT20G [91]	15 arcsec	PCCS2 143 GHz [138]	3 arcmin
NORTH20CM [146]	2 arcmin	PCCS2 217 GHz [138]	3 arcmin
CRATES [68]	15 arcsec	PCCS2 353 GHz [138]	3 arcmin
Far IR / IR catalog	**Searching Radius**	**Optical Catalog**	**Searching Radius**
SPIRE250 [127]	15 arcsec	USNO-B1 [87]	10 arcsec
SPIRE250 [127]	15 arcsec	SDSS Dr14 [20, 3]	10 arcsec
SPIRE250 [127]	15 arcsec	HST GSC2.3.2 [75]	10 arcsec
2MASS [129]	10 arcsec	Pan-STARRS Dr1 [29]	10 arcsec
AllWISE [36]	10 arcsec	Gaia Dr1 [53, 52]	10 arcsec
UV / X-ray Catalog	**Searching Radius**	**γ-ray Catalog**	**Searching Radius**
UVOT SSC 1.1 [104, 151]	15 arcsec	Fermi 3FGL [6]	20 arcmin
GALEX [89, 18]	15 arcsec	Fermi 2FHL [8]	20 arcmin
XMMOMSUSS 3 [105]	15 arcsec	Fermi 3FHL [135]	20 arcmin
XRT spectral data [a]	15 arcsec	Fermi FL8Y [b]	20 arcmin
BAT 105 Months [16]	10 acrmin	1BIGB SED [12]	10arcmin

[a] http://vo.bsdc.icranet.org/xrtspec/xrtspec/cone/info

[b] https://fermi.gsfc.nasa.gov/ssc/data/access/lat/fl8y/

Table 4.3: Catalogs applied in the second phase

The position error of CRATES, SDSS, USNO, and GALEX could not be retrieved from the catalogs, and there were assumed 5, 0.5, 0.5, and 1 arcsec for them, respectively. Besides, some of the catalogs (WISH352, ATPMN, AT20G, NORTH20CM, and GSC) gives only the accuracy of the position instead of a real error value. For those catalogs, the position errors are applied as 10 times of the accuracy, assuming the actual errors are not larger than the applied one.

There was applied likelihood analysis for every sources from 4.8 GHz, PLANK, far IR, or *Fermi* with every first-phase candidates within their error circle, not only the interested one been specified to the second phase. As the positional error of these catalogs is relatively larger than that of from IR, optical, or UV catalogs, the likelihood test is applied only for them. The likelihood, for example, of a far IR source or a *Fermi* source is the counterpart of the candidate is calculated using

$$
\begin{aligned}
\text{LIKELIHOOD} &= \frac{Q(\leq S)\exp^{-\frac{r^2}{2}}}{2\pi n(\leq S)\sigma^2} \\
\sigma &= \sqrt{{\sigma_1}^2 + {\sigma_2}^2} \\
r^2 &= 2(\frac{\Delta}{\sigma})^2
\end{aligned}
\tag{4.1}
$$

where S is the intensity or flux of the first-phase candidates, σ represents the propagation of the position errors of the two sources being tested, and Δ means distant between the two sources. $Q(\leq S)$ is the a priori probability that a "true" counterpart brighter than the S exists in the association. For simplicity, the $Q(\leq S)$ is fixed to 1, assuming that there always were counterpart found in every trial. Number density $n(\leq S)$ is estimated with NVSS sample with breaking line.

The "best" counterpart among the first-phase candidates for a far IR source or a *Fermi* source will be the one with largest LIKELIHOOD value. When the "best" counterpart is the interested candidate specified, the far IR or Fermi data will be shown on SED, assuming that the far IR or *Fermi* source is the counterpart of the interested candidate. However, sometimes, the likelihood method does not always work especially in the case of there are other bright sources very close to the candidate. In that case, the tool will ignore the result from likelihood method.

Next, the tool cross-matches every sources from the catalogs applied in the second phase with the interested candidate. Following what have done in the first phase, the matched radius is the propagation of the position errors from both sources to be matched, with the minimum accepted value of 2 arcsec. Sometimes, there is more than one source from the same catalog inside the matched radius, like there are two WISE detections within the combined position errors of candidate and WISE. The VOU-Blazars accepts the closer detection as the counterpart for the candidate when there are multiple detections from the same catalog.

After all the counterparts for the interested candidate are defined, the tool will show every matched counterpart from the second phase. Other information like the spectral slope between radio and IR, radio and UV, UV and X-ray, γ-ray photon index...etc are also displayed. The tool then outputs files that contain all the counterparts flux and position error of the candidate (See section 4.3 for more details). At the end of the second phase, an SED and an error circle map, examples are shown in Figure 4.3, will be illustrated as well. An SED file could be uploaded to SSDC SED tool is available to compare the differences between the SED produced by VOU-Blazars and from the SED tool.

The user could keep specifying interested sources until inserting "q" to stop the VOU-Blazars. Before going to the next candidate, there were saved the SED, error circle map, and conesearch results from the second phase. The final thing that VOU-Blazars do is to remove original files from VO conesearch, which produces a file for every catalogs searched if there are sources found in the catalogs.

4.2.5 SED mode

The SED mode of VOU-Blazars is designed to illustrate the SED of a source at a given position quickly without going through the processes of finding blazar candidates. In SED mode, the tool finds all the counterparts from every catalogs applied in the first phase and second phase. Comparing with the usual Find Candidate mode, the SED mode only returns flux and error circle along with the SED and error circle map for all the matched counterparts rather than returns a list and a map of potential candidates. Thus, the user does not need to further specified an interested candidate during the working process. Cross-matched radius in SED mode is the position error of each searching catalogs.

4.3 Results from the VOU-Blazars

```
Searching 28 catalogs
( 1 / 28 ) FIRST : NO SOURCES FOUND
( 2 / 28 ) SUMSS : NO SOURCES FOUND
( 3 / 28 ) SDS82 : NO SOURCES FOUND
( 4 / 28 ) SDSSWHL : NO SOURCES FOUND
( 5 / 28 )  ZWCLUSTERS : SUCCESS
( 6 / 28 ) PSZ2 : NO SOURCES FOUND
( 7 / 28 )  5BZCat : SUCCESS
( 8 / 28 )  3HSP : SUCCESS
( 9 / 28 ) IPC2E : NO SOURCES FOUND
( 10 / 28 ) ABELL : NO SOURCES FOUND
( 11 / 28 ) MCXC : NO SOURCES FOUND
( 12 / 28 ) SWXCS : NO SOURCES FOUND
( 13 / 28 )  CRATES : SUCCESS
( 14 / 28 )  Fermi8YL : SUCCESS
( 15 / 28 ) 1BIGB : NO SOURCES FOUND
( 16 / 28 ) BMW : NO SOURCES FOUND
( 17 / 28 ) PULSAR : NO SOURCES FOUND
( 18 / 28 )  WGACAT : SUCCESS
( 19 / 28 )  SXPS : SUCCESS
( 20 / 28 )  XMMSL : SUCCESS
( 21 / 28 ) IPCSL : NO SOURCES FOUND
( 22 / 28 ) F2PSR : NO SOURCES FOUND
( 23 / 28 )  3FHL : SUCCESS
( 24 / 28 )  NVSS : SUCCESS
( 25 / 28 )  3FGL : SUCCESS
( 26 / 28 )  RASS : SUCCESS
( 27 / 28 ) CHANDRA : NO SOURCES FOUND
( 28 / 28 )  3XMM : SUCCESS
```

Figure 4.5: Output from conesearch. If there were source found in the searching catalog, it will be illustrated with bold green.

The outputs of the VOU-Blazars, including detailed descriptions for the figures and the terminal outputs, will be explained in this section. There were illustrated some of the outputs with six examples, which includes a neutrino source, 2 FL8Y sources, and 3 random assigned positions. First of all, the output from conesearch of the neutrino detection during the first phase are depicted in Figure 4.5.

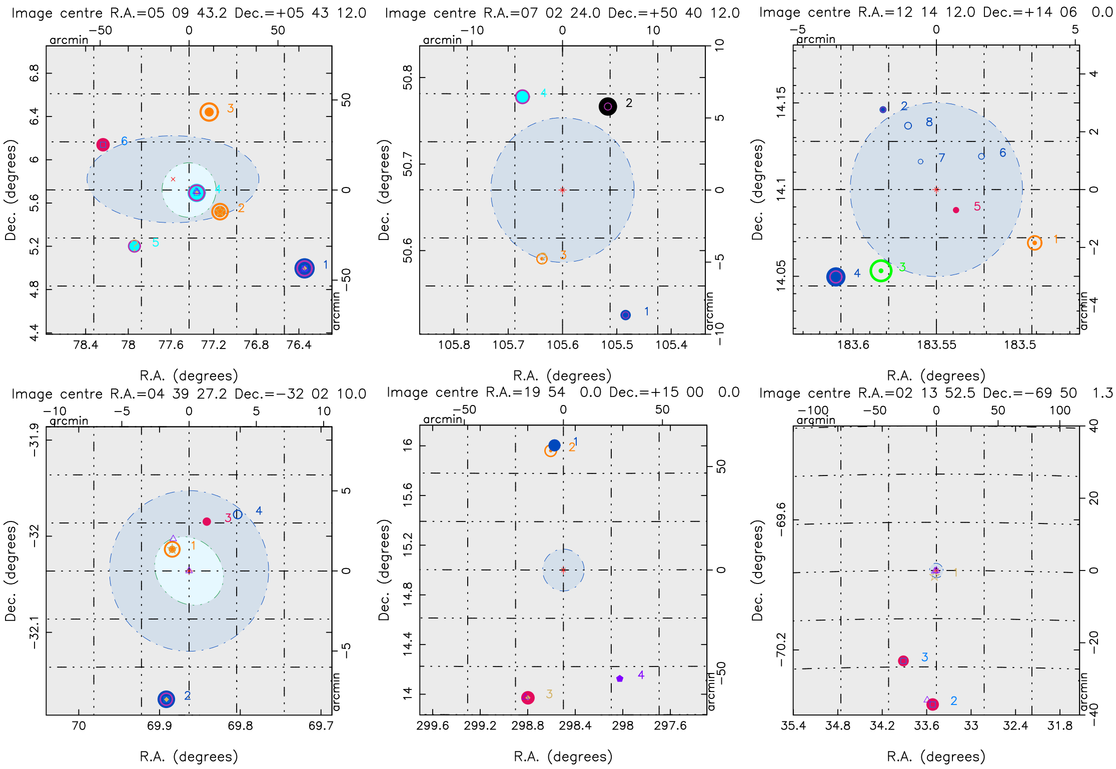

Figure 4.6: Candidate map examples.

After the first phase is done, the tool will list all the candidates with a map. Examples of candidate map for all 6 cases are shown in Figure 4.6, and the meaning of the symbols in source map from VOU-Blazars are explained in Table 4.4.

Case 1, the upper left in Figure 4.6, is the candidate map which lists all the possible counterparts for a neutrino event, IceCube-170922A [136]. The larger error elliptical is the 90 % of the neutrino position, and the smaller error circle is set to 15 arcmins for testing. Source number 4, and ISP, TXS 0506+056, also cataloged in 5BZCat (5BZBJ0509+0541) and CRATES (J050926+054143) with the blue square and golden diamond on the figure, is the closet and most possible counterpart [100] for the neutrino event. The ISP is also detected by *Fermi* and in 3FHL catalog (3FHL J0509.4+0542), with purple triangles nearby. Two HBL candidates found around the neutrino detection, source number 2 are inside the 90% error elliptical and in 3HSP catalog (3HSP J050833.3+053109, with golden star) as well, while source number 3 is not in the error elliptical.

Source number 1 is an LSP candidate in 5BZCat (5BZQ J0505+0459) and CRATES

Color	Meaning	Symbol	Meaning
Orange	HBL candidate	Hallow Circle	X-ray component
Light Blue	IBL candidate	Filled Circle	Radio component
Dark Blue	LBL candidate		
Green	Non-jetted AGN candidate		
Black	Unknown type source		
Symobol and Color	Meaning	Symobol and Color	Meaning
Gold Star	3HSP source	Red Filled Circle	Single radio source
Gold Diamond	5BZCat source	Blue Hallow Circle	Single X-ray source
Question Mark	Cluster	Purple Pentagon	Pulsar
Blue Square	Crates source	Purple triangle	γ-ray sources

Table 4.4: Symbol meaning of the candidate map and Radio-X-ray map

(J050523+045945), and source number 5 is an ISP candidate close to galaxy cluster (zw 4472), with the question mark on the figure. There are γ-ray detections (3FHL J0505.4+0458 and FL8Y J0505.3+0459), purple triangles around candidate number 1 as well. There is a CRATES source, J051256+060835, without radio-X-ray matched, source number 6, shows as the red filled circle with the blue square on it. Note that for candidate number 1, 4, and 5, the X-ray counterpart converted to size on candidate map is smaller than that of for radio counterpart, causing the hollow circle will be covered by the filled circle and could not be distinguished. In these situations, the X-ray counterparts are illustrated with magenta color.

Case 2 and Case 3, the middle up and upper right candidate maps in the Figure, are the result maps from random positions, (105.6 , 50.67) and (183.55 , 14.1), with applied error circles roughly half of the searching radius. Candidate number 2 in case 2 is classified as unknown type, and source number 3 in case 3 is a non-jet AGN candidate. Besides, there are an LSP, an ISP, and an HSP candidate found in Case 2, and two LSPs and an HSP candidate found in Case 3, with source number 3 in case 2 also might be a cluster member (zw 5047). Several interested single X-ray sources and a single radio source (blue hallow circles and red filled circle) in the specified error circle are selected from the Intermediate phase in case 3.

In case 4, the lower left in the Figure 4.6, there were run the VOU-Blazars with the position of a *Fermi* FL8Y source, FL8Y J0439.4-3202. The smaller error elliptical is the error region for that FL8Y source, and the larger circle is a trial value which is approximately half of the searching radius. The candidate map around the source suggests that there are a 3HSP (3HSP J043932.2-320052) and a 5BZCat LSP (5BZU J0439-3210), which is also in CRATES (J043929-320956), within the specified radius. The 3HSP source, candidate number 1, is inside the error region of the *Fermi source* and may be the most possible counterpart for that. Two extra single radio and X-ray sources within the assigned larger error circle are found and may be worth checking as well.

In case 5, the middle low candidate map in the Figure, the tool is run with an arbitrary coordinate (298.5 , 15.0) with error radius set to 10 arcmins. An LSP and an HSP candidate are found in this case. Candidate number 3 is a 5BZCat source (5BZQ J1955+1358) without X-ray detection yet; the candidate is also detected by *Fermi*. Furthermore, there is a Pulsar, PSR J1952+1410, source number 4 with the purple pentagon, in the searching region.

The last case, case 6 in the lower right, is a trial with FL8Y detection, FL8Y J0213.8-6950. The candidate map shows that the most probable counterpart for the FL8Y source is 3HSP J021358.6-695137, source number 1, without radio counterpart. Another two CRATES sources (J021405-702701 and J021545-701448) without radio-X-ray matched also are found as well within the searching radius. The two sources might be interested especially for the candidate number 2, the source might be *Fermi* counterpart as there is another FL8Y source (FL8Y J0214.3-7025) nearby.

```
 RASS/NVSS ra dec 05 05 23.2, 04 59 42.9 radio flux d.   986.400 flux-ratio     45. arx  0.800                        possible LBL  Dist.
77.971 arcmin
 XRT/NVSS ra dec 05 05 23.2, 04 59 42.9 radio flux d.   986.400 flux-ratio     17. arx  0.852                        possible LBL  Dist.  7
7.971 arcmin
 Match nr.   1        ra dec:  76.34662,  4.99525
 ................Cataloged sources.................
  5BZQ J0505+0459
  CRATES J050523+045945

 XMMSLEW/NVSS ra dec 05 08 33.5, 05 31 12.4 radio flux d.   45.300 X-ray/radio flux-ratio   1081. arx  0.632 Log(nu_p) 16.2+/-~1  possible
HBL Dist.  21.087 arcmin
 Match nr.   2        ra dec:  77.13954,  5.52011
 ................Cataloged sources.................
  3HSP J050833.3+053109

 RASS/NVSS ra dec 05 08 58.0, 06 26 29.1 radio flux d.   19.200 X-ray/radio flux-ratio   6628. arx  0.536 Log(nu_p) 18.1+/-~1  possible HBL
 Dist.  44.722 arcmin
 Match nr.   3        ra dec:  77.24154,  6.44142
 ................Cataloged sources.................

 RASS/NVSS ra dec 05 09 26.0, 05 41 35.7 radio flux d.  535.900 X-ray/radio flux-ratio     78. arx  0.770 Log(nu_p) 13.4+/-~1  possible IBL
 Dist.   4.577 arcmin
 XRT/NVSS ra dec 05 09 26.0, 05 41 35.7 radio flux d.  535.900 X-ray/radio flux-ratio     75. arx  0.772 Log(nu_p) 13.4+/-~1  possible IBL
Dist.   4.577 arcmin
 Match nr.   4        ra dec:  77.35821,  5.69325
 ................Cataloged sources.................
  5BZB J0509+0541
  CRATES J050926+054143

 3XMM/NVSS ra dec 05 11 46.1, 05 12  2.9 radio flux d.   42.200 X-ray/radio flux-ratio    116. arx  0.749 Log(nu_p) 13.8+/-~1  possible IBL
 Dist.  43.655 arcmin
 Match nr.   5        ra dec:  77.94204,  5.20081
 ................Cataloged sources.................
  zw  4472

 Candidate nr.   6, Known flat spectrum radio source with no radio/X-ray match: CRATES J051256+060835 found at a distance of  54.283 arcmin
```

Figure 4.7: Output from first phase

Figure 4.7 is the example output from the terminal after the first phase is done for case

1; the other cases are shown in Appendix A. VOU-Blazars will list all the possible blazars candidates, as well as the no radio-X-ray, cataloged sources after the first phase. For each candidates, every radio detections and X-ray detections are illustrated to the user; for a candidate with multiple radio detections, there were assigned the same number and considered as repeated radio counterpart. The tool will show if the candidates already in some blazars, galaxy clusters, or pulsar catalog as well. For the other without both radio and X-ray counterparts but cataloged in some catalogs like 5BZCat, 3HSP, CRATES, Pulsars...etc, they will also be presented.

```
----------------------------------------
 69.84179  -31.98492 radio source    35.896 mJy
GALEX : 22.172   0.000            35.364 arcsec away
      radio-UV slope:  0.629
GALEX : 22.458   0.000            51.639 arcsec away
      radio-UV slope:  0.648
GALEX : 20.915   0.000            21.033 arcsec away
      radio-UV slope:  0.548
GALEX : 22.228   0.000            71.833 arcsec away
      radio-UV slope:  0.633
GALEX : 22.551   0.000            64.604 arcsec away
      radio-UV slope:  0.654
GALEX : 22.005   0.000            50.262 arcsec away
      radio-UV slope:  0.618
GALEX : 22.030   0.000            30.248 arcsec away
      radio-UV slope:  0.620
----------------------------------------
 69.80316  -31.97737 X-ray source with 1 keV flux  3.939E-14
GALEX : 21.103   0.000             3.221 arcsec away
      UV-X-ray slope:  1.270
```

Figure 4.8: Output from intermediate phase

```
ra , dec = 69.88425 , -32.01353

Candidate nr.   1,  3fgl   1  point(s)
Candidate nr.   1,  3fhl   1  point(s)
Candidate nr.   1,  fermi8yr   1  point(s)
Candidate nr.   1,  gaia   1  point(s)
Candidate nr.   1,  galex   3  point(s)
Candidate nr.   1,  hst   1  point(s)
Candidate nr.   1,  panstarrs   1  point(s)
Candidate nr.   1,  uvot   5  point(s)
Candidate nr.   1,  wise   1  point(s)
```

Figure 4.9: Output from second phase. The conesearch result from every catalogs.

There were selected a candidate from case 4 shown here, candidate number 1 in case 4, and the candidate is also cataloged in 3HSP; more examples are illustrated in Appendix A. After specifying the number of the interested candidate, the tool will list it's RA dec and how many points in available catalogs, like Figure 4.9 depicts, and then will find extra counterparts for the candidate. The terminal output from the second phase is presented in Figure 4.10. Figure 4.11 depicts the SED and error circle map for several interested candidates The meaning of color for each error radius is shown in Table 4.5.

```
   1  candidate with average radio 1.4 GHz flux density    10.600 ,  average X-ray 1 keV flux  4.691E-13
      average X-ray-radio spectral slope:  0.575
6x,R.A. , Dec. =  69.88425  ,-32.01353

 NO WISH object within  5.63 arcsec
 .......................5 GHz Radio....................
 No 5 GHz detection within  30.  arcsec
 ................100 GHz Radio.......................
           0
 No 100 GHz detection within   3.  arcmin
 ................Far Infrared.......................
 No far IR detection within  30.  arcsec
 ....................IR............................
WISE     IR-X-ray slope:  0.961,  radio-IR slope:  0.280,    3.606 arcsec away
 ......................Optical.......................
 GAIA        18.9489994
GAIA     Optical slope: 99.990,    3.646 arcsec away
 HST         0.00000000       20.9762993       0.00000000       0.00000000       0.00000000
HST      Optical slope: 99.990,    3.566 arcsec away
 PANSTARRS   0.00000000       19.3813992       0.00000000       0.00000000       0.00000000
PANSTARRS Optical slope: 99.990,    3.646 arcsec away
 ......................UV..........................
GALEX    UV-X-ray slope:  1.014,  radio-UV slope:  0.408,    4.151 arcsec away
 GALEX       20.9399891       19.8577003
UVOT     UV-X-ray slope: 99.990,  radio-UV slope: 99.990,    4.002 arcsec away
 UVOT        19.6289005       0.00000000       0.00000000       0.00000000       0.00000000       0.00000000
 UV slope   99.9899979
UVOT     UV-X-ray slope:  0.994,  radio-UV slope:  0.410,    3.905 arcsec away
 UVOT        0.00000000       0.00000000       0.00000000       19.8530006       0.00000000       0.00000000
 UV slope   99.9899979
 ......................hard X-ray and XRT spectral data.................
 NO BAT or XRT detection within   4.413 arcmin
 ......................Gamma-ray.................
3FGL     photon index: 1.771,    1.760 arcmin away
3FHL     photon index: 2.222,    0.647 arcmin away
Fermi8YL photon index: 1.850,    1.720 arcmin away
 ......................TeV.................
 NO TeV detection within 10 arcmin
 ......................source type and cataloged.................
 Already in 3HSP!!
```

Figure 4.10: Output from second phase. The counterparts of the interested candidate.

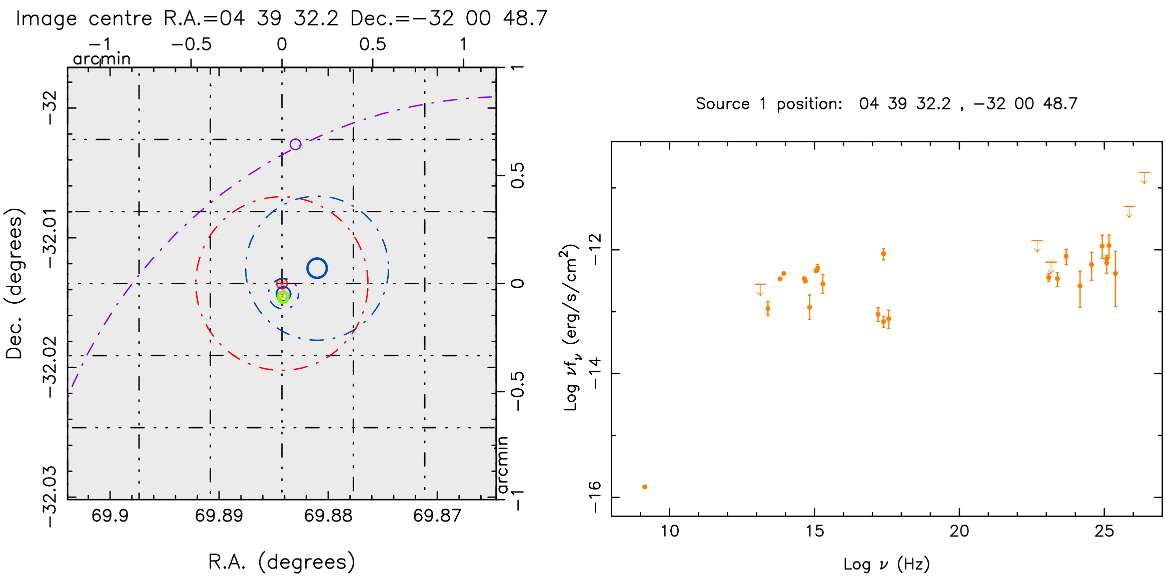

Figure 4.11: The error circle map and the SED.

All the counterparts for the interested candidate are shown in the second phase. There were listed fluxes and slope information for every counterparts as well. The SED of this 3HSP shows that there is variability in X-ray and the synchrotron peak may locate at

$\approx 10^{15.4}$ Hz; γ-ray data also consistent with the Synchrotron emission. According to the error circle map, there is no wrong or problematic counterparts for the candidate.

Color	Waveband
Red	Radio
Orange	Infrared
Gold	Optical
Green	Ultraviolet
Blue	X-ray
Purple	γ-ray

Table 4.5: Color represented in error circle map

Next, there were introduced some good applications for the VOU-Blazars. First of all, there were many good HSPs found by running the tool; specifically, some of the new sources add to the 3HSP in section 2.4 are selected with the VOU-Blazars. The tool retrieved data from more catalogs (GAIA, PanSTARRS, XMMOM...etc) or the latest version of some catalogs (GALEX, XMM, Swift XRT...etc) than the SED tool. Thus, the SED built by VOU-Blazars may contain more data and could identify more HSP candidates. With more data, the synchrotron peak value could be refined as well.

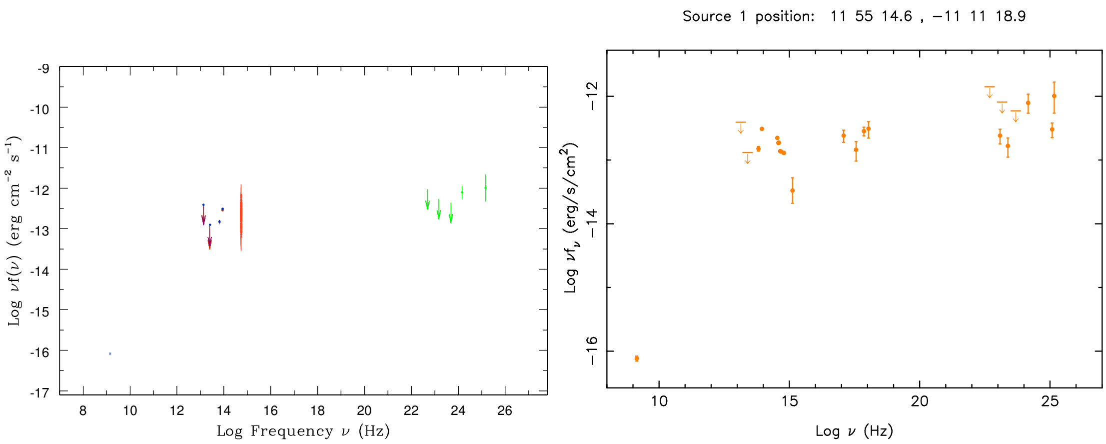

Figure 4.12: Extra sources found with VOU-Blazars

Figure 4.12 illustrates a new 3HSP source found by the tool. The Figure shows that from the SED builder, the SED lacks UV and X-ray data to be verified as an HSP. However, the SED from VOU-Blazars contains extra X-ray data from SWIFT deepsky and extra UV data from GALEX. With additional data, the source could be classified as an HSP with ν_{peak} at ≈ 17.3 Hz.

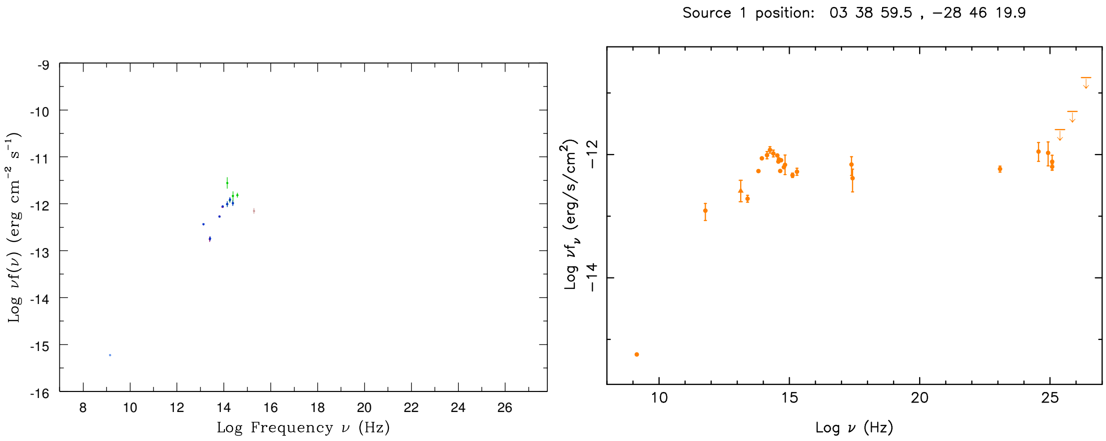

Figure 4.13: Peak refined with VOU-Blazars

As Figure 4.13 shown, VOU-Blazars also helps to revise the ν_{peak}. There is no X-ray data from SED builder, and without the X-ray data, the position of the synchrotron peak could not be evaluated precisely. There were latest version XMMSL data applied by the tool and the peak could be estimated more accurately with extra X-ray data. In this case, with XMM data, the peak is known at $\approx 10^{16.3}$ Hz. Moreover, additional data from far IR and UV make the illusion of the synchrotron emission on VOU-Blazars SED more explicit.

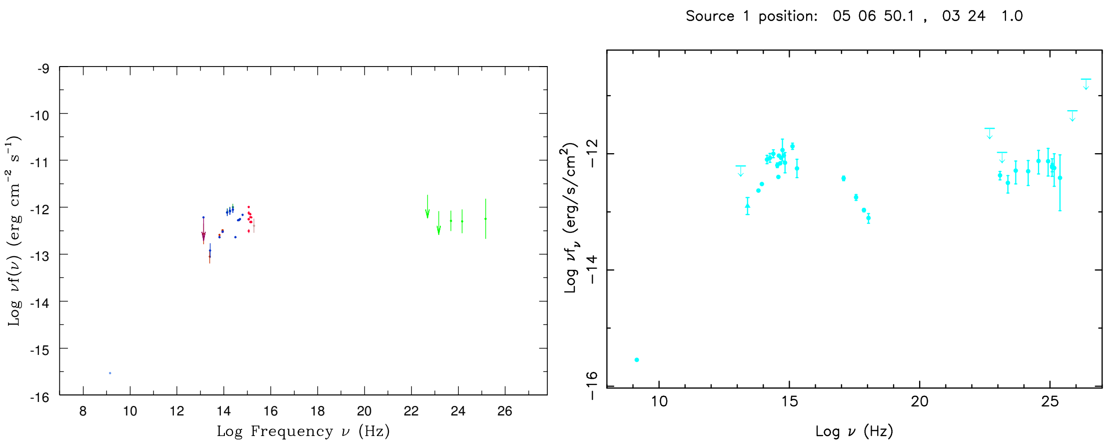

Figure 4.14: Peak refined with VOU-Blazars

There is another example how estimation of ν_{peak} could benefit with VOU-Blazars, illustrated in Figure 4.14. Without the X-ray data, like the SED from SED builder, it is not possible to estimate a real value for the synchrotron peak. Given that the Swift Deepsky pipeline provides dedicated X-ray analysis and further deep X-ray data and that VOU-Blazars could retrieve the data from the pipeline, there is extra X-ray data from

XRT on VOU-Blazars SED. After calling Swift Deepsky when running the VOU-Blazars, the peak could be refined at ≈ 15.8 instead of putting an upper limit.

Last but not least, the VOU-Blazars could quickly recognize all the possible counterparts for a VHE detection within a relatively large area, given that most of the VHE sources are known to be blazars. For example, the tool has been applied to identify the probable counterparts for an neutrino detection, IceCube-170922A [100]. Among these candidate counterparts, the TXS 0506+056 might be the most possible counterpart for IceCube-170922A, after dedicated multi-frequency data analysis. For sure there will be more VHE sources whose counterpart be identified with VOU-Blazars in future.

4.3.1 Ouput files

There will be up to 20 files generated after the whole process are done with VOU-Blazars. The eventually outputs from the VOU-Blazars are concluded as following,

(I) First and Intermediate phase

- **RX_map.eps**
  A map shown all the radio and X-ray sources.
- **candidates.eps**
  A map shown all the possible blazar / blazar candidats.
- **phase1**
  First phase output that list all the candidates information.
- **output1.csv**
  VO conesearch results for the first phase. The original data retrieved from every catalog are store in this csv file.
- **find_out_temp.txt**
  A List with the candidates coordinate and code for plotting.
- **output_int.csv**
  VO conesearch results for the intermediate phase.
- no_matched_temp.txt
  A list with the sources that will send to intermediate phase, containing R.A., Dec., flux, position error information.
- Sed_temp.txt
  A list with the sources that will pass to second phase, containing R.A., Dec.,

flux, position error information.

- RX_sorted.txt

  A list with all radio and X-ray source coordinate and code for plotting.

- catlist1.txt

  List all the name of the catalogs which have found the data with conesearch in first phase.

- catlist_int.csv

  List all the name of the catalogs which have found the data with conesearch in intermediate phase.

- Intermediate_out.txt

  Output from intermediate phase, list of the sources that will send to second phase. Have similar format as find_out_temp.txt and SED_temp.txt, and will be add to them later.

(II) Second phase

- **sed.eps**

  Sed for the interested source.

- **error_map.eps**

  Error circle map for the source.

- **phase2**

  Second phase output that list the couterpart and slope at each waveband.

- **output2.csv**

  VO conesearch results for the second phase.

- **Sed.txt**

  SED data with frequency, flux, upper limit flux, and lower limit flux.

- **Out4SedTool.txt**

  SED data in SSDC SED tool format.

- **error_map.txt**

  The file of the error circle

- catlist2.txt

  List all the name of the catalogs which have found the data with conesearch in second phase.

4.4 To be developed

Even though the current version of the VOU-Blazars is good enough to achieve goals that finding good blazars candidates and finding the possible counterpart for VHE sources, there are still some points need to be done. The first cardinal thing needs to be improved is the matching algorithm and position in the second phase. For example, sometimes, there are no IR counterparts around the radio-X-ray matched sources but with UV or optical counterparts around that, and the tool needs to identify this kind of case. Besides, the optical, IR, and UV counterparts, usually with a better position, might not be close to radio position for radio extended sources, causing the tool to miss those counterparts.

The likelihood method also needs to be modified to reduce the percentage that making a wrong association. Moreover, the likelihood is not applied to IR, optical and UV yet, and later with the logN-logS from these bands are estimated, it will be used to estimate the counterparts in these frequencies. Confidential level of the likelihood estimation will be applied to the tool as well.

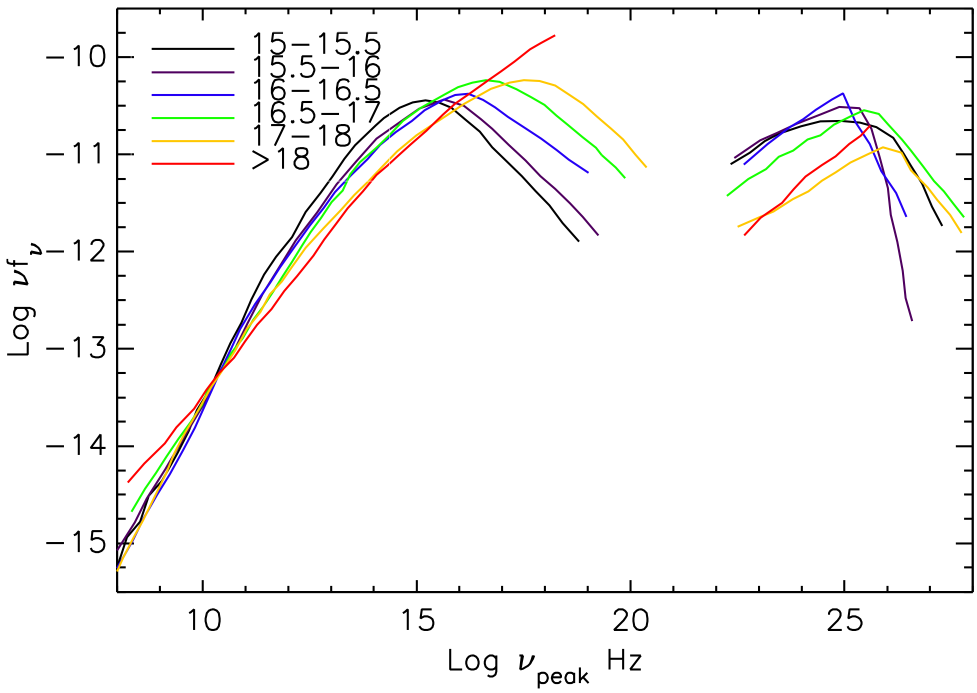

Figure 4.15: HSP SED template for different $\nu_{\rm peak}$

Another crucial thing needs to be done is to solve the problem of multiple radio detections. Those detections from the same source might be farther than 0.1 arcmins, which is applied in current VOU-Blazars. To solve the problem, a new method to carefully define radio counterpart is necessary.

Currently, the tool classifies the sources based on only radio-X-ray slope ratio. Later, there will be updated to define the source type according to more information, like slope from other bands and the photon index of γ-ray. Eliminating uncertain (too few non-thermal data) sources is another purpose of the VOU-Blazars in near future.

Apart from that, there were more catalogs such as RASS FSC and BSC, VLA, VLASS, and MAGIC, could be applied to the tool to make the searching more complete and have more data on SED. An HSP model according to different $\nu_{\rm peak}$also will be illustrated, like Figure 4.15, as well as the SED. With these templates, it is easier to tell if a source is a good HSP. The templates are built by collecting, averaging, and rescaling the SED of 5 3HSP sources, and then extracting the data by Plot Digitizer [12] in each bin.

Finally, there will be a configuration file read by the VOU-Blazars containing all the critical parameters such as various slope values to classify the sources or the VO links for conesearch. Machine learning is another goal to be applied to VOU-Blazars later. From previous resulted slope values and classifications with the help of machine learning, the tool could automatically update the values in a configuration file. With all the above modifications, there will be an updated and better version of VOU-Blazars in near future.

[12]http://plotdigitizer.sourceforge.net/

Catalog	Band	Zero-magnitude flux	Effective wavelength	Reference
2MASS	J	1594 Jy	12350 Å	Skrutskie et al. 2006[129]
	H	1024 Jy	16620 Å	
	K	666.7 Jy	21590 Å	
AllWISE	W1	309.540 Jy	34000 Å	Cutri et al. 2013[36]
	W2	171.787 Jy	46000 Å	
	W3	31.674 Jy	120000 Å	
	W4	8.363 Jy	220000 Å	
USNO	B	4260 Jy	4400 Å	Bessell 1979[17]
	R	3080 Jy	6400 Å	
SDSS	u	3631 Jy	3568 Å	Doi et al. 2010[42]
	g	3631 Jy	4653 Å	
	r	3631 Jy	6148 Å	
	i	3631 Jy	7468 Å	
	z	3631 Jy	8863 Å	
GSC	U	1810 Jy	3600 Å	Bessell 1979[17]
	B	4260 Jy	4400 Å	
	V	5500 Jy	3640 Å	
	R	3080 Jy	6400 Å	
	I	2550 Jy	7900 Å	
PanSTARRs	g	3631 Jy	4810 Å	Tonry et al. 2012[139]
	r	3631 Jy	6170 Å	
	i	3631 Jy	7520 Å	
	z	3631 Jy	8660 Å	
	y	3631 Jy	9620 Å	
GAIA	G	2918 Jy [a]	6730 Å	Jordi et al. 2010[72]
UVOT	u	3631 Jy	3501Å	Poole et al. 2008[117]
	b	3631 Jy	4329Å	
	v	3631 Jy	5402Å	
	w1	3631 Jy	2634Å	
	m2	3631 Jy	2231Å	
	w2	3631 Jy	2030Å	
GALEX	FUV	3631 Jy	1538.6Å	Morrissey et al. 2012[89]
	NUV	3631 Jy	2315.7Å	
XMMOM	u	3631 Jy	3440Å	Page et al. 2012[105]
	b	3631 Jy	4500Å	
	v	3631 Jy	5430Å	
	w1	3631 Jy	2910Å	
	m2	3631 Jy	2310Å	
	w2	3631 Jy	2120Å	

[a] The G band magnitude is measured in Vega system, depend on the flux densities of A0V star, the zero magnitude flux here is obtain from A0V star template from STSDAS calibrated database system at `http://www.stsci.edu/hst/observatory/crds/calspec.html`.

Table 4.6: Magnitude reduction details for catalogs applied in second phase

Chapter 5

Very High Energy astronomy with HSP Blazars

5.1 High energy emission from blazars

5.1.1 Extreme peaked HSPs

HSP blazars are believed to be the only few kinds of extragalactic object that emit in high energy or even very high energy (VHE). The synchrotron $\nu_{\rm peak}$ of HSPs are the highest among blazars, usually with values around 10^{16} to 10^{17} Hz, sometimes extending up to 10^{18} Hz in the most extreme cases. Accordingly, the Inverse Compton peak of these extreme cases may be few tens of even few hundreds TeVs, the highest energy end of the electromagnetic spectrum. Values of $\nu_{\rm peak}$ $\gtrsim 10^{18}$ Hz imply that the electrons responsible for the synchrotron radiation must be accelerated to extremely high energies (see the Introduction and, for example, Rybicki & Lightman 1986; Costamante et al. 2001 [121, 35]). Those extreme peaked HSPs obviously are particularly crucial sources for TeV astronomy.

There are 82 sources in the 3HSP sample with $\nu_{\rm peak}$ around or above 10^{18} Hz. Table G.1 gives the list of all the extreme sources with $\nu_{\rm peak} \geq 10^{17.9}$ Hz or sources with lower limit $\nu_{\rm peak}$; this includes many more such objects than any previous catalog. These extreme sources are particularly important since they may be candidate VHE, neutrino, or ultra-high energy cosmic ray (UHECR) sources (section 5.2 and 5.4). Figures 5.1 to 5.3 illustrate five examples of SEDs of representative objects from Table G.1.

Sometimes, it is hard to estimate the positions of the synchrotron peak for such extreme sources, since the available data in the X-ray band is often limited to a few keV, where most of the sensitive existing detectors operate. For about 20 sources the frequency of the synchrotron peak could not be estimated accurately since the soft X-ray data show a still rising spectrum in the SED, and no hard X-ray data exist to cover the peak of the emission. In these cases, there were only estimated a lower limit to $\nu_{\rm peak}$. For some strong X-ray variable sources with many X-ray observations we also could not obtain well-estimated $\nu_{\rm peak}$ values with the third degree polynomial fitting in SSDC SED tool since the curvature in the X-ray spectrum (and with it $\nu_{\rm peak}$) changes with time. However, in all these cases, the available multi-frequency data imply that the synchrotron peak is within the X-ray band; in these sources, there were estimated an average $\nu_{\rm peak}$ value using a second-degree polynomial in the X-ray band.

- **3HSP J023248.5+201717 (1ES0229+200)**. This is an extreme source with VHE data available. The ebl-deabsorbed VHE data (shown as dark blue filled circles) are from Finke et al. 2015 [48]. The synchrotron peak is at $\sim 10^{18} - 10^{19}$ Hz and the peak frequency is one of the highest among the 3HSP sources. In the VHE band, with the VHE fluxes after correcting for EBL absorption, the inverse Compton peak will be at energies $>$ 1 TeV. Since the inverse Compton peak is at VHE, this could also be a good candidate for neutrino event during the flaring.

- **3HSP J035257.4−683117**. This is a known blazar with log $\nu_{\rm peak} \approx 18.1$. It has hard X-ray and γ-ray detections, but no TeV detection and not in 5BZCat yet. This source might be a good target for next generation TeV telescopes.

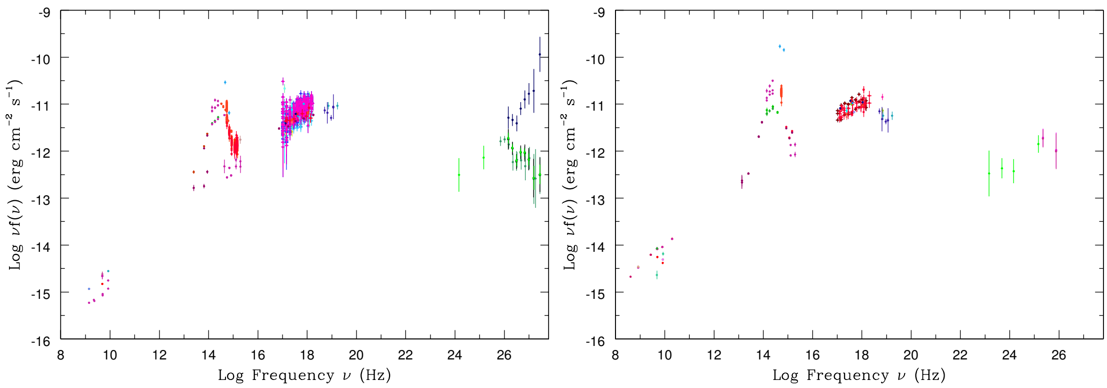

Figure 5.1: The SED of the extreme objects 3HSP J023248.5+201717 and 3HSP J035257.4−683117. The dark blue points are ebl- deabsorbed data from [48]. See text for details.

- **3HSP J215305.2−004229 (5BZBJ2153−0042)**. This source has a very hard X-ray spectrum and the SED in the X-ray band keeps increasing up to the highest energies, implying a $\nu_{\rm peak}$ larger that 10^{18} Hz. The X-ray emission is not likely to be related to a cluster of galaxys since it is compact. According to the γ-ray data from the source, it may be a good candidate for TeV obsersvation as well.

- **3HSP J143342.7−730437**. This is another example of a extremely hard X-ray SED source. The source has UV data but so far did not have any γ-ray data untill 3FHL [135]; moreover, this source is in the list of new γ-ray detections in Arsioli and Chand 2017; Arsioli et al. 2018 [13, 12] (The gree and yellow data).

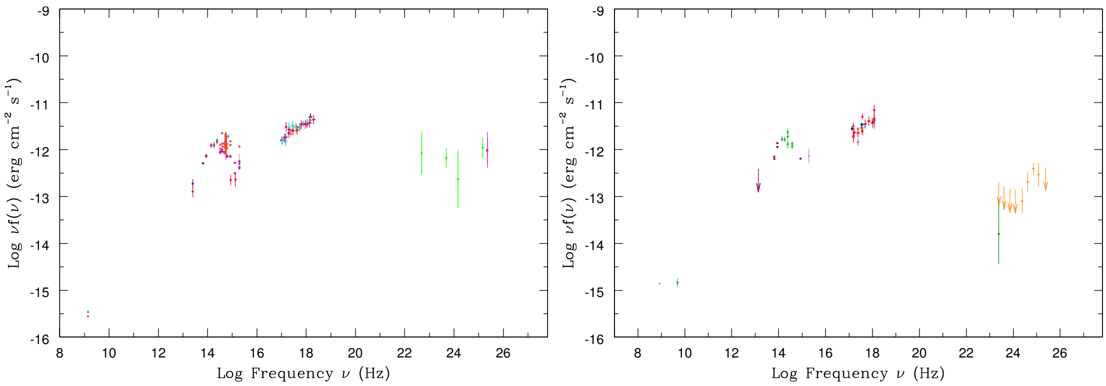

Figure 5.2: The SED of the extreme objects 3HSP J215305.2−004229 and 3HSP J143342.7−730437.

.

- **3HSP J165352.2+394536**. This is the well-known HSP, MRK501. On average, $\log \nu_{\rm peak} \sim 17.9$ Hz; however, during an X-ray flare, as shown by the BeppoSAX data (yellow points in the SED, Giommi et al. 2002 [55]), $\nu_{\rm peak}$ reached $> 10^{18}$ Hz. Note that in [113], they discussed the BeppoSAX observation of MRK501 in April 1997 and showed that the $\nu_{\rm peak}$of that shift at least two orders of magnitude with regard to previous observations. This was the first time this scenario had been seen. The source also is detected in TeV, and may be a good seed for neutrino observation as well.

5.2 HE and VHE observations for 3HSP

The main purpose of building the 3HSP sample is finding seed sources for HE or VHE surveys. As the emission from HSPs are expected to reach the HE part of the electromagnetic spectrum, HSP catalog provides good candidates for the search of sources in *Fermi* catalogs and in the VHE band. There are still around half of the sources in 3HSP

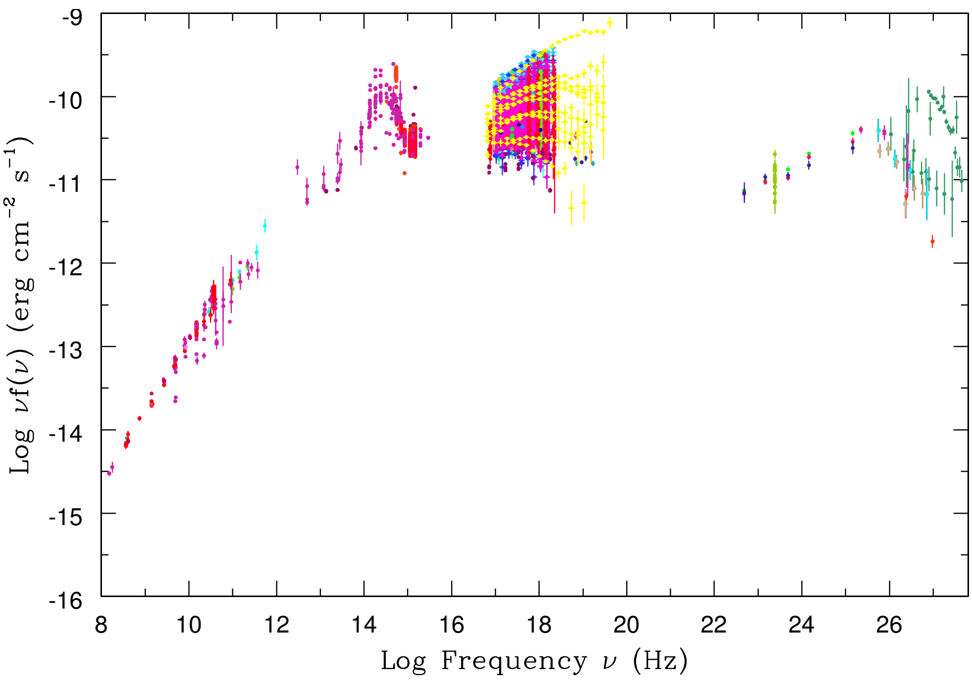

Figure 5.3: The SEDs of the extreme object 3HSP J165352.2+394536.

without any γ-ray or VHE detection yet. Some of them may be too faint to be detected by current VHE instruments, while the other of them already could be detected with finer analysis.

For example, 3HSP J083724.6+145820 (see Fig. 5.4), has $\nu_{\rm peak} \sim 10^{16.7}$ Hz and $\nu_{\rm peak} f_{\nu_{\rm peak}} \sim 10^{-11}$ erg cm^{-2} s^{-1} (or FOM= 2), but it had no γ-ray counterpart until recently. The green points in Fig. 5.4 correspond to the new γ-ray data presented in [13]. Another example is 3HSP J225147.5−320611, which has $\nu_{\rm peak} > 10^{18}$ Hz and $\nu_{\rm peak} f_{\nu_{\rm peak}} > 10^{-11.3}$ erg cm^{-2} s^{-1} (FOM $>$ 1), but also had no γ-ray counterpart in current available γ-ray or VHE catalogs (1/2/3 FGL, 1/2 FHL, and TeVCat) until it was detected by [13] according to 3HSP coordinate, which points to promising HE/VHE targets.

Apart from that, the CTA flux limit/sensitivity could be as low as 3×10^{-13} erg cm^{-2} s^{-1} [120] or $\sim$ 1 mCrab at 1 TeV for 50-hour exposure. Clearly, from Fig. 5.4, 3HSP J083724.6+145820 and 3HSP J225147.5−320611 may be detected by CTA in the future (since they are above the CTA sensitivity for an exposure time of 50 hours, the blue lines).

The Figure of Merit (FOM), defined in [14] is reported for all 3HSP sources and gives an objective way to assess the likelihood that a given HSP may be detectable as a TeV source. The two sources in Figure 5.4 have high FOM, thus later, with better/higher

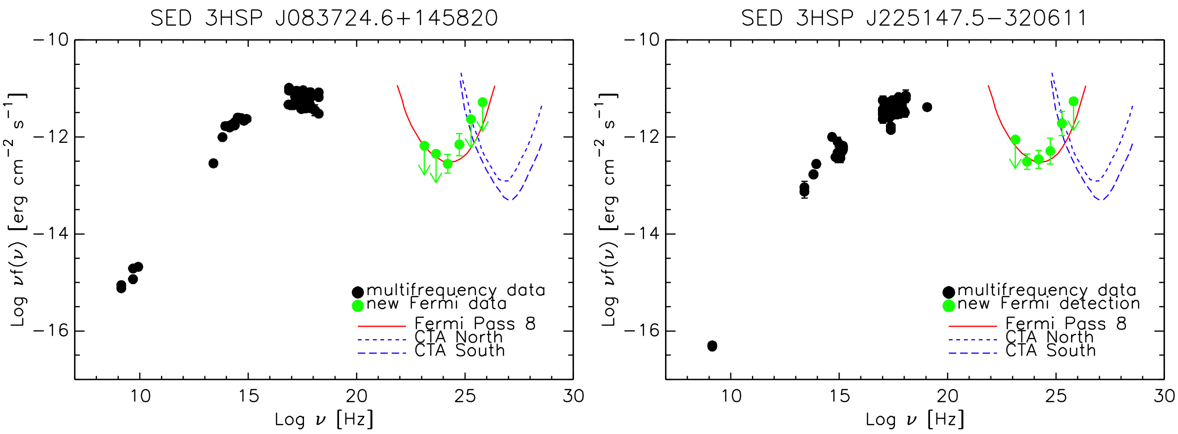

Figure 5.4: VHE observations candidates. Right: 3HSP J083724.6+145820; Left: 3HSP J225147.5−320611. The red line and blue lines are the *Fermi* Pass 8 and CTA sensitivities, respectively. The green circles are the data from *Fermi* Pass 8, and the black points are the data from other wavebands. The Pass 8 data are obtained from the *Fermi* tool with the 3HSP position. These sources are not yet in the 3FGL catalog [13].

resolution instruments, the high energy counterpart of these sources might be found. As discussed in Arsioli et al. 2015 [14], relatively high FOM sources (FOM > 0.1) are good targets for observation with the upcoming Cherenkov Telescope Array (CTA). Another upcoming instrument, the Large High Altitude Air Shower Observatory (LHAASO), is currently designed to survey with unprecedented sensitivity the whole northern sky for γ-ray sources above 300 GeV. Therefore, high FOM 3HSP sources may also provide seed-positions for searches of γ-ray signature embedded in LHAASO data [25].

Recently, a new TeV source, PGC 2402248, was detected by the MAGIC collaboration [86], which is also in 3HSP. This is another good example that extreme peaked HSP provided good candidates for TeV instruments. Furthermore, as section 2.4.2 described, there were 147 new XRT detections proposed by 3HSP sources. In conclusion, with the benefit of multi-wavelength work, like 3HSP catalog, there were provided many candidates for future VHE observations.

5.2.1 The 1BIGB catalog

Less than half of the 3HSP sources are cataloged in *Fermi* catalogs till now. To better assess the percentage of detection of HSP blazars in the γ-ray band, [13] have recently performed a dedicated γ-ray analysis of bright 2WHSP sources (previous version of 3HSP) with FOM ≥ 0.16, using archival *Fermi*-LAT Pass 8 observations integrated over 7.2 years of observations. By applying the position of 2WHSP sources as seeds for the data analysis, ≈ 85 sources were identified at the $> 5\sigma$ (TS > 25) level, and another 65 at a less significant ($10 <$ TS < 25) level. In total, 150 new γ-ray detections without FGL counterparts yet were found, the new detections are named first Brazil ICRANet gamma-ray blazar catalog (1BIGB).

The success of 1BIGB catalog demonstrates the potential of HSP catalogs for the detection and identification of γ-ray and VHE sources. With the more complete 3HSP catalog, for sure, there will be more γ-ray sources found in future. In fact, there will be a new γ-ray catalog, 2BIGB, in near future, with extra 120 new γ-ray detections, which is not in any *Fermi* catalogs before, above 10 GeV from HSPs. Conclusively, applying γ-ray analysis at a more precise position, proposed by multi-wavelength data, leads to 270 new γ-ray sources found.

5.2.2 Counterpart for *Fermi* catlaogs

Since HSPs are the dominant population in the extragalactic VHE sky, there were supposed that the majority of the non-associated *Fermi* sources may be HSP blazars as well. With thorough analysis, there were 26 HSPs proposed in table 5.1 may be the counterpart for *Fermi* 3FHL and 3FGL. All the 26 sources have no association in the catalogs yet. In future, as there will be more and more γ-ray detection from *Fermi* and more and more HSPs found, HSP catalog will play a more crucial role in associated for *Fermi* sources.

5.3 Prediction of the HE flux

In this section, the relationship between the Synchrotron emission and Inverse Compton emission for the HSPs are being discussed. To investigate the relation between two peaks, there were calculated the ratio between *Fermi* fluxes and synchrotron peak fluxes. There were applied de-absorbed *Fermi* 3FHL photon fluxes (10-1000 GeV fluxes) and FL8Y flux (1-100 GeV fluxes) to compare with synchrotron peak fluxes.

Given that the TeV photons are extremely easily absorbed by the extragalactic background from galaxies and quasars (EBL absorption), photon fluxes from 3FHL need to be calibrated with EBL absorption. There were applied the EBL correction for 10-1000 GeV fluxes with the optical depth template by [43] assuming no any extra emission or contribution from EBL (See Appendix E for more details). Figure 5.5 illustrates the flux ratio between 1-100 GeV (FL8Y) and synchrotron peak fluxes ratio with respect to synchrotron peak frequencies, and Figure 5.6 is the same plot but the γ-ray flux is between 1-1000

Source	R.A.	Dec.	3FGL	3FHL
3HSPJ015624.5−242003	29.10228	−24.33438	J0156.5−2423	J0156.2−2419
3HSPJ023246.2+063742	38.19263	6.62851	J0232.6+0646	—
3HSPJ025111.5−183112	42.79803	−18.52021	J0251.1−1829	J0251.2−1830
3HSPJ025857.5+055243	44.73981	5.87889	J0258.9+0552	J0258.9+0554
3HSPJ040111.2−535458	60.29668	−53.91626	J0401.0−5359	J0401.0−5355
3HSPJ043837.0−732921	69.65448	−73.48933	J0437.7−7330	J0438.0−7328
3HSPJ072547.8−054832	111.4495	−5.809	J0725.7−0550	J0725.7−0548
3HSPJ074710.0−073724	116.79181	−7.62359	J0747.4−0734	—
3HSPJ091926.2−220042	139.85933	−22.01187	J0919.5−2200	—
3HSPJ101620.6−424722	154.08614	−42.78961	J1016.6−4244	J1016.2−4245
3HSPJ102432.3−454426	156.13491	−45.74081	J1024.4−4545	J1024.5−4543
3HSPJ105224.5+081410	163.10221	8.23599	J1052.0+0816	—
3HSPJ114600.8−063854	176.50357	−6.64859	J1146.1−0640	J1145.9−0637
3HSPJ115514.8−111122	178.81193	−11.18959	J1155.3−1112	—
3HSPJ122014.5−245948	185.06058	−24.99685	J1220.0−2502	J1220.1−2459
3HSPJ122327.4+082030	185.8646	8.34183	J1223.3+0818	—
3HSPJ124021.2−714857	190.08841	−1.81605	J1240.3−7149	J1240.5−7148
3HSPJ141046.0+740511	212.69171	74.08647	J1410.9+7406	J1410.8+7406
3HSPJ154439.8−112741	236.16406	−11.46805	J1544.6−1125	—
3HSPJ194333.7−053353	295.89084	−5.56492	J1944.0−0535	—
3HSPJ210415.9+211808	316.06635	21.30228	J2104.7+2113	J2104.5+2117
3HSPJ211522.0+121802	318.84169	12.30074	J2115.2+1215	J2115.2+1218
3HSPJ214239.7−202819	325.66579	−20.472	J2142.6−2029	J2142.5−2029
3HSPJ214429.5−563848	326.12322	−56.64697	J2144.6−5640	—
3HSPJ224531.8−173358	341.38274	−17.56637	—	J2245.5−1734
3HSPJ230848.7+542611	347.20309	54.43645	J2309.0+5428	J2308.8+5424

Table 5.1: Fermi sources without association

GeV from *Fermi* 3FGL.

Both Figures imply that there is an anti-correlation between γ-ray photon flux Synchrotron flux ratio and $\nu_{\rm peak}$. The red triangles represent the average ratio in each $\nu_{\rm peak}$ bins, and the errors here are the 1σ standard deviation of the sources in every bins. Green lines are the best fitting for all the sources, and most of the sources are within 1σ standard deviation. The 1σ error is ≈ 0.3 in log, meaning that the deviation of the data is around a factor of 2 of the average value. Note that in Figure 5.6, some of the points are much higher than the mean value and fitted line, indicating that those sources might undergo strong variability due to flaring stage. Since there were applied the average value for both γ-ray photon fluxes and synchrotron peak fluxes, those obviously high ratios may imply extra components from γ-ray or VHE, as what have expected in a hadronic model for

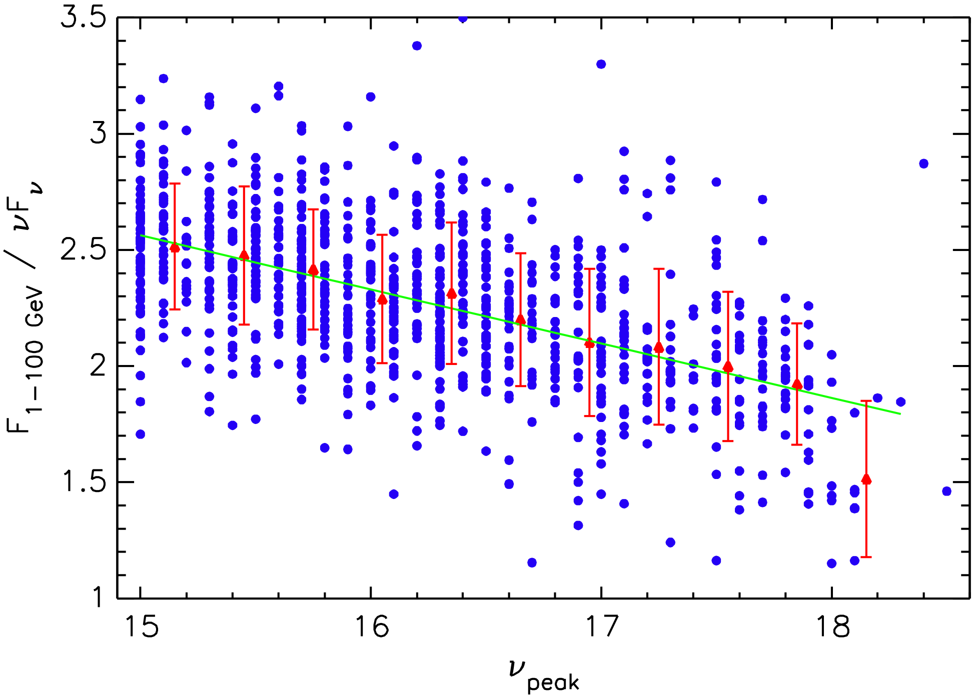

Figure 5.5: FGL flux-peak flux ratio w.r.t. ν_{peak}

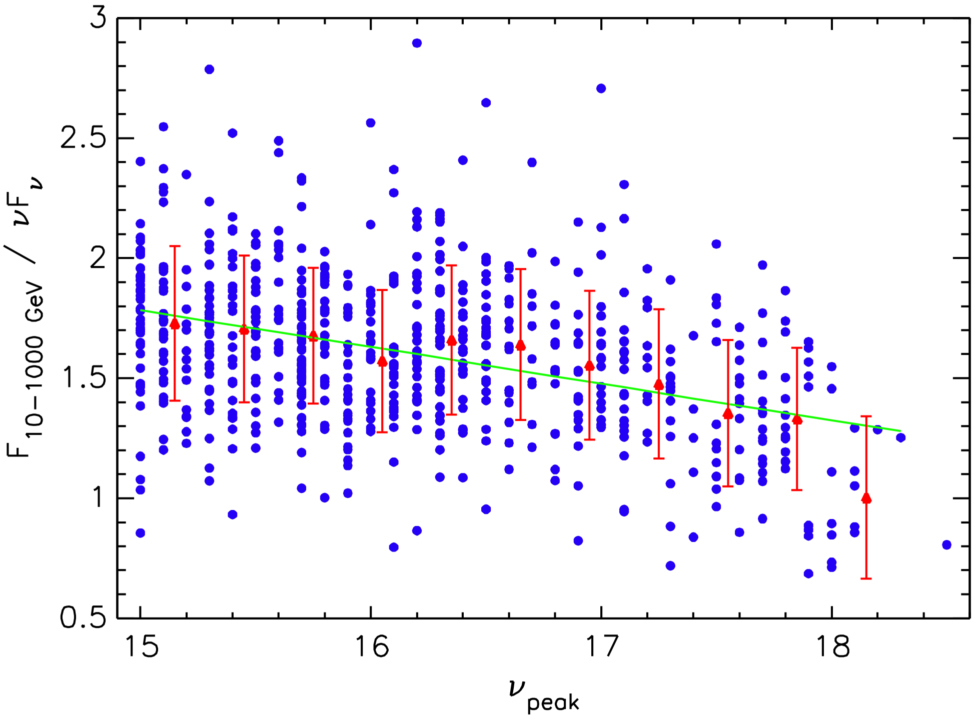

Figure 5.6: FHL flux-peak flux ratio w.r.t. ν_{peak}

blazars.

$$\log(\frac{F_{1-100\ \mathrm{GeV}}}{\nu_{\mathrm{peak}} f_{\nu_{\mathrm{peak}}}}) = -0.233 \times \log(\nu_{\mathrm{peak}}) + 6.061$$
$$\log(\frac{F_{10-1000\ \mathrm{GeV}}}{\nu_{\mathrm{peak}} f_{\nu_{\mathrm{peak}}}}) = -0.153 \times \log(\nu_{\mathrm{peak}}) + 4.072 \tag{5.1}$$

As there are still some of the sources without γ-ray flux or VHE flux yet, the expected γ-ray emission from these sources could be estimated from the anti-correlation. The ratio between the photon flux and $\nu_{\mathrm{peak}} f_{\nu_{\mathrm{peak}}}$ could be obtained with equation 5.1 Given that the deviation of the whole sample is only a factor of 2 of the mean value, there were predicted the HE fluxes for around 120 bright radio sources. The estimated *Fermi* photon fluxes between 1-100 GeV and 10-1000 GeV are shown in Table G.4. The estimated value may be useful for future γ-ray analysis.

5.4 Relation with VHE sources

Blazars have been considered as likely neutrino sources for quite some time [79]. [102] have suggested that blazars of the HSP type, where particles are accelerated to the highest energies, may be good candidates for neutrino emission and presented evidence for an association between HSP blazars and neutrinos detected by the IceCube South Pole Neutrino Observatory[1]. The first neutrino event catalog was published in [32]. [111] further modeled the HE SED of six HSPs selected by [102] as most probable neutrino sources and predicted their neutrino fluxes. All six predicted fluxes were consistent, within the errors, with the observed neutrino fluxes from IceCube, especially for two sources (MKN421 and H1914−194).

[103] have recently cross-matched two VHE catalogs and the 2WHSP with the most recent IceCube neutrino lists [70] at that time, measuring the number of neutrino events with at least one γ-ray counterpart. In all three catalogs, they observed a positive fluctuation with respect to the mean random expectation at a significance level between 0.4 and 1.3%, with a p-value of 0.7% for 2WHSP sources with FOM $\gtrsim 1$. The chance probability for 2WHSP FOM≈1 cross-matched with neutrino event randomly is 0.71 (average 12.7 random events out of 18 events); that is, only $\approx 6or7$ neutrino have "real" counterpart. [103] suggested 6 HBLs (1ES 1011+496, MKN421, H2356-309, PG 1553+113, 1H1914-194, and 1ES0414+009) which could be most probably counterparts of 5 neutrino events (id 9 10 17 22 41).

[103] concluded that HSPs are most promising counterparts for neutrino events among

[1]http://icecube.wisc.edu

blazars. All HBLs considered to be the most probable counterparts of IceCube neutrinos are 2WHSP sources, which strongly suggests that strong, VHE γ-ray HBLs are so far the most promising blazar counterparts of astrophysical neutrinos. At least part of the neutrino are from HSPs, and 3HSP provide a seed for future neutrino survey.

Apart from that, [119] have presented evidence of a direct connection between HSP, very high energy neutrinos, and ultra-high energy cosmic rays (UHECRs) by correlating the same catalogs used by [103] with UHECRs from the Pierre Auger Observatory [4, 137] and the Telescope Array [5]. A maximal excess of 80 cosmic rays (41.9 expected) was observed for 2FHL HBL. The chance probability for this to happen is 1.6×10^{-5}, which translates to 5.5×10^{-4} (3.26σ) after compensation for trials.

Chapter 6

Summary and Conclusions

This thesis was dedicated to the construction and to the scientific exploitation of 3HSP, the largest catalog of high synchrotron peaked Blazars (HSPs) (Chapter 2) catalog, which is an extention of the 2WHSP[30] and 1WHSP catalogs[14] ("W" stands for WISE here). Current, and virtually final version of the 3HSP catalog contains 2012 HSPs or HSP candidates, with 1633 of them also in the 2WHSP catalog and 999 of them having *Fermi* γ-ray counterparts. In the early fase of this work, the 2WHSP catalog was built from cross-matching among various radio catalogs (NVSS, First, and SUMSS), X-ray catalogs (3XMM, XMM slew, RASS, WGA, Chandra, XRT, BMW), and allWISE survey. We then applied slopes criteria, obtained from three well-known HSPs, and selected sources only with $\nu_{\rm peak} > 10^{15}$ Hz [97, 1]. To increase the completeness of the catalog, we checked extra good HSP candidates from *Fermi* 2FHL[8] and TeVCat[1], resulting in 1691 sources in the 2WHSP catalog.

Although relatively large, the 2WHSP catalog is not complete either in radio or in X-ray, and we need to add more HSPs or HSP candidates to the catalog. This has motivated further work into a new catalog, the 3HSP, dedicated to the selection of new HSPs and HSP candidates and aiming to improve the description of the HSP population. For the 3HSP catalog, We started from cross-matching NVSS and RASS catalogs and applying radio to X-ray flux ratio cut $\geq 9 \times 10^{-11}$. After removing those NVSS-RASS matched sources which are already in 2WHSP, there remains ≈ 4000 pre-selected candidates. To reduce the number of sources to be examined, we further cross-matched these 4000 sources with 5BZCat[82], 3FHL[135], and XMMOM[105] catalogs, individually. Apart from that, we also carefully reviewed every hard-photon-index *Fermi* 3FHL and FL8Y sources. The

[1] http://tevcat.uchicago.edu

procedures led to the selection of around 380 new HSPs/HSP candidates to the catalog. Combining with the 2WHSP sources, there are 2012 sources in the 3HSP catalog in total. The entire list of the 3HSP catalog is given in Table G.5.

Providing good candidates for high energy and very high energy (VHE) observations is the main motivation for building the 3HSP catalog (Chapter 5). The 3HSP catalog has been already used as a seed for HE or VHE observations, and several new detections from HE or VHE has been proposed according to the position of 3HSP sources. For example, a subsample of 3HSP sources with no or weak X-ray detections have been proposed for Swift XRT observations, and 97% of the sources observed have been detected by Swift XRT (See section 2.4.2). Moreover, a new VHE counterpart, PGC 2402248 (3HSP J073326.7+515355), was detected by MAGIC recently[86], showing that the 3HSP does contribute potential VHE candidates for future surveys. The 1BIGB catalog[13] is another successful example that demonstrated the presence of new gamma-ray sources found based on 3HSP sources. Therefore, with multi-frequency based catalogs, like 3HSP, it is more efficient to find more VHE sources/detections, as 3HSP could "point out" the possible location of VHE sources that were not known before. We note that some of the 3HSP sources are proposed to be the counterpart of unassociated *Fermi* sources, see Table 5.1.

The thesis also explored the intrinsic properties of HSP blazars with a complete 3HSP subsample (Chapter 3). As the data suggests, 3HSP subsample, which is flux-limited (cut) in radio and X-rays, is actually complete when $\nu_{\rm peak}$ is larger than 10^{16} Hz (See logN-logS, V/Vmax, and cumulative $\nu_{\rm peak}$ distribution); the subsample includes $\approx$ 900 sources. The loss of some low $\nu_{\rm peak}$ sources may result from the slop criteria applied during the selection processes or extremely faint X-ray emissions; the $\nu_{\rm peak}$ of these sources are on the threshold of the selection. It is possible to obtain the genuine statistical properties of HSPs with this largest ever and the most complete subsample of the 3HSP catalog. Especially, 88% of sources in 3HSP have estimated redshift, suggesting robust results for the statistical properties which depend on that (like the Luminosity function and V/Vmax) The new statistics indeed bring important new elements for long-lasting debates and controversy related to blazar population studies. The redshift estimations have been obtained mainly according to the optical spectra (either from SDSS or literature on NED/ADS). However, when no spectroscopic z was available, we estimated the photo-z with elliptical galaxy template from Coleman, Wu & Weedman (1980)[31] if the host galaxy features could be distinguished from the non-thermal emission on SED (Section 2.4.1) . Our results indicate that HSP blazars evolve negatively (See V/Vmax and luminosity function for different z or luminosity subsamples and section 3.5 for detail); they are less abundant or less luminous in the recent past. The negative evolution will make the finding of high luminous source more difficult and less amount of sources with fainter flux in a sample. The V/Vmax, luminosity function, and logN-logS for high ν_{peak} sources in this thesis could represent the intrinsic statistical of HSPs under de-evolution process. The "blazar sequences" is suggested to be a selection effect due to the evolution given that the high luminosity and high ν_{peak} sources are not easy to be found. In our radio luminosity function, slopes of that for different ν_{peak} subsamples of blazars are almost the same, which deviates from what is expected with a true sequence.

The current version of 3HSP may miss some good faint HSP blazars when the sensitivity of the available surveys is not sufficient to guarantee radio and X-ray matches. In addition, some VHE/neutrino detections have not been associated with any lower-frequency sources yet. A new tool, VOU-Blazars, has been developed to find more blazars candidates and to illustrate all the possible blazar counterparts in a large area immediately for VHE/neutrino detections at arbitrary postion (Chapter 4). The alpha version of the VOU-Blazars can be downloaded from the link `https://github.com/ecylchang/VOU_Blazars`. With the tool, all the interesting radio or X-ray sources with UV counterparts or Gamma-ray counterparts may not be missed anymore as it could return good blazars candidates from all available lists of radio and X-ray emitters after dedicated examination. In the future, with the help of VOU-Blazars, expectations are that more and more HSP blazars will be found, contributing to the identification of the VHE sources that might be discovered by current and future Cherenkov telescopes.

Appendix A

Extra output examples from VOU-Blazar

First of all, there were illustrated the radio-X-ray source maps for each cases.

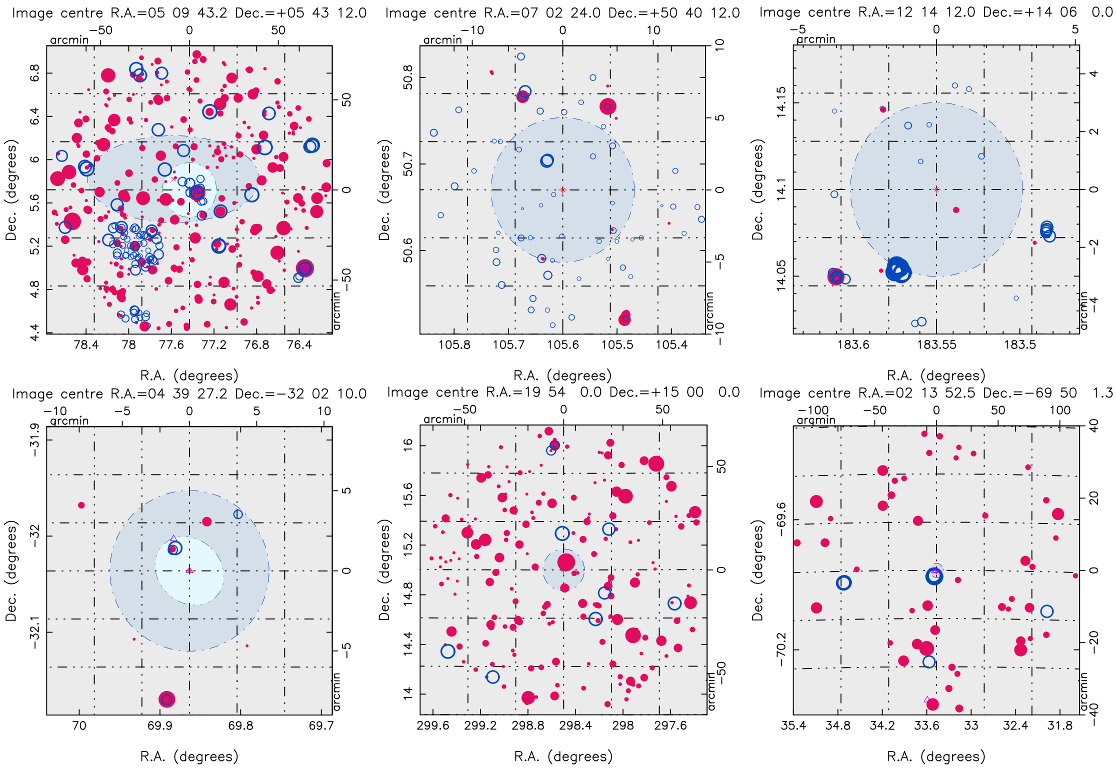

Figure A.1: Radio-X-ray source map examples.

The example output of first phase are shown in following figures.

```
XRT/FIRST ra dec 07 01 56.1, 50 31 31.5 radio flux d.    31.770 flux-ratio      9. arx  0.885                        possible
LBL  Dist.   9.738 arcmin
Match nr.   1       ra dec: 105.48381, 50.52543
................Cataloged sources.................

XRT/NVSS ra dec 07 01 56.7, 50 31 11.8 radio flux d.   106.900 flux-ratio      3. arx  0.949                        possible
LBL  Dist.   9.995 arcmin
              Repeated radio counterpart, 20.435  arcsec away from the matched nr.   1

XRT/FIRST ra dec 07 02  4.0, 50 45 59.4 radio flux d.   495.570 flux-ratio      1. arx  1.010             type unknown Dist.
  6.603 arcmin
Match nr.   2       ra dec: 105.51646, 50.76650
................Cataloged sources.................

XRT/NVSS ra dec 07 02  4.1, 50 45 59.2 radio flux d.   496.800 flux-ratio      1. arx  1.010             type unknown Dist.
 6.590 arcmin
              Repeated radio counterpart,  1.159  arcsec away from the matched nr.   2

XRT/NVSS ra dec 07 02 32.7, 50 35 24.6 radio flux d.    3.500 X-ray/radio flux-ratio    618. arx  0.661 Log(nu_p) 15.6+/-~1
possible HBL Dist.   4.985 arcmin
Match nr.   3       ra dec: 105.63629, 50.59017
................Cataloged sources.................
 zw  5047

XRT/FIRST ra dec 07 02 33.1, 50 35 25.9 radio flux d.    2.880 X-ray/radio flux-ratio    751. arx  0.651 Log(nu_p) 15.8+/-~1
possible HBL Dist.   4.982 arcmin
              Repeated radio counterpart,  3.803  arcsec away from the matched nr.   3

RASS/FIRST ra dec 07 02 41.7, 50 46 39.9 radio flux d.  111.370 X-ray/radio flux-ratio    188. arx  0.724 Log(nu_p) 14.3+/-~1
 possible IBL Dist.   7.046 arcmin
XRT/FIRST ra dec 07 02 41.7, 50 46 39.9 radio flux d.   111.370 flux-ratio     28. arx  0.825                        possible
LBL  Dist.   7.046 arcmin
Match nr.   4       ra dec: 105.67372, 50.77776
................Cataloged sources.................

RASS/NVSS ra dec 07 02 41.8, 50 46 39.9 radio flux d.  106.400 X-ray/radio flux-ratio    197. arx  0.721 Log(nu_p) 14.4+/-~1
possible IBL Dist.   7.052 arcmin
XRT/NVSS ra dec 07 02 41.8, 50 46 39.9 radio flux d.   106.400 flux-ratio     29. arx  0.823                        possible
LBL  Dist.   7.052 arcmin
              Repeated radio counterpart,  1.025  arcsec away from the matched nr.   4
```

Figure A.2: Other output examples from first phase

```
WGA/NVSS ra dec 12 13 57.8, 14 04  9.3 radio flux d.    4.000 X-ray/radio flux-ratio   6210. arx  0.539 Log(nu_p) 18.0+/-~1
possible HBL Dist.   3.898 arcmin
WGA/NVSS ra dec 12 13 57.8, 14 04  9.3 radio flux d.    4.000 X-ray/radio flux-ratio   2659. arx  0.584 Log(nu_p) 17.1+/-~1
possible HBL Dist.   3.898 arcmin
WGA/NVSS ra dec 12 13 57.8, 14 04  9.3 radio flux d.    4.000 X-ray/radio flux-ratio   2629. arx  0.585 Log(nu_p) 17.1+/-~1
possible HBL Dist.   3.898 arcmin
WGA/NVSS ra dec 12 13 57.8, 14 04  9.3 radio flux d.    4.000 X-ray/radio flux-ratio   4811. arx  0.553 Log(nu_p) 17.7+/-~1
possible HBL Dist.   3.898 arcmin
WGA/NVSS ra dec 12 13 57.8, 14 04  9.3 radio flux d.    4.000 X-ray/radio flux-ratio   5426. arx  0.547 Log(nu_p) 17.9+/-~1
possible HBL Dist.   3.898 arcmin
XRT/NVSS ra dec 12 13 57.8, 14 04  9.3 radio flux d.    4.000 X-ray/radio flux-ratio   4701. arx  0.554 Log(nu_p) 17.7+/-~1
possible HBL Dist.   3.898 arcmin
Match nr.   1       ra dec: 183.49100, 14.06925
................Cataloged sources.................

XRT/NVSS ra dec 12 14 19.7, 14 08 45.9 radio flux d.    9.500 flux-ratio     12. arx  0.868                     possible
LBL  Dist.   3.333 arcmin
Match nr.   2       ra dec: 183.58200, 14.14608
................Cataloged sources.................

 XMMSLEW/NVSS ra dec 12 14 20.0, 14 03 11.4 radio flux d.     4.300 flux-ratio  81794. arx  0.403            possible non-j
etted AGN Dist.   3.410 arcmin
 XMMSLEW/NVSS ra dec 12 14 20.0, 14 03 11.4 radio flux d.     4.300 flux-ratio  74574. arx  0.408            possible non-j
etted AGN Dist.   3.410 arcmin
 RASS/NVSS ra dec 12 14 20.0, 14 03 11.4 radio flux d.     4.300 flux-ratio 231319. arx  0.349           possible non-jett
ed AGN Dist.   3.410 arcmin
 WGA/NVSS ra dec 12 14 20.0, 14 03 11.4 radio flux d.     4.300 flux-ratio 138990. arx  0.376           possible non-jette
d AGN Dist.   3.410 arcmin
 WGA/NVSS ra dec 12 14 20.0, 14 03 11.4 radio flux d.     4.300 flux-ratio 208770. arx  0.354           possible non-jette
d AGN Dist.   3.410 arcmin
 WGA/NVSS ra dec 12 14 20.0, 14 03 11.4 radio flux d.     4.300 flux-ratio 125119. arx  0.381           possible non-jette
d AGN Dist.   3.410 arcmin
 WGA/NVSS ra dec 12 14 20.0, 14 03 11.4 radio flux d.     4.300 flux-ratio 234509. arx  0.348           possible non-jette
d AGN Dist.   3.410 arcmin
 WGA/NVSS ra dec 12 14 20.0, 14 03 11.4 radio flux d.     4.300 flux-ratio 248809. arx  0.345           possible non-jette
d AGN Dist.   3.410 arcmin
 WGA/NVSS ra dec 12 14 20.0, 14 03 11.4 radio flux d.     4.300 flux-ratio 124833. arx  0.381           possible non-jette
d AGN Dist.   3.410 arcmin
 WGA/NVSS ra dec 12 14 20.0, 14 03 11.4 radio flux d.     4.300 flux-ratio 107531. arx  0.389           possible non-jette
d AGN Dist.   3.410 arcmin
 XRT/NVSS ra dec 12 14 20.0, 14 03 11.4 radio flux d.    4.300 X-ray/radio flux-ratio  24777. arx  0.466 Log(nu_p) 19.5+/-~1
 possible HBL Dist.   3.410 arcmin
 IPC/NVSS ra dec 12 14 20.0, 14 03 11.4 radio flux d.     4.300 flux-ratio 157389. arx  0.369           possible non-jette
d AGN Dist.   3.410 arcmin
 IPC/NVSS ra dec 12 14 20.0, 14 03 11.4 radio flux d.     4.300 flux-ratio 119692. arx  0.383           possible non-jette
d AGN Dist.   3.410 arcmin
 IPC/NVSS ra dec 12 14 20.0, 14 03 11.4 radio flux d.     4.300 flux-ratio 239731. arx  0.347           possible non-jette
d AGN Dist.   3.410 arcmin
 Match nr.   3       ra dec: 183.58321, 14.05317
 ................Cataloged sources.................

WGA/NVSS ra dec 12 14 26.5, 14 02 58.7 radio flux d.   706.000 flux-ratio      8. arx  0.892                     possible
LBL  Dist.   4.631 arcmin
WGA/NVSS ra dec 12 14 26.5, 14 02 58.7 radio flux d.   706.000 flux-ratio      6. arx  0.906                     possible
LBL  Dist.   4.631 arcmin
WGA/NVSS ra dec 12 14 26.5, 14 02 58.7 radio flux d.   706.000 flux-ratio      7. arx  0.897                     possible
LBL  Dist.   4.631 arcmin
WGA/NVSS ra dec 12 14 26.5, 14 02 58.7 radio flux d.   706.000 flux-ratio     16. arx  0.854                     possible
LBL  Dist.   4.631 arcmin
WGA/NVSS ra dec 12 14 26.5, 14 02 58.7 radio flux d.   706.000 flux-ratio      6. arx  0.905                     possible
LBL  Dist.   4.631 arcmin
XRT/NVSS ra dec 12 14 26.5, 14 02 58.7 radio flux d.   706.000 flux-ratio      9. arx  0.884                     possible
LBL  Dist.   4.631 arcmin
Match nr.   4       ra dec: 183.61029, 14.04964
................Cataloged sources.................
```

Figure A.3: Other output examples from first phase

```
RASS/NVSS ra dec 04 39 32.2,-32 00 48.7 radio flux d.   10.600 X-ray/radio flux-ratio   5857. arx  0.543
Log(nu_p) 17.9+/-~1  possible HBL Dist.   1.720 arcmin
XRT/NVSS ra dec 04 39 32.2,-32 00 48.7 radio flux d.   10.600 X-ray/radio flux-ratio    465. arx  0.676
Log(nu_p) 15.3+/-~1  possible IBL Dist.   1.720 arcmin
Match nr.   1       ra dec:  69.88425,-32.01353
................Cataloged sources.................
 3HSP J043932.2-320052

XRT/SUMSS ra dec 04 39 33.9,-32 10 11.2 radio flux d.   554.600 flux-ratio     19. arx  0.844
            possible LBL  Dist.   8.145 arcmin
Match nr.   2       ra dec:  69.89133,-32.16978
................Cataloged sources.................
 5BZU J0439-3210
 CRATES J043929-320956

XRT/NVSS ra dec 04 39 34.0,-32 10 10.5 radio flux d.   373.700 flux-ratio     17. arx  0.849
           possible LBL  Dist.   8.136 arcmin
              Repeated radio counterpart,  1.048  arcsec away from the matched nr.   2
```

Figure A.4: Other output examples from first phase

```
XRT/NVSS ra dec 19 54 17.9, 16 00 14.6 radio flux d.    49.600 flux-ratio     64. arx  0.781
 possible LBL  Dist.  60.398 arcmin
Match nr.   1       ra dec: 298.57467, 16.00406
................Cataloged sources.................

XRT/NVSS ra dec 19 54 25.6, 15 57 36.9 radio flux d.    2.500 X-ray/radio flux-ratio   1698. arx  0.608 Log(nu_p)
16.6+/-~1  possible HBL Dist.  57.944 arcmin
Match nr.   2       ra dec: 298.60658, 15.96025
................Cataloged sources.................

Candidate nr.   3, Known blazar with no radio/X-ray match: 5BZQ J1955+1358 found at a distance of  64.113 arcmin
Pulsar  PSR J1952+1410   59.297  arcmin away

  No radio/X-ray matches were found.
 Candidate nr.   1, Known blazar with no radio/X-ray match: 3HSP J021358.6-695137 found at a distance of
1.683 arcmin
 Candidate nr.   2, Known flat spectrum radio source with no radio/X-ray match: CRATES J021405-702701 found
 at a distance of  37.100 arcmin
 Candidate nr.   3, Known flat spectrum radio source with no radio/X-ray match: CRATES J021545-701448 found
 at a distance of  26.593 arcmin
```

Figure A.5: Other output examples from first phase

Appendix B

Extinction

The blue light and UV light from an astronomical object will be scattered and absorbed by interstellar medium, causing the object seems redder than it is. In VOU-Blazars, the reddening of a object is estimated by absorbion template from Fitzpatrick 1999 [49] in UV and from CCM [26] in other bands. There were assumed $R_V = \frac{A_V}{E(B-V)} = 3.1$, which is the average oberved value all over the sky. A_V is estimated from nH value with according to Burstein and Heiles 1978 [24], assuming constant gas-to-dust ratio.

Note that

$$
\begin{aligned}
f_\lambda &= f^o_\lambda \ \exp^{-\tau_\lambda} \\
A_\lambda &= -2.5 \ \log(\frac{f_\lambda}{f^o_\lambda}) = 1.086 \ \tau_\lambda \\
E(B-V) &= A_B - A_V = 1.086 \ (-\tau_B - \tau_V) \\
\frac{A_\lambda - A_V}{A_B - A_V} &= \frac{E(\lambda - V)}{E(B-V)}
\end{aligned}
\tag{B.1}
$$

where τ_λ is the optical depth at λ, and f^o_λ is the observed flux density in case of only absorption situation.

Thus

$$
\begin{aligned}
A_\lambda &= [\frac{E(\lambda - V)}{E(B-V)}] \ E(B-V) + A_V \\
\frac{A_\lambda}{E(B-V)} &= [\frac{E(\lambda - V)}{E(B-V)}] + R_V
\end{aligned}
\tag{B.2}
$$

And the intrinsic magnitude will be

$$
m_{de-absorbed} = m_o - A_\lambda \tag{B.3}
$$

Appendix C

Slope criteria V.S. flux ratio convertion

With $C1 = -\log(\frac{\nu_r}{\nu_{W1}})$ and $C2 = -\log(\frac{\nu_{W2}}{\nu_x})$,

$$[\alpha_{r-W1} \times C1] + [\alpha_{W2-x} \times C2] = \log(\frac{F_r}{F_{W1}}) + \log(\frac{F_{W2}}{F_x}) = \log(\frac{F_r}{F_x}) + \log(\frac{F_{W2}}{F_{W1}}) \tag{C.1}$$

Assuming $\frac{F_{W1}}{F_{W2}} = (\frac{\nu_{W2}}{\nu_{W1}})^{-0.3}$ and $C3 = \log(\frac{\nu_{W2}}{\nu_{W1}})$

$$[\alpha_{r-W1} \times C1] + [\alpha_{W2-x} \times C2] = log(\frac{F_r}{F_x}) - 0.3 \times C3 \tag{C.2}$$

Thus,

$$\begin{aligned} \log(\frac{F_r}{F_x}) &= [\alpha_{r-W1} \times C1] + [\alpha_{W2-x} \times C2] + 0.3 \times C3 \\ \log(\frac{F_x}{F_r}) &= -[\alpha_{r-W1} \times C1 + \alpha_{W2-x} \times C2 + 0.3 \times C3] \end{aligned} \tag{C.3}$$

According to slope criteria,

$$\begin{aligned} 0.05 < \alpha_{1.4\mathrm{GHz}-3.4\mu\mathrm{m}} &< 0.45 \\ 0.4 < \alpha_{4.6\mu\mathrm{m}-1\mathrm{keV}} &< 1.1, \end{aligned} \tag{C.4}$$

Therefore,

$$\begin{aligned} 0.45\ C1 + 1.1\ C2 + 0.3\ C3 < \alpha_{r-W1} \times C1 + \alpha_{W2-x} \times C2 + 0.3\ C3 < 0.05\ C1 + 0.4\ C2 + 0.3\ C3 \\ -[0.05\ C1 + 0.4\ C2 + 0.3\ C3] < \log(\frac{F_x}{F_r}) < -[0.45\ C1 + 1.1\ C2 + 0.3\ C3] \end{aligned} \tag{C.5}$$

Note that assuming X-ray slope $\alpha = 0.9$ and for RASS sample,

$$\begin{aligned} F_r\ [\mathrm{Jy}] &= F_r\ [\mathrm{erg\ cm^{-2}\ s^{-1}}] \times 10^{23} \\ F_{0.1-2.4\mathrm{keV}} &= F_{1\mathrm{keV}} \times 2.418 \times 10^{17} \times \mathrm{CONV} \end{aligned} \tag{C.6}$$

where CONV $= \frac{(2.4)^{-\alpha+1}-(0.1)^{-\alpha+1}}{-\alpha+1}$

So,

$$2.418 \times 10^{17} \times \mathrm{CONV} \times 10^{-23} \times 10^{-\mathrm{AA}} < (\frac{\mathrm{F_x}}{\mathrm{F_r}}) < 2.418 \times 10^{17} \times \mathrm{CONV} \times 10^{-23} \times 10^{-\mathrm{BB}} \quad \text{(C.7)}$$

where AA = 0.05 C1 + 0.4 C2 + 0.3 C3 and BB = 0.45 C1 + 1.1 C2 + 0.3 C3
and $\frac{\mathrm{F_x}}{\mathrm{F_r}}$ is in unit of erg $\mathrm{cm^{-2}\ s^{-1}\ Jy^{-1}}$

With the trehold value from the slope criteria in equation C.4, there were obtained

$$\begin{aligned} 6.457 \times 10^{-12} < (\frac{\mathrm{F_x}}{\mathrm{F_r}})[\mathrm{erg\ cm^{-2}\ s^{-1}\ Jy^{-1}}] < 1.691 \times 10^{-7} \\ 0.198 < \alpha_{\mathrm{rx}} < 0.734 \end{aligned} \quad \text{(C.8)}$$

However, equation C.8 is not consistent with Figure 3.10 and in reality, the average $\alpha_{1.4\mathrm{GHz}-3.4\mu\mathrm{m}}$ is 0.3. Only few sources in 3HSP are with extremely low $\alpha_{1.4\mathrm{GHz}-3.4\mu\mathrm{m}}$ as 0.05. Thus, there were adjusted the slope criteria with the following equation when converting that into $\frac{\mathrm{F_x}}{\mathrm{F_r}}$ ratio

$$\begin{aligned} 0.3 < \alpha_{1.4\mathrm{GHz}-3.4\mu\mathrm{m}} &< 0.6 \\ 0.3 < \alpha_{4.6\mu\mathrm{m}-1\mathrm{keV}} &< 1.2, \end{aligned} \quad \text{(C.9)}$$

and the correspondint flux ratio between X-ray and radio becomes

$$\begin{aligned} 1.490 \times 10^{-11} < (\frac{\mathrm{F_x}}{\mathrm{F_r}})[\mathrm{erg\ cm^{-2}\ s^{-1}\ Jy^{-1}}] < 2.063 \times 10^{-9} \\ 0.43 < \alpha_{\mathrm{rx}} < 0.69 \end{aligned} \quad \text{(C.10)}$$

Appendix D

Converting the X-ray Flux / γ-ray Photon Flux to Flux Density

The X-ray intensity usually are observed in a relatively wide band (like RASS between 0.1-2.4 keV or Swift between 0.3-10 keV). To convert the X-ray flux to flux density, there were assumed X-ray spectrum following the power law relation $\mathrm{F_{x-ray}} \propto \nu^{-\alpha}$ and X-ray spectral slope $\alpha = 0.9$. That is, the flux density at 1 keV is

$$\mathrm{Flux_{1keV}} = \mathrm{K} \times 1\ \mathrm{keV}^{-\alpha} = \mathrm{K} \times (2.418 \times 10^{17})^{-\alpha} \tag{D.1}$$

Taking RASS for example, according to the calculus rule, the retrieved flux from band 0.1 keV to 2.4 keV is

$$\begin{aligned} \mathrm{Flux_{0.1-2.4keV}} &= \int_{0.1}^{2.4} \mathrm{K} \times (2.418 \times 10^{17} \times \mathrm{N})^{-\alpha} \mathrm{dN} \\ &= \frac{\mathrm{K}(2.418 \times 10^{17})^{-\alpha+1}}{-\alpha+1}[(2.4)^{-\alpha+1} - (0.1)^{-\alpha+1}] \\ &= \mathrm{Flux_{1keV}} \times (2.418 \times 10^{17})[\frac{(2.4)^{-\alpha+1} - (0.1)^{-\alpha+1}}{-\alpha-1}] \end{aligned} \tag{D.2}$$

where, N is in keV, and let CONV= $\frac{(\mathrm{bandu})^{-\alpha+1} - (\mathrm{bandl})^{-\alpha+1}}{-\alpha+1}$, bandu and bandl are the upper limit and lower limit of the frequency in keV of the intergral flux. Therefore, the flux density at 1keV coverted from intergrated flux is

$$\mathrm{Flux_{1keV}} = \frac{\mathrm{Flux_{intergrated}}}{\mathrm{CONV} \times 2.418 \times 10^{17}} \tag{D.3}$$

and the flux density at N keV is

$$\mathrm{Flux_{N\ keV}} = \frac{\mathrm{Flux_{intergrated}}}{\mathrm{CONV} \times 2.418 \times 10^{17}} \times \mathrm{N}^{-\alpha} \tag{D.4}$$

Thus, the flux at N keV is

$$\begin{aligned}\text{N keV} \times \text{Flux}_{\text{N keV}} &= \frac{\text{Flux}_{\text{intergrated}}}{\text{CONV} \times 2.418 \times 10^{17}} \times \text{N}^{-\alpha} \times (\text{N} \times 2.418 \times 10^{17}) \\ &= \frac{\text{Flux}_{\text{intergrated}}}{\text{CONV}} \times \text{N}^{-\alpha+1}\end{aligned} \tag{D.5}$$

In γ-ray the processes are very similar as that in X-ray, Photon are supposed to obey the power law like the Equation D.6.

$$\text{N(E)} = \frac{\text{dN}}{\text{dE}} = \text{N}_0(\frac{\text{E}}{\text{E}_0})^{-\Gamma} = \text{K} \times \text{E}^{-\Gamma} \tag{D.6}$$

where Γ is the photon index, N(E) = number of photon with energy E per square centimeter per second (photon flux at E), E_0 = the pivot energy = 30 GeV here, and N_0 = number of photon per square centimeter per second at pivot energy. The units of N(E) and N_0 are ph cm^{-2} s^{-1} MeV^{-1}.

The photon flux at N GeV could be converted following

$$\text{N GeV} \times \text{Flux}_{\text{N GeV}}[\text{ph cm}^{-2}\ \text{s}^{-1}] = \frac{\text{Flux}_{\text{intergrated}}}{\text{CONV}} \times \text{N}^{-\Gamma+1} \tag{D.7}$$

and the energy flux at N GeV is

$$\begin{aligned}\text{N GeV} \times \text{Flux}_{\text{N GeV}}[\text{erg cm}^{-2}\ \text{s}^{-1}] &= \frac{\text{Flux}_{\text{intergrated}}}{\text{CONV}} \times \text{N}^{-\Gamma+1} \times (1.602 \times 10^{-19} \times 10^{7}) \times (\text{N} \times 10^{9}) \\ &= \frac{\text{Flux}_{\text{intergrated}}}{\text{CONV}} \times \text{N}^{-\Gamma+2} \times 1.602 \times 10^{-3}\end{aligned} \tag{D.8}$$

Note that the intergrated energy flux coud be obtained by

$$\text{Flux}_{\text{intergrated}}[\text{erg cm}^{-2}\ \text{s}^{-1}] = 1.602 \times 10^{-3} \times \text{PH}[\frac{\text{E}_2^{\Gamma+2} - \text{E}_2^{\Gamma+2}}{\Gamma+2}][\frac{\Gamma+1}{\text{E}_2^{\Gamma+1} - \text{E}_2^{\Gamma+1}}] \tag{D.9}$$

where PH is the intergral photon flux in unit of ph cm^{-2} s^{-1}, E_1 and E_2 are the energy range for the intergral flux in GeV.

Appendix E

EBL Absorption

To estimatd the intrinsic TeV spectrum of a source before being absorbed by the extragalactic background, there were assumed the spectrum of each source following a break power law rule (Equation E.1).

$$\begin{aligned} \mathrm{N(E)} &= \mathrm{N_{break}}\ \mathrm{E_{break}^{\Gamma_1}}\ \mathrm{E^{-\Gamma_1}} && \text{if } \mathrm{E} \leq \mathrm{E_{break}} \\ &= \mathrm{N_{break}}\ \mathrm{E_{break}^{\Gamma_1}}\ (\frac{\mathrm{E_{break}^{\Gamma_2}}}{\mathrm{E_{break}^{\Gamma_1}}})\ \mathrm{E^{-\Gamma_2}} && \text{if } \mathrm{E} > \mathrm{E_{break}} \end{aligned} \tag{E.1}$$

where $\mathrm{E_{break}} = 200$ GeV, Γ_1 is the γ-ray photon index, and $\Gamma_2 = \Gamma_1 + 0.5$ is the TeV photon index.

The γ-ray photon indexes here are obtained from the *Fermi* 3FHL catalog [135]. If the sources were not in 3FHL, the photon indexes of them were assumed to be 1.8. Note that the EBL emission is depend on the redshifts, and for the sources without redshift measurement, they were assumed 0.3 in this section. The assumed redshift value is different then that of in section 3.4 and 3.3 since for a source already be observed or detected by Fermi will have average redshift around 0.3.

Based on the optical depth model from [43], the observed fluxes for a soruce with redshift z at a given energy E are absorbed by the factor ABS=$\exp^{-\tau(\mathrm{z,E})}$, where ABS is the absorbed fator, $\tau(\mathrm{z,E})$ is the optical depth. Therefore, taking 3FHL fluxes for example (10 GeV to 1000 GeV), the de-absorpted fluxes could be calculated with

$$\mathrm{de-absorbed\ flux} = \int_{10\mathrm{GeV}}^{1000\mathrm{GeV}} \mathrm{ABS(z,E)} \times \mathrm{N(E)\ dE} \tag{E.2}$$

ratio between the observed fluxe and de-absorbed flux is

$$\mathrm{de-absorbed\ ratio} = \frac{\int_{10\mathrm{GeV}}^{1000\mathrm{GeV}} \mathrm{ABS(z,E)} \times \mathrm{N(E)\ dE}}{\int_{10\mathrm{GeV}}^{1000\mathrm{GeV}} \mathrm{N(E)\ dE}} \tag{E.3}$$

Appendix F

Details of the luminosity function and V/Vmax

The estimation of the statistical properties, such as the logN-logS,V/Vmax, and luminosity function of a population of sources, requires the availability of flux-limited and complete samples. It is neccessary to take into account the incompleteness resulting from the fact that the only existing all sky X-ray survey is not sufficiently deep to ensure the detection of all radio and IR faint HSP blazars. Thus, there were applied radio-X-ray cutted subsample or radio-γ-ray subsample to estimate the statistic for 3HSP, and the RASS coverage were considered to calibrate the number count for X-ray selected subsample.

For each source in the 3HSP X-ray selected subsample, there were calculated a contribution n_i to the total density, as given by $n_i = 1/A_i$ deg^{-2}, where the parameter A_i is the sky area covered by RASS with sensitivity sufficient to detect the source in consideration. The logN-logS value is then the sum of the density contribution of all sources in a given flux/luminosity bin $N_{bin} = \sum n_i$. This approach is applied to estimate the logN-logS of HSP blazars with respect to the radio and X-ray flux density and cummulative ν_{peak} distribution in Figure 3.17. For γ-ray logN-logS, given that the sensitivity for *Fermi* is almost the same in the whole sky out of the Galactic region, there were counted the source for γ-ray selected sample without area calibration.

To obtained the V/Vmax value or luminosity function for a sources, maximum available z (Zmax) is neccessary. The Zmax is calculated by assuming a source with fix luminosity whose flux value is the flux limit (either specifyingarbitary or by defalut of the catalog applied) instead of the observed flux, and then estimating the corresponding maximum redshift with that luminosity and the flux limit. That is, the maximum distant is defined with a source could be detected with current instruments. If there were more than one flux limit applied, the maximum available redshift is then defined as the smaller one between the two limit redshifts estimated according to the flux limits. When the Zmax is smaller than the actual redshfit, Zmax is set to the same value as the redshift.

The comoving distant is then estimated using $r = D_L(z)/(1+z)$, and the comoving maximum volume will be $V_{max} = (1/3) \times AREA \times STR \times {r_{max}}^3$, where AREA is the sky coverage degrees, STR is steradian per degrees which is $4\pi/41252.96$, and D_L is the luminosity distant. Note that for X-ray selected subsample, the flux limits is not the same in the whole sky, and there were divided the sky with respect to every X-ray flux limit bins. For a given source in X-ray-radio cutted subsample, the $V_{max} = \sum(1/3) \times AREA^* \times STR \times {r^*_{max}}^3$, where AREA* is the corresponding area for a certain flux limit, $\sum AREA^* = AREA(= 34110.5 \text{ degrees}^2 \text{ for } |b| > 10^o)$, and ${r^*_{max}}^3$ is the comoving maximum distant for the $AREA^* with same flux limit$.

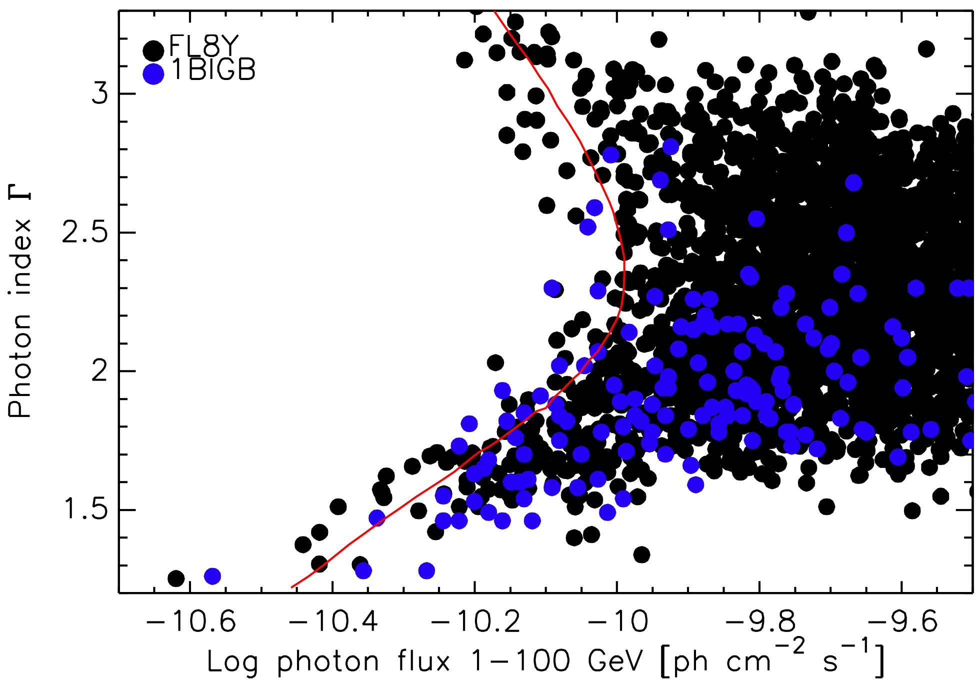

Figure F.1: *Fermi* limit applied in V/Vmax and luminosity function. The red line is the applied limit.

In γ-ray, the thing is simplier as there is no need to divide the volume according to the sensitivity in *Fermi* and flux limit. The γ-ray flux limit is assumed to be the same every where in the sky but depend on the photon index of observed object. Relationship between Γ and *Fermi* flux limit is shown in Figure F.1.

Appendix G

The 3HSP Tables

G.1 Extreme 3HSP sources

Table G.1: The extreme synchrotron peak sources. The sources marked with * are discussed in the text and shown in Figure 5.1 to 5.3.

Source	log $\nu_{\rm peak}$ Hz	log $\nu_{\rm peak}f_{\nu_{\rm peak}}$ erg cm^{-2} s^{-1}	BZCat	TeVCat
3HSPJ003322.4−203908	17.9	−11.9	–	
3HSPJ003552.6+595004	18.2	−10.3	5BZB	1ES0033+595
3HSPJ004013.8+405004	>17.5	−11.5	5BZU	
3HSPJ011501.7−340027	17.9	−11.6	5BZB	
3HSPJ012308.6+342048	18.0	−10.8	5BZB	
3HSPJ012340.3+421017	17.8	−11.7	5BZG	
3HSPJ013803.7−215530	>17.5	−12.0	–	
3HSPJ015657.9−530159	18.3	−11.1	5BZB	
3HSPJ020412.9−333340	17.9	−11.7	5BZB	
3HSPJ021216.8−022155	17.8	−11.7	–	
3HSPJ022539.7−190035	17.8	−12.9	–	
3HSPJ023248.5+201717*	18.5	−11.0	5BZG	1ES0229+200
3HSPJ032056.3+042448	17.9	−11.7	–	
3HSPJ032356.5−010833	>17.5	−11.9	5BZB	
3HSPJ034923.1−115927	17.9	−11.0	5BZB	1ES0347−121
3HSPJ035154.5−370344	17.9	−11.9	5BZB	
3HSPJ035257.4−683117*	18.1	−11.0	–	
3HSPJ035726.0−031759	>17.5	−12.1	–	
3HSPJ040324.5−242947	18.0?	−11.8	5BZB	
3HSPJ041238.4−392629	17.8	−12.2	–	
3HSPJ041855.8+132451	17.8	−12.1	–	
3HSPJ044127.4+150455	17.8	−11.5	5BZB	
3HSPJ050419.5−095632	17.9	−11.6	–	
3HSPJ050709.3−385948	>17.5	−12.2	–	
3HSPJ050756.1+673724	17.9	−10.7	5BZB	1ES0502+675
3HSPJ050938.1−040045	17.8	−11.4	5BZB	
3HSPJ055040.5−321616	18.1	−10.7	5BZG	PKS0548−322
3HSPJ055716.8−061706	17.8	−11.4	–	
3HSPJ064710.0−513547	17.9	−11.2	–	
3HSPJ071030.0+590820	18.1	−10.7	5BZB	RGBJ0710+591

Table G.1: continued.

Source	log $\nu_{\rm peak}$ Hz	log $\nu_{\rm peak} f_{\nu_{\rm peak}}$ erg cm^{-2} s^{-1}	BZCat	TeVCat
3HSPJ073326.7+515355	17.9	−11.2	–	
3HSPJ081917.5−075626	18.0	−11.5	5BZB	
3HSPJ083251.4+330011	18.0	−12.0	5BZB	
3HSPJ084452.2+280410	17.9	−12.3	–	
3HSPJ084712.9+113350	17.8	−11.2	5BZB	RBS0723
3HSPJ094620.2+010451	17.9	−11.8	5BZB	
3HSPJ102212.6+512400	18.2	−11.7	5BZG	
3HSPJ104651.4−253545	>18.0	−11.2	5BZB	
3HSPJ110804.9+164820	17.9	−12.7	–	
3HSPJ111939.5−304720	17.8	−12.1	5BZB	
3HSPJ113032.0−780105	17.9	−11.3	–	
3HSPJ113209.2−473853	>17.5	−11.6	–	
3HSPJ113630.1+673704	18.1	−11.1	5BZB	RXJ1136.5+6737
3HSPJ122208.7+030718	>17.5	−11.8	–	
3HSPJ122514.2+721447	>17.5	−11.8	5BZB	
3HSPJ125341.2−393159	17.9	−11.3	5BZG	
3HSPJ125708.3+264925	>17.5	−12.3	–	
3HSPJ132239.2+494336	>17.5	−12.1	–	
3HSPJ132541.8−022809	17.9	−12.0	5BZB	
3HSPJ133102.9+565541	17.8	−12.1	5BZG	
3HSPJ133529.7−295038	17.8	−11.8	5BZB	
3HSPJ140027.0−293936	>17.5	−12.1	–	
3HSPJ140121.1+520928	>17.5	−12.0	5BZB	
3HSPJ141427.0+035752	17.9	−11.9	–	
3HSPJ142238.8+580155	17.8	−11.3	5BZB	
3HSPJ142832.6+424020	18.1	−10.7	5BZB	H1426+428
3HSPJ143342.7−730438*	>18.0	−11.3	–	
3HSPJ150842.6+270908	17.8	−11.4	5BZB	
3HSPJ151041.1+333504	>17.5	−11.5	5BZG	
3HSPJ151618.7−152344	18.0	−11.7	5BZB	
3HSPJ153646.7+013800	>18.0	−11.7	5BZB	
3HSPJ154439.8−112741	18.4	−11.8	–	
3HSPJ155210.2+315909	17.8	−12.3	5BZG	
3HSPJ160519.0+542059	17.9	−12.0	5BZB	
3HSPJ161414.0+544251	17.8	−12.6	–	
3HSPJ161632.9+375603	18.0	−12.0	5BZG	
3HSPJ165352.2+394536*	17.9	−10.2	5BZB	Markarian501
3HSPJ174357.8+193509	17.8	−11.3	5BZG	1ES1741+196
3HSPJ182419.0+430949	17.8	−11.7	–	
3HSPJ184847.1+424539	17.8	−11.5	5BZB	
3HSPJ192325.3−250208	17.8	−12.0	–	
3HSPJ194333.7−053353	>17.5	−11.8	–	
3HSPJ194356.2+211822	18.1	−11.0	–	HESSJ1943+213
3HSPJ204008.2−711459	17.8	−11.2	–	
3HSPJ205528.2−002116	>18.0	−10.9	5BZB	
3HSPJ214410.0−195559	18.0	−12.4	–	
3HSPJ215015.5−141049	17.8	−11.3	5BZG	
3HSPJ215305.3−004230*	>18.0	−11.4	5BZB	
3HSPJ225147.5−320612	>18.0	−11.3	5BZU	
3HSPJ231305.8−600522	17.8	−12.3	–	
3HSPJ231347.8−692330	17.8	−11.8	–	
3HSPJ234753.2+543630	>17.5	−11.3	–	

G.2 3HSP sources with de-absorbed 3FHL flux

Table G.2: The table with de-EBL absorption flux. For sources without estimated redshift, there were assigned average value 0.3 to estimated the de-EBL absorbtion flux.

Source	Z	3FHL	3FHL Flux ph cm^{-2} s^{-1}	de-EBL Flux ph cm^{-2} s^{-1}	Γ
3HSPJ000132.7−415525	—	J0001.9−4155	4.323E−11	6.271E−11	1.782
3HSPJ000215.1−672653	>0.52	J0002.1−6728	5.009E−11	8.515E−11	1.811
3HSPJ000319.5−524727	0.37	J0003.3−5248	4.156E−11	7.32E−11	1.601
3HSPJ000835.3−233927	0.147	J0008.4−2339	7.46E−11	7.687E−11	2.739
3HSPJ000922.7+503028	0.25	J0009.4+5030	2.219E−10	3.737E−10	1.43
3HSPJ000949.7−431650	0.23	J0009.7−4319	2.419E−11	2.794E−11	2.204
3HSPJ001356.0−185406	0.094	J0013.8−1855	3.109E−11	3.452E−11	1.944
3HSPJ001411.4−502234	0.010?	J0014.0−5024	3.026E−11	3.095E−11	1.498
3HSPJ001442.0+580201	0.35	J0014.7+5801	5.674E−11	7.62E−11	2.001
3HSPJ001540.1+555144	0.15	J0015.7+5551	5.216E−11	6.618E−11	1.697
3HSPJ001827.7+294730	0.100?	J0018.6+2946	5.058E−11	5.988E−11	1.68
3HSPJ002200.0−514024	0.25	J0021.8−5140	6.679E−11	6.941E−11	2.856
3HSPJ002200.9+000657	0.306	J0022.0+0006	3.481E−11	8.843E−11	1.011
3HSPJ002635.6−460109	0.25	J0026.5−4602	2.461E−11	3.876E−11	1.543
3HSPJ002928.6+205333	0.367	J0029.4+2052	2.643E−11	5.612E−11	1.363
3HSPJ003020.4−164712	0.237	J0030.2−1648	5.981E−11	8.84E−11	1.625
3HSPJ003119.7+072453	—	J0031.2+0727	3.738E−11	4.234E−11	2.39
3HSPJ003334.3−192132	>0.506	J0033.5−1921	4.384E−10	6.836E−10	1.916
3HSPJ003514.7+151504	>0.64	J0035.2+1514	1.434E−10	1.957E−10	2.231
3HSPJ003552.6+595004	0.467?	J0035.9+5950	6.094E−10	9.659E−10	1.855
3HSPJ004013.8+405004	0.24	J0040.3+4049	2.475E−11	4.449E−11	1.3
3HSPJ004123.0+375855	0.38	J0041.5+3759	2.822E−11	4.214E−11	1.849
3HSPJ004141.2−160747	0.43	J0041.7−1608	2.08E−11	2.345E−11	2.564
3HSPJ004334.1−044300	>0.48	J0043.4−0443	2.83E−11	3.07E−11	2.805
3HSPJ004519.2+212740	>0.35	J0045.3+2127	2.577E−10	4.04E−10	1.733
3HSPJ004752.0+544745	0.26	J0047.9+5448	3.489E−11	5.122E−11	1.686
3HSPJ004755.2+394857	0.252	J0047.9+3947	8.365E−11	1.02E−10	2.074
3HSPJ004859.1+422351	0.37	J0049.0+4224	2.646E−11	3.58E−11	2.012
3HSPJ005116.6−624204	>0.3	J0051.2−6242	2.363E−10	3.096E−10	1.982
3HSPJ005446.7−245528	>0.12	J0054.7−2456	1.338E−10	1.578E−10	1.807
3HSPJ005542.7+450701	0.46	J0055.8+4507	2.108E−11	2.132E−11	3.752
3HSPJ005620.0−093630	0.1	J0056.3−0936	9.371E−11	1.093E−10	1.744
3HSPJ005758.3+632639	0.18	J0057.9+6325	6.088E−11	8.632E−11	1.533
3HSPJ005916.9−015017	0.114	J0059.3−0152	4.135E−11	4.63E−11	2.001
3HSPJ005931.4−351049	0.31	J0059.4−3513	2.88E−11	2.883E−11	4.643
3HSPJ010250.9−200158	0.270?	J0102.8−2001	2.436E−11	3.29E−11	1.865
3HSPJ010325.8+533713	0.15	J0103.5+5337	7.374E−11	7.796E−11	2.477
3HSPJ010956.5−402050	0.313	J0109.9−4020	3.129E−11	6.975E−11	1.17
3HSPJ011501.7−340027	0.482	J0114.9−3359	3.326E−11	9.277E−11	1.249
3HSPJ011546.1+251953	0.375	J0115.8+2519	1.069E−10	1.423E−10	2.047
3HSPJ011555.4−274431	>0.7	J0115.9−2746	2.263E−11	7.823E−11	1.284
3HSPJ011904.6−145858	0.29	J0119.0−1458	4.268E−11	7.265E−11	1.507
3HSPJ012152.6−391544	0.3	J0121.9−3917	2.092E−11	2.973E−11	1.819
3HSPJ012308.6+342048	0.27	J0123.0+3422	6.24E−11	8.174E−11	1.93
3HSPJ012338.3−231058	0.404	J0123.6−2309	7.772E−11	1.436E−10	1.586

Table G.2: continued.

Source	Z	3FHL	3FHL Flux ph cm^{-2} s^{-1}	de-EBL Flux ph cm^{-2} s^{-1}	Γ
3HSPJ012713.9+032300	—	J0127.2+0325	7.025E−11	9.459E−11	1.922
3HSPJ013107.2+612033	—	J0131.1+6120	2.533E−10	3.436E−10	1.907
3HSPJ013113.8+554512	0.036	J0131.1+5546	3.317E−11	3.32E−11	3.543
3HSPJ013309.2−453524	—	J0133.1−4533	2.202E−11	3.041E−11	1.872
3HSPJ013428.1+263843	>0.26	J0134.4+2638	7.789E−11	9.714E−11	2.033
3HSPJ013632.5+390559	—	J0136.5+3906	8.329E−10	1.334E−9	1.622
3HSPJ013750.4+581411	—	J0137.9+5815	1.652E−10	1.932E−10	2.276
3HSPJ013801.1+224808	0.26	J0138.0+2248	3.786E−11	6.822E−11	1.352
3HSPJ014347.3−584551	—	J0143.8−5846	1.807E−10	4.482E−10	1.023
3HSPJ014648.5−520233	0.098	J0146.8−5203	3.292E−11	3.476E−11	2.303
3HSPJ014820.3+520204	0.24	J0148.2+5201	1.014E−10	1.257E−10	2.011
3HSPJ014833.7+012901	0.940?	J0148.6+0127	3.357E−11	4.615E−11	2.383
3HSPJ015044.5−545004	0.28	J0150.6−5450	1.562E−11	2.352E−11	1.682
3HSPJ015239.5+014717	0.08	J0152.6+0147	1.249E−10	1.393E−10	1.83
3HSPJ015307.3+751742	—	J0152.8+7517	4.987E−11	5.935E−11	2.221
3HSPJ015325.8+711506	0.02	J0153.5+7115	4.447E−11	4.518E−11	2.155
3HSPJ015402.7+082351	0.681?	J0154.0+0823	1.636E−10	2.204E−10	2.282
3HSPJ015624.5−242003	—	J0156.2−2419	2.9E−11	4.329E−11	1.733
3HSPJ015646.0−474417	0.22	J0156.9−4744	2.449E−11	2.548E−11	2.786
3HSPJ015657.9−530159	0.25	J0156.7−5302	8.736E−11	1.419E−10	1.488
3HSPJ015934.3+104705	0.195	J0159.5+1047	8.967E−11	9.404E−11	2.656
3HSPJ020020.9−410935	0.500?	J0200.1−4109	5.055E−11	7.553E−11	1.974
3HSPJ020421.5+241750	0.18	J0204.3+2417	3.436E−11	3.51E−11	2.97
3HSPJ020838.1+352312	0.318	J0208.6+3522	3.804E−11	5.836E−11	1.719
3HSPJ020917.0+444946	0.27	J0209.2+4448	4.135E−11	5.844E−11	1.776
3HSPJ020921.6−522922	0.12	J0209.3−5229	2.191E−10	2.645E−10	1.72
3HSPJ021230.4−350330	0.393?	J0212.4−3503	3.046E−11	4.759E−11	1.795
3HSPJ021252.8+224452	0.459	J0213.0+2242	3.494E−11	5.98E−11	1.744
3HSPJ021358.6−695137	0.34	J0213.9−6950	4.574E−11	8.411E−11	1.494
3HSPJ021417.9+514451	0.049	J0214.5+5145	4.238E−11	4.818E−11	1.349
3HSPJ021517.8+755452	0.15	J0215.2+7555	1.99E−11	3.027E−11	1.23
3HSPJ021632.0+231450	0.288	J0216.4+2315	3.486E−11	4.061E−11	2.271
3HSPJ021650.8−663642	>0.673	J0217.0−6636	6.738E−11	7.149E−11	3.142
3HSPJ021900.4+244520	—	J0219.0+2445	3.942E−11	6.541E−11	1.568
3HSPJ021905.4−172512	0.128	J0219.1-1723	3.453E−11	3.969E−11	1.943
3HSPJ022304.5+682154	0.23	J0222.9+6821	4.843E−11	7.288E−11	1.573
3HSPJ022314.2−111738	>0.2	J0223.0−1119	3.991E−11	4.078E−11	3.011
3HSPJ022638.8−444122	>0.68	J0226.7−4440	3.127E−11	5.476E−11	1.896
3HSPJ022716.5+020200	0.45	J0227.3+0200	4.746E−11	7.844E−11	1.78
3HSPJ023109.2−575505	0.032	J0231.0−5755	3.687E−11	3.807E−11	2.025
3HSPJ023248.5+201717	0.139	J0232.8+2017	4.857E−11	6.399E−11	1.54
3HSPJ023340.9+065611	0.31	J0233.5+0657	2.694E−11	3.337E−11	2.126
3HSPJ023430.6+804337	0.5	J0233.9+8042	2.157E−11	5.414E−11	1.369
3HSPJ023536.6−293843	0.35	J0235.5−2938	2.32E−11	4.523E−11	1.436
3HSPJ023734.0−360328	0.411	J0237.6−3602	3.314E−11	7.905E−11	1.306
3HSPJ023832.4−311657	0.233	J0238.4−3117	1.229E−10	1.591E−10	1.885
3HSPJ024115.4−304140	0.3	J0241.0−3037	2.704E−11	2.788E−11	3.038
3HSPJ024121.7+654311	0.18	J0241.3+6543	9.896E−11	1.221E−10	1.878
3HSPJ024440.2−581954	0.26	J0244.4−5819	7.699E−11	1.346E−10	1.398
3HSPJ025037.9+171208	1.1	J0250.5+1712	6.623E−11	1.643E−10	1.755
3HSPJ025047.5+562935	0.27	J0250.7+5631	4.825E−11	5.218E−11	2.567
3HSPJ025111.5−183112	0.5	J0251.2−1830	3.463E−11	5.092E−11	1.999
3HSPJ025857.5+055243	—	J0258.9+0554	3.078E−11	3.105E−11	3.609
3HSPJ030326.3−240711	0.266	J0303.4−2407	6.378E−10	8.255E−10	1.95

Table G.2: continued.

Source	Z	3FHL	3FHL Flux ph cm^{-2} s^{-1}	de-EBL Flux ph cm^{-2} s^{-1}	Γ
3HSPJ030416.3−283218	0.400?	J0304.3−2833	2.872E−11	3.658E−11	2.169
3HSPJ030433.9−005404	0.511	J0304.5−0055	2.679E−11	4.722E−11	1.758
3HSPJ030515.0−160816	0.31	J0305.2−1609	4.735E−11	5.742E−11	2.182
3HSPJ031034.6−501631	0.26	J0310.6−5017	8.134E−11	9.009E−11	2.426
3HSPJ031235.6−222117	0.28	J0312.5−2221	5.018E−11	5.252E−11	2.829
3HSPJ031250.2+361519	0.071	J0312.8+3614	3.285E−11	3.735E−11	1.644
3HSPJ031423.9+061956	0.620?	J0314.3+0620	3.34E−11	8.466E−11	1.478
3HSPJ031612.7+090443	0.372?	J0316.2+0905	2.219E−10	3.036E−10	1.993
3HSPJ031614.3−643731	—	J0316.2−6439	6.364E−11	9.488E−11	1.735
3HSPJ031614.9−260757	0.443	J0316.5−2610	5.133E−11	6.518E−11	2.22
3HSPJ031951.7+184534	0.19	J0319.8+1845	1.069E−10	1.276E−10	2.01
3HSPJ032009.2−704533	0.37	J0319.2−7045	2.331E−11	2.361E−11	3.55
3HSPJ032159.9+233611	—	J0322.0+2336	1.452E−10	2.197E−10	1.71
3HSPJ032343.6−011146	>0.44	J0323.6−0109	7.348E−11	1.1E−10	1.912
3HSPJ032523.5−563544	0.6	J0325.4−5635	5.323E−11	7.572E−11	2.13
3HSPJ032541.0−164616	0.291	J0325.6−1646	1.62E−10	2.662E−10	1.565
3HSPJ032613.9+022514	0.147	J0326.3+0226	1.044E−10	1.131E−10	2.297
3HSPJ032852.6−571605	>0.48	J0329.2−5714	2.836E−11	3.675E−11	2.21
3HSPJ033118.4−615528	0.21	J0331.3−6157	3.898E−11	4.337E−11	2.314
3HSPJ033349.0+291631	—	J0333.7+2916	1.25E−10	1.38E−10	2.5
3HSPJ033356.7+653656	0.16	J0333.9+6537	1.109E−10	1.299E−10	1.991
3HSPJ033415.4−372542	>0.39	J0334.2−3726	1.953E−10	2.319E−10	2.341
3HSPJ033513.8−445943	—	J0335.1−4459	7.016E−11	9.751E−11	1.86
3HSPJ033623.7−034738	0.162	J0336.4−0348	2.295E−11	3.525E−11	1.28
3HSPJ033812.5−244350	0.251	J0338.1−2443	3.041E−11	6.092E−11	1.146
3HSPJ033829.2+130215	—	J0338.5+1302	1.879E−10	2.618E−10	1.855
3HSPJ033859.5−284619	0.27	J0338.9−2848	5.946E−11	8.933E−11	1.666
3HSPJ033913.6−173600	0.066	J0339.2−1736	6.029E−11	6.441E−11	2.026
3HSPJ034819.8+603508	0.4	J0348.3+6035	6.282E−11	8.073E−11	2.149
3HSPJ034923.1−115927	0.188	J0349.3−1159	5.822E−11	7.384E−11	1.826
3HSPJ034957.8+064126	0.26	J0350.0+0640	3.36E−11	5.943E−11	1.38
3HSPJ035028.3−514454	0.32	J0350.4−5143	2.039E−11	3.179E−11	1.697
3HSPJ035051.3−281632	0.47	J0350.8−2814	3.52E−11	5.429E−11	1.897
3HSPJ035257.4−683117	0.087	J0353.0−6832	6.1E−11	7.2E−11	1.606
3HSPJ035305.0−362308	0.31	J0352.9−3622	4.862E−11	6.9E−11	1.838
3HSPJ035308.4+825631	0.069?	J0353.4+8256	2.483E−11	2.963E−11	1.362
3HSPJ035309.5+565430	—	J0353.1+5655	4.658E−11	5.969E−11	2.032
3HSPJ035726.0−031759	0.3	J0357.3−0316	3.403E−11	4.252E−11	2.089
3HSPJ035923.4−023501	0.34	J0359.4−0235	3.899E−11	5.03E−11	2.07
3HSPJ040111.2−535458	0.59	J0401.0−5355	2.484E−11	6.115E−11	1.479
3HSPJ040254.4+643509	0.31	J0402.9+6433	2.562E−11	3.851E−11	1.739
3HSPJ040324.5−242947	0.357	J0403.2−2428	2.329E−11	5.6E−11	1.174
3HSPJ040928.5+320245	0.28	J0409.4+3201	3.307E−11	3.588E−11	2.564
3HSPJ041458.1−533943	—	J0414.6−5339	4.793E−11	5.213E−11	2.579
3HSPJ041652.4+010523	0.287	J0416.8+0105	1.032E−10	1.425E−10	1.851
3HSPJ042011.0−601505	0.33	J0420.2−6015	2.122E−11	3.116E−11	1.809
3HSPJ042013.4+401121	0.14	J0420.2+4011	4.165E−11	5.134E−11	1.743
3HSPJ042218.3+195054	0.516	J0422.3+1949	4.426E−11	1.016E−10	1.476
3HSPJ042525.3+632001	0.27	J0425.4+6319	8.955E−11	1.443E−10	1.552
3HSPJ042958.9−305935	0.21	J0429.9−3100	2.431E−11	3.075E−11	1.89
3HSPJ043145.0+740326	—	J0431.8+7403	7.782E−11	7.903E−11	3.343
3HSPJ043307.5+322840	—	J0433.1+3227	5.489E−11	8.409E−11	1.69
3HSPJ043344.1−572613	—	J0433.7−5725	4.193E−11	4.242E−11	3.473
3HSPJ043440.9+092348	0.21	J0434.7+0921	8.981E−11	1.071E−10	2.055

Table G.2: continued.

Source	Z	3FHL	3FHL Flux ph cm^{-2} s^{-1}	de-EBL Flux ph cm^{-2} s^{-1}	Γ
3HSPJ043837.0−732921	0.15	J0438.0−7328	4.518E−11	6.151E−11	1.505
3HSPJ043932.2−320052	0.4	J0439.5−3200	4.446E−11	8.365E−11	1.558
3HSPJ044018.6−245933	0.600?	J0440.3−2457	4.145E−11	5.638E−11	2.209
3HSPJ044050.3+275046	0.2	J0440.8+2749	8.476E−11	8.62E−11	3.114
3HSPJ044127.4+150455	0.109	J0441.6+1504	3.885E−11	4.495E−11	1.828
3HSPJ044240.6+614039	0.18	J0442.6+6142	4.58E−11	5.61E−11	1.9
3HSPJ044837.6−163243	0.350?	J0448.7−1632	1.053E−10	1.089E−10	3.067
3HSPJ044924.6−435008	>0.19	J0449.4−4350	1.273E−9	1.521E−9	2.006
3HSPJ045148.6+572141	0.31	J0451.9+5720	3.125E−11	4.044E−11	2.025
3HSPJ045804.8+115143	0.2	J0458.0+1151	2.949E−11	4.562E−11	1.426
3HSPJ050021.4+523801	0.12	J0500.3+5238	7.434E−11	8.549E−11	1.907
3HSPJ050043.9+190317	0.25	J0500.6+1903	3.562E−11	3.613E−11	3.293
3HSPJ050141.1+304825	0.31	J0501.6+3047	3.994E−11	4.46E−11	2.464
3HSPJ050335.4−111506	>0.4	J0503.5−1114	2.508E−11	6.141E−11	1.26
3HSPJ050339.5+451659	0.25	J0503.6+4518	6.718E−11	1.039E−10	1.574
3HSPJ050534.7+041554	0.424	J0505.5+0415	8.338E−11	1.069E−10	2.179
3HSPJ050558.7+611335	0.27	J0506.0+6113	5.183E−11	8.575E−11	1.507
3HSPJ050639.9−085801	0.28	J0506.7−0858	4.455E−11	5.019E−11	2.383
3HSPJ050650.1+032358	0.32	J0506.9+0323	4.117E−11	6.694E−11	1.633
3HSPJ050657.7−543503	>0.26	J0506.9−5434	1.178E−10	1.609E−10	1.824
3HSPJ050727.2−334635	0.390?	J0507.4−3347	3.792E−11	5.169E−11	2.021
3HSPJ050756.1+673724	0.340?	J0508.0+6737	4.983E−10	8.421E−10	1.612
3HSPJ050957.2−641741	—	J0509.9−6418	5.74E−11	7.101E−11	2.114
3HSPJ051631.2+735108	0.251	J0516.3+7350	4.613E−11	6.029E−11	1.9
3HSPJ052145.9+211251	0.108	J0521.7+2112	1.237E−9	1.456E−9	1.753
3HSPJ052542.4−601340	0.45	J0525.6−6013	7.862E−11	1.57E−10	1.551
3HSPJ052846.0−592003	1.130?	J0528.6−5920	3.857E−11	4.759E−11	2.707
3HSPJ052902.5+093435	0.3	J0529.2+0935	4.952E−11	6.136E−11	2.11
3HSPJ053629.0−334302	>0.34	J0536.4−3342	1.774E−10	2.728E−10	1.749
3HSPJ053748.9−571830	1.180?	J0537.8−5718	2.604E−11	4.975E−11	2.025
3HSPJ053810.3−390842	0.27	J0538.2−3908	2.246E−11	2.739E−11	2.105
3HSPJ054030.0+582338	—	J0540.5+5823	8.094E−11	1.323E−10	1.591
3HSPJ054106.9−485410	0.6	J0541.1−4855	2.595E−11	2.616E−11	4.136
3HSPJ054357.2−553207	0.273	J0543.9−5532	2.881E−10	3.537E−10	2.092
3HSPJ054906.8+325803	0.25	J0549.1+3258	3.938E−11	5.588E−11	1.728
3HSPJ055026.5−435703	0.4	J0550.4−4356	3.397E−11	4.408E−11	2.128
3HSPJ055040.5−321616	0.069	J0550.5−3215	3.147E−11	3.575E−11	1.63
3HSPJ055333.1−203418	>0.38	J0553.5−2034	5.267E−11	6.532E−11	2.211
3HSPJ055716.8−061706	0.29	J0557.3−0616	2.941E−11	5.28E−11	1.43
3HSPJ055806.4−383831	0.302	J0558.1−3838	7.465E−11	8.319E−11	2.461
3HSPJ055940.9+304228	0.3	J0559.6+3045	4.178E−11	4.623E−11	2.491
3HSPJ055959.3+640958	0.32	J0559.5+6409	2.144E−11	3.207E−11	1.763
3HSPJ060014.9+124343	0.12	J0600.3+1245	1.137E−10	1.277E−10	2.018
3HSPJ060200.4+531600	0.052	J0602.0+5316	8.705E−11	9.145E−11	2.049
3HSPJ060251.2−401845	—	J0602.7−4019	8.993E−11	9.897E−11	2.517
3HSPJ060408.6−481725	0.23	J0604.2−4816	6.021E−11	9.579E−11	1.47
3HSPJ060635.7−472954	0.037	J0606.3−4730	2.618E−11	2.721E−11	2.002
3HSPJ060915.0−024754	0.23	J0609.2−0247	1.193E−10	1.219E−10	3.067
3HSPJ061106.5+432357	0.28	J0611.2+4325	7.767E−11	1.159E−10	1.698
3HSPJ061740.9−171557	—	J0617.6−1715	1.054E−10	1.183E−10	2.428
3HSPJ062040.0+264331	0.14	J0620.6+2645	6.0E−11	7.042E−11	1.909
3HSPJ062046.1−503350	0.25	J0620.9−5033	2.257E−11	2.644E−11	2.192
3HSPJ062636.7−425805	0.27	J0626.5−4259	5.011E−11	5.086E−11	3.31
3HSPJ063059.5−240646	>1.239	J0630.9−2406	5.224E−10	2.223E−9	1.408

Table G.2: continued.

Source	Z	3FHL	3FHL Flux ph cm^{-2} s^{-1}	de-EBL Flux ph cm^{-2} s^{-1}	Γ
3HSPJ064007.1−125314	0.11	J0640.0−1254	8.691E−11	1.106E−10	1.477
3HSPJ064435.7+603851	0.33	J0644.4+6038	3.458E−11	4.61E−11	1.99
3HSPJ064443.7−285116	0.35	J0644.6−2854	3.942E−11	4.514E−11	2.414
3HSPJ064710.0−513547	0.22	J0647.0−5138	2.842E−11	3.059E−11	2.511
3HSPJ064847.6+151624	0.179	J0648.7+1517	2.678E−10	3.303E−10	1.877
3HSPJ064933.5−313920	—	J0649.5−3138	8.719E−11	1.349E−10	1.674
3HSPJ065035.3+205555	0.3	J0650.6+2055	9.192E−11	1.258E−10	1.89
3HSPJ065046.4+250259	0.203?	J0650.7+2503	4.454E−10	7.589E−10	1.259
3HSPJ065105.4+401338	0.18	J0651.1+4015	3.308E−11	3.439E−11	2.725
3HSPJ065610.6+423702	0.059	J0656.2+4235	2.751E−11	3.185E−11	1.394
3HSPJ065845.0+063711	0.23	J0658.5+0636	2.878E−11	3.758E−11	1.859
3HSPJ065932.9−674350	0.43	J0659.5−6743	1.826E−11	4.753E−11	1.244
3HSPJ070014.3+130424	0.21	J0700.1+1303	4.761E−11	5.816E−11	1.988
3HSPJ070132.1+250953	0.33	J0701.5+2512	2.224E−11	5.082E−11	1.213
3HSPJ070610.8+024449	0.22	J0706.1+0247	2.681E−11	4.975E−11	1.183
3HSPJ070631.6+374436	—	J0706.5+3744	1.879E−10	2.63E−10	1.847
3HSPJ070858.2+224135	—	J0708.9+2240	6.904E−11	8.886E−11	2.022
3HSPJ070912.5−152703	0.1	J0709.1−1525	6.821E−11	8.387E−11	1.529
3HSPJ070947.9−300905	—	J0709.7−3008	2.874E−11	3.651E−11	2.049
3HSPJ071030.0+590820	0.12	J0710.4+5908	1.006E−10	1.518E−10	1.022
3HSPJ072113.9−022054	0.38	J0721.1−0223	3.558E−11	6.789E−11	1.513
3HSPJ072259.6−073134	0.17	J0723.0−0732	5.527E−11	7.582E−11	1.576
3HSPJ072529.5−050336	0.1	J0725.5−0504	2.011E−11	2.442E−11	1.577
3HSPJ072547.8−054832	—	J0725.7−0548	5.402E−11	7.168E−11	1.952
3HSPJ072659.5+373423	0.35	J0726.7+3735	2.485E−11	2.559E−11	3.133
3HSPJ073026.0+330722	0.11	J0730.4+3307	4.129E−11	4.873E−11	1.752
3HSPJ073049.5−660218	0.106	J0730.8−6602	7.24E−11	8.687E−11	1.664
3HSPJ073326.7+515355	0.09	J0733.4+5152	3.482E−11	4.392E−11	1.345
3HSPJ073706.0−824840	0.23	J0737.5−8247	6.786E−11	9.003E−11	1.823
3HSPJ073927.3−672136	0.53	J0739.7−6720	2.183E−11	5.456E−11	1.406
3HSPJ074405.3+743358	0.314	J0744.1+7435	7.824E−11	1.017E−10	2.021
3HSPJ074627.0−022549	—	J0746.3−0225	8.674E−11	1.079E−10	2.099
3HSPJ074642.3−475455	—	J0746.6−4755	8.821E−11	1.078E−10	2.145
3HSPJ074716.2+851208	0.28	J0747.6+8513	5.417E−11	7.974E−11	1.721
3HSPJ074722.1+090548	0.28	J0747.4+0904	2.577E−11	3.726E−11	1.753
3HSPJ074724.7−492633	—	J0747.7−4927	2.5E−11	2.524E−11	3.561
3HSPJ075936.1+132117	>0.7	J0759.6+1322	4.986E−11	1.012E−10	1.746
3HSPJ080102.1+644449	0.200?	J0801.3+6443	1.935E−11	2.048E−11	2.589
3HSPJ080204.8+100637	>0.57	J0802.1+1006	2.297E−11	3.99E−11	1.826
3HSPJ080215.8−094210	—	J0802.2−0943	6.988E−11	1.007E−10	1.794
3HSPJ080312.1−033600	0.365	J0803.2−0336	7.333E−11	1.736E−10	1.236
3HSPJ080457.7−062426	0.27	J0804.9−0623	5.941E−11	6.945E−11	2.232
3HSPJ080526.6+753424	0.12	J0805.5+7534	1.701E−10	1.907E−10	2.029
3HSPJ080625.9+593106	0.300?	J0806.5+5930	3.501E−11	4.135E−11	2.244
3HSPJ080938.9+345537	0.083	J0809.7+3457	3.763E−11	4.467E−11	1.538
3HSPJ080949.1+521858	0.137	J0809.8+5218	5.032E−10	5.642E−10	2.086
3HSPJ081003.2−752723	>0.47	J0811.0−7529	2.804E−10	3.764E−10	2.129
3HSPJ081201.8+023732	0.2	J0811.9+0237	7.324E−11	9.657E−11	1.763
3HSPJ081231.2+282056	0.47	J0812.5+2821	2.8E−11	2.965E−11	2.965
3HSPJ081338.0−035716	0.33	J0813.7−0353	3.0E−11	4.75E−11	1.689
3HSPJ081421.2+294021	0.32	J0814.5+2941	2.182E−11	2.487E−11	2.394
3HSPJ081627.1−131152	>0.37	J0816.4−1311	2.708E−10	4.269E−10	1.753
3HSPJ081750.9+324340	0.32	J0817.8+3243	2.898E−11	2.944E−11	3.372
3HSPJ081917.5−075626	0.37	J0819.4−0756	3.728E−11	9.03E−11	1.188

Table G.2: continued.

Source	Z	3FHL	3FHL Flux ph cm^{-2} s^{-1}	de-EBL Flux ph cm^{-2} s^{-1}	Γ
3HSPJ082021.9−280159	—	J0820.2−2803	2.609E−11	5.137E−11	1.325
3HSPJ082051.1+235345	0.402	J0820.9+2353	2.403E−11	4.188E−11	1.655
3HSPJ082627.8−640415	—	J0826.3−6403	7.143E−11	1.296E−10	1.436
3HSPJ082706.1−070845	0.247?	J0826.9−0709	4.435E−11	6.98E−11	1.537
3HSPJ082814.2+415351	0.225	J0828.3+4153	1.67E−11	2.504E−11	1.566
3HSPJ084121.6−355505	—	J0841.3−3554	1.987E−10	2.573E−10	2.008
3HSPJ084701.5−233701	0.061	J0847.0−2337	1.555E−10	1.6E−10	2.389
3HSPJ084712.9+113350	0.198	J0847.2+1134	8.025E−11	1.399E−10	1.202
3HSPJ084839.6+050618	—	J0848.7+0508	3.971E−11	7.181E−11	1.441
3HSPJ085036.1+345522	0.145	J0850.6+3454	3.646E−11	4.511E−11	1.752
3HSPJ085310.5−365820	—	J0853.1−3657	1.022E−10	1.181E−10	2.315
3HSPJ085409.8+440830	0.23	J0854.3+4408	2.501E−11	2.728E−11	2.451
3HSPJ085410.1+275421	0.494	J0854.1+2752	1.722E−11	4.672E−11	1.29
3HSPJ085659.2+513554	0.77	J0856.8+5136	1.316E−11	5.593E−11	1.18
3HSPJ085802.8−313038	0.34	J0858.0−3131	4.626E−11	9.128E−11	1.404
3HSPJ090133.8+671316	0.55	J0901.5+6712	1.996E−11	3.184E−11	1.921
3HSPJ090534.9+135806	>0.34	J0905.5+1357	1.429E−10	1.733E−10	2.222
3HSPJ090900.6+231112	0.223	J0908.9+2311	1.116E−10	1.207E−10	2.486
3HSPJ091037.0+332924	0.350?	J0910.5+3329	1.362E−10	2.348E−10	1.599
3HSPJ091211.2+275927	>0.56	J0912.2+2800	3.453E−11	3.654E−11	3.062
3HSPJ091230.6+155527	0.212	J0912.4+1555	2.986E−11	4.517E−11	1.508
3HSPJ091300.2−210320	0.198	J0912.9−2103	1.35E−10	1.87E−10	1.646
3HSPJ091322.3+813305	0.639?	J0913.4+8132	3.525E−11	8.186E−11	1.574
3HSPJ091552.3+293324	>0.19	J0915.9+2933	2.151E−10	2.395E−10	2.267
3HSPJ092057.4−225721	0.32	J0920.9−2256	3.289E−11	4.503E−11	1.92
3HSPJ092542.8+595816	>0.7	J0925.8+5958	2.896E−11	4.239E−11	2.15
3HSPJ093037.5+495025	0.187	J0930.4+4952	3.405E−11	4.625E−11	1.655
3HSPJ093514.7−173658	0.29	J0935.2−1735	5.635E−11	7.101E−11	2.053
3HSPJ093623.1−211039	>0.53	J0936.4−2109	3.78E−11	5.37E−11	2.079
3HSPJ093754.7−143350	0.27	J0937.8−1434	3.398E−11	3.978E−11	2.227
3HSPJ094022.4+614826	0.21	J0940.5+6149	2.467E−11	4.447E−11	1.193
3HSPJ094620.2+010451	0.577	J0946.2+0104	5.574E−11	7.109E−11	2.324
3HSPJ094709.5−254059	0.0	J0947.2−2541	1.015E−10	1.21E−10	2.217
3HSPJ095224.1+750213	0.181	J0952.3+7502	3.306E−11	5.157E−11	1.335
3HSPJ095302.6−084018	>0.37	J0953.0−0840	3.509E−10	4.695E−10	2.034
3HSPJ095304.3−765801	0.25	J0953.3−7659	3.352E−11	4.589E−11	1.799
3HSPJ095409.8+491459	0.410?	J0954.2+4912	4.914E−11	1.034E−10	1.439
3HSPJ095419.6−251958	0.32	J0954.2−2520	3.235E−11	4.167E−11	2.047
3HSPJ095805.9−031740	0.43	J0957.9−0318	3.753E−11	5.084E−11	2.073
3HSPJ100234.4+221614	0.4	J1002.6+2216	3.05E−11	5.094E−11	1.709
3HSPJ100656.4+345445	0.612	J1006.9+3455	3.206E−11	4.587E−11	2.129
3HSPJ101015.9−311908	0.14	J1010.2−3119	1.085E−10	1.48E−10	1.45
3HSPJ101244.2+422957	0.365	J1012.6+4228	4.599E−11	7.021E−11	1.795
3HSPJ101504.1+492600	>0.2	J1015.0+4926	1.085E−9	1.309E−9	2.001
3HSPJ101620.6−424722	0.25	J1016.2−4245	5.548E−11	5.992E−11	2.543
3HSPJ102243.7−011302	0.22	J1022.7−0113	8.185E−11	9.568E−11	2.142
3HSPJ102339.7+300057	0.433	J1023.8+3002	2.586E−11	4.082E−11	1.826
3HSPJ102356.1−433601	>0.32	J1023.8−4335	2.286E−10	3.175E−10	1.893
3HSPJ102432.3−454426	0.37	J1024.5−4543	3.746E−11	3.912E−11	2.981
3HSPJ102634.3−854314	0.0	J1027.0−8543	1.332E−10	1.949E−10	1.767
3HSPJ102658.5−174858	0.114?	J1027.0−1749	1.677E−10	1.94E−10	1.854
3HSPJ102703.4+060933	0.449	J1026.9+0608	3.103E−11	5.421E−11	1.707
3HSPJ102724.9+631752	>0.58	J1027.5+6317	4.741E−11	7.134E−11	2.029
3HSPJ103040.3−203036	0.28	J1030.6−2029	9.675E−11	1.118E−10	2.286

Table G.2: continued.

Source	Z	3FHL	3FHL Flux ph cm^{-2} s^{-1}	de-EBL Flux ph cm^{-2} s^{-1}	Γ
3HSPJ103118.5+505335	0.16	J1031.3+5053	1.541E−10	2.109E−10	1.537
3HSPJ103332.1−503528	0.24	J1033.4−5033	8.052E−11	8.517E−11	2.669
3HSPJ103346.3+370824	0.448	J1033.7+3707	2.273E−11	4.541E−11	1.548
3HSPJ103438.4−464403	0.33	J1034.8−4645	2.281E−11	2.53E−11	2.521
3HSPJ103744.2+571155	>0.33	J1037.6+5711	3.579E−10	3.909E−10	2.598
3HSPJ104058.3+134150	>0.7	J1040.9+1341	2.37E−11	5.291E−11	1.653
3HSPJ104149.1+390119	0.21	J1041.7+3900	1.897E−11	1.965E−11	2.818
3HSPJ104202.9−412929	0.25	J1042.2−4128	2.879E−11	4.477E−11	1.565
3HSPJ104303.8+005420	0.4	J1042.8+0055	3.79E−11	6.406E−11	1.693
3HSPJ104651.4−253545	0.25	J1046.7−2532	3.199E−11	3.411E−11	2.626
3HSPJ104756.9−373730	—	J1047.9−3738	3.125E−11	4.57E−11	1.768
3HSPJ105125.3+394325	0.497	J1051.4+3942	5.052E−11	6.712E−11	2.173
3HSPJ105344.1+492956	0.14	J1053.6+4930	5.147E−11	6.941E−11	1.481
3HSPJ105534.3−012616	0.33	J1055.6−0125	4.417E−11	9.343E−11	1.301
3HSPJ105750.7−275410	0.091	J1057.8−2753	4.595E−11	5.347E−11	1.693
3HSPJ105837.7+562811	0.143	J1058.6+5628	3.102E−10	3.722E−10	1.843
3HSPJ110021.0+401927	0.225?	J1100.3+4020	6.663E−11	7.262E−11	2.446
3HSPJ110124.7+410847	0.38	J1101.4+4107	3.36E−11	6.34E−11	1.527
3HSPJ110337.6−232930	0.186	J1103.6−2328	8.018E−11	1.312E−10	1.264
3HSPJ110427.3+381231	0.03	J1104.4+3812	5.935E−9	6.219E−9	1.763
3HSPJ110748.0+150210	0.250?	J1107.8+1501	5.82E−11	6.44E−11	2.414
3HSPJ110916.1+241120	0.350?	J1109.3+2412	3.863E−11	4.705E−11	2.222
3HSPJ110938.5+373611	0.398	J1109.7+3735	3.027E−11	7.452E−11	1.251
3HSPJ111037.6+713356	—	J1110.4+7134	3.533E−11	5.318E−11	1.719
3HSPJ111706.2+201407	0.138	J1117.0+2014	1.639E−10	2.098E−10	1.625
3HSPJ111715.2−533813	—	J1117.2−5338	7.359E−11	7.745E−11	2.808
3HSPJ111757.2+535554	>0.44	J1118.0+5355	8.212E−11	1.113E−10	2.082
3HSPJ111939.5−304720	0.412	J1119.8−3047	2.599E−11	4.35E−11	1.721
3HSPJ112048.0+421212	>0.35	J1120.8+4212	3.167E−10	5.087E−10	1.697
3HSPJ112349.1+722959	0.38	J1123.7+7231	2.663E−11	4.409E−11	1.696
3HSPJ112453.8+493409	0.36	J1124.9+4933	8.616E−11	1.1E−10	2.118
3HSPJ112508.6−210105	0.24	J1125.1−2102	6.405E−11	7.542E−11	2.157
3HSPJ112551.9−074220	0.279	J1125.9−0743	2.83E−11	4.513E−11	1.588
3HSPJ113032.0−780105	0.23	J1130.5−7801	1.034E−10	1.456E−10	1.697
3HSPJ113046.1−313807	0.151	J1130.7−3137	2.01E−11	3.23E−11	1.097
3HSPJ113209.2−473853	0.21	J1132.2−4737	2.807E−11	4.032E−11	1.608
3HSPJ113626.4+700927	0.045	J1136.5+7009	1.739E−10	1.877E−10	1.701
3HSPJ113630.1+673704	0.134	J1136.4+6737	8.759E−11	1.031E−10	1.874
3HSPJ113650.1+255052	0.155	J1136.8+2549	4.696E−11	6.138E−11	1.635
3HSPJ113755.6−171042	0.6	J1137.8−1710	4.638E−11	5.078E−11	2.86
3HSPJ114023.4+152809	0.24	J1140.5+1528	4.595E−11	6.339E−11	1.762
3HSPJ114118.6+680429	0.57	J1141.4+6805	3.325E−11	9.693E−11	1.309
3HSPJ114600.8−063854	0.37	J1145.9−0637	5.792E−11	9.754E−11	1.659
3HSPJ115034.7+415439	>0.32	J1150.5+4154	2.72E−10	3.563E−10	2.013
3HSPJ115124.6+585917	>0.3	J1151.5+5858	1.084E−10	1.389E−10	2.032
3HSPJ115404.5−001009	0.254	J1154.1−0010	9.547E−11	1.172E−10	2.059
3HSPJ115520.5−341719	—	J1155.5−3418	4.32E−11	7.931E−11	1.42
3HSPJ115633.2−225004	—	J1156.6−2247	3.926E−11	4.2E−11	2.681
3HSPJ120317.8−392620	—	J1203.3−3924	5.816E−11	1.147E−10	1.323
3HSPJ120416.6−071009	0.184	J1204.2−0709	9.277E−11	1.196E−10	1.772
3HSPJ120837.1+612106	0.275	J1208.1+6120	1.852E−11	2.023E−11	2.519
3HSPJ121300.8+512935	0.796?	J1213.0+5128	2.379E−11	4.633E−11	1.846
3HSPJ121323.1−261807	0.278	J1213.2−2618	4.362E−11	5.901E−11	1.876
3HSPJ121603.2−024304	0.359?	J1216.0−0242	2.765E−11	3.595E−11	2.077

Table G.2: continued.

Source	Z	3FHL	3FHL Flux ph cm^{-2} s^{-1}	de-EBL Flux ph cm^{-2} s^{-1}	Γ
3HSPJ121945.7−031423	0.299	J1219.7−0312	6.483E−11	1.039E−10	1.619
3HSPJ122014.5−245948	0.48	J1220.1−2459	3.183E−11	4.293E−11	2.129
3HSPJ122019.8−371414	0.28	J1220.4−3714	4.252E−11	4.377E−11	3.032
3HSPJ122121.9+301037	0.18	J1221.3+3010	5.723E−10	8.345E−10	1.472
3HSPJ122337.0−303250	0.26	J1223.5−3033	2.939E−11	4.398E−11	1.652
3HSPJ122358.0+795328	0.29	J1223.6+7953	2.781E−11	3.413E−11	2.12
3HSPJ122424.1+243623	0.218	J1224.4+2436	1.561E−10	2.09E−10	1.774
3HSPJ122536.8−344721	0.31	J1225.4−3447	2.254E−11	3.404E−11	1.731
3HSPJ122644.2+063853	0.583	J1226.7+0635	4.352E−11	6.396E−11	2.065
3HSPJ123014.0+251807	0.135?	J1230.2+2517	2.256E−10	2.387E−10	2.425
3HSPJ123123.9+142124	0.256	J1231.4+1422	5.251E−11	6.746E−11	1.949
3HSPJ123131.3+641418	0.163	J1231.6+6415	4.177E−11	6.427E−11	1.281
3HSPJ123143.5+284749	0.236	J1231.7+2847	2.248E−10	2.776E−10	2.014
3HSPJ123235.9−372056	0.25	J1232.5−3720	5.175E−11	7.562E−11	1.673
3HSPJ123444.2−043622	—	J1234.8−0435	3.456E−11	5.098E−11	1.753
3HSPJ123623.0+390000	0.389	J1236.3+3858	2.638E−11	4.628E−11	1.63
3HSPJ124021.2−714857	0.21	J1240.5−7148	8.698E−11	9.379E−11	2.479
3HSPJ124149.3−145558	>0.44	J1241.8−1455	3.996E−11	5.029E−11	2.238
3HSPJ124232.3+763417	0.48	J1243.2+7634	1.771E−11	3.23E−11	1.687
3HSPJ124312.7+362743	>0.31	J1243.2+3627	3.234E−10	4.721E−10	1.788
3HSPJ124700.7+442318	0.600?	J1247.0+4421	4.46E−11	8.394E−11	1.756
3HSPJ124919.3−280834	0.15	J1249.2−2809	3.311E−11	3.388E−11	2.86
3HSPJ124946.7+370747	0.286?	J1249.8+3708	6.536E−11	8.209E−11	2.055
3HSPJ125341.2−393159	0.179	J1253.6−3934	3.442E−11	3.858E−11	2.211
3HSPJ125346.9+032630	0.066	J1253.7+0328	5.393E−11	6.355E−11	1.39
3HSPJ125359.3+624257	0.3	J1253.9+6242	2.427E−11	3.881E−11	1.625
3HSPJ125433.2+221103	>0.42	J1254.4+2210	3.775E−11	4.413E−11	2.421
3HSPJ125615.9−14637	0.058	J1256.2−1146	1.013E−10	1.06E−10	2.148
3HSPJ125820.8+612045	0.224	J1258.3+6121	1.737E−11	1.742E−11	3.949
3HSPJ125949.8−374858	0.23	J1259.9−3749	5.413E−11	8.203E−11	1.56
3HSPJ130420.9−435310	—	J1304.3−4353	3.085E−10	3.909E−10	2.055
3HSPJ130737.9−425938	—	J1307.6−4259	2.255E−10	3.396E−10	1.718
3HSPJ131012.1−115749	0.14	J1310.3−1158	5.052E−11	5.684E−11	2.081
3HSPJ131106.4+003509	0.418?	J1311.0+0033	5.948E−11	7.376E−11	2.252
3HSPJ131146.0+395317	0.159?	J1311.7+3954	1.84E−11	2.281E−11	1.799
3HSPJ131248.7−235047	0.29	J1312.7−2350	1.107E−10	1.367E−10	2.104
3HSPJ131503.3−423649	0.105	J1315.0−4237	7.41E−11	9.075E−11	1.579
3HSPJ131532.6+113331	0.36	J1315.6+1134	3.763E−11	3.89E−11	3.09
3HSPJ131552.9−073302	—	J1315.9−0732	7.286E−11	1.068E−10	1.764
3HSPJ131921.2+775822	0.21	J1319.9+7758	4.029E−11	5.752E−11	1.621
3HSPJ131931.7+140533	0.573	J1319.5+1404	3.552E−11	3.706E−11	3.219
3HSPJ132358.3+140559	0.32	J1323.9+1405	6.262E−11	7.351E−11	2.292
3HSPJ132840.6−472749	—	J1328.5−4728	1.201E−10	1.582E−10	1.971
3HSPJ133025.8+700138	0.23	J1330.5+7002	4.163E−11	6.43E−11	1.522
3HSPJ133529.7−295038	0.510?	J1335.3−2950	2.419E−11	7.806E−11	1.154
3HSPJ134029.8+441004	0.54	J1340.5+4410	3.279E−11	4.844E−11	2.026
3HSPJ134105.1+395945	0.172	J1341.2+3959	3.576E−11	4.474E−11	1.815
3HSPJ134706.8−295842	—	J1347.0−2959	3.257E−11	4.227E−11	2.003
3HSPJ135120.8+111453	>0.51	J1351.3+1115	1.1E−10	1.41E−10	2.26
3HSPJ135340.2−663957	—	J1353.6−6640	1.243E−10	2.926E−10	1.091
3HSPJ135345.1−393710	0.37	J1353.8−3936	2.823E−11	3.272E−11	2.395
3HSPJ140449.6+655431	0.363	J1404.8+6555	3.06E−11	4.454E−11	1.869
3HSPJ140450.8+040202	>0.37	J1404.9+0401	4.532E−11	8.255E−11	1.557
3HSPJ140609.5−250809	—	J1406.2−2508	3.309E−11	6.044E−11	1.427

Table G.2: continued.

Source	Z	3FHL	3FHL Flux ph cm^{-2} s^{-1}	de-EBL Flux ph cm^{-2} s^{-1}	Γ
3HSPJ140630.0−393509	0.37	J1406.7−3932	2.899E−11	4.089E−11	1.932
3HSPJ140659.1+164207	>0.54	J1406.6+1645	3.162E−11	6.85E−11	1.558
3HSPJ141046.0+740511	—	J1410.8+7406	5.496E−11	7.844E−11	1.811
3HSPJ141133.3−072253	0.32	J1411.5−0724	1.996E−11	4.185E−11	1.291
3HSPJ141208.2+383521	0.45	J1412.0+3835	2.377E−11	2.969E−11	2.265
3HSPJ141612.1−241813	0.136	J1416.1−2417	4.151E−11	4.833E−11	1.924
3HSPJ141756.6+254325	0.24	J1418.0+2543	6.722E−11	9.647E−11	1.684
3HSPJ141826.3−023333	>0.356	J1418.4−0233	4.443E−10	6.097E−10	1.967
3HSPJ141828.6+354249	0.47	J1418.4+3542	1.733E−10	2.095E−10	2.369
3HSPJ141900.3+773229	>0.27	J1419.0+7731	5.973E−11	7.796E−11	1.938
3HSPJ141927.4+044513	>0.7	J1419.4+0444	3.536E−11	3.886E−11	2.918
3HSPJ142238.8+580155	0.638	J1422.6+5801	4.439E−11	8.939E−11	1.712
3HSPJ142725.9−182303	0.36	J1427.4−1824	5.153E−11	5.716E−11	2.557
3HSPJ142832.6+424020	0.129	J1428.5+4240	1.761E−10	2.247E−10	1.589
3HSPJ143342.7−730438	0.23	J1433.5−7304	1.937E−11	3.529E−11	1.245
3HSPJ143441.4+664026	0.35	J1434.8+6641	2.837E−11	5.92E−11	1.353
3HSPJ143657.7+563925	0.381?	J1436.9+5639	7.595E−11	1.122E−10	1.868
3HSPJ143917.4+393242	0.344	J1439.3+3931	6.772E−11	1.005E−10	1.811
3HSPJ143950.8−395518	—	J1439.9−3955	4.046E−11	7.022E−11	1.499
3HSPJ143959.4−234140	0.25	J1440.2−2343	3.632E−11	4.044E−11	2.385
3HSPJ144037.8−384654	0.27	J1440.6−3846	1.084E−10	1.326E−10	2.097
3HSPJ144052.9+061016	0.396?	J1440.9+0610	5.866E−11	6.423E−11	2.663
3HSPJ144127.9−193552	—	J1441.3−1934	5.065E−11	5.407E−11	2.696
3HSPJ144236.4−462301	0.103	J1442.5−4621	3.305E−11	4.301E−11	1.346
3HSPJ144248.2+120040	0.16	J1442.8+1200	7.436E−11	8.789E−11	1.953
3HSPJ144334.4+251558	0.529	J1443.5+2515	2.679E−11	4.017E−11	1.994
3HSPJ144357.1−390839	0.065	J1443.9−3908	5.535E−10	6.0E−10	1.892
3HSPJ144506.2−032612	>0.31	J1445.0−0326	1.227E−10	1.597E−10	2.012
3HSPJ144656.8−265658	0.32	J1447.0−2657	3.034E−11	5.941E−11	1.376
3HSPJ144800.5+360831	>0.28	J1447.9+3608	1.941E−10	2.373E−10	2.115
3HSPJ145127.7+635419	0.65	J1451.2+6355	3.767E−11	1.345E−10	1.194
3HSPJ145427.1+512433	>0.39	J1454.5+5124	2.006E−10	2.368E−10	2.358
3HSPJ145543.6−760052	—	J1455.4−7559	2.993E−11	3.108E−11	2.945
3HSPJ145741.7−464210	0.16	J1457.8−4642	2.941E−11	5.109E−11	0.978
3HSPJ150316.5+165117	0.39	J1503.3+1651	2.175E−11	3.877E−11	1.613
3HSPJ150340.6−154113	>0.38	J1503.7−1541	1.319E−10	2.175E−10	1.702
3HSPJ150525.4−824231	0.39	J1505.8−8241	2.85E−11	5.589E−11	1.494
3HSPJ150644.4+081400	0.376?	J1506.7+0813	1.335E−10	1.721E−10	2.116
3HSPJ150716.4+172103	0.565	J1507.2+1722	5.281E−11	5.515E−11	3.2
3HSPJ150842.6+270908	0.27	J1508.7+2708	3.681E−11	5.672E−11	1.626
3HSPJ150947.9+555617	0.2	J1509.8+5556	4.538E−11	5.474E−11	2.002
3HSPJ151148.5−051346	—	J1511.8−0513	7.573E−11	1.134E−10	1.727
3HSPJ151212.7−225508	0.315	J1512.1−2254	7.681E−11	9.04E−11	2.277
3HSPJ151556.1+242620	0.228	J1515.9+2423	2.119E−11	2.945E−11	1.719
3HSPJ151747.5+652523	0.702	J1517.7+6525	1.375E−10	2.612E−10	1.817
3HSPJ151803.5−273131	0.14	J1518.0−2731	1.08E−10	1.248E−10	1.968
3HSPJ151838.8+404500	0.065	J1518.5+4044	3.064E−11	3.117E−11	2.637
3HSPJ152048.8−034851	—	J1520.7−0348	1.568E−10	1.997E−10	2.043
3HSPJ152810.8−673056	—	J1528.4−6730	2.908E−11	3.941E−11	1.909
3HSPJ153202.2+301628	0.065	J1531.9+3016	3.272E−11	3.658E−11	1.685
3HSPJ153311.2+185429	0.305	J1533.2+1855	5.466E−11	8.485E−11	1.678
3HSPJ153324.2+341640	>0.41	J1533.2+3416	2.715E−11	2.975E−11	2.674
3HSPJ153447.2+371554	0.143	J1534.9+3716	3.647E−11	3.928E−11	2.322
3HSPJ153500.7+532037	>0.59	J1534.9+5320	2.023E−11	6.663E−11	1.225

Table G.2: continued.

Source	Z	3FHL	3FHL Flux ph cm^{-2} s^{-1}	de-EBL Flux ph cm^{-2} s^{-1}	Γ
3HSPJ153941.2−112835	0.22	J1539.7−1127	5.929E−11	6.805E−11	2.207
3HSPJ154015.9+815505	—	J1540.1+8154	1.059E−10	1.504E−10	1.82
3HSPJ154150.0+141437	0.223	J1541.7+1413	2.433E−11	2.527E−11	2.811
3HSPJ154203.0−291509	>0.49	J1542.1−2915	4.566E−11	8.069E−11	1.735
3HSPJ154458.8−664146	0.23	J1544.9−6641	7.29E−11	9.167E−11	1.95
3HSPJ154546.5−233928	0.121	J1545.7−2338	3.272E−11	4.089E−11	1.613
3HSPJ154604.2+081913	>0.35	J1546.1+0818	7.83E−11	1.082E−10	1.946
3HSPJ154712.1−280221	0.28	J1547.2−2802	3.869E−11	7.214E−11	1.353
3HSPJ154849.7−225102	0.192	J1548.7−2250	1.73E−10	2.18E−10	1.854
3HSPJ154946.3−304501	—	J1549.7−3045	3.762E−11	4.564E−11	2.166
3HSPJ154952.0−065907	0.29	J1549.9−0659	1.114E−10	1.488E−10	1.922
3HSPJ155053.2−082246	0.27	J1550.8−0822	2.414E−11	3.897E−11	1.549
3HSPJ155333.5−311830	>0.21	J1553.6−3119	1.061E−10	1.164E−10	2.381
3HSPJ155424.1+201125	0.273	J1554.2+2010	2.358E−11	4.062E−11	1.452
3HSPJ155543.0+111124	0.360?	J1555.7+1111	2.71E−9	4.563E−9	1.645
3HSPJ160005.3−252439	0.26	J1559.9−2526	3.276E−11	3.441E−11	2.763
3HSPJ160339.4+500955	0.4	J1603.8+5010	2.532E−11	3.129E−11	2.241
3HSPJ160620.8+563017	0.45	J1606.2+5629	3.083E−11	4.371E−11	2.013
3HSPJ161046.4−664901	0.11	J1610.6−6649	4.767E−10	5.876E−10	1.595
3HSPJ162330.5+085724	0.533	J1623.4+0858	2.604E−11	2.789E−11	2.939
3HSPJ162625.8+351341	0.498	J1626.2+3515	2.255E−11	5.963E−11	1.319
3HSPJ162646.0+630048	0.2	J1626.4+6257	2.349E−11	2.679E−11	2.189
3HSPJ162712.9+314956	0.58	J1627.3+3148	2.727E−11	5.045E−11	1.76
3HSPJ163043.1+522138	—	J1630.7+5221	8.786E−11	9.855E−11	2.43
3HSPJ163213.8+580052	0.32	J1632.2+5801	1.831E−11	2.995E−11	1.627
3HSPJ163751.0−344915	—	J1637.8−3448	1.726E−10	2.125E−10	2.127
3HSPJ164011.0+062826	0.31	J1640.1+0629	2.292E−11	4.866E−11	1.252
3HSPJ164014.9+685234	0.26	J1640.3+6850	2.225E−11	2.285E−11	3.035
3HSPJ164328.9−064619	0.082	J1643.5−0646	3.588E−11	4.362E−11	1.421
3HSPJ164339.4+331647	0.42	J1643.7+3317	3.054E−11	3.27E−11	2.826
3HSPJ165139.9+721824	0.24	J1651.6+7219	4.286E−11	6.832E−11	1.494
3HSPJ165249.9+402310	>0.31	J1652.7+4024	3.324E−11	5.48E−11	1.597
3HSPJ165352.2+394536	0.03	J1653.8+3945	1.917E−9	2.034E−9	1.62
3HSPJ165655.1−201056	0.23	J1656.9−2010	1.098E−10	1.482E−10	1.785
3HSPJ170238.5+311543	0.32	J1702.6+3113	5.893E−11	6.508E−11	2.528
3HSPJ170409.5+123421	0.400?	J1704.2+1234	2.187E−11	2.419E−11	2.616
3HSPJ170433.8−052840	0.3	J1704.5−0527	1.098E−10	1.961E−10	1.458
3HSPJ171248.7+293116	>0.42	J1712.8+2932	5.069E−11	5.701E−11	2.563
3HSPJ171405.4−202752	0.09	J1714.0−2028	7.259E−11	8.509E−11	1.653
3HSPJ171553.2+884415	0.48	J1713.6+8844	1.9E−11	3.604E−11	1.641
3HSPJ171921.4+120721	0.34	J1719.3+1206	5.469E−11	8.603E−11	1.714
3HSPJ172504.3+115215	>0.18	J1725.0+1152	4.786E−10	5.749E−10	1.959
3HSPJ172818.6+501310	0.055	J1728.3+5013	2.918E−10	3.127E−10	1.888
3HSPJ173605.2+203301	—	J1736.0+2032	6.299E−11	7.527E−11	2.209
3HSPJ174357.8+193509	0.08	J1744.0+1935	8.083E−11	9.083E−11	1.787
3HSPJ174459.5−172639	0.0	J1744.9−1726	1.678E−10	2.564E−10	1.694
3HSPJ174537.7+395130	0.267	J1745.6+3950	1.986E−11	3.226E−11	1.532
3HSPJ174837.6−085440	0.33	J1748.5−0854	5.178E−11	1.018E−10	1.391
3HSPJ175615.9+552218	>0.657	J1756.3+5522	5.44E−11	8.878E−11	1.969
3HSPJ175713.0+703337	0.407	J1757.1+7031	2.7E−11	5.876E−11	1.397
3HSPJ180002.0+281045	0.44	J1800.2+2813	2.722E−11	3.758E−11	2.048
3HSPJ180732.1+642926	0.239	J1807.1+6429	2.247E−11	2.928E−11	1.883
3HSPJ180845.6+241905	0.45	J1808.7+2420	2.244E−11	4.075E−11	1.66
3HSPJ180925.4+204131	>0.28	J1809.4+2041	3.768E−11	4.722E−11	2.051

Table G.2: continued.

Source	Z	3FHL	3FHL Flux ph cm^{-2} s^{-1}	de-EBL Flux ph cm^{-2} s^{-1}	Γ
3HSPJ181118.0+034113	—	J1811.3+0341	1.001E−10	1.532E−10	1.692
3HSPJ182020.9+362343	0.33	J1820.4+3623	5.479E−11	7.847E−11	1.852
3HSPJ182338.5−345412	—	J1823.6−3454	2.103E−10	3.455E−10	1.583
3HSPJ182419.0+430949	0.487	J1824.5+4310	2.877E−11	5.182E−11	1.709
3HSPJ182854.7−241735	0.05	J1828.9−2416	5.259E−11	5.811E−11	1.579
3HSPJ182924.2+540259	—	J1829.4+5402	7.353E−11	8.814E−11	2.2
3HSPJ183806.7−600032	0.18	J1838.1−6000	3.06E−11	3.901E−11	1.789
3HSPJ183849.1+480234	0.300?	J1838.8+4802	2.567E−10	3.811E−10	1.742
3HSPJ184121.7+290940	0.18	J1841.3+2909	8.213E−11	1.036E−10	1.816
3HSPJ184147.0+321839	0.24	J1841.7+3217	9.893E−11	1.088E−10	2.425
3HSPJ184229.8−584157	0.33	J1842.4−5841	4.943E−11	1.085E−10	1.255
3HSPJ184425.3+154645	0.11	J1844.4+1547	1.54E−10	1.619E−10	2.395
3HSPJ184822.5+653657	0.364	J1848.4+6538	2.039E−11	3.719E−11	1.546
3HSPJ184847.1+424539	0.4	J1848.9+4247	3.316E−11	4.936E−11	1.877
3HSPJ184919.4−164723	0.16	J1849.2−1647	7.044E−11	9.113E−11	1.682
3HSPJ185024.0+263153	0.22	J1850.4+2631	2.578E−11	4.014E−11	1.479
3HSPJ190411.8+362658	0.13	J1904.1+3627	6.354E−11	7.109E−11	2.071
3HSPJ191052.1+285624	0.33	J1910.8+2856	6.193E−11	8.264E−11	1.988
3HSPJ191129.7−190824	0.16	J1911.5−1908	8.021E−11	9.542E−11	1.931
3HSPJ191401.8+443832	0.28	J1914.0+4438	3.769E−11	5.658E−11	1.687
3HSPJ191803.5+033031	0.23	J1917.9+0331	4.844E−11	7.267E−11	1.579
3HSPJ191809.6+375313	—	J1918.1+3752	2.966E−11	5.561E−11	1.391
3HSPJ192242.2−745356	0.36	J1922.6−7452	4.408E−11	6.863E−11	1.758
3HSPJ192325.3−250208	0.65	J1923.4−2502	4.282E−11	7.327E−11	1.904
3HSPJ192502.2+281542	0.16	J1925.0+2815	6.457E−11	7.837E−11	1.866
3HSPJ192519.0+370535	0.26	J1925.4+3706	3.206E−11	3.283E−11	3.084
3HSPJ192649.8+615442	—	J1926.9+6154	1.76E−10	2.36E−10	1.93
3HSPJ193109.2+093716	—	J1931.1+0937	4.525E−10	5.689E−10	2.074
3HSPJ193320.2+072621	0.17	J1933.3+0726	1.274E−10	1.57E−10	1.853
3HSPJ193412.7−241920	—	J1934.2−2419	2.6E−11	2.917E−11	2.429
3HSPJ193656.1−471950	0.265	J1936.9−4720	1.259E−10	1.6E−10	1.995
3HSPJ194247.4+103326	—	J1942.7+1033	4.385E−10	5.824E−10	1.95
3HSPJ194356.2+211822	0.22	J1943.9+2117	1.239E−10	1.96E−10	1.45
3HSPJ194422.3−452331	0.21	J1944.4−4523	4.503E−11	6.787E−11	1.509
3HSPJ194455.1−214319	0.28	J1944.9−2143	8.789E−11	1.461E−10	1.525
3HSPJ194934.1+090653	—	J1949.5+0906	8.336E−11	1.023E−10	2.136
3HSPJ195500.6−160338	0.23	J1955.0−1605	7.269E−11	1.002E−10	1.74
3HSPJ195502.8−564028	0.2	J1955.0−5640	3.912E−11	5.996E−11	1.444
3HSPJ195547.8+021512	—	J1955.7+0214	3.869E−11	6.171E−11	1.629
3HSPJ195800.4+243806	—	J1958.1+2437	5.601E−11	1.021E−10	1.43
3HSPJ195814.9−301111	0.119	J1958.3−3011	1.275E−10	1.463E−10	1.911
3HSPJ195945.6−472519	—	J1959.7−4725	1.762E−10	1.95E−10	2.489
3HSPJ195959.8+650854	0.047	J1959.9+6508	8.427E−10	8.929E−10	1.903
3HSPJ200112.8+435252	—	J2001.2+4353	5.212E−10	6.039E−10	2.307
3HSPJ200204.1−573645	—	J2002.1−5736	3.174E−11	3.78E−11	2.219
3HSPJ200227.2−711936	0.21	J2002.5−7119	2.971E−11	5.462E−11	1.133
3HSPJ200245.3+630233	—	J2002.6+6304	2.28E−11	3.674E−11	1.613
3HSPJ200505.9+700439	—	J2005.1+7004	7.426E−11	1.067E−10	1.799
3HSPJ200925.3−484953	0.071	J2009.4−4849	3.876E−10	4.287E−10	1.807
3HSPJ201428.6−004722	0.231	J2014.4−0047	4.38E−11	6.32E−11	1.652
3HSPJ201431.0+064852	0.341	J2014.5+0648	6.295E−11	1.231E−10	1.417
3HSPJ201503.8+162227	0.25	J2015.0+1622	2.812E−11	4.498E−11	1.514
3HSPJ201525.0−143203	0.31	J2015.3−1431	2.757E−11	3.187E−11	2.329
3HSPJ201619.5+495324	—	J2016.3+4953	5.411E−11	6.002E−11	2.479

Table G.2: continued.

Source	Z	3FHL	3FHL Flux ph cm^{-2} s^{-1}	de-EBL Flux ph cm^{-2} s^{-1}	Γ
3HSPJ202143.8−722611	0.29	J2022.2−7223	1.794E−11	3.655E−11	1.257
3HSPJ202429.3−084804	—	J2024.4−0847	5.817E−11	7.57E−11	1.997
3HSPJ202630.7+764448	0.29	J2026.2+7644	3.13E−11	5.472E−11	1.468
3HSPJ202658.4+334308	0.24	J2027.0+3343	3.82E−11	5.465E−11	1.69
3HSPJ203024.0−503413	0.53	J2030.2−5037	2.539E−11	6.298E−11	1.413
3HSPJ203027.9−143917	0.43	J2030.5−1439	4.063E−11	4.472E−11	2.673
3HSPJ203031.6+223439	—	J2030.4+2236	2.451E−11	2.678E−11	2.555
3HSPJ203057.1+193612	0.27	J2031.0+1936	8.637E−11	1.048E−10	2.118
3HSPJ203451.0−420038	0.29	J2034.9−4200	4.557E−11	6.686E−11	1.745
3HSPJ203649.4−332830	0.23	J2036.9−3328	7.537E−11	1.162E−10	1.526
3HSPJ203923.5+521950	0.053	J2039.4+5219	5.756E−11	6.499E−11	1.467
3HSPJ204008.2−711459	0.161	J2040.3−7116	1.044E−10	1.246E−10	1.923
3HSPJ204150.2−373339	0.098	J2041.9−3734	2.848E−11	3.643E−11	1.365
3HSPJ204201.9−731913	0.31	J2041.7−7319	3.765E−11	7.312E−11	1.366
3HSPJ204206.0+242652	0.104	J2042.0+2428	5.663E−11	6.833E−11	1.63
3HSPJ205242.5+081040	0.53	J2052.5+0810	2.433E−11	6.279E−11	1.376
3HSPJ205350.7+292314	0.23	J2053.8+2922	1.482E−10	1.634E−10	2.395
3HSPJ205456.8+001537	0.151	J2055.0+0014	3.828E−11	4.263E−11	2.164
3HSPJ205528.2−002116	0.44	J2055.4−0022	4.646E−11	9.868E−11	1.468
3HSPJ205642.6+494005	0.1	J2056.7+4940	2.349E−10	2.597E−10	2.009
3HSPJ205846.7−144304	0.078	J2058.8−1442	2.706E−11	2.811E−11	2.37
3HSPJ210338.3−623225	—	J2103.7−6232	9.772E−11	1.214E−10	2.104
3HSPJ210415.9+211808	0.36	J2104.5+2117	3.028E−11	6.215E−11	1.391
3HSPJ210421.9−021238	>0.45	J2104.2−0212	3.667E−11	4.54E−11	2.287
3HSPJ210844.7−025034	0.15	J2108.8−0251	2.568E−11	4.045E−11	1.143
3HSPJ210936.1+395513	—	J2109.6+3954	7.476E−11	1.113E−10	1.737
3HSPJ211011.1−861847	0.31	J2111.0−8618	6.584E−11	9.177E−11	1.871
3HSPJ211243.0+081835	0.27	J2112.7+0819	7.028E−11	7.758E−11	2.458
3HSPJ211522.0+121802	0.28	J2115.2+1218	3.729E−11	7.563E−11	1.237
3HSPJ211614.5+333920	0.12	J2116.2+3339	3.104E−10	3.352E−10	2.228
3HSPJ211754.9−324328	0.215	J2118.0−3243	3.58E−11	4.672E−11	1.826
3HSPJ212743.0+361305	>0.876	J2127.7+3612	1.469E−10	2.323E−10	2.132
3HSPJ213103.2−274657	>0.38	J2131.0−2746	1.185E−10	2.026E−10	1.652
3HSPJ213135.4−091523	0.449	J2131.5−0914	9.186E−11	1.566E−10	1.738
3HSPJ213151.5−251558	>0.86	J2131.8−2515	3.676E−11	1.06E−10	1.53
3HSPJ213349.1+664704	—	J2133.9+6647	7.692E−11	9.63E−11	2.084
3HSPJ213852.7−205347	0.29	J2138.7−2055	2.247E−11	4.234E−11	1.362
3HSPJ214226.4+365949	0.24	J2142.3+3659	3.684E−11	4.167E−11	2.301
3HSPJ214239.7−202819	0.53	J2142.5−2029	2.971E−11	6.44E−11	1.548
3HSPJ214247.6+195810	0.38	J2142.7+1959	2.396E−11	5.174E−11	1.365
3HSPJ214530.1+100605	0.37	J2145.5+1007	2.267E−11	3.579E−11	1.751
3HSPJ214552.2+071927	0.237	J2145.8+0718	2.463E−11	2.464E−11	5.094
3HSPJ214636.9−134400	>0.42	J2146.5−1343	2.256E−10	5.274E−10	1.339
3HSPJ215015.5−141049	0.22	J2150.2−1412	5.949E−11	8.888E−11	1.559
3HSPJ215123.2+415633	0.15	J2151.5+4155	6.224E−11	6.393E−11	2.796
3HSPJ215305.3−004230	0.341	J2153.1−0041	3.871E−11	5.122E−11	2.02
3HSPJ215601.6+181837	>0.36	J2156.0+1818	6.82E−11	1.291E−10	1.49
3HSPJ215852.0−301332	0.117	J2158.8−3013	2.374E−9	2.738E−9	1.881
3HSPJ215910.9−284116	0.271	J2159.2−2840	3.852E−11	5.811E−11	1.661
3HSPJ215936.1−461953	0.4	J2159.6−4619	3.081E−11	5.401E−11	1.645
3HSPJ220941.6−045110	0.255	J2209.7−0451	4.521E−11	7.932E−11	1.379
3HSPJ221108.3−000302	0.362	J2211.0−0003	4.419E−11	5.899E−11	2.029
3HSPJ222028.7+281355	0.15	J2220.5+2813	3.021E−11	3.98E−11	1.597
3HSPJ222129.2−522527	>0.34	J2221.5−5226	1.34E−10	1.689E−10	2.124

Table G.2: continued.

Source	Z	3FHL	3FHL Flux ph cm^{-2} s^{-1}	de-EBL Flux ph cm^{-2} s^{-1}	Γ
3HSPJ223928.8−243944	0.115	J2239.5−2439	2.178E−11	2.351E−11	2.211
3HSPJ224017.7−524113	0.25	J2240.3−5240	6.026E−11	6.834E−11	2.308
3HSPJ224340.3−123059	0.226	J2243.7−1232	5.59E−11	6.958E−11	1.968
3HSPJ224354.7+202103	—	J2243.9+2020	4.884E−10	7.146E−10	1.767
3HSPJ224531.8−173358	0.43	J2245.5−1734	2.636E−11	2.726E−11	3.176
3HSPJ224642.0−520640	0.098	J2246.6−5207	4.116E−11	5.18E−11	1.425
3HSPJ224753.2+441315	—	J2247.9+4413	9.313E−11	1.282E−10	1.878
3HSPJ224938.4−594422	0.29	J2249.6−5943	2.071E−11	2.365E−11	2.345
3HSPJ225005.7+382437	0.119	J2250.0+3825	1.27E−10	1.616E−10	1.536
3HSPJ225619.1−712115	0.4	J2256.0−7119	2.809E−11	3.69E−11	2.102
3HSPJ225818.9−552537	0.479	J2258.6−5525	2.344E−11	4.01E−11	1.765
3HSPJ230012.3+405225	0.34	J2300.0+4054	3.741E−11	5.991E−11	1.687
3HSPJ230436.7+370507	—	J2304.7+3705	1.087E−10	1.357E−10	2.091
3HSPJ230722.0−120517	0.32	J2307.4−1205	3.335E−11	3.47E−11	2.954
3HSPJ230848.7+542611	—	J2308.8+5424	5.073E−11	6.417E−11	2.059
3HSPJ230940.8−363248	—	J2309.7−3633	4.359E−11	6.886E−11	1.641
3HSPJ231347.8−692330	0.53	J2313.2−6922	2.142E−11	5.038E−11	1.466
3HSPJ231357.3+144423	0.162	J2314.0+1445	8.701E−11	1.179E−10	1.574
3HSPJ231731.9−453359	>0.59	J2317.3−4532	3.96E−11	4.05E−11	3.561
3HSPJ231905.9−420648	0.054	J2319.1−4206	2.222E−11	2.427E−11	1.723
3HSPJ232136.9−161928	—	J2321.6−1618	4.035E−11	7.538E−11	1.396
3HSPJ232240.3−422042	0.09	J2322.4−4222	1.82E−11	2.164E−11	1.589
3HSPJ232244.0+343613	0.094	J2322.6+3436	6.473E−11	7.662E−11	1.64
3HSPJ232254.4−491630	>0.38	J2322.8−4916	8.639E−11	1.62E−10	1.535
3HSPJ232352.0+421058	0.059?	J2323.8+4210	2.696E−10	2.846E−10	2.064
3HSPJ232444.6−404049	>0.24	J2324.7−4040	1.897E−10	2.256E−10	2.125
3HSPJ232914.2+375414	0.21	J2329.2+3755	9.919E−11	1.152E−10	2.144
3HSPJ232938.2+610114	—	J2329.7+6101	6.479E−11	7.086E−11	2.549
3HSPJ233920.8−740435	—	J2339.2−7404	4.875E−11	8.02E−11	1.581
3HSPJ234054.2+801515	0.274	J2340.8+8015	2.19E−10	2.879E−10	1.929
3HSPJ234333.5+343950	0.36	J2343.6+3439	6.57E−11	1.002E−10	1.79
3HSPJ234704.8+514217	0.044	J2347.0+5142	3.316E−10	3.541E−10	1.787
3HSPJ234753.2+543630	0.4	J2347.9+5435	7.071E−11	1.018E−10	1.933
3HSPJ235034.3−300604	0.23	J2350.5−3006	4.704E−11	5.604E−11	2.101
3HSPJ235116.1−760015	0.25	J2351.5−7559	3.569E−11	4.775E−11	1.847
3HSPJ235612.1+403644	0.331	J2356.2+4035	4.34E−11	5.699E−11	2.023
3HSPJ235729.9−171802	>0.85	J2357.4−1717	4.665E−11	1.262E−10	1.576
3HSPJ235825.1+382856	0.24	J2358.5+3829	4.211E−11	4.415E−11	2.747
3HSPJ235836.8−180717	>0.39	J2358.4−1808	4.868E−11	6.518E−11	2.053
3HSPJ235907.8−303740	0.165	J2359.1−3038	8.177E−11	8.956E−11	2.287
3HSPJ235919.5−204756	0.096	J2359.3−2049	3.056E−11	3.21E−11	2.34

G.3 3HSP sources proposed to SWIFT

Table G.3: XRT proposed sources which have been observed. The XRT flux are obtained from Swift DeepSky pipeline.

Source	RA XRT Deg.	Dec XRT Deg.	Exposure second	CRTs s^{-1}	Slope	Flux XRT erg cm^{-2} s^{-1}
3HSPJ000835.3−233927	2.14831	-23.65755	4617.5	0.148	1.253	1.298E−12
3HSPJ000949.7−431650	2.46013	-43.28014	2570.8	0.0065	0.8	8.47E−14
3HSPJ002928.6+205333	7.37099	20.89353	2324.9	0.0551	1.555	3.639E−13
3HSPJ003322.4−203908	8.3432	−20.6516	6384.3	0.111	0.99	1.229E−12
3HSPJ004334.1−044300	10.89192	−4.71715	5523.4	0.095	1.452	7.538E−13
3HSPJ010250.9−200158	15.7128	−20.03222	4165.1	0.0421	1.379	3.03E−13
3HSPJ011501.7−340027	18.75718	−34.00714	5331.8	0.218	0.929	2.649E−12
3HSPJ012338.3−231058	20.90928	−23.18286	7332.6	0.372	1.002	4.025E−12
3HSPJ012657.2+330730	21.73847	33.12438	5085.8	0.0506	1.122	5.675E−13
3HSPJ021205.7−255758	33.02414	−25.96668	1039.0	0.0464	0.8	6.07E−13
3HSPJ021358.6−695137	33.49224	−69.86088	8634.4	0.0893	1.2	9.233E−13
3HSPJ022048.4−084250	35.20046	−8.71334	1426.3	0.0177	0.8	2.524E−13
3HSPJ023340.9+065611	38.42109	6.93666	7745.7	0.109	1.228	1.178E−12
3HSPJ023536.6−293843	38.90185	−29.64542	6350.2	0.0275	1.382	1.996E−13
3HSPJ024151.3−160333	40.46337	−16.05822	3035.4	0.0149	0.8	2.033E−13
3HSPJ025707.8+335730	44.28288	33.95854	3979.0	0.0703	1.334	7.108E−13
3HSPJ030103.7+344101	45.26552	34.68342	8005.3	0.0944	1.117	1.231E−12
3HSPJ030246.3−192425	45.69382	−19.4062	5098.9	0.0185	0.648	2.82E−13
3HSPJ032647.3−340447	51.69664	−34.07978	8517.4	0.0435	1.477	2.761E−13
3HSPJ033832.0−570448	54.63128	−57.08106	988.9	0.0378	0.8	5.022E−13
3HSPJ035305.0−362308	58.27112	−36.38512	3161.5	0.135	1.608	7.217E−13
3HSPJ035856.1−305447	59.73467	−30.91226	4142.0	0.0779	1.388	5.377E−13
3HSPJ042026.3−651400	65.11018	−65.23338	4017.2	0.0281	1.129	2.871E−13
3HSPJ042900.1−323641	67.2508	−32.61072	7182.2	0.0601	1.43	4.139E−13
3HSPJ043726.9−462500	69.36357	−46.41618	5209.5	0.0234	0.836	2.913E−13
3HSPJ044328.3−415156	70.86903	−41.86408	4380.8	0.368	1.37	2.714E−12
3HSPJ050419.5−095632	76.08155	−9.94259	5363.2	0.202	0.919	2.845E−12
3HSPJ052645.4−151900	81.68932	−15.31698	7397.4	0.0257	2.029	1.119E−13
3HSPJ053626.8−254748	84.11115	−25.79687	4173.3	0.0384	1.611	2.097E−13
3HSPJ053645.3−255841	84.18811	−25.97804	7210.2	0.0164	0.968	1.859E−13
3HSPJ054903.4−215001	87.26313	−21.83326	8135.0	0.0214	1.128	2.174E−13
3HSPJ055716.8−061706	89.31975	−6.28499	4451.2	0.233	1.069	3.957E−12
3HSPJ062040.0+264331	95.16643	26.72582	3974.5	0.109	1.314	2.026E−12
3HSPJ062337.8−525756	95.90668	−52.96554	8709.1	0.0208	1.167	2.192E−13
3HSPJ064443.7−285116	101.18293	−28.85395	3906.9	0.0322	1.513	3.25E−13
3HSPJ065932.9−674350	104.88699	−67.73083	6973.9	0.107	1.264	1.179E−12
3HSPJ073329.5+351542	113.37313	35.2617	4534.4	0.0557	1.755	3.148E−13
3HSPJ074734.5+612650	116.89297	61.44714	4548.3	0.00658	0.8	9.687E−14
3HSPJ075212.5+040901	118.05327	4.14941	3663.3	0.0377	1.102	4.062E−13
3HSPJ075936.1+132117	119.90127	13.35473	4187.1	0.112	1.697	5.945E−13
3HSPJ080102.1+644449	120.25725	64.74688	10908.8	0.0342	1.187	3.489E−13
3HSPJ080135.9+463824	120.39997	46.63893	3457.1	0.034	0.627	5.614E−13
3HSPJ080625.9+593106	121.60669	59.51938	5498.4	0.0084	0.8	1.214E−13
3HSPJ081231.2+282056	123.12985	28.34886	2179.6	0.00653	0.8	9.001E−14
3HSPJ082706.1−070845	126.77537	−7.14598	4707.9	0.22	1.097	2.46E−12
3HSPJ082904.8+175415	127.27094	17.90411	4968.5	0.103	1.329	8.664E−13
3HSPJ083010.9+523027	127.54496	52.50736	1855.3	0.0465	1.121	5.053E−13
3HSPJ083955.1+121702	129.9797	12.28471	5449.4	0.00848	0.8	1.24E−13
3HSPJ090953.2+310603	137.47212	31.10064	6218.0	0.186	1.156	1.751E−12
3HSPJ091037.0+332924	137.6544	33.49031	8157.1	0.0413	1.832	1.676E−13
3HSPJ093239.3+104235	143.16587	10.70928	721.5	0.0492	0.8	6.838E−13
3HSPJ095409.8+491459	148.54015	49.24972	3642.1	0.0414	1.762	1.752E−13

Table G.3: continued.

Source	RA XRT Deg.	Dec XRT Deg.	Exposure second	CRTs s^{-1}	Slope	Flux XRT erg cm^{-2} s^{-1}
3HSPJ095622.6−095514	149.09445	−9.92124	8875.3	0.00592	0.8	8.744E−14
3HSPJ095849.8+703959	149.70704	70.66598	3778.2	0.0198	0.8	2.919E−13
3HSPJ100612.2+644011	151.55085	64.66981	7435.8	0.0356	1.533	2.332E−13
3HSPJ101244.2+422957	153.18458	42.49885	3982.4	0.128	1.205	1.123E−12
3HSPJ101616.8+410812	154.07096	41.1366	4252.3	0.0949	1.088	9.317E−13
3HSPJ103346.3+370824	158.44343	37.13982	7041.5	0.116	1.195	1.044E−12
3HSPJ104028.9+094753	160.12092	9.79804	3847.5	0.0516	0.926	6.296E−13
3HSPJ104651.4−253545	161.71541	−25.59613	4507.4	0.232	0.908	3.247E−12
3HSPJ105534.3−012616	163.89286	−1.43764	1147.7	0.125	1.676	7.282E−13
3HSPJ105707.4+551032	164.28122	55.17559	1474.9	0.0208	0.8	2.654E−13
3HSPJ110021.0+401927	165.08768	40.32364	3862.3	0.0349	0.8	4.528E−13
3HSPJ110357.2+261118	165.9878	26.18864	626.7	0.0386	0.8	5.036E−13
3HSPJ111717.5+000633	169.32132	0.10873	852.9	0.197	1.053	2.292E−12
3HSPJ112059.7+014456	170.249	1.74901	5611.4	0.00533	0.8	7.601E−14
3HSPJ112349.1+722959	170.95496	72.50002	3625.0	0.115	1.076	1.218E−12
3HSPJ112410.5−371002	171.04431	−37.16775	5939.5	0.0617	0.822	1.007E−12
3HSPJ113046.1−313807	172.69206	−31.63515	4574.9	0.0783	0.984	9.978E−13
3HSPJ113105.2−094406	172.77191	−9.73534	1547.5	0.0831	0.8	1.151E−12
3HSPJ114222.6−130643	175.59364	−13.11174	5507.5	0.00513	0.8	7.137E−14
3HSPJ115520.5−341719	178.83618	−34.28967	4846.9	0.0298	1.641	2.131E−13
3HSPJ115633.2−225004	179.13856	−22.8348	5732.6	0.018	1.644	1.079E−13
3HSPJ121158.6+224233	182.99424	22.70933	16810.4	0.247	0.979	2.861E−12
3HSPJ121510.9+073204	183.79561	7.53521	3892.1	0.177	1.076	1.782E−12
3HSPJ121603.2−024304	184.01393	−2.7177	8098.3	0.00229	0.8	3.095E−14
3HSPJ122307.2+110038	185.77973	11.01015	9430.9	0.0382	1.411	2.802E−13
3HSPJ123123.9+142124	187.8507	14.35616	4927.4	0.0219	0.8	2.996E−13
3HSPJ123131.3+641418	187.88151	64.23831	5093.5	0.216	1.119	2.147E−12
3HSPJ123417.1−385635	188.57005	−38.94371	3493.0	0.0052	0.8	7.978E−14
3HSPJ124141.4+344030	190.4227	34.67544	6118.9	0.21	1.238	1.781E−12
3HSPJ125134.8−295843	192.89532	−29.97827	3295.2	0.082	1.198	8.806E−13
3HSPJ130145.6+405624	195.4403	40.94022	7373.8	0.0459	1.645	2.373E−13
3HSPJ130903.9−040611	197.26622	−4.10288	4249.2	0.0215	0.686	3.135E−13
3HSPJ131012.1−115749	197.55192	−11.96239	7033.2	0.0432	1.453	3.126E−13
3HSPJ131155.7+085340	197.98198	8.89513	12146.3	0.0771	0.979	8.804E−13
3HSPJ131234.6−185901	198.14546	−18.98203	1469.7	0.00701	0.8	1.075E−13
3HSPJ132614.9+293330	201.56366	29.55842	5858.7	0.0933	1.261	7.637E−13
3HSPJ133529.7−295038	203.87335	−29.84436	8770.8	0.171	1.023	2.027E−12
3HSPJ133612.1+231958	204.05023	23.33276	5551.5	0.0408	1.4	2.825E−13
3HSPJ135328.0+560056	208.3662	56.01613	8468.2	0.0379	1.014	3.98E−13
3HSPJ140022.0−400823	210.09188	−40.13941	2885.0	0.066	1.224	6.857E−13
3HSPJ140630.0−393509	211.62501	−39.58556	4570.9	0.0933	1.182	1.036E−12
3HSPJ141029.5+282055	212.6233	28.34928	4758.3	0.00953	0.8	1.255E−13
3HSPJ142421.1+370552	216.08763	37.09803	12190.3	0.0402	1.155	3.641E−13
3HSPJ144446.0+474257	221.19132	47.71691	10454.8	0.0107	1.257	9.041E−14
3HSPJ144506.2−032612	221.27625	−3.43617	3963.8	0.517	1.202	5.565E−12
3HSPJ144941.8−091000	222.4246	−9.1665	6580.2	0.0257	1.539	2.02E−13
3HSPJ145543.6−760052	223.93161	−76.01459	2318.6	0.0337	0.8	5.566E−13
3HSPJ145827.3+483245	224.61297	48.54707	7948.9	0.0626	1.263	5.328E−13
3HSPJ150842.6+270908	227.178	27.15287	7934.8	0.29	0.82	4.018E−12
3HSPJ151041.1+333504	227.67022	33.58561	3551.8	0.0402	1.028	4.269E−13
3HSPJ151845.7+061356	229.68977	6.23271	4414.4	0.279	1.123	2.881E−12
3HSPJ152646.6−153026	231.69337	−15.50662	5459.2	0.00858	0.8	1.387E−13
3HSPJ153646.7+013800	234.19482	1.63402	5817.5	0.107	0.72	1.667E−12
3HSPJ153941.2−112835	234.92128	−11.47528	5905.1	0.0575	1.853	3.825E−13

Table G.3: continued.

Source	RA XRT Deg.	Dec XRT Deg.	Exposure second	CRTs s^{-1}	Slope	Flux XRT erg cm^{-2} s^{-1}
3HSPJ154203.0−291509	235.51295	−29.25205	3173.5	0.279	1.35	2.912E−12
3HSPJ154604.2+081913	236.51734	8.32099	6480.4	0.0233	1.563	1.479E−13
3HSPJ155424.1+201125	238.60073	20.19078	3447.4	0.3	1.215	2.873E−12
3HSPJ161327.1−190836	243.36147	−19.14174	4320.8	0.0139	0.8	2.408E−13
3HSPJ161632.9+375603	244.13671	37.93515	4500.1	0.0682	0.892	8.262E−13
3HSPJ163658.4−124836	249.24333	−12.80891	3740.6	0.0298	1.079	4.532E−13
3HSPJ170052.6+332431	255.22019	33.40895	4970.5	0.0205	0.8	2.732E−13
3HSPJ171105.8+120812	257.77395	12.13747	9581.3	0.00291	0.8	4.458E−14
3HSPJ174459.5−172639	266.24936	−17.44393	7288.9	0.357	1.484	5.131E−12
3HSPJ174702.5+493801	266.76086	49.6331	9881.9	0.154	1.039	1.716E−12
3HSPJ175713.0+703337	269.30555	70.56058	5385.5	0.151	1.109	1.627E−12
3HSPJ175949.1+703718	269.95444	70.62206	3716.4	0.00499	0.8	7.109E−14
3HSPJ180002.0+281045	270.00842	28.17979	9274.2	0.114	1.228	1.159E−12
3HSPJ180408.8+004222	271.03637	0.70702	6299.6	0.315	0.926	5.494E−12
3HSPJ180845.6+241905	272.19038	24.31877	8840.6	0.0429	1.01	6.157E−13
3HSPJ182833.5−592054	277.14088	−59.34822	4945.3	0.143	1.172	1.598E−12
3HSPJ184121.7+290940	280.34123	29.16215	3790.5	0.0794	1.401	9.135E−13
3HSPJ184822.5+653657	282.09422	65.61626	5409.4	0.0581	1.115	6.569E−13
3HSPJ185024.0+263153	282.6	26.53142	4280.3	0.0364	1.712	3.108E−13
3HSPJ194333.7−053353	295.89115	−5.56443	9181.0	0.0702	0.776	1.142E−12
3HSPJ194422.3−452331	296.09393	−45.39208	4762.2	0.0981	1.605	6.378E−13
3HSPJ195814.9−301111	299.56251	−30.18696	10007.6	0.544	1.135	6.677E−12
3HSPJ202429.3−084804	306.12292	−8.80096	4286.5	0.0711	1.5	5.173E−13
3HSPJ202803.6+720514	307.01625	72.0886	6441.0	0.00343	0.8	6.473E−14
3HSPJ204006.6−462017	310.02617	−46.3389	5652.9	0.118	1.279	1.016E−12
3HSPJ204150.2−373339	310.45892	−37.56121	3656.5	0.264	1.145	2.721E−12
3HSPJ205846.7−144304	314.69526	−14.71751	2885.3	0.0365	1.523	2.468E−13
3HSPJ210123.0−454949	315.34547	−45.82983	3457.1	0.148	1.098	1.565E−12
3HSPJ210721.1−145418	316.83864	−14.90519	502.2	0.0553	0.8	8.059E−13
3HSPJ213151.5−251558	322.96488	−25.26639	4948.0	0.28	1.335	2.337E−12
3HSPJ214552.2+071927	326.46795	7.32485	4833.8	0.156	1.008	1.931E−12
3HSPJ214625.7−474837	326.60724	−47.81105	4401.8	0.0662	1.122	6.53E−13
3HSPJ215305.3−004230	328.27247	−0.70873	4436.6	0.2	0.856	3.042E−12
3HSPJ215601.6+181837	329.00713	18.31029	5057.4	0.0579	1.552	4.369E−13
3HSPJ223812.7−394018	339.55288	−39.6725	3158.0	0.0571	1.009	6.142E−13
3HSPJ224910.7−130002	342.29448	−13.00103	8632.2	0.233	1.046	2.678E−12
3HSPJ225147.5−320612	342.94841	−32.10335	2970.9	0.381	1.013	4.067E−12
3HSPJ230344.5−043856	345.93563	−4.64845	6962.3	0.0208	1.282	1.914E−13
3HSPJ231952.8−011626	349.96929	−1.27346	933.5	0.0665	0.8	9.422E−13
3HSPJ232305.0−174802	350.77082	−17.8014	8035.6	0.0191	0.829	2.492E−13
3HSPJ235955.3+314600	359.97941	31.7664	9293.0	0.0599	1.501	4.552E−13

Source	R.A.	Dec.
3HSPJ004147.0−470136	10.44593	−47.02693
3HSPJ013309.2−453524	23.28867	−45.59002
3HSPJ013507.0+025542	23.77936	2.9285
3HSPJ034254.1−370737	55.72578	−37.12708
3HSPJ044240.6+614039	70.66938	61.67769
3HSPJ050601.6−382055	76.50697	−38.34876
3HSPJ071745.0−552021	109.43775	−55.33945
3HSPJ081201.8+023732	123.00779	2.62586
3HSPJ091322.3+813305	138.34319	81.55136
3HSPJ104857.6+500945	162.24008	50.16256
3HSPJ105750.7−275410	164.46153	−27.90304
3HSPJ105929.0−191221	164.87112	−19.20611
3HSPJ114930.3+243926	177.37647	24.65744
3HSPJ140108.7−232235	210.28655	−23.37653
3HSPJ143211.6+764355	218.04843	76.73221
3HSPJ144236.4−462301	220.65167	−46.38385
3HSPJ152559.4−242813	231.49755	−24.47033
3HSPJ152913.5+381217	232.30653	38.20488
3HSPJ153324.2+341640	233.35114	34.27789
3HSPJ155053.2−082246	237.72195	−8.37966
3HSPJ155432.5−121325	238.63577	−12.22366
3HSPJ160618.4+134532	241.57667	13.7591
3HSPJ162646.0+630048	246.69184	63.01353
3HSPJ164220.3+221143	250.58469	22.19551
3HSPJ164339.4+331647	250.91444	33.27996
3HSPJ164419.9+454644	251.08335	45.77892
3HSPJ165517.9−224045	253.82481	−22.67933
3HSPJ174929.9+463135	267.37472	46.52661
3HSPJ181403.4+382810	273.51432	38.46949
3HSPJ183200.9+382137	278.00408	38.36029
3HSPJ185813.4+432451	284.55597	43.41443
3HSPJ193412.7−241920	293.55322	−24.32236
3HSPJ194455.1−214319	296.22986	−21.72203
3HSPJ195547.8+021512	298.94942	2.25357
3HSPJ200204.1−573645	300.51749	−57.61264
3HSPJ215214.1−120541	328.05884	−12.09483
3HSPJ224340.3−123059	340.91792	−12.51647
3HSPJ232039.8−630918	350.16606	−63.15504
3HSPJ235917.0+021520	359.82104	2.25566

Table G.4: XRT proposed sources without observation yet

G.4 Estimated γ-ray flux for 3HSP sources without Fermi detection

Table G.5: Bright sources with estimated Fermi flux. The estimated flux are obtained from the equation 5.1.

Source	log $\nu_{\rm peak}$ Hz	log $\nu_{\rm peak}f_{\nu_{\rm peak}}$ erg cm^{-2} s^{-1}	est-Flux FL8Y ph cm^{-2} s^{-1}	est-Flux 3FHL ph cm^{-2} s^{-1}
3HSPJ000513.7−261438	15.4	−12.6	7.411E−11	1.323E−11
3HSPJ003539.6−181651	15.4	−11.9	3.714E−10	6.63E−11
3HSPJ004927.8+395003	16.4	−12.4	6.866E−11	1.475E−11
3HSPJ005040.9−254122	15.4	−12.2	1.862E−10	3.323E−11
3HSPJ011004.8+414950	15.9	−11.9	2.84E−10	5.562E−11
3HSPJ011009.7+042420	16.5?	−12.7	3.261E−11	7.139E−12
3HSPJ014918.2+203029	>15.0	−12.1	2.905E−10	4.815E−11
3HSPJ021515.2−161738	16.4	−12.1	1.37E−10	2.944E−11
3HSPJ022104.9+063939	16.1	−12.3	1.015E−10	2.064E−11
3HSPJ022657.2+082730	15.9	−12.4	8.98E−11	1.759E−11
3HSPJ031421.9−095453	16.5?	−12.2	1.031E−10	2.258E−11
3HSPJ033612.8−213128	16.6	−12.3	7.763E−11	1.731E−11
3HSPJ034054.7+782258	15.7	−12.2	1.585E−10	2.991E−11
3HSPJ034402.4+730114	16.4	−11.9	2.171E−10	4.666E−11
3HSPJ035154.5−370344	17.9	−11.9	9.702E−11	2.754E−11
3HSPJ041422.6−035017	16.1	−12.7	4.042E−11	8.217E−12
3HSPJ042850.8−380550	15.1	−12.7	6.916E−11	1.168E−11
3HSPJ044139.2−105735	15.6	−12.2	1.672E−10	3.097E−11
3HSPJ050833.3+053109	15.6	−11.7	5.287E−10	9.795E−11
3HSPJ051439.1−001104	15.4	−12.3	1.479E−10	2.64E−11
3HSPJ062445.0−323055	16.6	−12.4	6.166E−11	1.375E−11
3HSPJ063257.9+591541	16.9	−12.3	6.608E−11	1.558E−11
3HSPJ063331.0−162951	15.2	−11.4	1.308E−9	2.249E−10
3HSPJ064326.7+421418	17.2	−11.6	2.819E−10	7.028E−11
3HSPJ065751.3−284306	15.4	−12.0	2.95E−10	5.267E−11
3HSPJ071959.8+632228	15.3	−12.7	6.211E−11	1.088E−11
3HSPJ074709.4+062306	15.8	−12.0	2.38E−10	4.576E−11
3HSPJ075329.5+535111	15.1	−12.1	2.753E−10	4.649E−11
3HSPJ080610.6+020327	15.3	−12.1	2.473E−10	4.333E−11
3HSPJ082253.2+701357	15.5	−11.7	5.579E−10	1.015E−10
3HSPJ083713.3−185941	15.4	−12.3	1.479E−10	2.64E−11
3HSPJ084018.8−191028	15.3	−11.6	7.82E−10	1.37E−10
3HSPJ090051.6−154130	15.7	−12.2	1.585E−10	2.991E−11
3HSPJ091925.6+110659	15.9	−12.5	7.133E−11	1.397E−11
3HSPJ093848.5+441644	16.5?	−12.9	2.058E−11	4.505E−12
3HSPJ094340.7+444215	16.5	−12.6	4.105E−11	8.988E−12
3HSPJ100444.7+375211	16.4	−12.2	1.088E−10	2.338E−11
3HSPJ102004.7−120959	15.2	−12.5	1.039E−10	1.787E−11
3HSPJ102523.0+040229	16.2	−12.3	9.623E−11	1.993E−11
3HSPJ102839.3+170210	16.3	−12.3	9.12E−11	1.924E−11
3HSPJ103655.9−195423	16.2	−12.5	6.072E−11	1.257E−11
3HSPJ103838.1+675516	16.7	−12.2	9.262E−11	2.104E−11
3HSPJ105929.0−191221	15.3	−11.8	4.934E−10	8.646E−11
3HSPJ110356.1+002236	15.7	−12.4	9.998E−11	1.887E−11
3HSPJ110858.4−014931	16.7	−12.0	1.468E−10	3.335E−11
3HSPJ111112.5+584657	16.5?	−12.8	2.59E−11	5.671E−12

Table G.5: continued.

Source	log $\nu_{\rm peak}$ Hz	log $\nu_{\rm peak}f_{\nu_{\rm peak}}$ erg cm^{-2} s^{-1}	est-Flux FL8Y ph cm^{-2} s^{-1}	est-Flux 3FHL ph cm^{-2} s^{-1}
3HSPJ115709.5+282200	16.6	−12.3	7.763E−11	1.731E−11
3HSPJ115904.3+210209	16.6	−12.2	9.773E−11	2.18E−11
3HSPJ120106.1−000701	16.5	−12.4	6.507E−11	1.424E−11
3HSPJ121017.7+022343	16.0?	−12.4	8.51E−11	1.698E−11
3HSPJ121919.3+303937	15.7	−12.6	6.308E−11	1.191E−11
3HSPJ122107.7+474228	16.8	−12.2	8.778E−11	2.032E−11
3HSPJ122340.1+124203	15.9	−12.6	5.666E−11	1.11E−11
3HSPJ125408.1−280931	15.7	−11.8	3.98E−10	7.512E−11
3HSPJ125639.3+060907	16.5	−12.5	5.168E−11	1.132E−11
3HSPJ125908.6+412937	16.4	−12.3	8.643E−11	1.857E−11
3HSPJ130058.5−231215	15.6	−11.6	6.656E−10	1.233E−10
3HSPJ130531.2+385522	16.4	−12.2	1.088E−10	2.338E−11
3HSPJ130931.4−224425	16.2	−12.5	6.072E−11	1.257E−11
3HSPJ131330.1+020105	15.7	−12.2	1.585E−10	2.991E−11
3HSPJ133155.3−125816	15.1	−12.9	4.363E−11	7.367E−12
3HSPJ134223.4−313557	15.7	−11.9	3.162E−10	5.967E−11
3HSPJ134853.4+075647	16.1	−12.0	2.026E−10	4.118E−11
3HSPJ140150.2−294149	16.3	−12.2	1.148E−10	2.422E−11
3HSPJ140923.5+593940	15.6	−12.3	1.328E−10	2.46E−11
3HSPJ140954.8−104857	15.1	−12.3	1.737E−10	2.933E−11
3HSPJ141140.5+340424	16.4	−12.5	5.453E−11	1.172E−11
3HSPJ142421.1+370552	17.0	−12.3	6.263E−11	1.504E−11
3HSPJ143005.0+412707	16.6	−12.4	6.166E−11	1.375E−11
3HSPJ143824.0+085724	16.0?	−12.7	4.265E−11	8.511E−12
3HSPJ150826.6+014645	16.2	−12.8	3.043E−11	6.302E−12
3HSPJ150901.9+724354	15.3	−12.1	2.473E−10	4.333E−11
3HSPJ151641.5+291810	16.0	−12.1	1.698E−10	3.388E−11
3HSPJ152559.4−242813	16.5?	−12.1	1.298E−10	2.842E−11
3HSPJ153623.0+122211	15.6	−12.6	6.656E−11	1.233E−11
3HSPJ153646.7+013800	>18.0	−11.7	1.457E−10	4.215E−11
3HSPJ154418.7+045821	16.3	−12.1	1.445E−10	3.049E−11
3HSPJ160740.6+254113	17.0?	−11.7	2.493E−10	5.989E−11
3HSPJ161004.0+671026	17.5?	−11.9	1.203E−10	3.17E−11
3HSPJ162839.0+252756	16.7	−12.1	1.166E−10	2.649E−11
3HSPJ163920.6+560902	15.3	−12.6	7.82E−11	1.37E−11
3HSPJ164438.6−015202	15.7	−12.2	1.585E−10	2.991E−11
3HSPJ164549.6+792129	16.5	−12.1	1.298E−10	2.842E−11
3HSPJ165221.1+493253	17.1	−12.3	5.935E−11	1.452E−11
3HSPJ165746.7+675527	15.3	−12.2	1.964E−10	3.442E−11
3HSPJ170622.7+063847	16.3	−12.4	7.244E−11	1.528E−11
3HSPJ171105.8+120812	15.7	−12.4	9.998E−11	1.887E−11
3HSPJ172658.2+263436	16.5	−12.3	8.191E−11	1.793E−11
3HSPJ173328.9+451950	16.4	−12.6	4.332E−11	9.309E−12
3HSPJ175156.8+655117	15.2	−12.7	6.554E−11	1.127E−11
3HSPJ180408.8+004222	17.1	−11.2	7.472E−10	1.829E−10
3HSPJ184430.8+544144	15.2	−11.9	4.135E−10	7.113E−11
3HSPJ195755.0−241950	15.5	−11.9	3.52E−10	6.401E−11
3HSPJ205637.0+221845	16.0	−12.3	1.071E−10	2.138E−11
3HSPJ210451.0+050320	15.7	−11.8	3.98E−10	7.512E−11
3HSPJ210721.1−145418	17.2	−12.1	8.915E−11	2.222E−11
3HSPJ211207.4−144412	16.6	−12.1	1.23E−10	2.744E−11
3HSPJ211349.6+082501	15.1	−12.2	2.187E−10	3.692E−11
3HSPJ211353.7+133017	17.7	−12.0	8.581E−11	2.347E−11
3HSPJ211355.6−015540	15.4	−12.2	1.862E−10	3.323E−11

Table G.5: continued.

Source	log ν_{peak} Hz	log $\nu_{peak}f_{\nu_{peak}}$ erg cm^{-2} s^{-1}	est-Flux FL8Y ph cm^{-2} s^{-1}	est-Flux 3FHL ph cm^{-2} s^{-1}
3HSPJ212307.2−103648	16.6	−12.1	1.23E−10	2.744E−11
3HSPJ212839.9−194152	16.9	−12.3	6.608E−11	1.558E−11
3HSPJ213306.3−281536	15.1	−12.1	2.753E−10	4.649E−11
3HSPJ214410.0−195559	18.0	−12.4	2.908E−11	8.409E−12
3HSPJ214442.0−181800	16.7	−12.2	9.262E−11	2.104E−11
3HSPJ214453.3−185725	15.8	−12.7	4.749E−11	9.13E−12
3HSPJ220146.9−145439	15.7	−12.4	9.998E−11	1.887E−11
3HSPJ220451.3−181536	16.7	−11.9	1.848E−10	4.199E−11
3HSPJ221109.8−002327	15.6	−12.6	6.656E−11	1.233E−11
3HSPJ224819.4−003642	16.0	−12.8	3.388E−11	6.76E−12
3HSPJ230344.5−043856	15.9	−12.3	1.13E−10	2.214E−11
3HSPJ231952.8−011626	16.7	−12.2	9.262E−11	2.104E−11
3HSPJ233250.6+452936	15.4	−12.1	2.344E−10	4.183E−11
3HSPJ233404.0+084725	16.5?	−12.2	1.031E−10	2.258E−11
3HSPJ233653.7−232626	16.6	−12.4	6.166E−11	1.375E−11

G.5 Whole 3HSP table

Table G.6: The 3HSP sources.

Source	2WHSP	Log ν_{peak}	flag	Z	flag	γ-ray counterpart	FOM
3HSPJ000116.3+293534	Yes	16.0	2	0.58	5	–	0.03
3HSPJ000117.0−315043	Yes	15.5	2	0.45	4	–	0.1
3HSPJ000132.7−415525	Yes	15.8	1	—	0	3FGLJ0002.2−4152	0.4
3HSPJ000158.1−115047	Yes	16.2	1	0.53	5	–	0.06
3HSPJ000215.1−672653	Yes	15.8	1	0.52	3	3FGLJ0002.0−6722	0.32
3HSPJ000236.0−081532	Yes	16.0	1	0.39	5	–	0.1
3HSPJ000319.5−524727	Yes	16.9	1	0.37	5	3FGLJ0003.2−5246	0.25
3HSPJ000513.7−261438	Yes	15.4	1	0.32	1	–	0.05
3HSPJ000552.9−284503	Yes	15.4	1	0.57	5	–	0.06
3HSPJ000626.8+013610	Yes	16.4	1	0.787	2	3FGLJ0006.2+0135	0.05
3HSPJ000701.5+510500	Yes	15.6	1	0.47	5	–	0.06
3HSPJ000835.3−233927	Yes	17.0	1	0.147	1	3FGLJ0008.6−2340	0.4
3HSPJ000922.7+503028	Yes	15.1	1	0.25	5	3FGLJ0009.3+5030	0.32
3HSPJ000949.7−431650	Yes	15.3	1	0.23	4	FL8YJ0009.8−4317	0.2
3HSPJ000957.2+134058	Yes	16.3	1	0.43	5	–	0.16
3HSPJ001011.7+334851	Yes	15.4	1	—	0	–	0.25
3HSPJ001042.6−130817	Yes	15.5	1	0.53	5	–	0.05
3HSPJ001253.8−162656	Yes	15.8	1	0.35	5	–	0.1
3HSPJ001328.8+094930	Yes	17.3	1	0.29	5	J001328.8+094929	0.32
3HSPJ001356.0−185406	Yes	17.4	1	0.094	1	3FGLJ0013.9−1853	1.0
3HSPJ001411.4−502234	Yes	17.5	1	0.01	2	3FGLJ0014.0−5025	0.5
3HSPJ001442.0+162126	Yes	16.5	2	0.56	5	–	0.03
3HSPJ001442.0+580201	–	16.0	2	0.35	5	3FGLJ0014.7+5802	0.4
3HSPJ001527.9+353639	Yes	16.7	1	0.43	5	FL8YJ0015.3+3537	0.2
3HSPJ001540.1+555144	–	15.9	1	0.15	5	3FGLJ0015.7+5552	1.26
3HSPJ001541.8+121845	Yes	16.3	1	0.35	5	–	0.08
3HSPJ001827.7+294730	Yes	17.1	1	0.1	2	3FGLJ0018.4+2947	0.79

Source	2WHSP	Log $\nu_{\rm peak}$	flag	Z	flag	γ-ray counterpart	FOM
3HSPJ001916.2+053148	Yes	16.0	2	0.467	1	–	0.03
3HSPJ002200.0−514024	Yes	15.7	1	0.25	1	3FGLJ0022.1−5141	1.26
3HSPJ002200.9+000657	Yes	16.3	1	0.306	1	FL8YJ0022.0+0006	0.32
3HSPJ002209.5−670510	Yes	16.0	2	0.3	5	–	0.1
3HSPJ002254.9−341347	Yes	15.2	1	—	0	–	0.06
3HSPJ002259.0−244022	Yes	15.7	1	—	0	–	0.16
3HSPJ002611.6−073115	–	15.7	1	0.5	5	FL8YJ0026.1−0732	0.16
3HSPJ002635.6−460109	Yes	16.4	1	0.25	5	3FGLJ0026.7−4603	0.4
3HSPJ002928.6+205333	Yes	16.4	1	0.367	1	FL8YJ0029.4+2051	0.1
3HSPJ003020.4−164712	Yes	15.6	1	0.237	1	3FGLJ0030.2−1646	0.4
3HSPJ003119.7+072453	–	15.1	1	—	0	3FGLJ0031.3+0724	0.25
3HSPJ003120.5−233401	Yes	16.1	1	0.3	4	3FGLJ0031.2−2320	0.16
3HSPJ003120.7+051333	Yes	16.3	1	0.22	5	–	0.16
3HSPJ003222.5−472536	Yes	16.6	1	0.44	5	–	0.1
3HSPJ003322.4−203908	Yes	17.9	1	0.073	1	–	0.25
3HSPJ003333.2+502956	Yes	16.4	1	0.45	5	–	0.08
3HSPJ003334.3−192132	Yes	15.6	1	0.506	3	3FGLJ0033.6−1921	1.26
3HSPJ003358.8+390631	Yes	16.6	1	0.58	5	–	0.06
3HSPJ003514.7+151504	Yes	15.1	1	0.64	3	3FGLJ0035.2+1513	0.79
3HSPJ003532.8−131714	Yes	15.5	1	—	0	–	0.13
3HSPJ003539.6−181651	Yes	15.4	1	0.327	1	–	0.25
3HSPJ003552.6+595004	–	18.2	1	0.467	2	3FGLJ0035.9+5949	10.0
3HSPJ003631.6−031326	Yes	16.5	2	0.317	1	–	0.08
3HSPJ003736.2−230225	Yes	16.5	2	0.36	5	–	0.06
3HSPJ003908.2−222001	Yes	16.7	1	0.064	1	3FGLJ0039.0−2218	0.25
3HSPJ004013.8+405004	Yes	17.5	3	0.24	5	3FGLJ0040.3+4049	0.63
3HSPJ004040.8−232200	Yes	16.1	1	0.18	5	–	0.2
3HSPJ004123.0+375855	–	15.3	1	0.38	1	FL8YJ0041.4+3800	0.2
3HSPJ004141.2−160747	–	16.3	1	0.43	5	FL8YJ0041.7−1607	0.06
3HSPJ004143.2+083318	Yes	17.2	1	0.5	5	–	0.08
3HSPJ004147.0−470136	Yes	17.0	3	0.15	1	J004146.9−470136	0.32
3HSPJ004202.3−143600	Yes	16.2	1	0.5	5	–	0.05
3HSPJ004208.0+364112	Yes	16.3	1	0.33	5	3FGLJ0041.9+3639	0.32
3HSPJ004322.8+180846	Yes	16.5	1	0.322	1	–	0.08
3HSPJ004332.5+754518	Yes	16.0	1	0.27	5	–	0.13
3HSPJ004334.1−044300	Yes	16.5	1	0.48	3	3FGLJ0043.5−0444	0.32
3HSPJ004348.6−111606	Yes	15.7	1	0.264	1	3FGLJ0043.7−1117	0.5
3HSPJ004501.5+051215	Yes	16.1	1	0.27	5	–	0.06
3HSPJ004519.2+212740	Yes	15.8	1	0.35	3	3FGLJ0045.3+2126	1.0
3HSPJ004554.7−172328	Yes	16.0	2	0.096	1	–	0.16
3HSPJ004603.2+401346	Yes	15.2	1	0.67	5	–	0.02
3HSPJ004715.1−811135	Yes	16.6	1	0.3	5	–	0.08
3HSPJ004752.0+544745	–	16.5	1	0.26	5	3FGLJ0047.9+5447	0.2
3HSPJ004755.2+394857	Yes	16.1	1	0.252	1	3FGLJ0048.0+3950	0.25
3HSPJ004859.1+422351	Yes	16.3	1	0.37	5	3FGLJ0049.0+4224	0.16
3HSPJ004927.8+395003	Yes	16.4	1	0.19	5	–	0.08
3HSPJ004929.9−241844	Yes	16.4	1	0.49	5	–	0.08
3HSPJ004938.8−415137	Yes	16.3	1	0.38	5	3FGLJ0049.4−4149	0.2
3HSPJ005015.4−461811	Yes	16.1	1	0.33	5	–	0.06
3HSPJ005040.9−254122	Yes	15.4	1	0.777	2	–	0.13
3HSPJ005048.5−342850	Yes	16.1	1	0.32	5	–	0.06
3HSPJ005116.6−624204	Yes	15.8	1	0.3	3	3FGLJ0051.2−6241	0.79
3HSPJ005235.4−574636	Yes	16.1	1	0.256	1	–	0.13
3HSPJ005347.7−664517	–	17.0	2	0.31	5	FL8YJ0053.0−6643	0.32
3HSPJ005410.0+473611	Yes	16.7	1	0.5	5	–	0.1
3HSPJ005425.4−361131	Yes	16.2	1	0.31	5	–	0.06
3HSPJ005446.7−245528	Yes	15.7	1	0.12	3	3FGLJ0054.8−2455	1.0

Source	2WHSP	Log $\nu_{\rm peak}$	flag	Z	flag	γ-ray counterpart	FOM
3HSPJ005459.9−351917	–	15.1	1	0.057	2	–	0.08
3HSPJ005542.7+450701	–	15.0	3	0.46	5	FL8YJ0055.7+4507	0.06
3HSPJ005553.5+121733	Yes	16.1	1	0.29	5	–	0.08
3HSPJ005620.0−093630	Yes	15.9	1	0.1	1	3FGLJ0056.3−0935	0.5
3HSPJ005758.3+632639	–	16.8	1	0.18	5	FL8YJ0057.9+6326	0.5
3HSPJ005808.2−002417	–	16.2	1	0.6	4	–	0.03
3HSPJ005813.7−142929	Yes	16.7	1	0.3	4	–	0.08
3HSPJ005816.7+172313	Yes	17.4	1	0.42	5	J005816.6+172312	0.2
3HSPJ005916.9−015017	Yes	17.7	1	0.114	1	3FGLJ0059.2−0152	0.4
3HSPJ005931.4−351049	–	16.3	1	0.31	4	FL8YJ0059.5−3512	0.2
3HSPJ010010.7−023451	Yes	16.8	1	0.199	1	–	0.13
3HSPJ010116.2+273057	Yes	15.9	1	0.5	5	–	0.03
3HSPJ010142.0−545547	–	16.0	1	0.28	5	FL8YJ0101.7−5455	0.06
3HSPJ010250.9−200158	Yes	16.3	1	0.27	2	FL8YJ0102.7−2001	0.13
3HSPJ010325.8+533713	–	16.5	1	0.15	5	3FGLJ0103.4+5336	0.32
3HSPJ010353.2+351322	Yes	15.7	1	0.45	5	–	0.08
3HSPJ010501.8+503320	Yes	16.6	1	0.26	5	–	0.16
3HSPJ010528.1−171222	Yes	16.8	1	0.147	1	–	0.08
3HSPJ010547.1+393922	Yes	16.3	1	0.45	5	–	0.1
3HSPJ010956.5−402050	Yes	16.5	1	0.313	1	3FGLJ0109.9−4020	0.25
3HSPJ011004.8+414950	Yes	15.9	1	0.096	1	–	0.25
3HSPJ011009.7+042420	Yes	16.5	2	0.393	1	–	0.04
3HSPJ011049.9−125503	Yes	17.2	1	0.23	1	3FGLJ0110.9−1254	0.5
3HSPJ011130.1+053627	Yes	17.0	2	0.346	1	3FGLJ0111.5+0535	0.25
3HSPJ011231.3−750617	Yes	15.8	1	0.3	5	3FGLJ0112.9−7506	0.13
3HSPJ011232.7−320141	Yes	16.4	1	0.48	4	–	0.1
3HSPJ011314.3−190807	Yes	15.1	1	—	0	–	0.06
3HSPJ011501.7−340027	Yes	17.9	1	0.482	1	FL8YJ0114.9−3400	0.5
3HSPJ011533.3−030333	Yes	16.0	2	0.536	1	–	0.03
3HSPJ011546.1+251953	Yes	15.7	1	0.375	1	3FGLJ0115.8+2519	0.4
3HSPJ011555.4−274431	Yes	17.2	1	0.7	3	3FGLJ0116.2−2744	0.25
3HSPJ011637.0−281146	Yes	16.6	1	0.32	4	FL8YJ0116.5−2813	0.13
3HSPJ011724.3−222759	Yes	17.0	2	0.116	1	–	0.1
3HSPJ011746.9−244333	Yes	16.6	1	0.279	1	FL8YJ0117.5−2442	0.16
3HSPJ011823.2+324325	Yes	16.3	1	0.112	1	–	0.1
3HSPJ011828.7−511527	Yes	16.7	1	0.248	2	–	0.1
3HSPJ011831.4−142957	Yes	15.4	1	0.42	3	–	0.25
3HSPJ011904.6−145858	Yes	16.1	1	0.29	4	3FGLJ0118.9−1457	0.4
3HSPJ012048.3+212853	Yes	15.2	1	0.259	1	–	0.06
3HSPJ012152.6−391544	–	16.7	1	0.3	5	3FGLJ0121.8−3917	0.2
3HSPJ012203.7−300509	–	17.0	2	0.44	5	FL8YJ0122.1−3004	0.16
3HSPJ012308.6+342048	Yes	18.0	1	0.27	1	3FGLJ0122.8+3423	3.16
3HSPJ012338.3−231058	Yes	17.3	1	0.404	1	3FGLJ0123.7−2312	1.58
3HSPJ012340.3+421017	Yes	17.8	1	0.186	1	–	0.4
3HSPJ012430.5+324946	Yes	16.5	2	0.36	5	–	0.2
3HSPJ012443.7−314342	Yes	17.4	1	0.4	4	–	0.1
3HSPJ012523.5−292047	Yes	16.0	1	0.63	5	–	0.06
3HSPJ012629.5−350505	Yes	15.5	2	0.48	5	–	0.06
3HSPJ012652.1+003308	Yes	16.7	1	0.67	4	–	0.05
3HSPJ012657.2+330730	Yes	16.8	1	0.45	5	FL8YJ0127.1+3310	0.16
3HSPJ012713.9+032300	Yes	15.5	1	—	0	3FGLJ0127.2+0325	0.32
3HSPJ012722.1+211442	Yes	16.3	1	0.35	5	–	0.05
3HSPJ012750.8−001346	Yes	15.6	1	0.44	1	–	0.04
3HSPJ012917.9−034402	Yes	16.5	2	0.43	5	–	0.1
3HSPJ013025.7−212838	–	15.1	1	0.3	5	FL8YJ0130.5−2130	0.13
3HSPJ013107.2+612033	–	16.5	1	—	0	3FGLJ0131.2+6120	1.58
3HSPJ013113.8+554512	–	15.1	1	0.036	1	3FGLJ0131.3+5548	0.25

Source	2WHSP	Log $\nu_{\rm peak}$	flag	Z	flag	γ-ray counterpart	FOM
3HSPJ013241.1−080404	–	15.9	1	0.149	1	3FGLJ0132.5−0802	0.4
3HSPJ013309.2−453524	Yes	15.8	1	—	0	FL8YJ0133.2−4533	0.1
3HSPJ013312.1−351916	Yes	16.0	3	0.174	1	–	0.08
3HSPJ013314.1−435850	Yes	15.4	1	0.0	0	2FGLJ0133.4−4408	0.2
3HSPJ013428.1+263843	Yes	15.7	1	0.26	3	3FGLJ0134.5+2638	0.79
3HSPJ013507.0+025542	Yes	16.4	1	0.372	1	FL8YJ0135.1+0255	0.06
3HSPJ013523.6−272813	Yes	17.0	1	0.248	1	–	0.16
3HSPJ013548.7−201346	Yes	15.4	1	0.37	1	–	0.25
3HSPJ013626.6+302011	Yes	15.6	1	0.33	5	–	0.03
3HSPJ013632.5+390559	Yes	16.1	1	—	0	3FGLJ0136.5+3905	3.16
3HSPJ013750.4+581411	–	16.2	1	—	0	3FGLJ0137.8+5813	2.0
3HSPJ013801.1+224808	–	15.5	2	0.26	4	FL8YJ0138.0+2247	0.25
3HSPJ013803.7−215530	Yes	17.5	3	0.25	5	–	0.2
3HSPJ013834.5+245837	Yes	16.9	1	0.55	4	–	0.06
3HSPJ014040.8−075849	Yes	16.6	1	0.36	4	FL8YJ0140.6−0758	0.2
3HSPJ014347.1−012609	Yes	16.0	2	0.6	5	–	0.04
3HSPJ014347.3−584551	Yes	16.7	1	—	0	3FGLJ0143.7−5845	1.26
3HSPJ014357.9−651227	Yes	16.0	1	0.36	5	–	0.06
3HSPJ014522.8+045129	Yes	15.2	1	0.35	1	–	0.03
3HSPJ014557.6−282620	Yes	16.1	1	0.64	5	–	0.05
3HSPJ014558.0+213504	Yes	17.0	2	0.274	1	–	0.16
3HSPJ014620.2−024253	Yes	16.5	2	0.529	1	–	0.04
3HSPJ014648.5−520233	–	15.0	1	0.098	1	3FGLJ0147.0−5204	0.2
3HSPJ014715.8−000818	Yes	16.9	1	0.473	1	–	0.04
3HSPJ014748.7+203715	Yes	16.5	2	0.33	5	–	0.05
3HSPJ014753.6−602811	Yes	16.3	1	0.38	5	–	0.1
3HSPJ014820.3+520204	–	15.0	3	0.24	5	3FGLJ0148.3+5200	0.5
3HSPJ014833.7+012901	–	15.4	1	0.94	2	3FGLJ0148.6+0128	0.1
3HSPJ014918.2+203029	Yes	15.0	3	—	0	–	0.16
3HSPJ015044.5−545004	Yes	15.8	1	0.28	5	3FGLJ0150.5−5447	0.16
3HSPJ015219.8+364017	Yes	16.3	1	0.21	5	–	0.06
3HSPJ015239.5+014717	Yes	15.9	1	0.08	1	3FGLJ0152.6+0148	1.26
3HSPJ015307.3+751742	Yes	15.9	1	—	0	3FGLJ0152.8+7517	0.63
3HSPJ015313.1−110627	Yes	16.0	2	0.32	4	–	0.13
3HSPJ015325.8+711506	–	15.0	1	0.02	1	3FGLJ0153.4+7114	1.26
3HSPJ015402.7+082351	Yes	15.1	1	0.681	2	3FGLJ0154.0+0824	0.79
3HSPJ015553.6+053309	Yes	15.2	1	—	0	–	0.02
3HSPJ015608.2+054510	Yes	15.5	1	0.43	5	–	0.02
3HSPJ015624.5−242003	–	15.7	1	—	0	3FGLJ0156.5−2423	0.25
3HSPJ015646.0−474417	Yes	15.4	1	0.22	4	3FGLJ0156.9−4742	0.32
3HSPJ015657.9−530159	Yes	18.3	1	0.25	5	3FGLJ0157.0−5301	1.58
3HSPJ015700.6−323529	Yes	16.9	1	0.33	5	–	0.13
3HSPJ015721.5−215852	Yes	17.1	1	0.47	4	–	0.13
3HSPJ015743.9+003605	Yes	16.5	2	0.5	5	–	0.02
3HSPJ015809.9+251540	Yes	16.6	1	0.158	1	–	0.13
3HSPJ015934.3+104705	Yes	15.7	1	0.195	1	3FGLJ0159.4+1046	0.5
3HSPJ015953.5+004815	Yes	16.4	1	0.652	1	–	0.03
3HSPJ015958.1−364313	Yes	15.8	1	0.53	5	–	0.03
3HSPJ020020.9−410935	–	15.5	1	0.5	2	3FGLJ0200.3−4108	0.16
3HSPJ020106.1+003400	Yes	17.0	1	0.298	1	FL8YJ0201.1+0035	0.4
3HSPJ020110.9−434655	Yes	15.8	1	0.45	5	FL8YJ0201.1−4348	0.08
3HSPJ020121.7−225925	Yes	15.9	1	0.18	5	–	0.13
3HSPJ020226.4+084913	–	16.0	1	0.35	5	3FGLJ0202.3+0851	0.13
3HSPJ020239.7−313338	Yes	15.5	1	0.55	5	–	0.03
3HSPJ020252.2−022320	Yes	16.7	1	0.25	5	3FGLJ0203.1−0227	0.16
3HSPJ020314.0−323512	Yes	16.1	1	0.35	5	–	0.08
3HSPJ020356.0−244454	Yes	16.2	1	0.52	5	–	0.06

Source	2WHSP	Log $\nu_{\rm peak}$	flag	Z	flag	γ-ray counterpart	FOM
3HSPJ020412.9−333340	Yes	17.9	1	0.617	1	FL8YJ0204.0−3333	0.4
3HSPJ020416.4−314457	–	16.4	1	0.31	5	FL8YJ0204.3−3139	0.03
3HSPJ020421.5+241750	–	15.1	1	0.18	5	3FGLJ0204.2+2420	0.08
3HSPJ020430.0−213725	Yes	15.2	1	—	0	–	0.05
3HSPJ020441.6+004957	–	16.3	1	0.626	1	–	0.03
3HSPJ020615.8−095717	–	15.0	2	0.166	1	FL8YJ0206.0−0957	0.06
3HSPJ020838.1+352312	Yes	16.3	1	0.318	1	3FGLJ0208.6+3522	0.16
3HSPJ020917.0+444946	Yes	16.8	1	0.27	5	3FGLJ0209.5+4449	0.63
3HSPJ020921.6−522922	Yes	16.4	1	0.12	4	3FGLJ0209.4−5229	1.26
3HSPJ021205.7−255758	Yes	16.2	1	0.38	5	FL8YJ0212.3−2559	0.16
3HSPJ021216.8−022155	Yes	17.8	1	0.25	1	FL8YJ0212.2−0219	0.4
3HSPJ021230.4−350330	–	16.5	2	0.393	2	3FGLJ0212.8−3504	0.2
3HSPJ021252.8+224452	Yes	15.2	1	0.459	1	3FGLJ0213.0+2245	0.63
3HSPJ021358.6−695137	–	17.2	1	0.34	5	FL8YJ0213.8−6950	0.25
3HSPJ021409.8−473235	Yes	16.4	1	0.28	5	–	0.1
3HSPJ021411.9−353733	Yes	16.8	1	0.4	5	–	0.16
3HSPJ021417.9+514451	Yes	17.3	1	0.049	1	3FGLJ0214.4+5143	1.26
3HSPJ021502.9+032536	Yes	16.5	2	0.31	5	–	0.16
3HSPJ021515.2−161738	Yes	16.4	1	0.283	1	–	0.16
3HSPJ021517.8+755452	–	15.1	1	0.15	5	FL8YJ0215.2+7555	0.13
3HSPJ021552.3−402343	Yes	16.5	1	0.24	4	–	0.1
3HSPJ021616.6−481626	Yes	17.2	1	0.169	1	–	0.2
3HSPJ021632.0+231450	Yes	16.2	1	0.288	1	FL8YJ0216.5+2313	0.32
3HSPJ021650.8−663642	Yes	15.3	1	0.673	3	3FGLJ0217.0−6635	0.5
3HSPJ021729.3−642306	Yes	15.7	1	—	0	–	0.03
3HSPJ021900.4+244520	–	15.5	2	—	0	3FGLJ0219.0+2440	0.5
3HSPJ021905.4−172512	Yes	16.6	1	0.128	1	FL8YJ0219.1−1723	0.32
3HSPJ021915.4−493453	Yes	15.7	1	0.42	5	–	0.1
3HSPJ021931.2−642151	Yes	16.0	1	0.3	5	–	0.03
3HSPJ022006.3−391835	Yes	15.5	1	—	0	–	0.03
3HSPJ022048.4−084250	Yes	15.5	1	0.525	2	FL8YJ0220.8−0841	0.2
3HSPJ022104.9+063939	Yes	16.1	1	0.27	5	–	0.1
3HSPJ022211.4−213735	Yes	15.4	1	—	0	–	0.05
3HSPJ022304.5+682154	–	15.7	1	0.23	5	3FGLJ0223.3+6820	0.4
3HSPJ022314.2−111738	Yes	15.7	1	0.2	3	3FGLJ0222.9−1117	0.25
3HSPJ022539.7−190035	Yes	17.8	1	0.4	5	–	0.03
3HSPJ022540.7−561812	Yes	17.7	1	0.32	5	–	0.13
3HSPJ022638.8−444122	Yes	16.5	1	0.68	3	3FGLJ0226.5−4442	0.63
3HSPJ022657.2+082730	Yes	15.9	1	0.4	5	–	0.08
3HSPJ022716.5+020200	Yes	17.6	1	0.45	1	3FGLJ0227.2+0201	0.63
3HSPJ022855.8−292716	Yes	16.7	1	0.54	5	–	0.04
3HSPJ022941.1−412051	Yes	15.4	1	—	0	–	0.16
3HSPJ022948.2−512351	Yes	15.7	1	0.38	5	–	0.06
3HSPJ023005.9+194921	Yes	16.3	1	0.53	5	–	0.1
3HSPJ023109.2−575505	Yes	15.4	1	0.032	1	3FGLJ0230.6−5757	0.2
3HSPJ023231.1−251606	Yes	16.6	1	0.5	5	–	0.03
3HSPJ023237.5+313128	Yes	17.1	1	0.51	5	–	0.13
3HSPJ023241.9−112020	–	16.1	1	0.209	1	FL8YJ0232.5−1119	0.1
3HSPJ023246.2+063742	–	16.1	1	0.079	1	3FGLJ0232.6+0646	0.5
3HSPJ023248.5+201717	Yes	18.5	1	0.139	1	3FGLJ0232.8+2016	2.0
3HSPJ023340.9+065611	Yes	16.9	1	0.31	5	FL8YJ0233.5+0655	0.25
3HSPJ023410.2−062825	–	15.0	1	0.7	3	3FGLJ0234.2−0629	0.03
3HSPJ023430.6+804337	Yes	16.6	1	0.5	5	FL8YJ0234.0+8041	0.25
3HSPJ023536.6−293843	Yes	16.6	1	0.35	4	FL8YJ0235.6−2939	0.1
3HSPJ023605.5−215543	Yes	16.3	1	0.38	5	–	0.04
3HSPJ023734.0−360328	Yes	16.1	1	0.411	1	3FGLJ0237.5−3603	0.63
3HSPJ023800.6−390504	Yes	15.7	1	0.21	5	3FGLJ0238.3−3904	0.2

Source	2WHSP	Log $\nu_{\rm peak}$	flag	Z	flag	γ-ray counterpart	FOM
3HSPJ023813.6−092431	Yes	16.7	1	0.419	1	–	0.05
3HSPJ023832.4−311657	Yes	16.3	1	0.233	1	3FGLJ0238.4−3117	2.0
3HSPJ023853.8+255406	–	16.7	1	0.38	5	3FGLJ0239.0+2555	0.1
3HSPJ023905.5+132720	–	15.0	1	—	0	–	0.1
3HSPJ023927.2+132738	–	15.0	3	0.5	5	3FGLJ0239.4+1326	0.04
3HSPJ024115.4−304140	Yes	16.3	1	0.3	4	3FHLJ0241.0−3037	0.25
3HSPJ024121.7+654311	–	15.6	1	0.18	5	3FGLJ0241.3+6542	0.4
3HSPJ024151.3−160333	Yes	15.8	1	0.37	5	FL8YJ0241.8−1603	0.16
3HSPJ024302.9+004627	Yes	16.3	1	0.409	1	–	0.05
3HSPJ024440.2−581954	Yes	17.5	1	0.26	1	3FGLJ0244.8−5818	1.58
3HSPJ024507.8+184308	Yes	17.0	3	0.43	5	–	0.16
3HSPJ024641.8−334342	–	17.6	1	0.65	5	FL8YJ0246.6−3348	0.16
3HSPJ024743.3−481545	Yes	15.7	1	—	0	–	0.1
3HSPJ024751.6−225002	Yes	17.1	1	0.55	5	–	0.13
3HSPJ024752.1+004106	Yes	17.0	2	0.393	1	–	0.16
3HSPJ025018.9−212939	Yes	17.0	1	0.498	1	–	0.16
3HSPJ025024.5+454200	Yes	17.1	1	0.21	5	–	0.1
3HSPJ025037.9+171208	Yes	16.2	1	1.1	1	3FGLJ0250.6+1713	0.63
3HSPJ025047.5+562935	–	16.4	1	0.27	5	3FGLJ0250.6+5630	0.32
3HSPJ025056.8−324313	Yes	15.4	1	—	0	–	0.32
3HSPJ025057.2−122613	Yes	15.4	1	—	0	–	0.1
3HSPJ025111.5−183112	–	17.1	1	0.5	5	3FGLJ0251.1−1829	0.05
3HSPJ025211.5+320432	Yes	16.2	1	0.2	5	–	0.32
3HSPJ025347.1−103135	Yes	16.6	1	0.38	5	–	0.08
3HSPJ025426.3+160202	Yes	15.3	1	0.31	5	–	0.08
3HSPJ025434.3−454326	Yes	15.1	1	—	0	–	0.06
3HSPJ025448.1−125801	Yes	15.3	1	—	0	–	0.25
3HSPJ025707.8+335730	Yes	16.4	1	0.29	5	FL8YJ0257.0+3358	0.2
3HSPJ025756.1−271212	Yes	16.5	1	0.68	5	–	0.03
3HSPJ025857.5+055243	–	15.2	1	—	0	3FGLJ0258.9+0552	0.2
3HSPJ030036.9−361743	Yes	16.6	1	0.36	5	–	0.08
3HSPJ030103.7+344101	Yes	15.8	1	0.246	1	J030103.7+344100	0.13
3HSPJ030208.9+004626	Yes	16.6	1	0.63	5	–	0.1
3HSPJ030246.3−192425	Yes	15.5	1	—	0	–	0.5
3HSPJ030313.7−705026	Yes	16.6	1	0.33	5	–	0.1
3HSPJ030326.3−240711	Yes	15.7	1	0.266	1	3FGLJ0303.4−2407	3.98
3HSPJ030330.1+055430	Yes	15.8	1	0.196	1	FL8YJ0303.3+0554	0.4
3HSPJ030416.3−283218	Yes	17.7	1	0.4	2	3FGLJ0304.3−2836	0.5
3HSPJ030433.9−005404	Yes	15.9	1	0.511	1	FL8YJ0304.5−0055	0.16
3HSPJ030515.0−160816	–	17.0	1	0.31	5	3FGLJ0305.2−1607	0.2
3HSPJ030544.1+403510	Yes	16.7	1	0.24	5	J030544.1+403509	0.2
3HSPJ030718.6−205158	Yes	16.3	1	0.25	5	–	0.05
3HSPJ030816.8−285105	–	15.7	1	0.29	5	3FGLJ0308.4−2852	0.13
3HSPJ030926.0−395927	Yes	16.0	1	0.24	5	FL8YJ0309.4−4000	0.1
3HSPJ031034.6−501631	Yes	16.2	1	0.26	5	3FGLJ0310.4−5015	0.4
3HSPJ031103.2−440227	Yes	17.4	1	0.35	5	FL8YJ0311.4−4401	0.4
3HSPJ031205.3+312115	Yes	16.2	1	0.32	5	–	0.1
3HSPJ031234.1−322317	–	15.3	1	0.067	1	FL8YJ0312.4−3221	0.32
3HSPJ031235.6−222117	Yes	17.3	1	0.28	5	3FGLJ0312.7−2222	0.25
3HSPJ031250.2+361519	Yes	16.3	1	0.071	1	3FGLJ0312.7+3613	0.4
3HSPJ031311.5+244533	Yes	15.4	1	0.35	5	–	0.16
3HSPJ031421.9−095453	Yes	16.5	2	0.29	5	–	0.13
3HSPJ031423.9+061956	Yes	16.3	1	0.62	2	FL8YJ0314.3+0620	0.5
3HSPJ031432.6−090446	Yes	16.6	1	0.4	5	–	0.13
3HSPJ031527.1−264400	–	15.0	2	0.42	5	FL8YJ0315.4−2643	0.05
3HSPJ031612.7+090443	Yes	15.3	1	0.372	2	3FGLJ0316.1+0904	1.26
3HSPJ031614.3−643731	Yes	16.4	1	—	0	3FGLJ0316.2−6436	0.4

Source	2WHSP	Log ν_{peak}	flag	Z	flag	γ-ray counterpart	FOM
3HSPJ031614.9−260757	Yes	15.9	1	0.443	1	3FGLJ0316.1−2611	0.79
3HSPJ031615.1−224723	Yes	16.8	1	0.24	5	–	0.06
3HSPJ031633.7−221612	Yes	16.7	1	0.228	1	–	0.16
3HSPJ031746.6+201106	Yes	15.7	1	0.29	5	–	0.13
3HSPJ031749.7+010514	Yes	16.5	2	0.436	1	–	0.03
3HSPJ031855.5+190816	Yes	15.9	1	0.43	5	–	0.1
3HSPJ031916.7+190420	–	16.0	1	0.43	5	–	0.08
3HSPJ031951.7+184534	Yes	17.3	1	0.19	1	3FGLJ0319.8+1847	1.0
3HSPJ032009.2−704533	Yes	17.0	3	0.37	5	FL8YJ0319.4−7045	0.2
3HSPJ032038.0+112452	Yes	17.0	2	0.35	5	J032037.9+112451	0.1
3HSPJ032056.3+042448	Yes	17.9	1	0.46	5	FL8YJ0321.3+0424	0.4
3HSPJ032102.2−040851	Yes	15.9	1	0.45	5	–	0.16
3HSPJ032127.3−531055	Yes	17.1	1	0.5	5	–	0.08
3HSPJ032159.9+233611	Yes	15.6	1	—	0	3FGLJ0322.0+2335	0.79
3HSPJ032228.3−504539	Yes	16.5	1	0.53	5	–	0.03
3HSPJ032343.6−011146	Yes	15.1	1	0.44	3	3FGLJ0323.6−0109	0.4
3HSPJ032350.7+071737	Yes	17.0	2	0.31	1	–	0.32
3HSPJ032356.5−010833	Yes	17.5	3	0.392	1	1FGLJ0323.7−0106	0.25
3HSPJ032523.5−563544	Yes	16.5	1	0.6	1	3FGLJ0325.2−5634	0.32
3HSPJ032541.0−164616	Yes	15.6	1	0.291	1	3FGLJ0325.6−1648	1.26
3HSPJ032613.9+022514	Yes	15.9	1	0.147	1	3FGLJ0326.2+0225	1.0
3HSPJ032647.3−340447	Yes	16.2	1	0.51	5	FL8YJ0326.7−3404	0.2
3HSPJ032852.6−571605	Yes	17.3	1	0.48	3	FL8YJ0328.8−5715	0.25
3HSPJ033050.0−240611	–	16.5	2	0.43	5	FL8YJ0330.8−2407	0.16
3HSPJ033118.4−615528	Yes	15.7	1	0.21	5	3FGLJ0331.3−6155	0.32
3HSPJ033202.3−703948	Yes	16.6	1	0.24	5	–	0.13
3HSPJ033223.7+822645	–	15.7	1	—	0	FL8YJ0333.2+8227	0.13
3HSPJ033312.2−361946	Yes	17.5	1	0.308	1	–	0.16
3HSPJ033349.0+291631	Yes	15.2	1	—	0	3FGLJ0333.6+2916	1.26
3HSPJ033356.7+653656	–	15.2	1	0.16	5	3FGLJ0333.9+6538	0.63
3HSPJ033415.4−372542	–	15.0	1	0.39	3	3FGLJ0334.3−3726	1.58
3HSPJ033513.8−445943	–	15.3	1	—	0	3FGLJ0335.3−4459	0.4
3HSPJ033612.8−213128	Yes	16.6	1	0.35	5	–	0.1
3HSPJ033623.7−034738	Yes	17.3	1	0.162	1	FL8YJ0336.4−0348	0.25
3HSPJ033812.5−244350	Yes	16.5	2	0.251	1	3FGLJ0338.1−2443	0.13
3HSPJ033829.2+130215	Yes	15.8	1	—	0	3FGLJ0338.5+1303	0.63
3HSPJ033832.0−570448	Yes	16.6	1	0.3	5	FL8YJ0338.8−5706	0.4
3HSPJ033851.9−532425	Yes	16.0	1	0.37	5	–	0.06
3HSPJ033859.5−284619	–	16.3	1	0.27	5	FL8YJ0338.9−2848	0.13
3HSPJ033913.6−173600	–	15.6	1	0.066	1	3FGLJ0339.2−1738	0.5
3HSPJ034054.7+782258	Yes	15.7	1	0.31	5	–	0.13
3HSPJ034254.1−370737	Yes	17.1	1	0.201	1	–	0.32
3HSPJ034323.5−761448	Yes	15.1	1	0.22	5	–	0.13
3HSPJ034402.4+730114	Yes	16.4	1	0.28	5	–	0.25
3HSPJ034424.9+343017	–	15.7	1	—	0	FL8YJ0344.4+3432	0.04
3HSPJ034427.3−523557	Yes	15.6	1	—	0	–	0.13
3HSPJ034609.4−420505	Yes	16.5	2	0.47	5	–	0.08
3HSPJ034656.9−133830	Yes	15.4	1	—	0	–	0.32
3HSPJ034819.8+603508	–	17.5	2	0.4	5	3FGLJ0348.4+6039	0.79
3HSPJ034923.1−115927	Yes	17.9	1	0.188	1	3FGLJ0349.2−1158	2.0
3HSPJ034957.8+064126	–	17.6	1	0.26	5	FL8YJ0350.0+0640	0.32
3HSPJ035028.3−514454	–	17.6	1	0.32	5	FL8YJ0350.4−5144	0.4
3HSPJ035051.3−281632	Yes	17.5	1	0.47	5	3FGLJ0351.0−2816	0.16
3HSPJ035154.5−370344	Yes	17.9	1	0.165	1	–	0.25
3HSPJ035257.4−683117	Yes	18.1	1	0.087	1	3FGLJ0353.0−6831	2.0
3HSPJ035305.0−362308	Yes	16.8	1	0.31	5	3FGLJ0353.0−3622	0.32
3HSPJ035308.4+825631	Yes	16.4	1	0.069	2	FL8YJ0353.5+8257	0.32

Source	2WHSP	Log $\nu_{\rm peak}$	flag	Z	flag	γ-ray counterpart	FOM
3HSPJ035309.5+565430	–	16.4	1	—	0	3FGLJ0352.9+5655	0.5
3HSPJ035513.2−184308	–	15.0	3	0.28	5	FL8YJ0355.1−1841	0.16
3HSPJ035532.7−485134	Yes	16.7	1	0.47	5	–	0.02
3HSPJ035610.8−132905	–	15.7	1	0.35	5	FL8YJ0356.1−1328	0.1
3HSPJ035726.0−031759	–	17.5	3	0.3	5	FL8YJ0357.3−0319	0.16
3HSPJ035732.9−680932	–	16.6	1	0.089	1	FL8YJ0358.0−6807	0.08
3HSPJ035807.2−545139	Yes	15.4	1	—	0	–	0.1
3HSPJ035856.1−305447	Yes	16.7	1	0.65	2	FL8YJ0359.0−3053	0.25
3HSPJ035923.4−023501	–	15.5	2	0.34	5	FL8YJ0359.4−0236	0.08
3HSPJ040111.2−535458	–	16.8	1	0.59	5	3FGLJ0401.0−5359	0.13
3HSPJ040126.3−080159	Yes	16.4	1	0.147	2	–	0.1
3HSPJ040128.7+815311	Yes	16.7	2	0.215	1	–	0.25
3HSPJ040254.4+643509	–	15.3	1	0.31	5	FL8YJ0402.9+6433	0.1
3HSPJ040324.5−242947	–	18.0	2	0.357	1	FL8YJ0403.4−2432	0.32
3HSPJ040905.0−053235	Yes	16.7	1	0.346	1	–	0.05
3HSPJ040928.5+320245	–	16.5	2	0.28	5	3FGLJ0409.4+3158	0.79
3HSPJ041112.3−394143	Yes	16.6	1	0.7	3	J041112.2−394143	0.4
3HSPJ041238.4−392629	Yes	17.8	1	0.5	5	J041238.3−392629	0.13
3HSPJ041422.6−035017	Yes	16.1	1	0.36	5	–	0.04
3HSPJ041458.1−533943	Yes	16.9	1	—	0	FL8YJ0414.7−5339	0.63
3HSPJ041645.2−552529	Yes	15.5	2	0.33	5	–	0.03
3HSPJ041652.4+010523	Yes	16.5	1	0.287	1	3FGLJ0416.8+0104	3.16
3HSPJ041855.8+132451	Yes	17.8	1	0.27	5	–	0.16
3HSPJ041949.3+843835	Yes	16.3	1	0.5	5	–	0.1
3HSPJ042011.0−601505	–	16.2	1	0.33	5	3FGLJ0420.4−6013	0.16
3HSPJ042013.4+401121	–	16.1	1	0.14	5	FL8YJ0420.1+4011	0.25
3HSPJ042026.3−651400	Yes	15.3	1	—	0	–	0.32
3HSPJ042132.9−062903	Yes	17.0	1	0.39	1	–	0.25
3HSPJ042218.3+195054	Yes	17.5	1	0.516	1	3FGLJ0421.6+1950	0.32
3HSPJ042301.2−522716	Yes	15.2	1	—	0	–	0.06
3HSPJ042307.9−315958	Yes	16.1	1	0.58	5	–	0.06
3HSPJ042344.8−543150	Yes	15.5	2	0.29	5	–	0.05
3HSPJ042525.3+632001	–	17.5	2	0.27	5	3FGLJ0425.2+6319	0.25
3HSPJ042733.3−183010	Yes	17.5	1	0.22	5	–	0.32
3HSPJ042850.8−380550	–	15.1	1	0.15	1	–	0.04
3HSPJ042900.1−323641	Yes	16.4	1	0.34	4	FL8YJ0429.4−-3239	0.25
3HSPJ042958.9−305935	–	15.8	1	0.21	5	3FGLJ0430.1−3103	0.32
3HSPJ043046.3+030337	Yes	15.9	1	0.43	5	–	0.1
3HSPJ043145.0+740326	Yes	15.5	1	—	0	3FGLJ0431.6+7403	0.32
3HSPJ043154.9−653635	Yes	15.9	1	0.33	5	–	0.1
3HSPJ043307.5+322840	Yes	15.7	1	—	0	3FGLJ0433.1+3228	0.4
3HSPJ043332.8−104232	Yes	16.1	1	0.29	5	–	0.13
3HSPJ043344.1−572613	–	15.0	1	—	0	3FGLJ0434.0−5726	0.1
3HSPJ043440.9+092348	–	16.1	1	0.21	5	3FGLJ0434.6+0921	0.79
3HSPJ043517.7−262122	Yes	16.5	1	0.31	4	FL8YJ0435.4−2624	0.32
3HSPJ043726.9−462500	Yes	15.3	1	—	0	–	0.32
3HSPJ043837.0−732921	–	15.6	1	0.15	5	3FGLJ0437.7−7330	0.04
3HSPJ043837.4+311939	Yes	15.1	1	—	0	–	0.32
3HSPJ043932.2−320052	–	15.4	1	0.4	5	3FGLJ0439.6−3159	0.13
3HSPJ044018.6−245933	Yes	17.1	1	0.6	2	3FGLJ0440.3−2500	0.25
3HSPJ044050.3+275046	–	15.3	1	0.2	5	3FGLJ0440.8+2751	0.32
3HSPJ044127.4+150455	Yes	17.8	1	0.109	1	FL8YJ0441.5+1505	0.63
3HSPJ044139.2−105735	Yes	15.6	1	0.155	1	–	0.13
3HSPJ044230.2−001829	Yes	16.3	1	0.449	1	–	0.16
3HSPJ044240.6+614039	Yes	17.0	2	0.18	5	FL8YJ0442.7+6142	0.32
3HSPJ044328.3−415156	Yes	16.9	1	0.3	4	FL8YJ0443.3−4152	1.0
3HSPJ044458.3−583630	Yes	15.9	1	0.36	5	–	0.05

Source	2WHSP	Log $\nu_{\rm peak}$	flag	Z	flag	γ-ray counterpart	FOM
3HSPJ044627.1−434632	Yes	15.2	1	—	0	–	0.2
3HSPJ044757.9−354938	Yes	16.8	1	0.6	5	–	0.08
3HSPJ044837.6−163243	Yes	17.1	1	0.35	2	3FGLJ0448.6-1632	0.63
3HSPJ044855.0−101855	Yes	16.1	1	0.58	5	–	0.1
3HSPJ044917.0−422342	Yes	16.1	1	0.38	5	–	0.08
3HSPJ044924.6−435008	Yes	15.5	1	0.19	3	3FGLJ0449.4−4350	10.0
3HSPJ045039.2−160212	Yes	16.2	1	—	0	–	0.1
3HSPJ045107.5−232533	Yes	16.9	1	0.36	5	–	0.25
3HSPJ045148.6+572141	–	15.7	1	0.31	5	3FGLJ0451.7+5722	0.4
3HSPJ045215.3+210303	Yes	16.7	1	0.31	5	FL8YJ0452.0+2059	0.13
3HSPJ045249.4−000151	Yes	16.7	1	0.33	5	–	0.08
3HSPJ045658.5−080530	Yes	15.7	1	0.39	5	–	0.13
3HSPJ045741.6+062221	Yes	15.4	1	0.32	5	–	0.16
3HSPJ045744.2−014932	Yes	15.2	1	—	0	–	0.1
3HSPJ045804.8+115143	–	15.0	2	0.2	5	FL8YJ0458.0+1152	0.1
3HSPJ045823.5−864408	Yes	16.6	1	0.22	5	–	0.13
3HSPJ045834.7+085643	Yes	17.1	1	0.27	5	–	0.16
3HSPJ045936.9−541707	–	17.2	1	0.5	5	FL8YJ0459.6−5413	0.08
3HSPJ050021.4+523801	–	17.6	1	0.12	5	3FGLJ0500.3+5237	0.79
3HSPJ050043.9+190317	–	15.5	2	0.25	5	FL8YJ0500.6+1904	0.1
3HSPJ050130.0+020400	–	16.1	1	0.58	5	–	0.08
3HSPJ050141.1+304825	–	16.6	1	0.31	5	3FGLJ0501.8+3046	0.32
3HSPJ050240.7−120429	Yes	16.4	1	0.45	5	–	0.08
3HSPJ050244.8−450455	Yes	15.6	1	0.31	5	–	0.1
3HSPJ050305.8+653401	–	17.0	2	0.25	5	3FGLJ0503.5+6538	0.79
3HSPJ050319.0−390022	Yes	16.8	1	0.156	1	–	0.08
3HSPJ050335.4−111506	Yes	16.9	1	0.4	3	FL8YJ0503.5−1117	0.25
3HSPJ050339.5+451659	–	15.7	1	0.25	5	3FGLJ0503.4+4522	0.4
3HSPJ050419.5−095632	Yes	17.9	1	0.32	4	J050419.5−095631	0.5
3HSPJ050534.7+041554	Yes	15.8	1	0.424	1	3FGLJ0505.5+0416	0.5
3HSPJ050552.0−814358	Yes	15.6	1	0.37	5	–	0.06
3HSPJ050558.7+611335	Yes	15.8	1	0.27	5	3FGLJ0505.9+6114	0.2
3HSPJ050559.6−292630	Yes	15.5	1	0.44	5	–	0.1
3HSPJ050601.6−382055	Yes	16.2	1	0.182	1	FL8YJ0505.8−3818	0.2
3HSPJ050639.9−085801	Yes	15.3	1	0.28	5	3FGLJ0507.5−0906	0.16
3HSPJ050643.0−234419	Yes	16.7	1	0.45	4	–	0.08
3HSPJ050650.1+032358	–	15.8	1	0.32	5	3FGLJ0506.9+0321	0.16
3HSPJ050657.7−543503	Yes	16.1	1	0.26	3	3FGLJ0506.9−5435	1.0
3HSPJ050709.3−385948	Yes	17.5	3	0.55	5	–	0.13
3HSPJ050727.2−334635	Yes	17.7	1	0.39	2	FL8YJ0507.4−3346	0.32
3HSPJ050756.1+673724	Yes	17.9	1	0.34	2	3FGLJ0508.0+6736	3.98
3HSPJ050813.1−280742	Yes	16.7	1	0.26	5	–	0.08
3HSPJ050833.3+053109	Yes	15.6	1	—	0	–	0.4
3HSPJ050912.8−731755	Yes	16.2	1	—	0	–	0.2
3HSPJ050938.1−040045	Yes	17.8	1	0.304	1	3FGLJ0509.7−0400	0.79
3HSPJ050939.8−251403	Yes	16.5	2	0.264	1	–	0.13
3HSPJ050957.2−641741	–	17.4	1	—	0	3FGLJ0509.7−6418	0.79
3HSPJ051304.4−022034	Yes	15.9	1	0.29	5	–	0.1
3HSPJ051427.0−341225	Yes	16.7	1	0.4	2	–	0.13
3HSPJ051439.1−001104	Yes	15.4	1	0.28	5	–	0.1
3HSPJ051533.1−012355	–	15.6	1	0.25	5	3FGLJ0515.5−0123	0.4
3HSPJ051631.2+735108	Yes	16.2	1	0.251	1	3FGLJ0516.3+7351	0.25
3HSPJ051845.4−572055	Yes	17.0	1	0.4	4	–	0.08
3HSPJ052026.1−555430	Yes	15.4	1	0.37	5	–	0.1
3HSPJ052041.9+653351	Yes	17.4	1	0.4	5	–	0.2
3HSPJ052133.6−295748	Yes	16.1	1	0.45	5	–	0.08
3HSPJ052145.9+211251	Yes	15.1	1	0.108	1	3FGLJ0521.7+2113	5.01

Source	2WHSP	Log $\nu_{\rm peak}$	flag	Z	flag	γ-ray counterpart	FOM
3HSPJ052343.3−814201	Yes	16.4	1	0.28	5	–	0.08
3HSPJ052437.9+754000	Yes	16.1	1	0.5	5	–	0.1
3HSPJ052439.7−261554	Yes	17.2	1	0.26	4	–	0.16
3HSPJ052542.4−601340	Yes	16.2	1	0.45	5	3FGLJ0525.6−6013	0.04
3HSPJ052643.1−180813	Yes	15.7	1	—	0	–	0.16
3HSPJ052645.4−151900	Yes	15.7	1	0.21	5	FL8YJ0526.8−1519	0.79
3HSPJ052846.0−592003	–	15.2	1	1.13	2	3FGLJ0529.2−5917	0.25
3HSPJ052902.5+093435	Yes	17.7	1	0.3	5	3FGLJ0529.1+0933	0.63
3HSPJ053138.3+073039	–	15.7	1	0.5	5	–	0.08
3HSPJ053547.3−315342	Yes	16.2	1	0.5	5	–	0.05
3HSPJ053626.8−254748	Yes	15.9	1	—	0	FL8YJ0536.5−2548	0.03
3HSPJ053629.0−334302	Yes	16.0	1	0.34	3	3FGLJ0536.4−3347	1.0
3HSPJ053629.8−752412	Yes	16.1	1	0.56	5	–	0.13
3HSPJ053645.3−255841	Yes	17.2	1	0.32	5	J053645.2−255841	0.05
3HSPJ053737.4−233700	Yes	15.1	1	0.43	5	–	0.04
3HSPJ053737.6−140440	Yes	16.0	1	0.2	5	–	0.1
3HSPJ053748.9−571830	–	15.1	1	1.18	2	3FGLJ0537.4−5717	0.4
3HSPJ053809.7+031556	Yes	15.9	1	0.42	5	–	0.08
3HSPJ053810.3−390842	Yes	17.7	1	0.27	4	3FGLJ0538.4−3909	0.32
3HSPJ053949.5−102938	Yes	16.5	1	0.4	5	–	0.16
3HSPJ054030.0+582338	Yes	16.3	1	—	0	3FGLJ0540.4+5823	1.26
3HSPJ054106.9−485410	–	16.6	1	0.6	5	FL8YJ0541.1−4854	0.06
3HSPJ054357.2−553207	Yes	16.9	1	0.273	1	3FGLJ0543.9−5531	1.58
3HSPJ054449.1−193814	Yes	15.7	1	—	0	–	0.1
3HSPJ054504.4+065810	Yes	15.3	1	—	0	–	0.1
3HSPJ054655.2−685134	Yes	17.2	1	0.25	5	–	0.2
3HSPJ054656.7−220457	Yes	15.8	2	0.28	1	FL8YJ0546.8−2206	0.1
3HSPJ054746.5−460709	Yes	16.3	1	0.43	5	–	0.03
3HSPJ054903.4−215001	–	15.7	1	0.35	5	–	0.05
3HSPJ054906.8+325803	–	15.0	3	0.25	5	FL8YJ0549.0+3257	0.25
3HSPJ055026.5−435703	–	15.0	2	0.4	5	FL8YJ0550.4−4356	0.06
3HSPJ055040.5−321616	Yes	18.1	1	0.069	1	3FGLJ0550.6−3217	3.98
3HSPJ055102.0−472429	Yes	16.1	1	—	0	–	0.2
3HSPJ055333.1−203418	–	15.3	1	0.38	3	3FGLJ0553.5−2036	0.32
3HSPJ055411.0−275729	Yes	17.0	2	0.231	1	–	0.16
3HSPJ055716.8−061706	Yes	17.8	1	0.29	5	FL8YJ0557.3−0615	0.79
3HSPJ055734.3−685340	Yes	15.2	1	—	0	–	0.06
3HSPJ055806.4−383831	Yes	16.6	1	0.302	1	3FGLJ0558.1−3838	1.26
3HSPJ055940.9+304228	–	15.4	1	0.3	5	3FGLJ0559.8+3042	0.13
3HSPJ055959.3+640958	Yes	16.9	1	0.32	5	FL8YJ0559.8+6409	0.25
3HSPJ060014.9+124343	–	16.0	2	0.12	5	FL8YJ0600.3+1244	0.63
3HSPJ060200.4+531600	Yes	16.3	1	0.052	1	3FGLJ0602.2+5314	1.0
3HSPJ060251.2−401845	–	15.1	1	—	0	3FGLJ0602.8−4016	0.63
3HSPJ060408.6−481725	Yes	16.5	1	0.23	4	3FGLJ0604.1−4817	0.63
3HSPJ060433.7−403754	Yes	16.4	1	0.28	5	–	0.13
3HSPJ060450.0+833133	Yes	16.3	1	0.39	5	–	0.04
3HSPJ060635.7−472954	–	15.0	1	0.037	1	3FGLJ0606.4−4729	0.5
3HSPJ060714.3−251859	Yes	17.5	1	0.275	1	FL8YJ0607.2−2518	0.2
3HSPJ060736.4−742336	Yes	16.2	1	0.48	5	–	0.05
3HSPJ060915.0−024754	–	15.4	1	0.23	5	3FGLJ0609.4−0248	0.79
3HSPJ061104.1+682956	Yes	16.2	1	0.5	5	–	0.1
3HSPJ061106.5+432357	–	16.0	2	0.28	5	3FGLJ0611.2+4323	0.06
3HSPJ061518.2−782829	Yes	16.3	1	0.112	1	–	0.2
3HSPJ061610.2−173305	Yes	17.5	2	0.55	4	FL8YJ0616.1−1732	0.2
3HSPJ061702.7+434033	–	15.0	3	0.26	5	FL8YJ0617.0+4340	0.16
3HSPJ061740.9−171557	–	15.3	1	—	0	FL8YJ0617.6−1715	0.4
3HSPJ061742.8−171908	–	16.4	1	0.16	5	3FGLJ0617.6−1717	0.06

Source	2WHSP	Log $\nu_{\rm peak}$	flag	Z	flag	γ-ray counterpart	FOM
3HSPJ061841.8−173101	–	16.2	1	0.5	5	–	0.1
3HSPJ061949.5+573548	Yes	16.9	1	0.45	5	–	0.25
3HSPJ062040.0+264331	Yes	16.9	1	0.14	5	3FGLJ0620.4+2644	0.63
3HSPJ062046.1−503350	–	15.0	1	0.25	5	FL8YJ0620.7−5034	0.06
3HSPJ062149.6−341149	Yes	17.7	1	0.529	1	FL8YJ0621.7−3412	0.79
3HSPJ062337.8−525756	Yes	16.0	1	0.29	4	FL8YJ0623.9−5300	0.08
3HSPJ062445.0−323055	Yes	16.6	1	0.252	1	–	0.08
3HSPJ062550.3+485806	Yes	16.1	1	0.4	5	–	0.13
3HSPJ062626.2−171046	Yes	16.6	1	0.7	3	FL8YJ0626.4−1712	0.32
3HSPJ062636.7−425805	Yes	15.5	1	0.27	5	3FGLJ0626.6−4259	0.13
3HSPJ062753.3−151957	Yes	17.3	1	0.29	5	3FGLJ0627.9−1517	0.4
3HSPJ063015.0−201236	Yes	16.4	1	0.22	5	J063014.9−201236	0.32
3HSPJ063059.5−240646	Yes	15.1	1	1.239	3	3FGLJ0630.9−2406	1.26
3HSPJ063257.9+591541	Yes	16.9	1	0.28	5	–	0.1
3HSPJ063331.0−162951	–	15.2	1	—	0	–	0.79
3HSPJ063359.7+584035	–	15.0	3	0.29	5	FL8YJ0633.8+5840	0.08
3HSPJ063841.4−261744	Yes	15.6	1	—	0	–	0.13
3HSPJ064007.1−125314	Yes	17.1	1	0.11	5	3FGLJ0640.0−1252	2.51
3HSPJ064050.3+243319	–	16.4	1	0.27	5	FL8YJ0640.8+2432	0.16
3HSPJ064326.7+421418	–	17.2	1	0.089	1	–	0.5
3HSPJ064435.7+603851	–	15.5	1	0.33	5	3FGLJ0644.6+6035	0.1
3HSPJ064443.7−285116	Yes	16.1	1	0.35	4	3FGLJ0644.6−2853	0.25
3HSPJ064710.0−513547	Yes	17.9	1	0.22	5	3FGLJ0647.0−5134	1.26
3HSPJ064813.9+160656	–	16.9	1	0.35	5	3FGLJ0648.1+1606	0.32
3HSPJ064827.4+711313	Yes	15.1	1	—	0	–	0.1
3HSPJ064847.6+151624	Yes	16.6	1	0.179	1	3FGLJ0648.8+1516	1.58
3HSPJ064850.4−694522	Yes	17.1	1	0.28	5	–	0.32
3HSPJ064933.5−313920	Yes	16.8	1	—	0	3FGLJ0649.6−3138	0.79
3HSPJ065010.3−514421	–	15.0	3	0.31	5	FL8YJ0650.2−5144	0.2
3HSPJ065035.3+205555	–	16.7	1	0.3	5	3FGLJ0650.5+2055	0.4
3HSPJ065046.4+250259	Yes	16.7	1	0.203	2	3FGLJ0650.7+2503	3.98
3HSPJ065105.4+401338	Yes	15.2	1	0.18	5	3FGLJ0651.3+4014	0.32
3HSPJ065200.5−480859	Yes	15.9	1	—	0	3FGLJ0652.0−4808	0.16
3HSPJ065610.6+423702	–	15.8	1	0.059	1	3FGLJ0656.4+4232	0.32
3HSPJ065635.5+421524	–	16.5	2	0.45	5	FL8YJ0656.6+4218	0.16
3HSPJ065751.3−284306	Yes	15.4	1	0.25	5	–	0.2
3HSPJ065845.0+063711	–	15.5	1	0.23	5	3FGLJ0658.6+0636	0.16
3HSPJ065932.9−674350	Yes	17.4	1	0.43	5	FL8YJ0659.5−6743	0.2
3HSPJ070014.3+130424	–	15.1	1	0.21	5	3FGLJ0700.2+1304	0.25
3HSPJ070132.1+250953	–	17.0	2	0.33	5	FL8YJ0701.4+2512	0.5
3HSPJ070315.8+680831	–	15.6	1	0.27	5	FL8YJ0703.1+6809	0.08
3HSPJ070610.8+024449	–	16.0	1	0.22	5	FL8YJ0706.1+0246	0.4
3HSPJ070631.6+374436	Yes	15.4	1	—	0	3FGLJ0706.5+3744	0.5
3HSPJ070858.2+224135	–	15.3	1	—	0	3FGLJ0708.9+2239	1.0
3HSPJ070912.5−152703	–	16.9	1	0.1	5	FL8YJ0709.2−1527	2.51
3HSPJ070947.9−300905	–	16.4	1	—	0	FL8YJ0709.7−3008	0.2
3HSPJ071030.0+590820	Yes	18.1	1	0.12	1	3FGLJ0710.3+5908	3.98
3HSPJ071218.8+571948	Yes	17.6	1	0.095	2	FL8YJ0712.4+5721	0.16
3HSPJ071223.5+331333	–	16.8	1	0.41	5	FL8YJ0712.6+3311	0.08
3HSPJ071525.2−513738	Yes	15.7	1	—	0	–	0.25
3HSPJ071625.6+750700	Yes	16.1	1	—	0	–	0.05
3HSPJ071745.0−552021	Yes	15.4	1	0.35	5	FL8YJ0717.7−5519	0.16
3HSPJ071908.6−705403	Yes	16.4	1	0.33	5	–	0.05
3HSPJ071959.8+632228	Yes	15.3	1	—	0	–	0.04
3HSPJ072113.9−022054	–	16.9	1	0.38	5	3FGLJ0721.5−0221	0.4
3HSPJ072259.6−073134	–	16.3	1	0.17	5	3FGLJ0723.2−0728	0.63
3HSPJ072314.0+584120	Yes	17.2	1	0.26	5	FL8YJ0723.4+5842	0.13

Source	2WHSP	Log $\nu_{\rm peak}$	flag	Z	flag	γ-ray counterpart	FOM
3HSPJ072348.3+205130	Yes	16.1	1	0.21	5	3FGLJ0723.7+2050	0.25
3HSPJ072406.2+535114	Yes	15.2	1	—	0	–	0.32
3HSPJ072529.5−050336	–	16.3	1	0.1	5	FL8YJ0725.5−0504	0.4
3HSPJ072547.8−054832	–	16.4	1	—	0	3FGLJ0725.7−0550	0.25
3HSPJ072659.5+373423	Yes	15.7	1	0.35	4	FL8YJ0727.0+3735	0.1
3HSPJ073026.0+330722	Yes	15.4	1	0.11	1	3FGLJ0730.5+3307	0.5
3HSPJ073049.5−660218	Yes	15.6	1	0.106	1	3FGLJ0730.5−6606	0.63
3HSPJ073124.2−584122	Yes	15.1	1	0.33	5	–	0.1
3HSPJ073152.7+280433	Yes	16.5	1	0.248	1	FL8YJ0731.8+2804	0.4
3HSPJ073326.7+515355	Yes	17.9	1	0.09	5	3FGLJ0733.5+5153	1.26
3HSPJ073329.5+351542	Yes	16.3	1	0.177	1	FL8YJ0733.1+3522	0.2
3HSPJ073518.5+034735	Yes	15.3	1	—	0	–	0.2
3HSPJ073522.0+514641	Yes	16.7	1	0.45	5	–	0.08
3HSPJ073701.8+284646	Yes	15.7	1	0.272	1	–	0.1
3HSPJ073706.0−824840	–	15.7	1	0.23	5	3FGLJ0737.8−8245	0.32
3HSPJ073927.3−672136	–	17.0	1	0.53	5	FL8YJ0739.9−6721	0.25
3HSPJ074221.1−813136	–	15.0	3	0.43	5	3FGLJ0742.4−8133	0.1
3HSPJ074322.0−563254	Yes	15.6	1	0.38	5	–	0.08
3HSPJ074405.3+743358	Yes	16.5	1	0.314	1	3FGLJ0744.3+7434	0.79
3HSPJ074419.8−621100	Yes	16.6	1	0.38	5	–	0.16
3HSPJ074439.9−011430	Yes	16.0	1	0.48	5	–	0.1
3HSPJ074627.0−022549	–	15.3	1	—	0	3FGLJ0746.4−0225	0.32
3HSPJ074642.3−475455	Yes	15.4	1	—	0	3FGLJ0746.6−4756	1.0
3HSPJ074709.4+062306	Yes	15.8	1	—	0	–	0.2
3HSPJ074710.0−073724	–	15.5	1	0.32	5	3FGLJ0747.4−0734	0.03
3HSPJ074716.2+851208	Yes	17.1	1	0.28	5	3FGLJ0746.9+8511	0.32
3HSPJ074722.1+090548	Yes	17.2	1	0.28	5	3FGLJ0747.4+0904	0.4
3HSPJ074724.7−492633	Yes	15.8	1	—	0	3FGLJ0747.5−4927	0.5
3HSPJ074734.5+612650	Yes	15.5	2	0.32	5	–	0.13
3HSPJ074914.0+231316	–	15.5	1	0.175	1	FL8YJ0749.2+2313	0.1
3HSPJ074929.5+745144	Yes	16.1	1	0.607	2	FL8YJ0749.6+7450	0.25
3HSPJ075109.5+291335	Yes	15.8	1	0.185	1	–	0.03
3HSPJ075125.1+173050	Yes	17.2	1	0.187	1	–	0.2
3HSPJ075212.5+040901	Yes	15.5	1	—	0	–	0.4
3HSPJ075329.5+535111	Yes	15.1	1	0.26	5	–	0.16
3HSPJ075523.1+372619	Yes	17.2	1	0.605	1	–	0.08
3HSPJ075722.7+182929	Yes	16.3	2	0.26	1	–	0.1
3HSPJ075936.1+132117	Yes	16.3	1	0.7	3	FL8YJ0759.6+1321	0.4
3HSPJ080004.0+621015	Yes	15.8	1	0.48	5	–	0.08
3HSPJ080015.5+561107	Yes	16.0	1	0.38	5	FL8YJ0800.3+5610	0.13
3HSPJ080056.5+073235	–	15.4	1	0.44	5	FL8YJ0800.8+0732	0.1
3HSPJ080102.1+644449	Yes	16.4	1	0.2	2	FL8YJ0801.1+6444	0.16
3HSPJ080135.9+463824	Yes	16.0	1	0.369	1	J080135.8+463824	0.13
3HSPJ080204.8+100637	–	15.5	2	0.57	3	3FGLJ0802.0+1005	0.4
3HSPJ080215.8−094210	–	15.4	1	—	0	3FGLJ0802.3−0941	0.32
3HSPJ080312.1−033600	Yes	15.6	1	0.365	1	3FGLJ0803.3−0339	0.13
3HSPJ080323.0+481617	Yes	15.7	1	0.501	1	–	0.06
3HSPJ080457.7−062426	Yes	16.9	1	0.27	4	3FGLJ0805.0−0622	0.32
3HSPJ080508.9+685600	Yes	15.1	1	—	0	–	0.1
3HSPJ080526.6+753424	Yes	16.3	1	0.12	1	3FGLJ0805.4+7534	1.58
3HSPJ080610.6+020327	Yes	15.3	1	0.23	5	–	0.16
3HSPJ080625.9+593106	Yes	15.3	1	0.3	2	3FGLJ0806.6+5933	0.25
3HSPJ080938.9+345537	Yes	16.6	1	0.083	1	3FGLJ0809.6+3456	0.32
3HSPJ080949.1+521858	Yes	15.7	1	0.137	1	3FGLJ0809.8+5218	2.51
3HSPJ081003.2−752723	–	15.1	1	0.47	3	3FHLJ0811.0−7529	0.4
3HSPJ081012.0−703047	Yes	16.3	1	—	0	FL8YJ0809.9−7026	0.06
3HSPJ081201.8+023732	Yes	16.7	1	0.2	5	3FGLJ0812.0+0237	0.63

Source	2WHSP	Log $\nu_{\rm peak}$	flag	Z	flag	γ-ray counterpart	FOM
3HSPJ081231.2+282056	Yes	15.7	1	0.47	1	FL8YJ0812.6+2821	0.1
3HSPJ081240.8+650911	Yes	16.5	1	0.23	5	3FGLJ0813.3+6509	0.25
3HSPJ081258.3+153152	Yes	17.0	2	0.525	1	–	0.32
3HSPJ081305.6+714314	Yes	16.8	1	0.58	5	–	0.06
3HSPJ081338.0−035716	–	17.6	1	0.33	5	3FGLJ0813.5−0356	0.32
3HSPJ081343.5−754758	Yes	15.9	1	0.32	5	–	0.16
3HSPJ081421.2+294021	–	16.1	1	0.32	4	3FGLJ0814.5+2943	0.25
3HSPJ081435.3+183028	Yes	16.2	1	0.342	1	–	0.03
3HSPJ081539.8+655004	–	16.5	2	0.47	5	FL8YJ0815.4+6552	0.1
3HSPJ081602.9−121553	Yes	16.1	1	0.31	5	–	0.1
3HSPJ081627.1−131152	Yes	16.6	1	0.37	3	3FGLJ0816.4−1311	2.0
3HSPJ081750.9+324340	–	15.1	1	0.32	4	3FGLJ0818.0+3237	0.1
3HSPJ081915.3+064221	Yes	16.0	2	0.68	4	–	0.03
3HSPJ081917.5−075626	Yes	18.0	1	0.37	4	FL8YJ0819.4−0756	0.63
3HSPJ081941.8+053023	–	16.6	1	0.37	5	FL8YJ0819.5+0532	0.1
3HSPJ082021.9−280159	–	15.9	1	—	0	FL8YJ0820.2−2801	0.4
3HSPJ082030.8−031413	Yes	16.6	1	0.45	5	–	0.16
3HSPJ082051.1+235345	–	15.6	1	0.402	1	FL8YJ0820.9+2353	0.2
3HSPJ082130.2+213721	Yes	16.1	1	0.67	5	–	0.03
3HSPJ082253.2+701357	Yes	15.5	1	0.168	2	–	0.4
3HSPJ082314.5−632930	Yes	16.1	1	0.23	4	FL8YJ0823.2−6329	0.16
3HSPJ082320.5+112551	Yes	17.1	1	0.44	1	–	0.08
3HSPJ082355.6+394747	Yes	17.2	1	0.53	5	–	0.1
3HSPJ082406.5+613619	Yes	15.2	1	0.401	1	–	0.25
3HSPJ082427.8+624937	Yes	15.6	1	0.097	2	–	0.06
3HSPJ082555.2+401332	Yes	16.6	1	0.406	1	–	0.08
3HSPJ082627.8−640415	Yes	16.7	1	—	0	3FGLJ0826.3−6400	1.58
3HSPJ082706.1−070845	Yes	16.3	1	0.247	2	3FGLJ0827.2−0711	0.5
3HSPJ082707.0+084121	Yes	17.0	2	0.41	5	–	0.1
3HSPJ082707.1−310923	–	15.0	1	—	0	–	0.2
3HSPJ082801.1+231217	–	16.2	1	0.5	4	FL8YJ0828.0+2308	0.08
3HSPJ082814.2+415351	Yes	17.0	1	0.225	1	FL8YJ0828.4+4153	0.2
3HSPJ082904.8+175415	Yes	16.4	1	0.089	1	FL8YJ0829.1+1755	0.32
3HSPJ083010.9+523027	Yes	17.1	1	0.205	1	FL8YJ0830.0+5231	0.1
3HSPJ083015.1−094455	Yes	16.9	1	0.5	5	–	0.32
3HSPJ083117.3+513350	Yes	17.1	1	0.57	5	–	0.02
3HSPJ083133.0+174630	–	15.0	3	0.3	4	FL8YJ0831.5+1747	0.13
3HSPJ083251.4+330011	Yes	18.0	1	0.671	1	–	0.2
3HSPJ083357.0+472653	Yes	16.4	1	0.494	1	–	0.16
3HSPJ083417.5+182501	Yes	15.0	1	0.33	1	–	0.06
3HSPJ083713.3−185941	Yes	15.4	1	—	0	–	0.1
3HSPJ083724.6+145820	Yes	16.7	1	0.278	1	FL8YJ0837.3+1458	2.0
3HSPJ083918.7+361855	Yes	15.4	1	0.335	1	–	0.08
3HSPJ083952.6−054547	Yes	15.8	1	—	0	–	0.16
3HSPJ083955.1+121702	Yes	16.0	1	0.336	1	–	0.16
3HSPJ084018.8−191028	Yes	15.3	1	—	0	–	0.5
3HSPJ084121.6−355505	–	15.9	1	—	0	3FGLJ0841.3-3554	2.0
3HSPJ084225.5+025252	–	15.5	1	0.425	1	FL8YJ0842.4+0252	0.08
3HSPJ084310.2+503410	Yes	16.4	1	0.439	1	–	0.1
3HSPJ084345.8−194808	Yes	15.5	2	0.55	5	–	0.06
3HSPJ084452.2+280410	Yes	17.9	1	0.453	1	–	0.1
3HSPJ084701.5−233701	Yes	16.5	1	0.061	1	3FGLJ0846.9−2336	0.4
3HSPJ084712.9+113350	Yes	17.8	1	0.198	1	3FGLJ0847.1+1134	1.26
3HSPJ084827.9+811147	Yes	16.0	3	0.175	1	–	0.13
3HSPJ084839.6+050618	–	17.2	1	—	0	FL8YJ0848.7+0508	0.16
3HSPJ085036.1+345522	–	15.4	1	0.145	1	3FGLJ0850.2+3500	0.25
3HSPJ085102.9+054905	Yes	15.8	1	0.48	1	–	0.1

Source	2WHSP	Log $\nu_{\rm peak}$	flag	Z	flag	γ-ray counterpart	FOM
3HSPJ085242.9+430254	Yes	16.7	1	0.53	5	–	0.1
3HSPJ085310.5−365820	–	15.3	1	—	0	3FGLJ0853.0−3654	2.0
3HSPJ085315.8+072229	Yes	15.9	1	0.49	5	–	0.13
3HSPJ085406.5+482324	Yes	15.3	2	0.114	2	–	0.03
3HSPJ085409.8+440830	Yes	15.9	1	0.23	4	3FGLJ0854.2+4408	0.4
3HSPJ085410.1+275421	–	16.1	1	0.494	1	FL8YJ0854.0+2753	0.04
3HSPJ085440.1+162902	Yes	16.2	1	0.58	5	–	0.03
3HSPJ085549.3+423710	–	16.6	1	0.517	1	–	0.05
3HSPJ085627.2+602040	Yes	16.0	2	0.24	1	–	0.05
3HSPJ085659.2+513554	Yes	16.5	2	0.77	4	3FHLJ0856.8+5136	0.03
3HSPJ085730.1+062727	Yes	16.2	1	0.338	1	–	0.06
3HSPJ085749.8+013530	Yes	15.4	1	0.281	1	FL8YJ0857.6+0139	0.25
3HSPJ085802.8−313038	–	17.0	2	0.34	5	3FGLJ0858.1−3130	0.32
3HSPJ085834.3−071839	Yes	15.6	1	—	0	–	0.1
3HSPJ085910.2+834500	Yes	17.0	3	0.33	1	–	0.32
3HSPJ085920.5+004712	Yes	16.4	1	0.57	2	FL8YJ0859.8+0053	0.25
3HSPJ085930.6+621730	Yes	16.3	1	0.38	4	3FGLJ0859.1+6219	0.1
3HSPJ085958.4+560239	Yes	16.5	2	0.6	5	–	0.06
3HSPJ085958.6+294424	Yes	17.0	2	0.481	1	–	0.03
3HSPJ090038.6+674223	–	15.1	1	—	0	3FGLJ0900.0+6754	0.05
3HSPJ090051.6−154130	Yes	15.7	1	0.28	5	–	0.13
3HSPJ090132.0−043001	Yes	15.7	1	0.38	5	–	0.16
3HSPJ090133.8+671316	–	16.5	2	0.55	5	FL8YJ0901.5+6711	0.06
3HSPJ090200.1+431001	Yes	15.4	2	0.646	1	–	0.04
3HSPJ090314.6+405559	–	16.6	1	0.188	1	FL8YJ0903.5+4058	0.1
3HSPJ090317.9+344339	Yes	16.8	2	0.61	1	–	0.04
3HSPJ090416.8+725945	Yes	16.0	2	0.25	5	–	0.08
3HSPJ090523.0−053146	Yes	15.6	1	0.7	5	–	0.03
3HSPJ090534.9+135806	Yes	15.2	1	0.34	3	3FGLJ0905.5+1358	1.0
3HSPJ090802.2−095937	Yes	17.3	1	0.054	1	J090802.2−095936	0.32
3HSPJ090809.1−072708	Yes	16.4	1	0.22	5	–	0.06
3HSPJ090812.1+603540	Yes	16.2	2	0.294	1	–	0.16
3HSPJ090849.6+444604	Yes	16.9	2	0.348	1	–	0.04
3HSPJ090858.6−211854	Yes	15.7	1	0.33	5	2FGLJ0908.7−2119	0.25
3HSPJ090900.6+231112	Yes	15.2	1	0.223	1	3FGLJ0909.0+2310	0.32
3HSPJ090953.2+310603	Yes	17.0	1	0.272	1	FL8YJ0909.7+3105	0.5
3HSPJ091003.8−181612	–	16.5	2	0.45	5	FL8YJ0910.0−1815	0.08
3HSPJ091037.0+332924	Yes	15.0	1	0.35	2	3FGLJ0910.5+3329	1.58
3HSPJ091211.2+275927	–	15.1	1	0.56	3	3FGLJ0912.4+2800	0.1
3HSPJ091222.9−251825	Yes	16.5	2	0.33	5	–	0.16
3HSPJ091230.6+155527	Yes	17.1	1	0.212	1	3FGLJ0912.7+1556	0.2
3HSPJ091256.8+520947	Yes	17.7	2	0.411	1	–	0.06
3HSPJ091300.2−210320	Yes	17.1	1	0.198	1	3FGLJ0912.9−2104	1.58
3HSPJ091322.3+813305	Yes	17.0	2	0.639	2	FL8YJ0913.4+8134	0.16
3HSPJ091326.7+782923	Yes	16.1	1	0.47	5	–	0.04
3HSPJ091408.2−015945	Yes	15.9	1	—	0	FL8YJ0914.2−0202	0.08
3HSPJ091429.7+684508	–	15.0	3	0.45	5	FL8YJ0914.4+6844	0.1
3HSPJ091522.5−203625	Yes	15.6	1	—	0	–	0.1
3HSPJ091552.3+293324	Yes	15.4	1	0.19	3	3FGLJ0915.8+2933	1.58
3HSPJ091552.9+473820	Yes	16.5	2	0.407	1	–	0.04
3HSPJ091651.9+523828	Yes	15.9	1	0.19	1	FL8YJ0916.7+5238	0.4
3HSPJ091714.6−034314	Yes	16.6	1	0.308	1	3FGLJ0917.3−0344	0.2
3HSPJ091925.6+110659	Yes	15.9	1	0.425	1	–	0.06
3HSPJ091926.2−220042	Yes	15.8	1	0.45	5	3FGLJ0919.5−2200	0.08
3HSPJ092015.5+391013	Yes	17.0	1	0.607	1	–	0.03
3HSPJ092057.4−225721	Yes	17.7	1	0.32	4	3FGLJ0921.0−2258	0.4
3HSPJ092113.0+684902	Yes	15.4	1	—	0	–	0.06

Source	2WHSP	Log $\nu_{\rm peak}$	flag	Z	flag	γ-ray counterpart	FOM
3HSPJ092252.0+755403	Yes	16.4	1	0.4	5	–	0.08
3HSPJ092339.0+052649	Yes	16.0	2	0.27	5	–	0.13
3HSPJ092401.0+053345	Yes	16.8	1	0.57	1	3FGLJ0924.2+0534	0.25
3HSPJ092405.8+530033	Yes	16.5	2	0.64	1	–	0.03
3HSPJ092542.8+595816	Yes	15.8	1	0.7	3	3FGLJ0925.6+5959	0.08
3HSPJ092637.3−131233	Yes	16.7	1	0.138	1	–	0.08
3HSPJ092702.3+513733	Yes	16.7	1	0.413	1	–	0.03
3HSPJ092818.4+042109	Yes	16.1	1	0.3	5	–	0.08
3HSPJ092837.4+404845	–	15.4	1	0.55	3	3FGLJ0928.5+4048	0.2
3HSPJ093004.0+494331	Yes	17.4	1	0.573	1	–	0.03
3HSPJ093037.5+495025	Yes	17.5	1	0.187	1	3FGLJ0930.0+4951	1.0
3HSPJ093056.8+393335	Yes	17.0	2	0.639	1	–	0.1
3HSPJ093239.3+104235	Yes	16.2	1	0.361	1	FL8YJ0932.7+1041	0.2
3HSPJ093303.4+045235	Yes	16.6	1	0.378	1	–	0.08
3HSPJ093321.9+213211	Yes	16.1	1	0.43	5	–	0.03
3HSPJ093430.1−172120	Yes	17.7	1	0.25	1	FL8YJ0934.5−1720	0.5
3HSPJ093514.7−173658	–	15.2	1	0.29	5	3FGLJ0935.1−1736	0.16
3HSPJ093623.1−211039	–	16.2	1	0.53	3	3FGLJ0936.3−2114	0.08
3HSPJ093754.7−143350	–	15.1	1	0.27	5	3FGLJ0937.9−1435	0.2
3HSPJ093848.5+441644	Yes	16.5	2	0.615	1	–	0.03
3HSPJ093904.5+491622	Yes	16.3	1	0.403	1	–	0.05
3HSPJ093938.5−031503	Yes	15.6	1	—	0	–	0.13
3HSPJ094022.4+614826	Yes	16.3	1	0.21	1	3FGLJ0941.0+6151	0.32
3HSPJ094223.2+284414	–	15.7	1	0.366	1	FL8YJ0942.2+2841	0.03
3HSPJ094309.4+135132	Yes	16.0	2	0.569	1	–	0.03
3HSPJ094340.7+444215	Yes	16.5	1	0.48	5	–	0.05
3HSPJ094355.5−070950	Yes	17.6	1	0.433	1	–	0.1
3HSPJ094432.3+573535	Yes	15.9	1	0.717	2	–	0.06
3HSPJ094502.0−044833	Yes	16.2	1	0.43	5	–	0.05
3HSPJ094537.1−301333	Yes	16.1	1	0.43	5	–	0.08
3HSPJ094606.1+215138	Yes	16.7	1	0.489	1	–	0.04
3HSPJ094620.2+010451	Yes	17.9	1	0.577	1	3FGLJ0946.2+0103	0.32
3HSPJ094630.6+105202	Yes	16.9	1	0.161	1	FL8YJ0946.5+1051	0.16
3HSPJ094709.5−254059	Yes	15.7	1	—	0	3FGLJ0947.1−2542	0.79
3HSPJ094933.9+480826	Yes	16.8	1	0.728	1	–	0.02
3HSPJ095040.9+383044	Yes	16.5	2	0.5	4	–	0.04
3HSPJ095127.8+010210	Yes	15.5	1	0.5	2	–	0.1
3HSPJ095202.2−171443	Yes	16.2	1	0.45	5	–	0.05
3HSPJ095214.7+393615	Yes	16.5	1	0.58	4	FL8YJ0952.1+3932	0.13
3HSPJ095224.1+750213	Yes	17.6	1	0.181	1	FL8YJ0952.3+7503	0.2
3HSPJ095249.5+071330	–	15.3	1	0.31	5	3FGLJ0952.8+0711	0.1
3HSPJ095302.6−084018	Yes	15.3	1	0.37	3	3FGLJ0953.0−0839	1.0
3HSPJ095304.3−765801	Yes	16.1	1	0.25	5	3FGLJ0953.1−7657	0.4
3HSPJ095409.8+491459	Yes	16.3	1	0.41	2	3FGLJ0954.2+4913	0.2
3HSPJ095419.6−251958	–	15.0	2	0.32	5	FL8YJ0954.2−2520	0.08
3HSPJ095507.9+355100	Yes	17.7	1	0.557	2	FL8YJ0955.1+3551	0.32
3HSPJ095518.4−294611	Yes	15.1	1	—	0	–	0.2
3HSPJ095549.6+101429	Yes	15.8	1	0.373	1	–	0.04
3HSPJ095622.6−095514	Yes	15.8	1	0.31	5	–	0.13
3HSPJ095628.2−095719	Yes	17.3	1	0.161	1	FL8YJ0956.5−0957	0.32
3HSPJ095649.5+015601	Yes	17.0	2	0.65	4	–	0.04
3HSPJ095800.5+473734	Yes	15.3	1	0.485	1	2FGLJ0957.7+4735	0.03
3HSPJ095805.9−031740	Yes	16.6	1	0.43	4	3FGLJ0958.3−0318	0.2
3HSPJ095813.0−675242	Yes	16.3	1	0.21	5	3FGLJ0958.4−6752	0.5
3HSPJ095849.0+013219	Yes	17.4	1	0.42	4	–	0.08
3HSPJ095849.8+703959	Yes	16.2	1	0.31	5	FL8YJ0958.8+7039	0.05
3HSPJ095904.2−074413	Yes	15.1	1	—	0	–	0.13

Source	2WHSP	Log $\nu_{\rm peak}$	flag	Z	flag	γ-ray counterpart	FOM
3HSPJ095929.8+212321	Yes	16.5	1	0.36	1	3FGLJ0959.7+2124	0.25
3HSPJ095947.7−113725	Yes	16.3	1	0.45	5	–	0.06
3HSPJ100008.9−000319	Yes	17.4	1	0.63	5	–	0.02
3HSPJ100202.3+340836	Yes	16.4	1	0.412	1	–	0.03
3HSPJ100234.4+221614	Yes	17.3	1	0.4	4	3FGLJ1002.3+2220	0.32
3HSPJ100313.9+705912	Yes	15.0	2	—	0	–	0.04
3HSPJ100316.6+434401	Yes	15.0	1	0.48	5	–	0.03
3HSPJ100326.6+020455	–	15.9	1	0.48	4	FL8YJ1003.4+0205	0.1
3HSPJ100342.8−213809	–	17.0	2	0.17	5	FL8YJ1003.6−2138	0.2
3HSPJ100408.1+144909	Yes	17.0	1	0.712	1	–	0.04
3HSPJ100444.7+375211	Yes	16.4	1	0.44	1	–	0.13
3HSPJ100520.4+240504	Yes	16.5	1	0.476	1	–	0.08
3HSPJ100612.2+644011	Yes	15.9	1	0.39	4	FL8YJ1006.5+6441	0.16
3HSPJ100652.8−075545	Yes	15.2	1	0.4	5	–	0.06
3HSPJ100656.4+345445	Yes	15.0	1	0.612	1	3FGLJ1006.7+3453	0.13
3HSPJ100811.4+470521	Yes	17.4	1	0.343	1	–	0.5
3HSPJ101015.9−311908	Yes	16.8	1	0.14	1	3FGLJ1010.2−3120	1.58
3HSPJ101244.2+422957	Yes	16.9	1	0.365	1	3FGLJ1012.7+4229	0.32
3HSPJ101258.3+393238	Yes	15.7	1	0.17	1	–	0.08
3HSPJ101312.4+083209	Yes	16.5	1	0.602	1	–	0.06
3HSPJ101436.6−210142	Yes	16.3	1	0.45	5	–	0.1
3HSPJ101504.1+492600	Yes	16.4	1	0.2	3	3FGLJ1015.0+4925	3.98
3HSPJ101514.2−113803	Yes	17.2	2	0.151	1	–	0.1
3HSPJ101616.8+410812	Yes	17.3	1	0.27	1	–	0.2
3HSPJ101619.3−040705	Yes	15.5	1	0.48	5	–	0.05
3HSPJ101620.6−424722	–	15.5	1	0.25	5	3FGLJ1016.6−4244	0.2
3HSPJ101659.7+213316	Yes	16.3	1	—	0	–	0.02
3HSPJ101706.6+520247	Yes	15.8	1	0.379	1	FL8YJ1017.4+5204	0.06
3HSPJ101717.9−154933	Yes	15.8	1	0.53	5	–	0.08
3HSPJ101724.3+253956	–	15.0	2	0.417	1	FL8YJ1017.5+2535	0.05
3HSPJ101834.0+312833	Yes	17.0	3	0.161	1	–	0.2
3HSPJ101858.3+215958	Yes	15.8	1	0.572	2	–	0.06
3HSPJ102004.7−120959	Yes	15.2	1	—	0	–	0.06
3HSPJ102100.3+162554	Yes	16.1	1	0.556	2	FL8YJ1021.1+1625	0.2
3HSPJ102123.5−300220	Yes	16.4	1	0.29	4	–	0.08
3HSPJ102128.9+380644	Yes	16.2	1	0.467	1	–	0.06
3HSPJ102212.6+512400	Yes	18.2	1	0.142	1	–	0.4
3HSPJ102243.7−011302	Yes	17.1	1	0.22	4	3FGLJ1022.8−0113	1.0
3HSPJ102251.2+452141	Yes	16.5	2	0.58	5	–	0.03
3HSPJ102339.7+300057	Yes	16.0	1	0.433	1	3FGLJ1023.7+3000	0.13
3HSPJ102345.5−055523	Yes	17.6	1	0.423	1	–	0.05
3HSPJ102356.1−433601	Yes	15.9	1	0.32	3	3FGLJ1023.9−4335	2.0
3HSPJ102404.8−161935	Yes	15.7	1	0.44	5	–	0.06
3HSPJ102432.3−454426	–	17.0	1	0.37	5	3FGLJ1024.4−4545	0.16
3HSPJ102519.0−104106	Yes	16.0	1	0.6	5	–	0.05
3HSPJ102523.0+040229	Yes	16.2	1	0.208	1	–	0.1
3HSPJ102634.3−854314	Yes	15.0	1	—	0	3FGLJ1026.4−8542	0.63
3HSPJ102658.5−174858	Yes	15.7	1	0.114	2	3FGLJ1026.9−1750	0.79
3HSPJ102703.4+060933	Yes	16.5	1	0.449	1	3FGLJ1027.0+0609	0.2
3HSPJ102704.3+671618	Yes	15.7	1	0.27	5	–	0.05
3HSPJ102724.9+631752	Yes	15.5	1	0.58	3	3FGLJ1027.7+6316	0.13
3HSPJ102732.3+352622	Yes	17.2	1	0.47	4	–	0.1
3HSPJ102827.6+055515	Yes	16.0	1	0.234	1	–	0.03
3HSPJ102839.3+170210	Yes	16.3	1	0.169	1	–	0.1
3HSPJ103040.3−203036	Yes	15.2	1	0.28	5	3FGLJ1030.4−2030	0.1
3HSPJ103118.5+505335	Yes	16.9	1	0.16	4	3FGLJ1031.2+5053	2.0
3HSPJ103137.8−260716	Yes	17.0	3	0.25	5	–	0.2

Source	2WHSP	Log ν_{peak}	flag	Z	flag	γ-ray counterpart	FOM
3HSPJ103317.9+422236	–	15.8	1	0.211	1	FL8YJ1033.5+4222	0.08
3HSPJ103332.1-503528	–	15.7	1	0.24	5	3FGLJ1033.4−5035	0.5
3HSPJ103335.8−143627	Yes	15.9	1	0.367	1	–	0.16
3HSPJ103346.3+370824	Yes	17.1	1	0.448	1	FL8YJ1033.7+3707	0.13
3HSPJ103438.4−464403	–	17.1	1	0.33	5	FL8YJ1034.7−4645	0.25
3HSPJ103655.9−195424	Yes	16.2	1	0.3	5	–	0.06
3HSPJ103744.2+571155	Yes	15.5	1	0.33	3	3FGLJ1037.5+5711	1.58
3HSPJ103838.1+675516	Yes	16.7	1	0.5	5	–	0.13
3HSPJ103931.1+545548	Yes	17.7	1	0.617	2	–	0.05
3HSPJ104028.9+094753	Yes	16.7	1	0.304	1	–	0.13
3HSPJ104058.3+134150	Yes	16.8	1	0.7	3	3FGLJ1040.8+1342	0.32
3HSPJ104108.5−120330	Yes	15.4	1	0.31	5	3FGLJ1040.9−1205	0.05
3HSPJ104144.4+594257	Yes	15.9	1	0.425	1	–	0.03
3HSPJ104149.1+390119	Yes	16.5	1	0.21	1	3FGLJ1041.8+3901	0.13
3HSPJ104202.9−412929	–	15.3	1	0.25	5	3FGLJ1042.1−4126	0.16
3HSPJ104303.8+005420	Yes	17.1	1	0.4	4	FL8YJ1042.8+0054	0.32
3HSPJ104516.2+275133	Yes	15.4	1	0.7	3	–	0.1
3HSPJ104549.8−414310	Yes	16.4	1	0.26	4	–	0.2
3HSPJ104551.1−400041	Yes	16.3	1	0.243	1	–	0.1
3HSPJ104603.0+754040	Yes	16.4	1	0.52	5	–	0.08
3HSPJ104651.4−253545	Yes	18.0	3	0.25	1	3FGLJ1046.9−2531	1.26
3HSPJ104654.5−002835	Yes	15.4	1	0.74	5	–	0.01
3HSPJ104705.8+673758	–	15.0	2	0.5	5	FL8YJ1047.2+6741	0.03
3HSPJ104745.8+543741	Yes	15.8	1	0.54	2	–	0.05
3HSPJ104756.9−373730	Yes	15.9	1	—	0	3FGLJ1047.8−3737	0.25
3HSPJ104810.9+855958	Yes	16.0	2	0.23	5	–	0.1
3HSPJ104857.6+500945	Yes	17.2	1	0.403	1	FL8YJ1049.6+5012	0.08
3HSPJ104920.7+431525	Yes	16.5	2	0.5	4	–	0.05
3HSPJ104938.7+274212	–	16.4	1	0.144	1	FL8YJ1049.8+2741	0.05
3HSPJ105040.2+331004	Yes	16.7	1	0.63	4	–	0.05
3HSPJ105125.3+394325	Yes	16.8	1	0.497	1	3FGLJ1051.4+3941	0.25
3HSPJ105224.5+081409	–	16.8	1	0.223	1	3FGLJ1052.0+0816	0.25
3HSPJ105344.1+492956	Yes	15.8	1	0.14	1	3FGLJ1053.7+4929	0.32
3HSPJ105437.8+202740	Yes	16.7	1	0.225	1	–	0.08
3HSPJ105451.4+162607	Yes	15.8	1	0.505	1	–	0.06
3HSPJ105526.7+634234	Yes	15.4	1	—	0	–	0.04
3HSPJ105534.3−012616	Yes	16.2	1	0.33	4	FL8YJ1055.5−0126	0.25
3HSPJ105606.6+025213	Yes	17.7	1	0.236	1	–	0.63
3HSPJ105707.4+551032	Yes	15.7	1	0.7	3	FL8YJ1057.2+5510	0.08
3HSPJ105723.0+230318	Yes	16.9	1	0.379	1	–	0.32
3HSPJ105750.7−275410	Yes	16.3	1	0.091	1	3FGLJ1057.6−2754	0.32
3HSPJ105757.6+293714	Yes	16.9	1	0.57	5	–	0.06
3HSPJ105833.7+593218	Yes	17.4	2	0.591	1	–	0.01
3HSPJ105837.7+562811	Yes	15.1	1	0.143	1	3FGLJ1058.6+5627	2.0
3HSPJ105929.0−191221	Yes	15.3	1	0.222	1	–	0.32
3HSPJ110021.0+401927	Yes	16.2	1	0.225	2	3FGLJ1100.5+4020	0.5
3HSPJ110021.0+421053	Yes	16.0	1	0.323	1	–	0.08
3HSPJ110124.7+410847	Yes	15.6	1	0.38	4	3FGLJ1101.5+4106	0.13
3HSPJ110253.0−014906	Yes	16.6	1	0.56	5	FL8YJ1102.8−0148	0.08
3HSPJ110312.8+440116	Yes	15.5	2	0.411	1	–	0.06
3HSPJ110337.6−232930	Yes	17.3	1	0.186	1	3FGLJ1103.5−2329	5.01
3HSPJ110339.1−402402	Yes	15.5	1	0.22	5	–	0.25
3HSPJ110356.1+002236	Yes	15.7	1	0.275	1	–	0.08
3HSPJ110357.2+261118	Yes	17.1	1	0.712	2	FL8YJ1104.0+2610	0.13
3HSPJ110424.9+423454	Yes	17.0	1	0.453	1	–	0.08
3HSPJ110427.3+381231	Yes	16.3	1	0.03	1	3FGLJ1104.4+3812	39.81
3HSPJ110530.6+311436	Yes	15.4	1	0.42	2	–	0.05

Source	2WHSP	Log ν_{peak}	flag	Z	flag	γ-ray counterpart	FOM
3HSPJ110600.3+375445	Yes	16.5	2	0.64	5	–	0.02
3HSPJ110651.8+650604	Yes	16.5	2	0.73	5	–	0.04
3HSPJ110748.0+150210	Yes	15.6	1	0.25	2	3FGLJ1107.8+1502	0.32
3HSPJ110804.9+164820	Yes	17.9	1	0.476	1	–	0.04
3HSPJ110858.4−014931	Yes	16.7	1	0.106	1	–	0.2
3HSPJ110916.1+241120	–	15.7	1	0.35	2	3FGLJ1109.4+2411	0.2
3HSPJ110938.5+373611	–	15.0	2	0.398	1	3FGLJ1109.6+3734	0.13
3HSPJ111008.3−392615	Yes	15.8	1	0.29	5	–	0.06
3HSPJ111037.6+713356	Yes	15.2	1	—	0	3FGLJ1110.0+7134	0.2
3HSPJ111112.5+584657	Yes	16.5	2	0.642	2	–	0.03
3HSPJ111130.8+345203	Yes	17.1	1	0.68	3	–	0.32
3HSPJ111158.9+485701	Yes	16.1	1	0.44	4	FL8YJ1111.8+4858	0.06
3HSPJ111207.9+260803	Yes	16.1	1	0.45	1	–	0.16
3HSPJ111224.5+175121	Yes	16.9	1	0.42	1	3FGLJ1112.6+1749	0.25
3HSPJ111603.4+371036	Yes	15.7	1	0.269	1	–	0.1
3HSPJ111644.6+402635	–	15.7	1	0.202	1	–	0.08
3HSPJ111706.2+201407	Yes	15.9	1	0.138	1	3FGLJ1117.0+2014	2.0
3HSPJ111709.7+585921	Yes	16.0	1	0.081	1	–	0.1
3HSPJ111715.2−533813	–	15.9	1	—	0	3FGLJ1117.2−5338	0.2
3HSPJ111717.3+580124	Yes	16.0	2	0.75	5	–	0.01
3HSPJ111717.5+000633	Yes	17.3	1	0.451	1	J111717.5+000633	0.4
3HSPJ111757.2+535554	Yes	15.6	1	0.44	3	3FGLJ1117.9+5355	0.4
3HSPJ111806.8−813619	Yes	16.5	1	0.35	5	–	0.1
3HSPJ111810.8−164339	Yes	16.1	1	0.4	5	–	0.08
3HSPJ111939.5−304720	Yes	17.8	1	0.412	1	3FGLJ1119.7−3046	0.16
3HSPJ112048.0+421212	Yes	16.2	1	0.35	3	3FGLJ1120.8+4212	1.0
3HSPJ112059.7+014456	Yes	16.1	1	0.368	1	–	0.13
3HSPJ112211.6+431647	Yes	16.3	1	0.435	1	–	0.08
3HSPJ112313.2−090425	Yes	16.5	2	0.37	5	–	0.1
3HSPJ112318.0−323218	Yes	17.0	2	0.34	2	FL8YJ1123.2−3233	0.25
3HSPJ112349.1+722959	Yes	17.2	1	0.38	5	3FGLJ1123.6+7231	0.25
3HSPJ112405.3+204553	–	15.3	1	0.54	3	FL8YJ1124.1+2044	0.16
3HSPJ112410.5−371002	Yes	15.3	1	—	0	–	0.06
3HSPJ112414.7+234032	Yes	17.2	1	0.68	5	–	0.13
3HSPJ112453.8+493409	Yes	16.9	1	0.36	4	3FGLJ1124.9+4932	0.25
3HSPJ112502.8−265402	Yes	16.1	1	0.44	5	–	0.16
3HSPJ112503.6+214300	–	16.0	1	0.36	4	FL8YJ1124.9+2143	0.16
3HSPJ112508.6−210105	Yes	15.4	1	0.24	5	3FGLJ1125.0−2101	0.4
3HSPJ112551.9−074220	Yes	15.7	1	0.279	1	3FGLJ1125.8−0745	0.25
3HSPJ112611.9−203724	Yes	17.1	1	0.35	4	J112611.8−203723	0.2
3HSPJ112635.6−425212	Yes	16.7	1	0.29	5	–	0.2
3HSPJ112727.2+290829	Yes	16.5	2	0.57	4	–	0.04
3HSPJ112912.5−101349	Yes	15.5	1	—	0	FL8YJ1129.1−1014	0.08
3HSPJ112946.2+585057	Yes	15.4	1	0.75	4	–	0.02
3HSPJ113032.0−780105	Yes	17.9	1	0.23	5	3FGLJ1130.7−7800	1.0
3HSPJ113046.1−313807	Yes	16.9	1	0.151	1	FL8YJ1130.7−3137	0.25
3HSPJ113105.2−094406	Yes	16.4	1	0.33	5	FL8YJ1131.0−0944	0.25
3HSPJ113209.2−473853	Yes	17.5	3	0.21	5	3FGLJ1132.0−4736	0.5
3HSPJ113302.9+184704	Yes	16.7	1	0.716	1	–	0.1
3HSPJ113405.9+483904	Yes	16.5	1	0.749	1	–	0.04
3HSPJ113444.6−172901	Yes	17.6	1	0.571	1	FL8YJ1134.8−1730	0.16
3HSPJ113459.5+213456	Yes	16.7	2	0.602	1	–	0.02
3HSPJ113626.4+700927	Yes	16.8	1	0.045	1	3FGLJ1136.6+7009	3.16
3HSPJ113630.1+673704	Yes	18.1	1	0.134	1	3FGLJ1136.6+6736	1.58
3HSPJ113641.1+234726	Yes	15.4	1	0.38	5	–	0.1
3HSPJ113650.1+255052	–	15.2	1	0.155	1	3FGLJ1136.9+2551	0.2
3HSPJ113755.6−171042	Yes	17.7	1	0.6	1	FL8YJ1137.9−1708	0.79

Source	2WHSP	Log $\nu_{\rm peak}$	flag	Z	flag	γ-ray counterpart	FOM
3HSPJ113900.7+553035	Yes	16.8	1	0.63	4	–	0.08
3HSPJ113921.8+312930	Yes	16.5	2	0.509	1	–	0.04
3HSPJ113922.3+612644	Yes	15.4	1	0.53	5	–	0.01
3HSPJ114023.4+152809	Yes	16.2	1	0.24	1	3FGLJ1140.4+1529	0.5
3HSPJ114117.5+064123	Yes	17.0	3	0.672	2	–	0.08
3HSPJ114118.6+680429	Yes	15.3	1	0.57	5	3FGLJ1141.2+6805	0.03
3HSPJ114141.8−140754	Yes	16.4	1	0.32	5	3FGLJ1141.6−1406	0.25
3HSPJ114221.7+334201	Yes	15.8	1	0.409	1	–	0.06
3HSPJ114222.6−130643	Yes	15.3	1	0.33	5	–	0.1
3HSPJ114352.6+155821	Yes	16.6	1	0.67	2	–	0.08
3HSPJ114523.3+334744	Yes	16.5	2	0.51	5	–	0.06
3HSPJ114535.1−034001	Yes	16.9	1	0.167	1	–	0.25
3HSPJ114600.8−063854	–	16.3	1	0.37	5	3FGLJ1146.1−0640	0.13
3HSPJ114708.9−323003	Yes	16.7	1	0.37	4	–	0.2
3HSPJ114746.4+673906	Yes	16.4	1	0.78	5	–	0.01
3HSPJ114747.9−211640	Yes	16.8	1	0.35	5	–	0.13
3HSPJ114755.0+220539	Yes	16.3	2	0.276	1	–	0.2
3HSPJ114830.4−074508	Yes	15.2	1	—	0	–	0.2
3HSPJ114930.3+243926	Yes	17.1	1	0.402	1	3FGLJ1149.5+2443	0.5
3HSPJ115017.0+101652	Yes	17.5	1	0.284	1	–	0.1
3HSPJ115031.7−381832	Yes	15.8	1	0.3	5	–	0.1
3HSPJ115034.7+415439	Yes	15.6	1	0.32	3	3FGLJ1150.5+4155	0.63
3HSPJ115124.6+585917	–	15.0	1	0.3	3	3FGLJ1151.4+5858	1.0
3HSPJ115244.8+340638	Yes	16.5	2	0.705	2	–	0.03
3HSPJ115257.6+241345	Yes	17.6	2	0.175	1	–	0.08
3HSPJ115404.5−001009	Yes	16.6	1	0.254	1	3FGLJ1154.2−0010	0.25
3HSPJ115514.8−111122	–	17.3	1	0.47	5	3FGLJ1155.3−1112	0.05
3HSPJ115518.2+092641	Yes	15.3	1	0.47	4	–	0.06
3HSPJ115520.5−341719	Yes	15.5	1	—	0	3FGLJ1155.4−3417	0.5
3HSPJ115522.0−135110	Yes	15.3	1	0.47	5	–	0.04
3HSPJ115531.3+060855	Yes	16.7	1	0.368	1	–	0.03
3HSPJ115633.2−225004	Yes	15.3	1	—	0	3FGLJ1156.7−2250	0.16
3HSPJ115646.5+423807	Yes	16.2	1	0.172	1	–	0.06
3HSPJ115653.1+241246	Yes	16.2	1	0.145	1	–	0.2
3HSPJ115709.5+282200	Yes	16.6	1	0.3	1	–	0.1
3HSPJ115803.7−033337	Yes	16.5	2	0.37	5	–	0.06
3HSPJ115853.2+081943	Yes	16.1	1	0.29	1	3FGLJ1158.9+0818	0.13
3HSPJ115904.3+210209	Yes	16.6	1	0.35	1	–	0.13
3HSPJ115912.6−143154	–	16.5	2	0.48	5	FL8YJ1158.9−1430	0.08
3HSPJ120055.1−143039	–	16.2	1	0.48	5	3FGLJ1200.9−1432	0.08
3HSPJ120106.1−000701	Yes	16.5	1	0.165	1	–	0.08
3HSPJ120136.0−060734	Yes	15.4	1	—	0	–	0.08
3HSPJ120205.7+283326	Yes	17.0	1	0.379	1	–	0.06
3HSPJ120317.8−392620	Yes	15.7	1	—	0	3FGLJ1203.5−3925	0.4
3HSPJ120412.1+114555	Yes	16.6	1	0.296	1	3FGLJ1204.0+1144	0.5
3HSPJ120416.6−071009	–	15.0	1	0.184	1	3FGLJ1204.3−0708	0.79
3HSPJ120440.3+503927	Yes	15.1	1	0.7	5	–	0.01
3HSPJ120444.8−032144	Yes	16.6	1	0.7	5	–	0.08
3HSPJ120454.1+533037	Yes	17.3	1	0.402	1	–	0.03
3HSPJ120543.2+582933	Yes	16.3	1	0.4	2	–	0.04
3HSPJ120711.4−174605	–	17.3	1	0.7	3	–	0.25
3HSPJ120744.6+314851	Yes	16.8	1	0.67	1	–	0.13
3HSPJ120804.3+301549	–	15.0	3	0.33	4	FL8YJ1208.0+3017	0.13
3HSPJ120818.0−293759	Yes	16.4	1	0.249	1	–	0.1
3HSPJ120837.1+612106	–	15.6	1	0.275	1	FL8YJ1208.4+6121	0.13
3HSPJ120850.6+452951	Yes	17.5	2	0.654	1	–	0.04
3HSPJ120905.1−462948	Yes	15.4	1	—	0	FL8YJ1209.1−4629	0.08

Source	2WHSP	Log $\nu_{\rm peak}$	flag	Z	flag	γ-ray counterpart	FOM
3HSPJ120938.2+021017	Yes	16.2	1	0.291	2	–	0.1
3HSPJ121017.7+022343	Yes	16.0	2	0.383	1	–	0.08
3HSPJ121026.5+392908	Yes	17.7	1	0.617	1	–	0.25
3HSPJ121038.3−252713	Yes	16.6	1	0.47	5	–	0.13
3HSPJ121128.9−072239	Yes	16.3	1	0.28	5	–	0.06
3HSPJ121158.6+224233	Yes	17.6	1	0.453	1	FL8YJ1212.0+2242	0.5
3HSPJ121300.8+512935	Yes	16.0	1	0.796	2	3FGLJ1212.6+5135	0.13
3HSPJ121323.1−261807	Yes	17.7	1	0.278	1	3FGLJ1213.1−2619	1.0
3HSPJ121407.5+290328	Yes	16.6	1	0.469	1	–	0.06
3HSPJ121510.9+073204	Yes	16.3	1	0.137	1	FL8YJ1215.1+0731	0.5
3HSPJ121603.2−024304	Yes	15.9	1	0.359	2	FL8YJ1216.1−0242	0.13
3HSPJ121606.2+092909	–	15.9	1	0.094	1	FL8YJ1216.1+0930	0.16
3HSPJ121618.3+205957	Yes	16.8	2	0.607	1	–	0.1
3HSPJ121815.7+322344	Yes	17.0	1	0.63	1	–	0.02
3HSPJ121902.9+402442	Yes	15.7	1	0.5	5	–	0.04
3HSPJ121919.3+303937	Yes	15.7	1	0.243	1	–	0.05
3HSPJ121945.7−031423	Yes	16.0	1	0.299	1	3FGLJ1219.7−0314	0.32
3HSPJ122012.1−000306	Yes	15.8	1	0.7	3	–	0.1
3HSPJ122014.5−245948	–	17.0	3	0.48	5	3FGLJ1220.0−2502	0.32
3HSPJ122019.8−371414	Yes	16.0	1	0.28	5	3FGLJ1220.1−3715	0.32
3HSPJ122033.6+033807	Yes	15.7	1	0.8	5	–	0.01
3HSPJ122044.5+690525	Yes	17.0	2	0.36	5	3FGLJ1218.5+6912	0.2
3HSPJ122107.7+474228	Yes	16.8	1	0.21	1	–	0.13
3HSPJ122114.4+352239	Yes	16.7	1	0.51	1	–	0.03
3HSPJ122121.9+301037	Yes	16.8	1	0.18	1	3FGLJ1221.3+3010	3.16
3HSPJ122147.5−135158	Yes	15.0	1	0.26	5	–	0.08
3HSPJ122158.0+493413	Yes	16.5	1	0.598	1	–	0.02
3HSPJ122208.7+030718	Yes	17.5	3	0.503	1	–	0.32
3HSPJ122211.4+354058	Yes	15.3	1	0.57	3	–	0.1
3HSPJ122239.3−345841	Yes	16.0	1	—	0	–	0.1
3HSPJ122304.9+453444	Yes	17.0	1	0.43	5	–	0.03
3HSPJ122307.2+110038	Yes	16.4	1	0.5	4	FL8YJ1223.1+1059	0.1
3HSPJ122327.4+082030	–	15.1	1	—	0	3FGLJ1223.3+0818	0.06
3HSPJ122337.0−303250	Yes	16.3	1	0.26	5	3FGLJ1223.3−3028	0.4
3HSPJ122340.1+124203	Yes	15.9	1	0.34	5	–	0.05
3HSPJ122352.1+302726	Yes	16.7	1	0.63	5	–	0.03
3HSPJ122353.0+465048	Yes	15.5	1	0.25	1	FL8YJ1223.8+4650	0.06
3HSPJ122358.0+795328	–	15.1	1	0.29	5	3FGLJ1222.7+7952	0.04
3HSPJ122401.0+223939	–	15.6	1	0.482	1	FL8YJ1224.1+2239	0.06
3HSPJ122424.1+243623	Yes	16.1	1	0.218	1	3FGLJ1224.5+2436	1.26
3HSPJ122514.2+721447	Yes	17.5	3	0.114	1	–	0.32
3HSPJ122525.2−155317	Yes	16.2	1	0.34	5	–	0.08
3HSPJ122536.8−344721	–	16.3	1	0.31	5	3FGLJ1225.4−3448	0.2
3HSPJ122644.2+063853	Yes	15.9	1	0.583	1	3FGLJ1226.8+0638	0.5
3HSPJ122809.1−022136	Yes	16.8	1	0.323	1	–	0.16
3HSPJ122820.5+155655	Yes	15.8	1	0.232	1	–	0.13
3HSPJ122903.0−140251	Yes	16.1	1	0.47	5	–	0.1
3HSPJ122944.5+164004	Yes	16.8	1	0.682	2	–	0.1
3HSPJ123014.0+251807	Yes	15.0	1	0.135	2	3FGLJ1230.3+2519	3.98
3HSPJ123123.9+142124	Yes	15.4	1	0.256	1	3FGLJ1231.8+1421	0.32
3HSPJ123131.3+641418	Yes	16.4	1	0.163	1	3FGLJ1231.5+6414	0.32
3HSPJ123143.5+284749	–	15.0	1	0.236	1	3FGLJ1231.7+2847	0.79
3HSPJ123204.9−105600	–	16.3	1	0.19	5	–	0.04
3HSPJ123235.9−372056	–	16.3	1	0.25	5	3FGLJ1232.5−3720	0.1
3HSPJ123305.1+170133	–	16.1	1	0.24	4	3FGLJ1232.3+1701	0.32
3HSPJ123353.4+145925	Yes	16.1	1	0.52	5	–	0.03
3HSPJ123402.3+281502	Yes	16.4	1	0.424	1	–	0.1

Source	2WHSP	Log $\nu_{\rm peak}$	flag	Z	flag	γ-ray counterpart	FOM
3HSPJ123417.1−385635	Yes	16.2	1	0.236	1	–	0.4
3HSPJ123444.2−043622	–	15.0	3	—	0	3FGLJ1234.7−0437	0.2
3HSPJ123511.1−140323	Yes	17.0	1	0.4	1	–	0.32
3HSPJ123554.7+055213	Yes	16.3	1	0.682	1	–	0.04
3HSPJ123623.0+390000	–	15.1	1	0.389	1	3FGLJ1236.6+3901	0.1
3HSPJ123705.6+302005	Yes	17.3	1	0.33	2	–	0.13
3HSPJ123739.0+625842	Yes	16.0	1	0.297	1	3FGLJ1237.9+6258	0.25
3HSPJ123800.1+263553	Yes	16.8	1	0.21	1	–	0.03
3HSPJ123826.0+443137	Yes	16.0	1	0.312	1	–	0.03
3HSPJ123922.6+413251	Yes	16.0	3	0.16	2	–	0.13
3HSPJ124021.2−714857	–	17.4	1	0.21	5	3FGLJ1240.3−7149	0.79
3HSPJ124112.0+495548	Yes	17.7	1	0.225	1	–	0.03
3HSPJ124141.4+344030	Yes	17.2	1	0.54	1	FL8YJ1241.6+3438	0.4
3HSPJ124148.2+063601	Yes	16.2	1	0.51	3	3FGLJ1241.9+0639	0.2
3HSPJ124149.3−145558	Yes	15.1	1	0.44	3	3FGLJ1241.6−1456	0.63
3HSPJ124232.3+763417	Yes	16.6	1	0.48	5	3FHLJ1243.2+7634	0.1
3HSPJ124312.7+362743	Yes	16.1	1	0.31	3	3FGLJ1243.1+3627	3.16
3HSPJ124430.7+351003	Yes	16.5	2	0.65	5	–	0.04
3HSPJ124700.7+442318	Yes	16.2	1	0.6	2	3FGLJ1247.0+4421	0.2
3HSPJ124816.6+074258	Yes	17.2	1	0.57	1	–	0.04
3HSPJ124919.3−280834	Yes	16.0	1	0.15	5	3FGLJ1249.1−2808	0.32
3HSPJ124946.7+370747	–	15.6	1	0.286	2	3FGLJ1249.7+3705	0.13
3HSPJ125015.5+315559	Yes	16.4	1	0.6	3	J125015.4+315559	0.16
3HSPJ125117.8+103907	Yes	15.6	1	0.245	1	3FGLJ1251.3+1041	0.25
3HSPJ125134.8−295843	Yes	17.0	1	0.48	1	–	0.2
3HSPJ125300.9+382625	Yes	16.9	1	0.372	1	–	0.2
3HSPJ125341.2−393159	Yes	17.9	1	0.179	1	FL8YJ1253.6−3934	1.0
3HSPJ125346.9+032630	–	15.7	1	0.066	1	3FGLJ1253.7+0327	0.4
3HSPJ125359.3+624257	Yes	16.4	1	0.3	4	3FGLJ1254.1+6240	0.1
3HSPJ125408.1−280931	Yes	15.7	1	—	0	–	0.32
3HSPJ125433.2+221103	–	15.1	1	0.42	3	3FGLJ1254.5+2210	0.5
3HSPJ125445.4+470132	Yes	16.5	1	0.4	5	–	0.05
3HSPJ125447.0+175623	Yes	16.6	1	0.57	5	–	0.03
3HSPJ125447.6−142150	Yes	16.3	1	0.55	5	–	0.1
3HSPJ125449.2+570452	Yes	15.3	1	0.84	2	–	0.03
3HSPJ125509.8+280417	Yes	16.8	1	0.69	5	–	0.03
3HSPJ125528.6+091100	Yes	17.2	1	0.7	5	–	0.1
3HSPJ125548.0+141108	Yes	16.4	1	0.6	5	–	0.1
3HSPJ125615.9−114637	–	15.7	1	0.058	1	3FGLJ1256.3−1146	0.63
3HSPJ125639.3+060907	Yes	16.5	1	0.423	1	–	0.06
3HSPJ125708.3+264925	Yes	17.5	3	0.375	1	–	0.1
3HSPJ125723.9+483232	Yes	15.3	2	0.727	2	–	0.03
3HSPJ125731.9+241240	Yes	16.9	1	0.14	1	FL8YJ1257.6+2413	0.63
3HSPJ125820.8+612045	–	15.3	1	0.224	1	3FGLJ1258.0+6120	0.1
3HSPJ125822.8+062827	Yes	16.1	1	0.542	1	–	0.08
3HSPJ125848.0−044744	Yes	16.7	1	0.586	1	FL8YJ1258.7−0452	0.5
3HSPJ125908.6+412937	Yes	16.4	1	0.278	1	–	0.1
3HSPJ125949.8−374858	–	15.0	1	0.23	5	3FGLJ1259.8−3749	0.16
3HSPJ130058.5−231215	–	15.6	1	0.129	1	–	0.5
3HSPJ130145.6+405624	Yes	15.7	1	0.649	3	FL8YJ1301.6+4057	0.25
3HSPJ130255.2+505617	Yes	17.3	1	0.688	1	–	0.16
3HSPJ130420.9−435310	Yes	15.5	1	—	0	3FGLJ1304.3−4353	2.0
3HSPJ130531.2+385522	Yes	16.4	1	0.376	1	–	0.13
3HSPJ130619.7−023642	Yes	16.5	2	0.73	5	–	0.03
3HSPJ130630.9+192244	Yes	17.6	1	0.314	1	–	0.16
3HSPJ130711.9+115316	Yes	16.0	1	0.085	1	–	0.16
3HSPJ130713.3−034430	Yes	15.5	1	0.27	5	J130713.3−034430	0.16

Source	2WHSP	Log ν_{peak}	flag	Z	flag	γ-ray counterpart	FOM
3HSPJ130737.9−425938	Yes	15.9	1	—	0	3FGLJ1307.6−4300	3.16
3HSPJ130750.6+124828	Yes	16.2	1	0.58	5	–	0.03
3HSPJ130903.9−040611	Yes	15.3	1	0.39	1	–	0.5
3HSPJ130931.4−224425	Yes	16.2	1	0.38	5	–	0.06
3HSPJ131012.1−115749	Yes	15.9	1	0.14	1	3FGLJ1310.2−1159	0.32
3HSPJ131106.4+003509	Yes	15.0	1	0.418	2	3FGLJ1311.0+0036	0.2
3HSPJ131146.0+395317	–	15.3	1	0.159	2	FL8YJ1311.8+3953	0.04
3HSPJ131155.7+085340	Yes	17.1	1	0.469	1	–	0.16
3HSPJ131234.6−185901	Yes	15.8	1	0.48	4	FL8YJ1312.5−1901	0.06
3HSPJ131248.7−235047	Yes	15.3	1	0.29	5	3FGLJ1312.7−2349	0.16
3HSPJ131330.1+020105	Yes	15.7	1	0.356	1	–	0.13
3HSPJ131440.6−090148	Yes	17.0	2	0.43	5	–	0.13
3HSPJ131503.3−423649	Yes	17.6	1	0.105	1	3FGLJ1314.7−4237	2.51
3HSPJ131532.6+113331	Yes	16.9	1	0.36	4	3FGLJ1315.4+1130	0.4
3HSPJ131552.9−073302	–	15.2	1	—	0	3FGLJ1315.7−0732	1.26
3HSPJ131639.8+205514	Yes	16.3	1	0.255	1	–	0.13
3HSPJ131654.5+301454	Yes	16.3	1	0.55	4	FL8YJ1316.6+3013	0.08
3HSPJ131719.9+543512	Yes	15.9	1	0.394	1	–	0.13
3HSPJ131921.2+775822	–	16.5	2	0.21	5	3FGLJ1319.6+7759	0.32
3HSPJ131931.7+140533	–	15.2	1	0.573	1	3FGLJ1319.3+1402	0.32
3HSPJ132001.1+344445	Yes	16.4	1	0.88	5	–	0.03
3HSPJ132057.4+222516	–	16.0	1	0.234	1	–	0.06
3HSPJ132140.6−343752	Yes	16.0	1	0.142	1	–	0.2
3HSPJ132231.4+134430	Yes	16.8	1	0.377	1	–	0.08
3HSPJ132239.2+494336	Yes	17.5	3	0.33	1	–	0.16
3HSPJ132244.2+664942	Yes	15.7	1	0.47	5	–	0.06
3HSPJ132301.0+043951	Yes	16.8	1	0.224	1	3FGLJ1322.9+0435	0.25
3HSPJ132358.3+140559	Yes	15.8	1	0.32	4	3FGLJ1323.9+1405	0.16
3HSPJ132527.5−280521	Yes	15.5	1	—	0	–	0.08
3HSPJ132531.7+662102	Yes	16.7	1	0.21	1	–	0.06
3HSPJ132541.8−022809	Yes	17.9	1	0.8	2	J132541.8−022809	0.2
3HSPJ132556.0+080928	Yes	16.5	2	0.46	5	–	0.06
3HSPJ132614.9+293330	Yes	16.3	1	0.431	1	3FGLJ1326.1+2931	0.32
3HSPJ132617.7+122958	Yes	16.8	1	0.204	1	FL8YJ1326.2+1231	0.25
3HSPJ132635.9+254958	Yes	16.8	1	0.698	1	–	0.03
3HSPJ132744.9−082936	Yes	16.2	1	0.5	5	–	0.08
3HSPJ132833.5+114520	Yes	17.3	1	0.49	2	FL8YJ1328.7+1144	0.2
3HSPJ132840.6−472749	Yes	15.4	1	—	0	3FGLJ1328.5−4728	0.32
3HSPJ132845.8+720402	Yes	15.8	1	0.25	5	–	0.1
3HSPJ132949.0+071418	Yes	15.3	2	0.582	1	–	0.02
3HSPJ133021.5+444120	Yes	15.6	1	0.31	4	3FGLJ1330.0+4437	0.16
3HSPJ133025.8+700138	Yes	15.0	1	0.23	5	3FGLJ1330.6+7002	0.16
3HSPJ133040.6+565520	Yes	15.4	1	0.41	4	–	0.05
3HSPJ133044.2+470359	Yes	16.3	1	0.69	5	–	0.01
3HSPJ133046.0+113940	Yes	17.6	2	0.53	1	–	0.04
3HSPJ133102.9+565541	Yes	17.8	1	0.27	1	FL8YJ1331.0+5653	0.16
3HSPJ133105.7−002221	Yes	16.1	1	0.243	1	–	0.05
3HSPJ133155.3−125816	–	15.1	1	0.53	5	–	0.03
3HSPJ133302.1−125916	–	15.8	1	0.1	5	–	0.1
3HSPJ133325.9+623541	Yes	16.1	1	0.48	4	–	0.06
3HSPJ133529.7−295038	Yes	17.8	1	0.51	2	3FGLJ1335.4−2949	0.32
3HSPJ133612.1+231958	Yes	16.1	1	0.267	1	FL8YJ1336.2+2319	0.16
3HSPJ133647.2+602048	Yes	16.5	2	0.32	1	–	0.04
3HSPJ133806.3−093114	Yes	15.0	1	—	0	–	0.03
3HSPJ133844.6+412231	Yes	17.0	1	0.469	1	–	0.02
3HSPJ133922.1+474212	Yes	16.3	1	0.54	5	–	0.03
3HSPJ133937.8+183059	Yes	16.3	1	0.11	1	–	0.13

Source	2WHSP	Log $\nu_{\rm peak}$	flag	Z	flag	γ-ray counterpart	FOM
3HSPJ134029.8+441004	Yes	17.2	1	0.54	1	3FGLJ1340.6+4412	0.25
3HSPJ134042.0−041006	Yes	15.2	1	0.25	5	3FGLJ1340.6−0408	0.2
3HSPJ134105.1+395945	Yes	17.7	1	0.172	1	3FGLJ1341.0+3955	0.5
3HSPJ134223.4−313557	Yes	15.7	1	—	0	–	0.25
3HSPJ134240.3+093911	Yes	15.5	1	0.43	4	3FGLJ1342.7+0945	0.08
3HSPJ134249.7+035846	Yes	16.0	1	0.57	4	–	0.05
3HSPJ134251.0−353142	Yes	16.1	2	0.125	1	–	0.13
3HSPJ134347.4+002023	Yes	16.8	1	0.242	1	–	0.03
3HSPJ134428.2+045029	Yes	17.4	2	0.472	1	–	0.03
3HSPJ134525.1+231038	Yes	16.1	1	0.32	1	–	0.05
3HSPJ134545.0+702903	Yes	16.0	1	0.6	5	–	0.06
3HSPJ134621.3+080837	Yes	16.5	2	0.56	4	–	0.05
3HSPJ134706.8−295842	Yes	15.3	1	—	0	3FGLJ1346.9−2958	0.63
3HSPJ134853.4+075647	Yes	16.1	1	0.25	1	–	0.2
3HSPJ134951.1+421647	Yes	17.0	1	0.289	1	–	0.1
3HSPJ135043.8−310927	Yes	15.4	1	—	0	–	0.2
3HSPJ135117.4−153015	–	15.0	2	0.25	5	3FGLJ1351.8−1524	0.16
3HSPJ135120.8+111453	Yes	16.0	1	0.51	3	3FGLJ1351.4+1115	0.4
3HSPJ135126.9−000116	Yes	15.2	1	—	0	–	0.02
3HSPJ135132.9−263318	Yes	15.5	1	—	0	–	0.25
3HSPJ135159.6+041212	Yes	15.8	1	0.257	1	–	0.05
3HSPJ135206.8+425237	Yes	16.5	2	0.57	4	–	0.05
3HSPJ135328.0+560056	Yes	16.4	1	0.404	1	FL8YJ1353.4+5600	0.2
3HSPJ135340.2−663957	Yes	15.6	1	—	0	3FGLJ1353.5−6640	1.0
3HSPJ135345.1−393710	Yes	16.1	1	0.37	5	FL8YJ1353.7−3937	0.16
3HSPJ135406.6+532744	Yes	17.6	1	0.472	1	–	0.05
3HSPJ135537.4+251508	Yes	17.3	1	0.546	1	–	0.03
3HSPJ135650.1−071336	Yes	17.2	1	0.3	4	–	0.08
3HSPJ135712.9−014600	Yes	17.0	2	0.547	1	–	0.13
3HSPJ135758.2+055128	Yes	15.8	1	—	0	–	0.02
3HSPJ135856.2+365424	Yes	16.6	1	0.47	4	–	0.03
3HSPJ135908.8+332206	Yes	15.7	1	0.442	1	–	0.03
3HSPJ135922.6−020010	Yes	16.8	1	0.57	4	–	0.08
3HSPJ140022.0−400823	Yes	16.4	1	0.27	5	FL8YJ1400.1−4010	0.16
3HSPJ140027.0−293936	Yes	17.5	3	0.48	5	–	0.16
3HSPJ140108.7−232235	Yes	15.4	1	0.34	3	–	0.32
3HSPJ140121.1+520928	Yes	17.5	3	0.482	1	–	0.2
3HSPJ140150.2−294149	Yes	16.3	1	0.094	1	–	0.13
3HSPJ140203.8+674104	Yes	15.7	1	—	0	–	0.13
3HSPJ140245.0+632020	Yes	16.5	2	0.34	1	–	0.06
3HSPJ140350.2+243304	Yes	15.8	1	0.34	1	–	0.1
3HSPJ140449.6+655431	Yes	16.5	1	0.363	1	3FGLJ1404.8+6554	0.25
3HSPJ140450.8+040202	Yes	15.6	1	0.37	3	3FGLJ1404.8+0401	0.79
3HSPJ140519.6+305351	Yes	15.5	1	0.34	1	–	0.05
3HSPJ140550.2+231113	Yes	16.3	1	0.53	4	–	0.04
3HSPJ140609.5−250809	Yes	15.0	1	—	0	3FGLJ1406.0−2508	0.2
3HSPJ140630.0−393509	Yes	17.1	1	0.37	4	FL8YJ1406.6−3934	0.2
3HSPJ140630.1+123620	Yes	17.0	2	0.45	4	–	0.2
3HSPJ140635.8−005548	Yes	16.4	1	0.255	1	–	0.16
3HSPJ140641.4+481824	Yes	16.0	1	0.098	2	–	0.06
3HSPJ140642.7+530833	Yes	16.1	1	0.458	1	–	0.03
3HSPJ140653.5+272606	Yes	16.7	1	0.203	1	–	0.1
3HSPJ140659.1+164207	Yes	17.2	1	0.54	3	3FGLJ1406.6+1644	0.32
3HSPJ140705.2+104810	Yes	15.7	1	0.33	4	–	0.06
3HSPJ140710.3+380335	Yes	16.6	1	0.83	5	–	0.03
3HSPJ140711.4−184215	–	16.2	1	0.33	5	–	0.06
3HSPJ140713.0−070939	Yes	16.6	1	0.45	5	–	0.08

Source	2WHSP	Log $\nu_{\rm peak}$	flag	Z	flag	γ-ray counterpart	FOM
3HSPJ140734.0+120941	Yes	16.6	1	0.72	5	–	0.03
3HSPJ140848.1+221433	Yes	16.7	2	0.291	1	–	0.06
3HSPJ140919.1+135240	Yes	16.6	2	0.58	1	–	0.16
3HSPJ140923.5+593940	Yes	15.6	1	0.496	1	–	0.1
3HSPJ140954.8−104857	Yes	15.1	1	—	0	–	0.1
3HSPJ141003.9+051557	Yes	15.4	1	0.544	1	–	0.04
3HSPJ141012.3+113547	Yes	16.5	1	0.52	5	–	0.06
3HSPJ141027.0+275954	Yes	16.3	1	0.63	5	–	0.03
3HSPJ141029.5+282055	Yes	15.9	1	0.521	1	3FGLJ1410.4+2821	0.25
3HSPJ141030.8+610012	Yes	17.1	1	0.384	1	–	0.1
3HSPJ141046.0+740511	–	15.1	1	—	0	3FGLJ1410.9+7406	0.08
3HSPJ141133.3−072253	–	16.7	1	0.32	5	3FGLJ1411.4−0724	0.08
3HSPJ141136.3−024033	Yes	16.0	2	0.28	5	–	0.02
3HSPJ141140.5+340424	Yes	16.4	1	0.421	1	–	0.06
3HSPJ141208.2+383521	–	16.1	1	0.45	4	FL8YJ1412.0+3837	0.03
3HSPJ141324.6+484535	Yes	15.6	1	0.66	5	–	0.0
3HSPJ141358.4+764455	Yes	15.3	1	0.18	5	–	0.79
3HSPJ141409.2+343058	Yes	15.7	1	0.275	1	–	0.08
3HSPJ141427.0+035752	Yes	17.9	1	0.669	2	–	0.25
3HSPJ141446.2+163907	Yes	16.5	2	0.65	5	–	0.03
3HSPJ141457.7−002058	–	15.3	1	0.139	1	–	0.05
3HSPJ141612.1−241813	–	15.9	1	0.136	1	3FGLJ1416.1−2417	0.13
3HSPJ141706.5+624638	Yes	17.0	2	0.323	1	–	0.04
3HSPJ141750.0+593527	Yes	15.5	1	0.629	2	–	0.03
3HSPJ141756.6+254325	Yes	17.6	1	0.24	1	3FGLJ1417.8+2540	1.58
3HSPJ141821.7+355355	–	16.2	1	0.33	5	–	0.03
3HSPJ141826.3−023333	Yes	15.5	1	0.356	3	3FGLJ1418.4−0233	2.0
3HSPJ141828.6+354249	–	15.4	1	0.47	5	3FGLJ1418.5+3543	0.13
3HSPJ141839.7+243332	Yes	16.0	2	0.7	5	–	0.03
3HSPJ141900.3+773229	Yes	16.0	1	0.27	3	3FGLJ1418.9+7731	0.4
3HSPJ141905.0+133346	Yes	16.3	1	0.45	5	–	0.08
3HSPJ141927.4+044513	–	15.0	1	0.7	3	3FGLJ1419.5+0449	0.16
3HSPJ142041.6+554449	Yes	16.5	2	0.72	5	–	0.02
3HSPJ142227.4+233740	Yes	16.4	1	0.726	1	–	0.04
3HSPJ142238.8+580155	Yes	17.8	1	0.638	1	3FGLJ1422.8+5801	1.0
3HSPJ142320.6+053000	Yes	16.3	1	0.543	1	–	0.04
3HSPJ142412.3−175008	–	15.6	1	0.082	1	3FGLJ1424.3−1753	0.25
3HSPJ142421.1+370552	Yes	17.0	1	0.29	1	–	0.1
3HSPJ142422.9+343356	Yes	16.6	1	0.576	1	–	0.2
3HSPJ142452.6−143101	Yes	15.9	1	0.42	5	–	0.1
3HSPJ142508.1+664938	Yes	16.0	1	—	0	–	0.04
3HSPJ142526.1−011825	–	15.0	1	0.4	4	FL8YJ1425.4−0120	0.05
3HSPJ142645.5+241523	Yes	16.2	1	0.44	4	–	0.16
3HSPJ142659.5−255833	Yes	17.0	1	0.31	4	–	0.25
3HSPJ142710.5+054130	Yes	16.2	1	0.36	4	–	0.2
3HSPJ142723.0+590730	Yes	16.5	2	0.73	5	–	0.02
3HSPJ142725.9−182303	–	15.0	2	0.36	5	FL8YJ1427.4−1823	0.13
3HSPJ142739.5−252102	Yes	16.0	3	0.318	1	–	0.16
3HSPJ142745.8+390832	Yes	15.8	1	0.165	1	–	0.05
3HSPJ142829.8+743002	Yes	16.7	1	0.31	5	FL8YJ1428.9+7428	0.06
3HSPJ142832.6+424020	Yes	18.1	1	0.129	1	3FGLJ1428.5+4240	3.98
3HSPJ142904.6+120410	Yes	16.5	2	0.7	3	–	0.13
3HSPJ142918.1−013854	Yes	17.1	1	0.5	5	–	0.1
3HSPJ143005.0+412707	Yes	16.6	1	0.663	1	–	0.08
3HSPJ143109.5+271020	Yes	16.0	1	0.2	1	–	0.08
3HSPJ143117.4+110833	Yes	16.2	1	0.48	4	–	0.08
3HSPJ143211.6+764355	Yes	16.0	1	0.53	5	FL8YJ1432.5+7647	0.08

Source	2WHSP	Log $\nu_{\rm peak}$	flag	Z	flag	γ-ray counterpart	FOM
3HSPJ143327.6+244117	Yes	16.0	1	0.33	4	–	0.1
3HSPJ143342.7−730438	Yes	18.0	3	0.23	5	J143342.7−730437	1.0
3HSPJ143441.4+664026	–	15.4	1	0.35	5	3FGLJ1434.6+6640	0.08
3HSPJ143554.9+395729	Yes	15.5	1	0.755	1	–	0.04
3HSPJ143657.7+563925	Yes	16.8	1	0.381	2	3FGLJ1436.8+5639	0.5
3HSPJ143803.2−031511	Yes	16.2	1	0.27	5	–	0.06
3HSPJ143824.0+085724	Yes	16.0	2	0.58	5	–	0.04
3HSPJ143825.5+120418	Yes	17.1	1	0.848	1	FL8YJ1438.8+1203	0.16
3HSPJ143917.4+393242	Yes	15.9	1	0.344	1	3FGLJ1439.2+3931	1.26
3HSPJ143921.2−124312	Yes	16.1	1	0.29	5	–	0.2
3HSPJ143924.4+390411	Yes	15.5	1	0.17	1	–	0.08
3HSPJ143932.0+064015	Yes	17.0	2	0.3	5	–	0.2
3HSPJ143950.8−395518	Yes	15.7	1	—	0	3FGLJ1440.0−3955	0.5
3HSPJ143959.4−234140	–	16.2	1	0.25	5	FL8YJ1440.0−2343	0.25
3HSPJ144037.8−384654	Yes	17.3	1	0.27	4	3FGLJ1440.4−3845	1.26
3HSPJ144052.9+061016	–	15.1	1	0.396	2	3FGLJ1440.9+0610	0.5
3HSPJ144110.2+010216	Yes	16.1	1	0.43	5	–	0.02
3HSPJ144127.9−193552	–	15.0	2	—	0	FL8YJ1441.3−1934	0.1
3HSPJ144201.5+064230	Yes	17.0	1	0.693	2	–	0.04
3HSPJ144236.4−462301	Yes	15.8	1	0.103	1	FL8YJ1442.6−4623	0.2
3HSPJ144248.2+120040	Yes	17.7	1	0.16	1	3FGLJ1442.8+1200	1.26
3HSPJ144334.4+251558	–	15.3	1	0.529	1	FL8YJ1443.6+2515	0.06
3HSPJ144357.1−390839	Yes	15.7	1	0.065	1	3FGLJ1444.0−3907	3.16
3HSPJ144434.9+633606	Yes	17.4	1	0.297	1	–	0.16
3HSPJ144436.9−250931	Yes	16.3	1	0.33	5	–	0.13
3HSPJ144446.0+474257	Yes	16.1	1	0.581	2	–	0.03
3HSPJ144503.7+080202	Yes	17.0	2	0.55	5	–	0.13
3HSPJ144506.2−032612	Yes	17.2	1	0.31	3	3FGLJ1445.0−0328	1.26
3HSPJ144644.8−182925	Yes	15.6	1	—	0	3FGLJ1446.8−1831	0.1
3HSPJ144656.8−265658	–	17.6	1	0.32	5	FL8YJ1447.0−2658	1.0
3HSPJ144743.6+460916	Yes	15.8	1	0.68	4	–	0.03
3HSPJ144800.5+360831	Yes	15.1	1	0.28	3	3FGLJ1448.0+3608	0.63
3HSPJ144941.8−091000	Yes	16.0	1	0.21	5	FL8YJ1449.7−0910	0.13
3HSPJ145021.3−273052	Yes	16.1	1	0.33	5	–	0.1
3HSPJ145044.4−065005	Yes	16.1	1	0.45	5	–	0.1
3HSPJ145127.7+635419	Yes	17.0	3	0.65	1	3FGLJ1451.2+6355	0.2
3HSPJ145224.5−414950	–	16.3	1	0.26	5	FL8YJ1452.0−4148	0.13
3HSPJ145301.9+255953	Yes	15.8	1	0.66	4	–	0.03
3HSPJ145400.8−120154	Yes	15.3	1	—	0	–	0.25
3HSPJ145427.1+512433	–	15.3	1	0.39	3	3FGLJ1454.5+5124	0.5
3HSPJ145508.2+192015	Yes	16.8	2	0.115	1	J145508.2+192014	0.13
3HSPJ145543.6−760052	Yes	16.0	1	—	0	FL8YJ1455.6−7600	0.32
3HSPJ145550.3+635906	Yes	15.7	1	0.39	5	–	0.1
3HSPJ145603.6+504826	Yes	17.1	1	0.479	2	FL8YJ1456.0+5050	0.4
3HSPJ145631.5+635035	Yes	16.1	1	0.29	5	–	0.08
3HSPJ145707.4+185438	Yes	16.6	2	0.373	1	–	0.05
3HSPJ145741.7−464210	–	15.5	2	0.16	5	FL8YJ1457.8−4642	0.63
3HSPJ145820.7+412101	Yes	15.5	1	0.17	1	–	0.08
3HSPJ145827.3+483245	Yes	17.2	1	0.541	2	–	0.25
3HSPJ145948.6+314112	Yes	16.7	1	0.636	2	–	0.02
3HSPJ150020.2−020122	Yes	16.4	1	0.273	1	–	0.06
3HSPJ150106.6+422235	Yes	16.2	1	0.298	1	–	0.03
3HSPJ150235.4−052823	Yes	16.5	2	0.53	5	–	0.16
3HSPJ150316.5+165117	–	15.0	2	0.39	4	FL8YJ1503.3+1651	0.1
3HSPJ150340.6−154113	Yes	17.6	1	0.38	3	3FGLJ1503.7−1540	1.0
3HSPJ150355.9+655941	Yes	17.0	2	0.52	5	–	0.05
3HSPJ150425.6−004742	Yes	16.0	1	0.35	5	–	0.05

Source	2WHSP	Log $\nu_{\rm peak}$	flag	Z	flag	γ-ray counterpart	FOM
3HSPJ150426.7+302405	Yes	16.5	2	0.45	5	–	0.06
3HSPJ150507.0+012129	Yes	16.9	2	0.641	1	–	0.01
3HSPJ150525.4−824231	Yes	16.5	2	0.39	5	3FGLJ1504.5−8242	0.16
3HSPJ150604.4+102232	Yes	16.0	2	0.67	5	–	0.05
3HSPJ150637.1−054004	Yes	17.1	1	0.518	1	FL8YJ1506.4−0540	0.2
3HSPJ150644.4+081400	Yes	15.3	1	0.376	2	3FGLJ1506.6+0811	0.5
3HSPJ150651.2+553209	Yes	16.6	1	0.68	5	–	0.01
3HSPJ150653.8+021904	Yes	16.5	2	0.22	1	–	0.04
3HSPJ150654.7−215925	Yes	15.4	1	0.13	2	–	0.2
3HSPJ150708.2+454334	Yes	16.0	2	0.356	1	–	0.02
3HSPJ150714.3+550420	Yes	15.4	1	0.474	1	–	0.03
3HSPJ150716.4+172103	Yes	15.7	1	0.565	1	3FGLJ1507.4+1725	0.1
3HSPJ150826.6+014645	Yes	16.2	1	0.507	1	–	0.03
3HSPJ150842.6+270908	Yes	17.8	1	0.27	1	3FGLJ1508.6+2709	0.79
3HSPJ150858.3+315438	Yes	16.0	2	0.58	5	–	0.03
3HSPJ150901.9+724354	Yes	15.3	1	—	0	–	0.16
3HSPJ150947.9+555617	–	15.0	1	0.2	4	3FGLJ1509.7+5556	0.25
3HSPJ151041.1+333504	Yes	17.5	3	0.114	1	J151041.0+333503	0.63
3HSPJ151136.8−165326	Yes	16.1	1	0.36	2	J151136.8−165326	0.2
3HSPJ151148.5−051346	Yes	17.1	1	—	0	3FGLJ1511.8−0513	1.26
3HSPJ151154.8+562936	Yes	17.0	2	0.56	1	–	0.02
3HSPJ151212.7−225508	Yes	15.5	1	0.315	1	3FGLJ1512.2−2255	0.32
3HSPJ151234.5+162840	Yes	17.5	1	0.187	1	–	0.05
3HSPJ151324.1−075451	Yes	16.8	2	0.04	1	–	0.16
3HSPJ151402.9+312612	Yes	16.5	1	0.57	5	–	0.08
3HSPJ151428.0−252053	Yes	15.9	1	0.42	5	–	0.08
3HSPJ151433.7+190319	Yes	15.7	1	0.36	4	–	0.08
3HSPJ151444.0−772254	–	16.3	1	—	0	FL8YJ1514.4−7719	0.25
3HSPJ151549.8−305817	Yes	15.4	1	—	0	–	0.2
3HSPJ151556.1+242620	Yes	16.3	1	0.228	1	FL8YJ1515.9+2423	0.05
3HSPJ151618.7−152344	Yes	18.0	1	0.33	5	J151618.7−152344	0.4
3HSPJ151641.5+291810	Yes	16.0	1	0.13	1	–	0.16
3HSPJ151747.5+652523	Yes	16.3	1	0.702	1	3FGLJ1517.6+6524	1.58
3HSPJ151802.4+651057	Yes	16.5	1	0.55	5	–	0.08
3HSPJ151803.5−273131	Yes	15.3	1	0.14	5	3FGLJ1518.0−2732	0.63
3HSPJ151826.6+075222	Yes	15.9	1	0.41	1	FL8YJ1518.4+0750	0.13
3HSPJ151838.8+404500	–	16.1	1	0.065	1	FL8YJ1518.6+4044	0.08
3HSPJ151845.7+061356	Yes	17.2	1	0.102	1	FL8YJ1518.6+0613	0.63
3HSPJ151915.8+553645	Yes	15.9	1	0.52	5	–	0.03
3HSPJ152039.3−054641	Yes	16.1	1	0.13	5	–	0.16
3HSPJ152048.8−034851	–	15.1	1	—	0	3FGLJ1520.8−0348	0.5
3HSPJ152110.6+104054	Yes	15.6	1	0.4	5	–	0.04
3HSPJ152213.8−074818	Yes	15.3	1	0.4	5	–	0.1
3HSPJ152316.0+583515	Yes	16.0	1	0.35	1	–	0.06
3HSPJ152418.5−414655	Yes	15.5	1	—	0	–	0.32
3HSPJ152559.4−242813	Yes	16.5	2	0.097	1	–	0.16
3HSPJ152603.1−083146	–	15.5	1	0.35	5	3FGLJ1525.8−0834	0.1
3HSPJ152624.8−070223	Yes	15.5	1	0.26	5	–	0.08
3HSPJ152625.0+575855	Yes	16.5	2	0.77	5	–	0.02
3HSPJ152646.6−153026	Yes	15.9	1	0.21	4	FL8YJ1526.7−1529	0.25
3HSPJ152810.8−673056	–	16.1	1	—	0	FL8YJ1528.4−6729	1.26
3HSPJ152835.7+200420	–	16.2	1	0.52	5	FL8YJ1528.5+2003	0.1
3HSPJ152913.5+381217	Yes	15.8	1	0.27	4	FL8YJ1529.2+3811	0.2
3HSPJ153103.7−861226	Yes	15.5	1	—	0	–	0.32
3HSPJ153120.7+564907	Yes	16.8	1	0.62	5	–	0.05
3HSPJ153152.3+262053	Yes	16.6	1	0.6	5	–	0.03
3HSPJ153202.2+301628	Yes	16.0	1	0.065	1	3FGLJ1532.0+3018	0.32

Source	2WHSP	Log $\nu_{\rm peak}$	flag	Z	flag	γ-ray counterpart	FOM
3HSPJ153211.5+482024	Yes	16.5	2	0.747	2	–	0.03
3HSPJ153305.8+524758	Yes	16.0	2	0.476	1	–	0.02
3HSPJ153311.2+185429	Yes	17.2	1	0.305	1	3FGLJ1533.2+1852	0.63
3HSPJ153324.2+341640	Yes	15.5	1	0.41	3	3FGLJ1533.5+3416	0.32
3HSPJ153447.2+371554	–	15.3	1	0.143	1	3FGLJ1535.0+3721	0.32
3HSPJ153500.7+532037	Yes	17.1	1	0.59	3	3FGLJ1534.4+5323	0.63
3HSPJ153529.6−313346	Yes	15.6	1	0.27	5	–	0.13
3HSPJ153544.8+155850	Yes	16.1	1	—	0	–	0.02
3HSPJ153623.0+122211	Yes	15.6	1	0.362	1	–	0.05
3HSPJ153646.7+013800	Yes	18.0	3	0.311	1	–	0.4
3HSPJ153651.0+394506	Yes	16.0	1	0.63	5	–	0.01
3HSPJ153737.0+340148	Yes	17.2	1	0.327	1	–	0.03
3HSPJ153941.2−112835	Yes	15.7	1	0.22	5	3FGLJ1539.8−1128	0.63
3HSPJ153955.2−181436	Yes	15.7	1	—	0	–	0.2
3HSPJ154015.9+815505	Yes	16.1	1	—	0	3FGLJ1540.1+8155	1.26
3HSPJ154150.0+141437	–	15.0	1	0.223	1	3FGLJ1541.6+1414	0.13
3HSPJ154203.0−291509	Yes	16.7	1	0.49	3	FL8YJ1541.9−2915	0.79
3HSPJ154347.1+163153	Yes	16.7	1	0.28	5	–	0.06
3HSPJ154418.7+045821	Yes	16.3	1	0.326	1	–	0.16
3HSPJ154433.1+322148	Yes	15.5	1	0.32	4	FL8YJ1544.9+3218	0.08
3HSPJ154439.3−112804	–	18.4	1	—	0	3FGLJ1544.6−1125	0.32
3HSPJ154458.8−664146	–	17.3	1	0.23	5	3FGLJ1545.0−6641	0.63
3HSPJ154512.4+091133	Yes	17.0	2	0.365	1	–	0.03
3HSPJ154534.6−001928	Yes	16.3	1	0.6	5	–	0.03
3HSPJ154546.5−233928	–	16.2	1	0.121	1	FL8YJ1545.7−2336	0.16
3HSPJ154604.2+081913	Yes	15.1	1	0.35	3	3FGLJ1546.0+0818	0.4
3HSPJ154625.0−285723	Yes	16.0	2	0.4	4	J154625.0−285723	0.13
3HSPJ154712.1−280221	Yes	15.8	1	0.28	4	3FGLJ1547.1−2801	0.16
3HSPJ154819.1−025903	Yes	15.5	1	—	0	–	0.06
3HSPJ154827.3−211106	Yes	16.4	1	0.44	5	–	0.1
3HSPJ154849.7−225102	Yes	16.2	1	0.192	1	3FGLJ1548.8−2250	1.26
3HSPJ154902.0+482157	Yes	16.5	2	0.63	4	–	0.05
3HSPJ154918.6+423500	Yes	16.0	1	0.49	4	FL8YJ1549.3+4235	0.06
3HSPJ154939.7+195355	Yes	17.0	2	0.748	2	–	0.03
3HSPJ154943.0−292349	Yes	16.2	1	0.38	5	–	0.1
3HSPJ154946.3−304501	Yes	16.3	1	—	0	3FGLJ1549.9−3044	0.16
3HSPJ154952.0−065907	Yes	16.3	1	0.29	5	3FGLJ1549.7−0658	0.4
3HSPJ154954.5+582607	Yes	17.0	2	0.35	5	–	0.1
3HSPJ155053.2−082246	Yes	15.7	1	0.27	5	FL8YJ1550.8−0822	0.32
3HSPJ155210.2+315909	Yes	17.8	1	0.584	1	–	0.1
3HSPJ155214.4+601710	Yes	16.5	2	0.5	5	–	0.02
3HSPJ155333.5−311830	–	15.3	1	0.21	3	3FGLJ1553.5−3118	1.0
3HSPJ155412.0+241426	Yes	16.8	1	0.301	1	–	0.16
3HSPJ155424.1+201125	Yes	17.4	1	0.273	1	3FGLJ1554.4+2010	0.63
3HSPJ155432.5−121325	Yes	16.7	1	0.33	5	FL8YJ1554.4−1215	0.16
3HSPJ155533.4+780929	Yes	15.8	1	—	0	–	0.06
3HSPJ155543.0+111124	Yes	15.6	1	0.36	2	3FGLJ1555.7+1111	7.94
3HSPJ155703.0+244218	Yes	16.0	2	0.438	1	–	0.03
3HSPJ155720.8+094321	Yes	17.0	3	0.201	1	–	0.08
3HSPJ155812.9+004452	Yes	16.6	1	0.59	4	–	0.1
3HSPJ155850.3−034552	Yes	15.7	1	0.5	5	–	0.06
3HSPJ155900.6+451657	Yes	16.7	1	0.53	4	–	0.06
3HSPJ155941.9+634415	Yes	15.9	1	0.55	5	–	0.06
3HSPJ160005.3−252439	Yes	16.4	1	0.26	5	3FGLJ1559.8−2525	0.2
3HSPJ160135.4+161239	Yes	16.7	1	0.528	1	–	0.08
3HSPJ160218.0+305109	Yes	15.5	1	0.47	3	FL8YJ1602.2+3051	0.25
3HSPJ160258.8+421203	Yes	17.0	3	0.466	1	–	0.32

Source	2WHSP	Log $\nu_{\rm peak}$	flag	Z	flag	γ-ray counterpart	FOM
3HSPJ160307.9−244949	Yes	16.8	1	—	0	–	0.1
3HSPJ160339.4+500955	–	16.5	1	0.4	4	FL8YJ1603.8+5009	0.1
3HSPJ160446.5+334521	Yes	17.2	1	0.177	1	–	0.06
3HSPJ160519.0+542059	Yes	17.9	1	0.212	1	FL8YJ1605.5+5424	0.2
3HSPJ160533.1+091745	Yes	15.8	1	0.205	2	–	0.13
3HSPJ160618.4+134532	Yes	16.0	1	0.29	1	J160618.4+134532	0.32
3HSPJ160620.8+563017	Yes	16.0	3	0.45	1	3FGLJ1606.1+5630	0.06
3HSPJ160740.6+254113	Yes	17.0	2	0.534	1	–	0.4
3HSPJ161003.3+451641	–	16.3	1	0.596	1	–	0.08
3HSPJ161004.0+671026	Yes	17.5	2	0.27	4	–	0.25
3HSPJ161046.4−664901	Yes	15.9	1	0.11	5	3FGLJ1610.8−6649	2.0
3HSPJ161139.7+852541	–	15.0	2	0.22	5	–	0.1
3HSPJ161140.1+234519	Yes	16.1	1	0.65	5	–	0.1
3HSPJ161204.8−043815	Yes	16.5	2	0.7	3	–	0.16
3HSPJ161327.1−190836	Yes	15.5	1	0.31	5	FL8YJ1613.4−1907	0.1
3HSPJ161414.0+544251	Yes	17.8	1	0.45	5	–	0.05
3HSPJ161443.9-085120	Yes	16.7	1	0.5	5	–	0.1
3HSPJ161608.4+224107	–	16.0	1	0.33	1	–	0.13
3HSPJ161632.9+375603	Yes	18.0	1	0.2	1	–	0.2
3HSPJ161737.7−104734	Yes	15.6	1	—	0	–	0.16
3HSPJ161757.9+602416	Yes	15.8	1	0.75	5	–	0.02
3HSPJ161946.5+193416	Yes	16.6	1	0.52	5	–	0.03
3HSPJ162007.8+323027	Yes	16.4	1	0.778	1	–	0.03
3HSPJ162044.3+343511	Yes	16.4	1	0.36	1	–	0.06
3HSPJ162115.2−003140	Yes	16.3	1	0.414	2	J162115.1−003140	0.16
3HSPJ162142.3+454828	Yes	16.3	1	0.389	1	–	0.03
3HSPJ162259.2+440142	Yes	16.3	1	0.38	4	–	0.1
3HSPJ162330.5+085724	Yes	17.0	3	0.533	1	FL8YJ1623.4+0857	0.13
3HSPJ162332.3+284129	Yes	15.2	1	0.377	2	–	0.1
3HSPJ162458.6+220330	Yes	16.5	2	0.68	5	–	0.03
3HSPJ162625.8+351341	Yes	16.0	1	0.498	1	3FGLJ1626.1+3512	0.2
3HSPJ162642.8+080314	Yes	16.5	1	0.25	1	–	0.04
3HSPJ162646.0+630048	Yes	17.1	1	0.2	5	FL8YJ1626.5+6257	0.2
3HSPJ162712.9+314956	–	15.0	2	0.58	1	FL8YJ1627.3+3148	0.04
3HSPJ162819.3+363010	Yes	16.7	1	0.77	5	–	0.03
3HSPJ162839.0+252756	Yes	16.7	1	0.22	1	–	0.16
3HSPJ162920.1+263352	Yes	16.1	1	0.65	5	–	0.04
3HSPJ162939.4+701449	Yes	16.0	1	—	0	–	0.04
3HSPJ162950.5+584050	Yes	15.5	1	—	0	–	0.04
3HSPJ162957.9+531105	Yes	16.4	1	0.345	1	–	0.08
3HSPJ163043.1+522138	–	15.3	1	—	0	3FGLJ1630.7+5222	0.4
3HSPJ163119.7+102404	Yes	15.8	1	0.42	5	–	0.04
3HSPJ163124.7+421702	Yes	16.5	1	0.47	1	–	0.13
3HSPJ163146.7+414632	–	15.7	1	0.58	5	FL8YJ1631.8+4143	0.05
3HSPJ163213.8+580052	–	15.4	1	0.32	5	FL8YJ1632.3+5801	0.13
3HSPJ163309.0+700550	Yes	15.9	1	—	0	–	0.03
3HSPJ163417.0+330520	Yes	17.0	3	—	0	–	0.02
3HSPJ163559.4+183158	Yes	15.4	1	0.3	5	–	0.08
3HSPJ163658.4−124836	Yes	17.5	1	0.24	1	–	0.16
3HSPJ163709.4+432600	–	15.3	1	0.343	1	FL8YJ1637.3+4326	0.16
3HSPJ163715.3+463948	Yes	16.5	2	0.67	5	–	0.02
3HSPJ163716.7+131438	Yes	15.8	1	0.559	2	3FGLJ1637.1+1314	0.1
3HSPJ163726.6+454749	–	15.4	1	0.192	1	FL8YJ1637.6+4548	0.16
3HSPJ163751.0−344915	–	15.0	1	—	0	3FGLJ1637.6−3449	0.79
3HSPJ163801.6+732615	Yes	16.0	1	—	0	3FGLJ1637.8+7325	0.13
3HSPJ163808.8+004222	–	15.7	1	0.35	5	FL8YJ1638.1+0041	0.13
3HSPJ163920.6+560902	Yes	15.3	1	—	0	–	0.05

Source	2WHSP	Log $\nu_{\rm peak}$	flag	Z	flag	γ-ray counterpart	FOM
3HSPJ164011.0+062826	–	15.0	3	0.31	5	FL8YJ1640.2+0629	0.08
3HSPJ164014.9+685234	Yes	15.9	1	0.26	5	FL8YJ1640.2+6850	0.32
3HSPJ164213.9+654308	Yes	16.3	1	0.57	5	–	0.05
3HSPJ164220.3+221143	Yes	16.5	1	0.592	1	FL8YJ1642.4+2212	0.2
3HSPJ164319.2+213107	–	16.0	2	0.154	1	–	0.1
3HSPJ164328.9−064619	Yes	15.3	1	0.082	1	3FGLJ1643.6−0642	0.2
3HSPJ164339.4+331647	Yes	15.7	1	0.42	5	FL8YJ1643.7+3317	0.04
3HSPJ164345.6−111925	Yes	16.3	1	0.4	5	–	0.06
3HSPJ164419.9+454644	Yes	16.3	1	0.225	1	FL8YJ1644.1+4545	0.2
3HSPJ164438.6−015202	Yes	15.7	1	—	0	–	0.13
3HSPJ164549.6+792129	Yes	16.5	1	0.16	5	–	0.16
3HSPJ164651.7−132848	–	15.4	1	0.3	5	3FGLJ1646.9−1332	0.13
3HSPJ164702.6+385001	Yes	16.5	2	0.135	1	–	0.03
3HSPJ164720.9+132306	Yes	16.2	1	0.5	5	–	0.04
3HSPJ164845.1+800512	Yes	16.6	1	0.18	5	–	0.1
3HSPJ165139.9+721824	Yes	16.5	1	0.24	5	3FGLJ1651.6+7219	0.16
3HSPJ165221.1+493253	Yes	17.1	1	0.3	4	–	0.1
3HSPJ165249.9+402310	Yes	15.4	1	0.31	3	FL8YJ1652.8+4024	0.16
3HSPJ165352.2+394536	Yes	17.9	1	0.03	1	3FGLJ1653.9+3945	12.59
3HSPJ165419.6+470803	Yes	15.1	1	—	0	–	0.06
3HSPJ165431.0+651952	Yes	15.3	1	—	0	–	0.02
3HSPJ165504.1+660100	Yes	16.2	1	0.5	5	–	0.03
3HSPJ165517.9−224045	Yes	16.5	2	0.4	4	J165517.8−224045	0.32
3HSPJ165655.1−201056	Yes	16.2	1	0.23	4	3FGLJ1656.8−2010	0.79
3HSPJ165746.7+675527	Yes	15.3	1	—	0	–	0.13
3HSPJ165937.9+682618	–	16.2	1	0.05	1	–	0.13
3HSPJ170052.6+332431	Yes	16.5	2	0.383	1	–	0.05
3HSPJ170054.3+462853	Yes	16.5	2	0.365	1	–	0.03
3HSPJ170132.2+381103	Yes	16.0	2	0.6	5	–	0.02
3HSPJ170238.5+311543	Yes	15.4	1	0.32	4	3FGLJ1702.6+3116	0.1
3HSPJ170409.5+123421	–	16.4	1	0.4	2	3FGLJ1704.1+1234	0.25
3HSPJ170433.8−052840	Yes	16.2	1	0.3	5	3FGLJ1704.4−0528	0.25
3HSPJ170534.8+604215	Yes	15.9	1	0.28	1	–	0.06
3HSPJ170622.7+063847	Yes	16.3	1	0.45	5	–	0.08
3HSPJ170807.7+473223	Yes	15.4	1	—	0	–	0.05
3HSPJ170941.6+623918	Yes	15.8	1	0.63	5	–	0.03
3HSPJ171002.1+552033	Yes	16.3	1	0.53	5	–	0.1
3HSPJ171008.9+610223	Yes	16.3	1	—	0	–	0.06
3HSPJ171105.8+120812	Yes	15.7	1	0.43	5	–	0.08
3HSPJ171108.6+024404	Yes	16.8	1	0.46	5	J171108.5+024403	0.2
3HSPJ171116.6+572518	Yes	16.4	1	0.43	5	–	0.08
3HSPJ171248.7+293116	–	15.3	1	0.42	3	3FGLJ1712.6+2932	0.32
3HSPJ171405.4−202752	Yes	16.6	1	0.09	5	3FGLJ1714.1−2029	1.0
3HSPJ171419.7+371612	Yes	16.5	2	0.48	5	–	0.06
3HSPJ171427.3+560155	Yes	16.6	1	0.401	1	–	0.04
3HSPJ171531.4+205935	Yes	16.1	1	0.177	1	–	0.13
3HSPJ171553.2+884415	Yes	16.3	1	0.48	5	3FGLJ1711.6+8846	0.1
3HSPJ171610.1+433756	Yes	15.6	1	0.48	5	–	0.04
3HSPJ171622.9+480246	Yes	15.4	1	0.43	5	–	0.05
3HSPJ171841.4+360522	Yes	16.2	1	0.35	1	–	0.04
3HSPJ171902.3+552434	Yes	17.5	1	0.627	2	–	0.06
3HSPJ171921.4+120721	Yes	15.7	1	0.34	5	3FGLJ1719.3+1206	0.08
3HSPJ172034.9+100511	Yes	16.0	2	0.5	5	–	0.06
3HSPJ172504.3+115215	Yes	15.7	1	0.18	3	3FGLJ1725.0+1152	2.51
3HSPJ172658.2+263436	Yes	16.5	1	0.26	5	–	0.1
3HSPJ172818.6+501310	Yes	17.0	1	0.055	1	3FGLJ1728.3+5013	3.16
3HSPJ172838.3+704102	Yes	16.8	1	0.551	1	–	0.1

Source	2WHSP	Log $\nu_{\rm peak}$	flag	Z	flag	γ-ray counterpart	FOM
3HSPJ172918.7+525559	Yes	16.1	1	0.349	1	–	0.25
3HSPJ173044.7+380454	Yes	16.1	1	0.22	5	–	0.05
3HSPJ173328.9+451950	Yes	16.4	1	0.317	1	–	0.05
3HSPJ173605.2+203301	Yes	16.8	1	—	0	3FGLJ1736.0+2033	0.5
3HSPJ173842.4+382102	Yes	16.5	2	0.31	5	–	0.16
3HSPJ174017.3+432450	Yes	16.7	1	0.48	5	–	0.04
3HSPJ174108.9−733814	Yes	16.2	1	0.29	5	–	0.25
3HSPJ174357.5+375310	Yes	15.7	1	—	0	–	0.05
3HSPJ174357.8+193509	Yes	17.8	1	0.08	1	3FGLJ1743.9+1934	1.0
3HSPJ174419.7+185218	Yes	15.8	1	0.39	5	FL8YJ1744.4+1851	0.2
3HSPJ174442.8+134802	–	16.2	1	0.23	5	–	0.16
3HSPJ174459.5−172639	–	16.4	1	—	0	3FGLJ1744.9−1725	1.26
3HSPJ174537.7+395130	–	16.2	1	0.267	1	3FGLJ1745.7+3952	0.13
3HSPJ174632.3+502810	–	16.5	2	0.43	5	–	0.04
3HSPJ174702.5+493801	Yes	17.7	1	0.46	1	FL8YJ1747.2+4937	0.2
3HSPJ174837.6−085440	–	17.0	2	0.33	5	FL8YJ1748.5−0854	0.04
3HSPJ174929.9+463135	Yes	16.3	1	0.53	5	–	0.06
3HSPJ175040.7+431131	Yes	15.9	1	—	0	–	0.06
3HSPJ175052.7+550750	Yes	15.2	1	0.29	5	–	0.04
3HSPJ175156.8+655117	Yes	15.2	1	0.42	5	–	0.04
3HSPJ175328.0+321848	Yes	17.6	1	0.5	5	–	0.06
3HSPJ175600.6+332924	Yes	15.2	1	—	0	–	0.03
3HSPJ175615.9+552218	Yes	16.9	1	0.657	3	3FGLJ1756.3+5523	0.79
3HSPJ175713.0+703337	Yes	17.3	1	0.407	1	3FGLJ1756.9+7032	0.32
3HSPJ175751.3−453506	Yes	15.7	1	—	0	–	0.25
3HSPJ175949.1+703718	Yes	15.5	1	—	0	FL8YJ1800.2+7038	0.1
3HSPJ175955.2+150109	Yes	17.5	2	0.6	5	–	0.04
3HSPJ180002.0+281045	Yes	17.1	1	0.44	5	FL8YJ1800.1+2812	0.2
3HSPJ180143.9+295055	Yes	17.0	2	0.45	5	FL8YJ1801.8+2948	0.13
3HSPJ180158.9+610938	Yes	15.6	1	—	0	–	0.13
3HSPJ180311.4+723504	Yes	15.1	1	—	0	–	0.04
3HSPJ180354.3+654825	Yes	16.0	1	0.085	2	FL8YJ1803.4+6548	0.04
3HSPJ180408.8+004222	Yes	17.1	1	0.087	1	–	1.26
3HSPJ180409.3+562122	Yes	16.6	1	0.55	5	–	0.08
3HSPJ180431.9+614112	Yes	15.1	1	0.27	5	–	0.03
3HSPJ180451.3+322026	Yes	16.3	1	0.31	5	–	0.1
3HSPJ180732.1+642926	–	15.0	1	0.239	1	3FGLJ1807.8+6427	0.08
3HSPJ180832.7+510407	Yes	15.4	1	0.29	5	–	0.16
3HSPJ180845.6+241905	Yes	17.3	1	0.45	5	FL8YJ1808.8+2419	0.1
3HSPJ180849.6+352042	–	15.0	2	0.22	5	3FGLJ1809.0+3517	0.08
3HSPJ180925.4+204131	Yes	15.0	1	0.28	3	3FGLJ1809.4+2040	0.63
3HSPJ181118.0+034113	Yes	15.8	1	—	0	3FGLJ1811.2+0340	1.0
3HSPJ181403.4+382810	Yes	15.9	1	0.35	5	FL8YJ1814.0+3828	0.16
3HSPJ182020.9+362343	Yes	16.3	1	0.33	5	3FGLJ1820.3+3625	0.16
3HSPJ182338.5−345412	Yes	16.6	1	—	0	3FGLJ1823.6−3453	2.51
3HSPJ182419.0+430949	Yes	17.8	1	0.487	1	3FGLJ1824.4+4310	0.4
3HSPJ182531.9+601922	Yes	16.2	1	0.25	5	–	0.06
3HSPJ182833.5−592054	Yes	17.7	1	—	0	–	0.32
3HSPJ182854.7−241735	–	16.2	1	0.05	5	3FGLJ1828.9−2417	0.32
3HSPJ182924.2+540259	–	15.0	1	—	0	3FGLJ1829.4+5402	0.32
3HSPJ183141.0+422130	Yes	15.9	1	0.6	5	–	0.06
3HSPJ183200.9+382137	Yes	15.6	1	0.22	5	FL8YJ1831.7+3822	0.13
3HSPJ183229.3+512128	Yes	15.1	1	—	0	–	0.03
3HSPJ183806.7−600032	Yes	15.5	1	0.18	5	3FGLJ1838.5−6006	0.2
3HSPJ183820.6−602522	Yes	15.9	2	0.121	1	FL8YJ1838.4−6022	0.2
3HSPJ183849.1+480234	Yes	16.0	1	0.3	2	3FGLJ1838.8+4802	1.58
3HSPJ184120.3+590608	Yes	16.5	1	0.53	1	–	0.06

Source	2WHSP	Log ν_{peak}	flag	Z	flag	γ-ray counterpart	FOM
3HSPJ184121.7+290940	Yes	16.1	1	0.18	5	3FGLJ1841.2+2910	0.5
3HSPJ184147.0+321839	Yes	16.2	1	0.24	5	3FGLJ1841.7+3218	0.25
3HSPJ184207.4+521702	Yes	16.0	1	0.43	5	–	0.06
3HSPJ184229.8−584157	–	17.1	1	0.33	5	3FGLJ1842.3−5841	0.79
3HSPJ184425.3+154645	–	15.1	1	0.11	5	3FGLJ1844.3+1547	0.79
3HSPJ184430.8+544144	Yes	15.2	1	0.234	2	–	0.25
3HSPJ184445.6−324641	–	15.0	2	—	0	FL8YJ1844.8−3248	0.25
3HSPJ184514.1+555242	Yes	16.4	1	0.61	5	–	0.06
3HSPJ184642.6+561627	Yes	17.4	1	0.32	5	–	0.08
3HSPJ184822.5+653657	Yes	17.7	1	0.364	1	FL8YJ1848.5+6537	0.13
3HSPJ184847.1+424539	Yes	17.8	1	0.4	5	3FGLJ1848.9+4247	0.63
3HSPJ184919.4−164723	–	16.5	2	0.16	5	3FGLJ1849.3−1645	0.5
3HSPJ184951.6+745318	Yes	15.2	1	0.4	5	–	0.05
3HSPJ185024.0+263153	Yes	16.1	1	0.22	5	FL8YJ1850.5+2631	0.2
3HSPJ185352.0+671355	Yes	17.2	2	0.212	1	FL8YJ1853.9+6715	0.2
3HSPJ185550.8+805223	Yes	15.7	1	—	0	–	0.03
3HSPJ185813.4+432451	Yes	17.4	1	0.17	5	FL8YJ1858.3+4321	0.25
3HSPJ190411.8+362658	Yes	17.5	2	0.13	5	3FGLJ1904.5+3627	0.32
3HSPJ191052.1+285624	–	16.7	1	0.33	5	3FGLJ1910.8+2855	0.32
3HSPJ191129.7−190824	–	17.0	2	0.16	5	3FGLJ1911.4−1908	0.5
3HSPJ191251.1−124918	–	15.4	1	—	0	FL8YJ1912.7−1249	0.25
3HSPJ191401.8+443832	–	15.7	1	0.28	5	3FGLJ1913.9+4441	0.32
3HSPJ191803.5+033031	–	16.2	1	0.23	5	FL8YJ1918.0+0331	0.1
3HSPJ191809.6+375313	Yes	16.2	1	—	0	3FGLJ1918.0+3750	0.5
3HSPJ192024.9+693537	Yes	15.7	1	0.74	5	–	0.02
3HSPJ192157.6+581701	–	16.4	1	0.4	5	FL8YJ1921.7+5817	0.08
3HSPJ192242.2−745356	Yes	16.3	1	0.36	5	3FGLJ1923.2−7452	0.32
3HSPJ192325.3−250208	–	17.8	1	0.65	4	FL8YJ1923.4−2502	0.2
3HSPJ192502.2+281542	–	16.3	1	0.16	5	3FGLJ1924.9+2817	0.5
3HSPJ192519.0+370535	–	16.6	1	0.26	5	FL8YJ1925.4+3706	0.32
3HSPJ192527.1−722044	Yes	15.3	1	—	0	–	0.25
3HSPJ192649.8+615442	Yes	15.8	1	—	0	3FGLJ1926.8+6154	0.79
3HSPJ193109.2+093716	Yes	15.9	1	—	0	3FGLJ1931.1+0937	3.98
3HSPJ193320.2+072621	Yes	16.2	1	0.17	5	3FGLJ1933.4+0727	0.4
3HSPJ193412.7−241920	Yes	16.2	1	—	0	FL8YJ1934.3−2419	0.79
3HSPJ193419.6+600139	Yes	15.5	1	—	0	3FGLJ1934.2+6002	0.2
3HSPJ193517.5+751933	Yes	16.2	1	0.27	5	–	0.08
3HSPJ193656.1−471950	Yes	17.7	1	0.265	1	3FGLJ1936.9−4719	1.26
3HSPJ193804.5−380117	Yes	15.5	2	0.3	5	–	0.1
3HSPJ194247.4+103326	Yes	15.3	1	—	0	3FGLJ1942.7+1033	2.0
3HSPJ194333.7−053353	Yes	17.5	3	0.5	5	3FGLJ1944.0−0535	0.32
3HSPJ194356.2+211822	Yes	18.1	1	0.22	5	FL8YJ1944.0+2117	2.0
3HSPJ194422.3−452331	Yes	15.9	1	0.21	5	3FGLJ1944.1−4523	0.5
3HSPJ194455.1−214319	Yes	17.1	1	0.28	4	FL8YJ1944.8−2143	0.2
3HSPJ194615.2−520848	Yes	16.5	1	0.23	5	–	0.13
3HSPJ194934.1+090653	Yes	15.5	1	—	0	FL8YJ1949.5+0906	0.5
3HSPJ195021.8+604753	Yes	16.3	1	0.25	0	–	0.16
3HSPJ195134.8−154930	Yes	15.9	1	—	0	–	0.16
3HSPJ195500.6−160338	Yes	16.4	1	0.23	4	3FGLJ1955.0−1605	0.4
3HSPJ195502.8−564028	Yes	16.0	1	0.2	5	3FGLJ1954.9−5640	0.63
3HSPJ195547.8+021512	Yes	15.7	1	—	0	3FGLJ1955.9+0212	0.79
3HSPJ195755.0−241950	Yes	15.5	1	—	0	–	0.25
3HSPJ195800.4+243806	–	16.0	1	—	0	3FGLJ1958.1+2436	0.79
3HSPJ195812.6+694325	–	16.1	1	0.28	5	FL8YJ1957.9+6941	0.08
3HSPJ195814.9−301111	Yes	17.0	1	0.119	1	3FGLJ1958.2−3011	1.0
3HSPJ195945.6−472519	Yes	15.3	1	—	0	3FGLJ1959.8−4725	0.79
3HSPJ195959.8+650854	Yes	16.9	1	0.047	1	3FGLJ2000.0+6509	15.85

Source	2WHSP	Log $\nu_{\rm peak}$	flag	Z	flag	γ-ray counterpart	FOM
3HSPJ200053.9−364226	Yes	16.1	1	—	0	–	0.13
3HSPJ200112.8+435252	Yes	15.1	1	—	0	3FGLJ2001.1+4352	3.98
3HSPJ200204.1−573645	Yes	15.7	1	—	0	FL8YJ2001.9−5737	0.4
3HSPJ200213.6−583736	Yes	15.9	1	0.35	5	–	0.13
3HSPJ200227.2−711936	–	16.5	2	0.21	5	FL8YJ2002.3−7119	0.25
3HSPJ200245.3+630233	Yes	16.3	1	—	0	3FGLJ2002.7+6303	0.16
3HSPJ200505.9+700439	Yes	16.6	1	—	0	3FGLJ2004.8+7003	0.32
3HSPJ200630.8+660412	Yes	15.2	1	—	0	–	0.13
3HSPJ200632.8+635549	Yes	15.4	1	0.29	5	–	0.08
3HSPJ200925.3−484953	Yes	15.4	1	0.071	1	3FGLJ2009.3−4849	10.0
3HSPJ201002.9−244737	Yes	15.9	1	0.32	5	–	0.1
3HSPJ201200.9−771219	Yes	16.7	1	0.33	5	J201200.9−771219	0.2
3HSPJ201213.7−523251	–	16.5	1	0.37	5	FL8YJ2012.2−5234	0.13
3HSPJ201428.6−004722	Yes	15.2	1	0.231	1	3FGLJ2014.3−0047	0.25
3HSPJ201431.0+064852	–	15.8	1	0.341	1	3FGLJ2014.5+0648	0.4
3HSPJ201503.8+162227	–	15.7	1	0.25	5	3FGLJ2014.9+1623	0.13
3HSPJ201525.0−143203	–	16.0	1	0.31	5	3FGLJ2015.3−1431	0.1
3HSPJ201619.5+495324	–	16.0	1	—	0	FL8YJ2016.3+4953	0.32
3HSPJ201924.7+712624	Yes	15.5	1	—	0	–	0.25
3HSPJ202143.8−722611	–	16.2	1	0.29	5	3FGLJ2022.2−7220	0.2
3HSPJ202429.3−084804	Yes	15.8	1	—	0	3FGLJ2024.4−0848	0.32
3HSPJ202630.7+764448	Yes	16.6	1	0.29	5	3FGLJ2026.3+7644	0.2
3HSPJ202658.4+334308	–	17.5	1	0.24	5	FL8YJ2027.1+3343	1.0
3HSPJ202803.6+720514	Yes	15.4	1	—	0	–	0.06
3HSPJ202830.2+764736	–	16.1	1	0.38	5	–	0.06
3HSPJ203024.0−503413	–	16.7	1	0.53	5	FL8YJ2030.4−5037	0.05
3HSPJ203027.9−143917	–	16.9	1	0.43	5	3FGLJ2030.5−1439	0.06
3HSPJ203031.6+223439	–	16.2	1	—	0	FL8YJ2030.5+2235	0.2
3HSPJ203057.1+193612	Yes	15.8	1	0.27	5	3FGLJ2031.0+1937	0.32
3HSPJ203156.0−345850	Yes	16.4	1	0.124	1	–	0.08
3HSPJ203451.0−420038	Yes	15.7	1	0.29	5	3FGLJ2034.6−4202	0.5
3HSPJ203508.6−471708	Yes	15.2	1	—	0	–	0.13
3HSPJ203649.4−332830	Yes	16.4	1	0.23	1	3FGLJ2036.6−3325	0.32
3HSPJ203844.9−263632	Yes	16.2	1	0.44	1	–	0.1
3HSPJ203856.7−185916	Yes	15.7	1	—	0	–	0.06
3HSPJ203923.5+521950	–	16.9	1	0.053	1	3FGLJ2039.5+5217	0.5
3HSPJ203941.1−422052	Yes	16.2	1	0.4	5	–	0.08
3HSPJ204006.6−462017	Yes	16.4	1	0.31	5	FL8YJ2040.1−4622	0.32
3HSPJ204008.2−711459	Yes	17.8	1	0.161	1	3FGLJ2040.2−7115	1.26
3HSPJ204150.2−373339	Yes	17.3	1	0.098	1	3FGLJ2041.7−3732	0.63
3HSPJ204201.9−731913	Yes	16.3	1	0.31	5	3FGLJ2041.9−7318	0.1
3HSPJ204206.0+242652	Yes	17.2	1	0.104	1	3FGLJ2042.1+2428	0.79
3HSPJ204600.5−343017	Yes	16.3	1	0.425	1	–	0.16
3HSPJ204735.0+793759	Yes	15.1	1	—	0	–	0.03
3HSPJ204735.9−290858	Yes	17.0	3	0.333	1	–	0.16
3HSPJ204921.7−003926	Yes	16.6	1	0.25	1	–	0.16
3HSPJ205242.5+081040	Yes	17.0	2	0.53	5	FL8YJ2052.5+0810	0.2
3HSPJ205253.9−261511	Yes	15.6	1	—	0	–	0.2
3HSPJ205350.7+292314	–	16.3	1	0.23	5	3FGLJ2053.9+2922	1.0
3HSPJ205456.8+001537	Yes	16.1	1	0.151	1	3FGLJ2055.0+0016	0.2
3HSPJ205528.2−002116	Yes	18.0	3	0.44	1	3FGLJ2055.2−0019	2.51
3HSPJ205637.0+221845	Yes	16.0	1	0.23	5	–	0.1
3HSPJ205642.6+494005	–	17.6	1	0.1	5	3FGLJ2056.7+4938	2.0
3HSPJ205846.7−144304	Yes	16.0	1	0.078	1	FL8YJ2058.8−1442	0.13
3HSPJ205938.5−003755	Yes	16.0	1	0.335	1	–	0.08
3HSPJ210050.6−430532	Yes	16.5	1	0.31	5	–	0.06
3HSPJ210123.0−454949	Yes	16.0	1	—	0	–	0.79

Source	2WHSP	Log $\nu_{\rm peak}$	flag	Z	flag	γ-ray counterpart	FOM
3HSPJ210123.8+091324	Yes	15.9	1	0.29	5	FL8YJ2101.4+0912	0.32
3HSPJ210338.3−623225	Yes	15.0	1	—	0	3FGLJ2103.9−6233	1.0
3HSPJ210415.9+211808	Yes	15.9	1	0.36	5	3FGLJ2104.7+2113	0.2
3HSPJ210421.9−021238	Yes	15.5	1	0.45	3	3FGLJ2104.2−0211	0.4
3HSPJ210451.0+050320	Yes	15.7	1	—	0	–	0.32
3HSPJ210721.1−145418	Yes	17.2	1	0.3	4	–	0.16
3HSPJ210844.7−025034	Yes	15.8	1	0.15	1	3FGLJ2108.6−0250	0.32
3HSPJ210936.1+395513	–	16.3	1	—	0	FL8YJ2109.6+3954	0.25
3HSPJ211011.1−861847	Yes	15.5	1	0.31	5	3FGLJ2108.6−8619	0.2
3HSPJ211207.4−144412	Yes	16.6	1	0.28	5	–	0.16
3HSPJ211243.0+081835	Yes	15.9	1	0.27	5	3FGLJ2112.7+0819	0.25
3HSPJ211349.6+082501	Yes	15.1	1	0.23	5	–	0.13
3HSPJ211353.7+133017	Yes	17.7	1	0.307	2	–	0.2
3HSPJ211355.6−015540	Yes	15.4	1	0.42	5	–	0.13
3HSPJ211501.4−005641	Yes	15.9	1	0.226	1	–	0.06
3HSPJ211522.0+121802	–	15.4	1	0.28	5	3FGLJ2115.2+1215	0.25
3HSPJ211544.0−012545	Yes	16.6	1	0.33	5	–	0.16
3HSPJ211605.0+251200	Yes	15.7	1	—	0	–	0.06
3HSPJ211614.5+333920	–	15.0	1	0.12	5	3FGLJ2116.1+3339	0.79
3HSPJ211754.9−324328	Yes	15.7	1	0.215	1	3FGLJ2118.0−3241	0.13
3HSPJ212125.4−831914	Yes	16.0	1	0.62	5	–	0.08
3HSPJ212233.7+192527	Yes	15.7	1	—	0	–	0.08
3HSPJ212307.2−103648	–	16.6	1	0.023	2	–	0.16
3HSPJ212743.0+361305	Yes	15.3	1	0.876	3	3FGLJ2127.7+3612	0.63
3HSPJ212839.9−194152	Yes	16.9	1	0.24	5	–	0.1
3HSPJ212940.6+003527	Yes	16.0	2	0.426	1	–	0.06
3HSPJ213004.7−563222	Yes	15.3	1	—	0	–	0.06
3HSPJ213103.2−274657	Yes	16.2	1	0.38	3	3FGLJ2130.8−2745	0.63
3HSPJ213135.4−091523	Yes	16.3	1	0.449	1	3FGLJ2131.5−0915	0.63
3HSPJ213151.5−251558	Yes	16.9	1	0.86	3	3FGLJ2131.8−2516	0.63
3HSPJ213306.3−281536	Yes	15.1	1	—	0	–	0.16
3HSPJ213314.3+252859	–	15.2	1	0.294	1	3FGLJ2133.3+2533	0.16
3HSPJ213349.1+664704	–	15.4	1	—	0	3FGLJ2133.8+6648	0.25
3HSPJ213448.2−164205	Yes	16.3	1	—	0	–	0.05
3HSPJ213510.9+224307	Yes	16.5	1	0.45	5	–	0.05
3HSPJ213818.3−352204	Yes	15.5	1	—	0	–	0.06
3HSPJ213821.1+355823	–	16.3	1	0.25	5	FL8YJ2138.3+3556	0.25
3HSPJ213852.7−205347	Yes	17.0	1	0.29	1	FL8YJ2138.8−2055	0.4
3HSPJ214130.8+211526	Yes	16.2	1	0.22	5	–	0.1
3HSPJ214226.4+365949	Yes	16.8	1	0.24	5	FL8YJ2142.4+3659	0.63
3HSPJ214239.7−202819	–	16.4	1	0.53	5	3FGLJ2142.6−2029	0.05
3HSPJ214247.6+195810	–	16.2	1	0.38	5	3FGLJ2142.7+1957	0.25
3HSPJ214255.6−391312	Yes	15.0	2	—	0	–	0.05
3HSPJ214410.0−195559	Yes	18.0	1	0.38	5	–	0.08
3HSPJ214429.5−563848	–	16.8	1	0.48	5	3FGLJ2144.6−5640	0.06
3HSPJ214442.0−181800	Yes	16.7	1	0.23	5	–	0.13
3HSPJ214453.3−185725	Yes	15.8	1	0.38	5	–	0.04
3HSPJ214530.1+100605	–	16.0	1	0.37	4	3FGLJ2145.5+1007	0.16
3HSPJ214533.3−043439	Yes	16.6	1	0.07	1	J214533.3−043438	0.2
3HSPJ214552.2+071927	Yes	17.5	1	0.237	1	3FGLJ2145.7+0717	0.4
3HSPJ214609.6+850148	Yes	15.7	1	0.28	5	–	0.25
3HSPJ214625.7−474837	Yes	17.1	1	0.461	1	–	0.16
3HSPJ214636.9−134400	Yes	15.7	1	0.42	3	3FGLJ2146.6−1344	0.5
3HSPJ214924.0−563112	Yes	16.1	1	0.27	5	–	0.06
3HSPJ215006.3−044130	Yes	16.6	1	0.53	5	–	0.06
3HSPJ215006.8−245723	Yes	15.0	1	—	0	–	0.1
3HSPJ215015.5−141049	Yes	17.8	1	0.22	1	3FGLJ2150.2−1411	1.0

Source	2WHSP	Log $\nu_{\rm peak}$	flag	Z	flag	γ-ray counterpart	FOM
3HSPJ215051.7+111916	–	16.1	1	0.495	1	FL8YJ2150.8+1119	0.13
3HSPJ215123.2+415633	–	15.7	1	0.15	5	3FGLJ2151.6+4154	0.4
3HSPJ215214.1−120541	Yes	16.3	1	0.121	1	FL8YJ2152.1−1206	0.2
3HSPJ215258.3+172459	Yes	15.3	1	0.283	2	–	0.05
3HSPJ215305.3−004230	Yes	18.0	3	0.341	1	3FGLJ2152.9−0045	0.79
3HSPJ215355.8−295444	Yes	17.5	1	0.68	4	–	0.1
3HSPJ215412.7+000423	–	16.3	1	0.217	1	–	0.01
3HSPJ215511.6−253754	Yes	16.0	2	0.46	5	–	0.1
3HSPJ215601.6+181837	Yes	15.7	1	0.36	3	3FGLJ2156.0+1818	0.4
3HSPJ215852.0−301332	Yes	15.4	1	0.117	1	3FGLJ2158.8−3013	25.12
3HSPJ215910.9−284116	–	15.5	1	0.271	1	3FGLJ2159.2−2841	0.1
3HSPJ215936.1−461953	–	15.9	1	0.4	5	FL8YJ2159.6−4619	0.13
3HSPJ220031.3+003541	Yes	16.9	1	0.098	1	–	0.06
3HSPJ220107.3−590640	Yes	16.3	1	0.21	5	FL8YJ2201.0−5906	0.32
3HSPJ220123.8+294934	Yes	15.6	1	0.24	5	FL8YJ2201.6+2953	0.08
3HSPJ220146.9−145439	Yes	15.7	1	0.38	5	–	0.08
3HSPJ220155.8−170700	Yes	17.7	1	0.169	1	FL8YJ2201.9−1707	0.2
3HSPJ220214.8+104130	–	16.3	1	0.362	1	–	0.08
3HSPJ220451.3−181536	Yes	16.7	1	0.26	5	–	0.25
3HSPJ220704.1+222231	–	16.0	1	0.558	1	FL8YJ2207.1+2222	0.08
3HSPJ220941.6−045110	Yes	15.6	1	0.255	5	3FGLJ2209.8−0450	0.2
3HSPJ221029.6+362159	Yes	16.9	1	0.37	5	FL8YJ2210.4+3624	0.2
3HSPJ221058.5+320341	–	16.6	1	0.32	5	FL8YJ2210.9+3202	0.13
3HSPJ221108.3−000302	Yes	16.3	1	0.362	1	FL8YJ2211.0−0003	0.2
3HSPJ221109.8−002327	Yes	15.6	1	0.448	1	–	0.05
3HSPJ221330.3−475425	–	15.0	1	—	0	3FGLJ2213.6−4755	0.16
3HSPJ221405.0+393857	Yes	16.2	1	—	0	–	0.16
3HSPJ221659.5−672800	–	16.0	1	0.27	5	FL8YJ2216.9−6725	0.04
3HSPJ221728.4−310620	Yes	17.0	1	0.46	1	–	0.25
3HSPJ221919.9−323033	Yes	15.0	2	0.27	5	–	0.16
3HSPJ222028.7+281355	Yes	15.8	1	0.15	5	3FGLJ2220.3+2812	0.2
3HSPJ222129.2−522527	Yes	15.7	1	0.34	3	3FGLJ2221.6−5225	1.26
3HSPJ222253.8−175321	Yes	16.1	1	0.29	1	–	0.16
3HSPJ222329.5+010226	–	15.1	1	0.51	3	3FGLJ2223.3+0103	0.2
3HSPJ222424.9+035458	Yes	15.6	1	0.3	5	3FGLJ2224.4+0351	0.1
3HSPJ222512.6+113600	Yes	15.5	1	0.4	5	–	0.1
3HSPJ222610.9−840622	Yes	16.5	1	0.3	5	–	0.13
3HSPJ222636.4+021037	Yes	16.3	1	0.35	5	FL8YJ2226.6+0210	0.2
3HSPJ222906.2−313020	Yes	16.7	1	0.65	5	–	0.03
3HSPJ223245.5−004032	Yes	16.9	1	0.505	1	–	0.1
3HSPJ223248.7−202226	Yes	17.5	1	0.31	5	3FGLJ2232.9−2021	0.4
3HSPJ223301.1+133601	Yes	17.0	3	0.214	1	FL8YJ2232.9+1335	0.79
3HSPJ223626.3+370713	Yes	15.7	1	0.2	5	FL8YJ2236.6+3706	0.32
3HSPJ223704.8+184055	–	15.1	1	0.5	4	FL8YJ2236.9+1840	0.03
3HSPJ223812.7−394018	Yes	17.2	1	0.25	1	–	0.2
3HSPJ223928.8−243944	–	16.4	1	0.115	1	3FHLJ2239.5−2439	0.08
3HSPJ224017.7−524113	–	15.0	2	0.25	5	FL8YJ2240.3−5241	0.13
3HSPJ224046.8+132602	–	16.2	1	0.66	1	–	0.16
3HSPJ224123.5+294247	–	17.0	2	0.48	5	FL8YJ2241.3+2943	0.2
3HSPJ224340.3−123059	Yes	16.5	2	0.226	1	3FGLJ2243.6−1230	0.5
3HSPJ224354.7+202103	Yes	15.1	1	—	0	3FGLJ2243.9+2021	1.58
3HSPJ224434.9−723314	Yes	16.3	1	0.55	5	–	0.1
3HSPJ224448.0−000619	Yes	15.8	1	0.7	3	FL8YJ2244.9−0008	0.13
3HSPJ224531.8−173358	–	15.3	1	0.43	5	3FHLJ2245.5−1734	0.05
3HSPJ224642.0−520640	Yes	17.7	1	0.098	1	3FGLJ2246.7−5205	1.26
3HSPJ224727.9−545206	Yes	16.5	2	0.28	4	–	0.08
3HSPJ224753.2+441315	Yes	16.3	1	—	0	3FGLJ2247.8+4413	0.79

Source	2WHSP	Log ν_{peak}	flag	Z	flag	γ-ray counterpart	FOM
3HSPJ224819.3−003641	–	16.0	1	0.212	1	–	0.03
3HSPJ224820.7−003221	–	16.6	1	0.249	1	–	0.04
3HSPJ224833.3+322334	Yes	16.1	1	0.45	5	–	0.08
3HSPJ224910.7−130002	Yes	17.6	1	0.35	4	FL8YJ2249.4−1301	0.63
3HSPJ224938.4−594422	–	15.3	1	0.29	5	3FGLJ2249.3−5943	0.08
3HSPJ225005.7+382437	Yes	16.2	1	0.119	1	3FGLJ2250.1+3825	1.26
3HSPJ225147.5−320612	Yes	18.0	3	0.246	1	FL8YJ2251.7−3208	1.0
3HSPJ225240.8+162755	Yes	16.1	1	0.7	5	–	0.05
3HSPJ225354.2+140436	Yes	15.6	1	0.327	1	3FGLJ2254.0+1403	0.16
3HSPJ225441.8+293436	Yes	15.4	1	0.35	5	–	0.08
3HSPJ225613.3−330338	Yes	16.5	1	0.243	1	FL8YJ2255.9−3256	0.2
3HSPJ225619.1−712115	–	16.6	1	0.4	5	3FHLJ2256.0−7119	0.08
3HSPJ225636.0−554709	Yes	16.7	1	0.2	5	–	0.1
3HSPJ225818.9−552537	Yes	15.7	1	0.479	1	3FGLJ2258.3−5526	0.4
3HSPJ230012.3+405225	Yes	17.3	1	0.34	5	3FGLJ2300.0+4053	0.4
3HSPJ230039.7−533111	Yes	17.2	1	0.263	1	–	0.16
3HSPJ230327.4−520033	Yes	15.6	1	—	0	–	0.04
3HSPJ230329.8+032156	Yes	15.9	1	0.47	5	–	0.1
3HSPJ230344.5−043856	Yes	15.9	1	0.18	4	–	0.1
3HSPJ230436.7+370507	Yes	16.4	1	—	0	3FGLJ2304.6+3704	0.79
3HSPJ230525.7+294811	Yes	16.1	1	0.63	5	–	0.1
3HSPJ230526.9−674304	Yes	16.3	1	0.28	5	–	0.04
3HSPJ230634.9−110348	Yes	17.5	2	0.45	5	FL8YJ2306.6−1105	0.25
3HSPJ230717.3−423616	Yes	17.0	2	0.31	4	–	0.13
3HSPJ230722.0−120517	Yes	16.1	1	0.32	4	3FGLJ2307.4−1208	0.32
3HSPJ230814.8−160446	Yes	15.8	1	0.29	5	–	0.13
3HSPJ230846.8−221948	Yes	16.8	1	0.137	1	–	0.16
3HSPJ230848.7+542611	–	15.9	1	—	0	3FGLJ2309.0+5428	0.32
3HSPJ230940.8−363248	Yes	15.7	1	—	0	3FGLJ2309.6−3633	0.5
3HSPJ231011.8−105903	Yes	16.6	1	0.31	4	–	0.13
3HSPJ231023.3+311949	Yes	16.1	1	0.48	5	–	0.06
3HSPJ231027.5−371912	Yes	16.7	1	1.03	3	–	0.25
3HSPJ231041.7−434734	Yes	17.2	1	0.089	1	–	0.25
3HSPJ231118.9−094622	–	16.8	1	0.49	1	–	0.06
3HSPJ231305.8−600522	Yes	17.8	1	0.48	4	–	0.1
3HSPJ231306.4−550406	Yes	15.7	1	0.28	5	–	0.06
3HSPJ231323.5+402816	Yes	15.1	1	0.17	5	–	0.32
3HSPJ231347.8−692330	Yes	17.8	1	0.53	5	3FGLJ2312.9−6923	0.32
3HSPJ231357.3+144423	Yes	17.7	1	0.162	1	3FGLJ2314.0+1443	0.25
3HSPJ231608.5−252702	–	16.1	1	0.3	5	–	0.08
3HSPJ231731.9−453359	Yes	15.4	1	0.59	3	3FGLJ2317.3−4534	0.32
3HSPJ231752.7−144324	Yes	15.3	1	—	0	–	0.25
3HSPJ231827.1+070124	Yes	16.6	1	0.85	4	–	0.03
3HSPJ231905.9−420648	–	16.4	1	0.054	1	3FGLJ2319.2−4207	0.4
3HSPJ231943.4+161149	–	15.0	1	—	0	FL8YJ2319.7+1609	0.32
3HSPJ231952.8−011626	Yes	16.7	1	0.284	1	–	0.13
3HSPJ232012.1+414605	–	16.9	1	0.152	1	–	0.25
3HSPJ232039.8−630918	Yes	16.2	1	0.2	1	FL8YJ2321.0−6308	0.4
3HSPJ232110.9−121601	Yes	16.4	1	0.42	5	–	0.13
3HSPJ232136.9−161928	–	15.8	1	—	0	3FGLJ2321.6−1619	0.32
3HSPJ232240.3−422042	–	15.7	1	0.09	1	–	0.2
3HSPJ232244.0+343613	Yes	15.7	1	0.094	1	3FGLJ2322.5+3436	0.25
3HSPJ232254.4−491630	Yes	15.7	1	0.38	3	3FGLJ2322.9−4917	0.4
3HSPJ232305.0−174802	Yes	15.8	1	0.717	1	–	0.79
3HSPJ232352.0+421058	Yes	15.5	1	0.059	2	3FGLJ2323.9+4211	1.0
3HSPJ232444.6−404049	Yes	15.4	1	0.24	3	3FGLJ2324.7−4040	2.0
3HSPJ232520.2−201212	–	15.6	1	0.31	5	FL8YJ2325.2−2010	0.13

Source	2WHSP	Log $\nu_{\rm peak}$	flag	Z	flag	γ-ray counterpart	FOM
3HSPJ232538.1+164642	Yes	15.4	1	0.25	5	3FGLJ2325.6+1650	0.2
3HSPJ232914.2+375414	Yes	16.4	1	0.21	5	3FGLJ2329.2+3754	0.5
3HSPJ232938.2+610114	–	16.1	1	—	0	3FGLJ2329.8+6102	1.0
3HSPJ233014.1−294550	–	15.0	2	0.297	1	FL8YJ2330.2−2948	0.04
3HSPJ233016.1−233641	Yes	15.3	1	0.32	5	FL8YJ2330.0−2329	0.08
3HSPJ233112.9−030130	Yes	16.9	1	0.35	4	FL8YJ2331.4−0259	0.1
3HSPJ233207.6−025245	Yes	15.3	1	—	0	–	0.1
3HSPJ233250.6+452936	Yes	15.4	1	0.32	5	–	0.16
3HSPJ233252.1−052142	Yes	16.5	2	0.4	5	–	0.08
3HSPJ233339.5−252710	Yes	16.5	2	0.4	2	–	0.16
3HSPJ233352.3−241659	Yes	17.2	1	0.45	5	–	0.06
3HSPJ233404.0+084725	Yes	16.5	2	0.34	5	–	0.13
3HSPJ233552.9−581015	–	16.3	1	0.35	5	FL8YJ2335.9−5811	0.08
3HSPJ233630.5−635634	Yes	15.1	1	—	0	–	0.16
3HSPJ233653.7−232626	Yes	16.6	1	0.12	2	–	0.08
3HSPJ233859.1+025109	Yes	17.3	1	0.041	1	3FGLJ2338.7+0251	0.08
3HSPJ233907.3+053426	Yes	15.8	1	0.74	2	–	0.08
3HSPJ233920.8−740435	Yes	16.8	1	—	0	3FGLJ2338.7−7401	0.25
3HSPJ234042.8+385511	Yes	15.6	1	0.35	5	3FGLJ2340.7+3847	0.13
3HSPJ234043.8−462112	Yes	16.9	1	0.3	5	–	0.13
3HSPJ234054.2+801515	–	15.1	1	0.274	1	3FGLJ2340.7+8016	0.63
3HSPJ234238.6+361838	Yes	16.3	1	0.35	5	–	0.13
3HSPJ234331.6+783143	Yes	15.6	1	—	0	–	0.16
3HSPJ234333.5+343950	Yes	17.3	1	0.36	1	3FGLJ2343.7+3437	0.63
3HSPJ234538.4−144928	Yes	16.6	1	0.224	1	–	0.2
3HSPJ234704.8+514217	Yes	17.7	1	0.044	1	3FGLJ2347.0+5142	1.58
3HSPJ234753.2+543630	–	17.5	3	0.4	5	3FGLJ2347.9+5436	1.0
3HSPJ234754.8−663045	Yes	16.4	1	0.28	5	–	0.08
3HSPJ234857.3−312217	Yes	16.1	1	0.5	5	–	0.02
3HSPJ235001.7+194151	Yes	16.5	2	0.517	1	–	0.04
3HSPJ235013.5+015146	Yes	16.2	1	0.47	5	–	0.1
3HSPJ235018.0−055927	Yes	17.4	1	0.515	1	–	0.2
3HSPJ235023.3−243602	Yes	16.0	3	0.19	1	–	0.16
3HSPJ235034.3−300604	Yes	15.7	1	0.23	1	3FGLJ2350.4−3004	0.13
3HSPJ235116.1−760015	Yes	15.5	1	0.25	5	3FGLJ2351.9−7601	0.13
3HSPJ235321.0−145857	Yes	17.0	2	0.5	5	J235320.9−145856	0.16
3HSPJ235604.0−002353	Yes	15.2	1	0.283	1	–	0.06
3HSPJ235612.1+403644	Yes	16.3	1	0.331	1	3FGLJ2356.0+4037	0.16
3HSPJ235725.1−171234	Yes	15.1	1	—	0	–	0.05
3HSPJ235729.9−171802	Yes	17.6	1	0.85	3	3FGLJ2357.4−1716	0.79
3HSPJ235825.1+382856	–	16.1	1	0.24	5	3FGLJ2358.5+3827	0.25
3HSPJ235836.8−180717	–	15.5	1	0.39	3	3FGLJ2358.6−1809	0.32
3HSPJ235907.8−303740	Yes	17.1	1	0.165	1	3FGLJ2359.3−3038	2.0
3HSPJ235917.0+021520	Yes	16.4	1	0.61	4	–	0.04
3HSPJ235919.5−204756	–	16.2	1	0.096	1	3FGLJ2359.5−2052	0.13
3HSPJ235921.3−131129	Yes	15.7	1	0.56	5	–	0.04
3HSPJ235955.3+314600	Yes	16.1	1	0.33	5	–	0.2

Appendix H

Articles

H.1 Paper in preparation

Chang, Y.-L.; Arsioli, B.; Giommi, P.; and Padovani, P., The 3HSP catalog (Chaper 2)

Chang, Y.-L.; Brandt, C.; Giommi, P., The VOU-Blazars tool (Chapter 4)

Chang, Y.-L.; Giommi, P.; Arsioli, B.; Padovani, P., The statistical properties of HSPs blazars (Chapter 3)

H.2 Paper already published

A&A 598, A17 (2017)
DOI: 10.1051/0004-6361/201629487

Astronomy & Astrophysics

2WHSP: A multi-frequency selected catalogue of high energy and very high energy γ-ray blazars and blazar candidates⋆

Y.-L. Chang (張淯翎)[1,2,3], B. Arsioli[1,2,4], P. Giommi[2,4], and P. Padovani[5,6]

[1] Sapienza Università di Roma, ICRANet, Dipartimento di Fisica, Piazzale Aldo Moro 5, 00185 Roma, Italy
e-mail: stsun1223@hotmail.com
[2] Italian Space Agency, ASI, via del Politecnico snc, 00133 Roma, Italy
[3] ICRANet, P.zza della Repubblica 10, 65122 Pescara, Italy
[4] ICRANet-Rio, CBPF, Rua Dr. Xavier Sigaud 150, 22290-180 Rio de Janeiro, Brazil
[5] European Southern Observatory, Karl-Schwarzschild-Str. 2, 85748 Garching bei München, Germany
[6] Associated to INAF–Osservatorio Astronomico di Roma, via Frascati 33, 00040 Monteporzio Catone, Italy
e-mail: yuling.chang@asdc.asi.it

Received 5 August 2016 / Accepted 18 September 2016

ABSTRACT

Aims. High synchrotron peaked blazars (HSPs) dominate the γ-ray sky at energies higher than a few GeV; however, only a few hundred blazars of this type have been cataloged so far. In this paper we present the 2WHSP sample, the largest and most complete list of HSP blazars available to date, which is an expansion of the 1WHSP catalogue of γ-ray source candidates off the Galactic plane.
Methods. We cross-matched a number of multi-wavelength surveys (in the radio, infrared and X-ray bands) and applied selection criteria based on the radio to IR and IR to X-ray spectral slopes. To ensure the selection of genuine HSPs, we examined the SED of each candidate and estimated the peak frequency of its synchrotron emission ($\nu_{\rm peak}$) using the ASDC SED tool, including only sources with $\nu_{\rm peak} > 10^{15}$ Hz (equivalent to $\nu_{\rm peak} > 4$ eV).
Results. We have assembled the largest and most complete catalogue of HSP blazars to date, which includes 1691 sources. A number of population properties, such as infrared colours, synchrotron peak, redshift distributions, and γ-ray spectral properties have been used to characterise the sample and maximize completeness. We also derived the radio log N–log S distribution. This catalogue has already been used to provide seeds to discover new very high energy objects within *Fermi*-LAT data and to look for the counterparts of neutrino and ultra high energy cosmic ray sources, showing its potential for the identification of promising high-energy γ-ray sources and multi-messenger targets.

Key words. galaxies: active – BL Lacertae objects: general – radiation mechanisms: non-thermal – gamma rays: galaxies

1. Introduction

Blazars are a class of radio-loud active galactic nuclei (AGN) hosting a jet oriented at a small angle with respect to the line of sight (Blandford & Rees 1978; Antonucci 1993; Urry & Padovani 1995). The emission of these objects is non-thermal over most or the entire electromagnetic spectrum, from radio frequencies to hard γ-rays. The observed radiation shows extreme properties, mostly owing to relativistic amplification effects. The observed spectral energy distribution (SED) presents a general shape composed of two bumps, one typically located in the infrared (IR), and sometimes extending to the X-ray band, and the other in the hard X-ray to γ-rays. If the peak frequency of the synchrotron bump ($\nu_{\rm peak}$) in $\nu - \nu F_\nu$ space is larger than 10^{15} Hz (corresponding to ∼4 eV), a source is usually called high synchrotron peaked (HSP) blazars (Padovani & Giommi 1995; Abdo et al. 2010). HSP blazars are also considered as extreme sources since the Lorentz factor of the electrons radiating at the peak of the synchrotron bump $\gamma_{\rm peak}$ are the highest within the blazar population, and likely of any other type of steady cosmic sources. Considering a simple SSC model, where $\nu_{\rm peak} = 3.2 \times 10^6 \gamma^2_{\rm peak} B\delta$ (e.g. Giommi et al. 2012), assuming B = 0.1 Gauss and Doppler factor δ = 10, HSPs characterized by $\nu_{\rm peak}$ ranging between 10^{15} and $\gtrsim 10^{18}$ Hz demand $\gamma_{\rm peak} \approx 10^4$–$10^6$.

The typical two-bump SED of blazars and the high energies that characterize HSPs imply that these objects occupy a distinct position in the optical to X-ray spectral index ($\alpha_{\rm ox}$) versus the radio to optical spectral index ($\alpha_{\rm ro}$) colour–colour diagram (Stocke et al. 1991). Considering the distinct spectral properties of blazars over the whole electromagnetic spectrum, selection methods based on $\alpha_{\rm ox}$ and $\alpha_{\rm ro}$ have long been used to search for new blazars. For example, Schachter et al. (1993) discovered 10 new BL Lacs via a multi-frequency approach with radio, optical, and X-ray data, and their BL Lac nature with optical spectra.

HSP blazars play a crucial role in very high energy (VHE) astronomy. Observations have shown that HSPs are bright and variable sources of high energy γ-ray photons (TeVCat)[1] and that they are likely the dominant component of the extragalactic VHE background (Padovani et al. 1993; Giommi et al. 2006; Di Mauro et al. 2014; Giommi & Padovani 2015; Ajello et al. 2015). In fact, most of the extragalactic objects detected so far above a few GeV are HSPs (Giommi et al. 2009; Padovani & Giommi 2015; Arsioli et al. 2015; Ackermann et al. 2016, see also TeVCat). However, only a few hundred HSP blazars are

⋆ Table 4 is only available at the CDS via anonymous ftp to cdsarc.u-strasbg.fr (130.79.128.5) or via http://cdsarc.u-strasbg.fr/viz-bin/qcat?J/A+A/598/A17

[1] http://tevcat.uchicago.edu

above the sensitivity limits of currently available γ-ray surveys. For example, the 1WHSP catalogue (Arsioli et al. 2015, hereafter Paper I), which was the largest sample of HSP blazars when it was published, shows that out of the 992 objects in the sample, 299 have an associated γ-ray counterpart in the *Fermi* 1/2/3FGL catalogues. Nevertheless there is a considerable number of relatively bright HSPs which still lack a γ-ray counterpart. These are likely faint, point-like sources at or below the *Fermi*-LAT, detectability threshold and were not found by the automated searches carried out so far. Indeed, Arsioli & Chang (2016) have detected ≈150 new γ-ray blazars based on a specific search around bright WHSP sources, using over seven years of *Fermi*-LAT Pass 8 data.

In the most energetic part of the γ-ray band photons from high redshift sources are absorbed by the extragalactic background light (EBL) emitted by galaxies and quasars (Dermer et al. 2011; Pfrommer et al. 2013; Bonnoli et al. 2015). Therefore, the TeV flux can drop by a very large factor compared to GeV fluxes, making distant TeV sources much more difficult to detect. Paper I has shown that, with the help of multiwavelength analysis, HSP catalogues can provide many good candidates for VHE detection.

The currently known HSP blazars are listed in catalogues such as the 5th *Roma-BZCAT* (Massaro et al. 2015, hereafter 5BZCat), the Sedentary Survey (Giommi et al. 1999, 2005; Piranomonte et al. 2007), Kapanadze (2013), and Paper I. However, the number of known HSPs is still relatively small with less than ≈1000 cataloged HSPs till now. Significantly enlarging the number of high energy blazars is important to better understand their role within the AGN phenomenon, and should shed light on the cosmological evolution of blazars, which is still a matter of debate.

The 5BZCat is the largest compilation of confirmed blazars, containing 3561 sources, around 500 of which are of the HSP type. It includes blazars discovered in surveys carried out in all parts of the electromagnetic spectrum and is also based on an extensive review of the literature and optical spectra. The Sedentary Survey comprises 150 extremely high X-ray to radio flux ratio ($\log f_x/f_r \geq 3 \times 10^{-10}$ erg cm^{-2} s^{-1} Jy^{-1}) HSP BL Lacs. The sample was obtained by cross-matching the RASS catalogue of bright X-ray sources (Voges et al. 1999) and the NVSS 1.4 GHz radio catalogue (Condon et al. 1998). Kapanadze (2013) built a catalogue of 312 HSPs with flux ratio ($f_x/f_r \geq 10^{-11}$ erg cm^{-2} s^{-1} Jy^{-1}) selected from various X-ray catalogues, the NVSS catalogue of radio sources, and the first edition of the *Roma-BZCAT* catalogue (Massaro et al. 2009). The 1WHSP sample relied on a pre-selection based on Wide-field Infrared Survey Explorer (WISE) IR colours, SED slope criteria, and $\nu_{\rm peak} > 10^{15}$ Hz. It includes 992 known, newly-identified, and candidate high galactic latitude ($b > |20°|$) HSPs.

In a series of papers, Massaro et al. (2011, 2012), D'Abrusco et al. (2012) show that most blazars occupy a specific region of the IR colour–colour diagram, which they termed the blazar strip. In Paper I, we extended the blazar strip in the WISE colour–colour diagram to include all the Sedentary Survey blazars and called it the *Sedentary WISE colour domain* (SWCD). The SWCD is wider than the WISE blazar strip since it contains some blazars whose host galaxy is very bright, such as MKN421 (2WHSP J110427.3+381230) and MKN 501 (2WHSP J165353.2+394536). We understood from previous works that many low-luminosity HSP blazars have the IR colours dominated by the thermal component of the host giant elliptical galaxy. Therefore, a selection scheme adopting IR colour restrictions may work effectively for selecting cases where the non-thermal jet component dominates the IR band but is less efficient for selecting galaxy-dominated sources (since they are spread over a larger area in the IR colour–colour plot).

In the present paper, we extend the previous 1WHSP catalogue to lower Galactic latitudes ($b > |10°|$) building the larger and more complete 2WHSP catalogue including over 1600 blazars expected to emit at VHE energies by means of multi-frequency data.

2. Building the largest sample of HSP blazars

2.1. Initial data selection by spatial cross-matching

Blazars are known to emit electromagnetic radiation over a very wide spectral range, from radio to VHE photons. As discussed in Paper I, an effective way of building large blazar samples is to work with multi-frequency data, especially from all-sky surveys, and to apply selection criteria based on spectral features that are known to be specific to blazar SEDs.

We followed Paper I and started by cross-matching the AllWISE whole sky infrared catalogue (Cutri et al. 2013) with three radio surveys (NVSS, FIRST, and SUMSS: Condon et al. 1998; White et al. 1997; Manch et al. 2003). To take into account the positional uncertainties associated with each target, we used matching radii of 0.3 arcmin for the NVSS and the SUMSS surveys and 0.1 arcmin for the FIRST catalogue. Then we performed an internal match for all IR-radio sources to eliminate duplicate entries coming from the different radio catalogues. Keeping only the best matches between radio and IR, we selected 2 137 505 objects.

After this we demanded all radio-IR matching sources to have a counterpart in one of the X-ray catalogues available to us (RASS BSC and FSC, 1SWXRT and deep XRT GRB, 3XMM, XMM slew, Einstein IPC, IPC slew, WGACAT, *Chandra*, and BMW: Voges et al. 1999, 2000; D'Elia et al. 2013; Puccetti et al. 2011; Rosen et al. 2016; Saxton et al. 2008; Harris et al. 1993; Elvis et al. 1992; White et al. 2000; Evans et al. 2010; Panzera et al. 2003). Therefore we cross-matched the IR-radio subsample with each X-ray catalogue individually, taking into account their positional errors. For instance, a radius of 0.1 arcmin was adopted for the cross-correlations (as in Paper I), unless the positional uncertainty of a source was reported to be larger than 0.1 arcmin, as in the case of many X-ray detections in the RASS survey. In these cases, we used the 95% uncertainty radius (or ellipse major axis) of each source as maximum distance for the cross-match. Some X-ray catalogues have a very wide range of positional uncertainties, thus we separated the data by positional errors and used different cross-matching radii for these X-ray catalogues. The radii used for cross-matching the IR-radio subsample with each X-ray catalogue are reported in Table 1. We also restricted the sample by Galactic latitude $|b| > 10°$ to avoid complications in the Galactic plane. We combined all the IR-radio-X-ray matching sources and applied an internal cross-check, keeping only single IR sources within 0.1 arcmin radius; this procedure reduced the sample to 28 376 objects.

2.2. Further selection based on broadband spectral slopes

Here we take advantage of the fact that HSP blazars show radio to X-ray SEDs that distinguish them from any other type of extragalactic sources by imposing two constraints on the spectral

Table 1. Cross-matching radii of the X-ray catalogues.

Catalogue	Error position	Cross-matched radius
RASS	0–36 arcsec	0.6 arcmin
	>37 arcsec	0.8 arcmin
Swift 1SWXRT	0–5 arcsec	0.1arcmin
	>5 arcsec	0.2 arcmin
Swift deep XRT GRB	all data	0.2 arcmin
3XMM DR4	0−5 arcsec	0.1 arcmin
	>5 arcsec	0.2 arcmin
XMM Slew DR6	all data	10 arcsec
Einstein IPC	all data	40 arcsec
IPC Slew	all data	1.2 arcmin
WGACAT2	all data	50 arcsec
Chandra	all data	0.1 arcmin
BMW	all data	0.15 arcmin

slopes, namely

$$0.05 < \alpha_{1.4\ \mathrm{GHz}-3.4\ \mu\mathrm{m}} < 0.45$$
$$0.4 < \alpha_{4.6\ \mu\mathrm{m}-1\ \mathrm{keV}} < 1.1, \quad (1)$$

where $\alpha_{\nu1-\nu2} = -\frac{\log(f_{\nu1}/f_{\nu2})}{\log(\nu_1/\nu_2)}$,

which are the same conditions applied to the 1WHSP catalogue, with the exception that here we do not apply the criterion $-1.0 < \alpha_{3.4\ \mu\mathrm{m}-12.0\ \mu\mathrm{m}} < 0.7$. This choice was necessary to prevent the loss of IR galaxy-dominated HSPs, which could still be promising VHE candidates (see Massaro et al. 2011; Arsioli et al. 2015, for details). The parameter ranges given above are derived from the shape of the SED of HSP blazars, which is assumed to be similar to those of three well-known bright HSPs, i.e. MKN 421, MKN 501, and PKS 2155−304 shown in Fig. 3 of Paper I, which also fit within the limiting slopes ($\alpha_{1.4\ \mathrm{GHz}-3.4\ \mu\mathrm{m}}$ and $\alpha_{4.6\ \mu\mathrm{m}-1\ \mathrm{keV}}$) used for the selection.

By avoiding the application of the IR slope constraints used for the 1WHSP sample, we select more HSP candidates, reducing the incompleteness at low radio luminosities where the IR flux is often dominated by the host galaxy.

2.3. Deriving ν_{peak} and classifying the sources

The final pre-selection led to a sample of 5518 HSP-candidates, 922 of which are also 1WHSP sources. We note that this initial sample includes most of the HSP blazars that had to be added to the 1WHSP sample as additional previously known sources that were missed during the original selection procedure. To refine and further improve the quality of the sample, we used the ASDC SED builder tool[2] to examine in detail all 5518 candidates, accepting only those with SEDs that are consistent with that of genuine HSPs. Finally the synchrotron component of each object that passed our screening was fitted using a third degree polynomial function to estimate parameters such as $\nu_{\rm peak}$, and $\nu_{\rm peak} f_{\nu_{\rm peak}}$, the energy flux at the synchrotron peak.

The host galaxies of HSP blazars are typically giant ellipticals, and their optical and near IR flux sometimes dominate the SED in these bands. To only fit the synchrotron component of HSP blazars, it is crucial to distinguish the non-thermal nuclear radiation from the flux coming from the host galaxy. To do so, we used the standard giant elliptical galaxy template of the ASDC SED builder tool to judge if the optical data points were due to the host galaxy or from non-thermal synchrotron radiation. If the source under examination had ultraviolet data (such as *Swift*-UVOT or GALEX measurements) it was straightforward to tell if there was non-thermal emission from the object.

In addition, to avoid selecting objects with misaligned jets, which are expected to be radio-extended, the accepted spatial extension of the radio counterparts (as reported in the original catalogues) was limited to 1 arcmin. This procedure was carried out whenever possible, based on the 1.4 GHz radio image from NVSS, which includes the entire sky north of $\delta = -40°$, similarly to what had been done for the 1WHSP catalogue. We could also identify radio extended sources from their SED, since radio extended objects typically display a steep radio spectrum. All cases where we could find evidence of radio (or X-ray, typically from clusters: see below) extension were eliminated from the sample. At the end of this process, we only accepted objects with $\nu_{\rm peak} > 10^{15}$ Hz (Padovani & Giommi 1995).

Clearly, most bright sources in the current list are also included in the 1WHSP catalogue. Many of the new catalogue entries are fainter sources or objects located at low Galactic latitudes ($10° < |b| < 20°$). In some cases the optical data were consistent with thermal emission from the host galaxy, and the few radio, IR, or X-ray measurements that could be related to non-thermal emission were very sparse. Clearly, more multi-frequency data are needed for these sources.

We still have a number of unclear cases owing to the lack of good multi-frequency data. We flagged them accordingly. In addition, since the positional accuracy in X-ray surveys is usually not as precise as that of optical or radio surveys, the position of the X-ray counterparts sometimes may be 20 to 40 arcsec away from the radio and optical counterparts, introducing more uncertainty.

Many of the 2WHSP candidates have been observed by SWIFT with multiple short exposures. To allow for a more accurate estimation of $\nu_{\rm peak}$ and $\nu_{\rm peak} f_{\nu_{\rm peak}}$, we summed all the SWIFT XRT observations that were taken within a three-week interval.

2.4. Avoiding X-ray contamination from cluster of galaxies

Blazars are certainly not the only objects that emit X-rays. For instance, galaxy clusters also show X-ray emission that is, however, normally spatially extended with a spectrum that peaks at ≈1−3 KeV resulting from the emission of giant clumps of hot and low density diffused gas (≈10^8 K and ≈10^{-3} atoms/cm^3: Sarazin 1988; Böhringer & Werner 2010; Pérez-Torres et al. 2009). Since blazars and radio galaxies are often located in clusters of galaxies, the X-rays from the hot gas, if not correctly identified, might cause the SED of the candidate 2WHSP source to look like that of an HSP object, introducing a source of contamination for our sample.

To avoid this problem we carried out an extensive check of bibliographic references[3] and catalogues of clusters of galaxies (e.g. ABELL, PGC, MCXC, ZW, WHL, etc.), excluding cases where cluster emission could be responsible for the observed X-rays. In addition, we used *Swift* XRT imaging data (which are available for ≈60% of our sample) to distinguish between X-ray emission from blazar jets, which is point-like in the XRT count maps, and that from the clusters, which is often extended. The same procedure was followed using XMM images, whenever these could be found in the public archive. In addition, we cross-matched our sample with the positions of

[2] http://tools.asdc.asi.it/SED

[3] For the cross-check with ADS references on each source we have used the Bibliographic Tool available on the ASDC website.

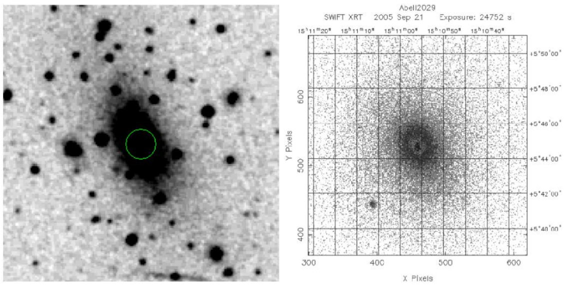

Fig. 1. Optical (*left*) and X-ray (*right*: XRT count map) images of WHL J151056.1+054441.

RASS extended sources and with those of the *Planck* catalogue of Sunyaev-Zeldovich sources (Planck Collaboration XXXII 2015).

Finally, we visually inspected optical images and the error circle maps built with the ASDC explorer tool[4] looking for targets that could be related to clusters of galaxies.

To illustrate how we removed objects that satisfy our multi-frequency selection criteria but where the X-ray flux is likely due to extended emission from a cluster of galaxies, we consider the example of WHL J151056.1+054441. This is a giant cluster of galaxies also cataloged as Abell2029. Since the strong X-ray emission is clearly extended both in the *Swift*-XRT and XMM images (see Fig. 1), this source was removed from our HSP catalogue.

Another example is shown in Fig. 2, where the candidate blazar is at the center of the cluster of galaxies LCRS B113851.7−115959. Although the X-ray emission is overall extended, the region around the sources shows clumps, and there are several X-ray detections; the non-thermal emission is very clear in the SED. Apparently, there is an AGN in the center that also emits in the UV. However, based on the available data, we cannot know if the X-ray is mainly from the non-thermal jet or from the cluster and, therefore, we did not include this source in the catalogue.

3. Improving the sample completeness

The procedure described above led to the selection of 734 new HSPs in addition to those already included in the 1WHSP catalogue, including previously known, newly discovered, and candidate blazars. For each source, we adopted as best coordinates those taken from the WISE catalogue.

To evaluate the efficiency of our method of selecting VHE emission blazars, we cross-matched the sample of 1647 objects with the Second Catalogue of Hard *Fermi*-LAT Sources (2FHL, Ackermann et al. 2016) and with TeVCat.

Only 146 of the 360 sources in the 2FHL catalogue (257 at $|b| > 10°$) are also in this preliminary sample. To verify if there are genuine HSPs in the 2FHL catalogue that were missed by our selection, we closely examined the remaining 214 2FHL sources to see if they are cataloged as blazars. We found 31 high Galactic latitude blazars with $\nu_{\rm peak} > 10^{15}$ Hz that could be added to the catalogue. These sources were initially missed since they just did not match the optical-X-ray slope criteria (Eq. (1)) during the preliminary selection process. This selection inefficiency could be due to flux variability, lack of sufficiently high quality multi-frequency data, or simply to a non-optimal choice of parameter

[4] `http://tools.asdc.asi.it`

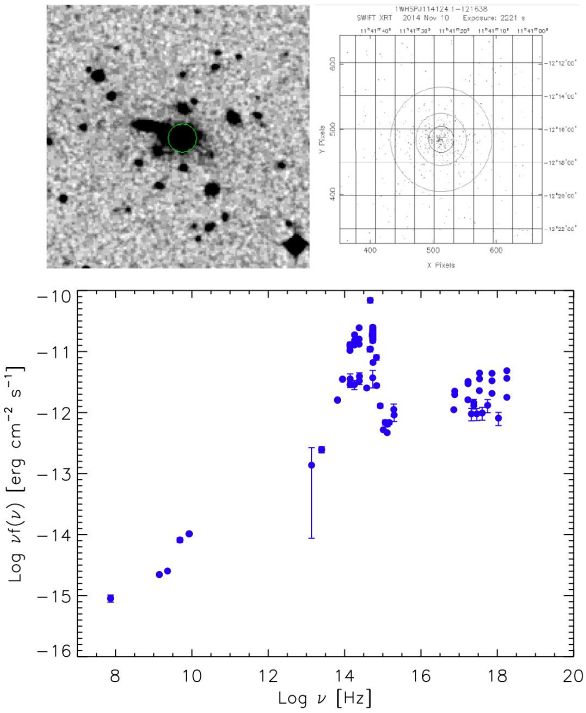

Fig. 2. *Top*: optical (*left*) and X-ray (*right*: XRT count map) images of LCRS B113851.7−115959. *Bottom*: SED of LCRS B113851.7−115959.

values in Eq. (1). Out of the 177 HSPs located at $|b| > 10°$ in the 2FHL catalogue, our selection method detected 146 objects, for an efficiency of 82.5%.

In addition, there are 14 HSP blazars in the 2FHL catalogue that are located at latitudes $|b| < 10°$, the area of sky that was not considered in our work as reducing complications connected to the Galactic plane. Since our aim is to provide the most complete list of HSPs, we added the 14 low latitude objects to the 2WHSP catalogue, as well as all additional HSPs found in the 2FHL catalogue, for a total of 45 sources. Only one good HSP blazar found among the 2FHL low Galactic latitude sources had no WISE data (2WHSP J135340.2−663958.0). We used the radio position instead of the IR position in this case.

We then checked catalogues of sources detected at TeV energies. Currently, the most complete list of objects detected in this band is TeVCat, which consists of 175 sources detected by Imaging Atmospheric/Air Cherenkov Telescope/Technique (IACT). At present there are three main IACT systems operating in the ~50 GeV to 50 TeV range: the High Energy Stereoscopic System (HESS), MAGIC (Major Atmospheric Gamma Imaging Cherenkov Telescopes), and VERITAS (Very Energetic Radiation Imaging Telescope Array System). There are 38 TeVCat sources that are also in the 2WHSP catalogue. We therefore checked the other high Galactic latitude sources to see if they were classified as HSP blazars, concluding that only one HSP source was missed. We note that, previously, we had already added three TeV sources to the 1WHSP catalogue, since these were missed during its selection. In total there are 39 HSPs at $|b| > 10°$ in TeVCat, 35 of which satisfy our selection criteria. Our selection efficiency in this case is 89.7%.

As in the case of the 2FHL catalogue, all missing sources have been lost because they just did not meet the slope criteria used in Sect. 2.2. In all cases, however, the spectral parameters turned out to be very close to the limits of the selection criteria, and $\nu_{\rm peak}$ was $\approx 10^{15}$ Hz.

The final 2WHSP catalogue includes a total of 1691 sources, 288 of which are newly identified HSPs, 540 are previously known HSPs, 814 are HSP candidates, 45 are HSP blazars taken from the 2FHL catalogue, and four from TeVcat. The complete list of 2WHSP sources is shown in Table 4.

We will further discuss the incompleteness owing to the inefficiency in finding sources peaking at or just above 10^{15} Hz in Sect. 4.1.

4. Discussion

4.1. The ν_{peak} distribution

The $\nu_{\rm peak}$ distribution of the 2WHSP sources is shown in Fig. 3. The peak of the distribution is located at $\approx 10^{15.5}$ Hz and not at the threshold of $\nu_{\rm peak} = 10^{15}$ Hz used for the sample selection. This is very likely due to incompleteness of the sample near the $\nu_{\rm peak}$ threshold, as our selection criteria were tuned to avoid too large an LSP contamination. The distribution is similar to that of the 1WHSP sample and of the subsample of HSP sources in the 5BZCat

When compared with other catalogues of extreme blazars, the peak value of the $\nu_{\rm peak}$ distribution of our sample is lower. For example the Sedentary and the Kapanadze (2013, hereafter K13) catalogues have peak values $\approx 10^{16.8}$ and $\approx 10^{16.7}$ Hz, respectively. This difference results from the criteria used and the different selected methods. The Sedentary and Kapanadze (2013) catalogues, for example, were tuned to select sources with very large $\nu_{\rm peak}$ values. We note that the $\nu_{\rm peak}$ of some sources is particularly high, with values $\gtrsim 10^{18}$ Hz. We discuss these extreme sources in the next section.

Sometimes, the severe variability of HSPs may result in displacements for $\nu_{\rm peak}$ in different phases, such as MRK501 (see Fig. 8); not to mention that the intense variability will make the $\nu_{\rm peak} f_{\nu_{\rm peak}}$ vary by an order of 1–2 or even worse. In these cases, we fit the $\nu_{\rm peak}$ and $\nu_{\rm peak} f_{\nu_{\rm peak}}$ with the mean values to estimate the proper values for the synchrotron component averagely. By doing so, we avoid having extreme values for the synchrotron peak and reduce the effects of variability.

4.2. The highest ν_{peak} blazars

There are several sources in the 2WHSP sample with $\nu_{\rm peak}$ around or above 10^{18} Hz; these are usually called extreme blazars. Values of $\nu_{\rm peak} \gtrsim 10^{18}$ Hz imply that the electrons responsible for the synchrotron radiation must be accelerated to extremely high energies (see the Introduction and, for example, Rybicki & Lightman 1986; Costamante et al. 2001).

It is hard to estimate the positions of the synchrotron peak for such extreme sources, since the available data in the X-ray band is often limited to a few keV, where most of the sensitive existing detectors operate. For about 20 sources we could not estimate the frequency of the synchrotron peak accurately since the soft X-ray data show a still rising spectrum in the SED, and no hard X-ray data exist to cover the peak of the emission. In these cases, we could only estimate a lower limit to $\nu_{\rm peak}$. For some strong X-ray variable sources with many X-ray observations we also could not obtain well-estimated $\nu_{\rm peak}$ values with

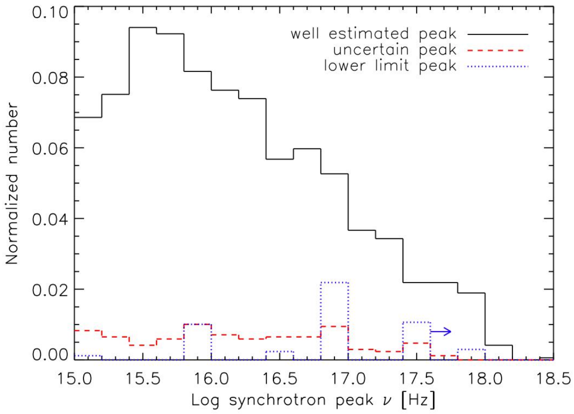

Fig. 3. $\nu_{\rm peak}$ distribution. The black solid line, blue dotted line, and red dashed line denote well-estimated $\nu_{\rm peak}$, uncertain $\nu_{\rm peak}$, and lower limits on $\nu_{\rm peak}$, respectively.

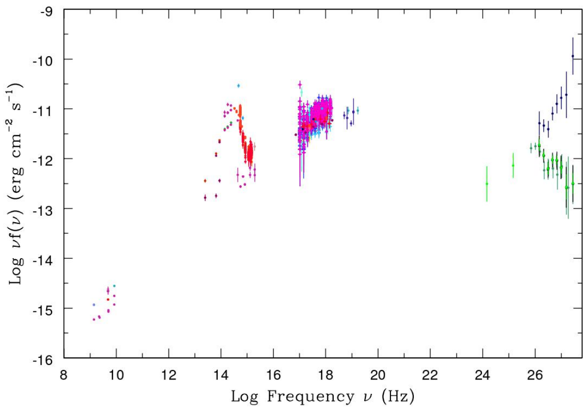

Fig. 4. SED of the extreme object 2WHSP J023248.5+201717. The dark blue points are ebl- deabsorbed data from Finke et al. (2015). See text for details.

the third degree polynomial fitting in ASDC SED tool since the curvature in the X-ray spectrum (and with it $\nu_{\rm peak}$) changes with time. However, in all these cases, the available multi-frequency data imply that the synchrotron peak is within the X-ray band; in these sources we estimated an average $\nu_{\rm peak}$ value using a second-degree polynomial in the X-ray band.

Table 2 gives the list of all the extreme sources with $\nu_{\rm peak} \geq 10^{17.9}$ Hz or sources with lower limit $\nu_{\rm peak}$; this includes many more such objects than any previous catalogue. These extreme sources are particularly importance since they may be candidate VHE, neutrino, or ultra high energy cosmic ray (UHECR) sources (Sects. 4.6 and 4.7). Figures 4 to 8 illustrate five examples of SEDs of representative objects from Table 2.

- *2WHSP J023248.5+201717 (1ES0229+200)*. This is an extreme source with VHE data available (the ebl-deabsorbed VHE data (shown as dark blue filled circles) are from Finke et al. 2015). The synchrotron peak is at $\sim 10^{18}$–10^{19} Hz and the peak frequency is one of the highest among the 2WHSP sources. In the VHE band, with the VHE fluxes for EBL absorption corrected, the inverse Compton peak will be at energies >1 TeV.

Table 2. Extreme synchrotron peaked sources.

Source	$\log\nu_{\rm peak}$	$\log\nu_{\rm peak}f_{\nu_{\rm peak}}$	Note
2WHSPJ003322.3−203907	17.9	−11.9	New HSP
2WHSPJ004013.7+405003	>17.5	>−11.5	5BZU, lower limit
2WHSPJ012308.5+342048	18.0	−10.8	5BZB, TeV source
2WHSPJ013803.7−215530	>17.5	>−12.0	blazar candidate lower limit
2WHSPJ015657.9−530159	18.0	−11.1	5BZB
2WHSPJ020412.9−333339	17.9	−11.7	5BZB, new γ-ray identification
2WHSPJ023248.5+201717	18.5	−11.0	5BZG, TeV source*
2WHSPJ032056.2+042447	17.9	−11.7	Blazar candidate, new γ-ray identification
2WHSPJ032356.5−010833	>17.5	>−11.9	5BZB, TeV source, lower limit
2WHSPJ034923.1−115926	17.9	−11.0	5BZB, TeV source
2WHSPJ035257.4−683117	18.1	−11.0	Previously known BL Lac*
2WHSPJ050419.5−095631	17.9	−11.6	New HSP, new γ-ray identification
2WHSPJ050709.2−385948	>17.5	>−12.2	Blazar candidate, lower limit
2WHSPJ050756.0+673723	17.9	−10.7	5BZB, TeV source
2WHSPJ055040.5−321615	18.1	−10.7	5BZG, TeV source
2WHSPJ055716.7−061706	17.9	−11.5	Blazar candidate, new γ-ray identification
2WHSPJ064710.0−513547	17.9	−11.2	Blazar candidate
2WHSPJ071029.9+590820	18.1	−10.7	5BZB, TeV source
2WHSPJ073326.7+515354	17.9	−11.3	Blazar candidate
2WHSPJ081917.5−075626	18.0	−11.5	5BZB, TeV source
2WHSPJ083251.4+330011	18.0	−12.0	5BZB, new γ-ray identification
2WHSPJ084452.2+280409	17.9	−12.3	New HSP
2WHSPJ092057.4−225720	>17.5	>−11.6	New HSP, lower limit
2WHSPJ094620.2+010450	17.9	−11.8	5BZB, TeV source
2WHSPJ095849.0+013218	17.9	−12.3	New HSP, new γ-ray identification
2WHSPJ102212.6+512359	18.2	−11.7	5BZG, new γ-ray identification
2WHSPJ104651.4−253544	>18.0	>−11.5	5BZB
2WHSPJ105606.6+025213	17.9	−11.5	5BZG
2WHSPJ110357.1+261117	17,9	−12.2	New HSP
2WHSPJ110651.7+650603	17.9	−12.7	Blazar candidate
2WHSPJ110804.9+164820	17.9	−12.7	New HSP
2WHSPJ112313.2−090424	17.9	−12.4	Blazar candidate
2WHSPJ113209.1−473853	>17.5	>−11.6	Blazar candidate, lower limit
2WHSPJ113630.1+673704	18.1	−11.1	5BZB, TeV source
2WHSPJ121323.0−261806	17.9	−11.2	5BZB
2WHSPJ122044.5+690525	>17.5	>−12.0	Blazar candidate, lower limit
2WHSPJ122208.6+030718	>17.5	>−11.8	New HSP, lower limit
2WHSPJ122514.2+721447	>17.5	>−11.8	Lower limit, 5BZB
2WHSPJ125341.2−393159	17.9	−11.3	5BZG, new γ-ray identification
2WHSPJ125708.2+264924	>17.5	>−12.3	New HSP, lower limit
2WHSPJ132239.1+494336	>17.5	>−12.1	New HSP, lower limit
2WHSPJ132541.8−022809	17.9	−12.0	5BZB, new γ-ray identification
2WHSPJ140027.0−293936	>17.5	>−12.1	Blazar candidate, lower limit
2WHSPJ140121.1+520928	>17.5	>−12.0	5BZB, lower limit
2WHSPJ142832.5+424020	18.1	−10.7	5BZB, TeV source
2WHSPJ143342.7−730437	>17.5	>−11.5	Blazar candidate, lower limit, new γ-ray identification*
2WHSPJ151041.0+333503	>17.5	>−11.5	5BZG, lower limit, new γ-ray identification
2WHSPJ151618.7−152344	18.0	−11.7	5BZB, new γ-ray identification
2WHSPJ153646.6+013759	>18.0	>−11.7	5BZB
2WHSPJ160519.0+542058	17.9	−12.0	5BZB, new γ-ray identification
2WHSPJ161004.0+671026	>17.5	>−11.8	5BZB, lower limit, new γ-ray identification
2WHSPJ161414.0+544251	17.9	−12.6	Blazar candidate
2WHSPJ161632.8+375603	18.0	−12.1	5BZG
2WHSPJ161632.8+375603	18.0	−12.1	5BZG
2WHSPJ162330.4+085724	>17.5	>−12.1	New HSP, lower limit, new γ-ray identification
2WHSPJ165352.2+394536	17.9	−10.2	Variability, flaring, 5BZB, TeV source*
2WHSPJ171902.2+552433	17.9	−12.5	Known blazar
2WHSPJ194333.7−053352	>17.5	>−11.8	Blazar candidate
2WHSPJ194356.2+211821	18.1	−11.0	New HSP, TeV source
2WHSPJ205528.2−002116	>18.0	>−10.9	5BZB, TeV source, lower limit
2WHSPJ214410.0−195559	17.9	−12.4	Blazar candidate
2WHSPJ215305.2−004229	>18.0	>−11.4	5BZB, lower limit*
2WHSPJ223248.7−202226	17.9	−11.7	Blazar candidate
2WHSPJ225147.5−320611	>18.0	>−11.3	5BZU, lower limit, new γ-ray identification

Notes. The sources marked with * are discussed in the text and shown in Figs. 4 to 8.

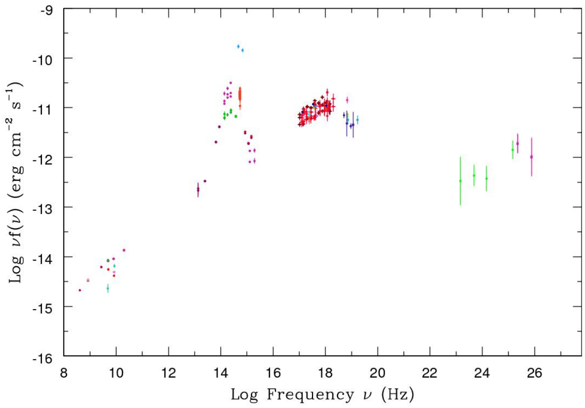

Fig. 5. SEDs of the extreme object 2WHSP J035257.4−683117. See text for details.

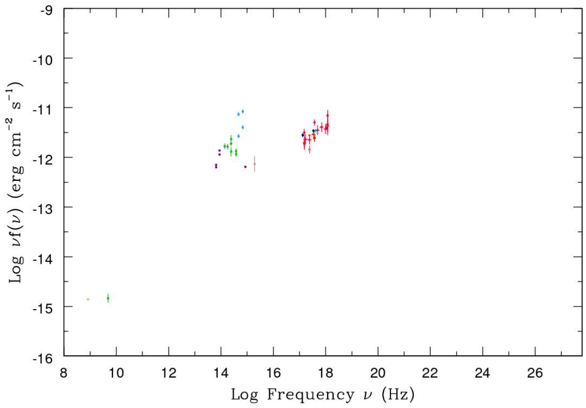

Fig. 7. SEDs of the extreme object 2WHSP J143342.7−730437. See text for details.

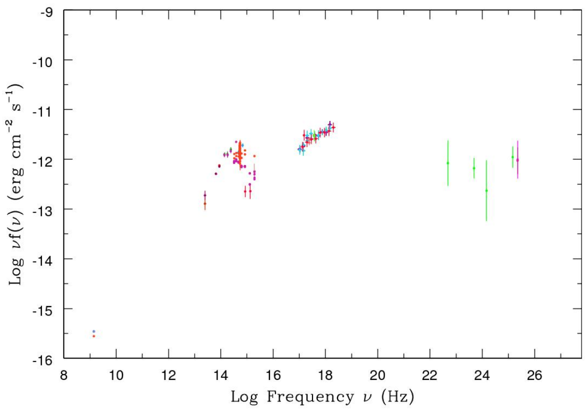

Fig. 6. SED of the extreme object 2WHSP J215305.2−004229. See text for details.

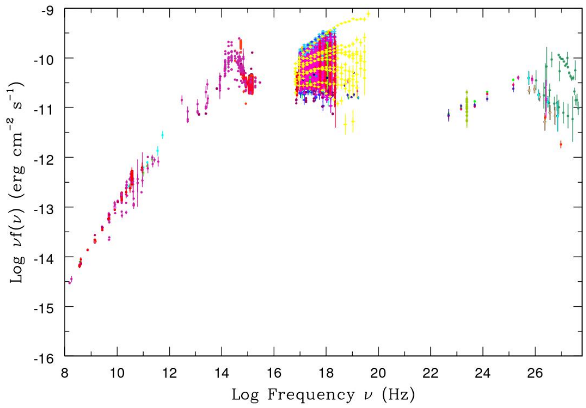

Fig. 8. SEDs of the extreme object 2WHSP J165352.2+394536. See text for details.

- *2WHSP J035257.4−683117*. This is a known blazar with $\log \nu_{\rm peak} \approx 18.1$. It has hard X-ray and γ-ray detections, but no TeV detection yet. This source might be a good target for next generation TeV telescopes. This source is not in 5BZCat yet.
- *2WHSP J215305.2−004229 (5BZBJ2153−0042)*. This source has a very hard X-ray spectrum and the SED in the X-ray band keeps increasing up to the highest energies, implying a $\nu_{\rm peak}$ larger that 10^{18} Hz. The X-ray emission is not likely to be related to a cluster of galaxys since it is compact. It has γ-ray data and may be a good TeV candidate source.
- *2WHSP J143342.7−730437*. This is another example of a very hard X-ray SED. This has UV data but so far did not have any γ-ray data; however, this source is in the list of new γ-ray detections in Arsioli & Chang (2016).
- *2WHSP J165352.2+394536*. This is the well-known HSP MRK501. On average $\log \nu_{\rm peak} \sim 17.9$ Hz; however, during an X-ray flare, as shown by the *Beppo*SAX data (yellow points in the SED, Giommi et al. 2002), $\nu_{\rm peak}$ reached $>10^{18}$ Hz. We note that in Pian et al. (1998), they discussed the *Beppo*SAX observation of MRK501 in April 1997 and showed that the $\nu_{\rm peak}$ of that shift at least two orders of magnitude with regard to previous observations. The was the first time this scenario had been seen.

4.3. The redshift distribution

Some 2WHSP sources lack redshift since their optical spectra are completely featureless. As in Paper I, we estimated lower limit redshifts for these sources. Assuming that in the optical band the host galaxy is swamped by the non-thermal emissions and leaves no imprint on the optical spectrum when the observed non-thermal flux is at least ten times larger than the host galaxy flux, we used the distance modulus (for details, see Eq. (5) in Paper I) to calculate the lower limits redshifts. For the others, we obtained the redshifts from the references listed in Table 4.

Figure 9 shows the redshift distribution, which peaks just above 0.2. For all 2WHSP sources, $\langle z_{\rm all} \rangle = 0.371 \pm 0.005$; for firm redshift 2WHSP sources, $\langle z \rangle = 0.331 \pm 0.008$. Clearly, sources without firm redshift are, on average, farther away than sources with firm redshift. High redshift sources in flux limited samples tend to have featureless optical spectra as the host galaxy contribution is overwhelmed by the synchrotron emission. Giommi et al. (2012) have predicted that the redshift distribution of BL Lacs without redshift in radio flux limited surveys will peak around $z_{\rm predict} \approx 1.2$. The results again suggest that all

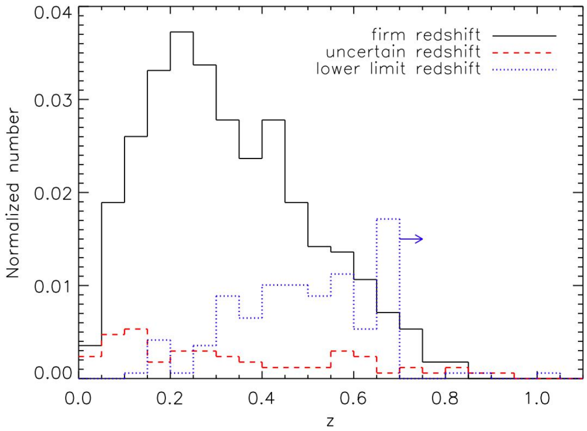

Fig. 9. Redshift distribution of 2WHSP sources. The black solid line represents the sources with firm redshifts, the red dashed line the sources with uncertain redshift, and the blue dotted line the lower limits.

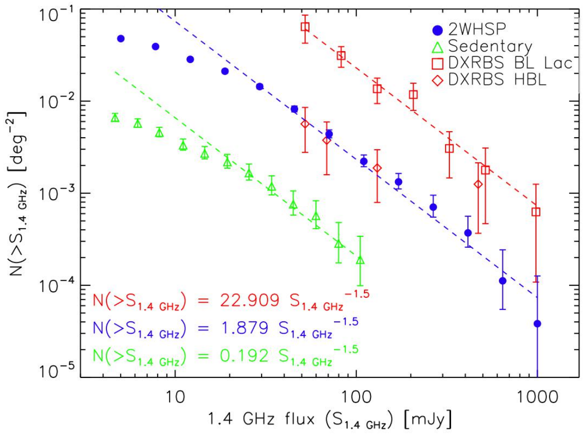

Fig. 10. Integral radio $\log N - \log S$ at 1.4 GHz. The blue filled circles denote the 2WHSP catalogue, the green open triangles indicate the Sedentary survey, the red open squares represent DXRBS BL Lacs of all types, while the red diamonds are the subsample of HBLs in the DXRBS (those in the HBL box: see Padovani et al. 2007, for details). The dashed lines have a slope of −1.5.

source with only lower limit redshift, or without redshift, could be much further away than objects with measured redshift.

Considering only sources with firm z values, the redshift distribution of 2WHSP sources is similar but not identical to other HSP catalogues/subsamples. The average redshift of the 1WHSP catalogue is $\langle z_{\rm 1whsp}\rangle = 0.306$, that of the subsample of HSPs ($\nu_{\rm peak} > 10^{15}$ Hz) in 5BZCat is $\langle z_{\rm bzcat}\rangle = 0.294$, that of the Sedentary sources is $\langle z_{\rm s}\rangle = 0.320$, and that of the K13 catalogue is $\langle z_k\rangle = 0.289$. For instance in K13, the redshifts range is $0.031 < z_k < 0.702$ while, in this paper, we selected a number of sources with relatively high redshift ($z > 0.7$) that are not in previous catalogues.

4.4. The radio log N–log S of HSP blazars

The estimation of the statistical properties, such as the $\log N - \log S$ of a population of sources, requires the availability of flux-limited and complete samples. Since we demand that all 2WHSP sources have a radio, IR, and X-ray counterpart, we must take into account the incompleteness resulting from the fact that the only existing all sky X-ray survey is not sufficiently deep to ensure the detection of all radio and IR faint HSP blazars.

To estimate the $\log N - \log S$, we then considered the subsample of 2WHSP sources that are included in the RASS X-ray survey, which covers the entire sky, albeit with sensitivity that strongly depends on ecliptic latitude (see Sect. 4.3 of Paper I for more details).

For each source in the 2WHSP-RASS subsample, we therefore calculated a contribution $n_{\rm i}$ to the total density, as given by $n_{\rm i} = 1/A_{\rm i}$ deg^{-2}, where the parameter $A_{\rm i}$ is the sky area covered by RASS with sensitivity sufficient to detect the source in consideration. We then sum the contribution of all sources in a given flux bin $N_{\rm bin} = \sum n_{\rm i}$ and obtain the $\log N - \log S$. We use this approach to estimate the $\log N - \log S$ of HSP blazars with respect to the radio flux density.

The integral radio $\log N - \log S$ for the 2WHSP sample is shown in Fig. 10, where we also plot the $\log N - \log S$ for the Sedentary HBL (Giommi et al. 1999, 2005; Piranomonte et al. 2007) for comparison. The dotted lines correspond to a fixed slope of –1.5, the expected value for a complete sample of a non-evolving population in a Euclidean Universe. Since the radio surveys that we use have different sensitivities in the northern and southern sky, we only considered sources with $\delta > -40°$ and radio flux density ≥5 mJy.

It is clear from Fig. 10 that the surface density of the 2WHSP sample is approximately a factor of ten larger than that of the Sedentary Survey, which is expected since the latter includes more extreme sources (its $\nu_{\rm peak}$ distribution peaks at $\log \nu_{\rm peak} \sim 16.8$, as compared to $\log \nu_{\rm peak} \sim 15.5$ for the 2WHSP sample). Apart from the different normalizations, the $\log N - \log S$ of the two samples show similar trends deviating from the Euclidean slope at radio flux densities lower than ≈20 mJy. The 2WHSP flattening, however, appears to be stronger than that of the Sedentary Survey, which suggests the onset of some degree of incompleteness at lower radio flux densities, on top of the evolutionary effects discussed by Giommi et al. (1999). The 2WHSP maximum surface density corresponds to a total of ∼1900 HSP blazars over the whole sky. Given that this number refers only to sources with 1.4 GHz flux density ≥5 mJy, and because of the incompleteness discussed above, this has to be considered a robust lower limit.

Figure 10 shows also the 5 GHz[5] number counts for the Deep X-ray Radio Blazar Survey (DXRBS) BL Lacs (red squares) and HBL only (red diamonds) from Padovani et al. (2007). The latter are in very good agreement with the 2WHSP number counts in the region of overlap, which shows that our selection criteria are robust. Moreover, a clear trend can be seen going from the Sedentary Survey to the 2WHSP sample and to the whole BL Lac population, with an increase in number by a factor ≈10 at every step. Given the unbiased nature of radio selection with respect to $\nu_{\rm peak}$, this is a direct consequence of BL Lac demographics, with HBL making up only ∼10% of the total (see also, for example, Padovani et al. 2007).

4.5. The IR colour–colour plot

Figure 11 shows the WISE IR colour–colour diagram of 2WHSP sources, with signal to noise ratio (S/N) in the W3 channel

[5] Given that BL Lacs typically have flat radio spectra, we did not convert the 5 GHz counts to 1.4 GHz.

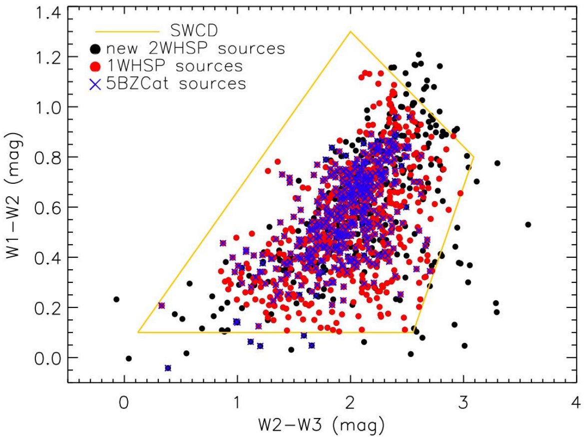

Fig. 11. IR colour–colour diagram. The black points are the sources we selected in 2WHSP but not in 1WHSP, the red points are the selected in 1WHSP, the blue crosses are the sources also in 5BZCat. The yellow line marks the SWCD region.

larger than 2, and the sources in the first WHSP sample and HSP blazars in the 5BZCat list. As expected, all of the 1WHSP sources are within the SWCD region since this was one of the criteria of the selection. By dropping the IR slope criterion ($-1.0 < \alpha_{3.4\ \mu m-12.0\ \mu m} < 0.7$) the 2WHSP sample includes more HSPs that are located in the bottom-left region within the SWCD than the 1WHSP sample.

There are also 47 sources outside the SWCD region (see Table 3), five of which are also in 5BZCat. The sources at the bottom are dominated by the host galaxy in the optical and near IR bands (Class 1). The right part of Fig. 11 is occupied by sources with problematic W3 photometry and sources whose W3 magnitude has relatively small S/N values (typically <4: Class 2). The sources located in the upper-right region have W1 fluxes similar or slightly lower than the W2 fluxes (Class 3). The class 3 sources may be IR variable sources or could be blazars at the border between ISP and HSP objects or might simply have poor W1 or W2 photometry. All 47 sources were checked individually and all of them are good HSP candidates. Thus, we suggest that the SWCD region needs to be extended to include all galaxy-dominated HSPs.

4.6. Candidates for GeV and VHE γ-ray observations

Since HSPs are the dominant population in the extragalactic VHE sky, the 2WHSP catalogue provides good candidates for the search of sources in *Fermi* catalogues and in the VHE band. The Figure of Merit (FOM, defined in Arsioli et al. 2015, as the ratio between the synchrotron peak flux $\nu_{\rm peak} f_{\nu_{\rm peak}}$ of a given source and that of the faintest blazar in the 1WHSP sample that has already been detected in the TeV band) was introduced to provide a simple quantitative measure of potential detectability of HSPs by TeV instruments. The FOM parameter is reported for all 2WHSP sources and gives an objective way to assess the likelihood that a given HSP may be detectable as a TeV source. As discussed in Paper I, relatively high FOM sources (FOM > 0.1) are good targets for observation with the upcoming Cherenkov Telescope Array (CTA). Another upcoming instrument, the Large High Altitude Air Shower Observatory (LHAASO), is currently designed to survey with unprecedented sensitivity the whole northern sky for γ-ray sources above 300 GeV. Therefore, high FOM 2WHSP sources may also provide seed-positions for searches of γ-ray signature embedded in LHAASO data (Cao et al. 2010).

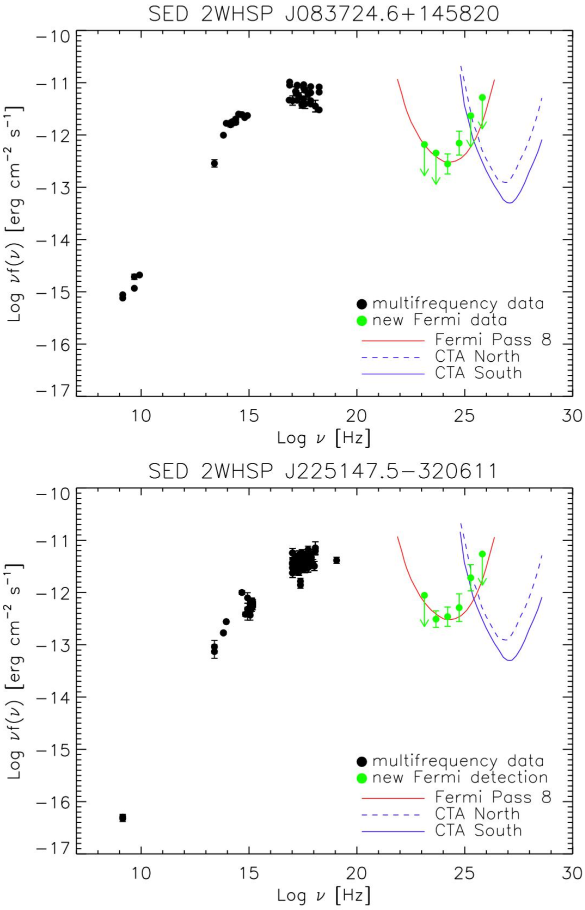

Fig. 12. VHE observations candidates. *Top*: 2WHSP J083724.6+145820; *bottom*: 2WHSP J225147.5−320611. The red line and blue lines are the *Fermi* Pass 8 and CTA sensitivities, respectively. The green circles are the data from *Fermi* Pass 8, and the black points are the data from other wavebands. The Pass 8 data are obtained from the *Fermi* tool using the 2WHSP position. These sources are not yet in the 3FGL catalogue (see Arsioli & Chang 2016).

For example, 2WHSP J083724.6+145820 (see Fig. 12), has $\nu_{\rm peak} \sim 10^{16.7}$ Hz and $\nu_{\rm peak} f_{\nu_{\rm peak}} \sim 10^{-11}$ erg cm^{-2} s^{-1} (or FOM = 2), but it had no γ-ray counterpart until recently. The green points in Fig. 12 correspond to the new γ-ray data presented in Arsioli & Chang (2016). Another example is 2WHSP J225147.5−320611, which has $\nu_{\rm peak} > 10^{18}$ Hz and $\nu_{\rm peak} f_{\nu_{\rm peak}} > 10^{-11.3}$ erg cm^{-2} s^{-1} (FOM > 1), but also had no γ-ray counterpart in current available γ-ray or VHE catalogues (1/2/3 FGL, 1/2 FHL, and TeVCat) until it was detected by Arsioli & Chang (2016) thanks to the 2WHSP, which points to promising x-ray targets.

To better assess the percentage of detection of HSP blazars in the γ-ray band, in fact, Arsioli & Chang (2016) have recently performed a dedicated γ-ray analysis of all 2WHSP sources with FOM ≥ 0.16, using archival *Fermi*-LAT observations integrated

Table 3. Sources outside the SWCD region.

Source	W1 mag	W2 mag	W3 mag	W3 S/N
Class 1: Host galaxy dominated				
2WHSPJ180408.8+004221	12.197	12.109	10.521	12.3
2WHSPJ085730.1+062726	13.349	13.303	12.101	2.7
2WHSPJ031250.2+361519	12.137	12.089	10.432	12.5
2WHSPJ090802.2−095936	11.586	11.523	10.406	15.0
2WHSPJ160740.0+254113	11.401	11.443	11.057	8.7
2WHSPJ013626.5+302011	15.961	15.914	12.905	2.2
2WHSPJ023109.1−575505	10.546	10.515	9.039	38.3
2WHSPJ085958.6+294423	14.881	14.802	12.166	3.0
2WHSPJ094537.0−301332	14.864	14.850	12.317	3.1
2WHSPJ120850.5+452951	14.811	14.749	12.629	2.6
2WHSPJ130711.8+115316	12.430	12.413	11.864	4.2
2WHSPJ195020.9+604750	12.675	12.679	12.640	3.2
2WHSPJ101514.2−113803	12.694	12.462	12.532	2.4
Class 2: Mainly problematic W3				
2WHSP J000552.9−284502	15.501	15.370	12.450	2.3
2WHSP J004501.4+051215	14.170	13.795	10.822	3.1
2WHSP J082030.7−031412	15.118	14.676	11.749	3.0
2WHSP J082355.6+394747	15.509	15.141	12.086	3.3
2WHSP J100520.4+240503	15.324	14.946	11.988	3.0
2WHSP J113405.8+483903	15.108	15.005	12.422	2.4
2WHSP J122304.9+453444	15.246	14.841	12.033	4.0
2WHSP J122944.5+164004	15.265	14.965	11.925	3.2
2WHSP J124430.7+351002	15.782	15.080	11.964	3.6
2WHSP J140125.3+031629	16.550	15.775	12.476	3.1
2WHSP J144446.0+474256	15.840	15.427	12.630	3.2
2WHSP J162939.4+701448	16.763	16.233	12.662	3.2
2WHSP J175955.2+150109	15.907	15.690	12.404	2.8
2WHSP J195134.7−154929	14.702	14.417	11.715	3.4
2WHSP J212233.7+192527	15.201	14.683	11.739	4.9
2WHSP J215355.8−295443	15.914	15.733	12.440	2.2
Class 3: W2 similar to or brighter than W1				
2WHSP J002258.9−244022	15.056	13.894	11.104	8.4
2WHSP J022941.1−412050	14.773	13.747	11.113	9.0
2WHSP J024743.3−481545	15.164	14.059	11.382	10.5
2WHSP J025057.1−122612	15.081	14.001	11.332	8.3
2WHSP J054504.3+065809	14.953	14.049	11.129	5.9
2WHSP J071625.6+750700	15.768	14.634	12.147	5.3
2WHSP J093938.5−031502	15.328	14.445	11.535	5.0
2WHSP J095518.4−294611	14.321	13.149	10.526	14.2
2WHSP J120136.0−060733	15.247	14.168	11.430	3.5
2WHSP J135043.7−310926	14.359	13.202	10.817	12.5
2WHSP J172746.3−754618	14.039	12.883	10.522	15.3
2WHSP J180158.9+610938	15.332	14.164	11.598	9.9
2WHSP J185550.8+805223	16.492	15.580	12.638	3.4
2WHSP J202803.5+720513	15.440	14.459	11.671	13.1
2WHSP J204734.9+793759	16.494	15.328	12.753	2.9
2WHSP J213533.7+314919	14.312	13.223	10.711	12.0
2WHSP J233207.6−025245	15.108	14.037	11.387	5.0
2WHSP J233630.4−635634	14.599	13.391	10.788	12.0

over 7.2 yr of observations. By using the position of 2WHSP sources as seeds for the data analysis, ≈85 sources were identified at the $>5\sigma$ (TS > 25) level, and another 65 at a less significant (10 < TS < 25) level. These results demonstrate the potential of HSP catalogues for the detection and identification of γ-ray and VHE sources.

Apart from that, the CTA flux limit/sensitivity could be as low as 3×10^{-13} erg cm^{-2} s^{-1} (Rieger et al. 2013) or ∼1 mCrab at 1 TeV for 50-h exposure. Clearly, from Fig. 12, 2WHSP J083724.6+145820 and 2WHSP J225147.5−320611 may be detected by CTA in the future (since they are above the CTA sensitivity for an exposure time of 50 h, the blue lines). Therefore, with the benefit of multi-wavelength work, we provide many candidates for future VHE observations.

4.7. HSP blazars as neutrino and cosmic ray emitters?

Blazars have been considered as likely neutrino sources for quite some time (e.g. Mannheim 1995). Padovani & Resconi (2014) have suggested that blazars of the HSP type, where particles are accelerated to the highest energies, may be good candidates for neutrino emission and presented evidence for an association between HSP blazars and neutrinos detected by the IceCube South Pole Neutrino Observatory[6].

Petropoulou et al. (2015) further modelled the HE SED of six HSPs selected by Padovani & Resconi (2014) as most probable neutrino sources and predicted their neutrino fluxes. All six predicted fluxes were consistent, within the errors, with the observed neutrino fluxes from IceCube, especially for two sources (MKN421 and H1914−194).

Padovani et al. (2016) have recently cross-matched two VHE catalogues and the 2WHSP with the most recent IceCube neutrino lists (IceCube Collaboration 2015), measuring the number of neutrino events with at least one γ-ray counterpart. In all three catalogues they observed a positive fluctuation with respect to the mean random expectation at a significance level between 0.4 and 1.3%, with a p-value of 0.7% for 2WHSP sources with FOM $\gtrsim$ 1. All HBLs considered to be the most probable counterparts of IceCube neutrinos are 2WHSP sources, which strongly suggests that strong, VHE γ-ray HBLs are so far the most promising blazar counterparts of astrophysical neutrinos.

Finally, Resconi et al. (2016) have presented evidence of a direct connection between HSP, VHE neutrinos, and ultra high energy cosmic rays (UHECRs) by correlating the same catalogues used by Padovani et al. (2016) with UHECRs from the *Pierre Auger* Observatory and the Telescope Array. A maximal excess of 80 cosmic rays (41.9 expected) was observed for 2FHL HBL. The chance probability for this to happen is 1.6×10^{-5}, which translates to 5.5×10^{-4} (3.26σ) after compensation for trials.

5. Conclusions

We have assembled the 2WHSP catalogue, currently the largest and most complete existing catalogue of HSP blazars, by using a multi-frequency method and a detailed comparison with existing lists of γ-ray emitting blazars. 2WHSP extends the previous 1WHSP catalogue (Arsioli et al. 2015) down to lower Galactic latitudes ($|b| > 10°$) and to fainter IR fluxes. In addition, it includes all the bright known HSP blazars close to the Galactic plane. The 2WHSP sample includes 1691 confirmed or candidates HSP blazars and was also put together to provide a large list of potential targets for VHE and multi-messenger observations.

The average $\nu_{\rm peak}$ for our catalogue is $\langle \log \nu_{\rm peak} \rangle = 16.22 \pm 0.02$ Hz and the average redshift is $\langle z \rangle = 0.331 \pm 0.008$. We have shown that the SWCD region needs to be extended to include HSPs in which the host galaxy is dominant.

Our radio $\log N - \log S$ shows that the number of HSP blazars over the whole sky is >2000 and that HBL make up ~10% of all BL Lacs.

Finally, we note that this catalogue has already been used to provide seeds for the identification of new *Fermi*-LAT objects and to look for astrophysical counterparts to neutrino and UHECR sources (Padovani et al. 2016; Resconi et al. 2016), which proves the relevance of having a large HSP catalogue for multi-messenger astronomy.

Acknowledgements. Y.L.C. is supported by the Government of the Republic of China (Taiwan), B.A. is supported by the Brazilian Scientific Program Ciências sem Fronteiras – Cnpq. This work was supported by the Agenzia Spaziale Italiana Science Data Center (ASDC) and the University La Sapienza of Rome, Department of Physics. P.P. thanks the ASDC for the hospitality and partial financial support for his visits. We made use of archival data and bibliographic information obtained from the NASA/IPAC Extragalactic Database (NED), data and software facilities from the ASDC managed by the Italian Space Agency (ASI). Extensive use was made of the TOPCAT software package (http://www.star.bris.ac.uk/~mbt/topcat/).

[6] http://icecube.wisc.edu

References

Abdo, A., Ackermann, M., Agudo, I., et al. 2010, ApJ, 716, 30
Ackermann, M., Ajello, M., Atwood, W. B., et al. 2016, ApJS, 222, 5
Ajello, M., Gasparrini, D., Sanchez-Conde, M., et al. 2015, ApJ, 800, L27
Antonucci, R. 1993, ARA&A, 31, 473
Arsioli, B., & Chang, Y.-L. 2016, A&A, in press, DOI: 10.1051/0004-6361/201628691
Arsioli, B., Fraga, B., Giommi, P., Padovani, P., & Marrese, P. M. 2015, A&A, 579, A34
Blandford, R., & Rees, M. 1978, in Pittsburgh Conf. BL Lac Objects, ed. A. M. Wolfe (Pittsburgh: University of Pittsburgh press), 341
Böhringer, H., & Werner, N. 2010, A&ARv, 18, 127
Bonnoli, G., Tavecchio, F., Ghisellini, G., & Sbarrato, T. 2015, MNRAS, 451, 611
Cao, Z., Bi, X. J., Cao, Z., et al. 2010, in 38th COSPAR Sci. Assem., Bremen, 2
Condon, J., Cotton, W., Greisen, E., et al. 1998, AJ, 115, 1693
Costamante, L., Ghisellini, G., Giommi, P., et al. 2001, A&A, 371, 512
Cutri, R. M., Wright, E. L., Conrow, T., et al. 2013, Explanatory Supplement to the AllWISE Data Release Products, Tech. rep.
D'Abrusco, R., Massaro, F., Ajello, M., et al. 2012, ApJ, 748, 68
D'Elia, V., Perri, M., Puccetti, S., et al. 2013, A&A, 551, A142
Dermer, C. D., Cavadini, M., Razzaque, S., et al. 2011, ApJ, 733, L21
Di Mauro, M., Donato, F., Lamanna, G., Sanchez, D. A., & Serpico, P. D. 2014, ApJ, 786, 129
Elvis, M., Plummer, D., Schachter, J., & Fabbiano, G. 1992, ApJS, 80, 257
Evans, I. N., Primini, F. A., Glotfelty, K. J., et al. 2010, ApJS, 189, 37
Finke, J. D., Reyes, L. C., Georganopoulos, M., et al. 2015, ApJ, 814, 20
Giommi, P., & Padovani, P. 2015, MNRAS, 450, 2404
Giommi, P., Menna, M. T., & Padovani, P. 1999, MNRAS, 310, 465
Giommi, P., Capalbi, M., Fiocchi, M., et al. 2002, in Blazar Astrophysics with *Beppo*SAX and Other Observatories, eds. P. Giommi, E. Massaro, & G. Palumbo, 63
Giommi, P., Piranomonte, S., Perri, M., & Padovani, P. 2005, A&A, 434, 385
Giommi, P., Colafrancesco, S., Cavazzuti, E., Perri, M., & Pittori, C. 2006, A&A, 445, 843
Giommi, P., Colafrancesco, S., Padovani, P., et al. 2009, A&A, 508, 107
Giommi, P., Padovani, P., Polenta, G., et al. 2012, MNRAS, 420, 2899
Harris, D. E., Forman, W., Gioia, I. M., et al. 1993, The Einstein Observatory catalogue of IPC X ray sources, Volume 1E: Documentation
IceCube Collaboration 2015, in 34th Int. Cosm. Ray Conf.
Kapanadze, B. 2013, AJ, 145, 31
Manch, T., Murphy, T., Buttery, H. J., et al. 2003, MNRAS, 342, 1117
Mannheim, K. 1995, Astropart. Phys., 3, 295
Massaro, E., Giommi, P., Leto, C., et al. 2009, A&A, 495, 691
Massaro, F., D'Abrusco, R., Ajello, M., Grindlay, J., & Smith, H. 2011, ApJ, 740, L48
Massaro, E., Nesci, R., & Piranomonte, S. 2012, MNRAS, 422, 2322
Massaro, E., Maselli, A., Leto, C., et al. 2015, Ap&SS, 357, 75
Padovani, P., & Giommi, P. 1995, ApJ, 444, 567
Padovani, P., & Giommi, P. 2015, MNRAS, 446, L41
Padovani, P., & Resconi, E. 2014, MNRAS, 443, 474
Padovani, P., Ghisellini, G., Fabian, A. C., & Celotti, A. 1993, MNRAS, 260, L21
Padovani, P., Giommi, P., Landt, H., & Perlman, E. S. 2007, ApJ, 662, 182
Padovani, P., Resconi, E., Giommi, P., Arsioli, B., & Chang, Y. L. 2016, MNRAS, 457, 3582
Panzera, M. R., Campana, S., Covino, S., et al. 2003, A&A, 399, 351
Pérez-Torres, M. A., Zandanel, F., Guerrero, M. A., et al. 2009, MNRAS, 396, 2237
Petropoulou, M., Dimitrakoudis, S., Padovani, P., Mastichiadis, A., & Resconi, E. 2015, MNRAS, 448, 2412
Pfrommer, C., Broderick, A. E., Chang, P., Puchwein, E., & Springel, V. 2013, ArXiv e-prints [arXiv:1308.6284]
Pian, E., Vacanti, G., Tagliaferri, G., et al. 1998, ApJ, 492, L17
Piranomonte, S., Perri, M., Giommi, P., Landt, H., & Padovani, P. 2007, A&A, 470, 787
Planck Collaboration XXXII. 2015, A&A, 581, A14

A&A 598, A134 (2017)
DOI: 10.1051/0004-6361/201628691

Astronomy & Astrophysics

Searching for γ-ray signature in WHSP blazars

Fermi-LAT detection of 150 excess signal in the 0.3−500 GeV band

B. Arsioli[1,2,3] and Y.-L. Chang[1,2]

[1] ASI Science Data Center, ASDC, Agenzia Spaziale Italiana, via del Politecnico snc, 00133 Roma, Italy
e-mail: bruno.arsioli@asdc.asi.it
[2] Sapienza Università di Roma, Dipartimento di Fisica, Piazzale Aldo Moro 5, 00185 Roma, Italy
[3] ICRANet-Rio, CBPF, rua Dr. Xavier Sigaud 150, 22290-180 Rio de Janeiro, Brazil

Received 11 April 2016 / Accepted 1 September 2016

ABSTRACT

Aims. A direct search of γ-ray emission centered on multifrequency selected candidates is a valuable complementary approach to the standard search adopted in current γ-ray *Fermi*-LAT catalogs. Our sources are part of the 2WHSP sample that was assembled with the aim of providing targets for Imaging Atmospheric Cherenkov Telescopes (IACT). A likelihood analysis based on their known position enabled us to detect 150 γ-ray excess signals that have not yet been reported in previous γ-ray catalogs (1FGL, 2FGL, 3FGL). By identifying new sources, we solve a fraction of the extragalactic isotropic γ-ray background (IGRB) composition, improving the description of the γ-ray sky.

Methods. We perform data reduction with the *Fermi* Science Tools using positions from 400 high synchrotron peaked (HSP) blazars as seeds of tentative γ-ray sources; none of them have counterparts from previous 1FGL, 2FGL and 3FGL catalogs. Our candidates are part of the 2WHSP sample (currently the largest set of HSP blazars). We focus on HSPs characterized by bright synchrotron component with peak flux $\nu f_{(\nu)} \geq 10^{-12.1}$ erg/cm^2/s, testing the hypothesis of having a γ-ray source in correspondence to the WHSP positions. Our likelihood analysis considers the 0.3−500 GeV energy band, integrating over 7.2 yr of *Fermi*-LAT observation and making use of the Pass 8 data release.

Results. From the 400 candidates tested, a total of 150 2WHSPs showed excess γ-ray signature: 85 high-significance detections with test statistic (TS) > 25, and 65 lower-significance detections with TS between 10 to 25. We assume a power law spectrum in the 0.3−500 GeV band and list the spectrum parameters describing all 150 new γ-ray sources. We study the γ-ray photon spectral index distribution, the likelihood of detection according to the synchrotron peak brightness (figure of merit parameter), and plot the measured γ-ray Log$N$-Log$S$ of HSP blazars, also discussing the portion of the IGRB that has been resolved by the present work. We also report on four cases where we could resolve source confusion and find counterparts for unassociated 3FGL sources with the help of high-energy TS maps together with multifrequency data. The 150 new γ-ray sources are named with the acronym 1BIGB for the first version of the Brazil ICRANet Gamma-ray Blazar catalog, in reference to the cooperation agreement supporting this work.

Key words. galaxies: active – BL Lacertae objects: general – radiation mechanisms: non-thermal – gamma rays: diffuse background – gamma rays: general

1. Introduction

Catalogs of γ-ray sources currently compiled by the *Fermi*-LAT team are based on γ-ray data only, and their standard detection method is blind with respect to information coming from other wavelengths. This approach is clean and unbiased with respect to any class of potential γ-ray emitters. However, there are populations of astrophysical objects that are now known to emit γ-rays, and the knowledge of their position in the sky can be used to facilitate the detection and identification of new γ-ray sources. Based on this principal, we select a sample of candidates to be used as seeds for a direct search of γ-ray signatures using likelihood analysis with the *Fermi* Science Tools.

Blazars are the most abundant γ-ray sources in the latest *Fermi*-LAT 3FGL catalog, being 1147 (660 BL Lacs and 487 flat spectrum radio quasars − FSRQ) of the total 3034 (Acero et al. 2015). Even so, one third of the known blazars from 5BZcat[1] are not confirmed as γ-ray emitters. Probably many of them are faint γ-ray sources that are hard to identify by automatic search methods only based on *Fermi*-LAT data. The blazar population has been extensively studied by means of a multifrequency approach considering dedicated databases on radio, microwave, infra-red (IR), optical, ultraviolet (UV), and X-ray, since they are characterized by radiation emission extending along the whole electromagnetic spectrum, up to TeV energies.

A particular family of extreme sources with the synchrotron component peaking at frequencies $\nu_{\rm peak}$ larger than 10^{15} Hz is classified as a high synchrotron peak blazar (HSP, Padovani & Giommi 1995; Abdo et al. 2010a) and is the dominant population associated with extragalactic very high-energy (VHE: E > 0.1 TeV, Rieger et al. 2013) sources in the 2nd Catalog of Hard *Fermi*-LAT Sources (2FHL, Ackermann et al. 2016b). Therefore, HSPs constitute a key population for the detection of point-like γ-ray sources within *Fermi*-LAT data.

[1] The 5BZcat (Massaro et al. 2015) is a large sample of 3561 identified blazars. Multifrequency data for the 5BZcat is available at http://www.asdc.asi.it/bzcat with a direct link to the SED-builder tool.

A large sample of HSP blazars was recently assembled using a multifrequency selection procedure that exploits the unique features of their spectral energy distribution (SED). This sample is known as the 1WHSP catalog (Arsioli et al. 2015) and was built using a primary source-selection based on IR colors (following Massaro et al. 2011), later demanding all potential candidates to have a radio, IR and X-ray counterpart. The sources had to satisfy broadband spectral slope criteria (from radio to X-rays) that were fine-tuned to match the SED of typical HSP blazars. In addition, their multifrequency SEDs were inspected individually using the SED-builder tool[2] fitting the synchrotron component with a third degree polynomial to determine the $\nu_{\rm peak}$ parameter, only keeping cases with $\nu_{\rm peak} > 10^{15}$ Hz. The catalog name "WHSP" stands for WISE high synchrotron peak blazars, since all sources have an IR counterpart from the WISE mission (Wright et al. 2010), which defines their positions. The 1WHSP catalog includes 992 objects at Galactic latitude $|b| > 20°$. A total of 299 1WHSPs have a confirmed γ-ray counterpart in 1FGL, 2FGL and 3FGL (Arsioli et al. 2015), but many HSPs with bright synchrotron peak are still not detected/confirmed in the γ-ray band.

Given the importance of finding new HSP blazars, an extension of the 1WHSP sample (the 2WHSP, Chang et al. 2017) has ben assembled. It considers sources located at latitudes as low as $|b| = 10°$ with a total of $\approx$1693 sources, 439 of which have counterparts within the error circles from the 3FGL catalog. The 2WHSP sample avoids the selection based on IR colors that was used as a primary step for the 1WHSP catalog. This brings an overall improvement in completeness[3], since some HSP blazars were out of the 1WHSP sample owing to the contamination of IR colors by the elliptical-galaxy thermal emission. Compared to the 1WHSP, the 2WHSP sample incorporates extra X-ray catalogs like Einstein IPC, IPC slew and *Chandra* (Harris et al. 1993; Elvis et al. 1992; Evans et al. 2010) as well as updated versions from 3XMM-DR5 and XMM-slew catalogs (Rosen et al. 2016; Saxton et al. 2008). In addition, *Swift*-XRT alone performed a series of ~160 new X-ray observation of WHSP sources (enabling us to better estimate synchrotron peak parameters) and an extensive study of X-ray extended sources helped to avoid contamination with spurious objects (more details are given by Chang et al. 2017)[4]. Since the 2WHSP catalog supersedes the 1WHSP (with improved selection and better estimate of synchrotron peak parameters), from now on we only refer to the 2WHSP sample.

Brightness of the synchrotron peak and detectability by Fermi-LAT The HSP blazars are characterized by hard γ-ray spectrum with average photon index $\langle\Gamma\rangle = 1.85 \pm 0.01$ (Arsioli et al. 2015; Ackermann et al. 2011, 2015b) favouring their detection in the high-energy band. Therefore, the 2WHSP catalog has collected an unprecedented number of remarkably rare and extreme sources that are expected to emit γ-rays.

In Fig. 1 we plot the distribution of synchrotron peak fluxes ($\nu_{\rm peak} f_{\nu_{\rm peak}}$) for the 2WHSP detected[5] and undetected

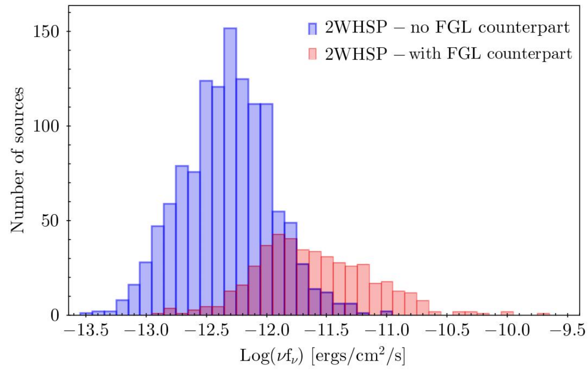

Fig. 1. Distribution of Log($\nu_{\rm peak} f_{\nu_{\rm peak}}$) synchrotron peak flux with indigo bars that represent the γ-ray subsample of 439 2WHSP-FGL sources, and light red-bars representing the 1255 γ-ray undetected 2WHSPs. The intersection between detected and undetected distributions suggests there may be numerous 2WHSP sources close to the detection threshold from *Fermi*-LAT. The 2WHSP catalog lists Log($\nu_{\rm peak} f_{\nu_{\rm peak}}$) values in 0.1 steps, and histogram-bins are centered on those values.

γ-ray sources. As seen, most of the bright 2WHSPs with Log($\nu_{\rm peak} f_{\nu_{\rm peak}}$) > -11.2 erg/cm²/s have already been unveiled by *Fermi*-LAT. The range between $-12.4 <$ Log($\nu_{\rm peak} f_{\nu_{\rm peak}}$) < -11.2 erg/cm²/s where histograms for detected and undetected sources have significant overlap, tells us that there must be a population of undetected 2WHSP blazars that is within the reach of *Fermi*-LAT; especially when taking into consideration integration time greater than 4 yr, as used to build the 3FGL catalog.

As a first step for testing the efficiency of a dedicated γ-ray sources-search, we performed a series of likelihood analysis on bright HSPs that were not included in previous *Fermi*-LAT catalogs 1FGL, 2FGL and 3FGL (FGL). It soon became clear that, when considering longer exposure time with improved event reconstruction of Femi-LAT Pass 8, a significant number of faint γ-ray sources could be detected. For the likelihood analysis, we define a subsample of 2WHSPs with a synchrotron component $\nu_{\rm peak} f_{\nu_{\rm peak}} \geq 10^{-12.1}$ erg/cm²/s simply for limiting the number of seeds to 400, indeed showing its potential for wider studies with the whole 2WHSP sample.

Our present effort for unveiling new γ-ray sources not only provides targets for future follow-up and variability studies, but also helps us to enhance the current understanding on the nature of the VHE γ-ray background, which probably has a strong contribution from unresolved point-like sources (Ajello et al. 2015). Especially at the $E > 10$ GeV band, unresolved HSP blazars may have increasing relevance (Giommi & Padovani 2015) as was confirmed by our results described in Sect. 4.

2. *Fermi*-LAT data reduction

The *Fermi*-LAT detector (Atwood et al. 2009) is characterized by a point spread function (PSF) which contains 68% of the 1 GeV events within 0.8°. The PSF decreases with energy, following a trend $\propto E^{-0.8}$ up 10's GeV, and is roughly constant at 0.1° from there to the highest energies considered in this paper.

Based on the position of a potential γ-ray source, we downloaded Pass 8 processed events from the public *Fermi*-database[6]

[2] http://www.asdc.asi.it

[3] Also to improve the completeness of the final sample, known HSP sources at $|b| < 10°$ were incorporate in the 2WHSP catalog.

[4] The catalogs are available at: www.asdc.asi.it/1whspor/2whsp; where multifrequency SEDs can be quickly built using open access online tools.

[5] We may use 2WHSP-FGL when referring to the subsample of 439 2WHSPs that have counterparts from the 1FGL, 2FGL, and 3FGL catalogs.

[6] http://fermi.gsfc.nasa.gov/ssc/data/access/

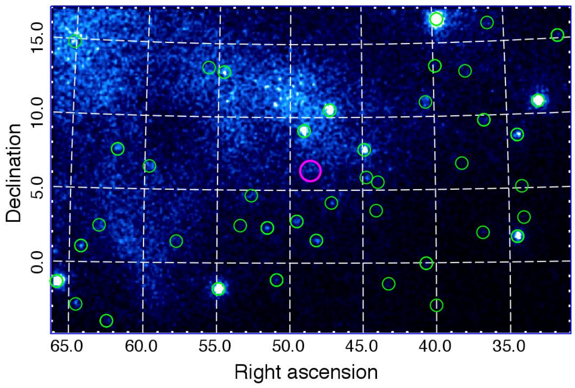

Fig. 2. *Fermi*-LAT γ-ray counts map in the energy range 0.3−500 GeV, over 7.2 yr, showing detected γ-ray sources, at the center of the green circles (only as indicative of their 3FGL positions). We highlight the source 2WHSP J031423.8+061955 (center of the magenta circle), which we detected in γ-rays with TS = 69.9. As seen, not all relevant sources are easy to unveil with only the CMAP inspection.

that includes all photons recorded in a region of interest (ROI) of 25° radius from the candidate's position, for the whole 7.2 yr of observations (MM/DD/YYYY: 08/04/2008 to 11/04/2015). In our analysis we used the *Fermi* Science Tools (v10r0p5), performing binned analysis to deal with the long integration time.

A series of quality cuts were applied to the raw data, starting with the selection of events having high probability of being photons (which is done by requiring *evclass* = 128 and *evtype* = 3 in the gtselect routine), working with maximum zenith angle-cut of 90°[7]. Given the fact that HSPs are characterized by hard γ-ray spectrum (with an average photon index $\langle\Gamma\rangle \approx 1.85$) we choose to work at $E > 300$ MeV, avoiding the need to calculate energy-dispersion correction during the data analysis (which is necessary for $E < 300$ MeV photons). With the gtmktime routine, we then generate a list of good time intervals (GTIs) to be considered in further analysis. In this step, some given flags ((DATA-QUAL > 0) and (LAT-CONFIG==1)) assure that only events acquired by LAT instrument in normal science data-taking mode are considered. Using the gtbin routine, we generate counts maps (CMAP) and counts cubes (CCUBE), having 500 × 500 and 350 × 350 pixels with 0.1°/pixel, respectively. The CCUBE is a series of CMAPs, each one having photons within a given energy bin, and here we consider 37 logarithmically spaced energy bins along 0.3−500 GeV.

As an example, the CMAP (Fig. 2) have green circles corresponding to known 3FGL sources, and a magenta circle to mark the 2WHSP J031423.8+061955 position. As seen, together with our candidate, other faint γ-ray sources may be present but cannot easily be distinguished from the counts map, demanding a dedicated data reduction to test the point-like source hypothesis.

A livetime cube is then generated using the gtltcube routine, holding information about the sky coverage as a function of inclination with respect to the LAT z-axis. An important parameter to set in this step is the cos(theta) which is related to the angle-binning, summing incoming photons from a particular solid angle; here we use 0.025° (following recommendations from the *Fermi*-LAT team). Later, the source map is created using the gtsrcmaps routine, and take into account the models describing all previously known γ-ray sources and background emission that are within 25° radius from the center candidate. The models that describe point-like and extended sources, as well as the diffuse Galactic and isotropic background are included in a single .xml file. This was built using the script make3FGLxml.py[8] and considers the 3FGL catalog for describing the point-like and extended sources known so far, loading parameters from the source file gll-psc-v16.fit. For the diffuse Galactic background content, the high-resolution model from the source file gll-iem-v06.fit was considered, and for the isotropic component we use the model from iso-source-v06.txt. We also considered the latest data and instrument response functions (IRFs) available at the time of work, P8R2 SOURCE V6, and event selection Pass 8 processed Source: front+back.

2.1. Adding γ-ray source candidates

Since our γ-ray candidates are not part of the latest *Fermi*-LAT catalog 3FGL, they have to be added to the source-input file (.xml) that contains the model parameters and the positions of all known γ-ray sources. In this work, the spectrum of each γ-ray candidate is always modeled as a power law:

$$\frac{\mathrm{d}N}{\mathrm{d}E} = N_0\left(\frac{E}{E_0}\right)^{-\Gamma} \tag{1}$$

where E_0 is a scale parameter (also known as pivot energy), N_0 is the pre-factor (corresponding to the flux density in units ph/cm^2/s/MeV at the pivot energy E_0), and Γ is the photon spectral index for the energy range under consideration. Usually, the starting guess-values were chosen to be consistent with SEDs from HSP blazars, therefore: E_0 = 1000 MeV, N_0 = 1.0×10^{-12} ph/cm^2/s/MeV, Γ = 1.8. Both Γ and N_0 are set as free parameters and further adjusted by the gtlike fitting routine. The source position and the scaling E_0 are set as fixed parameters. In the source-input xml file, all sources within 10° from the candidate are set free to vary their spectral fitting parameters, therefore 3FGL models that are based on four years of observation are adjusted, since we now integrate over 7.2 yr of data. This particular choice increases the computational burden of the analysis, but is crucial for adapting the model maps to the extra 3.2 yr of exposure that is considered.

A likelihood analysis is then performed by the gtlike routine, considering all the information from the livetime cube, source maps and source input files, together with the PSF and IRFs, in order to best fit the free parameter from the source input list. Finally it is calculated the test statistic (TS) parameter, which is defined as (Mattox et al. 1996)

$$\mathrm{TS} = -2\ln\left(\frac{L_{(\text{no source})}}{L_{(\text{source})}}\right) \tag{2}$$

where $L_{(\text{no source})}$ is the likelihood of observing a certain photon-count for a model without the candidate source (the null hypothesis), and $L_{(\text{source})}$ is the likelihood value for a model with the additional candidate source at the given location. The reported TS values correspond to a full band fitting, which constrains the

[7] The zenith angle-cut is used to avoid contamination with Earth's limb γ-ray photons, which are induced by cosmic-ray interactions with the atmosphere, and are known as strong source of background for the low-energy band covered by *Fermi*-LAT.

[8] The make3FGLxml.py is a python routine written by Johnson (2015), and provided by the *Fermi*-LAT team as an user contribution tool.

whole spectral distribution along 0.3−500 GeV to vary smoothly with energy and assuming no spectral break. Considering we have a good description of Galactic and extragalactic diffuse components, this is a measure of how strong a source emerges from the background, also assessing the goodness of free parameters fit. A TS $\approx$ 25 is equivalent to a 4−5σ detection Abdo et al. (2010b, depending on the strength of the background in the region), and only cases with TS > 25 are considered by the *Fermi*-LAT team as a positive detection of point-like source. We first run the gtlike with the fitting optimiser mode DRMNFB, which generates an enhanced source-input list with all the free parameters recalculated (the first interaction of the fitting procedure). We again feed the gtlike routine with the enhanced source-input list, and use the fitting optimiser mode NEWMINUIT to generate the final model for all sources in the ROI.

3. New γ-ray detections. Validation and population properties

Here we present the γ-ray detection of 85 2WHSP sources at TS > 25 level; and we extend the γ-ray analysis by considering another 65 2WHSPs with lower significance γ-ray signal, with TS ranging between 10 and 25. In Table A.1 we list relevant information for these 150 sources, including names, positions, redshift, γ-ray model parameters and their associated uncertainties. The new γ-ray sources are named with the acronym 1BIGB for the first version of the Brazil ICRANet Gamma-ray Blazar catalog, with source designation 1BIGB JHHMMSS.s±DDMMSS, and coordinates corresponding to the 2WHSP seed-positions. We also present a few examples of TS maps (Sects. 3.2 and 3.3) both for high and low-significance γ-ray signatures, showing that they all emerge as point-like sources, and should not be taken as spurious signals.

In Sect. 3.4 we test a direct source-search using the 3FGL catalog analysis setup, showing that we could successfully probe faint γ-ray emitters and add complementary γ-ray detections. In Sect. 3.5 we calculate the γ-ray detection efficiency based on the brightness of the synchrotron peak (≡figure of merit). In Sect. 3.6 we plot the photon spectral index (Γ) distribution for the newly-detected γ-ray sources and compare their spectral properties with the FGL counterparts from 2WHSP sources. We also show the Γ vs. flux (1−100 GeV band) so that the improvement, with respect to the flux threshold when considering detections down to TS = 10, can be evaluated. In Sect. 3.7 we comment on flux-fluctuations associated with sources close to the flux-threshold (Eddington bias effect) showing that this effect is not severe in our context.

3.1. High-significance γ-ray sources with TS > 25

In Sect. 1 we show that the natural candidates for our analysis are the bright 2WHSP sources[9] that have not yet been detected by *Fermi*-LAT (in previous 1FGL, 2FGL and 3FGL catalogs), as suggested from Fig. 1. Therefore, by sorting the 2WHSP source based on their synchrotron peak brightness, we considered cases down to $\text{Log}(\nu_{\text{peak}} f_{\nu_{\text{peak}}}) = -12.1$ erg/cm^2/s, selecting 400 γ-candidates, from which 85 (∼21%) have shown high-significance γ-ray signature with TS > 25.

For each source of interest, we inspected a region of 50′ radius around it, checking for any previous γ-ray detections or for the presence of bright blazars that could also be potential high-energy counterparts. For this task we made use of the Sky Explorer Tool, available from the ASDC web site (tools.asdc.asi.it), which displays all radio, optical, X-ray, and γ-ray detections for a given ROI. During the preparation of this work, the 2FHL catalog (Ackermann et al. 2016b), which contains only $E >$ 50 GeV detections was released, including six of the sources we were working with. Also Campana et al. (2015), as well as Campana et al. (2016), reported on possible counterparts of photon-clustering detected by *Fermi*-LAT at $E >$ 10 GeV, which included eight of our detections (two in common with the six 2FHL). We keep them in our Table A.1, indicated with "a" and "b" superscripts, respectively, since they constitute positive detections based on our primary approach, showing the intersection between valuable methods for unveiling new γ-ray sources.

The fact that few 2FHL-sources and Campana-sources are in common with our detections is certainly due to their analysis being based only on γ-rays, applied to $E >$ 50 GeV and $E >$ 10 GeV, respectively. Our energy threshold at $E >$ 300 MeV is much lower and well suited to the way we select our seeds (based on multifrequency information from radio to X-rays, not only on γ-ray data). Therefore, we are able to probe hard γ-ray sources, even if they have low flux at $E >$ 10 GeV (we do not depend on γ-ray photon clustering to identify our seeds). In fact, both approaches are powerful and should be seen as complementary, since they all apply to the goal of enriching our description of the γ-ray sky.

3.2. The TS map and γ-ray spectrum

A TS map consists of a pixel-grid where the existence of a point-like source is tested in each pixel. This is a demanding computational task when exposure time that is longer than few months are considered. Here we study the case of 2WHSP J021631.9+231449, defining a 25×25 grid with 0.05°/pixel, and evaluated each grid-bin using likelihood analysis from gttsmap routine. Given the fact that WHSP blazars are expected to be hard spectrum γ-ray sources, we built a TS map that only considers photons with energy larger than 3 GeV[10]. The cut in photon energy helps not only to save computation time, it also has another important purpose: since the PSF improves with increasing energy, working with high-energy photons help us to determine the TS-peak position with better precision. When building the TS map from Fig. 3, the input model (.xml file) does not contain our γ-candidate, so that the map alone can test the existence of point-like sources (with no previous bias), which may manifest as a TS peak that emerges from the background.

All sources within 7° from the grid center have their corresponding model parameters set as free to adjust for the current analysis. Also, we set as free parameters the Normalization (from the diffuse extragalactic background model) and ConstantValue (from the Galactic background model) to avoid having large TS values that are only due to an overestimated background flux. An overestimated background usually manifest as a smooth distribution of high TS values along the whole grid, therefore it is important to properly scale it in the studied region,

[9] By bright sources we mean: 2WHSPs with the largest flux density associated to the synchrotron peak $\nu f_{\nu-\text{peak}}$ component.

[10] For HSP sources with high-significance γ-ray signature, the cut at 3 GeV in many cases provided (and is therefore the reason why we choose it; see examples on Sect. 5) a good balance between computation time and ability to solve the γ-ray signature as a point-like source. Also, despite the fact we are dealing with HSP blazars (with mean γ-ray photon index ∼ 1.9) *Fermi*-LAT has relatively good sensitivity along the 1−100 GeV band, and improved PSF at >3 GeV, which helped to achieve better localization for the γ-ray sources when necessary.

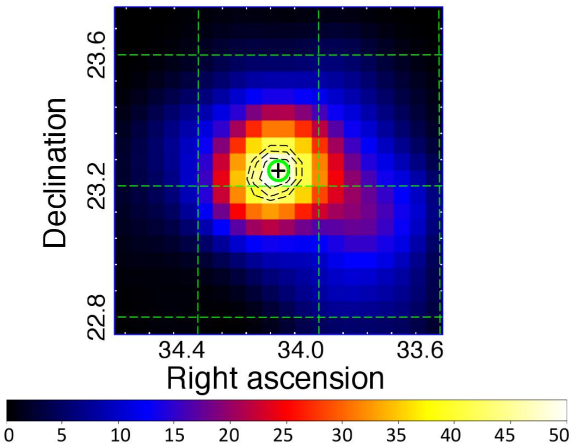

Fig. 3. TS map (3–500 GeV), having 20 × 20 pixels and built with resolution 0.05°/pixel, integrating over 7 yr of *Fermi*-LAT observations. The green circle centered on + highlights the position of 2WHSP J021631.9+231449; contour dashed lines correspond, respectively, to the 68%, 95%, and 99% confinement regions (from inner to outer lines) for the γ-ray signature position.

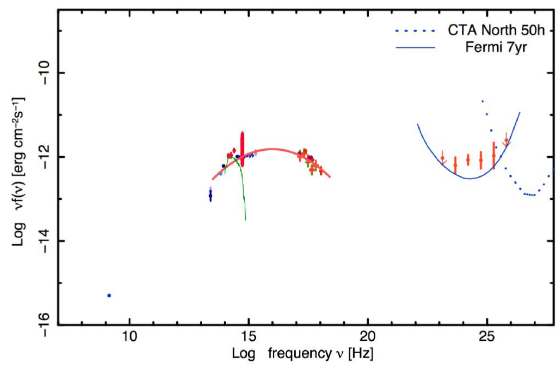

Fig. 4. SED for 2WHSP J021631.9+231449 adding new γ-ray description in the full energy band 0.3–500 GeV. The red line is a fitting for the nonthermal component in the synchrotron peak, the green line is the giant elliptical host galaxy template for $z = 0.288$, the blue line corresponds to the *Fermi*-LAT (7 yr) broadband sensitivity, and blue dashed line to CTA-North (50 h exposure, Bernlöhr et al. 2013).

and evaluate if the source emerges with high TS values from a low TS (≈0.0) background. When the background is not well described, it could affect (or mimic) a point-like source detection. Since we are mainly working at high Galactic latitude $|b| > 10°$, we avoid most of the Galactic diffuse emission (which is strong and highly structured at lower latitudes), preventing spurious detections. As seen in Fig. 3, the 2WHSP source is well within the 68% confinement region for γ-ray signature (Mattox et al. 1996), and TS values at the grid center contrasts with outer regions, ensuring that the observed TS peak is due to a point-like source rather than an overestimated background component.

In Fig. 4 we show the multifrequency SED[11] for 2WHSP J021631.9+231449. The γ-ray SED was calculated by dividing the full energy band 0.3–500 GeV into 6 bins, equally spaced in a logarithmic scale, to compensate for the lower number-counts when increasing the photon energy. The upper limits (u.l.) are computed only for energy bins with TS < 9, and considering a 95% confidence level on the integrated flux along the whole energy bin. The broadband sensitivity at a certain energy E (thin blue line in Fig. 4) is calculated as the maximum flux of a power law source at the LAT detection threshold, for any spectral index.

The source 2WHSP J021631.9+231449 ($\Gamma = 1.97 \pm 0.12$) is clearly a promising candidate for observation in the VHE domain with the future Cherenkov Telescope Array (CTA, Actis et al. 2011), or even in reach for present detectors during flaring events. This new γ-ray detection is only one example within the many cases listed in Table A.1, raising our expectations for future VHE studies. Currently, we do not have TS maps and γ-ray SEDs calculated for all sources[12]. However, we plan to make them available in the near future as a natural extensions of the present work, given the importance of HSP blazars for upcoming observations with CTA.

3.3. Lower significance γ-ray sources

Within the 400 2WHSPs studied, 65 had faint signatures of γ-ray emission with TS values ranging between 10 and 25, and are also listed in Table A.1. We call these lower-significance detections because these sources have TS < 25 (the threshold-limit assumed by the *Fermi*-LAT team) but they still represent relevant findings considering the number of seed-positions used in our present approach.

As known, the significance σ can be approximated as $\sigma \approx \sqrt{\mathrm{TS}}$ (Mattox et al. 1996) and, working with TS = 10 threshold, implies our detections have significance of the order of $\sim 3\sigma$. Since we performed a series of 400 binned likelihood analyses for positions only associated with WHSP sources, the number of spurious detections (N_{spur}) expected is $N_{\mathrm{spur}} \approx 400 \times 10^{-3} = 0.40$; therefore we do not consider spurious detections as a concern in our work. In fact, we have individuated a total of 150 γ-ray excess within TS > 10 level, which corresponds to ~37% positive signatures for all the 400 candidates tested.

It should be clear that we are not performing a blind-analysis of the whole γ-ray sky, therefore the number of seed-positions we inspect is very small. The strong threshold cut (TS > 25) adopted by the *Fermi*-LAT team manifest their rigour before validating any new populations of γ-ray emitters. In contrast, our candidates are a particularly small population of well-characterized (from radio to X-rays) blazars which are firmly established as a family of γ-ray emitters, therefore a 3σ detections threshold is suitable for our approach.

As a complementary test to evaluate if our lower-significance detections are consistent with point-like sources, we randomly choose six cases with TS in the range from 10 to 25 and calculate

[11] Here we make use of the Sky-Explorer tool from www.asdc.asi.it, quickly retrieving multifrequency information from public data bases, to cite: White & Becker (1992), Gregory et al. (1996), Cohen et al. (2007), Condon et al. (1998), Nieppola et al. (2007), White et al. (1997), Dixon (1970), Wright et al. (2010), Warren et al. (2007), Harris et al. (1996), Voges et al. (1999, 2000), Watson et al. (2009), Saxton et al. (2008), Puccetti et al. (2011), D'Elia et al. (2013), Alam et al. (2015).

[12] The computational demand for accomplishing such task is relatively large, and requires further planning together with our Computer-Cluster partners; to cite: Joshua-Cluster from ICRANet Italy, and Gauss-Cluster from CESUP Brazil.

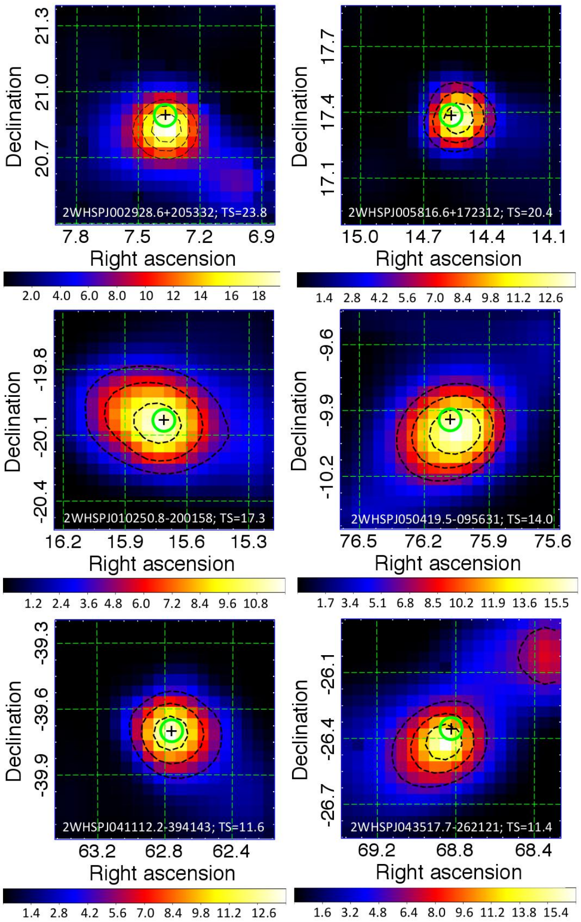

Fig. 5. TS maps in the 0.6−500 GeV band for six sources representing the lower-significance detections with TS between 10 to 25. At the bottom of each map, we write the corresponding source name and the reported TS value for a binned likelihood analysis when integration is over 7.2 yr of observations (along the full energy band 0.3−500 GeV). The 2WHSP positions are highlighted by thick green circles with their centered on +. The contour black dashed lines are TS surfaces representing 68%, 95%, and 99% containment region for the γ-ray signature (from inner to outer lines).

their corresponding TS maps (Fig. 5). Since lower-significance sources are hard to detect based only on >3 GeV photons, to improve the photon counts we go to lower energies (0.6−500 GeV), which helps to individuate the γ-ray signatures[13]. All six candidates studied clearly emerge from the background as point sources, and are consistent with the 2WHSP positions within the 68% confident radius for the γ-ray signature. In fact, this reinforces our view that assuming a TS > 10 threshold does not contaminate our results with spurious detections.

Given the variability of one order of magnitude is often observed for HSP blazars in the GeV−TeV bands[14], most of these lower-significance detections may be in reach of CTA during flaring episodes (see Fig. 4). In fact, the validation of lower-significance detections associated with HSP blazars provide relevant hints about the population responsible for considerable portion of the high-energy isotropic γ-ray background (IGRB); and it is also important to account for their existence and imprints, since they add anisotropic contribution to the IGRB (Malyshev & Hogg 2011; Cuoco et al. 2012; Ackermann et al. 2012; Inoue 2014).

knowledge about the position and model-parameter for describing individual faint γ-ray sources may also help to improve tentative correlations of the IGRB with the large-scale structures/clusters (Ando et al. 2014; Prokhorov & Churazov 2014), since their contribution could be subtracted from the currently unresolved background (i.e., to clean the IGRB from faint point-like sources before trying any sort of correlation). By relying on multifrequency data to search for faint γ-ray source, we may improve our capability of resolving them. Moreover, since the present evaluation is primary driven by the position of HSP blazars, it is important to keep track of any case that shows a faint γ-ray signature even if not enough to fit in the current TS-limit for detection demanded by *Fermi*-LAT team.

3.4. A direct source-search as a complementary approach to probe faint γ-ray emitters

To evaluate the potential of using direct source-search as a complementary method when building γ-ray catalogs, we select 30 objects with the highest significance γ-ray signatures from our list of new-detections (all sources having TS > 45 in our analysis with Pass 8 data integrating over 7.2 yr). We then test if these sources could be detectable with high/lower-significance based on the γ-ray analysis setup used to build the 3FGL catalog. We download Pass 7 data[15] corresponding to the first four years of observations (MM/DD/YYYY: 08/04/2008 to 08/04/2012) and proceed with the likelihood analysis that considers a background of extended and point-like sources built based on the gll-psc-v14.fit list, with information available at that time. For the diffuse Galactic background content we consider the source file gll-iem-v05-rev1.fit, and the iso-source-v05.txt model for the isotropic component. We also choose the IRF corresponding to the preparation of 3FGL catalog P7REP SOURCE V15, and event selection Pass 7 reprocessed source data (front+back).

The results are listed in Table A.2, showing four high-significance detections at TS > 25 level, and 17 lower-significance cases with TS in between 10 to 25. Indeed, our test shows that a direct-source search can be used as a complementary method to refine the description of the γ-ray sky; not only revealing high-significance sources, but also allowing lower-significance sources to be successfully probed. The fact that we only present four extra sources that could fit the 3FGL detection threshold should not mislead us into thinking that these types of contributions are not worth to incorporate. As discussed,

[13] Also, we should add that the overall computation time for lower-energy TS maps integrating over 7 yr can easily became prohibitive (>weeks). Especially for bright sources; large photon-counts translate into large computational demand. Therefore, there is no absolute way to choose a working energy-range. We are always limited by the computation time, and many cases demand us to adapt (for example, see the lower-energy TS map from Sect. 5.1, where we had to work in a narrow energy range of 700−800 MeV to reach results in reasonable time).

[14] For dedicated studies on variability involving HSP blazars, see Krawczynski et al. (2004) reporting on 1ES 1959+650 ≡ 2WHSP J195959.8+650853, or Błażejowski et al. (2005), Sahu et al. (2016) reporting on Mrk 421 ≡ 2WHSP J110427.3+381230.

[15] Pass 7 data: http://heasarc.gsfc.nasa.gov/FTP/fermi/data/lat/weekly/p7v6/

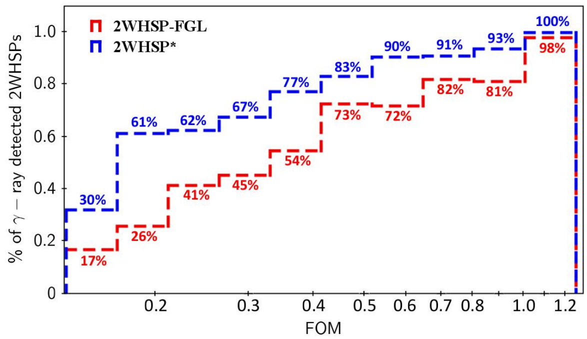

Fig. 6. γ-ray detection efficiency for each bin in FOM. Red represents the 2WHSP-FGL subsample (2WHSP sources with FGL counterparts: 439 objects), and blue the 2WHSP* subsample (2WHSP sources considering all 150 new + 439 FGL γ-ray counterparts). The first bin at FOM = 1.2 condensate all cases with FOM > 1.2 (sources with the brightest synchrotron peak flux $-11.2 < \text{Log}(\nu_{\text{peak}} f_{\nu_{\text{peak}}}) < -9.7$) since almost all of them have been already γ-ray detected, having a 3FGL counterpart.

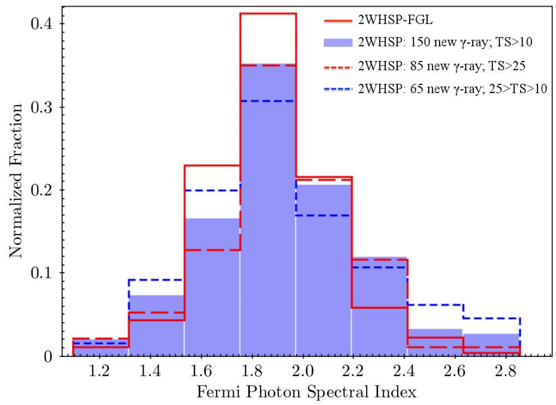

Fig. 7. Distribution of photon spectral index Γ for the 439 2WHSP-FGL sources (red-continuous line). For the new γ-ray signatures we have: solid indigo bars considers all the 150 detections at TS > 10, red dashed line only for the 85 detections at TS > 25 level, and blue dashed line only for the 65 lower-significance detections with TS in between 10 to 25.

this test considers only a few sources, and an extended study over the whole blazar population could add a significant complementary contribution. Also, with increasing integration time from *Fermi*-LAT data, we reach a lower flux threshold (S), and the source number-count may improve $\propto\sim S^{-1.5}$; therefore the impact of a direct source-search probably has increasing relevance to the building of the next γ-ray catalogs.

Clearly, most of our new high-significance detections based on 7.2 yr with Pass 8 data are mainly driven by a longer integration time (from four years, enhanced to 7.2 yr) and improved event reconstruction (from Pass 7 to Pass 8). However, all 150 detections presented in our work (Table A.1) were only possible because we knew where to look, using selected seed positions selected when considering multifrequency data. In this regard, multifrequency selected seeds are indeed very promising for driving new γ-ray detections just as γ-ray seeds are, and here we emphasise their complementarity. Also, a likelihood analysis based on seeds selected from populations of γ-ray emitter enabled us to successfully probe a population of lower-significance emitters (using Pass 7–4 yr) that are later confirmed with TS > 45 when working with 7.2 yr of Pass 8 data.

3.5. Detection efficiency according to FOM parameter

The figure of merit (FOM) parameter (Arsioli et al. 2015) is defined as the ratio between the synchrotron peak flux $\nu_{\text{peak}} f_{\nu_{\text{peak}}}$ of a given source and that of the faintest 1WHSP blazar already detected in the TeV band ($\nu_{\text{peak}} f_{\nu_{\text{peak}}} = 10^{-11.3}$ erg/cm^2/s); FOM = $\nu_{\text{peak}} f_{\nu_{\text{peak}}}$ / $10^{-11.3}$. The FOM then provides an objective way of assessing the likelihood for GeV−TeV detection of HSP blazars, based on the synchrotron peak brightness, and is not affected by absorption of VHE photons owing to the interaction with extragalactic background light (EBL, Franceschini et al. 2008).

Figure 6 illustrates this concept, showing the fraction of 2WHSPs already detected in γ-ray according to different FOM bins, considering the subsample of 439 2WHSP-FGL sources (in red), and the subsample of 589 2WHSP*[16], which represents all γ-ray detections (in blue). Clearly, the detection efficiency increases with increasing FOM, and there is a considerable increment in the fraction of sources detected for each FOM-bin when accounting for the 150 sources listed in Table A.1. Therefore, the 2WHSP sample shows its potential for unveiling high/lower-significance γ-ray sources, emphasising the power of considering multifrequency information to select VHE γ-ray targets for CTAs, as discussed in Arsioli et al. (2015) and Chang et al. (2017). In addition, given that γ-ray detected HSP blazars have been suggested as counterparts of IceCube astrophysical neutrinos (Padovani et al. 2016), our present work may contribute to discussions in the realm of multi-messenger astrophysics, especially when studying cross-correlations between extreme γ-ray blazars and astro-particles.

[16] We may use 2WHSP* when referring to the total 589 sources that include: 439 2WHSP-FGL + our 150 γ-ray detections at TS > 10 level.

3.6. The γ-ray spectral properties of 2WHSP blazars

In Fig. 7 we present the photon spectral index (Γ) distribution for the 150 new γ-ray excess signals (indigo), and compare it with the Γ distribution for the 439 2WHSP-FGL sources (red continuous line). The histogram is normalized with respect to the size of each subsample, so we can visualise their distribution-shape more accurately. A Kolmogorov-Smirnov (KS) test comparing both histograms gives a $p_{\text{value}} = 0.991$, meaning the distributions are fully consistent with the same parent population and have similar γ-ray distribution properties. Also, the mean photon spectral index only associated with the 150 new γ-ray sources is $\langle\Gamma\rangle_{\text{new}} = 1.94 \pm 0.03$ in good agreement with that calculated for the 2WHSP-FGL sample $\langle\Gamma\rangle_{\text{2WHSP-FGL}} = 1.89 \pm 0.01$. Considering all γ-ray detections together (the 2WHSP* subsample) we have $\langle\Gamma\rangle_{\text{2WHSP*}} = 1.90 \pm 0.01$.

When comparing the photon spectral index distribution of 2WHSP-FGL with the subsample only having our 85 new γ-ray detections at TS > 25; also with the one only having our 65 lower-significance γ-ray detections, the p-values are respectively: $p_{\text{value}}^{(\text{TS}>25)} = 0.987$ and $p_{\text{value}}^{(10<\text{TS}<25)} = 0.763$. Therefore, since all the cases we compared showed $p_{\text{value}} > 0.05$, we should not reject the hypothesis that all distributions are similar, consistent with a single-parent population.

The Γ vs. $S_{1-100\ \text{GeV}}$ plot (Fig. 8) shows how we went into lower flux-limit (blue dashed line) compared to previous γ-ray

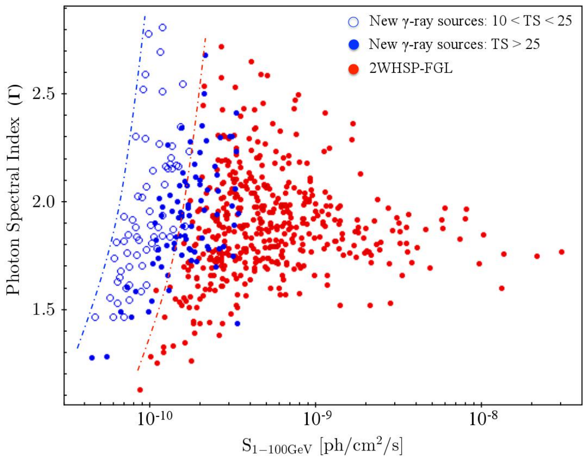

Fig. 8. Photon spectral index Γ plotted against total flux $S_{1-100\ \mathrm{GeV}}$ for the 439 2WHSP-FGL sources (in red), the 85 new detections with TS > 25 (filled-in blue), and for the 65 lower-significance detections with TS between 10 and 25 (blue outlines). The dashed lines represent the flux limit achieved by 3FGL-4 yr (red) and by our direct search based on 7.2 yr of data (blue) down to TS = 10.

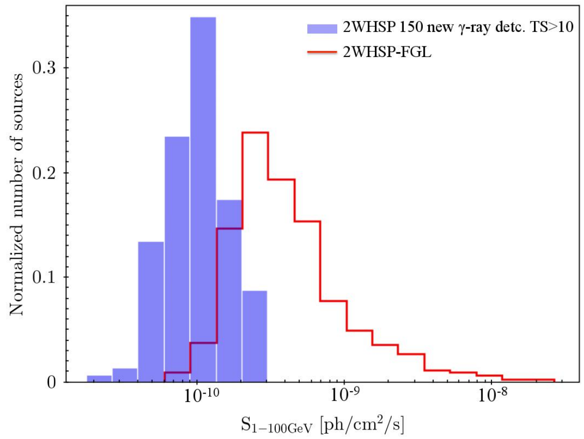

Fig. 9. Histogram comparing the flux distribution $S_{1-100\ \mathrm{GeV}}$ for the γ-ray subsamples of 439 2WHSP-FGL (red line), and the 150 newly detected WHSPs at TS > 10 level (indigo box).

catalogs (red dashed line). This improvement is a combination of many elements: our dedicated search for γ-ray counterparts based on WHSP positions, the larger exposure time used (since we integrate over 7.2 yr of observations), better events reconstruction (from Pass7 to Pass 8), and also the fact that we consider sources down to TS > 10.

The overlapping between red and blue dots (Fig. 8) in the range $1-4 \times 10^{-10}$ ph/cm²/s illustrates how we improved completeness for our HSP γ-ray sample, when considering the new detections presented in Table A.1. We note that the γ-ray threshold sensitivity for HSP blazars has little dependence on the photon spectral index down to $S^{\mathrm{limit}}_{1-100\ \mathrm{GeV}} = 7 \times 10^{-11}$ ph/cm²/s, so that sub-samples with flux-limit $>S^{\mathrm{limit}}_{1-100\ \mathrm{GeV}}$ have low bias arising from Γ. On the other hand, the threshold dependence on Γ is much stronger when considering the integrated flux along the whole band 0.1−100 GeV, as reported in Nolan et al. (2012) and Acero et al. (2015). Therefore, the discussion in Sect. 4 considers the 1−100 GeV energy range[17] for the flux distribution histogram (Fig. 9) and also for the γ-ray Log*N*-Log*S* studies (Figs. 11 and 12).

If we plot the histogram of γ-ray flux for the 2WHSP-FGL subsample, comparing it to our 150 γ-ray detections with TS > 10 (Fig. 9), we see that our sources dominate the faint-end. A KS test comparing both histograms gives a *p*-value of 0.062, which is relatively low, almost excluding the hypothesis that the histograms are similar with respect to the flux distribution. In fact, it shows that our new γ-ray detections (Table A.1) are part of a population of faint sources that was not probed before, and represents a contribution to the IGRB that was previously unresolved.

As is clear from Fig. 9, there is a region in the $S_{1-100\ \mathrm{GeV}}$ histogram where our new detections overlap the 2WHSP-FGL sources. For fluxes lower than $\sim 2.7 \times 10^{-10}$ ph/cm²/s the detection efficiency from the 3FGL catalog drops considerably (also shown by a sharp cut in differential number counts d*N*/d*S*, Fig. 12 in Sect. 4). As discussed in Sect. 3.4, our new detections at the faint-end of $S_{1-100\ \mathrm{GeV}}$ histogram are mainly driven by longer integration time, improved event reconstruction, and a lower TS threshold; not only, a direct search can bring complementary sources that improve detection efficiency close to the flux-limit. In addition, the *Fermi*-LAT exposure is not uniform (Acero et al. 2015, see their Fig. 1) and therefore sky-regions inspected with lower exposure (4-yr with Pass 7) now benefit from better sensitivity owing to longer exposure, revealing new sources at the same faintest flux levels probed by the 3FGL setup. Therefore, taking all of this into consideration, we naturally expect an overlap in the $S_{1-100\ \mathrm{GeV}}$ faint-end.

3.7. Comments on the Eddington bias effect

Ackermann et al. (2016a) has called attention to the statistical fluctuations of photon flux, especially for faint γ-ray sources close to the *Fermi*-LAT detection limit, which could lead to overestimated flux-values. The statistical fluctuation of sources close to the flux threshold of any sample is known as an Eddington bias (Eddington 1913) and has a direct impact on the number counts (Log*N*-Log*S*) or any other study relying upon the measured flux. For the 2FHL catalog it has been shown through simulations (Ackermann et al. 2016a) that the measured fluxes along 50 GeV−2 TeV band could be overestimated up to 10× for the faintest sources. However, we should note that this factor also has a strong dependence on the γ-ray spectral properties from individual sources.

Especially, the $\Gamma_{(50\ \mathrm{GeV}-2\ \mathrm{TeV})}$ distribution for the 2FHL sample ranges from ≈1.0 to 5.5 (see Fig. 10) with mean value $\langle\Gamma\rangle_{\mathrm{2FHL}} = 3.20 \pm 0.08$. Naturally, statistical fluctuations on photon flux measurements are more extreme for the steepest γ-ray spectra (Fig. 10, right side).

In this case, we may be subject to the same effect, however the $\Gamma_{(0.3-500\ \mathrm{GeV})}$ distribution for the 2WHSP* sample is well confined to the 1.2 to 2.8 range, with mean value

[17] The integral flux for the energy range 1−100 GeV is commonly reported in all *Fermi*-LAT catalogs (1FGL, 2FGL and 3FGL). For practical reasons we work in the same energy range, making it easy to combine flux information from our current list (Table A.1) with the 1−100 GeV flux reported in *Fermi*-LAT catalogs. Moreover, since the 1−100 GeV band is covered with relatively good sensitivity by *Fermi*-LAT, the power law modeling of faint hard-spectrum γ-ray sources is more reliable in this range.

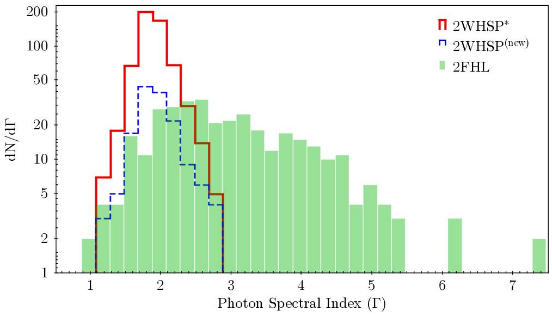

Fig. 10. Histogram comparing the photon spectrum index (Γ) distribution for the γ-ray samples 2FHL (all sources), 2WHSP* (all γ-ray detected 2WHSPs down to TS = 10), and 2WHSP$^{(new)}$ (only the 150 new γ-ray detections). Note that this is a qualitative comparison given that Γ parameter for the 2FHL sample is measured in the 50 GeV−2 TeV energy band.

$\langle\Gamma\rangle_{2WHSP^*} = 1.90 \pm 0.01$. Since the mean γ-ray spectrum for the 2WHSP* sources is close to flat, the effect of statistical flux fluctuations is much less severe in our sample, and does not compromise the measured-flux.

To estimate the effect of the Eddington bias in the faint-end of our sample we compare the parameter $S_{1-100 \text{ GeV}}$ from Tables A.1 and A.2 that were calculated for the same sources, but with different flux limits (see Sect. 3.4). In the first case, the likelihood setup is based on 7.2 yr Pass 8 data, and the second one is based on 4 yr Pass 7 data; therefore different flux-thresholds.

From Table A.2 let us assume that the 17 sources with $\text{TS}^{\text{Pass 7}}_{4 \text{ yr}}$ in between 10−25 are a good representative of our lower-significance detections, for which the measured fluxes $\text{S}^{\text{meas}}_{1-100 \text{ GeV}}$ could be overestimated. When analyzing these same 17 sources with an advanced setup of 7.2 yr with Pass 8 (Table A.1) all of them become γ-ray detected with relatively high-significance $\text{TS}^{\text{Pass 8}}_{7.2 \text{ yr}} > 45$, and their measured fluxes can be considered as the true ones, $\text{S}^{\text{true}}_{1-100 \text{ GeV}}$, since the flux threshold is now relatively improved.

We then calculate $\langle\text{S}^{\text{meas}}_{1-100 \text{ GeV}}\rangle/\langle\text{S}^{\text{true}}_{1-100 \text{ GeV}}\rangle = 0.79$ as an estimate for the order of magnitude of flux fluctuations for 2WHSP sources close to the *Fermi*-LAT threshold. This is far from the $10\times$ factor that could affect FHL sources, especially the ones with a steep γ-ray spectrum. Clearly, the effect is not representative for our sample and does not compromise further results. Moreover, in systematically overestimating the flux from faint sources, the Eddington bias would manifest as re-steepening in the number counts, which is not observed (see Figs. 11 and 12).

In conclusion, the $\langle\text{S}^{\text{meas}}_{1-100 \text{ GeV}}\rangle/\langle\text{S}^{\text{true}}_{1-100 \text{ GeV}}\rangle$ value tells us that the γ-ray variability associated with HSP blazars probably dominates eventual oscillations of the $\langle S_{1-100 \text{ GeV}}\rangle$ parameter when the two likelihood analysis-setups are compared. Also, it shows that the overlapping between γ-ray subsamples in Fig. 9 is mainly driven by better detection efficiency (from longer exposure time and improved event reconstruction from Pass 8) rather than statistical flux fluctuations.

4. The isotropic γ-ray background: contribution from HSP blazars to the diffuse component

Since we unveil and model a relatively large number of γ-ray emitters down to TS = 10, we try to evaluate quantitatively what is the impact of our approach for resolving the

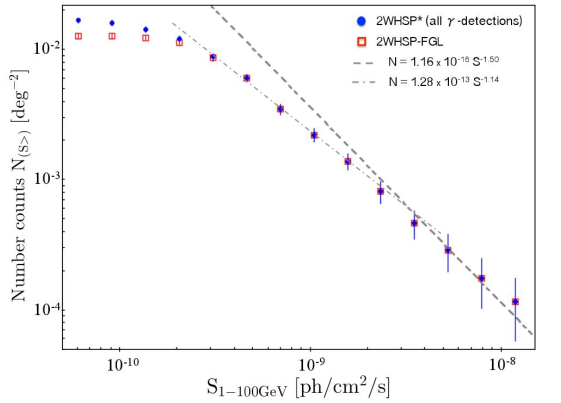

Fig. 11. Measured γ-ray Log$N$-Log$S$ of 2WHSP sources, plotting the cumulative number counts with integrated fluxes larger than $S_{1-100 \text{ GeV}}$, at $|b| > 10°$. The dashed lines represent a broken power law fit to the 2WHSP* sample, with an early break at $S_{\text{break}-1} = 3.5 \times 10^{-9}$ ph/cm^2/s and fitting parameters given in Eq. (3). This plot is not corrected for nonuniform exposure from *Fermi*-LAT.

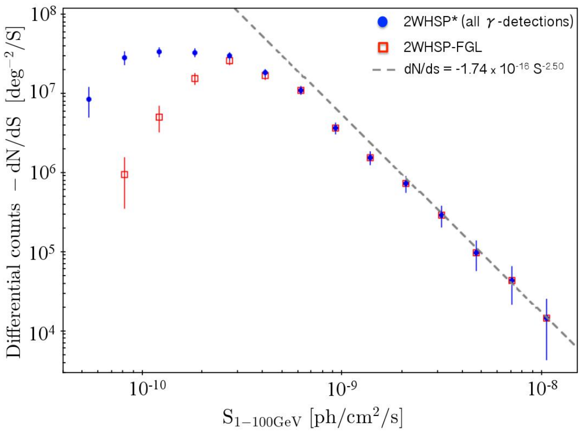

Fig. 12. Differential number counts ($-\text{d}N/\text{d}S$) with respect to $S_{1-100 \text{ GeV}}$ for HSP blazars at $|b| > 10°$. The dashed and dash-dotted lines represent the derivative for the power law fit from Eq. (3).

extragalactic γ-ray background (EGB), and isotropic γ-ray background (IGRB) components.

Following the discussion from Ackermann et al. (2015a), we refer to EGB as the sum of all resolved and unresolved contributions from individual extragalactic sources (Blazars, misaligned AGNs and Starburst Galaxies) plus the diffuse emission coming from outer Milky Way regions (which could be related to dark-matter annihilation, intergalactic shocks, and γ-ray cascades induced by ultra high-energy cosmic rays). The exact EGB composition is a matter of intense debate[18], and it is well known that contributions owing to unresolved sources may build-up

[18] Ackermann et al. (2015a) also discuss the challenges for measuring the EGB component, which demands a proper modeling of the diffuse Galactic emission (DGE) especially as a result of cosmic rays interacting with the Milky Way gas and photon fields. The DGE has intensity comparable to the EGB, and to obtain the EGB, both the DGE and the known Galactic sources have to be subtracted from the total-sky γ-ray counts. The reported EGB flux (1.1−200 GeV) is $I_{\text{EGB}} \approx 4.74 \times 10^{-7}$ ph/cm^2/s/sr.

Table 1. Integral contribution from our new γ-ray sources for different energy bins, compared to EGB and IGRB fluxes reported in (Ackermann et al. 2015a).

$E_{\rm bin}$ (GeV)	$I_{\rm EGB}$	$I_{\rm IGRB}$	$I^{\rm TS>25}_{\rm new-detc}$	%EGB	%IGRB	$I^{\rm TS>10}_{\rm new-detc}$	%EGB	%IGRB
1.1–13	4.5×10^{-7}	2.7×10^{-7}	1.22×10^{-9}	0.27%	0.45%	1.73×10^{-9}	0.38%	0.65%
13–36	1.4×10^{-8}	8.2×10^{-9}	8.48×10^{-11}	0.61%	1.0%	1.19×10^{-10}	0.86%	1.4%
36–51	1.8×10^{-9}	1.1×10^{-9}	1.59×10^{-11}	0.88%	1.4%	2.24×10^{-11}	1.2%	2.0%
51–72	1.1×10^{-9}	6.3×10^{-10}	1.19×10^{-11}	1.1%	1.9%	1.68×10^{-11}	1.5%	2.7%
72–100	6.2×10^{-10}	3.6×10^{-10}	8.69×10^{-12}	1.4%	2.4%	1.23×10^{-11}	2.0%	3.4%
100–140	3.1×10^{-10}	1.5×10^{-10}	6.89×10^{-12}	2.2%	4.6%	9.82×10^{-12}	3.2%	6.5%
140–200	1.9×10^{-10}	9.8×10^{-11}	5.63×10^{-12}	2.9%	5.7%	8.05×10^{-12}	4.2%	8.2%

Notes. Columns headed %EGB show the significance of new detections with respect to the total EGB component, and columns headed %IGRB show the fraction of IGRB component we have solved in the present work. The superscripts TS identify the cases where we only consider our new detections at TS > 25 level, and the case considering all new detections at TS > 10 level. Here we take into account our detections at $|b| > 10°$, and all intensities reported are in units [ph/cm^2/s/sr].

a dominant fraction of the diffuse EGB. Therefore, resolving point-like sources translates directly into narrowing the window available for putative truly-diffusive components, especially when constraining the upper-limits of dark-matter annihilation cross-section as discussed by e.g. Ajello et al. (2015) and Fornasa & Sánchez-Conde (2015).

Another term commonly used is isotropic γ-ray background (IGRB), and it is obtained by subtracting the known extragalactic sources from the EGB. Therefore IGRB represents the sum of a true extragalactic diffuse component, plus the contribution of unresolved sources (which mimic and contaminate the diffuse component). According to Di Mauro et al. (2014), Di Mauro (2015) and Giommi & Padovani (2015), unresolved HSPs/BL lacs may be the dominant component of the IGRB at $E > 10$ GeV and indeed, here we bring evidence of a population composed of faint γ-ray HSP blazars near the detectability threshold from *Fermi*-LAT, that was previously undetected.

Based on the model for individual sources, we calculate their corresponding fluxes for each energy bin ($E_{\rm bin}$ are listed in Table 1), and sum over our γ-ray detections at $|b| > 10°$ listed in Table A.1. We then normalize these values multiplying by $A_{\rm sky}/(4\pi \times A_{|b|>10°})$, where $A_{\rm sky} = 41252.96$ deg^2 is the total sky area, $A_{|b|>10°} = 34110.3$ deg^2 is the sky area out of the Galactic disk, and the factor 4π normalize the integral flux per unit of steradian, [ph/cm^2/s/sr], written as $I_{\rm new-detc}$. We compared $I_{\rm new-detc}$ with the IGRB and EGB intensities ($I_{\rm IGRB}$ and $I_{\rm EGB}$) as reported by Ackermann et al. (2015a), following the same $E_{\rm bin}$ steps as theirs. Since our source-modeling does not account for broken power law features that may arise from EBL absorption, especially for large redshift sources, we extend our calculations up to 200 GeV only.

Table 1 lists the corresponding IGRB and EGR fractions we resolved, showing that the subsample of previously undetected γ-ray HSP blazars has increasing relevance for the background composition at higher energies. We evaluate separately the impact owing to all new detections at TS > 10 level, and also owing only to the cases reported with TS > 25. This helped us understand what to expect (in terms of ability to solve the IGRB) from dedicated source-searches based on catalogs of potential γ-ray candidates, and also to evaluate the importance of taking into account lower-significance detections from faint γ-ray blazars. As can be seen, their contribution is not negligible, showing an increment of the order of 40% larger %IGRB solved for each energy bin if we compare the subsamples of our new γ-ray sources detected at TS > 25 and TS > 10.

We also report on the Log$N$-Log$S$ for HSP blazars using all γ-ray information currently available for the 2WHSP sample. Especially, we incorporate a complementary description for the HSP population at lower γ-ray fluxes by considering our 150 new γ-ray detections down to TS = 10 level. We define the 2WHSP* γ-ray sample (which encloses all 2WHSP-FGL sources together with our new detections) and compare it to the 2WHSP-FGL.

In Fig. 11 we plot the cumulative number counts N [deg^{-2}] with flux $S_{1-100\ \rm GeV}$ larger than the corresponding value on the x-axis. By fitting the γ-ray Log$N$-Log$S$ with a broken power law (Fig. 11), we consider an Euclidian behavior for the bright-end, and an early break[19] at $S_{\rm break-1} = 3.5\times10^{-9}$ ph/cm^2/s:

$$N_{(S)} = \begin{cases} 1.16\times10^{-16} S^{-1.50} & S > S_{\rm break-1} \\ 1.28\times10^{-13} S^{-1.14} & S < S_{\rm break-1}. \end{cases} \quad (3)$$

As a test of consistency, we calculate the number of sources n predicted by the fitting (Eq. (3)), which have flux in the interval $S_{\rm min} < S < S_{\rm max}$ (with $S_{\rm max} = 1.0\times10^{-8}$ and $S_{\rm min} = 3.0\times10^{-10}$ ph/cm^2/s) where the Log$N$-Log$S$ is well described by the broken power law. The number of sources predicted is: $n_{\rm (fit)} = A_{|b|>10°} \int_{S_{\rm min}}^{S_{\rm max}} {\rm d}N/{\rm d}S \times {\rm d}S$, where the parameter $A_{|b|>10°} = 34110.3$ deg^2 is the sky area at high Galactic latitudes $|b| > 10°$, resulting in $n_{\rm (fit)} \approx 309.5$, which is in very good agreement with the number of γ-ray sources expected from the 2WHSP* sample in this same interval, $n_{\rm (2WHSP*)} = 311$.

An important point to mention is that our new detections only add improvements to the Log$N$-Log$S$ after the second break. The region in between the first and the second break is not affected by the incompleteness of the 2WHSP γ-ray sample. However, even if the Log$N$-Log$S$ for $S < S_{\rm break-1}$ deviates from the Euclidian prediction, it is early to argue we are probing evolution of HSP blazars; further studies need to introduce corrections owing to nonuniform exposure from *Fermi*-LAT.

[19] To confirm the presence of this early break in the number counts, we extracted the Log$N$-Log$S$ data from Acero et al. (2015) paper (their Fig. 29) plotting the cumulative energy flux $S_{\rm energy}$ distribution for the clean sample of HSP blazars (also uncorrected for nonuniform sensitivity and detection efficiency). Although they do not mention the fitting parameters, we found good agreement with a broken power law that has similar slopes as ours: $N_{(S>S_{\rm break-1})} = 3.2\times10^{-19}\ S_{\rm energy}^{-1.5}$, $N_{(S<S_{\rm break-1})} = 1.8\times10^{-15}\ S_{\rm energy}^{-1.14}$. In this case $S_{\rm break-1} \approx 3.5\times10^{-11}$ erg/cm^2/s, but there is also a strong cut at $S_{\rm break-2} \approx 7.0\times10^{-12}$ erg/cm^2/s. Therefore also manifesting two breaks that probably have the same origin as in our case.

When plotting the differential number counts $-\mathrm{d}N/\mathrm{d}S$ vs. $S_{1-100\ \mathrm{GeV}}$ (Fig. 12), the low flux threshold ($S_{\mathrm{break-2}}$) is evidenced. This manifests as a sharp cut in $\mathrm{d}N/\mathrm{d}S$ at $S \sim 2.7 \times 10^{-10}$ ph/cm^2/s, showing that incompleteness becomes severe for both samples (2WHSP-FGL and 2WHSP*) at that particular flux level. Figure 12 also clearly presents how we increment the γ-ray sample completeness, specially at the faint-end where the 2WHSP* (blue) detaches from the 2WHSP-FGL (red).

If we assume there is no cut owing to the flux threshold at $S_{\mathrm{break-2}}$, so that the power law (Eq. (3)) is a good description for the number counts when extrapolating to the faint-end (from $S_{\mathrm{max}} = 1.0 \times 10^{-8}$ down to $S_{\mathrm{min}} = 6.0 \times 10^{-11}$ ph/cm^2/s)[20], it is possible to estimate the integral contribution of HSP blazars to the EGB in the 1−100 GeV band, $I_{1-100\ \mathrm{GeV}}$:

$$I^{\mathrm{HSPs}}_{(1-100\ \mathrm{GeV})} = \frac{A_{\mathrm{sky}}}{4\pi} \int_{S_{\mathrm{min}}}^{S_{\mathrm{max}}} S \frac{\mathrm{d}N}{\mathrm{d}S} \mathrm{d}S \quad [\mathrm{ph/cm^2/s/sr}] \tag{4}$$

where $A_{\mathrm{sky}} = 41252.96$ deg^2, and the factor 4π is for normalizing the total flux per unit of sky-steradian. The total 1−100 GeV flux generate by HSP blazars is of the order $I^{\mathrm{HSPs}}_{(1-100\ \mathrm{GeV})} \approx 4.80 \times 10^{-8}$ ph/cm^2/s/sr, which represents ≈8.5% when compared to the total EGB content for the same energy band $I^{\mathrm{EGB}}_{(1-100\ \mathrm{GeV})} = 5.63 \times 10^{-7}$ ph/cm^2/s/sr (Ackermann et al. 2015a, their Table 3).

We should note (from Fig. 11) that the fitting presented in Eq. (3) is suitable for the flux range $S > S_{\mathrm{break-2}}$ ($\approx 2.7 \times 10^{-10}$ ph/cm^2/s), which is well described by the 2WHSP-FGL subsample even without incorporating the 150 new γ-ray detections.

In fact, our new detections mainly address the problem of incompleteness at $S_{1-100\ \mathrm{GeV}} < 2.7 \times 10^{-10}$ ph/cm^2/s, as evidenced from Fig. 12. However, we are now confident of extrapolating Eq. (3) down to $S_{\mathrm{min}} = 6.0 \times 10^{-11}$ ph/cm^2/s only because our new detections push to a lower flux threshold. We emphasise that the measured γ-ray Log$N$-Log$S$ was calculated without corrections for nonuniform *Fermi*-LAT exposure. Therefore, the total flux estimated when extrapolating the Log$N$-Log$S$ to lower fluxes should be regarded as a lower bound to the true contribution of HSP blazars in the 1−100 GeV band, bearing in mind that HSPs have increasing relevance for the high-energy channels (Table 1).

Other intervening factors to mention, that may add corrections to the Log$N$-Log$S$ fitting are:

- The PSF and effective area from *Fermi*-LAT depends on energy, therefore the true sensitivity-limits rely on the intrinsic source spectrum properties.
- The data taken mode is turned off during *Fermi*-LAT passages along the South Atlantic Anomaly inducing ≈15% sensitivity differences between north and south hemisphere.
- Another bias is related to the incompleteness introduced by the poor all-sky coverage in X-rays, and probably an extra component owing to limitations imposed by current radio surveys (SUMMS and NVSS) that were used when building the 2WHSP sample. Evolution of the HSP Population could play an important role as well and demands further investigation.

Therefore, a refined representation of the γ-ray Log$N$-Log$S$ for HSP blazars demands further corrections (see Ackermann et al. 2016a, for a practical example) that needs to incorporate parameters like the *Fermi*-LAT detection efficiency, sensitivity nonuniformities along the sky, and selection-efficiency of current blazar catalogs.

[20] We choose the faint-end to be $S_{\mathrm{min}} = 6.0 \times 10^{-11}$ ph/cm^2/s since this is consistent with our flux threshold; as can be seen in Fig. 9, there is a sharp cut in the number of γ-ray sources for fluxes lower than that.

5. Addressing unassociated sources and confusion

In Sect. 1 we described the selection of ~400 2WHSP sources to search for their γ-ray signatures using the *Fermi* Science Tools. Before any likelihood analysis takes place, we inspect the region within 60′ radius from all candidates, considering multifrequency databases from radio to γ-rays (using the Sky-Explorer Tool at tools.asdc.asi.it).

In this process, we found four cases where the 2WHSP γ-ray candidates were close to one of the 3FGL sources, but outside, or at the border of, 3FGL error-circles. In the following we study these fields in more details by working with energy dependent TS maps, trying to improve the γ-ray signature description and confirm the association.

The cases studied are 3FGL J0536.4-3347, 3FGL J0935.1-1736, 3FGL J0421.6+1950, and 3FGL J1838.5-6006; well representative examples of how a multifrequency approach can lead to refined scientific products, especially for γ-ray confused sources.

In particular we draw attention to 3FGL J0935.1-1736 and 3FGL J0421.6+1950 which are currently unassociated. As known, a large number of 3FGL objects (1058) have no official association to date, despite the fact that many of them have blazars and AGNs as main association-candidates (especially the 541 unassociated γ-ray sources out of the Galactic plane $|b| > 10°$, Fujinaga et al. 2015; Doert & Errando 2013).

Although a clear picture that accounts for the large fraction of unassociated 3FGL source is yet to be build, there is evidence of sources that are not clearly related to pulsars nor to AGNs (Acero et al. 2013). In this context, any new association may help to clarify the true nature of current unassociated γ-ray source, and therefore we report on those two cases for which we propose new associations.

5.1. 3FGL J0536.4-3347: a case of source confusion

Source 3FGL J0536.4-3347 is one of the unassociated γ-ray detections in the 3FGL catalog. At this sky position the 2FHL catalog (Ackermann et al. 2016b) reports the source 2FHLJ0536.4-3342, which has been associated with 5BZBJ0536-3343 (=2WHSPJ053628.9-334301) with SED shown in Fig. 13. The γ-ray description of this source is very rich, being detected in the 1FGL, 2FGL and 3FGL catalogs (blue/red/green points); pink dots and u.l. correspond to the 2FHL counterpart at $E > 50$ GeV. For this case, there is a steep+hard component (Fig. 13) in the γ-ray SED, which may be hard to explain as intrinsic emission from a single source.

Exploring the sky area around 3FGL J0536.4-3347 with the ASDC error circle tool (Fig. 14) we note that blazar 2WHSP J053628.9-334301 is just outside the γ-ray error ellipse. Also, there is a bright FSRQ (5BZQ J0536-3401) within 15′ from the 3FGL source, and it could contribute to the overall γ-ray flux that is observed.

A likelihood analysis, assuming two γ-ray sources instead of one (with position corresponding to 5BZQ J0536-3401 and 2WHSP J053628.9-334301), results in a model adjustment with a very large statistical significance for both, as reported in Table 2. Each of the resolved sources is associated with a distinct γ-ray spectral component (one steep and one hard) in agreement

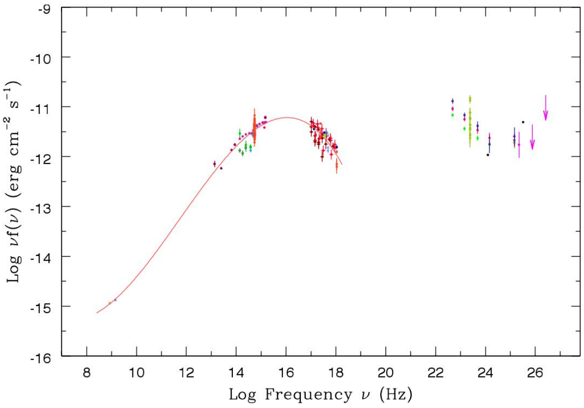

Fig. 13. SED for 2WHSP J053628.9-334301 (≡5BZBJ0536-3343) with red thin line showing a fitting for the synchrotron component (radio to X-rays), and its corresponding γ-ray spectrum from 3FGL J0536.4-3347 (≡2FHL J0536.4-3342).

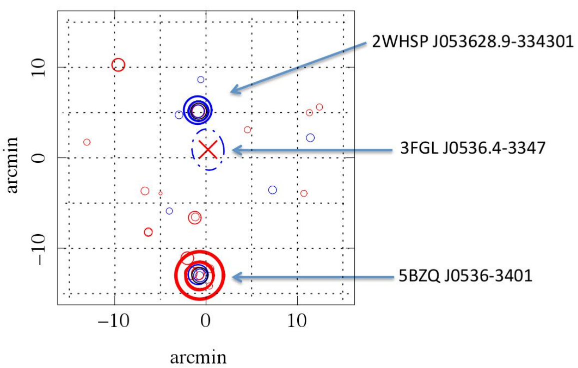

Fig. 14. Sky-Explorer view around 3FGL J0536.4-3347 with position indicated by ×, and γ-ray error-circle shown as dotted line. The 2WHSP J053628.9-334301 (top), and 5BZQ J0536-3401 (bottom) are indicated. X-ray and radio detections in the field are represented by blue and red circles, respectively.

Table 2. Source model parameters from *Fermi* Science Tools, assuming a power law to describe the γ-ray spectrum within 0.3−500 GeV, with N_0 given in [ph/cm^2/s/MeV].

Source	N_0 (10^{-13})	Γ	TS
5BZQ J0536-3401	17.82 ± 0.97	2.75 ± 0.05	813.9
2WHSP J053628.9-334301	7.08 ± 0.84	1.76 ± 0.05	482.8

with expectations: hard for the 2WHSP source and steep for the BZQ object.

We then consider 2WHSP J053628.9-334301 as part of the 2WHSP-FGL sample (with updated γ-ray parameters), but 5BZQ J0536-3401 does not count as part of the 150 new detections associated with 2WHSP blazars (since this source is not an HSP).

To validate our modeling, we also calculated TS maps for the region, taking into consideration different energy bands: 3−500 GeV (high-energy map), and 700−800 MeV (lower-energy map[21]).

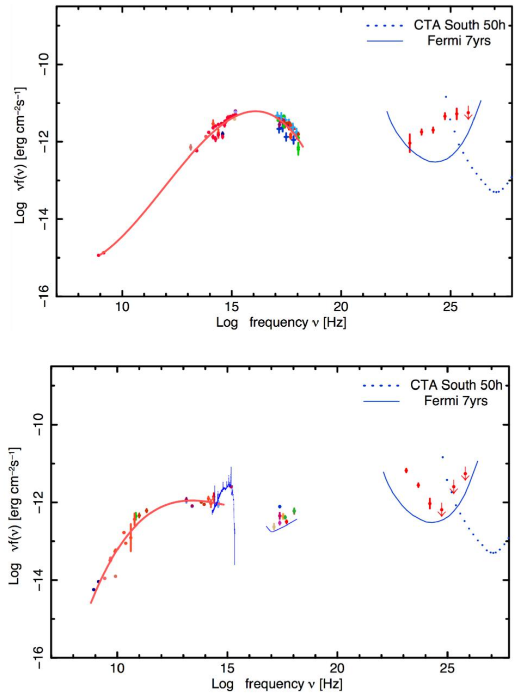

Fig. 15. *Top panel*: multifrequency SED for 2WHSP J053628.9−334301; source with hard γ-ray spectrum $\Gamma_{\rm WHSP}$ = 1.76. *Bottom panel*: multifrequency SED for 5BZQ J0536−3401; source with steep γ-ray spectrum $\Gamma_{\rm BZQ}$ = 2.75 (also showing the FSRQ template (Vanden Berk et al. 2001) as a thin blue-line along the optical to X-ray band). In the GeV−TeV band, both plots show the sensitivity curve for *Fermi*-LAT 7 yr broadband detection, and for CTA-South considering 50h of exposure.

We build the high-energy map so that the hard γ-ray spectrum source dominates, driving the TS-map peak over the 2WHSP J053628.9-334301, left side of Fig. 16. The lower-energy map was build so that the steeper source dominates, driving the TS peak over 5BZQ J0536−3401, right side of Fig. 16. This approach can be applied for disentangling confused γ-ray components within 10′−15′, just as shown in Fig. 15 where we plot the resolved SED for both sources.

One of the main reasons for source confusion is related to the PSF strong dependence on photon energy. The final position associated to the confused γ-ray sources is misplaced from their real counterparts, since the arrival direction of photons originating from distinct source are competing. In the case of close-by sources with steep/hard components, the improved PSF at high-energies may favour the association with the hard γ-ray spectrum sources (as seen in Fig. 14).

[21] In the lower-energy map we use lower resolution, to account for the larger PSF with respect to high-energy photons. In this case, the particular lower-energy range was chosen to try to balance between "going to the lowest energies probed by *Fermi*-LAT" and "still acceptable computation time" of the order of two weeks. A lower energy range could be used, but since it is a bright γ-ray source, photon-counts (and therefore computation time) escalate very rapidly.

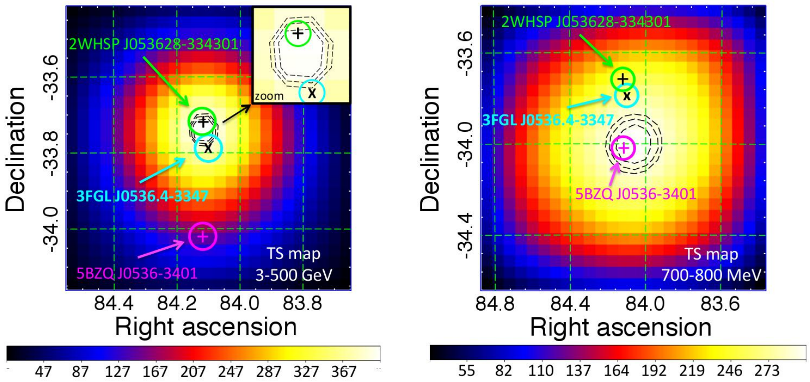

Fig. 16. Energy-dependent TS maps indicating three objects in the studied field; 3FGL J0536.4-3347's position is highlighted with a cyan circle, centered on ×, 2WHSP J053628.9-334301 and 5BZQ J0536-3401 are highlighted with green and magenta circles, centered on + symbol. Contour dashed lines in black (from inner to outer lines) represent the 68%, 95%, and 99% containment region for the γ-ray signature. *Left*: high-energy TS map (20×20, 0.05°/pixel) taking into consideration only 3−500 GeV photons; zooming into central TS-peak region, the source 2WHSP J053628.9-334301 (hard γ-ray spectrum, $\Gamma_{\rm 2WHSP} = 1.76$) is within the 68% containment region for the high-energy γ-ray signature. *Right*: lower-energy TS map (20×20, 0.08°/pixel) considering only 700−800 MeV photons. In this case, the TS-peak position is dominated by the 5BZQ J0536-3401 (steep γ-ray spectrum source, $\Gamma_{\rm BZQ} = 2.75$) well within the 68% containment region for the lower-energy γ-ray signature.

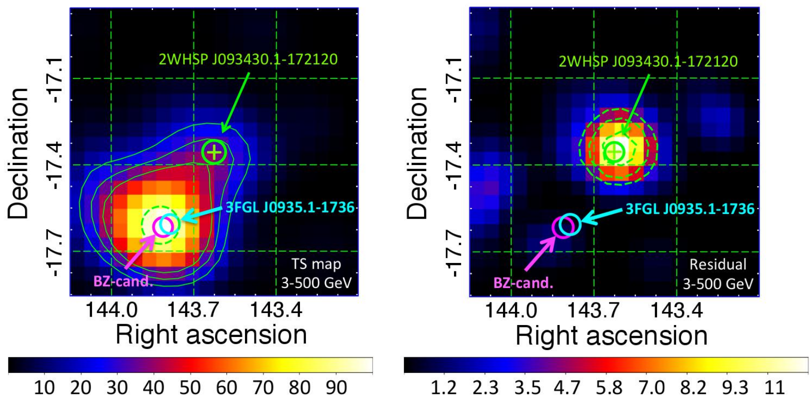

Fig. 17. High-energy TS-maps 3−500 GeV with 20×20 grid 0.05°/pixel, integrating over 7 yr of data. In both maps the 2WHSP J093430.1-172120 position is highlighted by a thick green circle centered on +; the 3FGL J0935.1-1736 is in the center of the thick cyan circle, and a blazar candidate (possible counterpart for the 3FGL source) is indicated with a thick magenta circle. *Left panel*: for this map, the 3FGL source is removed from the model input, showing the pure shape of TS distribution in the region. Green dashed line represents the 99% containment region for the γ-ray signature, which is compatible both with 3FGL and blazar candidate positions. The thin contour lines refer to TS surfaces of 40-30-20, only to show how the γ-ray signature is extended, matching the 2WHSP J093430.1-172120. *Right panel*: residual TS map (built using the 3FGL in the background) showing excess signal consistent with a point-like source. The green dashed lines correspond to the 68%, 95%, and 99% containment region for the γ-ray signature (from inner to outer lines).

The source 2WHSP J053628.9−334301 is a promising candidate for observation with Imaging Atmosphere Cherenkov Telescope (IACTs) and probably a future targets for the CTA-South array (Rieger et al. 2013). Therefore, any dedicated γ-ray analysis has strong motivations, especially when modeling the high-energy component of TeV candidates properly. In this case we have combined multifrequency knowledge of potential GeV−TeV emitters with information from the TS-maps, showing that higher quality scientific products can be extracted from the currently available data bases.

Other cases that have their γ-ray SED characterized by steep + hard component may help to identify potential cases of confusion. Source confusion between objects with similar photon spectral index seems harder to identify, but a multifrequency study in the vicinity of each γ-ray detection is useful to evaluate the presence of potential γ-ray emitters. In a hypothetical case, where a steep+hard γ-ray spectrum could emerge from a single source (multiple blobs scenario), the present treatment would help to evaluate/rule-out the possibility of source confusion for any candidate under study.

5.2. Solving a case of source confusion for the unassociated source 3FGL J0935.1-1736

The source 3FGL J0935.1-1736 is one of the unassociated 3FGL objects. Here we provide strong evidence for source confusion in γ-rays involving two objects: a blazar candidate (brighter γ-ray source in the field) and 2WHSP J093430.1-172120 (fainter γ-ray source in the field).

In Fig. 17 we study the γ-ray signature in the 3−500 GeV band, to revel the TS distribution that is based on improved PSF photons. For the left-grid marked with TS map, we removed the 3FGL source from the input-model, to show the TS distribution

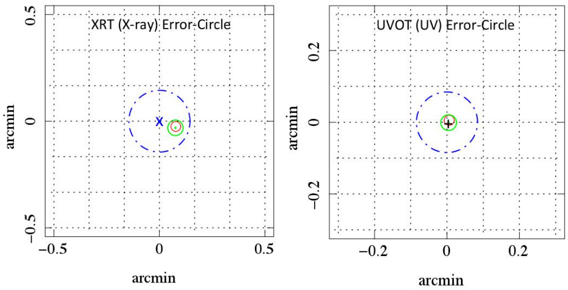

Fig. 18. Sky-Explorer view around NVSS J093514-173658 (blazar candidate). *Left side*: XRT field with the X-ray detection marked as ×. *Right side*: UVOT detection indicated as +. The X-ray and UV error-circle are shown with a dotted blue line. The radio-source is marked in red, and its optical counterpart USNOB1.0 (J2000 Ra, Dec: 143.8116°,-17.6163°) is shown in green.

Table 3. Source model parameters from *Fermi* Science Tools, assuming a power law to describe 3FGL J0935.1-1736 γ-ray spectrum within 0.3−500 GeV, with N_0 given in ph/cm^2/s/MeV.

Source	N_0 (10^{-13})	Γ	TS
NVSSJ093514-173658	3.46 ± 0.87	1.92 ± 0.12	102.9
2WHSP J093430.1-172120	1.26 ± 0.73	1.87 ± 0.24	21.7

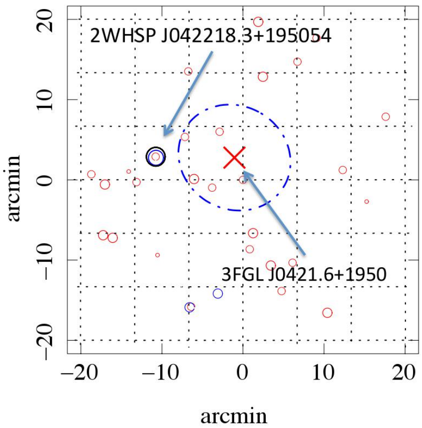

Fig. 19. Sky-Explorer view around 3FGL J0421.6+1950 positions indicated as a red cross. The blue dash-dotted line represents the error circle for the γ-ray detection reported in the 3FGL catalog. As shown, within 15′ from the unassociated γ-ray source there is a 2WHSP blazar. X-ray and radio detections in the field are represented by blue and red circles, respectively.

without any bias from the 3FGL catalog. As can be seen, the TS peak matches the 3FGL position (within 99% confinement radius, shown as dashed green line), but the γ-ray signature clearly extends towards the 2WHSP source, embracing it with high-significance $TS_{\mathrm{surfaces}} > 30$.

To test if the extended signature is due to an extra γ-ray source in the field, we built a residual map, as shown in Fig. 17, right. It corresponds to a TS map that considers the 3FGL J0935.1-1736 source is in the background (therefore, it is part of the input-model and positioned at the center of the magenta circle). In this case, the TS distribution is a result of excess photons with respect to the modeled background, which includes

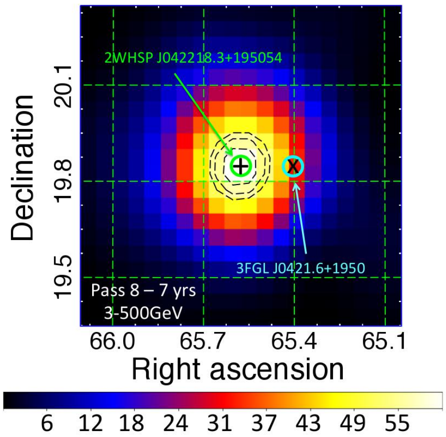

Fig. 20. High-energy 3−500 GeV TS-map, integrating 7 yr of data. The contour black dashed lines are TS surfaces representing 68%, 95% and 99% containment region for the γ-ray signature (from inner to outer lines). The 2WHSP J042218.3+195054 position is highlighted by a thick green circle centered on +. The 3FGL J0421.6+1950 position is highlighted by the cyan circle centered on ×, ≈9.7′ away from the high-energy TS peak.

point sources and the diffuse component. Clearly, the residual map shows our 2WHSP blazar matching the TS peak, well within the 68% containment region for the γ-ray signature.

This is clearly a case of source confusion where the 2WHSP is a counterpart for the residual γ-ray signature, and the brighter source is a counterpart of an, as yet, unidentified object. However, when inspecting this region searching information from other wavelengths, we find the radio-source NVSS J093514-173658 (Fig. 18, in red).

Recent measurements with *Swift* satellite XRT/UVOT show both UV and an X-ray signatures matching the radio source within their error ellipses (Fig. 18). Together with IR, optical, UV and X-ray counterparts we study the multifrequency SED for NVSS J093514-173658 which turns to be a blazar candidate[22] with synchrotron-peak parameters $\nu_{\mathrm{peak}} \approx 10^{15.0}$ Hz and $\nu f_\nu = 10^{-12.0}$ erg/cm^2/s, marked as BZ-cand in Fig. 17, and probable counterpart for the high-significance TS peak.

A likelihood analysis that considers two sources (with positions corresponding to the 2WHSP and NVSS, removing the 3FGL from the field) results in a relatively good adjustment, as shown in Table 3. Although the blazar candidate could be of HSP type, it is not part of the 2WHSP catalog (because the X-ray data was not available at the time of the sample selection) and therefore we do not count it within the 2WHSP-FGL γ-ray subsample; the source 2WHSP J093430.1-172120 is considered a lower-significance γ-ray detection, so we count it within the 150 sources listed in Table A.1.

5.3. Improved position for the unassociated source 3FGL J0421.6+1950

In Fig. 19 we show a chart that includes the 3FGL J0421.6+1950 source (indicated with a red ×) and its corresponding error-ellipse, which is determined over the entire *Fermi*-LAT energy range. However, it is well known that the detection of

[22] The term blazar candidate refers to a source with multifrequency SED characteristic of blazars, but missing optical identification (optical spectrum is not available).

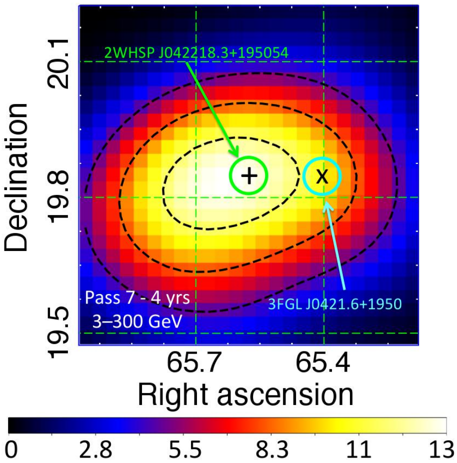

Fig. 21. High-energy 3−300 GeV TS map, integrating 4 yr of data (in this case, the highest energy used is 300 GeV following recommendations for the use of Pass 7 data). The contour black dashed lines are TS surfaces representing 68%, 95%, and 99% containment region for the γ-ray signature (from inner to outer lines). The 2WHSP J042218.3+195054 position is highlighted by a thick green circle centered on +, well within the 68% containment, while the 3FGL J0421.6+1950 source (position highlighted by the cyan circle centered on ×) is localized within the 95% containment region.

lower-energy photons ($E < 1$ GeV) from point-like sources have large PSF, so that the γ-ray signature can spread along a region of the order of 1°, as shown in the right side of Fig. 16.

Since the unassociated 3FGL J0421.6+1950 is ≈10′ away from a 2WHSP source (see Fig. 19), we tried to better evaluate the γ-ray signature localization by studying the high-energy TS map ($E > 3$ GeV), which benefits from smaller PSF with respect to lower-energy photons.

For the TS map in Fig. 20, we removed 3FGL J0421.6+1950 from the model-input so that the TS distribution has no bias from previous γ-ray catalogs. The TS map peaks at the position of 2WHSP J042218.3+195054 (thick green circle centered on +) well within the 68% confinement region for the γ-ray signature, which is ≈9.7′ away from the position reported in the 3FGL catalog (thick circle centered on ×). This source is taken as part of the 2WHSP-FGL subsample, using 3FGL parameters to describe it (since there is no γ-ray confusion in this particular case).

Although the 3FGL positions are based on information associated with the full energy band 0.1−300 GeV, we attempted to improve the γ-ray signature localization by selecting only high-energy photons that are know to have better PSF. In fact, we also improve the localization owing to longer exposure time (since we now integrate along seven years of *Fermi*-LAT observations instead of four years in the 3FGL), but it is important to mention that the high-energy maps, integrated over four years of Pass 7 data (with the same analysis setup used to build the 3FGL catalog, as described in Sect. 3.4) already enabled this kind of study, as seen in Fig. 21.

Probably, when using the full energy range from *Fermi*-LAT (0.1−500 GeV), lower-energy photons with the largest position uncertainties could be degrading the final source localization. Indeed, based on currently available data, there is room for improvements which may bring complementary and relevant information for describing the γ-ray sky.

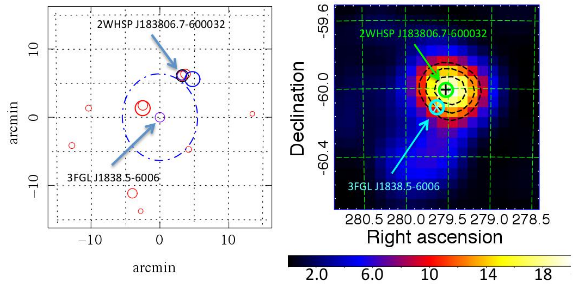

Fig. 22. *Left panel*: error-circle (dash-dotted) associated with the 3FGL source. *Right panel*: high-energy 3−500 GeV TS map, integrating over 7 yr of *Fermi*-LAT observations. The contour black dashed lines are TS surfaces representing 68%, 95% and 99% containment region for the γ-ray signature (from inner to outer lines). The 2WHSP J183806.7-600032 (thick green circle centered on +). The 3FGL J1838.5-6006 position is shows in cyan (centered on ×), ≈6.9′ away from the high-energy TS peak.

Working with high-energy TS maps proved to be very useful when searching for candidate-counterparts of current unassociated γ-ray sources, and could be applied systematically as a complementary refinement for the building of upcoming catalogs with the potential to improve source localization for the whole γ-ray sample. In the next subsection, we discuss a case where the 3FGL association has already been done, but we still improve the γ-ray localization using high-energy TS maps.

5.4. Improved position for the 3FGL J1838.5-6006 source

Here we study 3FGL J1838.5-6006, which is associated with the radio-source SUMSS J183806-600033 (≡2WHSP J183806.7-600032). In this case, the 2WHSP blazar is just at the border of the 3FGL error-circle (Fig. 22, left) and therefore we try improving the γ-ray source localization by working only with high-energy photons only. As shown in Fig. 22, the high-energy TS peak is few arcminutes away from the 3FGL position, and matches our 2WHSP source (which is within the 68% confinement radius for the γ-ray signature).

Although the association is correct, this is another example where we could improve the γ-ray signature localization (≈6.9′ drift) just by working with $E > 3$ GeV photons. We also study this region at a lower-energy band (850−950 MeV) and there is no evidence of another close-by source that could be the cause of the offset position. Therefore, it could be that, for some cases the determination of the source position based on the broad-band counts 0.1−500 GeV is non optimal, probably because of the large PSF associated with lower-energy photons. Building high-energy TS maps may help to improve source positioning, especially for cases with hard γ-ray spectrum, as shown for 3FGL J0421.6+1950 and 3FGL J1838.5-6006.

6. Conclusions and perspectives

The 2WHSP catalog was built to select promising VHE candidates for the present and future generation of Cherenkov Telescope Arrays, therefore we have tested the efficiency of a direct search for γ-ray signatures associated with 2WHSP blazars, achieving significant results.

We have detected 150 γ-ray excess signals out of 400 seed positions based on 2WHSP sources that had no counterpart in previous 1FGL, 2FGL, and 3FGL catalogs. A total of 85 sources were found with high-significance with TS > 25, and we also report on 65 lower-significance detections with TS between 10 to 25. The 150 new γ-ray sources presented in Table A.1 are named with acronym 1BIGB (first version of the Brazil ICRANet Gamma-ray Blazar catalog) which corresponds with the 2WHSP seed-positions used for our likelihood analysis. Clearly, the subsample of 2WHSP blazars that have not yet been detected by *Fermi*-LAT is a key representative population of faint γ-emitters, and we show how the new detections down to TS > 10 level can probe the faint-end of the flux-distribution (see Figs. 8 and 9). As discussed in Sect. 3.3, a γ-ray source-search based on the seed positions from HSP blazars can be used to unveil faint HE sources down to TS = 10 without compromising the γ-ray sample with spurious detections.

Our current work enabled us to associate a relevant fraction of the IGRB to a population of faint γ-ray emitters that had been previously unresolved. Moreover, we show the increasing relevance of faint-HSPs for the IGRB composition with respect to energy (see Table 1), specially for $E > 10$ GeV, reaching 6−8% in the 100−200 GeV band. Motivated by this first assessment, we plan to perform a complete γ-ray analysis of the 2WHSP sample, down to the lowest fluxes, and probably extend the search to other blazar families with potential to improve the γ-ray description of lower-significance γ-ray blazars, also helping to constrain the origins of the extragalactic diffuse γ-ray background.

We have worked out the possibility of solving source confusion when considering multifrequency data for identifying potential γ-ray emitters in a certain ROI, and building energy dependent TS maps to help disentangle hard-steep components from confused sources.

We also addressed cases of unassociated 3FGL sources by studying high-energy TS maps to evaluate possible counterparts. This could be a key for solving cases of unassociated γ-ray sources (just as discussed in Sects. 5.2–5.4) showing that we can improve the γ-ray signature localization based on currently available databases. Certainly, it is interesting to evaluate if this kind of approach could be applied systematically as a complementary refinement for the building of upcoming γ-ray catalogs.

Acknowledgements. B.A. is supported by the Brazilian Scientific Program Ciências sem Fronteiras from Cnpq, Y.L.C. is supported by the Government of the Republic of China (Taiwan). We thank ICRANet and Prof. Carlo Bianco for the cooperation that enabled us to perform part of the data reduction at Joshua Cluster, Rome-Italy. We thank the Centro Nacional de Supercomputação (CESUP) Porto Alegre-Brazil, and Carlos Brandt, for the cooperation that enabled us to perform part of the data reduction using CESUP machines. This work was supported by the ASDC, Agenzia Spaziale Italiana Science Data Center; and University La Sapienza of Rome, Department of Physics. We thank the guidance and comments from Prof. Paolo Giommi, and the special attention from Dr. Dario Gasparrini, Dr. Sara Cutini, Dr. Stefano Ciprini and Prof. Toby Brunett. This publication makes use of public data products and software from *Fermi*-LAT collaboration. We also make use of archival data and bibliographic information obtained from the NASA/IPAC Extragalactic Database (NED), data and software facilities from the ASDC managed by the Italian Space Agency (ASI).

References

Abdo, A. A., Ackermann, M., Agudo, I., et al. 2010a, ApJ, 716, 30
Abdo, A. A., Ackermann, M., Ajello, M., et al. 2010b, ApJS, 188, 405
Acero, F., Donato, D., Ojha, R., et al. 2013, ApJ, 779, 133
Acero, F., Ackermann, M., Ajello, M., et al. 2015, ApJS, 218, 23
Ackermann, M., Ajello, M., Allafort, A., et al. 2011, ApJ, 743, 171
Ackermann, M., Ajello, M., Albert, A., et al. 2012, Phys. Rev. D, 85, 083007
Ackermann, M., Ajello, M., Albert, A., et al. 2015a, ApJ, 799, 86
Ackermann, M., Ajello, M., Atwood, W. B., et al. 2015b, ApJ, 810, 14
Ackermann, M., Ajello, M., Albert, A., et al. 2016a, Phys. Rev. Lett., 116, 151105
Ackermann, M., Ajello, M., Atwood, W. B., et al. 2016b, ApJS, 222, 5
Actis, M., Agnetta, G., Aharonian, F., et al. 2011, Exp. Astron., 32, 193
Ajello, M., Gasparrini, D., Sánchez-Conde, M., et al. 2015, ApJ, 800, L27
Alam, S., Albareti, F. D., Allende Prieto, C., et al. 2015, ApJS, 219, 12
Ando, S., Benoit-Lévy, A., & Komatsu, E. 2014, Phys. Rev. D, 90, 023514
Arsioli, B., Fraga, B., Giommi, P., Padovani, P., & Marrezi, P. M. 2015, A&A, 579, A34
Atwood, W. B., Abdo, A. A., Ackermann, M., et al. 2009, ApJ, 697, 1071
Bernlöhr, K., Barnacka, A., Becherini, Y., et al. 2013, Astropart. Phys., 43, 171
Błażejowski, M., Blaylock, G., Bond, I. H., et al. 2005, ApJ, 630, 130
Campana, R., Massaro, E., Bernieri, E., & D'Amato, Q. 2015, Ap&SS, 360, 19
Campana, R., Massaro, E., & Bernieri, E. 2016, Ap&SS, 361, 183
Chang, Y.-L., Arsioli, B., Giommi, P., & Padovani, P. 2017, A&A, 598, A17
Cohen, A. S., Lane, W. M., Cotton, W. D., et al. 2007, AJ, 134, 1245
Condon, J. J., Cotton, W. D., Greisen, E. W., et al. 1998, AJ, 115, 1693
Cuoco, A., Komatsu, E., & Siegal-Gaskins, J. M. 2012, Phys. Rev. D, 86, 063004
Danforth, C. W., Keeney, B. A., Stocke, J. T., Shull, J. M., & Yao, Y. 2010, ApJ, 720, 976
D'Elia, V., Perri, M., Puccetti, S., et al. 2013, A&A, 551, A142
Di Mauro, M. 2015, in 5th Int. Fermi Symp. Nagoya, Japan, October 20−24, 2014
Di Mauro, M., Donato, F., Lamanna, G., Sanchez, D. A., & Serpico, P. D. 2014, ApJ, 786, 129
Dixon, R. S. 1970, ApJS, 20, 1
Doert, M., & Errando, M. 2013, in Proc. 3rd Int. Cosmic Ray Conf., Rio de Janeiro, 2−9 July 2013 [arXiv:1306.6529]
Eddington, A. S. 1913, MNRAS, 73, 359
Elvis, M., Plummer, D., Schachter, J., & Fabbiano, G. 1992, ApJS, 80, 257
Evans, I. N., Primini, F. A., Glotfelty, K. J., et al. 2010, ApJS, 189, 37
Fornasa, M., & Sánchez-Conde, M. A. 2015, Phys. Rep., 598, 1
Franceschini, A., Rodighiero, G., & Vaccari, M. 2008, A&A, 487, 837
Fujinaga, Y., Niinuma, K., Kimura, A., et al. 2015, PASJ, 68, 70
Furniss, A., Williams, D. A., Danforth, C., et al. 2013, ApJ, 768, L31
Giommi, P., & Padovani, P. 2015, MNRAS, 450, 2404
Gregory, P. C., Scott, W. K., Douglas, K., & Condon, J. J. 1996, ApJS, 103, 427
Harris, D. E., Forman, W., Gioia, I. M., et al. 1993, The Einstein Observatory catalog of IPC X ray sources, Vol. 1E: Documentation (Smithsonian Astrophysical Observatory)
Harris, D. E., Forman, W., Gioa, I. M., et al. 1996, VizieR Online Data Catalog: IX/13
Inoue, Y. 2014, Fifth Fermi Symposium Proceedings, Nagoya, Japan eConfC14102.1
Krawczynski, H., Hughes, S. B., Horan, D., et al. 2004, ApJ, 601, 151
Malyshev, D., & Hogg, D. W. 2011, ApJ, 738, 181
Masetti, N., Sbarufatti, B., Parisi, P., et al. 2013, A&A, 559, A58
Massaro, F., D'Abrusco, R., Ajello, M., Grindlay, J. E., & Smith, H. A. 2011, ApJ, 740, L48
Massaro, E., Maselli, A., Leto, C., et al. 2015, Ap&SS, 357
Mattox, J. R., Bertsch, D. L., Chiang, J., et al. 1996, ApJ, 461, 396
Nieppola, E., Tornikoski, M., Lähteenmäki, A., et al. 2007, AJ, 133, 1947
Nolan, P. L., Abdo, A. A., Ackermann, M., et al. 2012, ApJS, 199, 31
Padovani, P., & Giommi, P. 1995, ApJ, 444, 567
Padovani, P., Resconi, E., Giommi, P., Arsioli, B., & Chang, Y. L. 2016, MNRAS, 457, 3582
Pita, S., Goldoni, P., Boisson, C., et al. 2014, A&A, 565, A12
Prokhorov, D. A., & Churazov, E. M. 2014, A&A, 567, A93
Puccetti, S., Capalbi, M., Giommi, P., et al. 2011, A&A, 528, A122
Rieger, F. M., de Oña-Wilhelmi, E., & Aharonian, F. A. 2013, Frontiers of Physics, 8, 714
Rosen, S. R., Webb, N. A., Watson, M. G., et al. 2016, A&A, 590, A1
Sahu, S., Miranda, L. S., & Rajpoot, S. 2016, Eur. Phys. J. C, 76, 127
Saxton, R. D., Read, A. M., Esquej, P., et al. 2008, A&A, 480, 611
Sbarufatti, B., Treves, A., Falomo, R., et al. 2005, AJ, 129, 559
Shaw, M. S., Filippenko, A. V., Romani, R. W., Cenko, S. B., & Li, W. 2013a, AJ, 146, 127
Shaw, M. S., Romani, R. W., Cotter, G., et al. 2013b, ApJ, 764, 135
Vanden Berk, D. E., Richards, G. T., Bauer, A., et al. 2001, AJ, 122, 549
Voges, W., Aschenbach, B., Boller, T., et al. 1999, A&A, 349, 389
Voges, W., Aschenbach, B., Boller, T., et al. 2000, IAU Circ., 7432, 3
Warren, S. J., Cross, N. J. G., Dye, S., et al. 2007, ArXiv e-prints [arXiv:astro-ph/0703037]
Watson, M. G., Schröder, A. C., Fyfe, D., et al. 2009, A&A, 493, 339
White, R. L., & Becker, R. H. 1992, ApJS, 79, 331
White, R. L., Becker, R. H., Helfand, D. J., & Gregg, M. D. 1997, ApJ, 475, 479
Wright, E. L., Eisenhardt, P. R. M., Mainzer, A. K., et al. 2010, AJ, 140, 1868

Extreme blazars as counterparts of IceCube astrophysical neutrinos

P. Padovani[1,2⋆], E. Resconi[3], P. Giommi[4,5], B. Arsioli[4,5,6], Y. L. Chang[4,6]
[1] *European Southern Observatory, Karl-Schwarzschild-Str. 2, D-85748 Garching bei München, Germany*
[2] *Associated to INAF - Osservatorio Astronomico di Roma, via Frascati 33, I-00040 Monteporzio Catone, Italy*
[3] *Technische Universität München, Physik-Department, James-Frank-Str. 1, D-85748 Garching bei München, Germany*
[4] *ASI Science Data Center, via del Politecnico s.n.c., I-00133 Roma Italy*
[5] *ICRANet-Rio, CBPF, Rua Dr. Xavier Sigaud 150, 22290-180 Rio de Janeiro, Brazil*
[6] *Sapienza Università di Roma, ICRA, Dipartimento di Fisica, Piazzale Aldo Moro 5, I-00185 Roma, Italy*

Accepted 2016 January 25. Received 2016 January 22; in original form 2015 December 18

ABSTRACT

We explore the correlation of γ-ray emitting blazars with IceCube neutrinos by using three very recently completed, and independently built, catalogues and the latest neutrino lists. We introduce a new observable, namely the number of neutrino events with at least one γ-ray counterpart, N_ν. In all three catalogues we consistently observe a positive fluctuation of N_ν with respect to the mean random expectation at a significance level of $0.4 - 1.3$ per cent. This applies only to extreme blazars, namely strong, very high energy γ-ray sources of the high energy peaked type, and implies a model-independent fraction of the current IceCube signal $\sim 10 - 20$ per cent. An investigation of the hybrid photon – neutrino spectral energy distributions of the most likely candidates reveals a set of ≈ 5 such sources, which could be linked to the corresponding IceCube neutrinos. Other types of blazars, when testable, give null correlation results. Although we could not perform a similar correlation study for Galactic sources, we have also identified two (further) strong Galactic γ-ray sources as most probable counterparts of IceCube neutrinos through their hybrid spectral energy distributions. We have reasons to believe that our blazar results are not constrained by the γ-ray samples but by the neutrino statistics, which means that the detection of more astrophysical neutrinos could turn this first hint into a discovery.

Key words: neutrinos — radiation mechanisms: non-thermal — BL Lacertae objects: general — gamma-rays: galaxies — pulsars: general

1 INTRODUCTION

The IceCube South Pole Neutrino Observatory[1] has recently reported the first observations of high-energy astrophysical neutrinos[2] (Aartsen et al. 2013; IceCube Collaboration 2013, 2014). More recently, it has confirmed and strengthened these observations by publishing a sample of 54 starting events collected over about four years and with a deposited energy up to 2 PeV (IceCube Collaboration 2015a). These events are coming from the entire sky and consist of neutrinos of all flavours which interact inside the instrumented volume. The neutrino interaction vertex dominates the signature of these events, the majority of which are shower-like. The complementary sample of through-going charged current ν_μ from the northern sky has been also studied over a period of two (Aartsen et al. 2015) and four years (IceCube Collaboration 2015b) showing that the spectrum is inconsistent with the hypothesis of purely terrestrial origin at 3.7σ and 4.3σ level respectively. These track-like events confirm the general picture of a diffuse isotropic neutrino background although their energy spectrum $E^{-\gamma}$ is harder ($\gamma = 1.91 \pm 0.20$) with respect to the all sky one obtained from the starting events sample ($\gamma = 2.58 \pm 0.25$), suggesting a mixed origin of the signal observed by IceCube.

Many diverse scenarios for the astrophysical counterparts of IceCube neutrinos have been put forward (see, e.g. Ahlers & Halzen 2015, for a comprehensive discussion) but none has so far been statistically supported by the observational data described above. One of the candidate neutrino-emitting astronomical classes of sources is that of

⋆ E-mail: ppadovan@eso.org
[1] http://icecube.wisc.edu
[2] In this paper neutrino means both neutrino and antineutrino.

blazars. These are Active Galactic Nuclei (AGN) hosting a jet oriented at a small angle with respect to the line of sight with highly relativistic particles moving in a magnetic field and emitting non-thermal radiation (Urry & Padovani 1995). The two main blazar sub-classes, namely BL Lacertae objects (BL Lacs) and flat-spectrum radio quasars (FSRQ), differ mostly in their optical spectra, with the latter displaying strong, broad emission lines and the former instead being characterised by optical spectra showing at most weak emission lines, sometimes exhibiting absorption features, and in many cases being completely featureless. The general idea that blazars could be sources of high-energy neutrinos dates back to long before the detection of sub-PeV neutrinos and has since been explored in a number of studies (e.g. Mannheim 1995; Halzen & Zas 1997; Mücke et al. 2003; Kistler, Stanev, & Yüksel 2014; Murase, Inoue & Dermer 2014; Tavecchio & Ghisellini 2015, and papers from our group, as detailed below).

The spectral energy distributions (SEDs) of blazars are composed of two broad humps, a low-energy and a high-energy one. The peak of the low-energy hump ($\nu_{\rm peak}^S$) can occur at widely different frequencies, ranging from about $\sim 10^{12.5}$ Hz ($\sim$ 0.01 eV) to $\sim 10^{18.5}$ Hz ($\sim$ 13 keV). The high-energy hump, which may extend up to $\sim$ 10 TeV, has a peak energy that ranges between $\sim 10^{20}$ Hz ($\sim$ 0.4 MeV) to $\sim 10^{26}$ Hz ($\sim$ 0.4 TeV) (Giommi et al. 2012b; Arsioli et al. 2015). Based on the rest-frame value of $\nu_{\rm peak}^S$, BL Lacs can be further divided into Low energy peaked (LBL) sources ($\nu_{\rm peak}^S < 10^{14}$ Hz [$<$ 0.4 eV]), Intermediate (10^{14} Hz$< \nu_{\rm peak}^S < 10^{15}$ Hz [0.4 eV $< \nu_{\rm peak}^S <$ 4 eV)] and High ($\nu_{\rm peak}^S > 10^{15}$ Hz [$>$ 4 eV]) energy peaked (IBL and HBL) sources respectively (Padovani & Giommi 1995).

Padovani & Resconi (2014) (hereafter PR14), on the basis of a joint positional and energetic diagnostic using very high energy (VHE)[3] lists and studying γ-ray SEDs, have suggested a possible association between eight BL Lacs (all HBL) and seven neutrino events reported by the IceCube collaboration in 2014 (IceCube Collaboration 2014). Following up on this idea, Petropoulou et al. (2015) have modelled the SEDs of six of these BL Lacs using a one-zone lepto-hadronic model and mostly nearly simultaneous data. The SEDs of the sources, although different in shape and flux, were all well fitted by the model using reasonable parameter values. Moreover, the model-predicted neutrino flux and energy for these sources were of the same order of magnitude as those of the IceCube neutrinos. In two cases, i.e. MKN 421 and H 1914−194, a suggestively good agreement between the model predictions and the neutrino fluxes was found.

Very recently, Padovani et al. (2015) have calculated the cumulative neutrino emission from BL Lacs "calibrated" by fitting the spectral energy distributions of the sources studied by Petropoulou et al. (2015) and their (putative) neutrino spectra. Within the so-called *blazar simplified view* (Giommi et al. 2012a; Giommi, Padovani, & Polenta 2013; Padovani & Giommi 2015; Giommi & Padovani 2015) and by adding a hadronic component for neutrino production, BL Lacs as a class were shown to be able to explain the neutrino background seen by IceCube above $\sim$ 0.5 PeV while only contributing on average $\sim$ 10 per cent at lower energies. However, some room was left for individual BL Lacs to still make a contribution at the $\approx$ 20 per cent level to the IceCube low-energy events.

The hypothesis put forward by PR14 and Petropoulou et al. (2015), if correct, should materialise in an IceCube detection but this has not happened yet. At present, in fact, IceCube has not identified any point sources and therefore its signal remains unresolved. The published upper limits on blazars start to be in the ballpark of the scenario described above (PR14) although they do not rule it yet out (IceCube Collaboration 2015c).

Together with the larger neutrino samples recently provided by the IceCube Collaboration, new and better catalogues of high energy sources are now available, which overcome some of the limitations pointed out in PR 14, like the lack of an all-sky flux-limited TeV catalogue. The purpose of this paper is to study in a more quantitative way the possible connection between the IceCube astrophysical neutrinos and γ-ray emitting blazars. To this aim, we have selected a priori 2FHL (The Fermi-LAT Collaboration 2015) and 2WHSP (Chang et al. 2015, in preparation) as the best VHE catalogues, as detailed below. The *Fermi* 3LAC catalogue (Ackermann et al. 2015) was also used because of its size and all-sky coverage, although it reaches γ-ray photons of lower energy. We note that the scanning strategy and the intervals over which the connection between neutrinos and γ-ray sources was studied have also been fixed before any test was carried out.

Section 2 describes the neutrino and γ-ray catalogues used in this paper, while Section 3 discusses our statistical analysis. Section 4 gives our results, while in Section 5 we investigate the γ-ray counterparts and their SEDs. Section 6 summarises our conclusions. Appendix A deals with the 2FHL Galactic sources.

2 THE CATALOGUES

2.1 Neutrino lists

This work is based on the IceCube high-energy starting events (HESE) published by IceCube Collaboration (2014) and IceCube Collaboration (2015a), which cover the first four years of data plus the ν_μ selected from a large sample of high-energy through-going muons (see Aartsen et al. 2015, and the IceCube online link[4] for the full list). Finally, we also included the very high energy (2.6 PeV deposited energy) event announced by the IceCollaboration in July 2015 (Schoenen & Raedel 2015).

Following PR14 we made the following two cuts to the HESE list: 1. neutrino energy $E_\nu \geq 60$ TeV, to reduce the residual atmospheric background contamination, which might still be produced by mouns and atmospheric neutrinos and concentrates in the low-energy part of spectrum

[3] We adopt here the definitions used in Aharonian (2004) for γ-ray astronomy: "high energy" (HE) or GeV astronomy spans the 30 MeV to 30 GeV energy range while VHE or TeV astronomy refers to the 30 GeV to 30 TeV range.

[4] https://icecube.wisc.edu/science/data/HE_NuMu_diffuse

Table 1. Selected list of high-energy neutrinos detected by IceCube.

IceCube ID	Dep. Energy TeV	νf_ν [a] 10^{-11} erg/cm^2/s	RA (2000)	Dec (2000)	Median angular error deg	b_{II} deg
3	$78.7^{+10.8}_{-8.7}$	$1.4^{+3.3}_{-1.2}$	08 31 36	−31 12 00	≤1.4	+5
4	165^{+20}_{-15}	$0.8^{+1.9}_{-0.7}$	11 18 00	−51 12 00	7.1	+9
5	71.4±9.0	$1.3^{+3.0}_{-1.1}$	07 22 24	−00 24 00	≤1.2	+7
9	$63.2^{+7.1}_{-8.0}$	$2.1^{+4.7}_{-1.7}$	10 05 12	+33 36 00	16.5	+54
10	$97.2^{+10.4}_{-12.4}$	$1.2^{+2.8}_{-1.0}$	00 20 00	−29 24 00	8.1	−83
11	$88.4^{+12.5}_{-10.7}$	$1.1^{+2.5}_{-0.9}$	10 21 12	−08 54 00	16.7	+39
12	104±13.0	$0.9^{+2.1}_{-0.8}$	19 44 24	−52 48 00	9.8	−29
13	253^{+26}_{-22}	$1.2^{+2.7}_{-1.0}$	04 31 36	+40 18 00	≤1.2	−5
14	1041^{+132}_{-144}	$1.1^{+2.6}_{-0.9}$	17 42 24	−27 54 00	13.2	+1
17	200±27	$1.2^{+2.9}_{-1.0}$	16 29 36	+14 30 00	11.6	+38
19	$71.5^{+7.0}_{-7.2}$	$1.3^{+3.0}_{-1.1}$	05 07 36	−59 42 00	9.7	−36
20	1141^{+143}_{-133}	$1.1^{+2.6}_{-0.9}$	02 33 12	−67 12 00	10.7	−47
22	220^{+21}_{-24}	$0.7^{+1.7}_{-0.6}$	19 34 48	−22 06 00	12.1	−19
23	$82.2^{+8.6}_{-8.4}$	$1.5^{+3.5}_{-1.3}$	13 54 48	−13 12 00	≤1.9	+47
26	210^{+29}_{-26}	$1.1^{+2.6}_{-0.9}$	09 33 36	+22 42 00	11.8	+45
27	60.2±5.6	$1.8^{+4.0}_{-1.5}$	08 06 48	−12 36 00	6.6	+10
30	129^{+14}_{-12}	$0.8^{+1.9}_{-0.7}$	06 52 48	−82 42 00	8.0	−27
33	385^{+46}_{-49}	$1.4^{+3.2}_{-1.2}$	19 30 00	+07 48 00	13.5	−5
35	2004^{+236}_{-262}	$1.4^{+3.3}_{-1.2}$	13 53 36	−55 48 00	15.9	+6
38	201±16	$1.2^{+2.9}_{-1.0}$	06 13 12	+14 00 00	≤1.2	−2
39	101^{+13}_{-12}	$0.9^{+2.0}_{-0.7}$	07 04 48	−17 54 00	14.2	−5
40	157^{+16}_{-17}	$0.8^{+1.8}_{-0.6}$	09 35 36	−48 30 00	11.7	+3
41	$87.6^{+8.4}_{-10.0}$	$1.4^{+3.2}_{-1.2}$	04 24 24	+03 18 00	11.1	−30
44	$84.6^{+7.4}_{-7.9}$	$1.4^{+3.1}_{-1.1}$	22 26 48	+00 00 00	≤1.2	−46
45	430^{+57}_{-49}	$0.9^{+2.0}_{-0.7}$	14 36 00	−86 18 00	≤1.2	−24
46	158^{+15}_{-17}	$0.8^{+1.8}_{-0.7}$	10 02 00	−22 24 00	7.6	+26
47	$74.3^{+8.3}_{-7.2}$	$1.6^{+3.8}_{-1.4}$	13 57 36	+67 24 00	≤1.2	+48
48	105^{+14}_{-10}	$0.9^{+2.1}_{-0.8}$	14 12 24	−33 12 00	8.1	+27
51	$66.2^{+6.7}_{-6.1}$	$2.2^{+5.0}_{-1.8}$	05 54 24	+54 00 00	6.5	+14
52	158^{+16}_{-18}	$0.8^{+1.8}_{-0.7}$	16 51 12	−54 00 00	7.8	−6
	2600±300		07 21 22	+11 28 48	0.27	+12

[a] Fluxes in units of 10^{-8} GeV cm^{-2} s^{-1} can be obtained by multiplying the numbers in this column by 0.614.

(see Fig. 2 in IceCube Collaboration 2014); 2. median angular error $\leq 20°$, to somewhat limit the number of possible counterparts. The final list includes 30 HESE and 21[5] through-going ν_μ, for a total of 51 IceCube events. The former, together with the 2.6 PeV event, are listed in Tab. 1, which gives the deposited energy of the neutrino, the flux at the deposited energy in νf_ν units, the coordinates, the median angular error in degrees, and the Galactic latitude. For the through-going ν_μ, for which we refer the reader to the online IceCube link, we assumed a median angular error of 0.4°, as prescribed by the IceCube collaboration, apart from the 2.6 PeV event, for which the median angular error is 0.27° (Schoenen & Raedel 2015).

Neutrino fluxes have been derived as in PR14 but using a live time of detection of 1,347 days (IceCube Collaboration 2015a). This means that the values for the sources studied in PR14 are now smaller by a factor $1,347/998 = 1.363$. The derived fluxes are in the range $0.7 - 2.2 \times 10^{-11}$ erg cm^{-2} s^{-1} (i.e., $0.4 - 1.3 \times 10^{-8}$ GeV cm^{-2} s^{-1}) and errors are Poissonian for one event (Gehrels 1986).

[5] One of the ν_μ events coincides with HESE ID 5 and was therefore discarded.

2.2 γ-ray catalogues

2.2.1 *Fermi 2FHL*

The second catalogue of hard *Fermi*-Large Area Telescope (LAT) sources (2FHL: The Fermi-LAT Collaboration 2015) includes 360 sources and provides an all-sky view of VHE sources at $E > 50$ GeV. We remind the reader that 1FHL (Ackermann et al. 2013), the first *Fermi*-LAT catalogue of hard sources, had a 10 GeV threshold, i.e. still not on the VHE side. 2FHL, instead, bridges the gap between *Fermi*-LAT and ground based Cherenkov telescopes. Given its all-sky nature we can use 2FHL also to select a sample of Galactic sources. We then defined two subsamples: 1. the $|b_{II}| \geq 10°$ subsample, which contains 257 objects, of which a very large fraction ($\sim$ 90 per cent) are blazars[6]. The remaining sources are mostly still unclassified but very likely to be blazars; 2. the $|b_{II}| < 10°$ subsample, which contains 103 objects, of which a good fraction ($\sim$ 41 per cent) are still blazars. The remaining 59 per cent is composed of Galactic

[6] These and the following numbers reflect our own classification of many of the unclassified 2FHL sources, using also 2WHSP (see below), and are somewhat different from those given in the 2FHL paper.

objects, that is supernova remnants (SNR) and pulsar wind nebulae (PWN) (∼ 33 per cent), and unclassified sources (∼ 26 per cent), very likely to be Galactic as their VHE *Fermi* spectrum is harder than that of extragalactic sources (The Fermi-LAT Collaboration 2015). The Galactic sources are discussed in Appendix A.

We further subdivided the $|b_{\rm II}| \geq 10°$ subsample into HBL ($\nu^S_{\rm peak} > 10^{15}$ Hz) and non HBL. The former sample contains 149 sources, all BL Lacs, while the latter, which is made up of 108 objects, contains mostly blazars of the IBL and LBL type (∼ 69 per cent, including some FSRQs [∼ 9 per cent]), unclassified sources (∼ 23 per cent), and radio galaxies (∼ 8 per cent).

2.2.2 2WHSP

The 1WHSP catalogue (Arsioli et al. 2015) provided a large area ($|b_{\rm II}| > 20°$) catalogue of $\sim 1,000$ blazars and blazar candidates selected to have $\nu^S_{\rm peak} > 10^{15}$ Hz and therefore expected to radiate strongly in the HE and VHE bands. 1WHSP sources were characterized by a "figure of merit" (FoM), which quantified their potential detectability in the TeV band by the current generation of Imaging Atmospheric Cherenkov telescopes. This was defined as the ratio between the synchrotron peak flux of a source and that of the faintest blazar in the 1WHSP sample already detected in the TeV band. 1WHSP sources are all BL Lacs, with a large fraction of those with high FoM being known TeV sources (e.g., 36 per cent of those with FoM ≥ 1.2) and the remaining ones thought to be within reach of detection by current VHE instrumentation. Although technically not a γ-ray catalogue, 1WHSP represented at the time the best way to compensate for the lack of full sky coverage in the TeV band for blazars. Moreover, ∼ 30 per cent of the sources already had a *Fermi* 1FGL, 2FGL or 3FGL γ-ray counterpart.

Chang et al. (2015, in preparation) have updated the 1WHSP catalogue and produced 2WHSP, which reaches down to $|b_{\rm II}| \geq 10°$ and drops one of the previously adopted selection criteria (the IR colour-colour cut) to increase completeness at low IR fluxes and better include some HBL sources dominated in the optical and IR bands by the light from the host giant elliptical galaxy. The 2WHSP catalogue includes $\sim 1,700$ sources and therefore provides a ∼ 70 per cent increase in size as compared to 1WHSP. It reaches much lower VHE fluxes, and it is almost seven times larger, than 2FHL.

The 2FHL and 2WHSP catalogues do not have the same composition in terms of blazar types. Of the 240 sources in the 2FHL catalogue that are identified with a counterpart at other frequencies and are located at $|b_{\rm II}| \geq 10°$ only ∼ 71 per cent are also in 2WHSP. The remaining objects are all blazars with $\nu^S_{\rm peak} < 10^{15}$ Hz, which therefore cannot be included in the 2WHSP sample by definition. On the other hand, ∼ 93 per cent of the 2FHL HBL with $|b_{\rm II}| \geq 10°$ are also part of 2WHSP while ∼ 70 per cent of the 2WHSP subsample with FoM ≥ 2 are 2FHL HBL sources. We note that 2WHSP has an advantage over 2FHL, as it not affected by extragalactic background light (EBL) absorption, since the FoM is defined at $\nu^S_{\rm peak}$, while 2FHL is selected based on the flux at $E > 50$ GeV. A relatively high redshift source, for example is less likely to be in the 2FHL sample than in 2WHSP.

2.2.3 Fermi 3LAC

We also used the third catalogue of AGN detected above 100 MeV by the *Fermi*-LAT (3LAC: Ackermann et al. 2015), more specifically the "clean sample" of 1,444 sources at $|b_{\rm II}| \geq 10°$ and free of the analysis issues, which affect some of the 3LAC detections. Basically all objects (∼ 98.8 per cent) are blazars. We do not expect a neutrino signal from this sample, however, at least as far as the full sample is concerned, based on the results of Glüsenkamp et al. (2015), who found no evidence of neutrino emission and a maximal contribution from *Fermi* 2LAC (Ackermann et al. 2011) blazars ∼ 20 per cent. Moreover, Brown, Adams, & Chadwick (2015), using 70 months of *Fermi*-LAT observations, found no evidence of γ-ray emission associated with IceCube's track-like neutrino events.

We further subdivided the 3LAC sample into an HBL ($\nu^S_{\rm peak} > 10^{15}$ Hz), an FSRQ, and an "others" sample, which include 386, 415, and 645 sources respectively[7]. The "others" sample is made up for the most part of BL Lacs and "unclassified AGN" of the IBL and LBL type (∼ 97 per cent), with the remaining ∼ 3 per cent including steep-spectrum radio quasars and radio galaxies.

3 THE STATISTICAL ANALYSIS

To study the possible connection between the IceCube neutrinos and the source catalogues, we have introduced the observable N_ν defined as the number of neutrino events with at least one γ-ray counterpart found within the individual median angular error. To evaluate this, we also took into account the case of IceCube neutrinos with $|b_{\rm II}| < 10°$ but which could still be associated with a $|b_{\rm II}| > 10°$ γ-ray source given their large error radii. We do not only consider the whole γ-ray catalogues but within a given catalogue we scan versus flux, $N_\nu(f_\gamma)$ or, equivalently, versus FoM for 2WHSP, $N_\nu(FoM)$. If only the strongest sources are associated to IceCube events such a scan will reveal a deviation from the randomised cases. The chance probability $P_i(N_\nu(f_\gamma, i))$, or equivalently $P_i(N_\nu(FoM, i))$, to observe a certain N_ν for sources with $f_\gamma \geq f_\gamma, i$ is determined on an ensemble of typically 10^5 randomised maps. Where needed, the sampling has been done over 10^6 randomised maps. To determine the random cases, we explored three different procedures: 1. randomisation of the γ-ray sample coordinates by drawing an equal number of positions homogeneously distributed over the sky, making sure that only random sources with $b_{\rm II}$ values in the same range as the original γ-ray catalogue are considered. This leaves untouched the IceCube positions, which are known to be not uniformly distributed, but might lose any large scale structure present in the γ-ray sample; 2. to at least partially obviate this, we have also randomised only the γ-ray sample right ascensions; 3. randomisation of the IceCube right ascensions, making sure that only random sources that can be associated with the γ-ray catalogue within the relevant error circles are considered (for example, a $|b_{\rm II}| < 10°$ IceCube random source can still be associated

[7] These numbers sum up to 1,446 (and not 1,444) because two FSRQ happen to be HBL

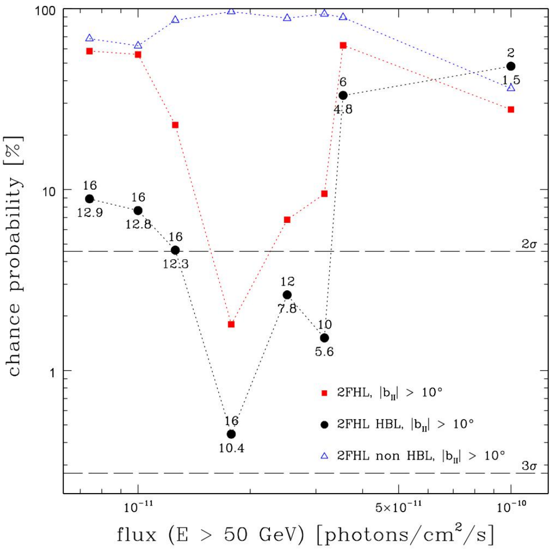

Figure 1. The chance probability of association of 2FHL with IceCube events for objects having $F(> 50$ GeV) larger than the value on the x axis for the whole high Galactic latitude sample (red squares), HBL (black circles), and non HBL (empty blue triangles). All cases refer to a randomisation of the γ-ray sample on right ascension. The numbers give the observed (above the points) and average random values (below the points) of N_ν for HBL. The two dashed lines denote the 2σ and 3σ values.

with a 2WHSP object provided it has a large enough error radius). This preserves any large scale structure present in the γ-ray sample plus the IceCube declinations. However, the requirement above does not conserve the total area sampled by the IceCube error circles, resulting in a biased test statistics. As a result, we used procedures 1 and 2, conservatively taking as our best estimate of the probability of random association the *largest* of the two probabilities. Since our three catalogues are somewhat overlapping, in particular at large fluxes and FoM (see Section 2.2.2), the number of bins per scan is < 10, and the points are not independent, we do not correct the probabilities for the "look elsewhere effect" (which would take into account the artificial p-value reduction due to the application of multiple tests). We have also fixed the catalogues studied at the beginning of this work as well as the bins in flux and FoM used for the scans.

4 RESULTS

4.1 *Fermi* 2FHL

Figure 1 shows the chance probability of association of 2FHL high Galactic latitude sources with IceCube events for objects having $F(> 50$ GeV) larger than the value on the x axis and a randomisation of the γ-ray sample on right ascension, which gives the most conservative result. Red squares indicate the whole high Galactic latitude sample, black circles denote HBL only, and blue triangles represent non HBL sources. The numbers give the observed (above the points) and average random value (below the points) of N_ν for HBL. Figure 1 shows the following:

- for the whole sample and for HBL the chance probability is strongly dependent on γ-ray flux, with an anti-correlation between probability and flux up to $F(> 50$ GeV) $\sim 1.8 \times 10^{-11}$ photon cm^{-2} s^{-1} with a p-value $< 10^{-4}$ according to a Spearman test. We attribute the turnover in p-value at very large γ-ray fluxes to small number statistics;
- p-values $\sim$ 1.8 per cent are reached for $F(> 50$ GeV) $\gtrsim 1.8 \times 10^{-11}$ photon cm^{-2} s^{-1} for the whole sample;
- p-values $\sim$ 0.4 per cent are reached for $F(> 50$ GeV) $\gtrsim 1.8 \times 10^{-11}$ photon cm^{-2} s^{-1} for HBL;
- non HBL sources display no correlation between γ-ray flux and p-value, the latter being always $\gtrsim 40$ per cent. This shows that the relatively low p-values reached by the whole sample are driven solely by HBL;
- at the flux at which p-value is minimum for HBL N_ν is 16, while the average value from the randomisation is 10.4, which means that only $\approx$ 6 IceCube events have a "real" counterpart;
- for the same flux the number of HBL γ-ray sources with a neutrino counterpart is 27, while the whole "parent" γ-ray sample includes 92 sources.

At this level of p-value this result would be significant for astronomers but only at the level of "a hint" for physicists, who require a 5σ level to claim a "discovery". We follow physicists here and consider this a potentially very interesting result, worth of further investigations. Therefore, we can say that a hint of an association between the 2FHL high Galactic latitude HBL and IceCube events is present in the data.

4.2 2WHSP

Figure 2 shows the chance probability of association of 2WHSP sources with IceCube events for objects having FoM larger than the value on the x axis and a randomisation of the γ-ray sample on both coordinates, which gives the most conservative result. The numbers give the observed (above the points) and average random values (below the points) of N_ν. The figure shows the following:

- the chance probability is dependent on FoM, with an anti-correlation between probability and flux up to FoM ~ 1 with a p-value $< 10^{-4}$ according to a Spearman test;
- p-values ~ 0.7 per cent are reached for FoM $\gtrsim 1$;
- at the flux at which p-value is minimum for HBL N_ν is 18, while the average value from the randomisation is 12.7, which means that only $\approx$ 5 IceCube events have a "real" counterpart;
- for the same flux the number of γ-ray sources with a neutrino counterpart is 32, while the whole "parent" γ-ray sample includes 137 sources.

Therefore, a hint of an association between the 2WHSP sample and IceCube events is present in the data. Note that a FoM ~ 1 is roughly equivalent to $F(> 50$ GeV) $\sim 2.5 \times 10^{-11}$ photon cm^{-2} s^{-1} (de-absorbed). Taking into account

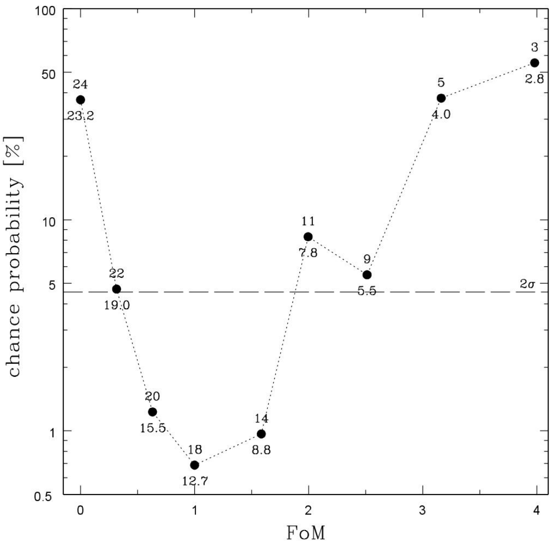

Figure 2. The chance probability of association of 2WHSP sources with IceCube events for objects having FoM larger than the value on the x axis for a randomisation of the γ-ray sample on both coordinates. The numbers give the observed (above the points) and average random values (below the points) of N_ν. The dashed line denotes the 2σ value.

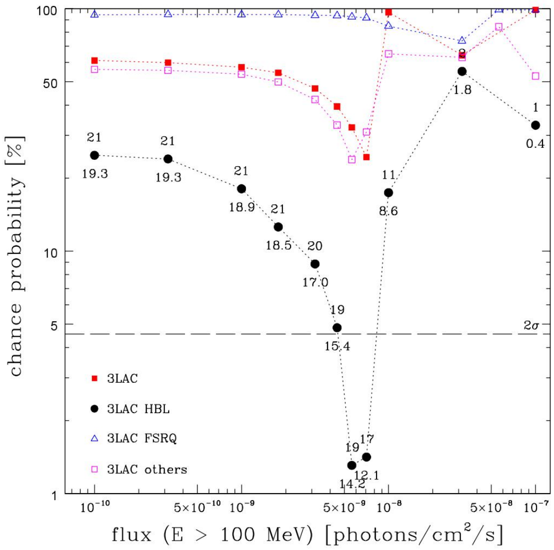

Figure 3. The chance probability of association of 3LAC "clean" sources with IceCube events for objects having $F(> 100$ MeV) larger than the value on the x axis for the whole sample (filled red squares), HBL (black circles), FSRQ (blue triangles), and others (non-HBL and non-FSRQ: empty red squares). Only HBL are randomised on right ascension, while the other samples are randomised on both coordinates. The numbers give the observed (above the points) and average random values (below the points) of N_ν for HBL. The dashed line denotes the 2σ value.

the EBL the corresponding flux is quite close to the value for which the p-value is minimum for 2FHL HBL.

4.3 *Fermi* 3LAC

Figure 3 shows the chance probability of association of 3LAC "clean" sources with IceCube events for objects having $F(> 100$ MeV) larger than the value on the x axis. Filled red squares indicate the whole sample, randomised on both coordinates, black circles denote HBL, randomised on right ascension, blue triangles represent FSRQ, while empty red squares are for other sources, namely non-HBL and non-FSRQ, both randomised on both coordinates. The numbers give the observed (above the points) and average random values (below the points) of N_ν for HBL. The figure shows the following:

- the chance probability is strongly dependent on γ-ray flux, with an anti-correlation between probability and flux up to $F(> 100$ MeV) $\sim 6 \times 10^{-9}$ photon cm^{-2} s^{-1} with a p-value $< 7 \times 10^{-3}$ for all samples apart from the FSRQ one;
- the minimum p-value for the whole 3LAC sample and for "others" is $\sim$ 24 per cent for $F(> 100$ MeV) $\sim 6 \times 10^{-9}$ photon cm^{-2} s^{-1};
- the minimum p-value for HBL is $\sim$ 1.3 per cent for $F(> 100$ MeV) $\sim 6 \times 10^{-9}$ photon cm^{-2} s^{-1};
- the minimum p-value for FSRQ is $\sim$ 74 per cent for $F(> 100$ MeV) $\sim 3 \times 10^{-8}$ photon cm^{-2} s^{-1};
- at the flux at which the p-value is minimum for HBL N_ν is 19, while the average value from the randomisation is 14.2, which means that only ≈ 5 IceCube events have a "real" counterpart;
- for the same flux the number of HBL γ-ray sources with a neutrino counterpart is 38, while the whole "parent" γ-ray sample includes 147 sources.

In summary, there is no evidence for an association between the 3LAC "clean" sample and IceCube events. As discussed in Section 2.2.3, this was to be expected for the full sample, as Glüsenkamp et al. (2015) did not make any cut on γ-ray flux. However, there is a hint of an association between the 3LAC HBL and IceCube events. This is not the case for the 3LAC FSRQ.

5 ASTROPHYSICS OF POSSIBLE ICECUBE COUNTERPARTS

The deviations from random expectation of N_ν for the 2FHL HBL and the 2WHSP samples are ~ 0.4 per cent for $F(> 50$ GeV) $\gtrsim 1.8 \times 10^{-11}$ photon cm^{-2} s^{-1} and ~ 0.7 per cent for FoM $\gtrsim 1$ respectively. We therefore examined in detail the corresponding counterparts to IceCube events, which are all HBL by definition.

Table 2 lists the main properties of the 2FHL HBL and 2WHSP sources satisfying the requirements mentioned above by giving the IceCube ID, the 2WHSP name (which includes the coordinates), the 2FHL name, the common

Table 2. 2FHL HBL sources with $F(> 50\text{ GeV}) \geq 1.8 \times 10^{-11}$ photon cm^{-2} s^{-1} and 2WHSP sources with FoM ≥ 1.0 in one median angular error radius around the positions of the IceCube events. The counterparts of the most probable matches are indicated in boldface.

ID	2WHSP name	2FHL name	Common name	offset deg	z	FoM	flux^a	Comments
9	J091037.0+332924	J0910.4+3327	Ton 1015	11.4	0.350	2.0	0.283	positional match (PR14)
	J091552.4+293324	J0915.9+2931	B2 0912+29	11.2	>0.19	2.5	0.324	positional match (PR14)
	J101504.1+492600	J1015.0+4926	**1ES 1011+496**	15.9	0.212	4.0	1.62	most probable match (PR14)
	J110427.3+381231	J1104.4+3812	**MKN 421**	12.8	0.031	57.5	12.4	most probable match (PR14)
10	J235907.8−303740		**H 2356−309**	4.7	0.165	2.0	0.69^b	most probable match (PR14)
11	J095302.7−084018	J0952.9−0841	1RXS J095303.4−084003	7.0	...	0.8	0.385	positional match (PR14)
	J102243.7−011302	J1022.7−0112	1RXS J102244.2−011257	7.7	>0.36	1.3	0.171	positional match (PR14)
	J102658.5−174858	J1027.0−1749	1RXS J102658.5−174905	9.0	0.267	1.0	0.196	most probable match?
12	J193656.1−471950	J1936.9−4721	PMN J1936−4719	5.6	0.265	1.3	0.240	most probable match?^{c}
	J195502.8−564028	J1954.9−5641	1RXS J195503.1−56403	4.2	...	1.0	0.127	positional match
	J195945.6−472519	J1959.6−4725	SUMSS J195945−472519	5.9	...	1.0	0.183	positional match
	J200925.3−484953	J2009.4−4849	PKS 2005−489	5.6	0.071	10.0	0.970	positional match (PR14)
14	J171405.4−202752	J1713.9−2027	1RXS J171405.2−202747	9.9	...	1.3	0.275	most probable match?
17	J155543.0+111124	J1555.7+1111	**PG 1553+113**	8.9	...	7.9	4.20	most probable match (PR14)
19	J050657.8−543503	J0506.9−5434	1RXS J050656.8−543456	5.1	>0.26	1.0	0.131	positional match (PR14)
	J054357.2−553207	J0543.9−5533	1RXS J054357.3−553206	6.4	...	2.5	0.527	positional match^d
20	J014347.3−584551	J0143.8−5847	SUMSS J014347−584550	10.1	...	2.0	0.161	positional match^e
	J035257.4−683117	J0352.7−6831	PKS 0352−686	7.6	0.087	2.0	0.228	positional match (PR14)
22	J191744.8−192131	J1917.7−1921	**1H1914−194**	4.8	0.137	1.6	0.814	most probable match (PR14)
		J1921.9−1607	PMN J1921−1607	6.7	...	...	0.397	most probable match?(PR14)^f
	J195814.9−301111	J1958.3−3011	1RXS J195815.6−30111	9.7	0.119	1.3	0.282	most probable match?(PR14)^f
26	J090534.9+135806	J0905.7+1359	MG1 J090534+1358	10.9	...	1.0	0.192	positional match (PR14)
	J091552.4+293324^g	J0915.9+2931	B2 0912+29	7.9	>0.19	2.5	0.324	positional match (PR14)
27	J081627.2−131152	J0816.3−1311	PMN J0816−1311	2.4	...	2.5	0.344	positional match^e
35	J130421.0−435310	J1304.5−4353	1RXS 130421.2−435308	14.3	...	2.0	0.235	positional match (PR14)
	J130737.9−425938	J1307.6−4259	1RXS 130737.8−425940	14.8	...	3.2	0.351	positional match (PR14)
	J131503.3−423649	J1315.0−4238	1ES 1312−423	14.6	0.105	2.5	0.157	positional match (PR14)
	J132840.6−472749	J1328.6−4728	1WGA J1328.6−4727	9.2	...	0.4	0.209	positional match
	J134441.7−451007		SUMSS J134441−451002	10.7	...	1.0		positional match
39		J0622.4−2604	PMN J0622−2605	12.8	0.414	...	0.258	positional match
	J063059.5−240646	J0631.0−2406	1RXS J063059.7−240636	10.0	...	1.6	0.322	positional match
	J064933.6−313920	J0649.6−3139	1RXS J064933.8−31391	14.2	...	0.8	0.225	most probable match?
40	J102356.1−433601		SUMSS J102356−433600	9.7	...	2.5	2.08^b	most probable match?
41	J041652.4+010523	J0416.9+0105	**1ES 0414+009**	2.9	0.287	3.2	0.269	most probable match
46	J094709.5−254100		1RXS J094709.2−254056	4.7	...	1.0		positional match
	J102658.5−174858^h	J1027.0−1749	1RXS J102658.5−174905	7.4	0.267	1.0	0.196	most probable match?
48	J144037.8−384655	J1440.7−3847	1RXS J144037.4−38465	8.0	...	1.3	0.184	positional match
51	J054030.0+582338	J0540.5+5822	GB6 J0540+5823	4.8	...	1.6	0.187	positional match
	J060200.4+531600	J0601.9+5317	GB6 J0601+5315	1.3	...	1.0	0.101	positional match

^{a} f (E > 50 GeV) in units of 10^{-10} ph/cm^2/s
^{b} not in 2FHL: 1FHL flux [f (E > 10 GeV)]
^{c} was positional match in PR14
^{d} was most probable match in PR14 but TeV upper limits rule that out
^{e} was most probable match in PR14 but 2FHL data rule that out
^{f} was positional match in PR14
^{g} also counterpart of ID 9
^{h} also counterpart of ID 11

name, the offset between the reconstructed position of the IceCube event and the blazar one, the redshift of the source (if available), the FoM, and the > 50 GeV flux from the 2FHL catalogue (if available). Given the very strong variability of blazars the flux values should be taken only as approximate. Nevertheless, on average a stronger neutrino source should also be a stronger γ-ray source, unless significant absorption is present.

The table contains 37 objects matched to 18 IceCube events. The overlap between the two samples, as expected, is quite large: 25 of the 27 2FHL objects are also 2WHSP sources, although three of them are below the FoM cut of 1, while 28 of the 32 2WHSP objects are also 2FHL sources, although five of them are below the γ-ray flux cut of $F(> 50\text{ GeV}) \gtrsim 1.8 \times 10^{-11}$ photon cm^{-2} s^{-1}. Two sources are matched to two different IceCube events: 2WHSPJ091552.4+293324 (ID 9 and 26) and 2FHL J1027.0−1749 (ID 11 and 46).

The comments in Table 2 refer to the hybrid photon – neutrino SED of the sources. Namely, following PR14 we have first put together the γ-ray SEDs of all sources using the SED builder[8] of the ASI Science Data Centre (ASDC) adding, if needed, VHE data taken from the literature. We have also included the flux per neutrino event at the specific energy. We then performed an "energetic" diagnostic by checking if a simple extrapolation succeeded in connecting the most energetic γ-rays to the IceCube neutrino in the hybrid SED, taking into account the rather large uncertainty in the flux of the latter. If this was the case we considered the source to be a "most probable" match. Otherwise, the object was considered a simple positional match. The idea behind this was to see how the neutrino and photon energetics compared and therefore have a much stronger discriminant than a simple cross-correlation.

We note that we do not include here the 3LAC counterparts for the simple reason that the few sources not overlapping with 2FHL or 2WHSP do not have, by definition, VHE γ-ray data and therefore the hybrid SED is not very informative.

As it turns out, the large majority of the sources in Table 2, that is all but six of those associated with the IceCube events discovered in the first three years of data, had already been considered by PR14. Based on the new data available and the revised neutrino fluxes (see Section 2.1), the classifications made by PR14 have been changed for six sources, as detailed in the Table.

The SEDs of sources associated with IceCube events having ID > 35 in Table 2, associated with the fourth year of IceCube data, were studied ex-novo. At least one, that is 1ES 0414+009, whose SED is shown in Fig. 4, is without doubt a most probable match, giving its rising SED and large de-absorbed TeV fluxes, while three more could be most probable matches.

The detailed SED study of the 2FHL and WHSP candidates suggests then that five IceCube events (9, 10, 17, 22, and 41) have most probable matches (with the respective counterparts highlighted in boldface), with a few more (11, 12, 14, 39, 40, and 46) having possible counterparts. SUMSS J102356−433600, however, the possible counterpart of ID 40, is an unlikely counterpart once one considers the Galactic source Vela Junior (see Appendix A and Fig. A1).

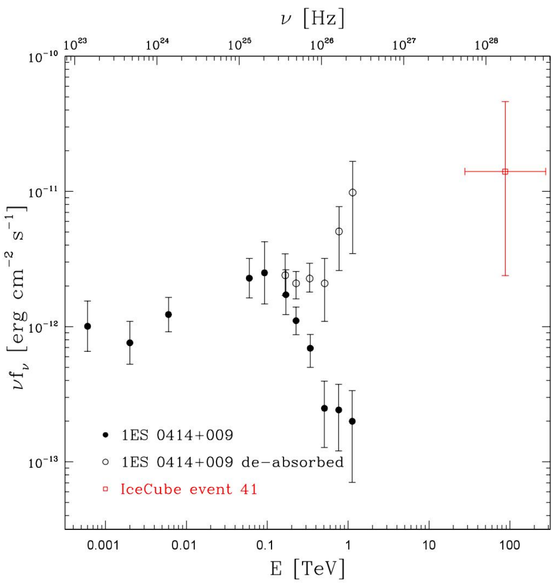

Figure 4. *Fermi* γ-ray SED (The Fermi-LAT Collaboration 2015; Acero et al. 2015) and HESS data observed (black filled circles) and corrected for absorption by the EBL (black open circles; Finke et al. 2015) of 1ES 0414+009, the only 2WHSP counterpart with FoM ≥ 2.5 in the IceCube error circle (ID 41). The (red) open square represents the neutrino flux for the corresponding IceCube event; vertical error bars are Poissonian for one event, while the horizontal one indicates the range over which the flux is integrated.

6 DISCUSSION

Consistently with PR14, HBL appear to be the only plausible blazar counterparts of at least some of the IceCube events. However, while in PR14 this statement could not be properly supported by a statistical analysis due to the lack of complete, all-sky, VHE catalogues, in this paper we have addressed this issue by introducing a new observable, N_ν, and by making use of the very recently completed, and independently built, 2FHL, 3LAC, and 2WHSP catalogues. The former is defined as the number of neutrino events with at least one γ-ray counterpart found within the individual median angular error.

The chance probability in the individual catalogues, $P_i(N_\nu(f_\gamma, i))$, reaches values $0.4 - 1.3$ per cent for HBL and appears to be strongly dependent on γ-ray flux and FoM, with a minimum at $F(>50\ \mathrm{GeV}) \gtrsim 1.8 \times 10^{-11}$ photon cm^{-2} s^{-1} (2FHL), $F(>100\ \mathrm{MeV}) \gtrsim 5.6 \times 10^{-9}$ photon cm^{-2} s^{-1} (3LAC), and FoM $\gtrsim 1$. We then carefully examined the SEDs of all these sources, applying the "energetic" test of PR14. This way we identified ≈ 5 HBL by checking if a simple extrapolation succeeded in connecting the most energetic γ-rays to the IceCube neutrino in an hybrid SED.

This number of most probable matches is in very good agreement with the value coming from our randomisations. Namely, we expect $\sim 10, 13,$ and 14 spurious matches on average (for the 2FHL, 2WHSP, and 3LAC catalogues respectively), which translates, based on the number of observed matches (16, 18, and 19), into $\sim 5 - 6$ "real" counterparts. This highlights once more the importance of the SED diagnostic in singling out the best candidates.

As found by Padovani et al. (2015) in a model-dependent fashion, it turns out that the neutrino signal from blazars is not a predominant component of current IceCube data: only ≈ 5 (up to ≈ 10 including the possible "most probable matches") IceCube events can be associated with HBL. These need to be compared with our list of 51 events, which includes 30 HESE and 21 through-going ν_μ, which corresponds to a model-independent fraction of the IceCube signal $\sim 10 - 20$ per cent. This does not exclude the possibility that this fraction might increase once IceCube reaches fainter fluxes.

Based on our results, to be a neutrino source candi-

[8] http://tools.asdc.asi.it/SED/

date a blazar needs to be: 1. a relatively strong source; 2. a VHE γ-ray source; 3. an HBL. This is relevant also to explain the lack of signal from *Fermi* blazars in IceCube Glüsenkamp et al. (2015), who, we note, did not make any cut on γ-ray flux, although they considered, apart from the whole 2LAC, also FSRQ, LBL, and IBL+HBL sub-samples.

We have in fact applied the same statistical tests not only to HBL but also to FSRQ and IBL and LBL in general, with null results (see Fig. 1 and 3). This leaves HBL as the only possible extragalactic γ-ray detected IceCube counterparts. We note that, since PR14 used TeVCat, 1WHSP, and 1FHL, the sensitivity to FSRQ was only marginal (e.g. only ~ 10 per cent of the sources in their Table 2 are FSRQ). This is not the case in this paper, since we also consider the 3LAC sample.

None of the matches in Tab. 2 are track-like events. To probe this further, we have re-done the statistical analysis separately for the 29 track-like events, with null results. Namely, no counterparts were observed for the full 2FHL and 3LAC HBL samples, while three were detected in the full 2WHSP catalogue (all with FoM ≤ 0.3). The corresponding curves in Fig. 1 to 3 would then be an horizontal line at 100% for the first two samples and a very similar line (with a small dip to $\sim 20\%$ only for FoM ≤ 0.3) for 2WHSP. The lack of track-like events in Tab. 2 persists even if we assume a median angular error of 1° for the ν_μ events. Only for an error of 2° one counterpart with FoM ≥ 2 appears in the 2WHSP catalogue, while ~ 0.5 are expected, based on our simulations. This indicates that by using tracks only we are still not sensitive to the HBL neutrino signal, as also expected from the fact that tracks trace only about 1/6 of the astrophysical signal under the assumption of a flavour ratio $\nu_e : \nu_\mu : \nu_\tau = 1 : 1 : 1$. We note that IceCube Collaboration et al. (2015) have looked for correlations between IceCube neutrinos and the highest-energy cosmic rays measured by the Pierre Auger Observatory and the Telescope Array. Even in their case the smallest of the p-values comes from the correlation between ultrahigh-energy cosmic rays with IceCube cascades (i.e. non track-like).

It is important to stress that we are not limited by the γ-ray samples but by the neutrino statistics. As illustrated, in fact, in Fig. 5, comparing the first half of the HESE sample with the four year one, the p-value decreases steadily at relevant γ-ray fluxes for the 2FHL HBL as the live time increases. Assuming there is indeed a signal, this gives us hope that the continuous accumulation of data from IceCube and future neutrino observatories (e.g. KM3NeT, IceCube-Gen2: Margiotta 2014; IceCube-Gen2 Collaboration 2014) can turn the hint we observed into a discovery.

7 CONCLUSIONS

We have investigated the correlation between γ-ray sources from the 2FHL, 2WHSP, and 3LAC samples with the latest list of IceCube neutrinos. This was done by first deriving the number of neutrino events with at least one γ-ray counterpart within the individual IceCube median angular error and then by estimating the related chance probability using an ensemble of $10^5 - 10^6$ random maps. For the three catalogues the p-values reach $0.4 - 1.3$ per cent for HBL and appears to be strongly dependent on γ-ray flux

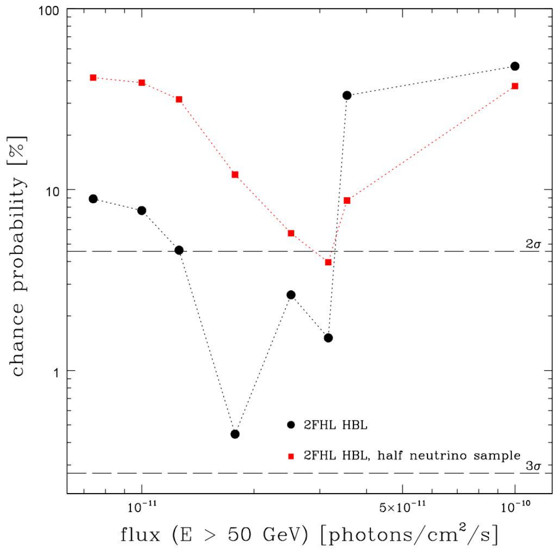

Figure 5. The chance probability of association of high Galactic latitude 2FHL HBL for objects having $F(> 50$ GeV) larger than the value on the x axis for the four year (black circles) and for the first half of the IceCube HESE sample (red squares). All cases refer to a randomisation of the γ-ray sample on right ascension.

and FoM. Through careful examination of the hybrid γ-ray – neutrino SEDs of the sources giving the strongest signal (the "energetic" test of PR14) we have identified ≈ 5 HBL as the most probable IceCube counterparts. This number is in very good agreement with the value coming from our randomisations, highlighting once more the importance of the SED diagnostic in singling out the best candidates, and corresponds to a model-independent fraction of the current IceCube signal $\sim 10 - 20$ per cent. Other types of blazars give null results, indicating that to be a neutrino source candidate a blazar needs to be a relatively strong VHE γ-ray source with $\nu^S_{\rm peak} > 10^{15}$ Hz. The p-values obtained for the 2FHL HBL by comparing the first half of the HESE sample with the four year one indicates that we are limited by the neutrino statistics. If a signal is indeed there, more data from IceCube and future neutrino observatories should turn our hint into a discovery.

As for Galactic sources, although we cannot perform a correlation study similar to that done for blazars due to the complications related to the randomisation in this case, we nevertheless studied their hybrid SEDs and found that two IceCube neutrinos have most probable Galactic 2FHL counterparts (with one more having a possible counterpart: see Appendix A).

ACKNOWLEDGMENTS

We thank Stefan Coenders for useful comments and the many teams, which have produced the data and catalogues used in this paper for making this work possible. ER is supported by a Heisenberg Professorship of the Deutsche Forschungsgemeinschaft (DFG RE 2262/4-1), BA by the Brazilian Scientific Program "Ciências sem Fronteiras" Cnpq, and YLC by a scholarship provided by the Government of the Republic of China (Taiwan). We acknowledge the use of data and software facilities from the ASDC, managed by the Italian Space Agency (ASI).

REFERENCES

Aartsen M. G., et al., 2013, Phys. Rev. Let., 111, 021103
Aartsen M. G., et al., 2015, Phys. Rev. Let., 115, 081102
Acero F., et al., 2013, ApJ, 773, 77
Acero F., et al., 2015, ApJS, 218, 23
Ackermann M., et al., 2011, ApJ, 743, 171
Ackermann M., et al., 2013, ApJS, 209, 34
Ackermann M., et al., 2015, ApJ, 810, 14
Aharonian F., 2004, Very High Energy Cosmic Gamma Radiation: A Crucial Window on the Extreme Universe. World Scientific Press, Singapore
Aharonian F., et al., 2006, ApJ, 636, 777
Aharonian F., et al., 2007, ApJ, 661, 236
Ahlers M., Halzen F., 2015, Rep. Prog. Phys., 78, 126901
Arsioli B., Fraga B., Giommi P., Padovani P., Marrese, M., 2015, A&A, 579, A34
Brown A. M., Adams J., Chadwick P. M., 2015, MNRAS, 451, 323
The Fermi-LAT Collaboration, 2015, ApJ, submitted (arXiv:1508.04449)
Finke J. D., Reyes L. C., Georganopoulos M., Reynolds K., Ajello M., Fegan S. J., McCann K., 2015, ApJ, 814, 20
Gehrels N. 1986, ApJ, 303, 336
Giommi P., Padovani P., Polenta G., Turriziani S., D'Elia V., Piranomonte S., 2012a, MNRAS, 420, 2899
Giommi P., et al., 2012b, A&A, 514, 160
Giommi P., Padovani P., Polenta G., 2013, MNRAS, 431, 1914
Giommi P., Padovani P., 2015, MNRAS, 450, 2404
Glüsenkamp T., for the IceCube Collaboration, 2015, proceedings of the RICAP-14 conference, Noto, Sicily (arXiv:1502.03104)
Halzen F., Zas E., 1997, ApJ, 488, 669
H.E.S.S. Collaboration, et al., 2014, A&A, 564, A9
IceCube Collaboration, 2013, Science, 342, 1242856
IceCube Collaboration, 2014, Phys. Rev. Lett., 113, 101101
IceCube Collaboration, 2015a, Contributions to the 34th International Cosmic Ray Conference (ICRC 2015), p. 45 (arXiv:1510.05223)
IceCube Collaboration, 2015b, Contributions to the 34th International Cosmic Ray Conference (ICRC 2015), p. 37 (arXiv:1510.05223)
IceCube Collaboration, 2015c, Contributions to the 34th International Cosmic Ray Conference (ICRC 2015), p. 5 (arXiv:1510.05222)
IceCube Collaboration, et al., 2015, submitted (arXiv:1511.09408)
IceCube-Gen2 Collaboration, 2014, arXiv:1412.5106
Kistler M. D., Stanev T., Yüksel H., 2014, Phys. Rev. D, 90, 123006
Mannheim K., 1995, Astroparticle Physics, 3, 295
Margiotta A., 2014, NIMPA, 766, 83
Mücke A. et al., 2003, Astroparticle Physics, 18, 593
Murase K., Inoue Y., Dermer C. D., 2014, Phys. Rev. D, 90, 023007
Padovani P., Giommi P., 1995, ApJ, 444, 567
Padovani P., Resconi E., 2014, MNRAS, 443, 474 (PR14)
Padovani P., Giommi P., 2015, MNRAS, 446, L41

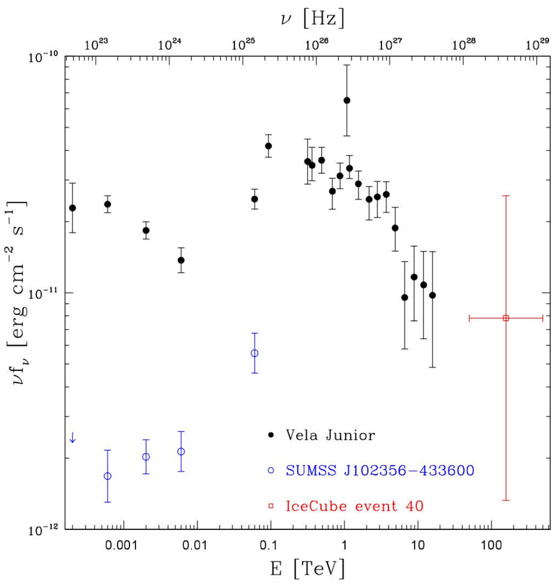

Figure A1. γ-ray SEDs of two sources in the error circle of ID 40, namely: the Vela Junior SNR (black filled circles: The Fermi-LAT Collaboration 2015; Acero et al. 2015; Aharonian et al. 2007) and the HBL SUMSS J102356−433600 (open blue circles: Acero et al. 2015). The (red) open square represents the neutrino flux for the corresponding IceCube event; error bars as described in the caption of Fig. 4.

Padovani P., Petropoulou M., Giommi P., Resconi E., 2015, MNRAS, 452, 1877
Petropoulou M., Dimitrakoudis S., Padovani P., Mastichiadis A., Resconi E., 2015, MNRAS, 448, 2412
Schoenen S., Raedel L., 2015, Astron. Telegram, 7856, 1
Urry C. M., Padovani P., 1995, PASP, 107, 803
Tavecchio F., Ghisellini G., 2015, MNRAS, 451, 1502

APPENDIX A: GALACTIC SOURCES

The case for Galactic sources is more complex: a randomisation of the γ-ray positions is, in fact, in this case meaningless because one loses the information on the concentration of sources at small b_{II} ($\lesssim 2^\circ$) values. And, as discussed in Sec. 3, the randomisation of the IceCube right ascensions would result in a biased test statistics.

Nevertheless, based on the results of PR14, who had singled out two PWN as most probable counterparts to two IceCube neutrinos, we list in Table A1 the main properties of all Galactic 2FHL matches with $|b_{II}| \leq 10^\circ$, defined as non blazar sources excluding the unclassified ones. The table gives the IceCube ID, the 2FHL name, the common name, the 2FHL coordinates, the offset between the reconstructed position of the IceCube event and the blazar one, the 2FHL > 50 GeV flux, and the class. Note that 3/5 events are also listed in Tab. 2.

We note that all sources in Table A1 associated with the IceCube events discovered in the first three years of data had been already considered by PR14. Based on the data

Table A1. 2FHL Galactic sources in one median angular error radius around the positions of the IceCube events. The counterparts of the most probable matches are indicated in boldface.

ID	2FHL name	Common name	RA (2000)	Dec (2000)	offset deg	f (E > 50 GeV) 10^{-10} ph/cm^2/s	Class[a]	Comments
14	J1745.7−2900	SgrA*	17 45 42.4	−29 00 37	1.3	1.070	Ext. Gal.	positional match (PR14)
	J1801.7−2358	HESS J1800−240B	18 01 47.0	−23 58 39	5.9	0.569	SNR	most probable match?
	J1801.3−2326	W28	18 01 21.5	−23 26 24	6.2	1.280	SNR	positional match (PR14)
	J1805.6−2136	W30	18 05 38.4	−21 36 36	8.2	2.680	Ext. Gal.	positional match (PR14)
33	J1911.0+0905	W49B	19 11 01.4	+09 05 13	4.9	0.462	SNR	positional match (PR14)
	J1923.2+1408	W51	19 23 16.8	+14 08 24	6.6	0.897	SNR	positional match (PR14)
35	J1303.4−6312	HESS J1303−631	13 02 59.9	−63 12 00	9.8	0.910	PWN	positional match (PR14)
	J1355.1−6420	HESS J1356−645	13 55 07.1	−64 20 24	8.5	0.833	PWN	positional match (PR14)
	J1443.2−6221	RCW86	14 43 16.8	−62 21 00	9.1	0.683	SNR	positional match (PR14)
	J1419.3−6047	HESS J1420−607	14 19 19.1	−60 48 00	6.0	1.650	PWN	positional match (PR14)
	J1514.0−5915	HESS J1514−591	15 14 02.3	−59 15 36	11.3	1.490	PWN	positional match (PR14)
40	J0833.1−4511	Vela Pulsar	08 33 09.5	−45 11 24	11.2	1.030	PWN	positional match
	J0835.3−4511	PSR J0835-4510	08 35 23.7	−45 11 09	10.8	0.274	Radio Pulsar	positional match
	J0852.8−4631	**Vela Junior**	08 52 48.0	−46 31 12	7.5	5.030	SNR	most probable match
52	J1615.3−5146	**HESS J1614−518**	16 15 19.2	−51 46 48	5.8	2.340	Ext. Gal.	most probable match
	J1616.2−5054	HESS J1616−508	16 16 14.4	−50 54 36	6.2	1.860	PWN	most probable match?
	J1633.5−4746	HESS J1632−478	16 33 00.0	−47 46 12	6.9	2.580	PWN	most probable match?
	J1640.6−4632	HESS J1641−463	16 40 41.7	−46 33 00	7.6	1.030	SNR	positional match

[a] SNR: supernova remnant; PWN: pulsar wind nebula; ext. Gal.: extended Galactic source

available now and the revised neutrino fluxes (see Section 2.1), we confirm the classification made by PR14 for all but one source: HESS J1800−240B was considered a positional match but we now believe it *could* be a most probable match. We note that none of the two PWN in Table 4 of PR14, namely HESS J1809−193 (connected to IceCube event 14) and MGRO J1980+06 (related to IceCube event 33) are in Table A1. This could be due to their relatively steep γ-ray spectra. Based on Figs. 6 and 7 of PR14 we still consider these two sources to be most probable matches.

The SEDs of the last seven 2FHL sources in Table A1, associated with the fourth year of IceCube data, were studied ex-novo. Of the first three, associated with ID 40, Vela Junior is without doubt a most probable match. Its SED is shown in Fig. A1, together with that of the HBL SUMSS J102356−433600. It turns out that the Galactic source is a better candidate. Of the last four 2FHL sources, all associated with ID 52, only the last one is a simple positional match, while none of the other three can be dismissed on the basis of the "energetic" diagnostic. Their SEDs are shown in Fig. A2. HESS J1614−518 might be more favoured simply because its SED does not drop at high energies like the other two sources for lack of data.

The detailed SED study of the 2FHL candidates suggests then that two IceCube events (40 and 52) have most probable Galactic 2FHL counterparts (with the respective counterparts highlighted in boldface), with one more (14) having a possible counterpart.

This paper has been typeset from a TEX/LATEX file prepared by the author.

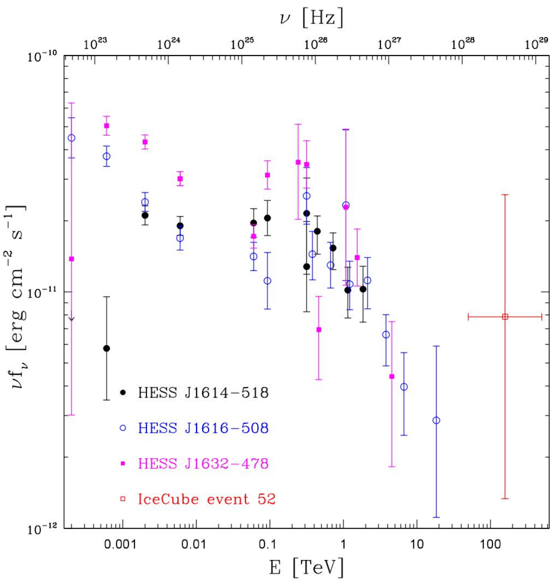

Figure A2. γ-ray SEDs of three sources in the error circle of ID 52, namely: the extended Galactic source HESS J1614−518 (black filled circles: The Fermi-LAT Collaboration 2015; Acero et al. 2015, 2013), the PWN HESS J1616−508 (blue open circles: The Fermi-LAT Collaboration 2015; Acero et al. 2015; Aharonian et al. 2006), and the PWN HESS J1632−478 (magenta filled squares: The Fermi-LAT Collaboration 2015; Acero et al. 2015; Aharonian et al. 2006). The (red) open square represents the neutrino flux for the corresponding IceCube event; error bars as described in the caption of Fig. 4.

Astronomy & Astrophysics manuscript no. Gamma-Ray-LSP-Blazars
April 30, 2018

The γ-ray emitting region in low synchrotron peak blazars

Testing self-synchrotron Compton and external Compton scenarios

B. Arsioli[1,2,4] and Y-L. Chang[1,3,5]

[1] Science Data Center della Agencia Spaziale Italiana, SSDC - ASI, Rome, Italy
[2] Instituto de Física Gleb Wataghin, UNICAMP, Rua Sérgio B. de Holanda 777, 13083-859 Campinas, Brazil
[3] Sapienza Università di Roma, Dipartimento di Fisica, Piazzale Aldo Moro 5, I-00185 Roma, Italy
[4] ICRANet-Rio, CBPF, Rua Dr. Xavier Sigaud 150, 22290-180 Rio de Janeiro, Brazil
[5] ICRANet, P.zza della Repubblica 10,65122, Pescara, Italy

e-mail: bruno.arsioli@ssdc.asi.it, arsioli@ifi.unicamp.br e-mail: yuling.chang@ssdc.asi.it

Preprint online version: April 30, 2018

ABSTRACT

Aims. From the early days in γ-ray astronomy, locating the origin of GeV emission within the core of an active galactic nucleus (AGN) persisted as an open question; the problem is to discern between near- and far-site scenarios with respect to the distance from the super massive central engine. We investigate this question under the light of a complete sample of low synchrotron peak (LSP) blazars which is fully characterized along many decades in the electromagnetic spectrum, from radio up to tens of GeV. We consider the high-energy emission from bright radio blazars and test for synchrotron self-Compton (SSC) and external Compton (EC) scenarios in the framework of localizing the γ-ray emission sites. Given that the inverse Compton (IC) process under the EC regime is driven by the abundance of external seed photons, these photons could be mainly ultraviolet (UV) to X-rays coming from the accretion disk region and the broad-line region (BLR), therefore close to the jet launch base; or infrared (IR) seed photons from the dust torus and molecular cloud spine-sheath, therefore far from jet launch base. We investigate both scenarios, and try to reveal the physics behind the production of γ-ray radiation in AGNs which is crucial in order to locate the production site.

Methods. Based on a complete sample of 104 radio-selected LSP blazars, with 37 GHz flux density higher than 1 Jy, we study broadband population properties associated with the nonthermal jet emission process, and test the capability of SSC and EC scenarios to explain the overall spectral energy distribution (SED) features. We use SEDs well characterized from radio to γ rays, considering all currently available data. The enhanced available information from recent works allows us to refine the study of Syn to IC peak correlations, which points to a particular γ-ray emission site.

Results. We show that SSC alone is not enough to account for the observed SEDs. Our analysis favors an EC scenario under the Thomson scattering regime, with a dominant IR external photon field. Therefore, the far-site (i.e., far from the jet launch) is probably the most reasonable scenario to account for the population properties of bright LSP blazars in cases modeled with a pure leptonic component. We calculate the photon energy density associated with the external field at the jet comoving frame to be $U'_{ext} = 1.69 \times 10^{-2}$ erg/cm^3, finding good agreement to other correlated works.

Key words. galaxies: active – Radiation mechanisms: nonthermal – Gamma rays: galaxies

1. Introduction

Locating the emission site where MeV-TeV photons are produced in active galactic nuclei (AGNs) has been as an open question since the early days of γ-ray astronomy (Vovk & Neronov 2013; Neronov et al. 2015); one of major limitations is the angular resolution of the current generation of satellite-borne MeV-GeV and ground-based GeV-TeV observatories. Currently, we do not have enough resolution to distinguish γ-ray substructures within the jets, even for close-by objects. The main class of AGNs detected from MeV up to tens of TeV are called blazars, and usually show extreme properties like high-power output together with short timescale variability (Aharonian et al. 2007), which are the main focus of studies trying to localize the γ-ray emission site.

In summary, blazars are a particular class of jetted AGNs corresponding to the very few cases where the jet is pointing close to our line of sight (Padovani et al. 2017). They are known to have a unique spectral energy distribution (SED) often characterized by the presence of two nonthermal bumps in the log(νf_ν) versus log(ν) plane, extending along the whole electromagnetic window, from radio up to TeV γ rays. Blazars are also known for their rapid and high-amplitude spectral variability. Usually, the observed radiation shows extreme properties owing to the relativistic nature of the jets, which result in amplification effects. Those objects are relatively rare. Only $\sim$ 4000 cases have been optically identified since the latest blazar surveys, 5BZcat Massaro et al. (2015) and 2WHSP Chang et al. (2017), and have been extensively studied by means of a multifrequency approach, which has cumulated impressive dedicated databases at radio, microwave, infrared (IR), optical, ultraviolet (UV), X-ray, and γ rays.

According to the standard picture (e.g., Giommi et al. 2012a), the first peak in the log(νf_ν) versus log(ν) plane is associated with the emission of synchrotron (Syn) radiation owing to relativistic electrons moving through the jet's collimated magnetic field. The second peak is usually described as a result of inverse Compton (IC) scattering of low-energy photons to the highest energies by the same relativistic electron population that generates the Syn photons (synchrotron self-Compton model, SSC). The seed photons undergoing IC scattering can also come from outside regions (external Compton models, EC), like the accretion disk, the broad-line region (BLR), the dust torus, and even from illuminated molecular clouds, adding extra ingredients for modeling the observed SED.

Since the peak-power associated with the synchrotron bump tell us at which frequency ($\nu_{\rm peak}^{\rm Syn}$) most of the AGN electromagnetic power is being released, the parameter $\log(\nu_{peak}^{Syn})$ has been extensively used to classify blazars. Following discussion from Padovani & Giommi (1995) and Abdo et al. (2010a), objects with $\log(\nu_{\rm peak}^{\rm Syn}) < 14.5$, between 14.5 and 15.0, and > 15.0 [Hz] are respectively called low, intermediate, and high synchrotron peak (LSP, ISP, HSP) blazars. Some blazars whose Syn peaks reach the hard X-ray band are called extreme HSP (EHSP) blazars; moreover, evidence for Syn peak at the MeV–GeV range are still under debate, with several cases of EHSP blazars already being studied, for example in Chang et al. (2017); Kaufmann et al. (2011); Tavecchio et al. (2011); Tanaka et al. (2014) and Arsioli et al. (2018). EHSP blazars are not easy to identify as they are typically faint in radio and hardly detected by current radio sky surveys; moreover, there is increasing attention from the physics community given the possibility that blazars might be associated with astrophysical neutrinos (Padovani et al. 2016, 2018) and with ultra-high-energy cosmic rays (Resconi et al. 2017). Given the broad context in which blazars play an important role for the future of astroparticle physics, studying the production site of γ rays for the subsample of LSP blazars may bring relevant elements for the understanding of high and very high-energy mechanisms in action for the entire blazar population.

From current leptonic-based models, synchrotron photons and external thermal photons interacting with relativistic particles in the jet may be scattered to much higher energies, characterizing the inverse Compton (IC) process. A simple treatment can show how this process works. In the electron frame l', the synchrotron photons moving along with electrons will appear to have much lower energy, $h\nu_1' \ll m_e c^2$. In the laboratory (astrophysical source) frame l, the relativistic Doppler shift formula is given by

$$\mathrm{h}\nu_1' = \gamma \mathrm{h}\nu_1 \big(1 + \beta \cos\theta\big)\,, \tag{1}$$

where θ is the angle between the propagation direction of photons and electrons, $\gamma = 1/\sqrt{1-\beta^2}$ represents the Lorentz factor for the relativistic electron[1], and $\beta = v/c$. In the electron comoving frame l', this angle seems much smaller $\sin\theta' = \frac{\sin\theta}{\gamma(1+\beta\cos\theta)}$ so that all photons will appear to approach in head-on collision, and Eq. 1 reduces to $\mathrm{h}\nu_1' \approx \gamma \mathrm{h}\nu_1 \big(1+\beta\big)$, since $\theta \ll 1$. Also, in l' frame the photon energy seems much lower ($\mathrm{h}\nu' \ll \mathrm{m_e c^2}$) and the interaction can be treated as elastic Thomson scattering. Therefore, in l' frame the photon energy does not change much during the collision $\mathrm{E}_1' \approx \mathrm{E}_2'$ and $\nu_1' \approx \nu_2'$. In the AGN source frame l, however, photons are scattered along the direction of the relativistic electrons with $\nu_2 = \delta\nu_2' \approx \delta\nu_1'$, where $\delta^{-1} = \gamma\big(1+\beta\cos\theta\big)$ is the beaming factor, which reduces to $\delta^{-1} \approx \gamma\big(1+\beta\big)$ so that we have $\nu_2 = \nu_1\big[\gamma\big(1+\beta\big)\big]^2$. In the relativistic limit, $\beta \approx 1$, and the frequency associated with the upscattered photon follows as $\nu_2 \approx 4\,\gamma^2\,\nu_1$.

Therefore, an important conclusion is that photons scattered by relativistic electrons gain energy with a γ^2 factor: $\mathrm{E}_2 \propto \gamma^2 \mathrm{E}_1$. Naturally, the luminosity $\mathrm{L_{IC}}$ of the inverse Compton component depends on the photon density n_{ph} available for up-scattering via the IC process. In the SSC model only photons generated by the synchrotron process itself may build up the available n_{ph}. In addition, the external contribution from thermal emission regions can be significant sources of low-energy photons, characterizing the EC models. In both cases we have $\mathrm{L_{IC}} \propto \mathrm{n_{ph}}\gamma^2\mathrm{E}_1$ (Rybicki & Lightman 1986).

As is known, the synchrotron emission can extend up to hard X-rays, and in some extreme cases can even peak in this region. When the photon energy reaches a level that is similar to the electron mass, the condition $h\nu' \ll mc^2$ is not valid in the electron's frame, and Klein–Nishina effect (described by applying quantum electrodynamics to the scattering process) acts to reduce the electron-photon cross section with respect to the case of classical Thomson scattering (σ_T). Therefore, the IC scattering might becomes less and less efficient for seed photons with the highest energies (e.g., $\sigma_{\rm KN}/\sigma_{\rm T} \approx 0.5$ at $\mathrm{E} = 300\,\mathrm{KeV}$), which influence the spectral energy distribution of blazars at very high energies $\mathrm{E} > 100\,\mathrm{GeV}$ and manifest as a strong break (steepening) in γ-ray emitted power. In fact, if the electron energy distribution follows $\mathrm{N_{(E)}} = \mathrm{kE^{-p}}$, the scattered IC spectrum will also be a power law with spectral index $\alpha = (1-\mathrm{p})/2$.

Although a pure leptonic IC process is well established as the mechanism that produce the second bump observed on the blazar's SED, there is still open debate on alternative scenarios like the ones considering hadronic plus leptonic components (Böttcher et al. 2013; Cerruti et al. 2015, 2017b). In addition, the location and AGN environment dependences associated with the production of γ rays are still unclear. Probing such information demands a set of multifrequency measurements together with model-dependent tests, as we discuss below. Given the many identified γ-ray sources, there is still a great deal of room to explore issues like variability (comparing the behavior at low and high energies) and probing the far end of SED at $\mathrm{E} > 10\,\mathrm{TeV}$ with the upcoming generation of Cherenkov telescope arrays (CTA, Bernlhr et al. 2013).

In this work we focus on modeling low synchrotron peak (LSP) blazars making use of a complete sample of radio-loud blazar AGNs described in details by Planck Collaboration et al. (2011). It consists of 104 northern and equatorial sources with declination greater then -10^o, flux density at 37 GHz exceeding 1 Jy as measured with the Metsähovi radio telescope. All 104 sources have been detected between 30 GHz and 857 GHz by the *Planck* mission (Planck Catalogue of Compact Sources PCCS, Planck Collaboration et al. 2014a) most of which were previously known. With the addition of PCCS data, many radio-bright blazars gained a better multifrequency description for their

[1] This is the same as Γ, which is commonly used as a representation for the Lorentz factor associated with the bulk motion of relativistic jet-plasma.

synchrotron (Syn) component, and here are referred to as radio-Planck sources.

It is important to note that the vast majority of these sources (103) are legitimate LSP blazars (two cases at the border line, ν_{peak} $\approx 10^{14.5}$ Hz, BZQJ 0010+1058 and BZBJ 0050-0929); only one bright HSP blazar (BZBJ 1653+3945) was removed or properly highlighted during the preparation of following studies. Out of those 104 sources, 83 have a confirmed γ-ray counterpart in at least one of the *Fermi*-LAT (Atwood et al. 2009) catalogs 1FGL, 2FGL, and 3FGL (Abdo et al. 2010b; Ackermann et al. 2011; Acero et al. 2015) and another 16 had their γ-ray spectrum recently described by Arsioli & Polenta (2018), who search for new γ-ray emitting blazars following the same approach as Arsioli & Chang (2017). We note that their study was based on a dedicated *Fermi*-LAT analysis showing that many of the previously γ-ray undetected LSPs are actually detectable when integrating over 7.5 years of observations.

The online SED builder tool[2] was used in previous work to compile and fit all available multifrequency data (Arsioli & Polenta 2018) that we now use for current analysis. This included relevant microwave flux measurements coming from the Planck mission, the new γ-ray data-points from the *Fermi*-LAT dedicated analysis, and extra UV to X-ray observations from Swift. From there, fitting parameters were extracted to describe the observed peak-frequency $\log(\nu_{peak})$ and peak-brightness $\log(\nu f_{\nu})$ for both Syn and IC bumps. We now use those measurements to gain further insight on the population properties of LSP blazars, calculating parameters like the Lorentz factor associated with relativistic electrons in the jet, the product Bδ (δ stands for the beaming factor), the luminosity associated with Syn and IC peaks, and the external photon field energy density (U_{ext}) calculated when assuming an EC models.

2. LSPs jets and nonthermal emission mechanism

As argued in the literature (Paliya et al. 2017; Lister et al. 2015) LSP blazars with $\nu_{\rm peak} < 10^{13.4}$Hz may show a typical inverse Compton peak below 0.1 GeV, and thus out of the *Fermi*-LAT sensitivity bandwidth at 0.1–500 GeV. In the case of LSP blazars, we might probe only the very end of the IC component, and this is why a considerable percentage of LSPs ($\sim$20%) had no counterpart in the latest *Fermi*-LAT catalogs (1FGL, 2FGL, and 3FGL). The relation between Syn and IC peaks is explored in Abdo et al. (2010a); Gao et al. (2011); Zhang et al. (2012), with Şentürk et al. (2013) showing a correlation between peak frequencies, since ν^{IC}_{peak} is decreasing with respect to HBL-LBL-FSRQ. There is a clear connection between the distributions of $\log(\nu^{\rm Syn}_{\rm peak})$ and $\log(\nu^{\rm IC}_{\rm peak})$ when a complete sample of LSPs is considered, such that a characteristic peak ratio (PR = $\log(\nu^{\rm IC}_{\rm peak}/\nu^{\rm Syn}_{\rm peak})$ is very suitable for describing the average relation between their distributions (PR $\approx$ 8.6, Arsioli & Polenta 2018). However, when taken case by case, they show that an intrinsic and direct relation between peak frequencies is nontrivial and most probably highly dependent on its SSC or EC dominance nature and variability.

[2] The SED builder is an online tool dedicated to multifrequency data visualization, together with fitting routines useful for extracting refined scientific products. Provided by the Space Science Data Center (SSDC): http://www.ssdc.asi.it

Intrinsic jet properties like the beaming factor (δ) and the dominant IC regime (either synchrotron self-Compton, SSC, or external Compton, EC) may in fact have a strong influence on the γ-ray variability, and also affect the *Fermi*-LAT detectability of a few radio-loud blazars. Lister et al. (2009) have shown that the γ-ray sources detected during the first three months of *Fermi*-LAT operations are on average the ones associated with the highest apparent jet speeds (based on radio measurements with the Very Large Baseline Array, VLBA) and therefore the most powerful accelerators with the highest δ values.

In a simple SSC scenario (Maraschi et al. 1992; Marscher & Travis 1996) the intensity boosting factor scales as $\delta^{3+\alpha}$, where α is the spectral index given that the flux scales as $S_{\nu} \propto \nu^{-\alpha}$. When considering typical blazar SEDs in the S_{ν} versus ν plane, the spectrum tends to be flat at radio frequencies and steep in γ rays. As a consequence, the intensity boosting is more pronounced in γ rays than in the radio bands, and thus the γ-ray detection of faint sources is favored during flaring episodes.

Considering the mechanism involved for the IC scattering, additional photon fields could be present and even dominant with respect to synchrotron photons (Dermer 1995; Jones et al. 1974). For instance, the jet might interact with external photons produced by the accretion disk, reflections, and IR thermal emission from surrounding gas clouds and dust torus. In such scenarios, a considerable amount of the γ-ray emission would be produced by Compton scattering of those external photons which is associated with an additional boosting factor $\delta^{1+\alpha}$ enhancing the IC intensity.

Given that nearly all radio-Planck sources are now well described in γ rays, we study their population properties to probe the leading emission mechanism, either SSC or EC, looking for hints to locate the γ-ray emitting region in LSP blazars.

3. Comments on synchrotron self-Compton and external Compton scenarios

Identifying the dominant IC mechanism can help to locate the γ-ray emitting region and to better understand its underlying physics. If the IC emission is dominated by EC process and happens close to the black hole (0.1–1 pc distance, embedded in the BLR) it could explain the observed γ-ray short timescale variability of a few hours (Aharonian et al. 2007; Pittori et al. 2018). In this case, since optical-UV BLR photons would be available for up-scattering, there should be a strong correlation between γ-ray and optical-UV flares. However, an alternative scenario considers that the γ-ray emission originates farther from the black hole (BH) at distance $\gg$1 pc. In this case, an IR photon field generated by the molecular clouds and dust torus (through reprocessing radiation from the accretion disk, or even by illumination from the jet synchrotron emission itself) are possible dominant sources of seed photons for up-scattering to higher energies (Breiding et al. 2018).

Both SSC and EC scenarios with γ rays originating far from the BH (out of the BLR region) demands that the jet structure should be a very narrow opening ($\approx$0.8 pc scale) or have N substructures ($\approx 0.8/\sqrt{N}$ pc), as invoked by multicomponent scenarios, to reconcile with the short timescale variability observed in the GeV–TeV band (Agudo et al. 2011).

There are indeed plenty of arguments supporting the far-site emission. One is related to radio-mm observations with the Very Long Baseline Array (VLBA) which shows radio-mm variability (at a distance on the order of 12–14 pc from the BH, for the BL Lac AO 0235+164 and OJ 287, Agudo et al. 2011; Agudo et al. 2013) to be correlated in time with γ-ray flares, and therefore supposed to happen in the same site. If this is true, there remains the question of how all the power gets transferred so efficiently farther away from the BH to produce the VHE component we observe. In addition, BL Lacs are usually dominated by nonthermal emission along the whole spectrum, with no trace of disk or dust torus thermal component.

Agudo et al. (2013) has interpreted the far emission site for BL Lacs AO 0235+164 and OJ 287 in the framework of SSC scenario since no other evident photon field is present for up-scattering other then the nonthermal synchrotron photons. However, similar work from Ackermann et al. (2012) for the same object and flaring event (AO 0235+164, 2008) describes the IC component within an EC scenario, assuming the external photon field is dominate by IR photons from the surrounding dust torus, which are up-scattered to HE. An extra IR component could also be present and dominant as a consequence of illumination and sublimation of the molecular cloud (MC) torus in a spine-sheath geometry as described by Breiding et al. (2018) and MacDonald et al. (2015). We should not avoid mentioning several works, such as Nalewajko et al. (2014) and Neronov et al. (2015) in favor of a close-site emission at the vicinity of the AGN supermassive black hole.

Even though we do not have evidence of MC or dust torus thermal components in BL Lacs, we should note that the nonthermal jet synchrotron emission is beamed and dominant because our observer frame is watching a relativistic jet pointing close to our line of sight. Thermal components from the MC and dust torus could well be present, nevertheless swamped by the jet beamed emission. Given the relativistic nature of the jet, even a relatively faint photon field with energy density U_{ext} would be boosted in the jet's "$\prime$" reference frame $U'_{ext} \propto U_{ext}\Gamma^2$ (Ghisellini & Madau 1996). This could become much more relevant or even dominant with respect to the Syn photon field produced by the jet itself, and strongly depending on the Lorentz factor (Γ).

The discussion surrounding the γ-ray emitting region in AGNs is ample, and interpretations are always subject to multiple free parameters that can be fine-tuned for different scenarios. We try to contribute to that understanding by studying general properties of the radio-Planck sample as a fair representation of powerful LSP blazars.

4. Lorentz factor of jet's relativistic electrons

Assuming a homogeneous SSC to describe the blazar SED, high-energy photons are generated by the up-scattering of low-energy Syn photons due to their interaction with relativistic electrons from the jet. In this scenario, a single population of relativistic electrons is then responsible for the entire SED, resulting in a strong correlation between the Lorentz factor of the electrons $\gamma_{\rm peak}$ emitting at the peak of the Syn component, and the peak frequency from the Syn and IC components:

$$\gamma_{peak} \simeq \sqrt{3/4 \times \nu^{IC}_{peak}/\nu^{Syn}_{peak}} \quad (2)$$

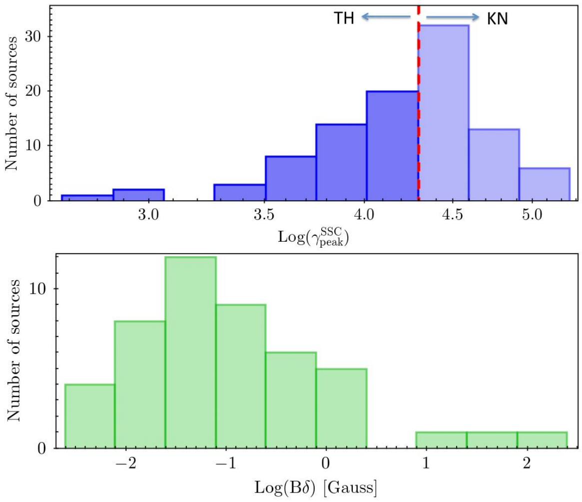

Fig. 1. Top: Distribution of Lorentz factor $\gamma^{\rm SSC}_{\rm peak}$ for electrons emitting in the peak of the Syn component (eq. 2). The red dashed line shows the limit for $\gamma^{\rm SSC}_{\rm peak}$ values where the transition from TH to KN scattering regime occurs. Bottom: Distribution of the Bδ parameter for LSP sources assuming a SSC model, and considering only sources with $\gamma^{\rm SSC}_{\rm peak} < 2\times10^4$ (under TH regime).

However, this trend is valid only under Thomson regime (TH) of the IC scattering, that is for $\gamma_{\rm peak} < 2\times10^4$, where the transition to the Klein–Nishina (KN) regime occurs. We use eq. 2 to calculate $\gamma^{\rm SSC}_{\rm peak}$ for all 99 sources with Syn and IC parameters available (Table 1), and plot its distribution in fig. 1, top. The histogram shows a Gaussian distribution with slightly negative skewness, and characterized by mean $\langle\log(\gamma^{\rm SSC}_{\rm peak})\rangle = 4.24\pm0.05$. Therefore, half of the sample have $\gamma^{\rm SSC}_{\rm peak} > 2\times10^4$, which is in tension with the fact that we are dealing with bright LSPs. Apart from a single HSP (Mrk501), all sources have $\nu^{\rm Syn}_{\rm peak} < 10^{14.6}$ Hz and the transition from TH to KN regime is only expected for $\nu^{\rm Syn}_{\rm peak} > 10^{14.7}$ Hz in the case of a single-zone SSC model.

In a simple single-zone self-synchrotron model, the $\nu^{\rm Syn}_{\rm peak}$ can be written in terms of jet magnetic field (B), beaming factor (δ), and peak Lorentz factor ($\gamma_{\rm peak}$). As discussed in Abdo et al. (2010a), assuming an emitting region of size R$\sim10^{15}$cm[3], and a log-parabola to describe the distribution of Lorentz factor: $n_{(\gamma)} = k\times10^{r\,\log(\gamma/\gamma_{\rm peak})^2}$ (curvature parameter r = 2.0, γ ranging from 10^2 to 6×10^5, and electron density of $\sim 1.0\,{\rm cm}^{-3}$; Tramacere et al. 2010), we have

$$\nu^{Syn}_{peak} = 3.2\times10^6(\gamma_{peak})^2 B\delta/(z+1)\ , \quad (3)$$

which is valid up to $\nu^{\rm Syn}_{\rm peak} \approx 10^{14.7}$ Hz, where the transition to KN scattering regime occurs. Following the discussion from Abdo et al. (2010a), $\gamma^{\rm SSC}_{\rm peak} \approx \gamma_{\rm peak}$ under TH regime, therefore we use eq. 3 to calculate the Bδ parameter as Bδ =

[3] Given that $R < \frac{c\Delta t\delta}{(1+z)}$, assuming z on the order of 1.0, and $\delta \sim 10-20$, with characteristic variability timescale of a few days ($\sim5\times10^5$ s), jet length is on the order of $R \approx 10^{15}$ cm.

$\nu_{\rm peak}^{\rm Syn}(1+{\rm z})/(3.2\times10^6\times(\gamma_{\rm peak}^{\rm SSC})^2)$, only for the subsample of 48 sources having $\gamma_{\rm peak}^{\rm SSC} < 2\times10^4$. These 48 sources are the ones under TH regime if we assume a single-zone SSC model. We plot the Bδ distribution in Fig. 1 (bottom) which peaks at $\langle B\delta\rangle$=$0.066^{+0.020}_{-0.015}$ gauss. This is also in tension with the expected value for the Bδ parameter for blazars, which is usually assumed to be $\langle {\rm B}\delta\rangle_{\rm expected}$ = 10 gauss, with beaming factor δ on the order of $\sim$20 (ranging from 5 to 35 for LSP blazars, Kang et al. 2014) and B on the order of $\sim$0.5 gauss (ranging from 0.3 to 1.5 gauss, Tramacere et al. 2010). Most probably, the γ^{SSC}_{peak} values that we have calculated from eq. 2 are highly overestimated, leading to low Bδ values. Therefore a simple single-zone SSC model seems insufficient to account for the overall SEDs observed for LSP blazars.

4.1. Tramacere plane: log(γ^{SSC}_{peak}) versus log(ν^{Syn}_{peak})

Tramacere et al. (2010) proposes the use of the log(γ^{SSC}_{peak}) versus log(ν^{Syn}_{peak}) plane to better understand the dominant emission mechanism in blazars (either SSC or EC) for individual sources and populations, as also mention by Abdo et al. (2010a). In fig. 2 we show the radio-Planck sources in this plane, with $\gamma_{\rm peak}^{\rm SSC}$ values estimated using eq. 2, directly from the Syn and IC peak-power parameters measured from fitting the SEDs case by case (Table 1).

In this plane, the blue dashed line (extracted from Tramacere et al. 2010, their Fig. 3) represents a SSC numerical model which incorporates the TH to KN transition, and therefore corrects for the decreasing e$^-$+γ cross-section which reduces the efficiency of IC scattering and affects the cooling time of relativistic electrons in the jet. The black dashed line represents the synchrotron emission, simply plotting eq. 3 for the SSC model with no correction on the TH to KN transition (assuming R$\sim$10^{15}cm and Bδ/(1+z)=1.3 to match with the SSC-TH estimate from the numerical modeling). The purple dashed line (Tramacere et al. (2010), also from their Fig. 3) represents a numerical model for the EC regime assuming benchmark values for the jet parameters: R$\sim$10^{15}cm, a log-parabola to describe the distribution of Lorentz factor (γ) of the jet's relativistic electron, assuming a dominant UV external photon field produced by the accretion disk (modeled as a blackbody with T profile having innermost T of $\approx$10^5 K), and assuming an extra component reflected by the BLR toward the jet, with efficiency τ=10%. Those models are described and applied in a series of works: Tramacere & Tosti (2003); Massaro et al. (2006); Tramacere (2007); Tramacere et al. (2009).

We separate sources according to their classification in the 5BZcat catalog (BZBs, BZQs, Uncertain types, Massaro et al. (2015)), and also mark cases with the highest Compton Dominance (CD) values (CD$>$6.0 to select the top 10% of sources). Most sources cluster in the region above the blue dashed line, meaning they are mainly out of the SSC domain. This region is characteristic of blazars where there might be an external photon field ranging from IR to UV playing an important role.

In conclusion, an EC mechanism under the TH scattering regime should be more suitable to study those sources. The Tramacere plane then gave us an overview on the dominant IC mechanism in play for bright LSP blazars, and also

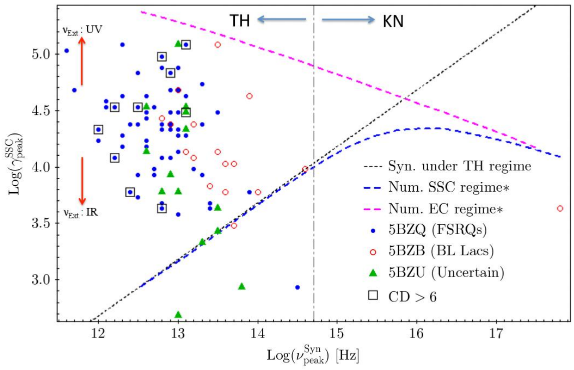

Fig. 2. The log($\gamma_{\rm peak}^{\rm SSC}$) vs. log($\nu_{\rm peak}^{\rm Syn}$) plane. Sources are divided according to their classification in the 5BZcat: blue circles for 5BZQs (FSRQ), red empty circles for 5BZBs (BL Lacs), and green triangles for 5BZUs (unclassified). Blue and purple dashed lines correspond to γ^{SSC}_{peak} calculated from numerical simulations considering SSC and EC scenarios incorporating the transition from TH and KN regimes. The vertical dot-dashed line indicates the ν^{Syn} domains for which TH and KN regimes apply. The black dashed line represents eq. 3 using Bδ/(1+z)$\approx$1.3 gauss, with no correction for the TH to KN transition.

shows that there is no significant differences (data clustering) with respect to the γ^{SSC}_{peak} parameter depending on blazar type or Compton dominance.

4.2. Assuming a dominant EC scenario

If we assume that a source can be described via the EC model under the TH regime, the frequency associated with the IC peak ($\nu_{\rm peak}^{\rm EC}$) should be well described by (Abdo et al. 2010a)

$$\frac{\nu_{\rm peak}^{\rm EC}}{\nu_{\rm peak}^{\rm ext}\Gamma} = \frac{4}{3}(\gamma_{\rm peak})^2\frac{\delta}{(1+{\rm z})}, \quad (4)$$

where γ_{peak} is the Lorentz factor associated with jet electrons emitting in the peak of the synchrotron component (see eq. 2) and $\nu_{\rm peak}^{\rm ext}$ is the peak frequency associated with the external photon field in the rest frame from the emitting zone (either accretion disk, BLR, MC, or dust torus). When $\nu_{\rm peak}^{\rm ext}$ is multiplied by the bulk Lorentz factor Γ associated with the relativistic outflow, it transforms this frequency to the jet rest frame. We use the notation $\gamma_{\rm peak}^{\rm EC}$ to represent $\gamma_{\rm peak}$ when assuming an EC scenario.

We use eq. 3 to calculate $\gamma_{\rm peak}^{\rm EC}$ for all sources with available IC data, considering $\nu_{\rm peak}^{\rm IC}$ ($\equiv \nu_{\rm peak}^{\rm EC}$) as reported in Table 1. To perform this calculation we assume the Doppler (beaming) factor $\delta = [\Gamma(1-\beta\cos\theta)]^{-1} \approx \Gamma$ (Dermer 2015) valid for sources observed close to the line of sight, $\theta < 5°$.

We assume $\langle\delta\rangle\approx 20\pm2$, following Kang et al. (2014), which presents a list of δ parameter for 15 bright LSPs, as estimated from the model constrained by SED fitting[4]

[4] The adopted model considers an EC leptonic scenario, assuming external photon fields from BLR (UV), molecular, and dust torus (IR), with the last resulting in better fittings.

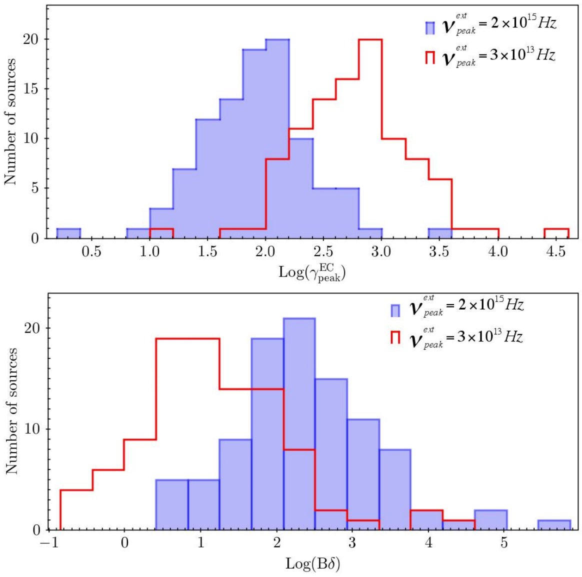

Fig. 3. Top: Distribution of $\log(\gamma^{\rm EC}_{\rm peak})$ for the radio-Planck sample based on eq. 4 when assuming $\Gamma = 20$, and for two different external photon fields: dust torus photons peaking at IR $\nu^{\rm ext}_{\rm IR} = 3\times10^{13}$Hz (in red); near-UV photons from the BLR region, peaking close to Ly$_\alpha$, $\nu^{\rm ext}_{\rm UV} = 2\times10^{15}$Hz (full indigo bars). Bottom: Corresponding distribution of log(Bδ) calculated from eq. 3 for $\gamma_{\rm peak} = \gamma^{\rm EC}_{\rm peak}$, and considering ν^{Syn}_{peak} and ν^{IC}_{peak} from Table 1.

and in agreement with estimates from radio variability and brightness temperature (confirming early measurements made by Jorstad et al. (2005)). Also, Saikia et al. (2016) introduced a new independent method based on the optical fundamental plane of black hole activity[5] to estimate the Γ distribution, showing a valid range from 1 to 40, with $N_{(\Gamma)} \propto \Gamma^{-2.1\pm0.4}$, or an even more restrictive range with Γ between 15 and 30 (Nalewajko et al. 2014), as deduced from a study of γ-ray flares, with a multifrequency approach and testing EC scenarios.

There are two different setups that are important to consider, and that are related to the photon-frequency (ν) associated with the external photon field. The first one assumes that seed photons originate mainly from the dust torus. This view is supported by Cleary et al. (2007) who deduced from observations with *Spitzer* that the torus may heat up to 150–200 K by absorbing accretion disk radiation and emitting like a blackbody, and therefore with dominant IR emission peaking at $\nu^{\rm ext}_{\rm IR} = 3\times10^{13}$Hz. There is a similar scenario where the illumination and sublimation of molecular clouds, owing to synchrotron jet emission in a spine-sheath geometry (Breiding et al. 2018), could also play important role in producing a dominant IR photon field. In the second setup the external photon field originates from the BLR and accretion disk regions, with dominant emission peaking close to Ly$_\alpha$ in near UV, at $\nu^{\rm ext}_{\rm UV} = 2.0\times10^{15}$Hz (Tavecchio & Ghisellini 2008; Ghisellini & Tavecchio 2008).

In Fig. 3 (top) we plot the distribution of $\log(\gamma^{\rm EC}_{\rm p})$ for the radio-Planck sample, which leads us to the following conclusion. When using an EC model with external photon field ranging from UV to IR, and assuming $\langle\delta\rangle \approx \langle\Gamma\rangle = 20$, almost all sources are under the TH scattering regime. This is in agreement with expectations since the radio-Planck sample is dominated by LSP blazars, $\nu^{\rm Syn}_{\rm peak} < 10^{14}$ Hz. We find $\langle\log(\gamma^{\rm EC}_{\rm peak})\rangle$ ranging from 2.80±0.05 to 1.93±0.05 depending on the external photon field, UV and IR, respectively. Compared to γ^{SSC}_{peak} values calculated when assuming a simple SSC model (Fig. 1), we see that γ^{SSC}_{peak} is highly overestimated by almost two orders of magnitude in any scenario.

As mention previously, eq. 3 is only valid under the TH regime. Therefore, we recalculate the Bδ parameter according to $B\delta = \nu^{\rm Syn}_{\rm peak}(1+z)/(3.2\times10^6\times(\gamma^{\rm EC}_{\rm peak})^2)$, which now applies to the subsample of 98 sources having $\gamma^{\rm EC}_{\rm peak} < 2\times10^4$. We plot the B$\delta$ distribution in Fig. 3 (bottom), which peaks at $\langle\log(B\delta)\rangle = 2.72\pm0.09$ for the UV external field and at $\langle\log(B\delta)\rangle = 0.99\pm0.09$ for the IR external field. Therefore, assuming $\langle\delta\rangle = 20$ we get an estimate for the magnetic field in the jet $\langle B_{\rm UV}\rangle = 26.2$ gauss, and $\langle B_{\rm IR}\rangle = 0.48$ gauss. In particular, the estimate for $\langle B_{\rm UV}\rangle$ is not consistent with the constraints from SED fitting when assuming an emission site within the BLR (Cao & Wang 2013), owing to underestimated $\gamma^{\rm EC}_{\rm peak}$ values. However, the estimate for $\langle B_{\rm IR}\rangle$ is in good agreement with expectations from SED fitting from Kang et al. (2014) for γ-ray emission out of the BLR region (far-site) at a distance $\gg 0.1$ pc from the BH.

This suggests that an IR external photon field might be the dominant driver in the EC scenario for the population of bright LSP blazars, also in agreement with findings from Abdo et al. (2015). One important aspect to note is that the energy density (U) from external photon fields are boosted in the jet's comoving frame "$\prime$" according to $U'_{\rm ext} = U_{\rm ext}\Gamma^2$ (Sikora et al. 2009), therefore strongly dependent on the jet's bulk Lorentz factor Γ and accounting for $U'_{\rm ext}$ being dominant with respect to the self-synchrotron photon field.

If we assume an UV external photon field from the BLR region, forcing the magnetic field to $0.5 < B < 2.0$ gauss as expected from SED fitting derived from Cao & Wang (2013), it may lead to highly overestimated γ^{EC}_{peak} values, as also reported by Abdo et al. (2010a). In fact, when relaxing the value associated with $\langle\delta\rangle$, it is possible to adjust UV dominant scenarios for some individual sources, and that is a known degeneracy associated with the Bδ parameter.

4.3. Syn versus IC luminosity correlation

We have calculated the Syn and IC peak luminosities based on the flux density νf_ν [ergs/cm^2/s] measurements listed in Table 1. Luminosity is given by

$$L = \frac{4\pi d_L^2\ \nu f_\nu}{(1+z)^{1-\alpha}} \equiv 4\pi d_L^2\ \nu f_\nu^{\rm peak}, \qquad (5)$$

where d_L is the luminosity distance calculated based on ΛCDM cosmology (with H_0=67.3 Km/s/Mpc, ω_Λ=0.685,

[5] The method (Saikia et al. 2015) is based on the fundamental plane of black hole activity in X-rays. The proposed "optical fundamental plane of BH activity" relies on the OIII forbidden-line intensity (independent of beaming and viewing angle) as a tracer for the accretion rate instead of the X-ray flux, which is heavily contaminated by a nonthermal jet component in blazars.

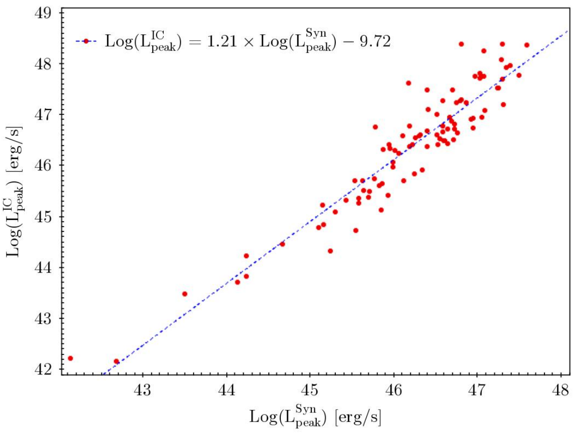

Fig. 4. Syn vs. IC luminosity plane showing a tight correlation that extends for seven decades in luminosity. Blue dashed line is a linear fit to the data.

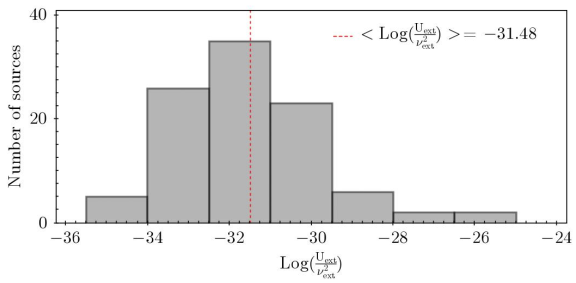

Fig. 5. Distribution for the $\log(U_{ext}/\nu^2_{ext})$ parameter, as derived from eq. 8 when considering measurements from Table 1. The mean value associated with $\log(U_{ext}/\nu^2_{ext})$ is highlighted with dashed red line.

ω_K=0, and ω_M=0.315, Planck Collaboration et al. (2014b)). Given that we calculate the luminosity at the Syn and IC peaks measured from the SEDs in the ν versus νf_ν plane, the photon spectral index is $\Gamma^{IC,Syn}_{peak} = 2.0$; therefore, $\alpha = (\Gamma - 1) = 1.0$, and the K-correction term simplifies to $(1 + z)^{1-\alpha} = 1.0$. As seen from Fig. 4 the scatter in the $\log(L_{Syn})$ versus $\log(L_{IC})$ plane is very tight, holding along seven decades in luminosity, with a strong Pearson correlation coefficient of 0.94. The correlation is described by

$$\log(L^{IC}_{peak}) = 1.21 \times \log(L^{Syn}_{peak}) - 9.72 \quad (6)$$

This relation was also probed by Gao et al. (2011) using an early data release from *Fermi*-LAT after three months of observations, plotting the total Syn against IC luminosities. Their relation between $\log(L_{IC})$ and $\log(L_{Syn})$ had a slope of 1.1, similar to our value. Although their correlation coefficient is much lower, 0.58 (owing to larger uncertainties in the γ-ray band, especially because of low *Fermi*-LAT exposure and its early detector calibration at the time), the agreement is remarkably good.

In the luminosity plane (Fig. 4) we are most likely probing the mean behavior of both Syn and IC emission. Especially for the γ-ray band, the spectral data points were calculated integrating over a few years of *Fermi*-LAT observations; therefore, short flaring states (day-week scale) are smoothed and the IC luminosity we plot is a fine representation of the mean emitted power.

The correlation we see at the luminosity plane is probably related to a constant ratio between external photon field (U'_{Ext}) and the magnetic field (U'_B) energy densities in the jet comoving frame. Assuming an EC scenario in this case, this correlation could be taken as observational evidence of the established balance between a dynamic radiative-drag and the magnetic energy density. On the one hand, the radiative-drag is induced by the jet interaction with a boosted external photon field U'_{Ext}, as discussed in Moderski et al. (2003) and Madejski et al. (1999), which is directly connected to the loss energy mechanism for the relativistic electrons (cooling) even imposing limitations to the jet's Lorentz factor (Γ). On the other hand, following Keppens et al. (2008), the magnetic energy density U_b might be directly connected to the particles acceleration (energy gain – bulk plasma heating) and jet structure collimation.

Therefore, the argument put forward by Tavecchio et al. (1998) and Gao et al. (2011) where the ratio between IC and Syn luminosities are directly related to the energy densities U_{ext} and U_b is based on the underling dynamic-mechanisms at work, i.e., the mechanisms responsible for particle acceleration and deceleration within the jet structure. In fact, given that synchrotron and external photons might undergo IC scattering, $L_{IC} \propto U'_{Ext} + U'_{Syn}$ should be more suitable for describing luminosity ratios in general, and $L_{IC} \propto U'_{Ext}$ might hold as the best approach to describe EC scenarios where U'_{Ext} is dominant with respect to U'_{Syn} (using "′" to refer to jet rest-frame quantities):

$$\frac{L_{IC}}{L_{Syn}} = \frac{U'_{Ext} + U'_{Syn}}{U'_B} \ (a) \Rightarrow \frac{U'_{Ext}}{U'_B} \ (b) \quad (7)$$

Also, we should note that the characteristic slope and tight correlation in the L_{IC} versus L_{Syn} plane is in agreement with the CD distribution for LSP blazars (as reported by Arsioli & Polenta 2018), which is Gaussian-like and peaks at log(CD) slightly higher than zero, at $\approx$ 0.17. The fact that the slope associated with $\log(L_{IC})$ versus $\log(L_{Syn})$ is well established at > 1.0 is probably related to the number of strong and fast flaring events in γ rays which pushes the $\langle L_{IC} \rangle$ to higher values when we integrate the observed flux from steady + flaring states over many years. In addition, it is telling us that the more powerful (luminous) blazars are the ones undergoing γ-ray flares more frequently. This could be a hint for the existence of an extra component apart from external and synchrotron photons that might be contributing to the IC bump during flaring events, especially for the most powerful (luminous) blazars. This is in agreement with the possibility of having hadronic or ultra-high-energy cosmic rays (UHECR) cascade components connected to the IC bump, just as considered by Cerruti et al. (2017a).

As discussed by Hu et al. (2017), contributions from external photon fields (IR and UV, from accretion disk, BLR, and dust Torus) are relevant for describing the HE bump from blazar SEDs, and currently the major difficulty is the lack of precise knowledge about the AGN environment so that a multicomponent EC model can be fitted properly. In this scenario, it is hard to conclude the most relevant γ-ray emission site for individual sources, but as we describe here (from our population studies) the IR field tends to be more suitable to model the IC component of bright LSP blazars. Therefore, on average, a far-site emission for MeV-GeV photons is favored, suggesting that an efficient acceleration mechanism might operate far from the core region, as mention by Sikora et al. (2009).

From Tavecchio et al. (1998) and Gao et al. (2011), when using eq. 7.b, the external photon density U_{ext} transforms to the jet comoving frame according to $U'_{\rm ext} = (17/12)\Gamma^2 U_{\rm ext}$ as derived in Ghisellini & Madau (1996). Then, assuming the synchrotron peak $\nu^{\rm Syn}_{\rm peak} = (4/3)\nu_{\rm L}\gamma^2_{\rm peak}\delta$ and $\nu^{\rm EC}_{\rm peak} = (4/3)\nu^{\rm ext}_{\rm peak}\gamma^2_{\rm peak}\Gamma\delta$, where $\gamma_{\rm peak}$ is the Lorentz factor for electrons emitting in the Syn peak, $\nu_{\rm L} = {\rm eB}/(2\pi {\rm m_e c})$ is the Larmor frequency, and $\nu^{\rm ext}_{\rm peak}$ is the peak frequency associated with the external photon field. From this Gao et al. (2011) obtain

$$\frac{L_{\rm IC}}{L_{\rm Syn}} \simeq \frac{17e^2}{6\pi m_e^2 c^2}\frac{U_{\rm Ext}}{\nu^2_{\rm ext}}\Big(\frac{\nu^{\rm EC}_{\rm peak}}{\nu^{\rm S}_{\rm peak}}\Big)^2 \qquad (8)$$

Using measured values for $L_{\rm Syn}$, $L_{\rm IC}$, and assuming $\nu^{\rm EC}_{\rm peak} \equiv \nu^{\rm IC}_{\rm peak}$, with $\frac{17e^2}{6\pi m_e^2 c^2} = 2.79 \times 10^{14}\ [\frac{\rm cm^3}{\rm erg.s^2}]$, we infer the distribution of energy density $(U_{\rm ext}/\nu^2_{\rm ext})$ associated with the external photon field at the AGN source frame (fig. 5, which has mean value $\langle \log(U_{\rm ext}/\nu^2_{\rm ext})\rangle = -32.53 \pm 0.17$. Given the discussion from Sect. 4.2, if we assume the external photon field to be dominant in IR, with $\nu_{\rm ext} = \nu_{\rm IR} = 3 \times 10^{13}$ Hz, the characteristic IR-photon energy density for LSP blazar under EC regime is $\langle U_{\rm ext}\rangle = 2.98 \times 10^{-5}$ erg/cm^3 at the AGN rest frame; The photon field seen by the jet (comoving jet frame) is then: $U'_{\rm ext} = (17/12)\Gamma^2 U_{\rm ext} = 1.69 \times 10^{-2}$ erg/cm^3. Our estimate for $\langle U'_{\rm ext}\rangle$ is in good agreement with Breiding et al. (2018), which assumes a far-site emission zone for γ-ray photons as a result of an IC upscattering of IR seed photons (originating from an illuminated molecular torus and assuming a spine-sheath geometry). We note that we follow the discussion from Sect. 4.2 and assume $\langle\Gamma\rangle = 20$, the bulk Lorentz factor associated with the relativistic outflow.

4.4. The γ-ray photon spectral index versus the synchrotron peak frequency

In Fig. 6 we show the correlation between the γ-ray photon spectral index and the logarithm of the Syn peak frequency $\log(\nu^{Syn}_{peak})$, considering all the 99 radio-Planck sources that had available data in the MeV to GeV band. To expand the description beyond LSP sources and extend the test to higher ν^{sync}_{peak} values, in this same plot we add the 2WHSP sources (Chang et al. 2017) which is a highly confident sample of high synchrotron peak (HSP) blazars. A linear fitting in the Γ versus $\log(\nu^{Syn}_{peak})$ plane reveals a clear negative trend,

$$\langle\Gamma\rangle = -0.119 \times \log(\langle\nu^{\rm Syn}_{\rm peak}\rangle) + 3.85, \qquad (9)$$

showing, on average, that increasing synchrotron peak frequency is related to the hardening of the γ-ray spectrum in the 0.1 to 500 GeV band, as also reported by Acero et al. (2015) and Arsioli et al. (2015). This is usually explained as a consequence of the fixed observational energy window from *Fermi*-LAT (~100 MeV up to 500 GeV) which probes different regions of the IC bump: after its peak (soft spectra with decaying power $P_{(\nu)}$) in case of LSPs, and before its peak (hard spectra with increasing power $P_{(\nu)}$) in the case of HSPs. This is usually taken as observational evidence that ν^{IC}_{peak} is moving to higher energies according to ν^{Syn}_{peak}.

The connection between ν^{IC}_{peak} and ν^{Syn}_{peak} is actually very hard to probe directly, simply because we have limited data to describe the IC bump in the case of HSP blazars. For HSPs, the IC bump extends farther than the *Fermi*-LAT main sensitivity window, and despite the many detections with ground-based very high-energy observatories (VHE, at E > 100 GeV), the absorption of VHE photons due to scattering with low-energy extragalactic background light (EBL) hinders the description of the IC peak.

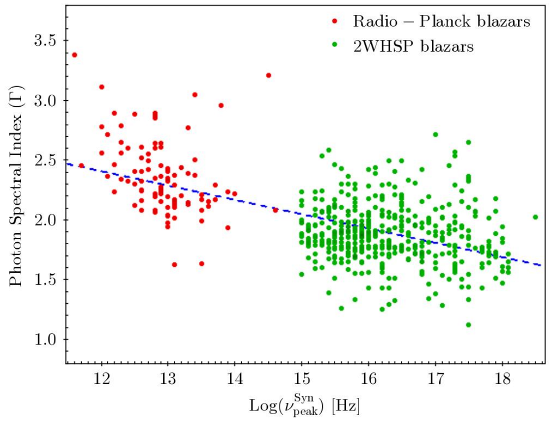

Fig. 6. Gamma-ray photon spectral index (Γ) vs. the Syn peak $\log(\nu^{\rm Syn}_{\rm peak})$ parameter: in red, the radio-Planck sources (LSP blazars); in green, the 2WHSP sources (HSP blazars); blue dashed line is the linear fitting considering all sources in the Γ vs. $\log(\nu^{\rm Syn}_{\rm peak})$ plane.

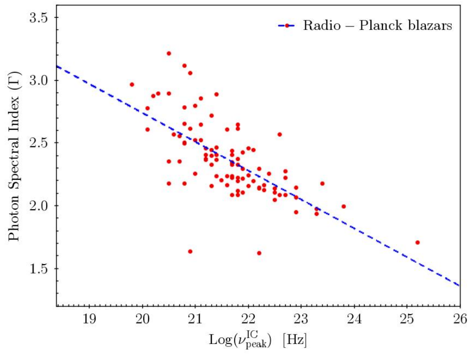

Fig. 7. Gamma-ray photon spectral index (Γ) vs. the inverse Compton peak $\log(\nu^{\rm IC}_{\rm peak})$ parameter. In red, the radio-Planck sources with good estimates for the IC peak; the blue dashed line is the linear fitting for the data.

If we consider only the complete radio-Planck sample of LSP blazars (Arsioli & Polenta 2018), a scatter plot with $\log(\nu_{\rm peak}^{\rm Syn})$ versus $\log(\nu_{\rm peak}^{\rm IC})$ shows no clear correlation. A complete sample of blazars spanning a wider range in $\log(\nu_{\rm peak})$ space might be needed to better probe the $\nu_{\rm peak}^{\rm Syn}$ to $\nu_{\rm peak}^{\rm IC}$ connection. In Fig. 7 we plot the γ-ray photon spectral index against the $\log(\nu_{\rm peak}^{\rm IC})$, this time only for the radio-Planck sources with good estimates for the IC parameter (cases with the ? flag in Table 1 were eliminated). Even if we try to use a complete sample of HSP blazars, there is no good estimate of ν_{peak}^{IC} for all sources, and therefore we do not consider HSPs for this plot. A linear fitting in the Γ versus $\log(\nu_{\rm peak}^{\rm IC})$ gives

$$\langle\Gamma\rangle = -0.229 \times \log(\langle\nu_{\rm peak}^{\rm IC}\rangle) + 7.34 \quad (10)$$

Both correlations, as in eq. 9 and eq. 10, tell us that LSP blazars are associated with the steepest γ-ray sources in the 0.1–500 GeV band, with an IC peak located around the MeV band. Faint point-like sources of this kind are difficult to detect with *Fermi*-LAT, especially in regions close to the galactic disk $|b| < 10°$ where the MeV diffuse component is dominant. In pure leptonic SSC and EC scenarios, a correlation between spectral parameters derived from the Syn and IC components is expected (Giommi et al. 2012b, 2013) given that both components depend directly on the jet's relativistic electrons producing synchrotron radiation and acting for the up-scattering of low-energy photons to γ rays.

5. Conclusions

We evaluate the jet's Lorentz factor γ_{peak} and Bδ parameters for LSP blazars in the radio-Planck sample, assuming at first a simple single-zone SSC model. In this case, we show that Bδ is probably underestimated owing to overestimated γ_{peak}^{SSC} values; therefore, a SSC model can hardly describe the SED observed for LSP blazars.

We studied the Tramacere plane $\log(\gamma_{\rm peak}^{\rm SSC})$ versus $\log(\nu_{\rm peak}^{\rm Syn})$ to show that most sources in the radio-Planck sample are above the limits associated with a dominant SSC regime. In fact, they populate a region that is characteristic of the EC regime under TH scattering, spreading along a parameter-space that is attributed to external photon fields ranging from IR to UV.

Assuming an EC model, we reevaluate the γ_{peak}^{EC} and Bδ parameters for LSP blazars. We assume two different external photon fields, one dominated by UV photons (consistent with BLR emission) and another dominated by IR photons (consistent with dust torus emission, and MC emission in spine-sheath geometry). We conclude that on average an IR field is probably more suitable, resulting in distributions with the corresponding mean values $\langle\log({\rm B}\delta)\rangle \approx 0.99$ and $\langle\log(\gamma_{\rm peak}^{\rm EC})\rangle \approx 2.80$ consistent with expectations from Kang et al. (2014) and Cao & Wang (2013). This hints to a γ-ray emission region which is out of the BLR domain, far from the BH, at a distance $\gg$ 0.1 pc. Moreover, it demands the jet structure to be a very narrow opening (or with substructures) to reconcile with the short timescale variability observed in the GeV-TeV band (Agudo et al. 2011). We calculate the photon energy density associated with the external field at the jet comoving frame to be $U'_{\rm ext} = 1.69 \times 10^{-2}$ erg/cm^3, finding good agreement with Breiding et al. (2018).

We calculate the luminosity associated with the peak-power for both Syn and IC components, and plot $\log(L_{\rm IC})$ versus $\log(L_{\rm Syn})$ in what we called "the luminosity plane". There we show a tight correlation spanning seven orders of magnitude in luminosity, with slope slightly larger than one, which is probably related to a nearly constant ratio of the energy density associated with external + synchrotron photon fields to the magnetic energy density, $(U'_{\rm Ext} + U'_{\rm Syn})/U'_{\rm B}$, implying a balance between the particle's acceleration and deceleration mechanisms in the jet. In fact, the slope we measure in the luminosity plane is larger than 1.0 and could be induced by the γ-ray flaring activity, which is proving to be more relevant for the most luminous (powerful and extreme) sources.

We probe the correlation between the γ-ray photon spectral index (0.1–500 GeV band) with both $\nu_{\rm peak}^{\rm Syn}$ and $\nu_{\rm peak}^{\rm IC}$ parameters, showing a trend of hardening Γ for increasing ν_{peak}^{Syn} and $\nu_{\rm peak}^{\rm IC}$, noting that LSP blazars are characterized by steep γ-ray spectrum in the 0.1–500 GeV band, which hinders the detection of faint LSP sources with *Fermi*-LAT.

Acknowledgements. During this work, BA was supported by the Brazilian Scientific Program Ciências sem Fronteiras - Cnpq, and later by São Paulo Research Foundation (FAPESP) with grant n. 2017/00517-4. YLC is supported by the Government of the Republic of China (Taiwan). We would like to thank Prof. Paolo Giommi and Prof. Gianluca Polenta for their comments during the preparation of this work, Prof. Marcelo M. Guzzo and Prof. Orlando L.G. Peres for the full support granting the author's partnership with FAPESP. We thank SSDC, the Space Science Data Center from the Agenzia Spaziale Italiana; University La Sapienza of Rome, Department of Physics; And State University of Campinas - Unicamp, IFGW Department of Physics for hosting the authors. We make use of archival data and bibliographic information obtained from the NASA-IPAC Extragalactic Database (NED), and data and software facilities from the SSDC (www.ssdc.asi.it).

References

Abdo, A. A., Ackermann, M., Agudo, I., et al. 2010a, The Astrophysical Journal, 716, 30
Abdo, A. A., Ackermann, M., Ajello, M., et al. 2015, The Astrophysical Journal, 799, 143
Abdo, A. A., Ackermann, M., Ajello, M., et al. 2010b, The Astrophysical Journal Supplement Series, 188, 405
Acero, F., Ackermann, M., Ajello, M., et al. 2015, ApJS, 218, 23
Ackermann, M., Ajello, M., Allafort, A., Antolini, E., & Atwood, e. a. 2011, ApJ, 743, 171
Ackermann, M., Ajello, M., Ballet, J., et al. 2012, The Astrophysical Journal, 751, 159
Agudo, I., Marscher, A., Jorstad, S. G., & Gómez, J. L. 2013, in Highlights of Spanish Astrophysics VII, ed. J. C. Guirado, L. M. Lara, V. Quilis, & J. Gorgas, 152–157
Agudo, I., Marscher, A. P., Jorstad, S. G., et al. 2011, The Astrophysical Journal Letters, 735, L10
Aharonian, F., Akhperjanian, A. G., Bazer-Bachi, A. R., et al. 2007, The Astrophysical Journal Letters, 664, L71
Arsioli, B., Barres de Almeida, U., Prandini, E., Fraga, B., & Foffano, L. 2018, ArXiv e-prints
Arsioli, B. & Chang, Y.-L. 2017, A&A, 598, A134
Arsioli, B., Fraga, B., Giommi, P., Padovani, P., & Marrese, P. M. 2015, A&A, 579, A34
Arsioli, B. & Polenta, G. 2018, ArXiv e-prints
Atwood, W. B., Abdo, A. A., Ackermann, M., et al. 2009, ApJ, 697, 1071
Bernlhr, K., Barnacka, A., Becherini, Y., et al. 2013, Astroparticle Physics, 43, 171 , seeing the High-Energy Universe with the Cherenkov Telescope Array - The Science Explored with the CTA

References

[1] Abdo, A. A., Ackermann, M., Agudo, I., Ajello, M., Aller, H. D., Aller, M. F., Angelakis, E., Arkharov, A. A., Axelsson, M., Bach, U., , and et al. The spectral energy distribution of fermi bright blazars. *The Astrophysical Journal 716*, 1 (jun 2010), 30–70.

[2] Abell, G. O., Corwin, H. G. J., and Olowin, R. P. A catalog of rich clusters of galaxies. *The Astrophysical Journal Supplement Series*, 70 (1989), 1–138.

[3] Abolfathi, B., Aguado, D. S., Aguilar, G., Prieto, C. A., Almeida, A., Ananna, T. T., Anders, F., Anderson, S. F., Andrews, B. H., Anguiano, B., , and et al. The Fourteenth Data Release of the Sloan Digital Sky Survey: First Spectroscopic Data from the extended Baryon Oscillation Spectroscopic Survey and from the second phase of the Apache Point Observatory Galactic Evolution Experiment. *The Astrophysical Journal Supplement Series 235* (2018), 42.

[4] Abraham, J., Aglietta, M., Aguirre, I. C., Albrow, M., Allard, D., Allekotte, I., Llison, P., Alvarez Muñiz, J., Do Amaral, M. G., Ambrosio, M., , and et al. Properties and performance of the prototype instrument for the Pierre Auger Observatory. *Nuclear Instruments and Methods in Physics Research Section A 525* (2004), 50–95.

[5] Abu-zayyad, T., Aida, R., Allen, M., Anderson, R., and Azuma, R. The surface detector array of the Telescope Array experiment. *Nuclear Instruments and Methods in Physics Research A 689* (2012), 87–97.

[6] Acero, F., Ackermann, M., Ajello, M., Albert, A., Atwood, W. B., Axelsson, M., Baldini, L., Ballet, J., Barbiellini, G., Bastieri, D., , and et Al. Fermi Large Area Telescope Third Source Catalog. *The Astrophysical Journal Supplement Series 218*, 2 (2015).

[7] Ackermann, M., Ajello, M., Atwood, W., Baldini, L., Ballet, J., Barbiellini, G., Bastieri, D., Gonzalez, J., Bellazzini, R., Bissaldi, E., , and et al. The Third Catalog of Active Galactic Nuclei Detected by the Fermi Large Area Telescope. *The Astrophysical Journal 810* (2015), 14.

[8] Ackermann, M., Ajello, M., Atwood, W. B., , and et al. 2FHL: The second catalog of hard fermi-LAT sources. *The Astrophysical Journal Supplement Series 30-July-20* (2015).

[9] Ajello, M., Gasparrini, D., Sanchez-Conde, M., Zaharijas, G., Gustafsson, M., Cohen-Tanugi, J., Dermer, C. D., Inoue, Y., Hartmann, D., Ackermann, M., Bechtol, K., , and et al. The Origin of the Extragalactic Gamma-Ray Background and Implications for Dark-Matter Annihilation. *The Astrophysical Journal 800*, 2 (2015), L27.

[10] Ajello, M., Romani, R. W., Gasparrini, D., Shaw, M. S., Bolmer, J., Cotter, G., Finke, J., Greiner, J., Healey, S. E., King, O., Max-Moerbeck, W., Michelson, P. F., Potter, W. J., Rau, A., Readhead, A. C. S., Richards, J. L., and Schady, P. THE COSMIC EVOLUTION OF Fermi BL LACERTAE OBJECTS. *The Astrophysical Journal 780*, 1 (2014), 73.

[11] Antonucci, R. Unified Models for Active Galactic Nuclei and Quasars. *Annual Review of Astronomy and Astrophysics 31*, 1 (1993), 473–521.

[12] Arsioli, B., Barres de Almeida, U., Prandini, E., Fraga, B., and Foffano, L. Extreme & High Synchrotron Peaked Blazars at the limit of Fermi-LAT detectability: the gamma-ray spectrum of 1BIGB sources. *Monthly Notices of the Royal Astronomical Society submitted* (2018).

[13] Arsioli, B., and Chang, Y.-L. Searching for gamma-ray signature in WHSP blazars: Fermi-LAT detection of 150 excess signal in the 0.3-500 GeV band. *Astronomy and Astrophysics 598* (2017), A134.

[14] Arsioli, B., Fraga, B., Giommi, P., Padovani, P., and Marrese, P. M. 1WHSP: An IR-based sample of ˜1000 VHE <i>γ</i> -ray blazar candidates. *Astronomy & Astrophysics 579* (2015), A34.

[15] Avni, Y., and Bahcall, J. N. On the simultaneous analysis of several complete samples - The V/Vmax and Ve/Va variables, with applications to quasars. *The Astrophysical Journal 235* (1980), 694–716.

[16] Baumgartner, W. H., Tueller, J., Markwardt, C. B., Skinner, G. K., Barthelmy, S., Mushotzky, R. F., Evans, P. A., and Gehrels, N. The 70 month swift-bat all-sky hard X-ray survey. *The Astrophysical Journal Supplement Series 207*, 2 (2013).

[17] Bessell, M. S. UBVRI photometry. II - The Cousins VRI system, its temperature and absolute flux calibration, and relevance for two-dimensional photometry. *Publications of the Astronomical Society of the Pacific 91*, October (1979), 589.

[18] Bianchi, L., dela Vega, A., Shiao, B., and Bohlin, R. New UV-source catalogs, UV spectral database, UV variables and science tools from the GALEX surveys. *Astrophysics and Space Science 363*, 3 (2018), 56.

[19] Blandford, R., and Rees, M. Some comments on radiation mechanisms in Lacertids. In *Pittsburgh Conference on BL Lac Objects* (Pittsburgh, 1978), A. M. Wolfe, Ed., University of Pittsburgh press, pp. 341–347.

[20] Blanton, M. R., Bershady, M. A., Abolfathi, B., Albareti, F. D., Prieto, C. A., Almeida, A., Alonso-García, J., Anders, F., Anderson, S. F., Andrews, B., , and et al. Sloan Digital Sky Survey IV: Mapping the Milky Way, Nearby Galaxies, and the Distant Universe. *The Astronomical Journal 154*, 28 (2017).

[21] Böhringer, H., and Werner, N. X-ray spectroscopy of galaxy clusters: Studying astrophysical processes in the largest celestial laboratories. *Astronomy and Astrophysics Review 18*, 1-2 (2010), 127–196.

[22] Boller, T., Freyberg, M. J., Truemper, J., Haberl, F., Voges, W., and Nandra, K. Second ROSAT all-sky survey (2RXS) source catalogue. *Astronomy and Astrophysics 103* (2016), 1–26.

[23] Bonnoli, G., Tavecchio, F., Ghisellini, G., and Sbarrato, T. An emerging population of BL Lacs with extreme properties: towards a class of EBL and

cosmic magnetic field probes? *Monthly Notices of the Royal Astronomical Society 451*, April (2015), 611–621.

[24] Burstein, D., and Heiles, C. H I, galaxy counts, and reddening - Variation in the gas-to-dust ratio, the extinction at high galactic latitudes, and a new method for determining galactic reddening. *The Astrophysical Journal*, 225 (1978), 40–55.

[25] Cao, Z., Bi, X. J., Cao, Z., Chan, J. F., Chen, G., He, H. S., Chen, M. J., Chen, S. Z., Jiang, L. H., He, H. H., , and et al. 38th COSPAR Scientific Assembly 2010. In *38th COSPAR Scientific Assembly* (Bremen, 2010).

[26] Cardelli, J. A., Clayton, G. C., and Mathis, J. S. The relationship between infrared, optical, and ultraviolet extinction. *The Astrophysical Journal 345* (1989), 245.

[27] Carroll, B. W., and Ostlie, D. A. *An Introduction to Mordern Astrophysics*, 2 ed. Addison-Wesley, 2006.

[28] Carroll, S. M., Press, W. H., and Turner, E. L. The cosmological constant. *Annual Review of Astronomy and Astrophysics 30* (1992), 499–542.

[29] Chambers, K. C., Magnier, E. A., Metcalfe, N., Flewelling, H. A., Huber, M. E., Waters, C. Z., Denneau, L., Draper, P. W., Farrow, D., Finkbeiner, D. P., , and et al. The Pan-STARRS1 Surveys. *ArXiv e-prints 1612.05560* (2016).

[30] Chang, Y.-L., Arsioli, B., Giommi, P., and Padovani, P. 2WHSP: A catalog of HE and VHE gamma-ray blazars and blazar candidates. *Astronomy and Astrophysics 598* (2017), A17.

[31] Coleman, G. D., Wu, C.-C., and Weedman, D. W. Colors and magnitudes predicted for high redshift galaxies. *The Astrophysical Journal Supplement Series 43* (1980), 393–416.

[32] collaboration, I. Evidence for High-Energy Extraterrestrial Neutrinos at the IceCube Detector. *Science 342* (2013), 1242856.

[33] Condon, J. J. The 1.4 gigahertz luminosity function and its evolution. *The Astrophysical Journal 338* (1989), 13–23.

[34] Condon, J. J., Cotton, W. D., Greisen, E. W., Yin, Q. F., Perley, R. A., Taylor, G. B., and Broderick, J. J. 1.4 GHz NRAO VLA Sky Survey (NVSS). *The Astronomical Journal 115*, 5 (1998), 1693–1716.

[35] Costamante, L., Ghisellini, G., Giommi, P., Tagliaferri, G., Celotti, A., Chiaberge, M., Fossati, G., Maraschi, L., Tavecchio, F., Treves, A., and Wolter, A. Extreme synchrotron BL Lac objects Stretching the blazar sequence. *Astronomy and Astrophysics 371* (2001), 512–526.

[36] Cutri, R. M., Wright, E. L., Conrow, T., Fowler, J. W., Eisenhardt, P. R. M., Grillmair, C., Kirkpatrick, J. D., Masci, F., McCallon, H. L., Wheelock, S. L., , and et al. Explanatory Supplement to the AllWISE Data Release Products. Tech. rep., 2013.

[37] D'Abrusco, R., Massaro, F., Ajello, M., Grindlay, J., Smith, H., and Tosti, G. Infrared Colors of the Gamma-Ray-detected Blazars. *The Astrophysical Journal 748* (2012), 68.

[38] De Breuck, C., Tang, Y., de Bruyn, A. G., Röttgering, H., and van Breugel, W. A sample of ultra steep spectrum sources selected from the Westerbork In the Southern Hemisphere (WISH) survey. *Astronomy & Astrophysics 394*, 1 (2002), 59–69.

[39] D'Elia, V., Perri, M., Puccetti, S., Capalbi, M., Giommi, P., Burrows, D. N., Campana, S., Tagliaferri, G., Cusumano, G., Evans, P., Gehrels, N., Kennea, J., Moretti, A., Nousek, J. A., Osborne, J. P., Romano, P., and Stratta, G. The seven year Swift -XRT point source catalog (1SWXRT). *Astronomy and Astrophysics 551* (2013), A142.

[40] Dermer, C. D., Cavadini, M., Razzaque, S., Finke, J. D., Chiang, J., and Lott, B. TIME DELAY OF CASCADE RADIATION FOR TeV BLAZARS AND THE MEASUREMENT OF THE INTERGALACTIC MAGNETIC FIELD. *The Astrophysical Journal 733*, 2 (2011), L21.

[41] Di Mauro, M., Donato, F., Lamanna, G., Sanchez, D. A., and Serpico, P. D. Diffuse Γ-Ray Emission From Unresolved Bl Lac Objects. *The Astrophysical Journal 786*, 2 (2014), 129.

[42] Doi, M., Tanaka, M., Fukugita, M., Gunn, J. E., Yasuda, N., Ivezić, Ž., Brinkmann, J., de Haars, E., Kleinman, S. J., Krzesinski, J., and Leger, R. F. Photometric Response Functions of the Sloan Digital Sky Survey Imager. *The Astronomical Journal 139*, 4 (2010), 1628–1648.

[43] Domínguez, A., Primack, J. R., Rosario, D. J., Prada, F., Gilmore, R. C., Faber, S. M., Koo, D. C., Somerville, R. S., Pérez-Torres, M. A., Pérez-González, P., , and et al. Extragalactic background light inferred from AEGIS galaxy-SED-type fractions. *Monthly Notices of the Royal Astronomical Society 410*, 4 (2011), 2556–2578.

[44] Edelson, R. A Survey of Ultraviolet Variability in Blazars. *The Astrophysical Journal 401* (1992), 516–528.

[45] Edelson, R., Krolik, J., Madejski, G., Maraschi, L., Pike, G., Urry, C. M., Brinkmann, W., Courvoisier, T. J.-L., Ellithorpe, J., Horne, K., , and et al. Multiwavelength monitoring of the BL Lacertae object PKS 2155-304. 4: Multiwavelength analysis. *The Astrophysical Journal 438* (1995), 120–134.

[46] Evans, I. N., Primini, F. A., Glotfelty, K. J., Anderson, C. S., Bonaventura, N. R., Chen, J. C., Davis, J. E., Doe, S. M., Evans, J. D., Fabbiano, G., , and et al. The Chandra source catalog. *Astrophysical Journal, Supplement Series 189*, 1 (2010), 37–82.

[47] Evans, P. A., Osborne, J. P., Beardmore, A. P., Page, K. L., Willingale, R., Mountford, C. J., Pagani, C., Burrows, D. N., Kennea, J. A., Perri, M., Tagliaferri, G., and Gehrels, N. 1SXPS: A deep swift X-ray telescope point source catalog with light curves and spectra. *The Astrophysical Journal Supplement Series 210*, 1 (2014), 8.

[48] Finke, J. D., Reyes, Luis C. Georganopoulos, Markos Reynolds, K., Ajello, M., Fegan, S. J., and McCann, K. Constraints on the intergalactic magnetic field with gamma-ray observations of blazars. *The Astrophysical Journal 814* (2015), 20.

[49] Fitzpatrick, E. L. Correcting for the Effects of Interstellar Extinction. *Publications of the Astronomical Society of the Pacific 111* (1999), 63–75.

[50] Fossati, G., Celotti, A., Ghisellini, G., and Maraschi, L. Unifying models for X-ray-selected and radio-selected BL Lac objects. *Monthly Notices of the Royal Astronomical Society 289*, 1 (1997), 136–150.

[51] Fossati, G., Maraschi, L., Celotti, A., Comastri, A., and Ghisellini, G. A unifying view of the spectral energy distributions of blazars. *Monthly Notices of the Royal Astronomical Society 299* (1998), 433–448.

[52] Gaia Collaboration. The Gaia mission. *Astronomy & Astrophysics 595* (2016), A1.

[53] Gaia Collaboration, Brown, A. G. A., Vallenari, A., Prusti, T., de Bruijne, J., Mignard, F., Drimmel, R., and Co-authors, . Gaia Data Release 1. Summary of the astrometric, photometric, and survey properties. A2.

[54] Gehrels, N. Confidence limits for small numbers of events in astrophysical data. *The Astrophysical Journal 303* (1986), 336–346.

[55] Giommi, P., Capalbi, M., Fiocchi, M., Memola, E., Perri, M., Piranomonte, S., Rebecchi, S., and Massaro, E. A Catalog of 157 X-ray Spectra and 84 Spectral Energy Distributions of Blazars Observed with BeppoSAX. In *Blazar Astrophysics with BeppoSAX and Other Observatories* (2002).

[56] Giommi, P., Colafrancesco, S., Cavazzuti, E., Perri, M., and Pittori, C. Non-thermal Cosmic Backgrounds from Blazars: the contribution to the CMB, X-ray and gamma-ray Backgrounds. *Astronomy and Astrophysics 445* (2006), 843–855.

[57] Giommi, P., Colafrancesco, S., Padovani, P., Gasparrini, D., Cavazzuti, E., and Cutini, S. The number counts, luminosity functions and evolution of microwave-selected (WMAP) blazars and radio galaxies. *Astronomy and Astrophysics 508* (2009), 107–115.

[58] Giommi, P., Menna, M. T., and Padovani, P. The sedentary multifrequency survey - I. Statistical identification and cosmological properties of high-energy peaked BL Lacs. *Monthly Notices of the Royal Astronomical Society 310* (1999), 465–475.

[59] Giommi, P., and Padovani, P. A simplified view of blazars: contribution to the X-ray and gamma-ray cosmic backgrounds. *Monthly Notices of the Royal Astronomical Society 450* (2015), 2404–2409.

[60] Giommi, P., Padovani, P., Polenta, G., Turriziani, S., D'Elia, V., and Piranomonte, S. A simplified view of blazars: clearing the fog around long-standing selection effects. *Monthly Notices of the Royal Astronomical Society 420* (2012), 2899–2911.

[61] Giommi, P., Piranomonte, S., Perri, M., and Padovani, P. The Sedentary Survey of Extreme High Energy Peaked BL Lacs. II. The Catalog and Spectral Properties. *Astronomy and Astrophysics 434*, 1 (2005), 385–396.

[62] Gregory, P. C., and Condon, J. J. 87GB Catalog of radio sources. *VizieR Online Data Catalog* (1992).

[63] Gregory, P. C., Scott, W. K., Douglas, K., and Condon, J. J. The GB6 Catalog of Radio Sources. *The Astrophysical Journal Supplement Series 103* (1996), 427.

[64] Griffith, M. R., and Wright, A. E. The Parkes-MIT-NRAO (PMN) surveys. I - The 4850 MHz surveys and data reduction. *The Astronomical Journal 105*, 5 (1993), 1666.

[65] Griffith, M. R., Wright, A. E., Burke, B. F., and Ekers, R. D. The Parkes-MIT-NRAO (PMN) surveys. 3: Source catalog for the tropical survey (-29 deg less than delta less than -9 deg .5). *The Astrophysical Journal Supplement Series 90* (1994), 179.

[66] Griffith, M. R., Wright, A. E., Burke, B. F., and Ekers, R. D. The Parkes-MIT-NRAO (PMN) surveys. 6: Source catalog for the equatorial survey (-9.5 deg less than delta less than +10.0 deg). *The Astrophysical Journal Supplement Series 97* (1995), 347.

[67] Harris, D. E., Forman, W., Gioia, I. M., Hale, J. A., Harnden, F. R., J., Jones, C., Karakashian, T., Maccacaro, T., McSweeney, J. D., and Primini, F. A. The Einstein Observatory catalog of IPC X ray sources. Volume 1E: Documentation. *Einstein Observatory Catalog of IPC X-ray Sources* (1990).

[68] Healey, S. E., Romani, R. W., Taylor, G. B., Sadler, E. M., Ricci, R., Murphy, T., Ulvestad, J. S., and Winn, J. N. CRATES: An AllSky Survey of FlatSpectrum Radio Sources. *The Astrophysical Journal Supplement Series 171*, 1 (2007), 61–71.

[69] Helfand, D. J., White, R. L., and Becker, R. H. The last of first: The final catalog and source identifications. *The Astrophysical Journal 801*, 1 (2015), 26.

[70] IceCube Collaboration. The IceCube Neutrino Observatory. In *34th International Cosmic Ray Conference* (2015).

[71] Irwin, M., Maddox, S., and McMahon, R. The APM Sky Catalogues. *IEEE Spectrum 2* (1994), 14–16.

[72] Jordi, C., Gebran, M., Carrasco, J. M., de Bruijne, J., Voss, H., Fabricius, C., Knude, J., Vallenari, A., Kohley, R., and Mora, A. Gaia broad band photometry. *Astronomy and Astrophysics 523* (2010), A48.

[73] Kapanadze, B. Catalog and Statistical Study of X-Ray Selected Bl Lacertae Objects. *The Astronomical Journal 145*, 2 (2013), 31.

[74] Landt, H., Padovani, P., Perlman, E. S., Giommi, P., Bignall, H., and Tzioumis, A. The Deep X-Ray Radio Blazar Survey (DXRBS) - II. New identifications. *Monthly Notices of the Royal Astronomical Society 323* (2001), 757.

[75] Lasker, B. M., Lattanzi, M. G., McLean, B. J., Bucciarelli, B., Drimmel, R., Garcia, J., Greene, G., Guglielmetti, F., Hanley, C., Hawkins, G., , and et al. The second-generation guide star catalog: Description and properties. *The Astronomical Journal 136*, 2 (2008), 735–766.

[76] Liu, T., Tozzi, P., Tundo, E., Moretti, A., Rosati, P., Wang, J. X., Tagliaferri, G., Campana, S., and Giavalisco, M. The swift X-ray telescope cluster survey. III. Cluster catalog from 2005-2012 archival data. *The Astrophysical Journal Supplement Series 216*, 2 (2015).

[77] Manch, T., Murphy, T., Buttery, H. J., Curran, J., Hunstead, R. W., Piestrzynski, B., Robertson, J. G., and Sadler, E. M. SUMSS: A wide-field radio imaging survey of the southern sky - II. The source catalogue. *Monthly Notices of the Royal Astronomical Society 342*, 4 (2003), 1117–1130.

[78] Manchester, R. N., Hobbs, G. B., Teoh, A., and Hobbs, M. The Australia Telescope National Facility Pulsar Catalogue. *The Astronomical Journal 129* (2005), 1993–2006.

[79] Mannheim, K. High-energy neutrinos from extragalactic jets. *Astroparticle Physics 3* (1995), 295–302.

[80] Marziani, P., Sulentic, J. W., Dultzin-Hacyan, D., Calvani, M., and Moles, M. Comparative Analysis of the High- and Low-Ionization Lines in the Broad-Line Region of Active Galactic Nuclei. *The Astrophysical Journal Supplement Series* (1996), 37–70.

[81] Massaro, E., Giommi, P., Leto, C., Marchegiani, P., Maselli, A., Perri, M., Piranomonte, S., and Sclavi, S. Roma-BZCAT: a multifrequency catalogue of blazars. *Astronomy and Astrophysics 495*, 2 (2009), 691–696.

[82] Massaro, E., Maselli, A., Leto, C., Marchegiani, P., Perri, M., Giommi, P., and Piranomonte, S. The 5th edition of the Roma-BZCAT. A short presentation. *Astrophysics and Space Science 357* (2015), 75.

[83] Massaro, E., Nesci, R., and Piranomonte, S. The colours of BL Lac objects: a new approach to their classification. *Monthly Notices of the Royal Astronomical Society 422*, 3 (2012), 2322–2331.

[84] Massaro, F., D'Abrusco, R., Ajello, M., Grindlay, J. E., and Smith, H. A. Identification of the infrared non-thermal emission in blazars. *The Astrophysical Journal Letters 740*, 2 (2011), L48.

[85] McConnell, D., Sadler, E. M., Murphy, T., and Ekers, R. D. ATPMN: Accurate positions and flux densities at 5 and 8GHz for 8385 sources from the PMN survey. *Monthly Notices of the Royal Astronomical Society 422*, 2 (2012), 1527–1545.

[86] Mirzoyan, R. First detection of very-high-energy gamma-ray emission from the extreme blazar PGC 2402248 with the MAGIC telescopes. *The Astronomer's Telegram, No. 11548* (2018).

[87] Monet, D. G., Levine, S. E., Canzian, B., Ables, H. D., Bird, A. R., Dahn, C. C., Guetter, H. H., Harris, H. C., Henden, A. A., Leggett,

S. K., , and et Al. The USNO-B Catalog. *The Astronomical Journal 125*, 2 (2003), 984–993.

[88] Morris, S. L., Stocke, J. T., Gioia, I. M., Schild, R. E., Wolter, A., Maccacaro, T., and della Ceca, R. The luminosity function and cosmological evolution of X-ray-selected BL Lacertae objects. *The Astrophysical Journal 380* (1991), 49.

[89] Morrissey, P., Conrow, T., Barlow, T. A., Small, T., Seibert, M., Wyder, T. K., Budavari, T., Arnouts, S., Friedman, P. G., Forster, K., , and et al. The Calibration and Data Products of GALEX. *The Astrophysical Journal Supplement Series 173*, 2 (2007), 682–697.

[90] Munz, E. D. The Einstein Slew Survey. *The Astrophysical Journal Supplement Series 80* (1992), 257–303.

[91] Murphy, T., Sadler, E. M., Ekers, R. D., Massardi, M., Hancock, P. J., Mahony, E., Ricci, R., Burke-Spolaor, S., Calabretta, M., Chhetri, R., , and et al. The Australia Telescope 20 GHz Survey: The source catalogue. *Monthly Notices of the Royal Astronomical Society 402*, 4 (2010), 2403–2423.

[92] Netzer, H. Revisiting the Unified Model of Active Galactic Nuclei. *Annual Review of Astronomy and Astrophysics 53* (2015), 365.

[93] Padovani, P. Gamma-ray Emitting AGN and Unified Schemes. In *the XXXII Moriond Conference 'Very High Energy Phenomena in the Universe'* (1997).

[94] Padovani, P. The blazar sequence: Validity and predictions. *Astrophysics and Space Science 309*, 1-4 (2007), 63–71.

[95] Padovani, P., Alexander, D. M., Assef, R. J., De Marco, B., Giommi, P., Hickox, R. C., Richards, G. T., Smolcic, V., Hatziminaoglou, E., Mainieri, V., and Salvato, M. Active Galactic Nuclei: what's in a name? *Astronomy and Astrophysics Review 25* (2017), 2.

[96] Padovani, P., Ghisellini, G., Fabian, A. C., and Celotti, A. Radio-loud AGN and the extragalactic gamma-ray background. *Monthly Notices of the Royal Astronomical Society 260*, 2 (1993), L21–L24.

[97] Padovani, P., and Giommi, P. The connection between x-ray- and radio-selected BL Lacertae objects. *The Astrophysical Journal 444* (1995), 567.

[98] Padovani, P., and Giommi, P. A simplified view of blazars: the very high energy gamma-ray vision. *Monthly Notices of the Royal Astronomical Society: Letters 446* (2015), L41–L45.

[99] Padovani, P., Giommi, P., Landt, H., and Perlman, E. S. The deep x-ray radio blazar survey (DXRBS). III. radio number counts, evolutionary properties, and luminosity function of blazars. *The Astrophysical Journal 662* (2008), 182.

[100] Padovani, P., Giommi, P., Resconi, E., Glauch, T., Arsioli, B., and Sahakyan, N. Dissecting the region around IceCube-170922A: the BL Lac TXS 0506+056 as the first cosmic neutrino source. *Monthly Notices of the Royal Astronomical Society submitted* (2018).

[101] Padovani, P., Perlman, E. S., Landt, H., Giommi, P., and Perri, M. What Types of Jets Does Nature Make? A New Population of Radio Quasars. *The Astrophysical Journal 588*, 1 (2003), 128–142.

[102] Padovani, P., and Resconi, E. Are both BL Lacs and pulsar wind nebulae the astrophysical counterparts of IceCube neutrino events? *Monthly Notices of the Royal Astronomical Society 443* (2014), 474–484.

[103] Padovani, P., Resconi, E., Giommi, P., Arsioli, B., and Chang, Y. L. Extreme blazars as counterparts of IceCube astrophysical neutrinos. *Monthly Notices of the Royal Astronomical Society 457*, 4 (2016), 3582–3592.

[104] Page, M., Yershov, V., Breeveld, A., Kuin, N. P., Mignani, R. P., Smith, P. J., Rawlings, J. I., Oates, S. R., Siegel, M., and Roming, P. W. The Swift UVOT serendipitous source catalogue. *Proceedings of Science*, December (2014).

[105] Page, M. J., Brindle, C., Talavera, A., Still, M., Rosen, S. R., Yershov, V. N., Ziaeepour, H., Mason, K. O., Cropper, M. S., Breeveld, A. A., , and et al. The XMM-Newton serendipitous ultraviolet source survey catalogue. *Monthly Notices of the Royal Astronomical Society 426*, 2 (2012), 903–926.

[106] Panzera, M. R., Campana, S., Covino, S., Lazzati, D., Mignani, R. P., Moretti, A., and Tagliaferri, G. The Brera Multi-scale Wavelet ROSAT HRI source catalogue. *Astronomy & Astrophysics 399* (2003), 351–364.

[107] Paturel, G., Petit, C., Prugniel, P., Theureau, G., Rousseau, J., Brouty, M., Dubois, P., and Cambrésy, L. HYPERLEDA. I. Identification and designation of galaxies. *Astronomy and Astrophysics 412* (2003), 45–55.

[108] Pérez-Torres, M. A., Zandanel, F., Guerrero, M. A., Pal, S., Profumo, S., Prada, F., and Panessa, F. The origin of the diffuse non-thermal X-ray and radio emission in the Ophiuchus cluster of galaxies. *Monthly Notices of the Royal Astronomical Society 396*, 4 (2009), 2237–2248.

[109] Perlman, E. S., Padovani, P., Giommi, P., Sambruna, R., Jones, L. R., Tzioumis, A., and Reynolds, J. The Deep X-Ray Radio Blazar Survey. I. Methods and First Results. *The Astronomical Journal 115* (1998), 1253.

[110] Peterson, B. M. *An Introduction to Active Galactic Nuclei.* Cambridge University Press, 1997.

[111] Petropoulou, M., Dimitrakoudis, S., Padovani, P., Mastichiadis, A., and Resconi, E. Photohadronic origin of γ -ray BL Lac emission : implications for IceCube neutrinos. *Monthly Notices of the Royal Astronomical Society 448* (2015), 2412.

[112] Pfrommer, C., Broderick, A. E., Chang, P., Puchwein, E., and Springel, V. The physics and cosmology of TeV blazars in a nutshell. *ArXiv e-prints* (2013).

[113] Pian, E., Palazzi, E., Chiappetti, L., Maraschi, L., Tavecchio, F., Ghisellini, G., Tagliaferri, G., Fossati, G., Treves, A., Urry, C. M., and Vacanti, G. BeppoSAX Observations of BL Lac Object MKN 501 in an Intermediate State. In *BL Lac Phenomenon, Astronomical Society of the Pacific Conference Series* (1999).

[114] Piffaretti, R., Arnaud, M., Pratt, G. W., Pointecouteau, E., and Melin, J.-B. The MCXC: a meta-catalogue of x-ray detected clusters of galaxies. *Astronomy & Astrophysics 534* (2011), A109.

[115] Piranomonte, S., Perri, M., Giommi, P., Landt, H., and Padovani, P. The sedentary survey of extreme high-energy peaked BL Lacs. *Astronomy and Astrophysics 470*, 2 (2007), 787–809.

[116] Planck Collaboration. Planck 2015 results. XXVII. The second Planck catalogue of Sunyaev-Zeldovich sources. *Astronomy & Astrophysics 594* (2016), A27.

[117] Poole, T. S., Breeveld, A. A., Page, M. J., Landsman, W., Holland, S. T., Roming, P., Kuin, N. P. M., Brown, P. J., Gronwall, C., Hunsberger, S., , and et al. Photometric calibration of the Swift ultraviolet/optical telescope. *Monthly Notices of the Royal Astronomical Society 383*, March (2008), 627–645.

[118] Puccetti, S., Capalbi, M., Giommi, P., Perri, M., Stratta, G., Angelini, L., Burrows, D., Campana, S., Chincarini, G., Cusumano, G., Gehrels, N., Moretti, A., Nousek, J., Osborne, J., and Tagliaferri, G. The Swift serendipitous survey in deep XRT GRB fields (SwiftFT). I. The X-ray catalog and number counts. *Astronomy and Astrophysics 528* (2011), A122.

[119] Resconi, E., Coenders, S., Padovani, P., Giommi, P., and Caccianiga, L. Connecting blazars with ultra high energy cosmic rays and astrophysical neutrinos. *Monthly Notices of the Royal Astronomical Society 468* (2017), 597.

[120] Rieger, F. M., de Oña-Wilhelmi, E., and Aharonian, F. A. TeV Astronomy. *Frontiers of Physics 8* (2013), 714–747.

[121] Rybicki, G. B., and Lightman, A. P. *Radiative Processes in Astrophysics*. Wiley-VCH, 1986.

[122] Sarazin, C. *X-ray emission from clusters of galaxies*, vol. 58. Cambridge Astrophysics Series, Cambridge, 1986.

[123] Saxton, R. D., Read, A. M., Esquej, P., Freyberg, M. J., Altieri, B., and Bermejo, D. The first XMM-Newton slew survey catalogue: XMMSL1. *Astronomy and Astrophysics 480* (2008), 611–622.

[124] Schachter, J. F., Stocke, J. T., Perlman, E., Elvis, M., Remillard, R., Granados, A., Luu, J., Huchra, J. P., Humphreys, R., Urry, C. M.,

and Wallin, J. Ten new BL Lacertae Objects Discovered by an Efficient X-ray/Radio/Optical Technique. *The Astrophysical Journal 412* (1993), 541–549.

[125] Schmidt, M. Space Distribution and Luminosity Functions of Quasi-Stellar Radio Sources. *The Astrophysical Journal 151* (1968), 383.

[126] Schmidt, M., and Green, R. F. Counts, evolution, and background contribution of X-ray quasars and other extragalactic X-ray sources. *The Astrophysical Journal 305* (1986), 68–82.

[127] Schulz, B., Valtchanov, I., and María, A. SPIRE Point Source Catalog Explanatory Supplement. *ArXiv e-prints* (2017).

[128] Siebert, J., Brinkmann, W., Drinkwater, M. J., Yuan, W., Francis, P. J., Peterson, B. A., and Webster, R. L. X-ray properties of the Parkes sample of flat-spectrum radio sources: Dust in radio-loud quasars? *Monthly Notices of the Royal Astronomical Society 301*, 1 (1998), 261–279.

[129] Skrutskie, M. F., Cutri, R. M., Stiening, R., Weinberg, M. D., Schneider, S., Carpenter, J. M., Beichman, C., Capps, R., Chester, T., Elias, J., , and et al. The Two Micron All Sky Survey (2MASS). *The Astronomical Journal 131*, 2 (2006), 1163–1183.

[130] Stocke, J. T., Morris, S. L., Gioia, I., Maccacaro, T., Schild, R. E., and Wolter, A. No Evidence for Radio-Quiet BL Lacertae Objects. *The Astrophysical Journal 348* (1990), 141–146.

[131] Stocke, J. T., Morris, S. L., Gioia, I. M., Maccacaro, T., Schild, R., Wolter, A., Fleming, T. A., and Henry, J. P. The Einstein Observatory Extended Medium-Sensitivity Survey. II - The optical identifications. *The Astrophysical Journal Supplement Series 76* (1991), 813–874.

[132] Stoughton, C., Lupton, R. H., Bernardi, M., Blanton, M. R., Burles, S., Castander, F. J., Connolly, A. J., Eisenstein, D. J., Frieman, J. A., Hennessy, G. S., , and et al. SLOAN DIGITAL SKY SURVEY : EARLY DATA RELEASE. *The Astronomical Journal 123* (2002), 485–548.

[133] Strauss, M. A., Huchra, J. P., Davis, M., Yahil, A., and Fisher, K. B. A redshift survey of IRAS galaxies. VII - The infrared and redshift data for the 1.936 Jansky sample. *The Astrophysical Journal Supplement Series 83* (1992), 29.

[134] The Fermi-LAT Collaboration. The Second Fermi Large Area Telescope Catalog of Gamma-ray Pulsars. 17.

[135] The Fermi-LAT Collaboration. 3FHL: The Third Catalog of Hard Fermi-LAT Sources. *The Astrophysical Journal Supplement Series* (2017).

[136] The IceCube Collaboratioin. The IceCube Neutrino Observatory - Contributions to ICRC 2017 Part II: Properties of the Atmospheric and Astrophysical Neutrino Flux. *ArXiv e-prints 1710.01191 1819885288*, 44 (2017).

[137] The Pierre Auger Collaboration. The Pierre Auger Cosmic Ray Observatory. *ArXiv e-prints* (2015).

[138] The Plank Collaboration. Planck 2015 results. XXVI. The Second Planck Catalogue of Compact Sources. *Astronomy & Astrophysics 594* (2016), A26.

[139] Tonry, J. L., Stubbs, C. W., Lykke, K. R., Doherty, P., Shivvers, I. S., Burgett, W. S., Chambers, K. C., Hodapp, K. W., Kaiser, N., Kudritzki, R. P., Magnier, E. A., Morgan, J. S., Price, P. A., and Wainscoat, R. J. The pan-starrs1 photometric system. *The Astrophysical Journal 750*, 2 (2012).

[140] Urry, C. M., and Padovani, P. Unified Schemes for Radio-Loud Active Galactic Nuclei. *Publications of the Astronomical Society of the Pacific 107* (1995), 803–845.

[141] Voges, W., Aschenbach, B., Boller, T., Braeuninger, H., Briel, U., Burkert, W., Dennerl, K., Englhauser, J., Gruber, R., Haberl, F., , and et al. The ROSAT All-Sky Survey Bright Source Catalogue. *Astronomy and Astrophysics 349* (1999), 389–405.

[142] Voges, W., Aschenbach, B., Boller, T., Brauninger, H., Briel, U., Burkert, W., Dennerl, K., Englhauser, J., Gruber, R., Haberl, F., , and et al. ROSAT all-sky survey faint source catalogue. In *International Astronomical Union Circular* (2000), vol. 7432, p. 1.

[143] Watson, M. G., Schröder, A. C., Fyfe, D., Page, C. G., Lamer, G., Mateos, S., Pye, J., Sakano, M., Rosen, S., Ballet, J., Barcons, X., , and et al. The XMM-Newton serendipitous survey. *Astronomy & Astrophysics 493*, 1 (2009), 339–373.

[144] Wen, Z. L., Han, J. L., and Liu, F. S. Galaxy clusters identified from the sdss dr6 and their properties. *The Astrophysical Journal Supplement Series 183*, 2 (2009), 197–213.

[145] White, N., Giommi, P., and Angelini, L. The WGACAT version of the ROSAT PSPC Catalogue, Rev. 1. *VizieR Online Data Catalog* (2000).

[146] White, R. L., and Becker, R. H. A new catalog of 30,239 1.4 GHz sources. *Astrophysical Journal Supplement Series (ISSN 0067-0049) 79* (1992), 331–467.

[147] White, R. L., Becker, R. H., Helfand, D. J., and Gregg, M. D. A Catalog of 1.4 GHz Radio Sources from the FIRST Survey. *The Astrophysical Journal 475*, 2 (1997), 479–493.

[148] Wright, A. E., Griffith, M. R., Burke, B. F., and Ekers, R. D. The Parkes-MIT-NRAO (PMN) surveys. 2: Source catalog for the southern survey (delta greater than -87.5 deg and less than -37 deg). *The Astrophysical Journal Supplement Series 91* (1994), 111.

[149] Wright, A. E., Griffith, M. R., Hunt, A. J., Troup, E., Burke, B. F., and Ekers, R. D. The Parkes-MIT-NRAO (PMN) Surveys. VIII. Source Catalog for the Zenith Survey (-37.0 degrees < delta < -29.0 degrees). *The Astrophysical Journal Supplement Series 103* (1996), 145.

[150] Yentis, D. J., Cruddace, R. G., Gursky, H., Stuart, B. V., Wallin, J. F., MacGillivray, H. T., and Collins, C. A. The Cosmos/ukst Catalog of the Southern Sky. In *Digitised Optical Sky Surveys.* (Edinburgh, Scotland, 1992), Academic Kluwer and Boston Dordrecht, p. 67.

[151] Yershov, V. N. Serendipitous UV source catalogues for 10 years of XMM and 5 years of Swift. *Astrophysics and Space Science 354*, 1 (2014), 97–101.

[152] Zwicky, F., Herzog, E., Wild, P., Karpowicz, M., and Kowal, C. T. *Catalogue of galaxies and of clusters of galaxies.* 1968.